

Energy Research and Development Division  
FINAL PROJECT REPORT

**AIR-QUALITY IMPACTS OF HEAT  
ISLAND CONTROL AND  
ATMOSPHERIC EFFECTS OF URBAN  
SOLAR PHOTOVOLTAIC ARRAYS**

Prepared for: California Energy Commission

Prepared by: Altostratus Inc.



DECEMBER 2011  
CEC-500-2013-061

**Prepared by:**

**Primary Author(s):**

Haider Taha

Altostratus Inc.  
Martinez, California

**Contract Number: 500-08-007**

**Prepared for:**

**California Energy Commission**

Marla Mueller  
**Contract Manager**

Guido Franco  
**Program Area Lead**  
**Energy-Related Environmental Research**

Linda Spiegel  
**Office Manager**  
**Energy Generation Research Office**

Laurie ten Hope  
**Deputy Director**  
**ENERGY RESEARCH AND DEVELOPMENT DIVISION**

Robert P. Oglesby  
**Executive Director**

#### **DISCLAIMER**

This report was prepared as the result of work sponsored by the California Energy Commission. It does not necessarily represent the views of the Energy Commission, its employees or the State of California. The Energy Commission, the State of California, its employees, contractors and subcontractors make no warrant, express or implied, and assume no legal liability for the information in this report; nor does any party represent that the uses of this information will not infringe upon privately owned rights. This report has not been approved or disapproved by the California Energy Commission nor has the California Energy Commission passed upon the accuracy or adequacy of the information in this report.

## Acknowledgements

This report was prepared as the result of work sponsored by the California Energy Commission. The project managers acknowledge Marla Mueller, California Energy Commission, and Nicole Davis, Global Environmental Research. The project advisory committee is also acknowledged: Phil Martien, Bay Area Air Quality Management District; Carol Bohnenkamp, U.S. Environmental Protection Agency; Ash Lashgari, California Air Resources Board; David Nunes and Katy Linebach, San Joaquin Valley Unified Air Pollution Control District, Aaron Katzenstein and Satoru Mitsutomi, South Coast Air Quality Management District, and Robert Bornstein, San Jose State University.

Information in this report does not necessarily represent the views of the California Energy Commission, Global Environmental Research, or the project advisory committee. They have not approved or disapproved it, nor do they assume any legal liability for the findings presented in this report.

# PREFACE

The California Energy Commission Energy Research and Development Division supports public interest energy research and development that will help improve the quality of life in California by bringing environmentally safe, affordable, and reliable energy services and products to the marketplace.

The Energy Research and Development Division conducts public interest research, development, and demonstration (RD&D) projects to benefit California.

The Energy Research and Development Division strives to conduct the most promising public interest energy research by partnering with RD&D entities, including individuals, businesses, utilities, and public or private research institutions.

Energy Research and Development Division funding efforts are focused on the following RD&D program areas:

- Buildings End-Use Energy Efficiency
- Energy Innovations Small Grants
- Energy-Related Environmental Research
- Energy Systems Integration
- Environmentally Preferred Advanced Generation
- Industrial/Agricultural/Water End-Use Energy Efficiency
- Renewable Energy Technologies
- Transportation

*Air-Quality Impacts of Heat Island Control and Atmospheric Effects of Urban Solar Photovoltaic Arrays* is the final report for the Multi-episodic and Seasonal Impacts of and Emissions Credits from Heat Island Mitigation Strategies Modeling project (Contract Number 500-08-007) conducted by Altostratus Inc. The information from this project contributes to Energy Research and Development Division's Energy-Related Environmental Research Program.

For more information about the Energy Research and Development Division, please visit the Energy Commission's website at [www.energy.ca.gov/research/](http://www.energy.ca.gov/research/) or contact the Energy Commission at 916-327-1551.

# ABSTRACT

Many California air districts seek to reduce energy use, emissions, and air pollution. Because higher air temperatures increase electricity use and ozone production, research has focused on cooling urban heat islands—areas that produce and retain more heat than rural surroundings. The goal of this study is to evaluate the effectiveness of heat-island control on local meteorology, emissions, and ozone air quality under a range of summer conditions typically experienced in several California regions. The range of interest, over a period of 10 years, includes conditions that produce very high, high, and moderate ozone concentrations. Another goal of the study is to evaluate the potential atmospheric impacts of large-scale urban solar photovoltaic (PV) deployment. The purpose is to identify the important factors and parameters in evaluating the local and regional meteorological impacts of PV arrays.

The modeling results show that the impacts of urban heat island mitigation are relatively consistent and significant across a range of summer conditions in California. The air-quality improvements are significant in areas where surface modifications (to control heat islands) are carried out. Downwind of and around these modified areas, the air-quality impacts depend on meteorological conditions (for example, wind flow patterns).

In terms of urban deployment of solar PV, modeling of the Los Angeles Basin (as an example) shows that there are no negative impacts on air temperature or heat islands from large-scale PV deployment. For the range of solar conversion efficiencies currently available or expected to become available in the near future, the deployment of solar PV can also cool the urban environment. It is only under hypothetical future-year scenarios of cool cities (highly-reflective urban areas) and high-density deployment of urban solar PV arrays that there might be some negative impacts on the atmosphere (heating). But the heating effect is small.

If findings from this project result in implementation of recommended heat-island control measures, California will benefit by reducing cooling-energy demand, reducing emissions of air pollutants, and improving air quality.

**Keywords:** Air quality, albedo, meteorological modeling, ozone, photochemical modeling, solar photovoltaic, surface modifications, urban heat island

Please cite this report as follows:

Taha, Haider. Altostratus Inc. 2013. *Air-Quality Impacts of Heat Island Control and Atmospheric Effects of Urban Solar Photovoltaic Arrays*. California Energy Commission. Publication number CEC-500-2013-061.

# TABLE OF CONTENTS

<b>Acknowledgements</b> .....	<b>i</b>
<b>PREFACE</b> .....	<b>ii</b>
<b>ABSTRACT</b> .....	<b>iii</b>
<b>TABLE OF CONTENTS</b> .....	<b>iv</b>
<b>EXECUTIVE SUMMARY</b> .....	<b>1</b>
Introduction .....	1
Purpose of Study and Project Objectives .....	1
Project Outcomes .....	2
Heat Island Control .....	2
Solar Photovoltaic (PV) .....	4
Recommendations.....	6
Benefits to California .....	6
<b>CHAPTER 1: Introduction and Background</b> .....	<b>9</b>
<b>CHAPTER 2: Purpose of This Study</b> .....	<b>11</b>
<b>CHAPTER 3: Approach</b> .....	<b>12</b>
<b>CHAPTER 4: Study Domains</b> .....	<b>13</b>
<b>CHAPTER 5: Meteorological, Air-Quality, and CART Analysis</b> .....	<b>16</b>
5.1 Meteorological Data.....	16
5.2 Air-Quality / Air-Pollutant Data .....	17
5.3 Meteorological and Air-Quality Data Analysis and CART Development .....	18
<b>CHAPTER 6: Episodes</b> .....	<b>37</b>
<b>CHAPTER 7: Surface Characterization and Input</b> .....	<b>41</b>
<b>CHAPTER 8: Models and Data</b> .....	<b>45</b>
8.1 Mesoscale Meteorological Model.....	45
8.2 Meso-urban Meteorological Model .....	46
8.3 Photochemical Model .....	48
<b>CHAPTER 9: Model Performance Evaluation</b> .....	<b>50</b>
<b>CHAPTER 10: Meteorological Modeling Results</b> .....	<b>51</b>
10.1 BASE METEOROLOGY .....	53
10.1.1 BASE-CASE 2000 (Central California) .....	53
10.1.2 BASE-CASE 1999 (Central California) .....	55

10.1.3	BASE CASE 2005 (Southern California).....	58
10.1.4	Modeled Multi-episodic Characterization.....	59
10.2	METEOROLOGY PERTURBATION SCENARIOS.....	61
10.2.1	PERTURBATION 2000 (Central California).....	61
10.2.2	PERTURBATION 1999 (Central California).....	62
10.2.3	PERTURBATION 2005 (Southern California).....	64
10.3	MULTI-EPISODIC ANALYSIS OF METEOROLOGY PERTURBATIONS .....	65
10.3.1	Central California.....	65
10.3.2	Southern California.....	71
<b>CHAPTER 11: Emissions Impacts of Surface Modifications.....</b>		<b>74</b>
<b>CHAPTER 12: Photochemical/Air-Quality Modeling Results .....</b>		<b>76</b>
12.1	2000 Episode (Central California).....	79
12.1.1	Air-Quality Impacts with Year2000 Emissions .....	79
12.1.2	Air-Quality Impacts with Future Emissions (Year 2018).....	80
12.2	1999 Episode (Central California).....	81
12.2.1	Air-Quality Impacts with Year 1999 Emissions .....	81
12.2.2	Air-Quality Impacts with Future Emissions (Year 2018).....	82
12.3	2005 Episode (Southern California).....	83
12.4	Multi-Episodic Air-Quality Analysis .....	84
12.4.1	Impacts on the 1-hour Peak Ozone at Monitors .....	84
12.4.2	Peak 8-hour Ozone and Relative Reduction Factor Analysis .....	89
12.4.3	Cumulative Concentrations Changes .....	96
<b>CHAPTER 13: Emissions Equivalents.....</b>		<b>99</b>
<b>CHAPTER 14: Potential Atmospheric Impacts of Urban Solar PV Arrays .....</b>		<b>105</b>
14.1	Deployability (Technical Potential) .....	106
14.2	Effective Albedo of Solar PV Systems.....	108
14.3	Evaluation of Potential Radiative Impacts .....	109
14.4	Modeling of Potential Meteorological Impacts.....	110
14.5	Results and Discussion.....	114
<b>CHAPTER 15: Summary and Conclusions.....</b>		<b>120</b>
15.1	Heat-Island Control .....	120
15.1.1	Meteorology .....	120

15.1.2 Air Quality .....	123
15.2 Solar PV Deployment .....	127
15.3 Recommendations.....	129
<b>Appendix A: Monitor Locations.....</b>	<b>A-1</b>
<b>Appendix B: Classification and Regression Trees.....</b>	<b>B-1</b>
<b>Appendix C: Meteorological and Air-Quality Impact Cross-Section Figures.....</b>	<b>C-1</b>
<b>Appendix D: Degree-hour Changes .....</b>	<b>D-1</b>
<b>Appendix E: Degree-hour Changes Time Series.....</b>	<b>E-1</b>
<b>Appendix F: Impacts on 1-hour Peak Ozone .....</b>	<b>F-1</b>
<b>Appendix G: Emission Reduction Cross Sections and Carrying Capacity Diagrams .....</b>	<b>G-1</b>
<b>Appendix H: 8-hour Peak Ozone Cross Sections.....</b>	<b>H-1</b>
<b>Appendix I: Impacts of Solar PV Deployment Cross Sections .....</b>	<b>I-1</b>

## LIST OF FIGURES

Figure 4.1 (left): Central California Modeling Domains. Figure 4.2 (right): Southern California Modeling Domains .....	13
Figure 5.1. Surface Meteorological Stations and Air-quality Monitor Locations (Small Black Circles) and Upper-air Data Stations (Large Green Circles).....	18
Figure 5.2 (a,b,c): Total Number of Hours at Each Monitor in Each 30-ppb Ozone Bin Interval	22
Figure 5.2 (d,e,f,g): Total Number of Hours at Each Monitor in Each 30-ppb Ozone Bin Interval .....	23
Figure 5.3a: Frequency Distribution of Ozone <i>Daily Peaks</i> (ppb) on <i>Weekdays</i> for Years 2000–2005 .....	24
Figure 5.3b: Frequency Distribution of Ozone <i>Daily Peaks</i> (ppb) on <i>Weekdays</i> for Years 2000–2005 .....	24
Figure 5.3c: Frequency Distribution of Ozone <i>Daily Peaks</i> (ppb) on <i>Weekdays</i> for Years 2000–2005 .....	25
Figure 5.3d: Frequency Distribution of Ozone <i>Daily Peaks</i> (ppb) on <i>Weekdays</i> for Years 2000–2005 .....	25
Figure 5.3e: Frequency Distribution of Ozone <i>Daily Peaks</i> (ppb) on <i>Weekdays</i> for Years 2000–2005 .....	26
Figure 5.3f: Frequency Distribution of Ozone <i>Daily Peaks</i> (ppb) on <i>Weekdays</i> for Years 2000–2005 .....	26

Figure 6.1: Fire Events on July 23, 2002.....	38
Figure 6.2: Fire Events on July 25, 2002.....	39
Figure 6.3: Fire Events on July 30, 2002.....	39
Figure 7.1:Fresno-Area Surface Characterization (4 km): Albedo (top-left), Soil Moisture (top-right), Thermal Inertia (bottom-left), in Joules per square meter per degree Kelvin per 1/square root second ( $J m^{-2} K^{-1} s^{-0.5}$ ), and Roughness Length (bottom-right), m.....	41
Figure 7.2: San Francisco Bay Area Surface Characterization (4 km): Albedo (top-left), Soil Moisture (top-right), Thermal Inertia (bottom-left), $J m^{-2} K^{-1} s^{-0.5}$ , and Roughness Length (bottom-right), m.....	42
Figure 7.3: Los Angeles Region Surface Characterization (5 km): Albedo (top-left), Soil Moisture (top-right), Thermal Inertia (bottom-left), $J m^{-2} K^{-1} s^{-0.5}$ , and Roughness Length (bottom-right), m .....	43
Figure 7.4: Sacramento Region Surface Characterization (1 km): Albedo (top-left), Soil Moisture (top-right), Thermal Inertia (bottom-left), $J m^{-2} K^{-1} s^{-0.5}$ , and Roughness Length (bottom-right), m .....	43
Figure 10.1: Vertical Profile (Variation) of Normalized Nudging-Coefficients Weight .....	52
Figures 12.1 and 12.2: Impacts on the Episodic 8-hour Peak During the 2000 and 1999 Central California Episodes.....	91
Figures 12.3 and 12.4: Impacts on the Episodic 8-hour Peak for Runs A1 and B for Central California.....	92
Figures 12.5 and 12.6: Impacts on the Episodic 8-hour Peak for Runs C and D for Central California.....	92
Figures 12.7 and 12.8: Impacts on the Episodic 8-hour Peak for Runs E and H1 for Central California.....	93
Figures 12.9 and 12.10: Impacts on the Episodic 8-hour Peak for Runs I and J for Central California.....	93
Figures 12.11 and 12.12: Impacts on the Episodic 8-hour Peak for Runs K and M for Central California.....	94
Figures 12.13 and 12.14: Impacts on the Episodic 8-hour Peak for Runs N and O for Southern California.....	95
Figures 12.15 and 12.16: Impacts on the Episodic 8-hour Peak for Runs P and Q for Southern California.....	95
Figure 12.17: Impacts on the Episodic 8-hour Peak for Run R for Southern California .....	96

Figure 12.18: Changes in Cumulative Concentration-Time (ppb-hr) above 0 and 60 ppb Thresholds, for the San Francisco Bay Area .....	97
Figure 12.19: Changes in Cumulative Concentration-Time (ppb-hr) above 0 and 60 ppb Thresholds, for the Sacramento Area .....	97
Figure 12.20: Changes in Cumulative Concentration-Time (ppb-hr) above 0 and 60 ppb Thresholds, for the Fresno Area.....	98
Figure 14.1: Solar Photovoltaic Deployment Potential (% of 200 m Cells) for the Los Angeles Basin.....	108

## LIST OF TABLES

Table 4.1: Meteorological Model Grid Configurations for Central California .....	13
Table 4.2: Meteorological Model Grid Configurations for Southern California .....	13
Table 4.3: Photochemical Model Grid Definitions.....	14
Table 4.4: Vertical Structure of Modeling Domains .....	15
Table 5.1: Air Quality System Data File Contents .....	17
Table 5.2: California Counties ID (for Counties Used in the Air-quality Analysis in This Section) .....	20
Table 5.3. Air-quality Monitors of Interest Used in the Present Analysis.....	20
Table 5.4: Ranking of Monitors by Peak 1-hr Ozone Concentrations (Top, Second, and Third 20 Percent) and Frequency of Occurrences of Peaks within Each 20 Percent Concentration Bin 27	
Table 5.4.A: South Coast / Los Angeles Region .....	27
Table 5.4.B: Fresno / Bakersfield Region.....	28
Table 5.4.C: Sacramento Valley Region.....	28
Table 5.4.D: San Francisco Bay Area .....	29
Table 5.4.E: Frequency of occurrence of 1-hr peaks in concentration bins of 20% (based on observational data from 2000 through 2005).....	30
Table 5.5: Example Results from CART (Classification) Analysis at Various Counties .....	32
Table 5.6: Meteorological Conditions Corresponding to the Highest of Mean Ozone at Several Nodes from CART Analysis for Monitors in California.....	33
Table 6.1: Final Episodes Selected for Modeling in This Study.....	40

Table 7.1: Surface-Based Albedo Modifications Used in Modeling the Reasonably High Increase Scenario of Albedo Change .....	44
Table 10.1: Central California Modeled Meteorology.....	60
Table 10.2: Southern California Modeled Meteorology.....	61
Table 10.3: Summary of Changes in Degree-Hours per Day as a Total over All Monitors in the Central California Domain for Each Episode (for the 15°C Threshold).....	68
Table 10.4: Percentage-wise Changes in Degree-Hours at Monitors in Placer County for Four Temperature Thresholds. These changes are averaged over all episodes.....	69
Table 10.5: Percentage-wise Changes in Degree-Hours at Monitors in Sacramento County for Four Temperature Thresholds. These changes are averaged over all episodes.....	69
Table 10.6: Percentage-wise Changes in Degree-Hours at Monitors in Santa Clara County for Four Temperature Thresholds. These changes are averaged over all episodes.....	70
Table 10.7: Percentage-wise Changes in Degree-Hours at Monitors in Contra Costa County for Four Temperature Thresholds. These changes are averaged over all episodes.....	70
Table 10.8: Percentage-wise Changes in Degree-Hours at Monitors in Alameda County for Four Temperature Thresholds. These changes are averaged over all episodes.....	70
Table 10.9: Percentage-wise Changes in Degree-Hours at Monitors in Fresno County for Four Temperature Thresholds. These changes are averaged over all episodes.....	70
Table 10.10: Summary of Changes in Degree-Hours per Day as a Total over All Monitors in the Southern California Domain for Each Episode (for the 15°C Threshold).....	72
Table 10.11: Percentage-wise Changes in Degree-Hours at Monitors in San Bernardino County for Four Temperature Thresholds. These changes are averaged over all episodes.....	73
Table 10.12: Percentage-wise Changes in Degree-hours at Monitors in Los Angeles County for Four Temperature Thresholds. These changes are averaged over all episodes.....	73
Table 10.13: Percentage-wise Changes in Degree-Hours at Monitors in Riverside County for Four Temperature Thresholds. These changes are averaged over all episodes.....	73
Table 12.1: Air-Quality Monitors of Interest in This Analysis.....	76
Table 12.2: Domain-wide Simulated Base-Case Episodic Ozone Peak .....	79
Table 12.3: Largest Changes in Daily Ozone in Central California with Year 2000 Emissions ....	80
Table 12.4: Largest Changes in Daily Ozone in Central California with Year 2018 Emissions ....	81
Table 12.5: Largest Changes in Daily Ozone in Central California with Year 1999 Emissions ....	82
Table 12.6: Largest Changes in Daily Ozone in Central California with Year 2018 Emissions ....	82

Table 12.7: Largest Changes in Daily Ozone in Southern California with Year 2005 Emissions .	83
Table 12.8: Impacts on the 1-hr Peak Ozone in Central California .....	85
Table 12.9: Impacts on the 1-hr Peak Ozone in Southern California .....	88
Table 12.10: Domain-Wide, Episodic 8-hr Peak Ozone in Central and Southern California .....	90
Table 12.11: Domain-Average Change in 8-hr Episodic Peak in Central California .....	91
Table 12.12: Domain-Averaged Changes in the 8-hr Episodic Peak in Southern California .....	94
Table 12.13: Average Changes in Cumulative Concentration Differences in Central California...	96
Table 13.1: Summary of Carrying-Capacity Sensitivities .....	101
Table 13.2: NO <sub>x</sub> and ROG Equivalences for Central California.....	103
Table 13.3: Central California Episode-Averaged Emissions Equivalence.....	103
Table 13.4: NO <sub>x</sub> and ROG Emission Equivalence for Southern California .....	104
Table 13.5: Southern California Episode-Averaged Emissions Equivalence.....	104
Table 14.1: Technical Potential for Solar PV (Based on Navigant 2007).....	107
Table 14.2: Technical Potential for Solar PV Based on Taha (2011).....	107
Table 14.3: Deployment Scenarios (Technical Potential) at 200 m Resolution .....	112
Table 14.4: Perturbation Scenarios for $\epsilon$ .....	112
Table 14.5: Modeling Scenarios of Solar PV Deployment in Southern California .....	113
Table 15.1: Changes in Degree-Hours (per day) Totalized over All Monitors in the Central California Domain for Each Episode (Relative to the 15°C Threshold) .....	121
Table 15.3: Changes in Degree-Hours (Per Day) Totalized over All Monitors in the Southern California Domain for Each Episode (Using the 15°C Threshold).....	122
Table 15.4: Range of Percentage-wise Changes in Degree-Hours across Monitors in Counties (Averaged over All Episodes) for Southern California .....	122
Table 15.5: Ratio of Decrease-to-Increase (RDI) in 1-hr Peaks' Total ppb-hr .....	124
Table 15.6: Domain-Averaged Changes in 8-hr Episodic Maximum for Central California .....	124
Table 15.7: Domain-Averaged Changes in 8-hr Episodic Maximum for Southern California ...	124
Table 15.8: Average Changes in Cumulative Concentrations above 0 and 60 ppb for Central California.....	125
Table 15.9: Occurrence of Changes in 1-hr and 8-hr Peaks, and Cumulative Concentration Differences .....	126

Table 15.10. Central California Episode-Averaged Emissions Equivalence(percent change in emissions)..... 126

Table 15.11. Southern California Episode-Averaged Emissions Equivalence (percent change in emissions)..... 127

# EXECUTIVE SUMMARY

## Introduction

The federal Clean Air Act requires that non-attainment areas in the United States develop plans for reducing air pollution and improving air quality. State implementation plans consider and embody emission-control strategies that are typically quantifiable and enforceable in nature. For many areas in California with air quality problems, heat-island control measures could be a useful part of the plan to reduce energy demand and help reach ozone attainment. State-of-science meteorological, emissions, and photochemical air-quality modeling is used to evaluate the effectiveness of control measures and, in this particular case, provide a basis for further understanding and ultimately increasing the acceptance of heat-island mitigation measures in clean air plans.

Prior studies of heat island mitigation were focused on specific episodes typically used in regulatory modeling. While the results from these studies showed significant and beneficial effects in terms of improving air quality, the impacts under longer time scales and/or different large-scale meteorological conditions were unknown. Thus, recommendations were made to evaluate the effectiveness of these strategies under a broad range of summer conditions in California. From a modeling perspective, there also was a need to develop more robust models and data so as to increase the acceptance of the results in the regulatory environment.

## Purpose of Study and Project Objectives

The purpose of this study is to develop useable models and data in evaluating the effectiveness of heat-island control measures on local meteorology, emissions, and ozone air quality under a range of summer conditions typically experienced in several California regions. The goal is to further the analysis beyond the time scales and limited episodic conditions modeled in past efforts. The multi-episodic conditions analyzed in this study occur over a period of ten years.

The focus in this modeling effort is on the impacts of increasing albedo (reflectivity of roofing, paving, and other construction materials) in several California urban areas including the Sacramento Valley, the San Francisco Bay Area, the Fresno region, and the South Coast Air Basin (Los Angeles region). The goal is to evaluate and quantify the potential positive and negative impacts in each of these regions that can arise following surface modifications, over several episodes, under different summer synoptic conditions, and with different interactions among the regions (for example, pollutant transport). Thus, to accomplish these goals, the study developed several episodes to cover a range of meteorological conditions, associated emissions, and ozone air quality.

Another goal of the study is to identify factors for determining the atmospheric impacts of solar PV deployment and their links to air quality and energy use. The scoping analysis also includes extensive meteorological simulations to evaluate various scenarios and assumptions, as an example.

## Project Outcomes

### Heat Island Control

The modeling approach used in the study was developed over the prior phases of this effort and subsequently demonstrated to quantify impacts from heat island control strategies (such as cool roofs) over several long episodes/seasons in several urban areas in California.

Representative summer meteorological patterns and air-quality conditions were statistically grouped together to identify episodes that were then simulated with meteorological, emissions, and photochemical models to predict the impacts on air quality. The ozone air-quality impacts were then converted into emission-reduction equivalents.

The modeling shows that significant cooling of the urban atmosphere can be achieved, particularly during the daytime, with heat island mitigation, that is, increased urban albedo (such as cool roofs and cool pavements) in this case. During the central-California July–August 2000 episode, for example, the largest daily cooling ranges from 0.6°C to 1.1°C (1.1°F to 2°F), and sometimes larger in various parts of the domain. The simulations also show that the smaller reductions in air temperature in certain urban areas (such as Fresno versus the San Francisco Bay Area) occur because of the smaller modifiable surface area available for increasing albedo (some parts of cities have less surfaces that can be modified, thus we do not see large benefits in these areas). In the central California July 1999 episode, the range of largest daily temperature decrease is 0.7°C to 2.2°C (1.3°F to 4°F). On some days, the models show warming as well as cooling, but in general, the warming is smaller in magnitude than the cooling, is short lived, and affects much smaller areas in the domain. The reason some warming can occur is the reduced mixing downwind of or around modified areas. During the southern California episode of July 2005, the largest daily cooling ranges from 1.1°C to 3.9°C (2°F to 7°F) in different parts of the domain.

Since a large number of episodes were modeled in this study, a cumulative “degree-hour” metric was used to quantify cooling above certain temperature thresholds. A degree-hour is a measure of how many hours and how many degrees the temperature is above a certain threshold. For example, the changes in degree-hours as a total over all monitors in the central California domain, totalized for each episode (relative to the 15°C (59°F) temperature threshold) were computed. It was found that the range of these changes was from -90 to -155 degree-hours per day (above 15°C [59°F]) as a result of increased urban albedo. For southern California, the range was from -142 to -155 degree-hours per day. The modeling also shows that the range of impacts from increased albedo is relatively consistent and not very dependent on meteorology during the summer conditions analyzed in this study.

In terms of air quality impacts, several metrics were used to evaluate the effectiveness of heat island control across various regions and episodes. The effects are found to be significant and dominantly positive, meaning improved air quality. However, there also are increases in ozone at times during the episodes, but the areas affected by increases in ozone are much smaller than those affected by decreases and, thus, the dominant effect is an improvement in air quality. The local impacts on ozone air quality (for example, improvements) also appear to be relatively consistent and not very meteorology-dependent during the summer conditions studied here.

That is, within the areas where albedo is increased (modified areas), the impacts on air quality are relatively consistent across a range of summer conditions. In unmodified, downwind areas, the impact differs depending on the flow pattern. When such unmodified or marginally modified areas are downwind of modified ones, increases in ozone can be seen. When the relative up- and down-wind positions are reversed, no ozone increase is seen in the unmodified areas.

In addition to modeling several episodes, scenarios, and regions with current emissions, two central California base episodes, July–August 2000 and July 1999, were also modeled with future-year (2018) emissions to evaluate the effectiveness of heat island control on improving air quality in the future. The models show that in general, the impacts in 2018 are about 40 to 100 percent of what they are under present-day emissions (that is, year 1999 or 2000). There also are cases in which the impacts under year 2018 emissions are larger than those under present conditions. For example, in the base 2000 episode in central California, the largest daily decrease in ozone in the San Francisco Bay Area, Sacramento, and Fresno regions, under year 2000 emissions, ranges from 4–9, 1–8, and 3–10 parts per billion (ppb), respectively for these regions. Under year 2018 emissions, the largest daily decrease ranges from 4–8, 1–4, and 1–5 ppb, respectively. In the 1999 base episode, the largest daily decrease in ozone in the San Francisco Bay Area, Sacramento, and Fresno regions, under year 1999 emissions, ranges from 4–11, 2–3, and 4–8 ppb, respectively for these three regions. Under year 2018 emissions, the largest daily decrease ranges from 2–8, 4–14, and 1–4 ppb, respectively.

Since a large number of episodes were simulated, the results were also evaluated using cumulative metrics or summaries such as ppb-hour (ppb difference times hours), in addition to peaks, relative reduction factors, and emission-reduction equivalents. For central California, and across all episode days modeled in this study, the largest daily average decreases in the 1-hour peak range from 2.05–5.24 ppb (under present-day emissions), and the largest increases range from 0.28–2.75 ppb (but note that the increases and decreases mentioned here do not correspond to the same times or locations). The ratio of decrease-to-increase in the 1-hour peaks across all episodes ranges from a low of 2.06 to a high of 62.32. For southern California, the largest average daily decreases in the 1-hour peak range from 4.80–8.37 ppb under present-day emissions, and the largest increases range from 0.40–0.94 ppb. The ratio of decrease-to-increase in the 1-hour peaks across all episodes in southern California ranges from a low of 18.79 to a high of 98.52.

In terms of the 8-hour average ozone, the modeling shows that across all episodes and regions in central California studied here, the domain-average change in 8-hour episodic peak ranges from -0.9 to -1.9 percent and for the Los Angeles Basin, from -2.0 to -3.6 percent. This indicates an improvement in air quality.

In terms of emission equivalents—that is, conversion of changes in ozone concentrations into corresponding changes in precursor emissions—a separate modeling and analysis task was undertaken in this study. The findings show that for the central California domain, the emissions equivalents of heat-island mitigation across all episodes range from -66 to -185 tons per day of *anthropogenic* reactive organic gases (~3 to 9 percent reduction). For the Los Angeles

Basin, the range is from -51 to -77 tons per day of *anthropogenic* reactive organic gases (~5 to 8 percent reduction). These modeled reduction estimates are based on the assumption that all major urban areas in California are modified *simultaneously*. Also, the above estimates are relative to only the anthropogenic component of reactive organic gas emissions (relative to the entire reactive organic gas emissions inventory, the relative reductions will be smaller).

In summary, this study shows that it is doable and useful to evaluate, via multi-scale modeling, the effects of urban heat islands over longer time scales, multi-episodic, and seasonal conditions. Models and data, both input and output, were developed for a thorough evaluation of the potential impacts of urban heat island mitigation on energy, emissions, and air quality for a range of summer conditions typically experienced in California. The study shows that, overall, urban heat island mitigation is effective in cooling the urban environment, reducing energy use and emissions, and improving air quality.

## **Solar Photovoltaic (PV)**

In relation to urban heat islands and their mitigation, the potential atmospheric effects of large-scale deployment of solar PV arrays were also evaluated in this study. The deployment of solar PV in urban areas has two types of effects. The *direct* effect is that of generating electricity and reducing energy use; whereas, the *indirect* effect is the impact on the ambient environment; for example, air temperature. Depending on the configuration of the solar arrays (envelope-integrated or detached/elevated), additional direct effects can be accounted for as well, such as the shading effect of elevated solar panels on the underlying roof structures or parking lots. In addition, solar-power generation contributes to improving air quality and greenhouse gas emission reductions by avoiding/reducing the need for power generation and reducing energy use in buildings, for example, via shading. Both of these effects contribute to reducing emissions from power plants and are also considered part of the *direct* effect.

In this scoping analysis, the focus is on the *indirect* effect only—that is, the atmospheric impacts of solar PV deployment in urban areas. The goal is to identify the various factors to consider when evaluating such impacts. The South Coast Air Basin (the Los Angeles area) is used as an example in this study for modeling the potential atmospheric impacts; however, the methodology applies equally well to any other region.

From a radiative standpoint, and since current average urban albedo in U.S. cities is mostly in the range of 0.16 to 0.22 (an average of 0.18), it is anticipated that deployment of solar PV systems will have no negative impacts, even at a low conversion efficiency ( $\epsilon$ ) of 10 percent, assuming solar-panel reflectivity of 0.08. For  $\epsilon$  values greater than 10 percent, the solar PV systems will actually provide a cooling effect. On the other hand, the typical future-year urban albedo of *cool cities* (if heat-island mitigation strategies are implemented) will likely range from 0.25 to 0.28. In such cases, the conversion efficiency of the solar systems will need to reach about 0.17 to 0.20 to break even (that is, to exert no negative effects on air temperature). Such efficiencies exist in today's PV market or will in the near future.

However, the meteorological modeling performed in this study shows that deployment of solar PV systems has no impact on regional temperature and, more likely, will have a cooling effect.

It is emphasized that the modeling and simulations discussed as part of this scoping analysis are provided as examples of the methodology and approach used in evaluating the regional impacts of solar PV deployment. These are not results to be used “as is” for planning purposes. Two levels of deployment were modeled and are briefly discussed here: one is a “reasonably high” and the other is “high” deployment of solar PV arrays. These scenarios are defined in the report.

The meteorological modeling of a “reasonably high” level of deployment, at an  $\varepsilon$  value of 10% shows that the impacts of solar PV in the Los Angeles Basin in present-day conditions are non-existent. In other words, there are no negative impacts (nor positive) on air temperature because the effective albedo of the solar PV arrays is essentially similar to that of the present background urban albedo in the area. At a conversion efficiency of 15 percent, there still is not detectable impact (positive or negative) on air temperature, but when the conversion efficiency reaches 20 percent, some regional cooling can be detected. That cooling is very small, up to 0.05°C (0.09°F), but it covers a large area corresponding to that where the solar PV deployment occurs in the Los Angeles Basin. At conversion efficiency of 25 percent, the cooling effect increases slightly to between 0.05°C and 0.1°C (0.09°F and 0.2°F) and at conversion efficiency of 30 percent, the cooling effects reaches up to 0.15°C (0.27°F), a relatively small change.

In a future-year scenario of cool cities, based on high albedo-increase values assumed in this study, the background *urban* albedo would reach between 0.24 and 0.26. Modeling this scenario shows that with a conversion efficiency value of 10 through 25 percent, the impact of solar PV deployment on air temperature is nil. It is only at a conversion efficiency value of 30 percent that some cooling effects become noticeable (0.05°C [0.9°F]). In other words, the increase in albedo in the cool-city scenario (relative to present-day conditions) requires a larger conversion efficiency to initiate cooling than during present-day albedo.

Scenarios with “high” deployment of solar PV were also modeled and evaluated. At a conversion efficiency value of 10 percent, the “high” deployment level of solar PV causes an increase in air temperatures in the Los Angeles Basin if cool-city strategies are in place. The increase in air temperature is again small, reaching only 0.1°C (0.2°F), affecting an area spanning several counties. With a conversion efficiency value of 15 percent, the “high” deployment of solar PV can cause some very small (almost negligible) increases in air temperatures, reaching up to 0.05°C (0.09°F) in some small areas. At a conversion efficiency level of 25 percent, the effects turn into cooling the area by as much as 0.15°C (0.27°F). The cooling increases further at the conversion efficiency level of 30 percent to reach a decrease of 0.2°C (0.4°F) and cover a large swath of the Los Angeles Basin. This indicates that a “high” deployment level of solar PV (higher density) in a cool-city scenario can have larger negative effects at low conversion efficiency values but also larger cooling (at high conversion efficiency values) compared to scenarios with “reasonably high” deployment of solar PV.

Thus, for the scenarios and levels of deployment and conversion efficiencies used as examples in meteorological modeling of the Los Angeles Basin in this study, the results show that there are no negative impacts from urban solar PV deployment on heat islands and air quality. The deployment of solar PV, above certain conversion efficiencies, can also cool the urban

environment. It is only under hypothetical future-year scenarios of cool cities (highly reflective urban areas) and very high density deployment of urban solar PV that there might be some small negative impacts (0.1°C [0.2°F] or less in warming). But there can also be a cooling effect of up to 0.2°C (0.4°F).

In summary, the aspects to consider when evaluating the local impacts of solar PV arrays are (1) solar PV deployment level (density), (2) available modifiable area (such as roof area, parking-lot area, and open-space areas), (3) current background albedo of the target region, (4) actual albedo of the solar panels to be installed, (5) conversion efficiency of the solar PV systems planned for deployment (and thus the “effective” albedo of the panels), (6) potential future-year albedo changes, such as those from cool-cities measures, (7) solar availability at the location where deployment is planned, and (8) modeling the multi-seasonal atmospheric impacts of various scenarios of solar PV systems deployment.

## **Recommendations**

Based on the analysis performed in this study, it is recommended that the following aspects be addressed further in the future:

- Evaluating the effects of proximity among urban areas (such as down-wind) when one area is modified by increasing albedo and the other is not (this situation can increase ozone in non-modified downwind areas if close enough to upwind, modified ones). In such cases, considerations should be given to also modifying downwind urban areas, for example, by increasing their albedo. This should be modeled and evaluated on a case-by-case basis.
- Modeling the effects of site-specific changes in albedo that are market-based and neighborhood-specific, not theoretical/idealized or maximum feasible values.
- Evaluating the impacts of heat-island control strategies under conditions of future urbanization, per projected building and population growth trends.
- Evaluating the benefits of these strategies under scenarios of potential future climate change in California, to characterize impacts on radiative forcing (warming or cooling of the atmosphere due to radiation), local cooling, emissions, and air quality.

## **Benefits to California**

This study and related efforts provide several benefits to California. The first is the availability of new-generation, improved modeling capabilities that can be used in evaluating the potential impacts of heat-island control strategies in the State (as well as any other application that requires fine-resolution modeling capabilities). The second benefit is the actual savings in cooling-energy use, reductions in emissions, and improvements in air quality that would be achieved when heat-island control strategies are implemented in California. The third is that the models developed in this study, the data, and related configurations can also be used to evaluate the atmospheric, indirect effects of large-scale deployment of solar arrays, thus facilitating their marketing and deployment.



# CHAPTER 1:

## Introduction and Background

Several studies have evaluated the potential beneficial effects of urban heat island mitigation on energy use, emissions, and air quality. While evaluating the direct effects of this strategy on energy use and emissions is relatively straightforward and can be assessed over long periods of time (e.g., annual timescales), the indirect effects are relatively more difficult to quantify and are less certain. In addition, quantifying the atmospheric impacts of heat-island mitigation—that is, effects on meteorology and air quality—requires use of large datasets, complex models (meteorological, emissions, and photochemical/air quality), and data-processing that in turn requires more extensive computing resources, especially if the evaluations are to be carried out on longer time scales.

Thus, it has been a common practice to evaluate the air-quality impacts of control strategies on a time scale of about one week, in a manner that conforms to the typical regulatory air-quality modeling approach recommended by the U.S. Environmental Protection Agency (U.S. EPA 1999). The California Energy Commission supported two earlier studies (Phases I and II) of an extensive episodic modeling effort to evaluate the urban meteorological and ozone (O<sub>3</sub>) air-quality impacts and benefits of heat island mitigation (Taha 2005, 2007). In these studies of central and southern California, the modeling time frame was about one week using the regulatory episodes of July 27–August 3, 2000 (for central California) and August 3–7, 1997 (for southern California). These modeling studies resulted in a large amount of information on the effectiveness of heat-island control, via increased urban albedo and reforestation, in reducing energy use and emissions and improving ozone air quality.

Phase II of this study (prior phase) further improved the resolution of the simulations in computational domains of interest, e.g., the urban canopy layer (UCL). This goal was achieved by introducing and further developing new-generation fine-resolution meteorological (meso-urban) models (Taha 2007, 2008a,b; Dupont et al. 2004) and using them to drive fine-resolution photochemical air-quality simulations. The purpose of developing and using fine-resolution meso-urban and photochemical models in that phase was to evaluate in more detail the relevant dynamics, thermodynamics, physics, and photochemistry within the urban canopy layer. This layer is of interest because it is where the bulk of the population exists, where most emissions are initially injected, and where initial chemical reactions producing smog occur. Thus, improving the modeling of the urban atmospheric environment and the canopy layer is critical for a better assessment of environmental and air pollution/health impacts, as well as for regulatory air-quality planning purposes.

The objectives in Phase II were successfully met. The meso-urban model is now configured and available for use in California air-quality studies and a detailed morphological database for Sacramento (as a first prototype) is available as well. The development and use of fine-resolution meso-urban meteorological and corresponding fine-resolution photochemical models is critical because, in theory at least, such fine-resolution modeling capabilities and data are

useful not only in enabling fine-resolution photochemical air-quality modeling but also in developing fine-resolution four-dimensional emission inventories. Such modeling capabilities are also useful in the actual planning and implementation phases of heat-island control measures since they allow for a detailed evaluation of meteorological, energy, and air-quality impacts at a neighborhood scale or on a block-by-block basis if needed.

However, because the modeling in Phases I and II was done on relatively short time scales, as discussed above, it raised questions about the applicability of such results on longer time scales and during different synoptic conditions. It was also observed in the modeling of Phase II that heat island control could sometimes be more effective during less extreme conditions, i.e., not during the hottest days of the episodes. Thus, a number of factors and considerations led to the recommendation that the effects of heat island mitigation be further evaluated in multi-episodic conditions for a range of different ozone-producing regimes. It was also an intention for this study to use more recent modeling episodes and data.

## **CHAPTER 2: Purpose of This Study**

One purpose of this study is to evaluate the effectiveness of heat-island control measures, such as increased urban albedo, under a range of *summer* meteorological conditions that are typically experienced in various regions in California. The goal also is to evaluate the potential positive or negative impacts that can arise following deployment of high albedo over long periods of time, for example, long multi-episodic conditions. Thus, the study develops several episodes to cover and analyze a range of meteorological conditions, corresponding emissions, and ozone air quality.

Another purpose of the study is to evaluate the potential atmospheric impacts of large-scale deployment of urban solar photovoltaic (PV) arrays and to identify the variables that are important in such evaluations.

## **CHAPTER 3: Approach**

In this study, evaluating the impacts of heat-island mitigation (increased urban albedo) is done via state-of-science meteorological, emissions, and photochemical modeling, and generating the needed input: boundary conditions, surface characteristics, meteorological, and species concentrations input. For each region and episode selected for analysis, a full meteorological characterization is done with meso-scale and meso-urban modeling. Emission corrections follow this step; the focus here is on correcting biogenic volatile organic compound (BVOC) emissions only. The final step is the preparation of input to photochemical/air-quality simulations and performing the simulations. The resulting meteorological and air-quality impacts of heat-island mitigation are evaluated through a number of metrics and measures. The approach is discussed in detail in Taha (2005,2007).

# CHAPTER 4: Study Domains

This section presents the domain configurations and grid structures for the meteorological and photochemical models. Figures 4.1 and 4.2 show the horizontal grid structures for the central and southern California study domains, respectively. The horizontal dimensions and resolutions, as well as the corresponding vertical structures, are summarized in Tables 4.1, 4.2, and 4.3. The vertical structure and inter-model meshing of vertical layers is shown in Table 4.4.

**Figure 4.1 (left): Central California Modeling Domains. Figure 4.2 (right): Southern California Modeling Domains**

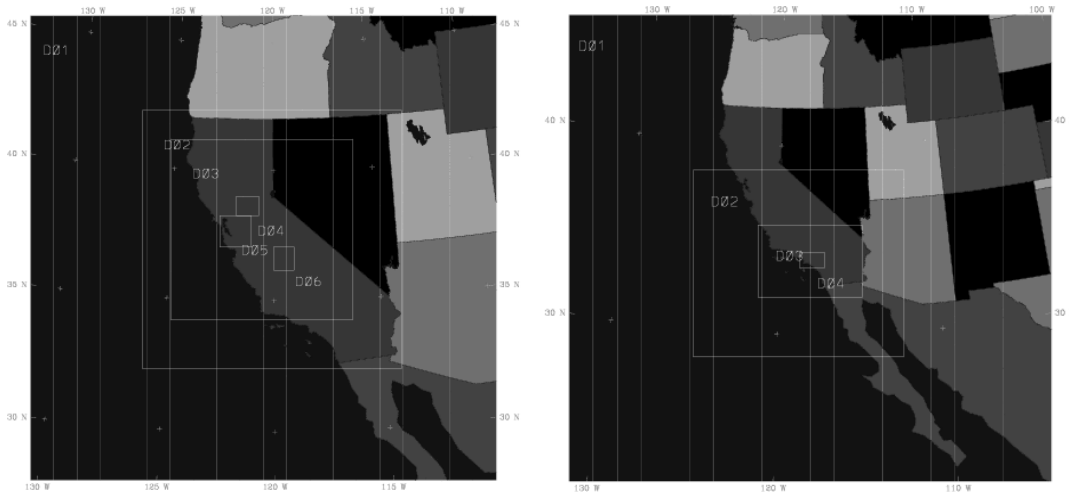


**Table 4.1: Meteorological Model Grid Configurations for Central California**

Meteorological-model domains	D01	D02	D03	D04	D05	D06
Resolution (km)	36	12	4	1	1	1
Dimensions (i,j,k)**	55, 55, 33	91, 91, 33	190, 190, 33	81, 93, 49	133,129, 49	97,85,49

\*\* i and j dimensions are in grid points; k-dimension in full- $\sigma$  levels

**Table 4.2: Meteorological Model Grid Configurations for Southern California**

Meteorological-model domains	D01	D02	D03	D04
Resolution (km)	45	15	5	1
Dimensions (i,j,k)**	61,63, 33	73,82, 33	85,121, 33	91,141, 49

\*\* i and j dimensions are in grid points; k-dimension in full- $\sigma$  levels

In coarse-grid simulations (down to 4 or 5 kilometer [km] resolution, depending on region), the first few model vertical levels near the ground are finer in resolution than those typically used in regulatory modeling. Furthermore, the fine-resolution meteorological model (uMM5),<sup>1</sup> discussed later in this report, uses 12 levels near the ground instead of the typical 2 used in conventional modeling (thus an additional 10 levels), and there are 16 levels in the canopy layer (the model is run with 49 full  $\sigma$  levels). The purpose of increasing the number of vertical levels near the ground is to more accurately capture the canopy-layer meteorology and to achieve better calculations in the emission models (more resolved meteorological input to emissions models near the ground) and in photochemical simulations. The photochemical (CAMx)<sup>2</sup> modeling grids are defined in Table 4.3.

**Table 4.3: Photochemical Model Grid Definitions**

Photochemical Modeling Domains		→	D01	D02
Central California	Resolution (km)	→	4	1
	Dimensions (x,y,z)*	→	185, 185, 20	124, 120, 20
Southern California	Resolution (km)	→	5	1
	Dimensions (x,y,z)*	→	116, 80, 16	n/a

\*The x, y, and z dimensions are in columns, rows, and layers, respectively.

The 4- and 5-km photochemical-model grids are thus slightly smaller than, and inscribed within, their corresponding 4- or 5-km meteorological-model grids; whereas, the 1-km photochemical grid is slightly smaller than and inscribed within the uMM5 domains (for central California). The purpose of this configuration is to create a buffer of a few grid cells around the photochemical model grids, relative to their corresponding meteorological-model grids.

The meshing of different model levels in the vertical direction is summarized in Table 4.4, which is constructed with the correct vertical orientation (bottom of table is at surface and top of table is at model top). The table shows the vertical meshing of the models MM5, uMM5, CAMx-4 km, and CAMx-1 km domains as configured in this study (the models will be discussed later). The red numbers in the table correspond to the additional 4 levels in CAMx used in the simulations of central California (20 levels) relative to those used for southern California, where the photochemical model is configured with 16 vertical levels.

<sup>1</sup>The urbanized MM5 model.

<sup>2</sup>Comprehensive Air quality Model with extensions

**Table 4.4: Vertical Structure of Modeling Domains**

MM5 33 full sigma	uMM5 49 full sigma	Layer mapping to CAMx	
		From MM5	From uMM5
0.0000	0.0000		
0.0232	0.0232		
0.0493	0.0493		
0.0788	0.0788		
0.1120	0.1120		
0.1495	0.1495		
0.1917	0.1917		
0.2394	0.2394		
0.2930	0.2930		
0.3536	0.3536		
0.4218	0.4218		
0.4954	0.4954	<b>21</b>	<b>37</b>
0.5635	0.5635	<b>20</b>	<b>36</b>
0.6254	0.6254	<b>19</b>	<b>35</b>
0.6809	0.6809	<b>18</b>	<b>34</b>
0.7301	0.7301	17	33
0.7733	0.7733	16	32
0.8107	0.8107	15	31
0.8431	0.8431	14	30
	0.8570		
0.8709	0.8709	13	28
	0.8828		
0.8946	0.8946	12	26
	0.9047		
0.9148	0.9148	11	24
	0.9234		
0.9319	0.9319	10	22
	0.9391		
0.9463	0.9463	9	20
	0.9524		
0.9585	0.9585	8	18
	0.9637		
0.9688	0.9688	7	16
	0.9731		
0.9774	0.9774	6	14
	0.9810		
0.9846	0.9846	5	12
	0.9877		
0.9907	0.9907	4	10
	0.9929		
0.9950	0.9950	3	8
0.9958	0.9958		
	0.9967		
0.9975	0.9975	1	5
	0.9980		
	0.9985		
	0.9990		
	0.9995		
1.0000	1.0000	surface	surface

## CHAPTER 5: Meteorological, Air-Quality, and CART Analysis

The initial task in this study was to obtain synoptic-scale observational surface- and upper-air meteorological data, meteorological analyses, and observed ozone air-quality data for various locations in California. The period for which data was obtained is 1995 to 2005, inclusive. The goal was to analyze the data in order to characterize and identify a number of episodes that capture a range of summer conditions for use in multi-episodic modeling of the potential impacts of heat-island mitigation. The observational data and their characteristics are discussed in this section.

### 5.1 Meteorological Data

Synoptic-scale observational surface- and upper-air meteorological data and meteorological analyses were obtained from several sources, relying mostly on data from the National Center for Atmospheric Research (NCAR) and the National Oceanic and Atmospheric Administration (NOAA). The following meteorological data were obtained:

- Eleven years of summer data (1995 through 2005). For each year, data from May 15 through August 30 were obtained and, because of lengthy processing for large datasets, each year's data was split into four parts corresponding to the periods 5/15–6/15; 6/15–7/15; 7/15–8/15; and 8/15–8/30.
- Analyses from the National Centers for Environmental Prediction (NCEP)-NCAR Reanalysis Project (NNRP) datasets for years 1995 through 2005
- NCAR upper-air and surface observational data for a window over central and southern California (116.25W–122.75W and 33.25N–39.25N) for the same dates and years identified above
- NCAR datasets *ds472* for years 1995 through 2005
- California climatological data from the Desert Research Institute (DRI)
- Synoptic weather maps for various pressure levels and for all years from the Plymouth University weather server.

These datasets were processed in this study for use in two main applications. The first is for use in Classification and Regression Trees (CART) analysis to statistically characterize air-quality (ozone) at a number of monitors based on variations in synoptic meteorological conditions. This analysis was done for the entire period 1995 through 2005, to facilitate selection of several episodes for modeling. The second purpose is to help generate the initial and boundary conditions needed by the meteorological and photochemical models in simulating the episodes and seasons selected in the previous step.

## 5.2 Air-Quality / Air-Pollutant Data

For air quality, focusing mainly on ozone, the main source of data used in this study was the U.S. EPA's Aerometric Information Retrieval System (AIRS) Air Quality System (AQS):

<http://www.epa.gov/ttn/airs/airsaqs/detaildata/downloadaqsdta.htm>.

The data are very extensive, and only certain subsets were obtained in this study. Table 5.1 shows the typical data file contents.

**Table 5.1: Air Quality System Data File Contents**

Field	Description	Field	Description
1	RD: Raw Data	9	Unit
2	Action code	10	Method
3	State code	11	Date
4	County code	12	Start time
5	Site ID	13	Sample value (e.g., [O <sub>3</sub> ])
6	Parameter ID (e.g., 44201 for O <sub>3</sub> )	14	Null data code
7	Parameter Occurrence Code	15	Sampling frequency
8	Sample duration	16	Monitor protocol

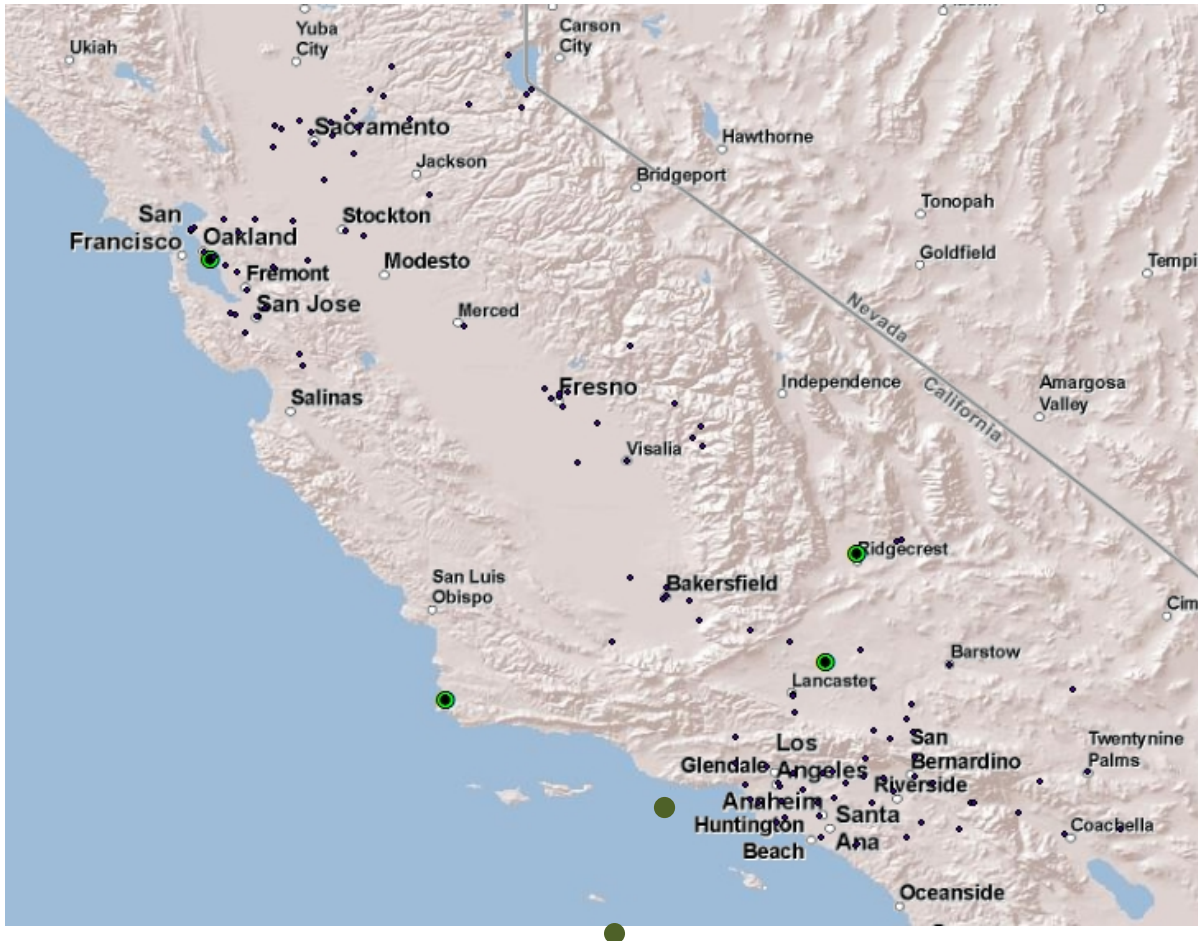
Past field No. 16, an additional 12 fields can be included, depending on available additional information (these 12 additional fields are not listed in Table 5.1). For a full explanation of the above fields and for a description of measurement units, county, city, and monitor identifications, information at the following three links is useful:

1. <http://www.epa.gov/ttn/airs/airsaqs/manuals/AQS%20Input%20Transaction%20Formats.pdf>
2. <http://www.epa.gov/ttn/airs/airsaqs/manuals/codedescs.htm>
3. [http://www.epa.gov/ttn/airs/airsaqs/manuals/city\\_names.pdf](http://www.epa.gov/ttn/airs/airsaqs/manuals/city_names.pdf)

Figure 5.1 shows the locations of surface meteorological and air-quality monitors used in this analysis (there are 134 such monitors/stations). While there are many more monitors not included in this figure (and analysis), the reason for using only the subset shown in Figure 5.1 is because of their continuous data coverage from 1995 through 2005. The large green dots in the figure represent locations of upper air data used in the large-scale forcing characterization. Thus, in the CART analysis, ozone from monitors in the San Francisco Bay Area (SFBA), Sacramento Valley, Lake Tahoe, and San Joaquin regions would preferably be correlated with upper-air meteorological variables from the Oakland airport soundings and profilers (OAK). The rest would preferably be correlated to upper-air variables from the Vandenberg Air Force Base (AFB), Point Mugu Naval Air Station (NAS), St. Nicholas Island, Edwards AFB, and China

Lake Naval Weapons Center (NWC) soundings and profilers. However, the analysis also correlates all monitor data with all six upper-air datasets.

**Figure 5.1. Surface Meteorological Stations and Air-quality Monitor Locations (Small Black Circles) and Upper-air Data Stations (Large Green Circles)**



### 5.3 Meteorological and Air-Quality Data Analysis and CART Development

In correlating ozone to meteorology, and in the CART analysis, the following meteorological variables were used: pressure (pressure heights), air temperature, humidity, wind speed, and wind direction. How each of these factors influences ozone formation, i.e., “ozone meteorology,” is discussed in many sources and textbooks, such as in Seinfeld and Pandis (1998). For this type of application in heat-island studies, these were also discussed in Taha (2007).

To select modeling episodes representing various ozone meteorologies, an approach similar to that of CART was followed in this study. The goal is to identify, for several major regions in California, the meteorological conditions conducive to high, moderate, and marginal ozone

concentrations. As discussed earlier in sections 5.1 and 5.2, data from 1995 through 2005 were obtained and analyzed for this purpose. Two analyses were performed: one using the entire 1995–2005 datasets and the other is using only 2000–2005 data. Results from the latter analysis were then used in developing the correlations, so as to minimize the impacts of emission control on air quality during more recent years. That is, the effects of emission controls from 1995 to 2005, if still included in CART analysis, could inadvertently affect the correlations we seek to develop. In the second analysis, we assume that no major emission reductions occurred from 2000 through 2005.

Selection of meteorological variables to include in the CART analysis depends on a region's synoptic characteristics, emission patterns, topographical and land-use features, and so on. But in general, certain variables are almost always present in such analyses. From a hundred meteorological variables and parameters, for example, Cox and Chu (1996) found maximum surface temperature, wind speed, relative humidity, mixing height, and cloud cover to be the most relevant for urban areas in the United States. Other researchers focused only on pressure and geo potential height in their analysis and assumed that these parameters are surrogates for other meteorological variables (Pryor et al. 1995). Upper-air variables have been included in CART analysis, as they are useful in predicting high-ozone episodes. That is because upper-air conditions are typically indicative of large-scale/synoptic weather patterns (Davis et al. 1998). Others have used some averaging of the data one way or another. For example, Horie (1988) used 1200Z (UTC time) upper air data averaged over two days at a time. They used air temperature at 850 and 900 hectopascals (hPa), air temperature at inversion base, relative humidity at surface, relative humidity at 900 and 950 hPa, and wind speed at surface. Yet other researchers used only geo potential height as a surrogate for everything else.

Because the relationships between ozone formation and meteorology are non-linear and differ from one region to another, it is not appropriate to develop correlations based on linear regression. However, CART analysis may be a more suitable approach (Thompson et al. 2000) to capture the inherent effects of non-linearities. In this study, the results from CART analysis provide the initial screening of episodes, which is then finalized using observational ozone data for several regions in California.

In this analysis, wind direction, wind speed, pressure height, dew point temperature, and air temperature are used as predictors in CART. These variables are diagnosed at three levels: 1000, 850, and 700 hPa. In the analysis discussed in this section, only weekdays are considered (to avoid the compounding weekend effect). In addition, only ozone is considered as a dependent variable (predict and); other pollutants are not considered. Lastly, and as discussed earlier, to minimize the effects of emission control measures in this CART analysis, only the years 2000 through 2005 are presented in this section (although the original analysis included all eleven years, from 1995 through 2005).

### **CART Analysis**

The first part in this analysis was to get the ozone data ready and processed for this application. The air-quality monitors that were used in creating the CART ozone datasets are identified below. Table 5.2 identifies the county codes and Table 5.3 identifies the monitors in each county.

**Table 5.2: California Counties ID (for Counties Used in the Air-quality Analysis in This Section)**

NSJV and Sacramento		Southern CA and SoCAB		Central CA and SSJV	
County	ID	County	ID	County	ID
Yolo	113	San Joaquin	077	Orange	059
Placer	061	Santa Clara	085	San Bernardino	071
El Dorado	017	Contra Costa	013	Los Angeles	037
Sacramento	067	Alameda	001	Riverside	065
Calaveras	009	Merced	047		
		Fresno	019		
		Kings	031		
		Kern	029		
		Tulare	107		

**Table 5.3. Air-quality Monitors of Interest Used in the Present Analysis**

County	Monitors
Yolo	0004, 0005, 1003
Placer	0002, 0004, 0006, 0007, 3001
El Dorado	0010, 0011, 0012, 0013, 0020, 2003
Sacramento	0002, 0006, 0010, 0011, 0012, 0013, 1001, 5002, 5003
Calaveras	0001
San Joaquin	0009, 1002, 3002, 3003
Santa Clara	0002, 0004, 0005, 1001, 1002, 2004, 2005, 2006, 2007
Contra Costa	0002, 0003, 0010, 1002, 1003, 1004, 3001
Alameda	0003, 0005, 0006, 0007, 0010, 1001, 2001
Merced	0003
Fresno	0007, 0008, 0010, 0242, 0243, 0244, 4001, 5001
Kings	1004
Kern	0007, 0008, 0010, 0011, 0014, 0232, 1005, 5001, 6001, 9000
Tulare	0005, 0006, 0007, 0008, 0009, 2002
Orange	0001, 0007, 1003, 2001, 2022, 5001
San Bernardino	0001, 0005, 0012, 0014, 0015, 0017, 0217, 0306, 1004, 1234, 2002, 4001, 4003, 9000, 9002, 9003, 9004, 9006, 9007, 9008
Los Angeles	0002, 0016, 0030, 0031, 0113, 0206, 1002, 1103, 1201, 1301, 1601, 1701, 2005, 4002, 5001, 5005, 6002, 6012, 9002, 9006, 9033
Riverside	0002, 0003, 0008, 0012, 1002, 2002, 5001, 6001, 8001, 9001, 9003

These monitors were shown in Figure 5.1 and some of them, discussed in the air-quality impact analysis, are shown in more detail in Figures A1 through A9 at the end of Appendix A of this report.

Two types of CART analysis were performed in this study. The initial analysis was a *classification* and the second was a *regression*. For the classification analysis, the observed ozone concentrations range was “binned” into 30-part per billion (ppb) bins ranging from 50 to 260 ppb. This range captures ozone concentrations from background values (~50 ppb ozone) to the highest concentration found at any monitor in California during the 1995–2005 period analyzed in this study (even though the second stage focused only on years 2000–2005). That highest value was 256 ppb, in San Bernardino County in August 1995, at monitor 0005.

Figure 5.2(a–g) shows example results from this analysis, namely, the total number of hours in each 30-ppb bin at several counties/monitors for years 1995–2005. Note that the vertical scale was intended to be different from one figure to another, for ease of reading as the number of hours becomes smaller in higher-concentration bins. These results (shown in Figure 5.2) were also used in screening counties for further analysis within each ozone concentrations bin.

Figure 5.3 provides another way to summarize the observational ozone data. While Figure 5.2 shows the data at all monitors but in different ozone concentration bins, Figure 5.3 shows the data at monitors in each county or region separately. Figure 5.3 (a–f) shows the frequency distributions of ozone *daily peaks* (ppb) on *weekdays* for years 2000–2005 (15 May–30 August on each year). That is, the figures show the number of occurrences of the daily peaks (vertical axis) in 10 ppb bins (defined on the horizontal axis). From this information, the relevant monitors can be selected for further analysis (e.g., those monitors with largest ozone, or those with highest frequencies in certain bins) in CART, and thus in episode selection.

Figure 5.2 (a,b,c): Total Number of Hours at Each Monitor in Each 30-ppb Ozone Bin Interval





Figure 5.3a: Frequency Distribution of Ozone *Daily Peaks* (ppb) on *Weekdays* for Years 2000–2005

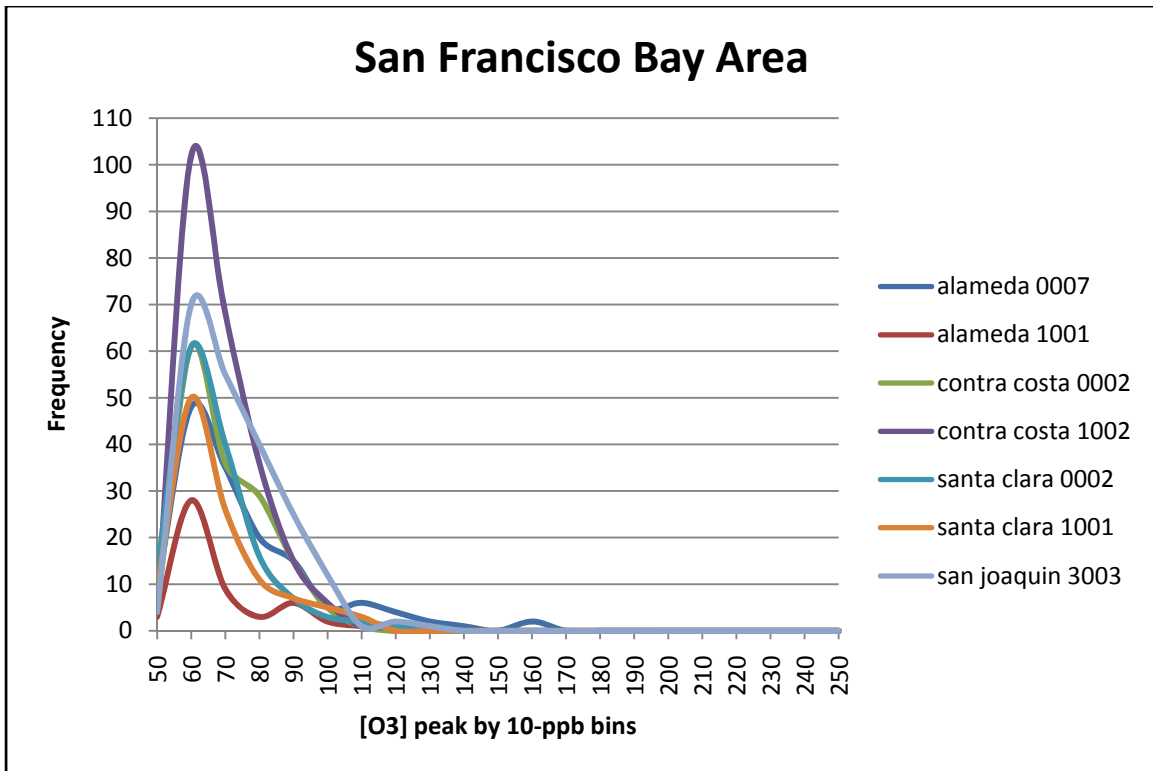


Figure 5.3b: Frequency Distribution of Ozone *Daily Peaks* (ppb) on *Weekdays* for Years 2000–2005

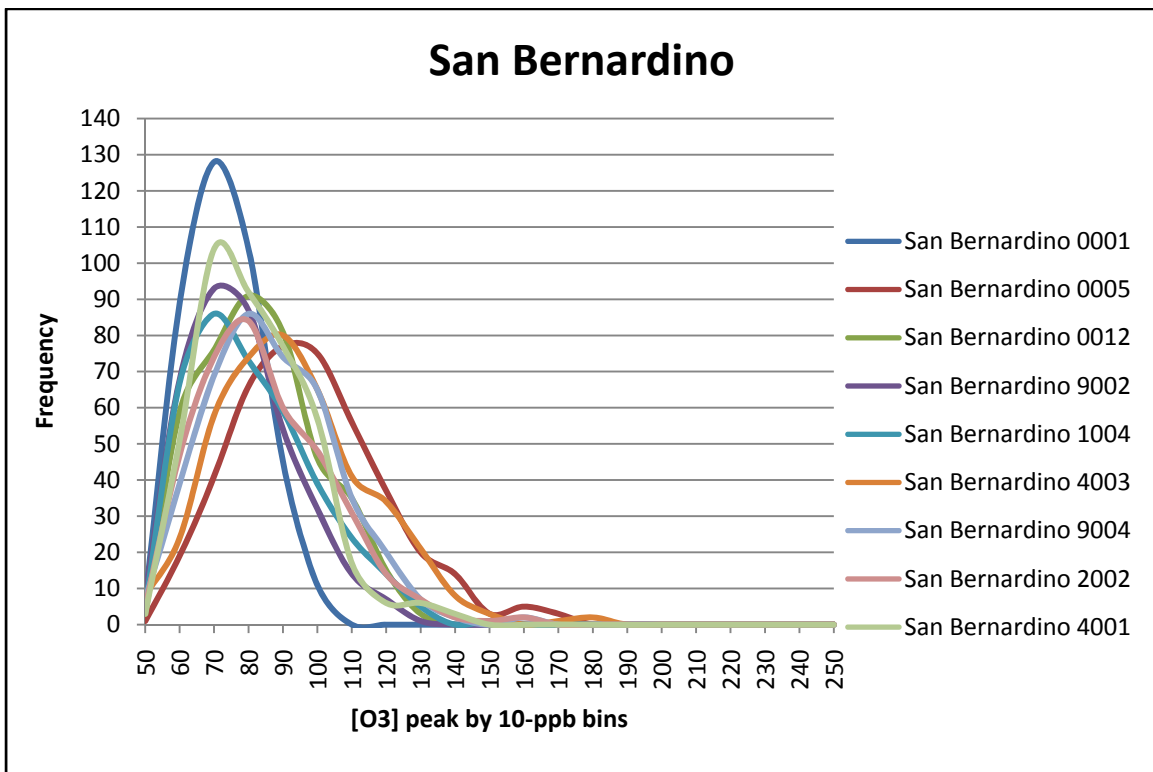


Figure 5.3c: Frequency Distribution of Ozone *Daily Peaks* (ppb) on *Weekdays* for Years 2000–2005

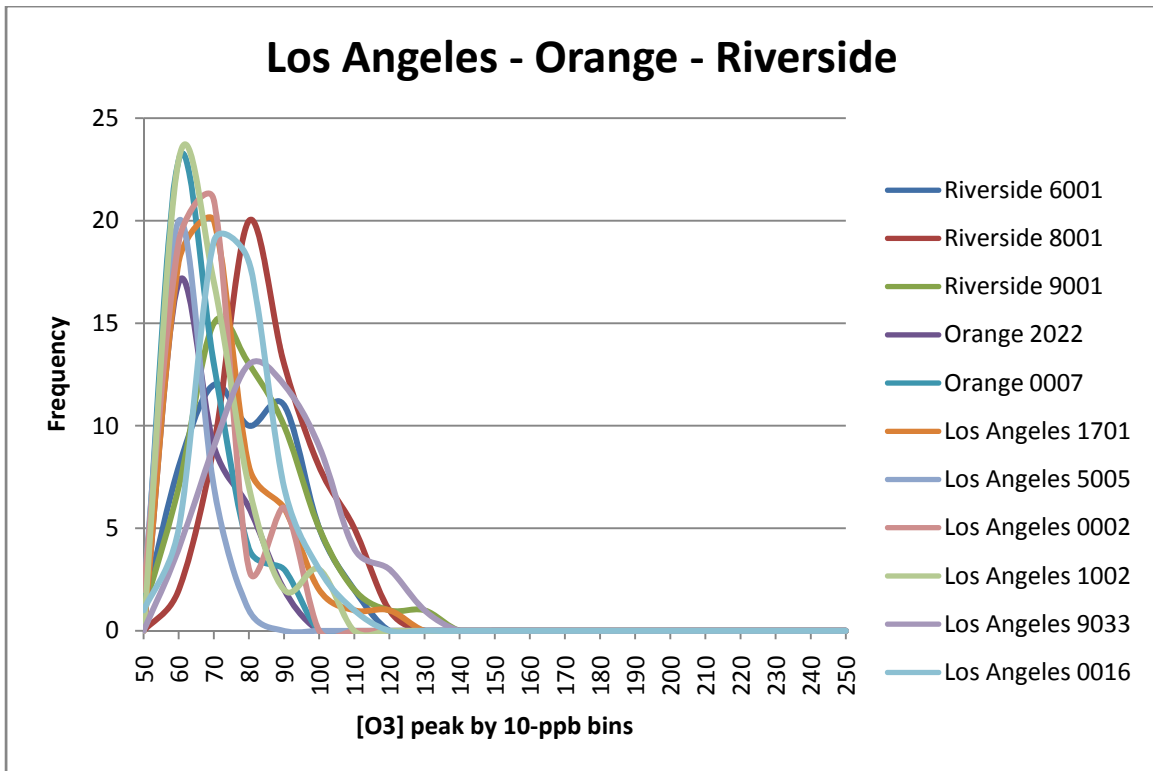


Figure 5.3d: Frequency Distribution of Ozone *Daily Peaks* (ppb) on *Weekdays* for Years 2000–2005

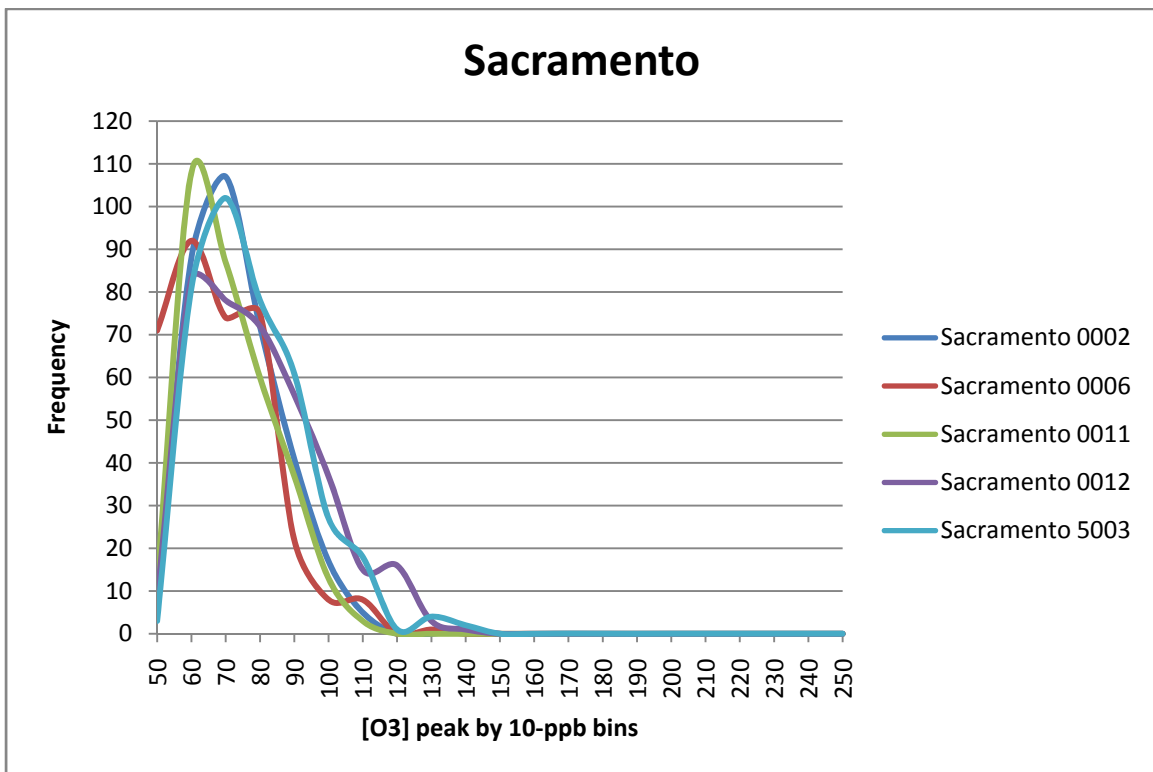


Figure 5.3e: Frequency Distribution of Ozone *Daily Peaks* (ppb) on *Weekdays* for Years 2000–2005

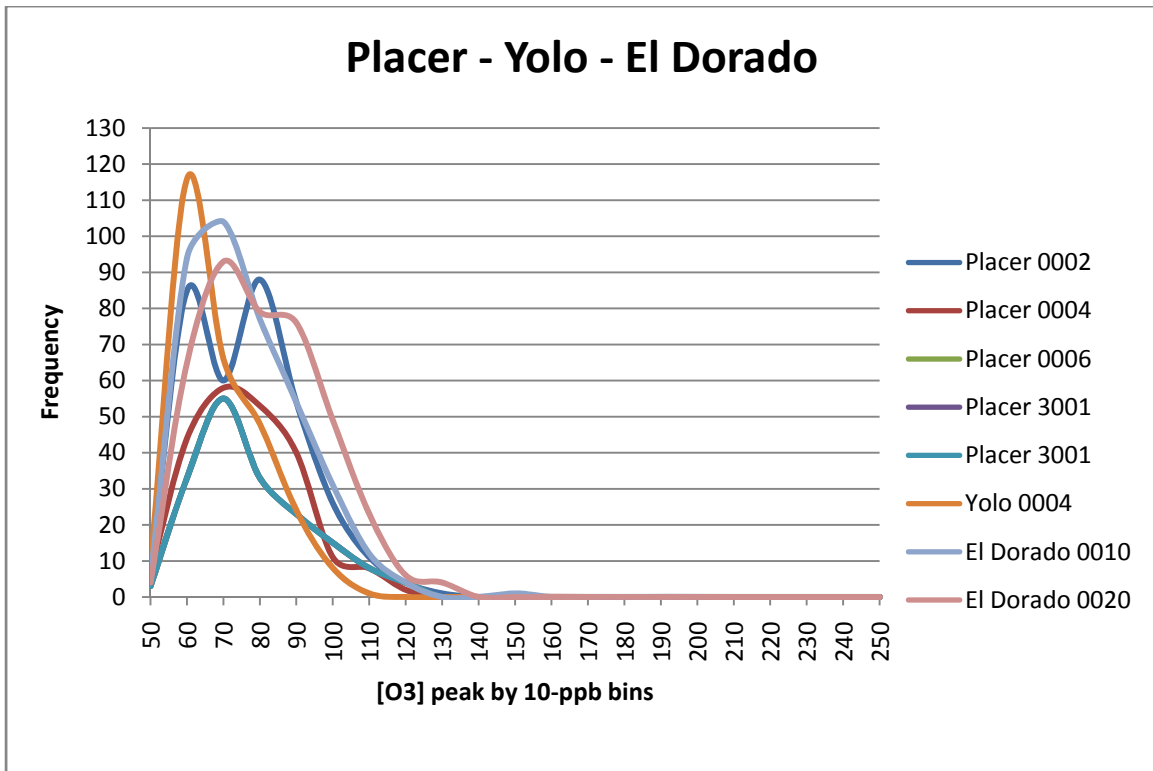
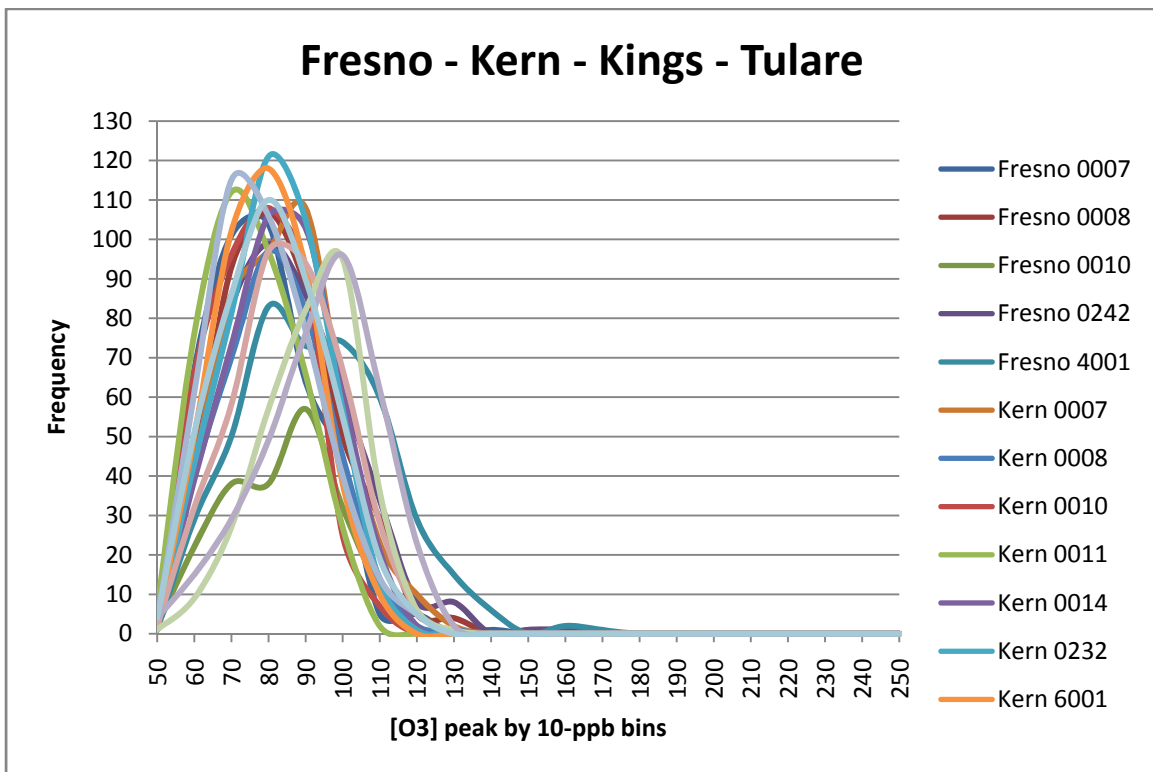


Figure 5.3f: Frequency Distribution of Ozone *Daily Peaks* (ppb) on *Weekdays* for Years 2000–2005



Based on observational data analysis and the binning discussed above, air-quality monitors and their ozone values were then grouped into percentiles, e.g., top 20 percent, second 20 percent, and so on. The goal in this study was to select modeling episodes that capture the range of ozone in the top, second, and third 20 percent. Table 5.4 (A–D) summarizes the grouping.

**Table 5.4: Ranking of Monitors by Peak 1-hr Ozone Concentrations (Top, Second, and Third 20 Percent) and Frequency of Occurrences of Peaks within Each 20 Percent Concentration Bin**

**Table 5.4.A: South Coast / Los Angeles Region**

**South Coast / Los Angeles Basin**

San Bernardino County

top 20%			2nd 20%			3rd 20%		
Rank	Monitor	O3 range	Rank	Monitor	O3 range	Rank	Monitor	O3 range
1	4003	172-174	1	4003	147	1	4003	119-124
2	0005	158-163	2	0005	135-140	2	0005	112-116
3	2002	156-158	3	2002	131	3	2002	109-113
4	9004	151-154	4	9004	128-129	4	9004	107-112
5	0012	145	5	0012	125-126	5	0012	102-107
6	1004	142	6	1004	118-122	6	1004	100-105
7	4001	138-140	7	4001	121	7	4001	99-104
8	9002	125	8	9002	107-110	8	9002	90-95
9	0001	94-99	9	0001	84-89	9	0001	74-79

Riverside County

top 20%			2nd 20%			3rd 20%		
Rank	Monitor	O3 range	Rank	Monitor	O3 range	Rank	Monitor	O3 range
1	0012	141	1	0012	118-119	1	0012	100-102
2	9001	129	2	9001	109-113	2	9001	92-97
3	5001	125	3	5001	106-107	3	5001	90-92
4	8001	119	4	8001	103-106	4	8001	88-93
5	6001	104	5	6001	88-93	5	6001	78-82
6	2002	92-97	6	2002	86-88	6	2002	75-79

Los Angeles County

top 20%			2nd 20%			3rd 20%		
Rank	Monitor	O3 range	Rank	Monitor	O3 range	Rank	Monitor	O3 range
1	6012	155	1	6012	134	1	6012	108-112
2	9033	120-123	2	9033	103	2	9033	89-94
3	1201	112-113	3	1201	95-98	3	1201	83-87
4	1701	111	4	1701	95-96	3	1701	83-87
5	0016	97-102	5	0016	87-88	4	0016	76-81
6	1002	94-96	6	1002	82-83	5	1002	74-75
7	0002	86-90	7	0002	82	6	0002	69-74
8	2005	82-86	8	2005	73-77	7	2005	66-71
9	5005	75	9	5005	65-69	8	5005	60-65

**Table 5.4.B: Fresno / Bakersfield Region**

**Fresno - Bakersfield**

Fresno County top 20%			2nd 20%			3rd 20%		
Rank	Monitor	O3 range	Rank	Monitor	O3 range	Rank	Monitor	O3 range
1	4001	164	1	4001	137	1	4001	114-118
2	0242	155	2	5001	113-117	2	0242	108-113
3	5001	134	3	0007	111-114	3	5001	95-100
4	0007	132	4	0008	105-110	4	0007	94-99
5	0008	121-125	5	0010	100-103	5	0008	90-95
6	0010	114-119	NA	0242	NA	6	0010	86-90

Kern County top 20%			2nd 20%			3rd 20%		
Rank	Monitor	O3 range	Rank	Monitor	O3 range	Rank	Monitor	O3 range
1	0007	121-126	1	0007	105-110	1	0007	90-95
2	0008	123	2	0008	103-108	2	0008	88-93
3	0014	111-115	3	0014	97-102	3	0014	84-89
4	0232	107-111	4	0232	93-98	4	0232	81-86
5	5001	106-111	4	5001	93-98	4	5001	81-86
6	6001	104-109	5	6001	92-97	5	6001	80-85
7	0010	103-108	6	0010	93-96	6	0010	79-84
8	0011	103-107	7	0011	91-95	6	0011	79-84

Tulare County top 20%			2nd 20%			3rd 20%		
Rank	Monitor	O3 range	Rank	Monitor	O3 range	Rank	Monitor	O3 range
1	0009	121-126	1	0009	105-110	1	0009	90-95
2	0008	119-121	2	0008	101-106	2	0008	87-92
3	2002	120	3	2002	101-105	2	2002	87-92
4	0006	111-115	4	0006	97-102	3	0006	84-89

**Table 5.4.C: Sacramento Valley Region**

**Sacramento Valley**

Sacramento County top 20%			2nd 20%			3rd 20%		
Rank	Monitor	O3 range	Rank	Monitor	O3 range	Rank	Monitor	O3 range
1	0006	134	1	5003	117	1	0006	95-100
2	5003	129-134	2	0006	114-116	1	5003	95-100
3	0012	129-132	3	0012	111 115	2	0012	94-99
4	0002	131	4	0011	91-96	3	0002	93-98
5	0011	108	NA	0002	NA	4	0011	79-84

Placer County top 20%			2nd 20%			3rd 20%		
Rank	Monitor	O3 range	Rank	Monitor	O3 range	Rank	Monitor	O3 range
1	0006	130	1	0006	110	1	0006	93-98
2	0002	120-125	2	0002	106-108	2	0002	90-95
3	3001	114-118	3	3001	99-104	3	3001	85-90
4	0004	112-115	4	0004	97-101	4	0004	84-89

El Doarado County top 20%			2nd 20%			3rd 20%		
Rank	Monitor	O3 range	Rank	Monitor	O3 range	Rank	Monitor	O3 range
1	0010	141	1	0010	117-119	1	0010	99-104
2	0020	121-126	2	0020	105-108	2	0020	90-95
3	0012	78-82	3	0012	70-75	3	0012	64-69

**Table 5.4.D: San Francisco Bay Area**

**San Francisco Bay Area**

Alameda County			2nd 20%			3rd 20%		
top 20%								
Rank	Monitor	O3 range	Rank	Monitor	O3 range	Rank	Monitor	O3 range
1	0007	151-152	1	0007	128	1	0007	107-111
2	0003	134	2	1000	86-91	2	1001	78-81
3	1001	99-102	3	2001	81-84	3	2001	76
4	2001	95	NA	0003	NA	NA	0003	NA

Contra Costa County			2nd 20%			3rd 20%		
top 20%								
Rank	Monitor	O3 range	Rank	Monitor	O3 range	Rank	Monitor	O3 range
1	1002	130	1	0002	87-91	1	1002	93-98
2	3001	111	NA	1002	NA	2	3001	81-86
3	0002	98-103	NA	3001	NA	3	0002	77-81

Santa Clara County			2nd 20%			3rd 20%		
top 20%								
Rank	Monitor	O3 range	Rank	Monitor	O3 range	Rank	Monitor	O3 range
1	0002	120-121	1	0002	104	1	0002	87-89
2	2006	113-117	2	2006	101-102	2	2006	85-90
3	1001	102-106	3	1001	89-94	3	1001	80-81

Table 5.4.E summarizes the frequency of occurrences for each 20 percent bin in several counties of interest (not at monitor level). For each county, the occurrences are averaged over a number of monitors. The range of these averaged occurrences corresponding to concentrations from 50 ppb to the highest value in each county is then divided into 20 percent bins. The number of occurrences in each 20 percent bin is then computed based on the data shown in Figures 5.3.a through 5.3.f. Table 5.4.E will be referred to later when evaluating the relative importance of changes in the peaks and other measures; that is, the frequency of occurrences such changes represent. Note that the values of the peaks in Table 5.4.E do not match those in Figures 5.4a through 5.4f, because the values in Table 5.4.E are averaged over a number of monitors.

**Table 5.4.E: Frequency of occurrence of 1-hr peaks in concentration bins of 20% (based on observational data from 2000 through 2005).**

Counties	Range	Concentrations range (ppb) in 10-ppb bins	Frequency of occurrence (%)
Alameda and Contra Costa	Top 20%	140–160	0.68
	2nd 20%	120–140	0.96
	3rd 20%	100–120	3.83
Santa Clara	Top 20%	120–130	1.25
	2nd 20%	100–120	3.28
	3rd 20%	90–100	6.87
San Bernardino	Top 20%	140–160	0.66
	2nd 20%	120–140	4.24
	3rd 20%	100–120	16.91
Los Angeles	Top 20%	110–120	2.80
	2nd 20%	100–110	6.00
	3rd 20%	80–100	16.40
Riverside	Top 20%	110–120	4.07
	2nd 20%	100–110	12.22
	3rd 20%	80–100	27.77
Orange	Top 20%	90	6.15
	2nd 20%	80–90	9.23
	3rd 20%	70–80	16.41
Sacramento	Top 20%	130–140	0.74
	2nd 20%	110–130	2.67
	3rd 20%	90–110	11.73
Fresno	Top 20%	120–130	1.81
	2nd 20%	100–120	8.76
	3rd 20%	90–100	26.66

Note that in Table 5.4.E the 20 percent ranges correspond to different concentration (bin) values in different counties and also within each county at times. Where only one value for the concentrations range is provided, the 20 percent in corresponds to a range of less than 10 ppb.

Following the binning and categorization of observed ozone as discussed above, the next step was to analyze the surface and upper-air meteorological data corresponding to those observations, that is, develop a correspondence in space (monitor location) and in time (dates) among the two datasets. To perform the matching or crosswalk between ozone and surface- and upper-air meteorology, FORTRAN programs were written and used to identify the binned ozone data and search for the corresponding meteorological data from the 1995–2000 record. Pairing between ozone monitors and upper-air meteorology stations was done to develop a tree at each monitor. The county-station pairings were as follows:

<u>County</u>	<u>Upper-airstation</u>
Alameda	KOAK
Calaveras	KOAK
Contra Costa	KOAK
El Dorado	KOAK
Fresno	KOAK + VAFB
Kern	VAFB + PMNAS
Kings	KOAK + VAFB
Los Angeles	PMNAS
Merced	KOAK
Orange	PMNAS
Placer	KOAK
Riverside	PMNAS
Sacramento	KOAK
San Bernardino	VAFB + PMNAS
San Joaquin	KOAK
Santa Clara	KOAK
Tulare	KOAK + VAFB
Yolo	KOAK

KOAK = Metropolitan Oakland International Airport, VAFB = Vandenberg Air Force Base, PMNAS = Point Mugu Naval Air Station

The CART analysis was performed using a model (GUIDE)<sup>3</sup> and methodology developed by Loh (2002, 2006, 2008). GUIDE was used in this study for developing both *classification* and *regression* tree correlations. Thus, both binned and non-binned ozone data were prepared as input to the model, and used accordingly. Figure B1 in Appendix B shows some examples of results from *classification*; whereas, Figure B2 shows results from *regression*.

Figure B1 shows tree examples of various complexities based on different levels of pruning. Of interest is the relatively high importance of air temperature as the main splitting variable of the trees. For example, in Figure B1-A (Alameda), the top splitting variable is air temperature at 1,000 hPa with a value of 288 Kelvin (K) (about 15°C [59°F]). Above that value, most high concentrations of ozone occur, including the peak bin of 110–140 ppb. For Contra Costa (in the very abridged tree shown in Figure B1-B), the splitting variable is air temperature at 850 hPa with a value of 286.75 K (about 13°C [55.4°F]), above which, higher concentrations of ozone are found (e.g., 80–110 ppb). This can also be seen in the rest of the B1 figures. These and the foregoing two examples are summarized in Table 5.5. Clearly, there are other variables that define each pathway, but the table lists only the top node.

---

<sup>3</sup>GUIDE stands for Generalized, Unbiased, Interaction Detection and Estimation.

**Table 5.5: Example Results from CART (Classification) Analysis at Various Counties**

County	Top-Node Splitting Variable	Level	Value	Figure
Alameda	Air temperature	1000 hPa	15.0°C (59.0°F)	B1-A
Contra Costa	Air temperature	850 hPa	13.5°C (56.3°F)	B1-B
El Dorado	Air temperature	850 hPa	25.3°C (77.5°F)	B1-C
Riverside	Air temperature	850 hPa	17.5°C (63.5°F)	B1-D
Sacramento	Air temperature	700 hPa	9.7°C (49.5°F)	B1-E

On the other hand, Figures B2-1 through B2-51 show examples from *regression-tree* analysis of ozone versus meteorological parameters and at various levels of complexity (pruning). The CARTs shown in the figures are for ozone  $\geq 50$  ppb, years 2000–2005, and weekdays only.

In the *classification* trees, the node number is given inside the circle, the splitting criterion and its value are given to the left of the node, the ozone bin range is given immediately below each terminal node, and below that is a misclassification cost associated with the estimates for that node. To the left of each node is the number of occurrences for this condition. Conditions meeting the splitting criterion follow the path to the left of the node, otherwise to the right. In the *regression* trees, all indicators are the same as with classification trees, with one exception. That is, the ozone bin range (under each terminal node) is replaced with the average ozone concentration represented by that path (averaged over the number of occurrences of that node).

Table 5.6 provides a summary of pathways to certain nodes of interest in this CART regression analysis, e.g., nodes with high ozone concentrations, for the SFBA, Southern California, Sacramento Valley, and San Joaquin Valley. Note that the trees not only evaluate the pathways (i.e., identify the most important splitting variables) but can also show that various ranges of ozone concentrations (e.g., high ozone) can be reached via several different pathways. Table 5.6 lists the highest ozone (highest mean ozone at each node) from CART analysis for monitors in California counties and pertaining criteria. In the table, the entries are in the following order: county, corresponding upper-air/rawinsonde data station, and monitor ID. Then for each pressure level of 700, 850, and 1000 hPa,  $Ta$  is air temperature (K),  $Td$  is dew-point temperature (K),  $V$  is wind speed (in meters per second [ $\text{m s}^{-1}$ ]),  $\theta$  is wind direction, and  $Pz$  is pressure height (in meters [m]).

For each entry in the table, the CART-specific criteria are provided (of course this discussion is specific to the dataset being examined here but should provide an idea as to the most important splitting variables). In some cases, more than one “highest” ozone node is provided, to show how such concentrations can be reached via different pathways in the trees. Entries are rounded to the nearest decimal point (except for wind speed). The nodes at which the splitting variables and conditions are reported in Table 5.6 are identified in Appendix B on Figures B2-1 through

B2-49 with black circles next to the nodes. Node 1 splitting variables (the top of the tree) are shown in red font. The abbreviations in the table are as follows:

Upper-air sites:

1 = KOAK, 2 = VAFB, 3 = PMNAS

Counties:

(SFBA)	(SoCAB)	(Sacramento)
AL = Alameda	SB = San Bernardino	SA = Sacramento
CC = Contra Costa	RS = Riverside	PL = Placer
SC = Santa Clara	OR = Orange	YO = Yolo
SJ = San Joaquin	LA = Los Angeles	ED = El Dorado

(Fresno-Bakersfield)

FR = Fresno  
 KR = Kern  
 KI = Kings  
 TU = Tulare

**Table 5.6: Meteorological Conditions Corresponding to the Highest of Mean Ozone at Several Nodes from CART Analysis for Monitors in California**

SFBA (No clearly defined main splitting variable at node 1)																		
County	UA station	Monitor	700 hPa					850 hPa					1000 hPa					
			Ta	Td	V	θ	Pz	Ta	Td	V	θ	Pz	Ta	Td	V	θ	Pz	
AL	1	0007	>285						<280				>1500					<127 >77
		0007	>283						<280				>1500				<201	<127 >77
		1001	>283									<330			>283			
CC	1	0002					<3166			>3.3					<1.6			
		0002				<297		>296		>3.3					<1.1			
		0002			<5.2		>3155			<3.3								
		1002		>273														
		1002							Eqn A				Eqn A	>288				
SC	1	0002					>3170		>269				>289		<1.4			
		1001																
SJ	1	3003					>292					<163						
		3003			<3.4							>163		<285				

Table 5.6: continued

Southern California (Ta 700 mb and Pz 700 mb dominate the splitting variables at node 1)																	
County	C/A station	Monitor	700 hPa					850 hPa					1000 hPa				
			Ta	Td	V	θ	Pz	Ta	Td	V	θ	Pz	Ta	Td	V	θ	Pz
SB	2	0001								<2.6	>115	>1504					
		0001								<2.3	<302	<1504					
		0005	>281									>352	>1466		>1.4	>3	<104
		0005	>281					>291						>286	<1.4	>202 <222	
		0005	>281							<5.9		>1520			>1.4	>32	<119 >104
		0005	>281					>293							>14	>33	>120
		0012	>282		<2.8	>112	<3176										
		0012	>282			>337					<317						
		9002				>313	<3144	>294	<276						<2.9		
		9002				>313			<276								
		9002				<313					>117					<172	
		1004	>283	>268			>3125	<298						<286			
		1004		<262			>3125	<298	>268					>284			
		4003					>3123										
		9004					>3151										
		9004					<3151				<5.9	<206					
		2002	>283	<248				>291									
		2002	>283	<270				>291									
4001	>277			Eqn B	>3098												
RS	3	6001								>298							
		8001	>283				>3130						>289			>110	
OR	3	2022				<167						>1500					
		0007					>3156							<1.3			
LA	3	1701											<284				
		5005						>292		>6.9		>1520					

Table 5.6: continued

Sacramento Valley (Ta 850 mb and Tdew 1000 mb dominate the splitting variables at node 1)																		
County	U/A station	Monitor	700 hPa					850 hPa					1000 hPa					
			Ta	Td	V	θ	Pz	Ta	Td	V	θ	Pz	Ta	Td	V	θ	Pz	
SA	1	0002				>327		Eqn c						Eqn c				
		0002					>3178	Eqn c						Eqn c		>308		
		0006			<0.8			Eqn d						Eqn d				
		0006			<4.8			Eqn d				>1544		Eqn d				
		0011				<305	Eqn e			>4.8	>185			Eqn e				
		0011				<211	Eqn e	<292		<4.8				Eqn e				
		0012						>293										
		5003	>283				>3169	>292		<4.4								
5003					<3169	>292			<167									
PL	1	0002						Eqn f				>284	Eqn f		>322	<116		
		0006	>272		>7.8										>210			
		0006	>272												<217			
		0004	>286			<230										>103		
		0004				<230			>267							<103		
		0004			<6.2	>230	>3100											
		3001					>3183	>287								>302		
YO	1	0004			<6.2	>194	>293	>273										
		0004			<6.2	<207	>293	<273										
		0004			<6.2	<193	>293								<259			
ED	1	0010	>282			<203												
		0020				>168	>3147	>298										
		0020				<168	>3147					<286						

Table 5.6: continued

San Joaquin Valley (Ta 850 mb dominates splitting variables at node 1)																		
County	UA station	Monitor	700 hPa					850 hPa					1000 hPa					
			Ta	Td	V	θ	Pz	Ta	Td	V	θ	Pz	Ta	Td	V	θ	Pz	
FR	1	0007	>284														<1514	
		0007	<284	>260							>8.0							
		0008		<247														
		0010														<2.8	>253	
		0242										<175	<1525					
		0242										>175	>1502					
		4001																
KR	2	0007						>3149	<295				<204	<1546				
		0007			>4.4		>3185	>295									>252	
		0007			>4.4			>295						>286			<252	
		0008						>294										
		0010						>295								<0.3		
		0010						>295						<285		>0.3		
		0011	>286															
		0014							>295		<2.5	<317						
		0014							>295		4.4	>317						
		0014							>295		<6.4		>1498					
		0232				<142			>295									
		6001						<3210	>295	<264				<1525				
6001							>295					>1550						
6001						>3210	>295					<1535						
KI	1						>3138											
TU	1	0006																
		0008		<266														
		0009		<266														
		0009	>283	<266				>3121	>287									
		2002						>3143	>293									

Where an equation is the splitting variable (in lieu of a single variable and value), it is identified as follows:

Eqn C:  $(-0.6529 \cdot \text{TDEW1000} + \text{TAIR850}) > 108.07$

Eqn D:  $(-0.8522 \cdot \text{TDEW1000} + \text{TAIR850}) > 49.89$

Eqn E:  $(-15.89 \cdot \text{WSP1000} + \text{HT700}) > 3085$

Examining the results from both the regression and classification analysis above, some of which is summarized in Tables 5.5 and 5.6, it becomes evident that splitting variables such as air temperature at 850 hPa and pressure height at 700 hPa are dominant (particularly air temperature at 850 hPa). The 850 hPa level is removed enough from the surface (thus not directly influenced by it), yet not too high as not to be influenced by local and sub-regional properties and processes. The results from the regression tree are used in conjunction with ozone analysis in selecting the episode-regions for modeling.

## CHAPTER 6: Episodes

Based on the analysis discussed in Section 5, a number of episode-region combinations were selected for modeling. This was based on the characterization of observed meteorology and ozone concentration ranges discussed earlier, followed by a last step to screen the selected episodes for fire/smoke events. Thus, based on the percentiles of ozone discussed in Section 5 and after screening for fire/smoke events, the following episodes were selected for modeling (the 20 percent bins represent the ranges of the 1-hour peaks):

### Fresno–Bakersfield

Top 20%	2002 / 7 / 10–23; 2002 / 8 / 8–11
2nd 20%	2000 / 8 / 2–25
	2002 / 7 / 10–12
3rd 20%	2000 / 6 / 14–27
	2001 / 5 / 18–31
	2002 / 8 / 8–20

### Sacramento Valley

Top 20%	2005 / 7 / 13–14
2nd 20%	2003 / 6 / 3–27
	2001 / 6 / 20–22 **
3rd 20%	2000 / 7 / 19 through 2000 / 8 / 22
	2002 / 7 / 4–19
	2005 / 7 / 25 through 2005 / 8 / 4

### San Francisco Bay Area

Top 20%	2000 / 6 / 14–15
2nd 20%	2003 / 6 / 25 through 2002 / 7 / 17
3rd 20%	2002 / 7 / 1–2 **

### Los Angeles Basin

Top 20%	2003 / 7 / 9–15
2nd 20%	2001 / 5 / 22 through 2001 / 6 / 8 **
	2003 / 7 / 9–24
3rd 20%	2000 / 5 / 23 through 2000 / 6 / 16
	2001 / 8 / 13–17 **
	2005 / 7 / 12–26

\*\* Very small / marginal fires and far downwind from episode-region of interest.

In addition to these episodes, three regulatory episodes were also selected for modeling. These are:

- July 27–August 4, 2000 (for central California)
- July 4–14, 1999 (for central California)
- July 14–20, 2005 (for southern California)

Table 6.1 lists the final episode selection. The episodes are listed in a manner to show the region-episode combinations that can be simulated simultaneously. At the 4- and 1-km grid levels, these episodes are split according to each region’s meteorological and air-quality analysis discussed above.

Figures 6.1 through 6.3 show example satellite data used in screening the episodes for fires or smoke events. The data were obtained from NOAA. In this case, there was a particular fire event affecting the episode July 10 through August 15, 2002, which was then removed as indicated in the top 20 percent bin for Fresno-Bakersfield in the table above. There was a fire event on July 23 in the Sequoia National Forest Area, but the smoke was not affecting California in general (but Nevada). Thus, for this period, the days July 10 through 23 will be used in modeling, and then August 8 through 11. Also, as indicated in the above table (with \*\*), there were other fire events, but they were generally too small or too far downwind to affect the modeling domains.

**Figure 6.1: Fire Events on July 23, 2002**

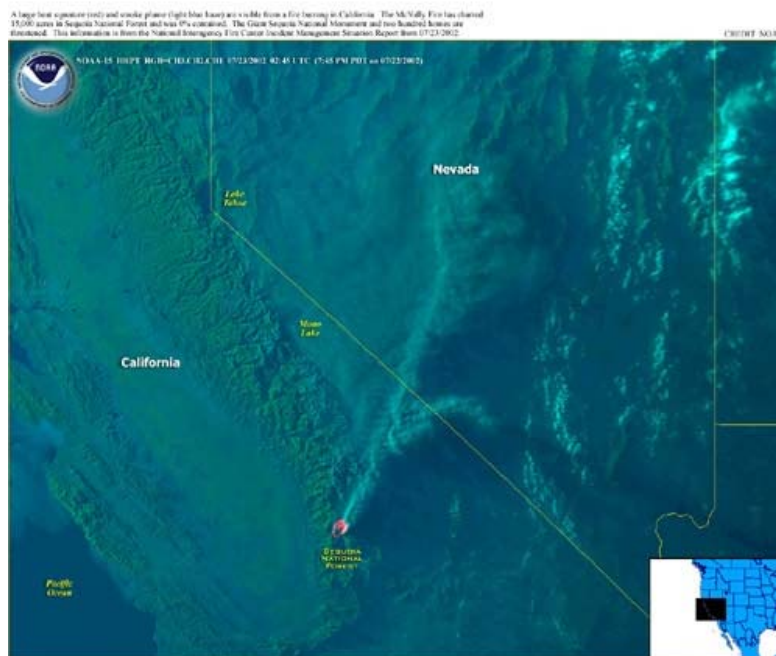


**Figure 6.2: Fire Events on July 25, 2002**



**Figure 6.3: Fire Events on July 30, 2002**

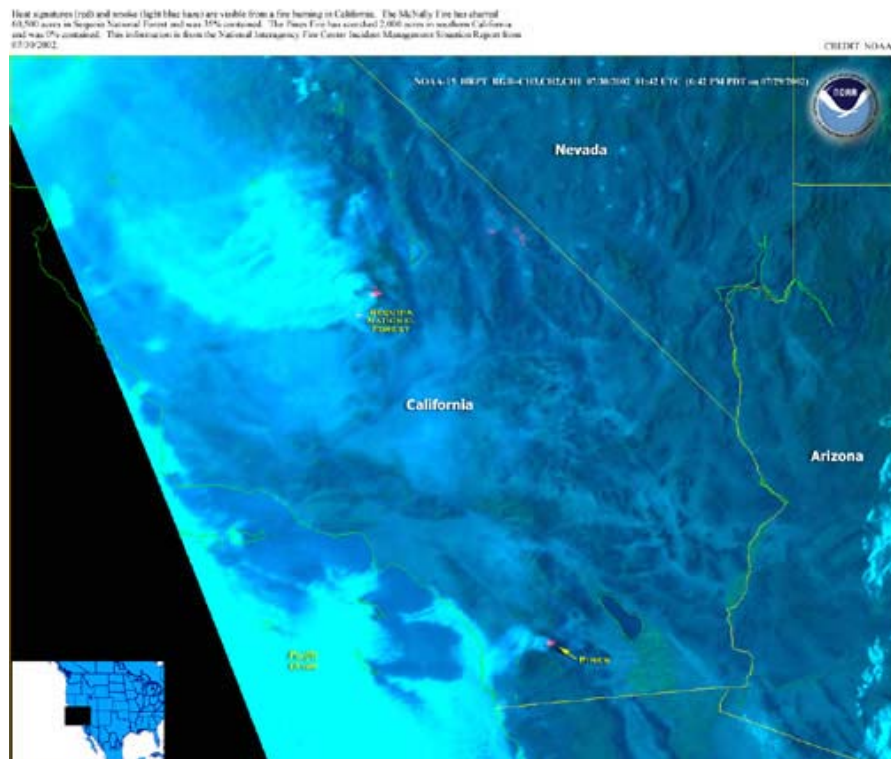


**Table 6.1: Final Episodes Selected for Modeling in This Study**

D01 and D02 base case runs	Central California					Based on CART / O <sub>3</sub> analysis ↓
	Domains through 4km		4km and/or 1km			
	Episode:	Splits into:	For region:	Number of days		
runA	2000	6/14–6/27	6/14–6/27	FV	14	3rd 20% for Fresno
			6/14–6/15	SFBA	2	Top 20% for the SFBA
runB	2000	7/19–8/1	7/19–8/1	SAC	14	3rd 20% for Sacramento
runC	2000	8/4–8/8	8/4–8/8	FV	5	2nd 20% for Fresno
			8/4–8/8	SAC	5	3rd 20% for Sacramento
runD	2000	8/11–8/18	8/11–8/18	FV	8	2nd 20% for Fresno
			8/11–8/18	SAC	8	3rd 20% for Sacramento
runE	2001	5/18–5/31	5/18–5/31	FV	14	3rd 20% for Fresno
runF	2001	6/20–6/22	6/20–6/22	SAC	3	2nd 20% for Sacramento
runG	2002	7/1–7/2	7/1–7/2	SFBA	2	Top 20% for the SFBA
runH	2002	7/4–7/22	7/4–7/19	SAC	16	3rd 20% for Sacramento
			7/10–7/22	FV	13	First two days are for 2nd 20% for Fresno and rest of episode is for top 20% for Fresno
runI	2002	8/8–8/20	8/8–8/20	FV	13	8/8–8/11 are top 20% for Fresno, then 8/12–8/20 are 3rd 20% for Fresno
runJ	2003	6/3–6/27	6/3–6/27	SAC	25	2nd 20% for Sacramento
runK	2003	6/25–7/17	6/25–7/17	SFBA	23	2nd 20% for the SFBA
runL	2005	7/13–7/14	7/13–7/14	SAC	2	Top 20% for Sacramento
runM	2005	7/25–8/4	7/25–8/4	SAC	11	3rd 20% for Sacramento
	Southern California					Based on CART / O <sub>3</sub> analysis ↓
	Domains through 5km		5km and/or 1km			
	Episode:	Splits into:	For region:	Number of days		
runN	2000	5/23–6/16	5/23–6/16	SB	25	3rd 20% for San Bernardino
runO	2001	5/22–6/8	5/22–6/8	SB	18	2nd 20% for San Bernardino
runP	2001	8/13–8/17	8/13–8/17	SB	5	3rd 20% for San Bernardino
runQ	2003	7/9–7/24	7/9–7/24	SB	16	7/9–7/15: top 20% for San Bernardino; 7/15–7/24: 2nd 20% for San Bernardino
runR	2005	7/12–7/26	7/12–7/26	SB	15	3rd 20% for San Bernardino

All of the episode-regions listed in Table 6.1 are simulated twice: one run for the base scenario and another for the high-albedo scenario.

# CHAPTER 7: Surface Characterization and Input

Surface characterization was performed based on the United States Geological Survey (USGS) Level II land-use/land-cover (LULC) classification system (Anderson et al. 2001). The approach used in developing surface characteristics, morphological, and physical properties is discussed in detail in Taha (2007) and Taha (2008a–c) and will not be repeated here. The results from this LULC processing is a full characterization of each domain in terms of surface albedo, roughness length, thermal inertia, soil moisture, emissivity, and a number of other relevant parameter as needed. Generation of additional parameters required by the fine-resolution model, uMM5, is discussed in detail in Taha (2007, 2008a,b) and will not be repeated here. Figures 7.1 through 7.4 show examples of the computed values for some surface parameters.

**Figure 7.1: Fresno-Area Surface Characterization (4 km): Albedo (top-left), Soil Moisture (top-right), Thermal Inertia (bottom-left), in Joules per square meter per degree Kelvin per 1/square root second ( $J m^{-2} K^{-1} s^{-0.5}$ ), and Roughness Length (bottom-right), m**

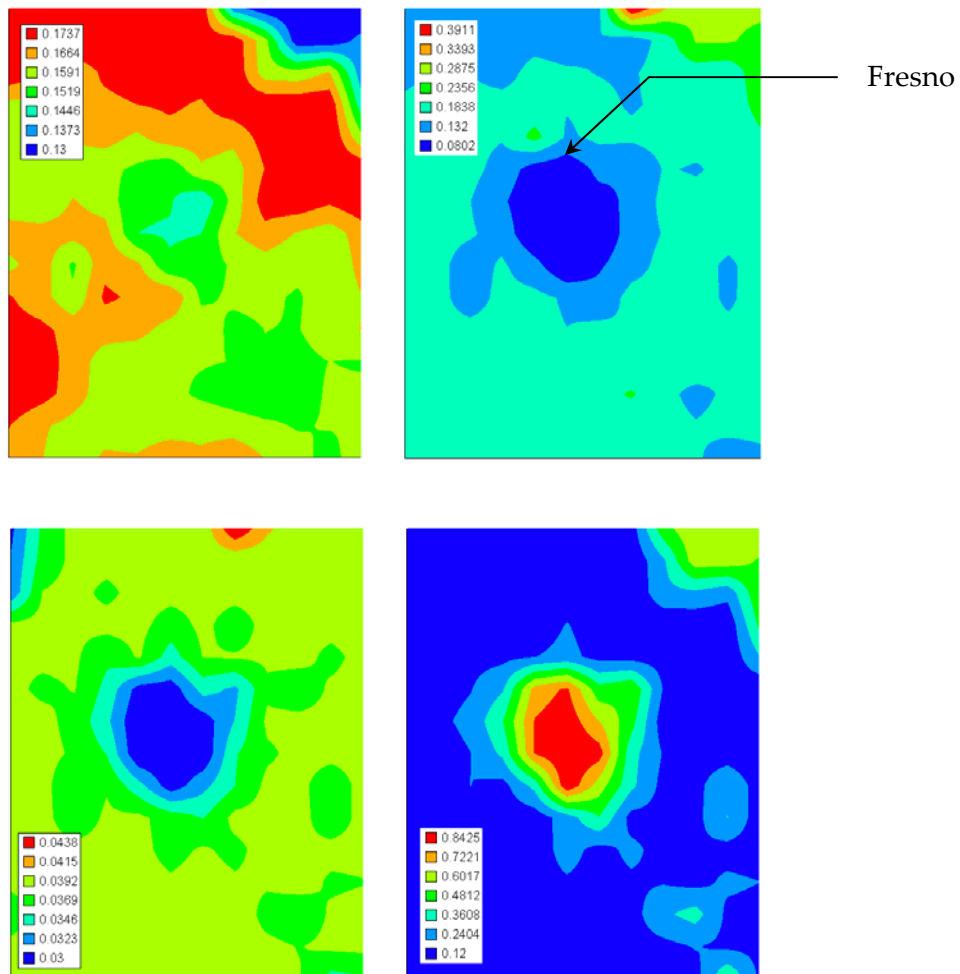


Figure 7.2: San Francisco Bay Area Surface Characterization (4 km): Albedo (top-left), Soil Moisture (top-right), Thermal Inertia (bottom-left),  $J m^{-2} K^{-1} s^{-0.5}$ , and Roughness Length (bottom-right), m

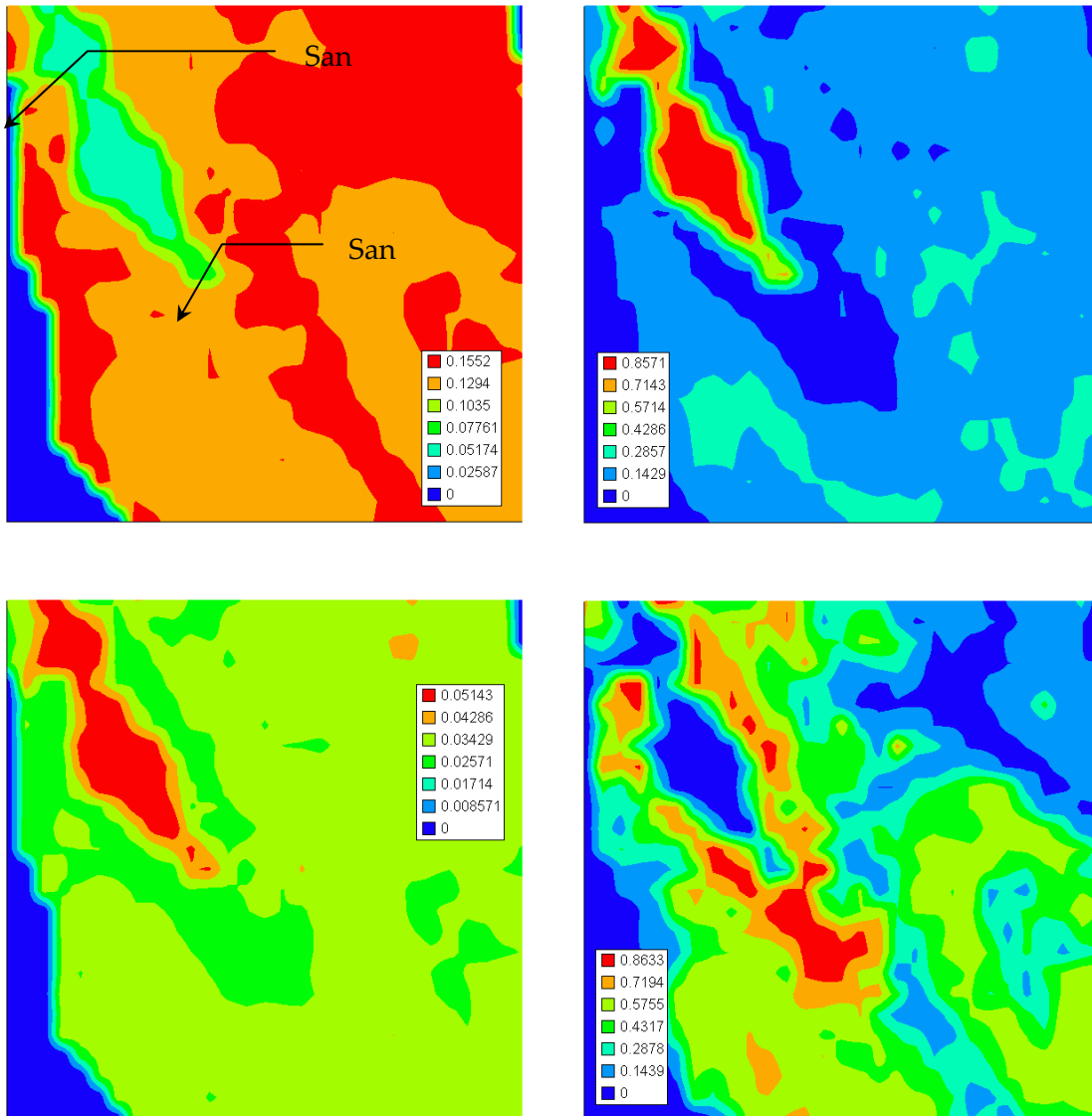


Figure 7.3: Los Angeles Region Surface Characterization (5 km): Albedo (top-left), Soil Moisture (top-right), Thermal Inertia (bottom-left),  $J m^{-2} K^{-1} s^{-0.5}$ , and Roughness Length (bottom-right), m

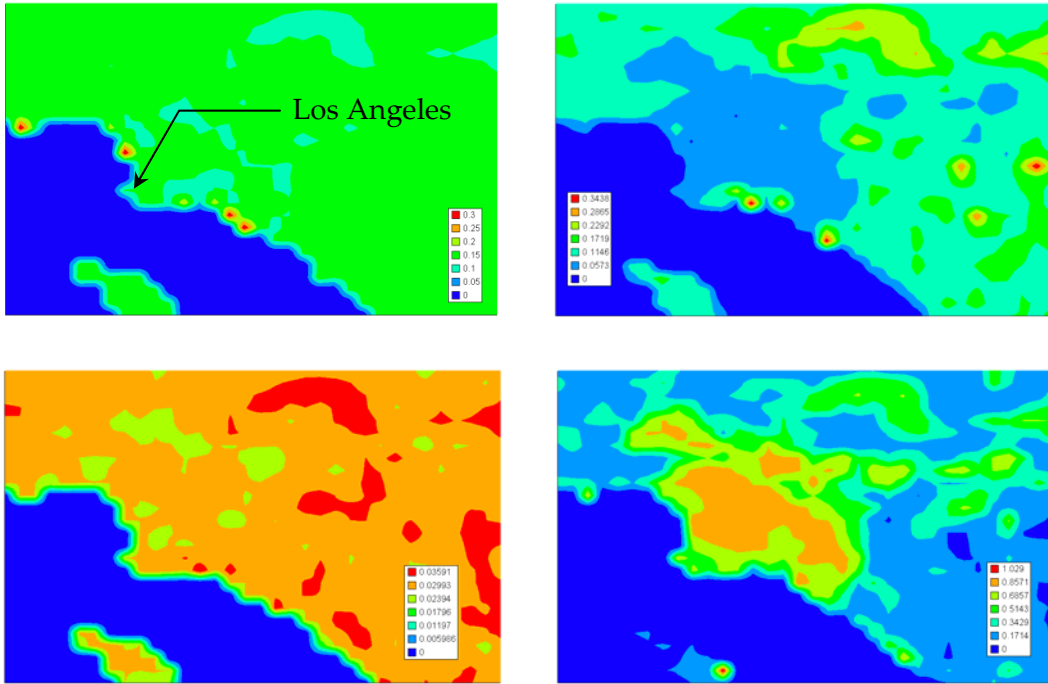
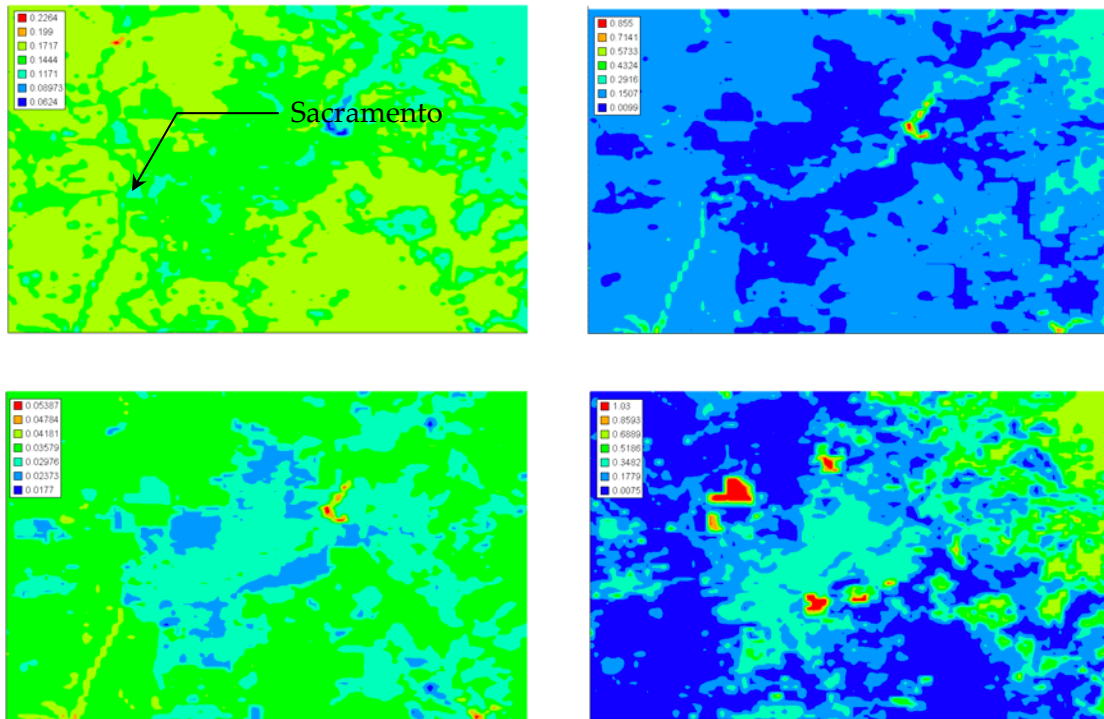


Figure 7.4: Sacramento Region Surface Characterization (1 km): Albedo (top-left), Soil Moisture (top-right), Thermal Inertia (bottom-left),  $J m^{-2} K^{-1} s^{-0.5}$ , and Roughness Length (bottom-right), m



The development of albedo perturbation scenarios was also discussed in detail in Taha (2005,2007) and will not be repeated here, except for a summary of the surface-based changes assumed in the modeling (Table 7.1)

**Table 7.1: Surface-Based Albedo Modifications Used in Modeling the Reasonably High Increase Scenario of Albedo Change**

	Specification of surface-specific albedo and change			
	Roof		Paved	
	$\Delta\alpha$	New $\alpha$	$\Delta\alpha$	New $\alpha$
Residential	0.45	0.55	0.22	0.30
Commercial/Services	0.55	0.65	0.27	0.35
Industrial	0.55	0.65	0.27	0.35
Transportation/Communication	0.25	0.35	0.20	0.28
Industrial and Commercial	0.55	0.65	0.27	0.35
Mixed Urban or Built Up	0.45	0.55	0.22	0.30
Other Urban or Built Up	0.45	0.55	0.22	0.30

# CHAPTER 8: Models and Data

## 8.1 Mesoscale Meteorological Model

In this study, we use the latest version of the Pennsylvania State University / National Center for Atmospheric Research mesoscale model (PSU/NCAR MM5) (v3-7-4) that has been modified for the particulars of this type of application (heat-island control), as discussed in Taha (2008c,2007). The PSU/NCAR MM5 (Dudhia 1993; Grell et al. 1994) is a widely used mesoscale meteorological model in conjunction with photochemical regulatory modeling, e.g., see Tesche et al. (2001), Seaman and Stauffer (1996), and Seaman et al. (1997). For simulating the potential impacts of urban heat island mitigation, a modified version of the MM5 was extensively used by Taha (2005, 2007) in prior phases of this project performed for the California Energy Commission (Energy Commission).

The MM5 is an Eulerian, three-dimensional grid, non-hydrostatic, primitive-equation prognostic model. The basis of the model is the three-dimensional prognostic equations for wind ( $u,v,w$ ), temperature, pressure perturbation, and water vapor mixing ratio. It uses a sigma-altitude ( $\sigma$ - $z$ ) terrain-following vertical coordinate system and allows for multiple nesting. The  $\sigma$  levels are defined according to a hydrostatic reference state and are time-independent (invariant) during the course of model integration. The MM5 allows for moving nests, as well as turning on and off selected nests during the simulation. There can be one-way nesting or two-way feedback, and various smoothing methods are available.

For sub-grid-scale parameterizations of turbulent fluxes, the model allows for a number of different (local and non-local) planetary boundary-layer (PBL) schemes, such as ETA and Gayno-Seaman, Medium-Range Forecast model (MRF) (Hong and Pan 1996), fine-resolution Blackadar (Zhang and Anthes 1982), and Mellor-Yamada (Burk and Thompson 1989). The model also allows for a number of physics, microphysics, and convection options. Microphysics options include stable precipitation parameterizations, such as warm rain (Hsie and Anthes 1984), ice physics (Dudhia 1993), ice and graupel (Tao and Simpson 1993), and the Schultz and Reisner schemes (Schultz 1995; Reisner et al. 1998).

The model also has a number of cumulus parameterization schemes, e.g., Grell et al. (1994), Kain and Fritsch (1993), Arakawa-Schubert (Grell et al. 1991), and Betts and Miller (1986). It allows for coupling land-surface models, e.g., the Oregon State University (OSU)/Noah model (Pan and Mahrt 1987; Chen and Dudhia 2001). The MM5 has four-dimensional data assimilation (FDDA) capabilities (Stauffer and Seaman 1990) for both analyses and observational (station, point) nudging. Use of FDDA can, in certain cases, improve model performance, especially over longer simulation time frames, depending on the actual conditions being simulated.

The model's grid is based on the Arakawa-B stagger configuration, where, in the horizontal direction, scalars are defined at the center of the grid; whereas, velocity variables are allocated at the corners. In the vertical, all variables are defined at half-sigma levels, except for the vertical component of velocity, which is defined at the full sigma levels. Practical minimum horizontal

grid resolution is in the order of 500 m (although in theory, the model can be run at smaller grid spacing). In the vertical, resolution is variable and the grid is stretched (for example: the layers can be a few meters thick near the ground to hundreds of meters thick near the model top). Of course, both horizontal and vertical resolutions can be significantly improved if sub-grid-scale parameterization is also modified, as is done in the uMM5 (Taha 2008a,b) discussed in Section 8.2.

Initialization of the model is based on integrated divergence removal. Initial and boundary-condition data are typically specified from large-scale (synoptic) three-dimensional analyses and applied to the coarsest grids of the domain, but can also be used in driving fine-resolution nests. For the top boundary conditions, the model uses a radiative or rigid layer; and at the bottom, a prognostic surface temperature, constant or varying water surface temperature, and a constant-flux surface layer (fluxes based on similarity theory). At the lateral boundaries, time-dependent inflow / outflow (relaxation) conditions are assumed. The model produces comprehensive forecast variables, e.g., wind field, temperature, water vapor, cloud rain and ice, boundary-layer fluxes and variables, perturbation pressure, etc., and host of derived quantities.

The MM5 requires as input: (1) meteorological initial conditions, (2) meteorological boundary conditions, and (3) surface characterizations (lower boundary characterization). The meteorological information consists of observational upper air and surface data that is supplemented by gridded four-dimensional analyses. In modeling urban heat islands and their mitigation, Taha (2003a-c, 2005, 2007) used the NCEP / NCAR Reanalysis Project data (NNRP; Kistler et al. 2001) for several reasons, including fine temporal resolutions. Thus, we continued the use of NNRP in this modeling effort.

In terms of surface characterization, the standard MM5 uses LULC information and a classification scheme based on the USGS land-use characterization system (Anderson et al. 2001), as discussed above. This information is used to indirectly assign, via lookup values, certain physical properties in the soil and land-surface models (LSM) as well as in the related boundary-layer calculations. In this study, we use this approach only in the coarsest grids, e.g., 36 and 12 km for central California and 45 and 15 km for southern California. For the 5- or 4-km and 1-km domains, different approaches are used, as explained later.

## **8.2 Meso-urban Meteorological Model**

The study also uses a version of the uMM5 (Taha 2008a) for 1-km simulations of selected sub-domains. The term “uMM5” is coined here to loosely refer to modifications, updates, and improvements that Taha (2008a-c) made, since 2003, on the Urban Canopy Parameterization version (UCP) MM5 of DuPont et al. (2004) resulting in a version more suitable for heat-island mitigation modeling. While modifications to the model are routinely made to suit specific project needs, there are generally two main versions of the uMM5: a drag-force-based scheme (DA) and a roughness-length-based scheme (RA). The latter involves modifications to the surface-layer similarity formulation (Monin-Obukhov Similarity Theory; MOST) such that roughness length is computed for each individual surface in a grid cell rather than only once at the grid level. Note that the DA approach is based solely on drag-force formulations and the RA

approach based strictly on MOST formulations. To calculate roughness length, the hybrid approach (used in this study) uses drag coefficients as well as DA-geometrical parameters.

Recent applications of the uMM5 (Taha 2005, 2006, 2007) include dispersion modeling, heat island studies, photochemical and air-quality modeling, and urban-induced precipitation studies. An emerging use of the uMM5 is to drive micro-scale and Computational Fluid Dynamics (CFD) models for various research and real-time applications. The purpose of using the uMM5 here is to improve the simulation of fine resolution phenomena, e.g., urban heat islands, canopy-layer meteorology, and flow divergence/convergence in the canopy layer. The uMM5 resolution in this study is 1 km in the horizontal and a few meters in the vertical, as discussed in Section 4.

The uMM5 (DA and RA versions) is fully described in Taha (2007) including all modified conservation relations and parameterizations. This discussion will not be repeated here. In terms of data, the uMM5 (whether DA, RA, or hybrid) requires special input beyond that needed by the standard MM5 discussed above in Section 8.1. Thus, in addition to the standard input (e.g., meteorological initial and boundary conditions, 4-D analyses, surface characterization), the uMM5 requires detailed 3-D fine-resolution morphological/geometrical parameter input (for a full discussion, refer to Taha [2007] and Taha [2008a,b]). These include:

- Land-use fraction
- Land-cover fraction (paved, vegetation, roof, water, and other categories)
- Mean orientation of streets and urban canyons
- Percent of paved surfaces/impervious areas that are linked to drainage system
- Building mean heights
- Vegetation mean heights
- Building Wall-to-plan ratios
- Building Height-to-width ratios
- Canopy mean heights
- Roughness lengths and displacement heights (for several wind approach directions)
- Frontal area density (function of height) for buildings (for wind approach directions)
- Vegetation frontal area density (function of height)(for wind approach directions)
- Top area density for buildings (function of height)
- Top area density for vegetation (function of height)
- Plan area density for buildings (function of height)
- Plan area density for vegetation (function of height)

- Sky-view factor

All of these parameters are gridded (developed specifically for each grid cell in the modeling domain).

### 8.3 Photochemical Model

In this study, version 4.51 of the CAMx photochemical model (Environ 2004, 2005, 2006) is used. CAMx (Yarwood et al. 1996) is an Eulerian, three-dimensional grid, photochemical model that allows simulation and assessment of “one atmosphere,” i.e., ozone (gaseous) and particulate matter (PM) air pollution. This state-of-science model is modular in structure, which facilitates updates, modifications, and integration of user-developed algorithms and routines. In addition, the model allows for a number of coordinate systems (map projections) and for nested configurations to provide detail and efficiency in simulating larger domains. More recent versions incorporate additional improvements in treatment of ozone and PM.

At its core, CAMx uses a continuity equation (advection-diffusion equation) closed by k-theory for both horizontal and vertical advection, transport, and diffusion. As with other similar photochemical models, e.g., UAM-V and CMAQ,<sup>4</sup> for example, CAMx solves the advection-diffusion equation and accounts for emissions (sources), dispersion/transport, chemical transformations, and removal (sinks). The chemistry term of the equation can be solved with different chemical and lumping mechanisms, e.g., CB-IV or SAPRC.<sup>5</sup> Finally, both dry and wet deposition (scavenging) can be accounted for in CAMx.

The model grid is based on the Arakawa-C stagger configuration (recall that the MM5 is based on the Arakawa-B stagger). In the horizontal, the Arakawa-C scalars and concentrations are located at cell center to represent cell-averaged conditions; whereas, wind vector is carried at the edges (cell interfaces), and the u- and v-components are staggered with respect to each other. In the vertical, scalars are situated at cell center (halfway between layer interfaces), except for vertical entrainment rate and vertical diffusivities, which are at the layer interfaces. The meteorological fields are passed from the meteorological model (e.g., MM5 or uMM5) to CAMx into this grid configuration via a mapping and interpolation step.

Some important features in CAMx include:

1. A flexible two-way nesting and feedback structure (as used in this study) and the ability to activate selected nested grids during the course of model integration
2. The availability of versions of the CB-IV and the SAPRC chemical mechanisms that provide alternate methods of VOC lumping into surrogate species
3. Options for standard or fast chemical kinetics solvers, which can provide significant model speedup where needed

---

<sup>4</sup>The Urban Airshed Model (UAM-V) and Community Multiscale Air Quality (CMAQ) models.

<sup>5</sup>Carbon Bond (CB-IV) and Statewide Air Pollution Research Center (SAPRC) chemical mechanisms.

4. Plume-in grid (PiG) simulation capabilities to handle the details of point-source plumes, e.g., nitrogen oxide (NO<sub>x</sub>) plumes, within the grid until the plume has dispersed well enough for accurate representation within the model grid structure
5. Ozone source apportionment technology (OSAT), which is a CAMx feature that allows users to track the source regions and/or source categories contributing to resulting ozone concentrations at specific (user-selected) grid cells
6. Process analysis (PA) capabilities, whereby the results can be evaluated in terms of model formulation and the relative role of various terms and processes (e.g., process rates for advection, diffusion, chemistry, deposition) in the conservation relations, or provide reaction rate data for all chemical mechanisms in selected grid cells
7. An advanced photolysis model (NCAR's Tropospheric Ultraviolet and Visible [TUV] radiative transfer and photolysis model) that allows modification of photolysis rates to account for changes in albedo, ozone column, zenith angle, elevation, etc., and an option to adjust these rates for the impacts of clouds based on the Regional Acid Deposition Model (RADM) (Chang et al. 1987)

CAMx requires the following as input:

1. Gridded four-dimensional meteorological fields
2. Initial and boundary conditions (observed or analyzed pollutant concentrations fields)
3. Species emission rates (emission inventories)
4. Gridded land-use information and deposition velocities
5. Ozone column and albedo data
6. Chemical parameters and photolysis rates

The meteorological fields are passed from the meteorological model (e.g., MM5 or uMM5) to CAMx, considering their specific grid configurations in the horizontal and vertical directions (after mapping from the Arakawa B to Arakawa C staggered configurations discussed above).

Emission inventories options, both CB-IV [or CB5] and SAPRC-speciated, are available in CAMx. In this study, the SPARC99 mechanism was used. The emission input data were obtained from the California Air Resources Board (ARB) for the episodes of interest. Other input files to CAMx were developed using CAMx-specific pre-processors along with meteorology post-processors.

## **CHAPTER 9: Model Performance Evaluation**

Performance evaluation for meteorological and photochemical models used here has been discussed in detail in (Taha 2007, 2008a-c) and will not be repeated here. Model performance was done for four “regulatory” episodes modeled in this study, including the Central California Ozone Study (CCOS) July–August 2000 episode, the CCOS July 1999 episode, and the Southern California Ozone Study (SCOS) 1997 and 2005 episodes. Model performance was found to be satisfactory in terms of recommended meteorological model benchmarks and photochemical model performance recommendations, e.g., U.S. EPA (1999), Tesche (1988), Tesche et al. (2001).

## CHAPTER 10: Meteorological Modeling Results

For each selected episode-region combination (Table 6.1), the meteorological model was run first for a base-case scenario and then for a scenario with increased urban albedo (heat-island control). Development of this high-albedo scenario is discussed in detail in Taha (2007), and its derivation/development will not be repeated here. The modeling was performed first for all coarse grids (e.g., 36 and 12 km for central California and 45 and 15 km for southern California). This was done for all episode-region combinations. Following these runs for coarse domains, model output was then downscaled to the 4- or 5-km grids (D03), depending on region, for each episode and scenario. In the next paragraphs, the model configuration for these sets of runs is described briefly.

Grids D01 and D02 (see Figure 4.1 a and b) were run with analysis/grid nudging (but no station nudging) throughout the horizontal and vertical domains, including nudging within the boundary layer. At the resolutions used for these domains, no control over the weight of nudging coefficients was done in the vertical. The surface was characterized using the default MM5 methodology (using, however, modified values in the land use lookup tables as discussed earlier). Other options that were selected for D01 and D02 (depending on actual scenario) include:

- MRF PBL or ETA PBL schemes (Hong and Pan 1996; Yamada and Mellor 1975).
- Simple ice physics (Dudhia 1993).
- Rapid Radiation Transfer Model (RRTM) atmospheric radiation scheme (Mlawer et al. 1997).
- Grell cloud scheme on D01 (Grell et al. 1991).
- Multi-layer soil model.
- Vertical moist diffusion in clouds.
- Grid nudging FDDA. In grid analysis for D01 and D02, temperature, moisture, and wind were all nudged.
- The nudging was also done through the boundary layer.

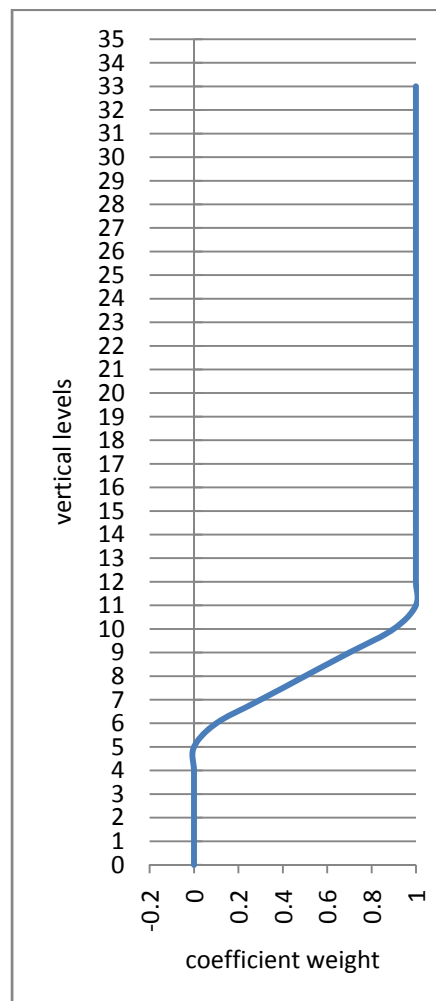
For the 4- or 5-km grids (D03), the configurations include:

- Modified surface characterization, as discussed earlier (i.e., the MM5 default input is overridden) especially in areas of interest (SFBA, Sacramento, Fresno, and Los Angeles basin)
- Use of a vertical profile for scaling the nudging coefficients, so as to increase in weight away from the boundary layer and the surface (see Figure 10.1)
- ETA PBL scheme

- Simple ice physics
- RRTM radiation scheme
- Multi-layer soil model for the hybrid RA meso-urban model.

With respect to *grid nudging*, a modified approach (Taha 2006,2007) was used in this study such that the weight of nudging coefficients was varied in the vertical direction according to a prescribed profile (Figure 10.1). The purpose of the vertical variation is to allow the model to freely develop unforced meteorological fields within the canopy layer and the lowest parts of the boundary layer, but is gradually restricted away from the surface towards the top of the domain. For grid D03 in both the central and southern California domains (33 full-sigma levels), full nudging was assumed from level 11 through the top of the domain (Figure 10.1). From levels 10 through 5, nudging weight decreases from 0.90 to 0.00 and remains at 0.00 until reaching the surface. Recall that this is not the *actual* value of the nudging coefficient but its weight (the factor by which it is multiplied).

**Figure 10.1: Vertical Profile (Variation) of Normalized Nudging-Coefficients Weight**



It would be a very lengthy task to discuss here the modeled meteorologies from all episodes. Some aspects of meteorology were already presented in the CART analysis. Thus here, we only describe, as an example, the base-case meteorology for the episodes July–August 2000, July 1999, and July 2005 (for central and southern California) that are considered “regulatory” modeling episodes. The base-case scenarios of all remaining episodes will not be discussed, only the differences in meteorology (i.e., air-temperature changes).

## 10.1 BASE METEOROLOGY

### 10.1.1 BASE-CASE 2000 (Central California)

#### 10.1.1.1 SFBA-Sacramento Domain

On 27 July, the highest temperature in the SFBA-Sacramento domain is 32°C (89.6°F) during the hours 1700 through 1900 Pacific Daylight Time (PDT). At 1700 PDT the area covered by higher temperatures is larger, and the peak temperature is found in north Sacramento County at 32°C (89.6°F). At that hour, Sacramento is within a 1°C heat island relative to upwind areas to the west. At 1500 PDT, a heat island of 2°C (4°F) in San Jose / Santa Clara County is seen (relative to upwind areas to the northwest). Figure C1-1 in Appendix C shows the temperature and wind fields at 1500 PDT on 27 July. The urban heat islands (UHI) are as follows: Livermore 1°C (2°F); Concord-Walnut Creek 1°C; and San Jose 1°C. The flow pattern at this time of day is generally westerly and is northwesterly in the southern part of the domain. During the earlier parts of the day, there is a coupling in the flow from the SFBA to Sacramento.

The same pattern is seen again on 28 July and the maximum temperature is 32°C (89.6°F). However, at 1500 PDT, the UHI is now 3°C (5°F) over San Jose and up to 3°C (37.4°F) in the Morgan Hills / Gilroy area. A small 1°C (2°F) UHI is found in the Mill Valley area and a 2°C (4°F) UHI in the Concord / Walnut Creek area. The Sacramento UHI is not well defined during these hours. Figure C1-2 shows the temperature and wind fields at 1500 PDT on 28 July. In Livermore, the UHI is 2°C (4°F). The flow pattern is similar to that of the day before, and there also is coupling from the SFBA to Sacramento during the earlier parts of the day.

On 29 July, the absolute temperature peaks at 34°C (93.2°F) in the northern parts of the domain shown in Figure C1-3. The majority of the land area is within the 30°C to 34°C (86.0°F to 93.2°F) range by 1700 PDT. Heat islands are as follows (relative to each upwind area): Mill Valley 2°C (4°F); San Mateo through San Jose to Gilroy 3°C (5°F); Santa Cruz 3°C (5°F); Concord-Walnut Creek 2°C (4°F); North Highlands-Roseville-Lincoln 1°C (2°F); and Livermore 2°C (4°F). The flow pattern is roughly similar to that of the day before but with a stronger westerly component. Earlier in the morning, sea-breeze flow provided a mechanism for coupling the SFBA and Sacramento regions.

The next day, 30 July, the highest temperature is again 34°C (93.2°F) and the flow/temperature patterns are similar to the day before. Heat islands at 1500 PDT are as follows: Mill Valley 2°C (4°F); Concord-Walnut Creek 2°C (4°F); (San Jose 2°C (4°F); Gilroy 3°C (5°F); Santa Cruz 3°C (5°F); Livermore 2°C (4°F); and Sacramento 2°C (4°F) (at 1700 PDT, not shown). Figure C1-4 shows the flow and temperature fields at 1500 PDT on 30 July.

On 31 July, the highest temperature is 36°C (96.8°F), and the flow pattern is mostly northwesterly, with no coupling from the SFBA to Sacramento. As seen in Figure C1-5, the entire land area is within high temperatures. Heat islands, while less defined, at 1500 PDT are as follows: Mill Valley 2°C (4°F); San Francisco 1°C (2°F); Concord-Walnut Creek 1°C (2°F); San Jose 4°C (7°F); Gilroy 4°C (7°F); Santa Cruz 3°C (5°F); Livermore 3°C (5°F); and Sacramento 1°C (2°F). Figure C1-5 shows the flow and temperature fields at 1500 PDT on 31 July.

On 1 August, the highest temperature is 36°C (96.8°F), and the flow pattern is mostly westerly, with no coupling from the SFBA to Sacramento earlier in the day. The flow was more northwesterly earlier in the morning. As seen in Figure C1-6, the entire land area of this domain is within high temperatures. Heat islands are less defined at this hour but more so at 1900 PDT. At that hour, their magnitudes are similar to those of the previous day.

Finally on 2 August, the peak temperatures reach 34°C (93.2°F), and the flow varies from earlier in the day to mid-day to later in the afternoon. At 1500 PDT, for example as seen in Figure C1-7, the flow has a westerly component but flow divergence (to the north and to the south) in the eastern part of the domain. Again, heat island intensities are similar to those of the previous two days.

#### *10.1.1.2 Fresno-Visalia Domain*

On 27 July, the highest temperature in the Fresno-Visalia domain is 36°C (96.8°F) during the hours 1500 through 1700 PDT. The flow pattern on that day is generally northwesterly and westerly through the area, turning southwesterly in the eastern parts of Fresno and Tulare counties. At 1700 PDT, the time of the maximum UHI over Fresno, the UHI is 1°C (2°F). A similar UHI is found over Visalia. Figure C2-1 shows the modeled fields for 1700 PDT 27 July. Smaller urban areas such as Madera and Hanford do not develop heat islands. Of note, which applies to other days of the episode as well, is that beginning about evening time, the flow in eastern Fresno County (and in the eastern part of the domain in general) acquires an easterly component because of the down slope flow from the eastern hills and mountains (this flow occurs in general, regardless of the flow pattern in the western part of the domain, unless it is stronger than a certain threshold).

On 28 July, the temperature and flow patterns are essentially similar to those of the day before. The heat island at 1500 PDT is 1°C (2°F) over both Fresno and Visalia, as seen in Figure C2-2 for 1500 PDT on 28 July. On 29 July, the maximum temperature reaches 36°C (96.8°F), as with the previous days. However, the flow field now has a stronger westerly component, with smaller veering towards the northeast than the days before. A 1°C (2°F) heat island is seen over Fresno at 1700 PDT (Figure C2-3) but none over Visalia.

On 30 July, the highest temperatures in the area reach up to 40°C (104°F) between 1500 and 1700 PDT. The flow pattern returns to that of the earlier days of the episode; that is, northwesterly in the western domain turning southwesterly in the eastern domain. A heat island of 1°C (2°F) is seen over the Fresno-Visalia area from 1500 through 1900 PDT. Figure C2-4 shows the modeled fields at 1500 PDT on 30 July.

On 31 July, the maximum temperatures and the flow pattern are similar to those of the day before. However, heat islands are not well defined on that day, except for a much smaller (spatial extent) heat island of 1°C (2°F) over Fresno at 1700 PDT. Figure C2-5 shows the simulated fields at 1700 PDT on 31 July.

On 1 August, the flow in the region is southerly and southwesterly during the early hours of the day (through 0900 PDT). It then becomes westerly, turning southwesterly in the afternoon. The maximum temperature is 40°C (104.0°F) and the UHI is 1°C (2°F) over Fresno and Visalia, as seen in Figure C2-6 for 1300 PDT on 1 August. On 2 August, the flow is disorganized through 1100 PDT, becoming southerly and southwesterly in the afternoon. The maximum temperature is 36°C (96.8°F) and a 1°C (2°F) relatively small UHI is seen over Fresno at 1500 PDT (Figure C2-7).

### 10.1.2 BASE-CASE 1999 (Central California)

#### 10.1.2.1 SFBA-Sacramento Domain

On 5 July, the highest temperature in the SFBA-Sacramento domain is 32°C (89.6°F) at 1700 PDT. At that hour, although not well defined, Sacramento is within a 1°C (2°F) heat island (especially in northwest Sacramento County) relative to upwind areas to the west. At 1500 PDT, a heat island of 2°C (4°F) in San Jose / Santa Clara County exists (relative to upwind areas to the northwest) and a 3°C (5°F) heat island in Gilroy also appears. Figure C9-1 shows the temperature and wind fields at 1500 PDT on 5 July. At that hour, Livermore has a 3°C (5°F) UHI and Concord-Walnut Creek 2°C (4°F) UHI. The flow pattern at this time of day is generally westerly in the northern half of the domain but dominantly northerly in the southern half of the domain. There is no coupling between the SFBA and Sacramento.

On 6 July, the maximum temperature is 32°C (89.6°F) in both the northern and southeastern parts of the domain (at 1700 PDT). This day is generally windier than the previous day in the central domain and, as a result, heat islands are essentially nonexistent over most urban areas in the SFBA and Sacramento, except for a 1°C (2°F) heat island over Gilroy and over Santa Cruz, as seen in Figure C9-2 (at 1500 PDT). The flow pattern shows a generally westerly flow (over the Golden Gate) that splits into southwesterly flow to Sacramento (thus coupling exists) and northwesterly towards San Joaquin and Madera counties. The flow is generally faster than the day before, now reaching up to or higher than 7 meters per second ( $\text{m s}^{-1}$ ) in western and central portions of the domain.

On 7 July, a relatively cooler day, the absolute temperature peaks at 30°C (86.0°F) during the hours 1500 through 1900 PDT. The higher temperatures are seen mainly in the northern parts of the domain, as in Figure C9-3 (1700 PDT on 7 July). Heat islands can be seen as follows (relative to each regions upwind area): Mill Valley 1°C (2°F); San Jose 2°C (4°F); Morgan Hills through Gilroy 1°C (2°F); Santa Cruz 2°C (4°F); Concord-Walnut Creek 2°C (4°F); and Livermore 1°C (2°F). The flow is predominantly northwesterly (thus no SFBA-Sacramento coupling), except over the SFBA, where it is westerly. Speeds are under 5  $\text{m s}^{-1}$  over most of the domain.

On 8 July, the highest temperature is again 32°C (89.6°F) between 1500 and 1900 PDT. Heat islands are not well defined on this day, except for a 1°C (2°F) heat island in the San Jose-Gilroy

area, a 2°C (4°F) heat island over Santa Cruz, and a 1°C (2°F) heat island over Concord-Walnut Creek. Figure C9-4 shows the flow and temperature fields at 1500 PDT on 8 July. The flow field is generally westerly in the northern domain and mainly northwesterly in the southern half of the domain.

The next day, 9 July, the highest temperature is 32°C (89.6°F) between 1500 and 1700 PDT. The flow pattern is westerly over the Golden Gate, turning generally southwesterly/southerly over the northern half of the domain and northwesterly/northerly over the southern half of the domain. Wind speeds range up to 5 m s<sup>-1</sup>. There is a weak coupling from the SFBA to Sacramento. As seen in Figure C9-5 (1500 PDT 9 July), heat islands are as follows: Mill Valley 1°C (2°F); Sacramento-Roseville-Lincoln 1°C (2°F); Concord 2°C (4°F); San Jose 2°C (4°F); Gilroy 3°C (5°F); Santa Cruz 2°C (4°F); and Livermore 2°C (4°F).

On 10 July, the highest temperature is 34°C (93.2°F) between 1700 and 1900 PDT, especially in the northern part of the domain. The flow pattern is similar to that of the day prior, except that over the Golden Gate, the flow has a more southwesterly component. There is weak coupling between the SFBA and Sacramento. As seen in Figure C9-6 (1500 PDT 10 July), heat islands are: 2°C (4°F) in Mill Valley; 1°C (2°F) in Sacramento; 1°C (2°F) in North-Highlands-Lincoln; 1°C (2°F) in Concord; 2°C (4°F) in Livermore; 1°C (2°F) in San Mateo-Palo Alto; 2°C (4°F) in San Jose-Morgan Hills-Gilroy; and 3°C (5°F) in Santa Cruz.

On 11 July, the peak temperatures reach 38°C at 1700 PDT. As seen in Figure C9-7 (at 1500 PDT on 11 July), heat islands are 1°C (2°F) over Sacramento, North Highlands, and Roseville; 1°C (2°F) over Mill Valley; 2°C (4°F) over Concord-Walnut Creek; 1–2°C (2°F–4°F) over Livermore; 1°C (2°F) over San Jose, Morgan Hills, and Gilroy; and 1°C (2°F) over Santa Cruz. The flow field shows very weak coupling between the SFBA and Sacramento, and the flow is mainly westerly in the north part of the domain, but northwesterly/northerly in the south part of the domain. There is also some easterly/northeasterly flow in the southern part of the domain.

The simulations show that 12 July is the hottest day of this episode, with temperature reaching 40°C (104°F) (at 1700 PDT). Figure C9-8 shows the modeled fields at 1500 PDT on 12 July. The flow is generally similar to that of the day before. Heat islands are 3°C (5°F) in Concord-Walnut Creek and 2°C (4°F) in San Jose. Other urban areas on this day do not have clearly identifiable heat islands.

Finally, on 13 July, a cooling trend begins, and the maximum temperature reaches up to only 32°C (89.6°F) during the hours 1300 through 1700 PDT. These high temperatures occur at various locations throughout the domain, and the wind flow pattern changes rapidly from one hour to another. As a result of the disorganized flow, e.g., as seen in Figure C9-9 (1300 PDT on 13 July), heat islands are not discernible on this day, but generally in the order of 1–2°C (2°F–4°F) at various times during the day.

#### 10.1.2.2 *Fresno-Visalia Domain*

On 5 July, the highest temperature in the Fresno-Visalia domain is 36°C (96.8°F) during the hours 1500 through 1900 PDT. The flow pattern on that day is generally northwesterly and westerly through the area, then turning southwesterly in the eastern parts of Fresno and Tulare

counties. At 1900 PDT, the UHI over Fresno and Visalia is 1°C (2°F) as seen in Figure C10-1 for 1900 PDT 5 July. Smaller urban areas such as Madera and Hanford have no heat islands on that day. Of note, and as discussed earlier for the July–August 2000 base episode, a feature that applies to other days of the episode in general as well is that beginning about evening time, the flow in eastern Fresno County (and in the eastern part of the domain in general) reverses and acquires an easterly component because of the down slope flow.

On 6 July, the maximum temperature is 38°C (89.6°F) at 1500 PDT. The flow pattern is essentially similar to that of the day before. The heat island at 1300 PDT is 1°C (2°F) over both Fresno and Visalia, as seen in Figure C10-2 (for 1300 PDT on 6 July). On 7 July, the maximum temperature reaches 32°C (89.6°F), and the flow pattern is similar to that of the previous two days. An urban heat island of 1°C (2°F) develops over Fresno at 1300 (as seen in Figure C10-3 for 1300 PDT) and remains through 1700 PDT. A heat island of the same magnitude develops later (between 1700 and 1900) over Visalia.

On 8 July, the highest temperatures in the area reach up to 34°C (93.2°F) between 1500 and 1900 PDT. These high temperatures are over the Madera-Fresno-Visalia region. A heat island of 1°C (2°F) develops over Fresno and Visalia, as seen in Figure C10-4 (for 1500 PDT on 8 July). The flow pattern is northwesterly over the western part of the domain and, unlike previous days, it retains a westerly component over the eastern part of the domain (rather than southwesterly as in the previous days).

On 9 July, the maximum temperatures reach 34°C (93.2°F) in the domain, from 1300 through 1700 PDT. The flow pattern is northwesterly in the western part of the domain and turns southwesterly in eastern Fresno County. However, after about 1700 PDT, the flow in the eastern part of the domain becomes disorganized and later acquires an easterly component in east Fresno County as a result of downslope flow from the mountains. A short-lived heat island of 1°C (2°F) is seen over Fresno and Visalia at 1300 PDT (Figure C10-5) and disappears between 1500 and 1700 PDT. On 10 July, the highest temperatures in the domain reach up to 34°C (93.2°F) from 1500 through 1900 PDT. Urban heat islands are difficult to discern on that day, but the Fresno-Visalia-Hanford area is about 1°C (2°F) warmer than in surrounding areas, as seen in Figure C10-6 for 1700 PDT (on 10 July).

On 11 July, the highest temperature is 36°C (96.8°F) from 1500 to 1700 PDT. The flow pattern on that day is generally opposite in direction to that in the previous days. As seen in Figures C10-7 (1500 PDT on 11 July), the flow has a general easterly and southeasterly flow, with higher speeds (greater than 5 m s<sup>-1</sup>). A heat island of 1°C (2°F) develops over Fresno and, at this hour, is displaced to the west and north (see Figure C10-7) by the southeasterly flow in the area. Later during this day, the flow acquires a northeasterly component throughout most of the domain that persists through the next morning hours (of 12 July).

On 12 July, the highest domain-wide temperature is 40°C (104°F) at 1500 PDT. Between 0900 and 1100 PDT, the flow changes from predominantly easterly to disorganized flow, which continues through the rest of the day, e.g., as seen in Figure C10-8 (for 1500 PDT). Urban heat islands are not discernible. Finally, on 13 July, the highest domain-wide temperature is 34°C

(93.2°F) from 1300 to 1900 PDT. The flow re-assumes the general pattern of the earlier days of the episode, that is, mostly northwesterly in the western part of the domain turning southwesterly in east Fresno County. However, the flow becomes more northerly after 1500 PDT, at which time the down slope flow also starts. As seen in Figure C10-9 (for 1700 PDT), there is a 1°C (2°F) heat island over Fresno and Visalia.

### 10.1.3 BASE CASE 2005 (Southern California)

This base case scenario is for the southern California domain. The regulatory episode is July 14 through 19, 2005 (the episode modeled here is much longer, as part of several other episodes). Thus, only those days (July 14–19) are discussed here. The other days of the episodes are discussed under the multi-episodic simulation runs analysis in Section 12.4. And since the year 2005 is not far off in the past (unlike the 2000 and 1999 episodes for CCOS), no future-year runs were made for southern California. Of note, due to the size of the Los Angeles Basin, the complexities of its topography, and its expansive *continuous* urbanization, urban heat islands are not well-defined and will not be discussed in this section. Thus, the figures presented here (since UHIs are not discussed) are arbitrarily selected to represent various hours during the episode. In this section, we discuss the base-case meteorological fields.

On 14 July, the highest domain-wide temperatures reach up to 44°C (111.2°F) between the hours of 1300 and 1700 PDT. These high temperatures occur in the desert areas to the west of Salton Sea (at the boundary between San Diego and Imperial counties), in the Palm Springs region, and in the San Bernardino desert (east of Twentynine Palms). The flow is westerly and northwesterly over the ocean and is generally westerly (though disorganized) over land. Figure C17-1 shows the modeled fields at 1500 PDT on 14 July.

On 15 July, the highest temperatures reach 44°C (111.2°F) between the hours of 1500 and 1700 PDT. These high temperatures, again, occur in the same areas identified above; that is, Salton City, Palm Springs, and Twentynine Palms. The flow pattern is similar to that on 14 July, in general, as seen in Figure C17-2 (for 1900 PDT on 15 July). On 16 July, the maximum domain-wide temperature is again 44°C (111.2°F) between 1500 and 1700 PDT in the areas identified above as well as in central San Bernardino County. As seen in Figure C17-3 (for 1500 PDT, 16 July), the flow is mostly westerly over the ocean, turning generally southerly and southwesterly over land.

On 17 July, the temperature pattern and maxima are similar to those of the day before. And, while the flow field is generally westerly over the ocean, it is now relatively disorganized over land, e.g., as seen in Figure C17-4 for 1500 PDT on 17 July. On 18 July, the highest temperature reaches up to 48°C (118.4°F) at 1500 PDT. These high temperatures occur in San Bernardino and Riverside counties (Figure C17-5 for 1500 PDT). The flow is mostly westerly over the ocean and disorganized over land, consistent with no-gradient, high-pressure situation.

On 19 July, the highest temperatures drop (relative to the day before) to 44°C (111.2°F) between the hours of 1300 through 1700 PDT. The flow over the ocean is generally northwesterly, and over land it becomes relatively more organized than during the day before. Now over land, the

flow has a dominant westerly or southwesterly component, as seen in Figure C17-6 (for 1700 PDT).

#### 10.1.4 Modeled Multi-episodic Characterization

Tables 10.1 and 10.2 provide a qualitative summary of temperature, wind, and cloud-cover fields of the episodes that will be discussed in the air-quality impacts analysis in Chapter 12. For central California, the dominant wind direction is provided in order to qualitatively evaluate transport and coupling between the SFBA and Sacramento or the SFBA and Fresno regions. In these tables, the entries are as follows:

- Column 1: Modeled episode and run ID
- Column 2: Domain-wide maximum daily air temperature (range over all episode days)
- Column 3: Dominant daytime surface wind direction (from) in the San Francisco Bay Area during the episode
- Column 4: Dominant daytime surface wind direction (from) in the Sacramento region during the episode
- Column 5: Dominant daytime surface wind direction (from) in the Fresno area during the episode
- Column 6: Daytime cloud-cover range over the Pacific Ocean part in the domain during the episode
- Column 7: Daytime cloud-cover range overland (over California) during the episode. Cloud-cover range as a fraction of either the Pacific Ocean (in the domain) or over California is as follows:
  - VL Zero or near zero (very low)
  - L Low (< 33 percent cover)
  - M Medium (> 33 percent and < 66 percent)
  - H High (> 66 percent cover)

Note that most of the clouds forming during daytime overland in central California are due to upslope flow near the eastern ranges of the central valley. However, cloud formations throughout the State are also noticed at times during the simulations. The tables below are based on a large number of simulations that are not shown in the figures, but are provided as summary.

**Table 10.1: Central California Modeled Meteorology**

1	2	3	4	5	6	7
		<b>Dominant Wind Direction</b>			<b>Cloud Cover</b>	
<b>Episode</b>	<b>Daily max Tair domain</b>	<b>SFBA</b>	<b>Sacramento</b>	<b>Fresno</b>	<b>Ocean / Coast</b>	<b>Overland</b>
Jul–Aug 2000 (run Reg.)	40–44°C (104.0–111.2°F)	NW/W	W/NW	NW/W	M/H	VL
Jul 1999 (run Reg.)	34–40°C (93.2–104.0°F)	NW/W/SW	W/NW/SW	NW/W/SW/SE	L/H	VL
Jun 14–27, 2000 (runA1)	34–42°C (93.2–107.6°F)	N/NW/W/SW	NW/SW	NW/W/SW	VL/L	VL/L
Jul 19–Aug 1, 2000 (runB)	41–42°C (105.8–107.6°F)	NW	NW	NW	VL/L	VL
Aug 4–8, 2000 (runC)	38–42°C (100.4–107.6°F)	W/NW	SW/NW	SW/W/NW	VL/L	VL
Aug 11–18, 2000 (runD)	38–42°C (100.4–107.6°F)	NW	NW	NW	VL	VL
May 18–31, 2001 (runE) ++	34–38°C (93.2–100.4°F)	NW/W	NW/W	NW/W	VL/L	VL
Jun 20–22, 2001 (runF)	40°C (104°F)	NW/W/SW	NW/W	W/SW	VL	VL
Jul 4–19, 2002 (runH1) **	40–46°C (104–114.8°F)	NW/W/SW	NW/W/SW	NW/W/SW	VL/L/M	VL
Jul 10–22, 2002 (runH2) ++	38–42°C (100.4–107.6°F)	NW/W/SW	NW/W/SW	NW/W/SW	VL/L/M	VL
Aug 8–20, 2002 (runI)	38–44°C (100.4–111.2°F)	NW/W/N	NW/W/SW	NW/W/SW	L/M	VL
Jun 3–27, 2003 (runJ)	34–40°C (93.2–104°F)	W/NW	W/SW/NW	W/NW/SW	L/M/VL	VL/L
Jun 25–Jul 17, 2003 (runK)	38–40°C (100.4–104°F)	N/NW/W	NW/W	NW/W	VL/L	VL
Jul 25–Aug 4, 2005 (runM)	38–42°C (100.4–107.6°F)	NW/W	NW/W	NW/W	L	VL

++ A low-pressure system develops over California

\*\* A high-pressure system develops over California, followed by a low-pressure system

**Table 10.2: Southern California Modeled Meteorology**

1	2	6	7
		<b>Cloud Cover</b>	
Episode	Daily max Tair domain	Ocean / Coast	Overland
May 23–Jun 16, 2000 (runN)	34–40°C (93.2–104°F)	VL/L	VL
May 22–Jun 8, 2001 (runO)	34–40°C (93.2–104°F)	VL/L	VL
Aug 13–17, 2001 (runP)	40–42°C (104–107.6°F)	VL/L	VL
Jul 9–24, 2003 (runQ)	40–44°C (104–111.2°F)	VL (0)	VL (0)
Jul 12–26, 2005 (runR)	40–44°C (104–111.2°F)	VL/L	VL

## 10.2 METEOROLOGY PERTURBATION SCENARIOS

This section presents the perturbations in air temperature at the lowest atmospheric layer of the model. These temperature changes correspond to the scenario of albedo increase discussed earlier. For compactness, we present here only those hours when the largest cooling occurs or hours around that time (as stated in each case).

### 10.2.1 PERTURBATION 2000 (Central California)

#### 10.2.1.1 SFBA-Sacramento

On 27 July at 1300 PDT, the largest cooling is 0.7°C (1.3°F) in both the SFBA and Sacramento. In the SFBA, areas surrounding the bay are cooled by up to 0.7°C (1.3°F), especially in the denser urban parts such as San Jose, East Bay, Concord-Walnut Creek, and Livermore. In the Sacramento area, the largest cooling is seen east of downtown, south of the American River, and in the Roseville-Lincoln areas. Figure C3-1 shows the temperature differences at 1300 PDT on 27 July. The absolute wind field of the high-albedo case is superimposed on the temperature difference.

On 28 July, the maximum cooling is 0.8°C (1.4°F) between 1100 and 1300 PDT. Figure C3-2 shows the modeled differences at 1100 PDT on that day. While the overall pattern is similar to that of the day before, temperature reductions are better defined, e.g., over San Jose, Oakland-Berkeley, and Concord-Walnut Creek. In the Sacramento area, the cooling is well defined south of the American River and north of it from downtown through North Highlands, and to Roseville-Lincoln.

On 29 July, the largest cooling occurs between 1100 and 1300 PDT, reaching up to 1°C (2°F), as seen in Figure C3-3 for 1100 PDT. Cooling is well defined around the San Francisco Bay, in San Jose (up to 1°C [2°F]), in Concord (up to 0.8°C [1.4°F]), and in Sacramento (south and north of the American River), up to 1°C (2°F) as well. The maximum temperature reduction reaches 1.1°C (2°F) at 1100 PDT on 30 July in both the San Jose and Sacramento areas. Figure C3-4 shows those differences at 1100 PDT. Again, the cooling is better defined in the San Jose and Sacramento regions.

On 31 July, the largest decrease in air temperature reaches 1.1°C (2.0°F) between the hours 0900 and 1100 PDT. Figure C3-5 shows the differences at 1100 PDT on that day. The largest cooling is seen around the San Francisco Bay Area, with peaks in San Francisco, Santa Clara and San Jose, Oakland, and Concord. In Sacramento, the cooling is largest east of downtown, south of the American River, and in Arden-Fair Oaks-Folsom area.

On 1 and 2 August, the cooling becomes larger—up to 2°C (4°F) or more—but the signal becomes relatively noisy, and therefore these days will not be considered in this analysis of cooling and impacts on air quality for the SFBA-Sacramento region.

#### 10.2.1.2 *Fresno-Visalia*

On 27 July, the maximum cooling achieved over Fresno reaches up to 0.8°C (1.4°F) at 1100 PDT, as seen in Figure C4-1. The cooling is well defined and centered over Fresno and slightly downwind of it. No changes in surface properties were assumed for Visalia (no increase in urban albedo) and, as a result, there is no cooling over that area. The same pattern is seen during the next three days on 28, 29, and 30 July at 1100 PDT, except now the largest decrease is 0.6°C (1.1°F), as seen in Figures C4-2, C4-3, and V4-4.

On 31 July at 1100 PDT (Figure C4-5), the largest decrease is 0.5°C (0.9°F) and has the same spatial characteristic as for the days prior. On 1 and 2 August, the cooling becomes larger—up to 1.5°C (2.7°F) or more—but as discussed above, the signal becomes relatively noisy, and these days are not considered in this analysis. The reason for the generally smaller temperature reductions in Fresno compared to the SFBA or Sacramento is the smaller modifiable area for increasing urban albedo.

### 10.2.2 PERTURBATION 1999 (Central California)

#### 10.2.2.1 *SFBA – Sacramento*

In this section, as with the July–August 2000 episode above, the impacts on meteorology (focus on air temperature) resulting from increased urban albedo are discussed. Figures are presented for the hour (on each day) with largest cooling effect. Recall that the differences presented in this report correspond to reasonably high increases in urban albedo, not extreme increases.

On 5 July, the largest cooling occurs at 1100 PDT and reaches up to 1.4°C (2.5°F) in San Jose. In the SFBA, areas surrounding the Bay area cooled by up to 1°C to 1.3°C (2°F to 2.3°F), especially in the denser urban parts such as San Jose, East Bay, and Concord-Walnut Creek. In the Sacramento area, the largest cooling, between 1°C and 1.2°C (2°F and 2.2°F), is seen east of downtown, south of the American River, to Folsom, and in the Roseville-Lincoln areas. Figure C11-1 shows the temperature differences at 1100 PDT on 5 July. As before, the absolute wind field of the high-albedo scenario is superimposed on the temperature difference.

On 6 July, the maximum cooling is between 1.6°C and 1.8°C (2.9°F and 3.2°F) in the San Jose area, again at 1100 PDT. Figure C11-2 shows the modeled differences at that hour on that day. The area affected by cooling is no longer contiguous, as in the day before, but is isolated over the San Jose area, East Bay, Concord-Walnut Creek, and Sacramento, North Highlands, Roseville, and Lincoln.

On 7 July, the largest cooling occurs at 1100 PDT and reaches up to 1.3°C (2.3°F). Instead of showing the same hour again (and the same spatial characteristics), the hour of 1300 PDT, with a relatively smaller cooling of up to 1°C (2°F) is shown instead, in Figure C11-3. It can be seen that, again, the largest cooling occurs around the San Francisco Bay Area, particularly in the San Jose area and in the East Bay. Smaller cooling of up to 0.8°C (1.4°F) can be seen in the Sacramento region, from Elk Grove-Florin to east of downtown, to Folsom, as well as over Roseville.

On 8 July, the largest cooling, up to 2°C (4°F), occurs at 1100 PDT, as seen in Figure C11-4. This largest cooling again occurs in the San Jose area, and significant cooling occurs around the San Francisco Bay Area. One can also notice smaller cooling in the Livermore area, as well as in Concord-Walnut Creek. In the Sacramento region, the largest cooling reaches up to 1°C to 1.2°C (2°F to 2.2°F) south of the American River and in Roseville. Most of Sacramento County is cooler, although by a range of temperatures differences.

On 9 July, the largest cooling occurs at hours 1100 and 1300 PDT, respectively reaching 1.6°C and 1.5°C (2.9°F and 2.7°F), respectively. Here we show the cooling at 1300 PDT (Figure C11-5). At this hour, the largest cooling affects an area from Palo Alto through San Jose (up to 1.5°C [2.7°F]), as well as around the San Francisco Bay Area at smaller reductions. In the Sacramento area, the largest cooling reaches up to 1°C (2°F) south of the American River and in the Roseville area. On 10 July, the largest cooling is achieved between the hours 1100 and 1500 PDT, reaching up to 1.5°C (2.7°F). Figure C11-6 shows the temperature change at 1100, and is generally similar to that of the day before, both in magnitude and spatial pattern.

On 11 July at 1100 PDT, the largest cooling achieved is 2.2°C (4°F) in the Palo Alto-to-San Jose area, as well as significant cooling around other areas in the SFBA and in the Sacramento region. As seen in Figure C11-7 (for 1100 PDT), there is now also some warming at that hour affecting a relatively small area, reaching up to 1°C (2°F). That warming is found over north Santa Cruz County and disappears during the subsequent hours. For the remaining days, 12 and 13 July, the cooling effect is larger than 2°C (4°F) in several areas, and there is also warming in other areas. However, the signal is not as clear as during the previous days (i.e., the association between changes in temperature and the modified regions is not clear). Part of this may also be a result of model noise. Thus, days 12 and 13 are not used or discussed in this report.

#### 10.2.2.2 *Fresno-Visalia*

As discussed before, the impact of increased urban albedo is mainly a reduction in daytime air temperature. There is no impact on nighttime temperatures, and therefore they are not shown in the figures. Of note, while the cooling effect persists throughout daylight hours, in this discussion we show only the hour when the largest cooling occurs.

On 5 July, the largest cooling over the Fresno area is 0.7°C (1.3°F) at 1100 PDT and is displaced to the southeast by the northwesterly flow. This can be seen in Figure C12-1 for 1100 PDT on that day. On the next day, 9 July, the largest cooling of 0.8°C (1.4°F) is achieved at 0900 PDT, with the same spatial character as the day before. Figure C12-2 shows the temperature

difference field at 0900 PDT on 6 July. As before, the wind field of the high-albedo scenario is superimposed on the temperature difference field.

On 7 July, the largest cooling is again at 1100 PDT and reaches up to 0.8°C (1.4°F) over the Fresno area. As seen in Figure C12-3 (for 1100 PDT), the cool area (temperature perturbation) is also displaced (advected) by the northwesterly flow. On 8 July, the largest cooling is achieved at 1100 over the Fresno area. It reaches up to 0.8°C (1.4°F) in cooling. At this hour some possible model noise is also evident in the temperature field, with both cooling and warming occurring elsewhere in the domain, as seen in Figure C12-4 (for 1100 PDT). The warming disappears in subsequent hours.

On 9 July, a similar pattern is seen, where the largest cooling of 0.8°C (1.4°F) occurs at 1300 PDT over the Fresno area. Two other areas are also affected by temperature change at this hour, as seen in Figure C12-5 (for 1300 PDT). One is an increase in temperature, the other a decrease. Both of these changes (increase and decrease), which are not over the Fresno area, disappear during subsequent hours. On 10 July, the largest cooling of 0.6°C to 0.7°C (1.1°F to 1.3°F) occurs between the hours of 0900 and 1100 PDT over the Fresno area. Figure C12-6 shows the temperature change at 1100 PDT. While the main temperature decrease occurs over Fresno, the perturbation is still advected to the southeast (all the way to Visalia) by the northwesterly flow. On 11, 12, and 13 July, the signal can no longer be directly associated with specific surface modifications. Therefore, these days will not be included in the analysis. Also, as discussed earlier, the reason for the smaller reduction in Fresno compared to the SFBA or Sacramento is the smaller modifiable area for increasing urban albedo.

### 10.2.3 PERTURBATION 2005 (Southern California)

On 14 July, the largest cooling of 2.8°C (5°F) occurs at 0900 PDT in both Los Angeles and Orange counties. At 1100, the largest cooling is 2°C (4°F), mainly in Los Angeles County, as seen in Figure C18-1 (for 1100 PDT). As before, the wind field for the high-albedo scenario is superimposed on the temperature-difference field. Notice in the figure that parts of San Bernardino County are also affected by the lowered air temperatures. Also of note is that other urban areas in the domain, in the counties of San Diego, Imperial, Ventura, Santa Barbara, San Luis Obispo, and Kern, do not see temperature decreases because no surface modifications were assumed in these areas.

On 15 July, the largest cooling occurs at 1100 PDT, as seen in Figure C18-2 (for 1100 PDT on 15 July). The largest cooling occurs in Los Angeles County and significant cooling is also seen in both Orange and San Bernardino counties. On 16 July, the largest cooling occurs at 0900 PDT, reaching up to 3.9°C (7°F) over Los Angeles and Orange counties. Some cooling can also be seen over San Bernardino County. Figure C18-3 show the modeled temperature perturbation at 0900 PDT on 16 July. On 17 July, the largest cooling is achieved at 0900 PDT reaching up to 2°C (4°F) in Los Angeles County. For the sake of providing diverse information, we show here the temperature reduction at 1700 PDT (Figure C18-4), when the largest cooling in the domain reaches 1.2°C (2.2°F) in several locations in the counties of Los Angeles and Orange. Cooling in the counties of Riverside and San Bernardino at this hour reaches up to 0.7°C (1.3°F).

On 18 July, the largest cooling occurs at 1300 PDT (as shown in Figure C18-5) mainly over Los Angeles County. Cooling in San Bernardino County at this hour reaches up to 1°C and in Orange County up to 1.4°C (2.5°F). Finally on 19 July, the largest cooling is at 1300 PDT reaching up to 1.4°C (2.5°F) over Los Angeles County (there also is a very small area affected by an increase of 1.4°C (2.5°F) that disappears in subsequent hours). Here we show the temperature change at 1500 PDT (Figure C18-6), where the largest cooling is 1.1°C (2°F) over both Los Angeles and Orange Counties.

## 10.3 MULTI-EPISODIC ANALYSIS OF METEOROLOGY PERTURBATIONS

In this section, results from the above three regulatory episodes are discussed, as are those from all the other episodes. These other episodes represent the bulk of the multi-episodic simulations done in this study. However, due to the large volume of data and model output, the base-case conditions for the other episodes are not discussed in this section. Here, only perturbations (differences) are evaluated. Thus, in the following discussion, the meteorological *changes* are presented for the multi-episodic runs identified earlier in Table 6.1, focusing on air temperature.

Figures A-1 through A-9 in Appendix A of the report show the locations of the monitors discussed in this section.

### 10.3.1 Central California

Figures D1 through D34 in Appendix D summarize in a compact manner a very large amount of data from the multi-episodic simulations of heat island control in the central California domain. The focus in these figures is on the “degree-hour” metric, more specifically, the differences in degree-hours per day across the various region-episode combinations that were evaluated in the modeling tasks. Several monitors (from the ones listed later in Table 12.1) are selected for this discussion. Most of these monitors will also be discussed again in the subsequent analysis of air-quality impacts, as well as in the emission-equivalent analysis (carrying capacity). In addition, Figures E-1 through E-6 show changes at each monitor (across all episodes), grouped by county.

For this analysis, four ambient-air temperature thresholds were selected. These are 15°C (59°F), 20°C (68°F), 25°C (77°F), and 30°C (86°F), respectively. The purpose is to show the effectiveness of increased urban albedo in affecting air temperature relative to different thresholds. Thus, the figures show at a glance the effectiveness of this control measure under various episodic conditions, at each monitor, and across several monitors.

Two types of figures are presented for central California. Figures D1 through D17 show the average degree-hour changes (i.e., in units of degree-hours per day as an average over the number of days in each respective episode) for the threshold air temperature of 15°C (59°F). The purpose is to show the effectiveness of the control measure across various episodes at each monitor (across figures), as well as across monitors within each episode (within each figure). The second set of figures, D18 through D34, shows the percentage-wise changes in degree-hours at each monitor for each temperature threshold listed above. If no data (no bars) are

shown for a certain location or episode, it means that no temperature higher than the threshold (i.e., no degree-hour exceedance) occurred in the base-case scenario for that episode and location.

Figures E-1 through E-6 in Appendix E show changes at each monitor (across all episodes), grouped by county and for the threshold of 15°C (59°F). The purpose is to identify, if any, the episodes with most effective UHI-control impacts, as well as identify locations with the largest impact (e.g., largest cooling) and those with the least impact, across the domains.

First, a qualitative scan of Figures D1 through D17 shows that the temperature changes, i.e., the average changes in degree-hours per day (DH/D), are relatively consistent and of the same magnitude (at each monitor) regardless of the different episodes. Overall, most of the changes fall within the range of 4 to 8 DH/D at each monitor. Of course there are actual differences from one episode to another, due to variations in cloud cover and wind flow patterns, but these differences are not large. This can be seen further in Figures E1 through E6. In these figures, it can be seen that except for one or two episodes, e.g., runs H1 and H2, the effects of the control measure in almost all of the remaining episodes are relatively similar and consistent within a relatively narrow range of change.

In Figure E1, the three monitors in Placer County have relatively constant reductions in average DH/D through all episodes, except for runs H1 and H2. The range of change across the monitors is from -3 to -8 DH/D. For run H1, corresponding to the episode 4 through 19 July 2002, there is slightly less reduction than the average and in run H2, corresponding to 10 through 22 July 2002, there is slightly larger reduction than the average. Run L, corresponding to 13 to 14 July 2005, also shows a slightly smaller impact from the control measure. Note that the sequence from the top line (series) to the bottom line in Figure E1 (showing the smallest to largest effects) is mainly due to urbanization. The smallest effect (top line, in Auburn) is a result of least urbanization (and thus the smallest impact from albedo modifications); whereas, the bottom line corresponding to Roseville (larger urbanization) and relatively larger impact from albedo increase. Thus, the lines in the figure from top to bottom correspond to the effects of increased albedo in increasingly urbanized (denser) areas. The same is observed in Figure E2 (Cool), where urbanization is small. The range of change is from -1 to -3 DH/D. See Figure A-1 through A-9 in Appendix A for the locations of these monitors.

In Figure E3, for Sacramento County, the lines are banded closer together (except for monitor 5003) indicating similar overall impacts at the monitors in that county (a narrow range of changes, from about -3 to -7 DH/D). This is indicative of similar urban conditions and levels of albedo increase in the urbanized Sacramento areas along the American River, except for the topmost line (067-5003) at Sloughouse, that has the least urbanization (rural site) and thus smaller impacts from albedo increases.

In Santa Clara County, as seen in Figure E4, there is a wide range of impacts across the various monitors (locations) in the county. The changes range from 0 to -12 DH/D. It is clear that the monitors of least impact (0002 and 2006) at the top of the chart (corresponding to Gilroy and Morgan Hills respectively), have the relatively smallest urban areas compared to those in and

around the greater San Jose region. The locations that have the larger effects are all within the larger San Jose area. The largest effects (greatest cooling) are seen at monitor 2004, corresponding to west of downtown. Another reason for the larger effects in these areas is that they are downwind of other urbanized areas (San Mateo County) and thus are affected by both local and transported cooler air.

In Contra Costa County (Figure E5), the range is relatively large, from 0 to -6 DH/D, but not as large as it is in Santa Clara. The top two series in Figure E5 correspond to locations in Pittsburg and Bethel Island (both low-density suburban and rural areas), and thus to smaller impacts from increased albedo. On the other hands, the two bottom lines (series) in the figure correspond to the Concord-Pleasant Hill-Walnut Creek region and the San Pablo-Richmond area, that are relatively more heavily built up.

In Alameda County, the range is relatively narrower (Figure E6) from -5 to -10 DH/D, and the largest effects (at monitor 0006) are in the San Leandro-Hayward area, which again is highly urbanized. Another observation is that some of the largest effects (largest reductions in degree-hours per day averages) throughout the central-California domain occur in Santa Clara and Alameda counties, both in the San Francisco Bay Area.

As highlighted earlier, the modeling shows that the effects of urban heat island control (e.g., increased urban albedo in this case) are relatively consistent across the various meteorological conditions of the different episodes. There are some variations, however, and these were due to mainly the local cloud cover and wind pattern. Thus, episodes H1 and H2 are discussed here as an example because of their relatively contrasting impacts on cooling (see Table 10.3), i.e., 90 versus 155 DH/D of cooling (as discussed below). In Figures E1 through E6, it can be seen that in episode H1, the impacts are relatively smaller than in episode H2.

Episode H2 starts with a typical northwesterly flow over the ocean as in episode H1 (see Figure E10 for episode H1), then develops a high-pressure system over California, as does episode H1. However, during the final days of episode H2 (days that are not included in episode H1), a low-pressure system forms over California and the flow becomes southerly instead of northwesterly, as in episode H1 (as seen in Figure E11). During these days in episode H2, the flow over the Pacific Ocean is southwesterly and southerly. In addition, episode H2 has slightly larger daytime cloud cover both offshore and overland than in episode H1 (compare Figures E11 and E12 to Figure E10). These are middle and low clouds at model levels 5 through 7 from the bottom and sometimes up to level 20 from the bottom. Table 10.1 shows that the peak air temperatures in episode H1 range from 40°C to 46°C (104°F to 114.8°F); whereas, for episode H2, they range from 38°C to 42°C (100.4°F to 107.6°F). Thus, episode H2 is generally cooler than H1 and represents milder summer conditions (with a low-pressure system overhead in the latter days), yet the albedo effects in episode H2 are larger than in episode H1 (in terms of temperature impacts). This suggests that the effectiveness of increased albedo is relatively independent of meteorology (in summer) and that it can be larger on cooler days than in hotter ones.

It is reiterated here that there was no particular reason for selecting these two episodes or specific days; it was simply to show that certain episodic days can have different meteorologies, yet the impacts on degree-hours (cooling) can be relatively similar or directionally opposite. Recall that the discussion here pertains to meteorological effects only and that impacts on air quality can be different, as will be discussed later.

In terms of relative changes across various temperature thresholds, Figures D18 through D34 in Appendix D summarize the effects of increased urban albedo on episodic degree-hours above the four thresholds discussed earlier. One can observe that the largest percentage-wise reductions in degree-hours over the four thresholds are consistently larger in Santa Clara, Contra Costa, and Alameda counties. This is both because temperatures are relatively lower in these areas than in other regions in the central California domain (thus the effects of increased urban albedo on exceedances above temperature thresholds are relatively larger) and that these areas are more urbanized and thus see larger impacts from increased albedo. Also, seen in Figures D28 and D29, the relative changes in percentage-wise exceedances above thresholds are similar in these two episodes (H1 and H2), despite the differences in synoptic conditions discussed above (e.g., temperature, cloud cover, and wind fields). This again suggests that the temperature-change signal from UHI control is relatively consistent regardless of large-scale summer meteorological conditions in the episodes studied here (summer episodes with varying partial cloud cover or wind field).

Table 10.3 summarizes the changes in degree-hours per day (DH/D) as a total over all monitors in the central California domain, averaged for each respective episode (for the 15°C (59°F) threshold). In other words, the table shows the sums of the DH/D changes across all monitors in each of figures D1 through D17. The purpose is to identify the effectiveness of increased urban albedo on a region-wide basis (in affecting air temperature) among various episodic conditions.

**Table 10.3: Summary of Changes in Degree-Hours per Day as a Total over All Monitors in the Central California Domain for Each Episode (for the 15°C Threshold)**

Episode/runID	Total DH/D change over all monitors
JulAug_2000	-116.63
July_1999	-132.33
run_A1	-120.43
run_A2	-133.00
run_B	-125.79
run_C	-107.80
run_D	-133.50
run_E	-123.64
run_F	-130.00
run_G	-118.50
run_H1	-90.00
run_H2	-155.23

Episode/runID	Total DH/D change over all monitors
run_I	-140.75
run_J	-115.52
run_K	-133.52
run_L	-111.50
run_M	-134.18

It can be seen in Table 10.3 that the range of impacts from increased urban albedo is relatively consistent and confined to between about -110 and -140 DH/D regardless of meteorology, except for the two episodes, which deviate somewhat from this range (episodes H1 and H2, discussed earlier).

While Figures D18 through D34 show the changes for each monitor and threshold for each episode, Tables 10.4 through 10.9 below show the changes (percentage-wise) at each monitor, but averaged over all episodes. Again, one can see the increase in percentage change as the temperature threshold increases, and that the largest changes are in Santa Clara, Contra Costa, and Alameda counties, as discussed earlier.

**Table 10.4: Percentage-wise Changes in Degree-Hours at Monitors in Placer County for Four Temperature Thresholds. These changes are averaged over all episodes.**

	Monitors	061-0002	061-0006	T061-3001
Threshold		(%)	(%)	(%)
15°C (59°F)		-1.46	-2.33	-1.88
20°C (68°F)		-2.63	-3.81	-3.04
25°C (77°F)		-5.07	-6.67	-4.77
30°C (86°F)		-11.62	-11.56	-10.18

**Table 10.5: Percentage-wise Changes in Degree-Hours at Monitors in Sacramento County for Four Temperature Thresholds. These changes are averaged over all episodes.**

Monitors	067-0002	067-0006	067-0010	067-0012	067-0013	067-1001	067-5003
Threshold	(%)	(%)	(%)	(%)	(%)	(%)	(%)
15°C (59°F)	-1.83	-2.10	-1.87	-1.99	-1.62	-1.98	-1.22
20°C (68°F)	-2.95	-3.39	-2.98	-3.32	-2.57	-3.23	-2.02
25°C (77°F)	-4.91	-5.62	-4.74	-5.66	-4.06	-5.28	-3.46
30°C (86°F)	-31.93	-13.94	-9.95	-12.98	-8.29	-11.29	-7.91

**Table 10.6: Percentage-wise Changes in Degree-Hours at Monitors in Santa Clara County for Four Temperature Thresholds. These changes are averaged over all episodes.**

	Monitors	085-0002	085-1002	085-2004	085-2005	085-2006	085-2007
Threshold		(%)	(%)	(%)	(%)	(%)	(%)
15°C (59°F)		-0.24	-3.57	-5.71	-3.32	-1.01	-3.55
20°C (68°F)		-0.44	-6.47	-8.99	-6.88	-1.80	-6.16
25°C (77°F)		-1.45	-13.70	-16.56	-17.32	-3.87	-12.60
30°C (86°F)		-19.33	-30.94	-31.06	-25.70	-8.80	-27.25

**Table 10.7: Percentage-wise Changes in Degree-Hours at Monitors in Contra Costa County for Four Temperature Thresholds. These changes are averaged over all episodes.**

	Monitors	013-0002	013-1002	013-1003	013-3001
Threshold		(%)	(%)	(%)	(%)
15°C (59°F)		-2.37	-0.41	-4.22	-0.52
20°C (68°F)		-4.21	-0.75	-9.54	-0.97
25°C (77°F)		-8.63	-1.41	-24.54	-2.27
30°C (86°F)		-18.73	-3.47	-26.95	-4.68

**Table 10.8: Percentage-wise Changes in Degree-Hours at Monitors in Alameda County for Four Temperature Thresholds. These changes are averaged over all episodes.**

	Monitors	001-0005	001-0006	001-1001
Threshold		(%)	(%)	(%)
15°C (59°F)		-5.65	-6.80	-4.54
20°C (68°F)		-15.82	-15.17	-9.24
25°C (77°F)		-40.03	-31.77	-21.92
30°C (86°F)		-51.67	-53.21	-34.19

**Table 10.9: Percentage-wise Changes in Degree-Hours at Monitors in Fresno County for Four Temperature Thresholds. These changes are averaged over all episodes.**

	Monitors	019-0007	019-0008	019-0242	019-0243	019-4001
Threshold		(%)	(%)	(%)	(%)	(%)
15°C (59°F)		-1.82	-2.18	-0.13	-0.86	-0.42
20°C (68°F)		-2.94	-3.49	-0.20	-1.38	-0.69
25°C (77°F)		-4.76	-5.73	-0.33	-2.17	-1.03
30°C (86°F)		-8.93	-10.81	-0.89	-4.26	-2.23

### 10.3.2 Southern California

Figures D35 through D44 summarize the changes in degree-hours for the Southern California domain, more specifically, the differences in DH/D across the various region-episode combinations that were evaluated in the modeling task. Several monitors (from the ones listed in Table 12.1) are selected for this discussion. In addition, Figures E-7 through E-9 show changes at each monitor (across all episodes), grouped by county.

For this analysis, as with central California, four ambient-air temperature thresholds were selected. The purpose is to show the effectiveness of increased urban albedo in changing air temperature in different temperature ranges. Figures D35 through D39 in Appendix D show the change in DH/D as an average over the number of days in each respective episode) for the air temperature threshold of 15°C (59°F). Figures D40 through D44 show the percentage-wise changes in DH/D at each monitor for each temperature threshold. Where no data (no bars) are shown for certain locations or episodes, there was no temperature higher than the threshold (i.e., no degree-hour exceedance) in the base-case scenario for that episode and location.

Figures D35 through D39 show that the effects of the control measure (increased urban albedo) are consistent, regardless of the summer episodic meteorological conditions. They also show that the largest effects (largest cooling) occur in Los Angeles County. Of course there are variations in space (monitor-to-monitor variations) and across the various episodes, but the pattern is generally similar and the differences are not large. In San Bernardino County, the changes in DH/D reach up to about -6 or -7 DH/D across all episodes, in Los Angeles County up to about -12 to -14 DH/D, and in Riverside County up to about -2 to -5 DH/D, across all episodes.

In Figures E7 through E9 in Appendix E, it can be seen that the impacts of increased urban albedo on DH/D are relatively more uniform across all episodes than in central California. The reason for this is that the modifications in the Los Angeles Basin are done over a large and more contiguous area, not separate urban regions as in central California. This approach produces a relatively uniform and continuous effect across the region and thus less episode-to-episode variations from one monitor to another.

In these figures (E7 through E9), it can again be seen that the cooling in Los Angeles County is the largest of the three counties in southern California that were examined in this analysis; in San Bernardino County, the largest change reaches up to -7 DH/D; in Los Angeles County, up to -16 DH/D; and in Riverside County, up to -5 DH/D. As in the earlier discussion, the effect of urbanization (density) is obvious in the cooling potential. For example, in San Bernardino County (Figure E7), the top-to-bottom series in the chart corresponds to Redlands, Upland, and San Bernardino, in increasing urban density. Thus, the effect at monitor 9004 (San Bernardino) is larger than that at monitor 4003 (Redlands). The same can be seen in Los Angeles County (Figure E8). The least impact (top of the chart) is at monitors 9006 and 9002, corresponding to Palmdale and Lancaster; whereas, the largest impact can be seen at the bottom of the figure, corresponding to the downtown Los Angeles area (monitors 0030 and 1103) and nearby, such as Lynwood (monitor 1301). Finally, the same can be observed in Figure E9. The sequence of the

lines (series) from top to bottom corresponds to increased urban density; the order being Hemet, Perris, Norco, and Rubidoux, in increasing order.

For relative changes across various temperature thresholds, Figures D40 through D44 summarize the effects of increased urban albedo. One observation that can be made is that the largest percentage-wise reductions in DH/D over the four thresholds are consistently found in Los Angeles County. This is mainly the result of two factors: (1) that these areas have relatively lower air temperatures than other regions in the southern California domain (such as San Bernardino or Riverside, which are further inland), and thus the effects of increased urban albedo on exceedances above the temperature thresholds are relatively larger, and (2) that Los Angeles county is the most urbanized of the three, and thus has the largest urban albedo modification potential. Also, as seen in these figures, the relative changes in percentage-wise exceedances above thresholds are generally similar in the five episodes, thus suggesting that the temperature-change signal from UHI control is relatively consistent, regardless of large-scale meteorological conditions in the summer episodes studied here.

Table 10.10 summarizes the changes in DH/D as a total over all monitors in the southern California domain, totaled for each episode (for the 15°C [59°F] threshold). The purpose is to identify the effectiveness of increased urban albedo (in affecting air temperature) among various episodic conditions. In other words, the table shows the sums of the DH/D changes across all monitors in each of figures D35 through D39 (for the 15 in Figure E9,C threshold).

**Table 10.10: Summary of Changes in Degree-Hours per Day as a Total over All Monitors in the Southern California Domain for Each Episode (for the 15°C Threshold)**

Episode/runID	Total DH/D change over all monitors
run_N	-141.96
run_O	-150.67
run_P	-155.40
run_Q	-144.94
run_R	-155.07

One can see from Table 10.10 that the range of total changes is narrow, relatively confined to about -140 to -155 DH/D, and that there is practically no difference in impacts on air temperature among the five episodes considered here.

While Figures D40 through D44 show the changes for each monitor and threshold for each episode, Tables 10.11 through 10.13 show the changes (percentage-wise) at each monitor, but averaged over all episodes. Again, one can see the increase in percentage change as the temperature threshold increases and also that the largest percentage-wise changes are in Los Angeles County.

**Table 10.11: Percentage-wise Changes in Degree-Hours at Monitors in San Bernardino County for Four Temperature Thresholds. These changes are averaged over all episodes.**

	<b>Monitors</b>	<b>071-1004</b>	<b>071-4003</b>	<b>071-9004</b>
<b>Threshold</b>		<b>(%)</b>	<b>(%)</b>	<b>(%)</b>
15°C (59°F)		-2.23	-1.42	-2.46
20°C (68°F)		-4.00	-2.51	-4.06
25°C (77°F)		-8.43	-5.35	-7.56
30°C (86°F)		-20.45	-13.09	-14.83

**Table 10.12: Percentage-wise Changes in Degree-hours at Monitors in Los Angeles County for Four Temperature Thresholds. These changes are averaged over all episodes.**

	<b>037-0002</b>	<b>037-0016</b>	<b>037-0030</b>	<b>037-0031</b>	<b>037-0113</b>	<b>037-0206</b>	<b>037-1002</b>	<b>037-1103</b>
<b>Threshold</b>	<b>(%)</b>	<b>(%)</b>	<b>(%)</b>	<b>(%)</b>	<b>(%)</b>	<b>(%)</b>	<b>(%)</b>	<b>(%)</b>
15°C (59°F)	-3.25	-2.08	-9.64	-8.18	-4.39	-3.36	-5.48	-8.62
20°C (68°F)	-5.96	-4.11	-16.90	-16.97	-9.69	-6.16	-9.59	-14.75
25°C (77°F)	-11.96	-10.57	-33.96	-39.17	-28.82	-12.82	-18.94	-28.87
30°C (86°F)	-27.35	-32.05	-73.17	-83.33	-52.68	-40.44	-47.59	-61.67
	<b>037-1301</b>	<b>037-1601</b>	<b>037-1701</b>	<b>037-2005</b>	<b>037-6002</b>	<b>T037-9002</b>	<b>037-9006</b>	
	<b>(%)</b>	<b>(%)</b>	<b>(%)</b>	<b>(%)</b>	<b>(%)</b>	<b>(%)</b>	<b>(%)</b>	
15°C (59°F)	-8.40	-7.32	-3.90	-6.88	-0.79	-0.09	-0.08	
20°C (68°F)	-14.77	-11.66	-6.86	-11.36	-1.36	-0.14	-0.13	
25°C (77°F)	-29.51	-20.51	-12.86	-20.44	-2.70	-0.27	-0.34	
30°C (86°F)	-61.28	-47.82	-30.15	-45.07	-7.01	-0.30	-0.43	

**Table 10.13: Percentage-wise Changes in Degree-Hours at Monitors in Riverside County for Four Temperature Thresholds. These changes are averaged over all episodes.**

	<b>Monitors</b>	<b>065-0003</b>	<b>065-1002</b>	<b>065-6001</b>	<b>065-8001</b>
<b>Threshold</b>		<b>(%)</b>	<b>(%)</b>	<b>(%)</b>	<b>(%)</b>
15°C (59°F)		-1.14	-0.04	-0.44	-2.03
20°C (68°F)		-1.95	-0.12	-0.77	-3.47
25°C (77°F)		-3.85	-0.23	-1.59	-6.23
30°C (86°F)		-11.98	-0.76	-4.28	-14.12

## CHAPTER 11: Emissions Impacts of Surface Modifications

As increasing urban albedo reduces air temperature in the affected areas; that is, where modifications are assumed and downwind of these areas, emissions of air pollutants are also affected. While there are a number of emissions sources that can be affected by changing air temperature (e.g., fuel storage, fugitive emissions, mobile-source hot soak, point sources), this study's focus is on adjusting biogenic volatile organic compound (BVOC) emissions for changes in air temperature and, if necessary, photosynthetically active radiation (solar radiation, PAR). Anthropogenic emissions are assumed unchanged as a result of increased urban albedo for the episodic periods of interest.

Thus, the focus of the intermediate emissions modeling step (between the meteorological and photochemical modeling stages) is to update the BVOC emissions. In general, isoprene and monoterpenes together represent more than 80 percent of total BVOC emissions (Fuentes et al. 2000), and thus are the most critical to update. Other BVOC, such as MBO (methyl butenol) and OVOC (oxygenated VOC) are not corrected in this study. The BVOC emissions corrections/updates are done using a top-down approach (Taha 2005,2007) whereby the emissions are adjusted for air temperatures changes on a grid cell-by-grid cell basis without affecting the emissions of other pollutants and precursors. That is, emissions are not regenerated from raw data but updated for each grid cell based on the change in air temperature (and PAR if necessary) at each time step (Taha 2007).

*Isoprene Temperature Correction Factor,  $C_T$ .*

The empirical formula of Guenther et al. (1993) is used in this study to estimate the temperature correction factor for isoprene. The equation is:

$$C_T = \frac{\exp\left(\frac{c_{T1} \cdot (T - T_S)}{R \cdot T_S \cdot T}\right)}{1 + \exp\left(\frac{c_{T2} \cdot (T - T_M)}{R \cdot T_S \cdot T}\right)}$$

where,  $c_{T1} = 95,000$  joules per mole ( $\text{J mol}^{-1}$ ),  $c_{T2} = 230,000$   $\text{J mol}^{-1}$ , and  $T_M = 314$  K are empirical coefficients;  $R = 8.314$   $\text{J K}^{-1} \text{mol}^{-1}$  is the ideal gas constant,  $T_S$  (303 K) is an empirical normalizing temperature, and  $T$  (K) is the leaf temperature, which is assumed to be the ambient temperature.

*Monoterpenes and OVOCs Temperature Correction Factor,  $C_T$ .*

The empirical formula suggested by Guenther et al. (1993) is used to estimate the temperature correction factor for monoterpenes and OVOC. The equation is:

$$C_T = \exp(\beta[T - T_S])$$

where  $\beta = 0.09 \text{ K}^{-1}$  is the empirical coefficient that can also be thought of as an inverse temperature scale;  $T_s = 303 \text{ K}$  is the normalizing temperature scale; and  $T \text{ (K)}$  is ambient temperature.

## CHAPTER 12: Photochemical/Air-Quality Modeling Results

Table 12.1 lists the monitors of interest in the air-quality analysis discussed in this section. Note that only monitors of relevance to UHI control have IY,IX values displayed next to them in the last two columns; that is, only those monitors close to or within areas where surface modifications have been assumed, or those areas immediately downwind of such modifications (to detect any negative impacts). Thus, some monitors are also included in this analysis (and listed in Table 12.1) not because they are located in modified areas but because data from those monitors are used to evaluate any negative effects on air quality in such unmodified locations.

**Table 12.1: Air-Quality Monitors of Interest in This Analysis**

County	County ID	Monitor ID	Address	Lat	Long	IY	IX
Placer	061	0002	DEWITT-108 "C" AVE, AUBURN	38.937778	-121.103889	126	82
		0004	CITY HALL-33 S MAIN ST, COLFAX	39.100278	-120.952778		
		0006	151 NO SUNRISE BLVD, ROSEVILLE	38.745833	-121.265278	121	78
		0007	2400 LAKE FOREST ROAD	39.184166	-120.12195		
		3001	5000 ROCKLIN ROAD, ROCKLIN	38.788889	-121.216667	122	79
El Dorado	017	0010	3111 GOLD NUGGET WAY, PLACERVILLE	38.727222	-120.818056		
		0011	3337 SANDY WAY, SOUTH LAKE TAHOE	38.945	-119.968889		
		0012	21200 HWY 50 -LITTLE NORWAY/ECHO SUMMIT	38.811667	-120.0325		
		0013	1901 AIRPORT ROAD	38.91028	-119.99528		
		0020	1400 AMERICAN RIVER TRAIL, COOL	38.890556	-121	125	84
		2003	BIG HILL LOOKOUT	38.84222	-120.4066		
Sacramento	067	0002	7823 BLACKFOOT WAY, NORTH HIGHLANDS	38.712778	-121.38	120	76
		0006	DEL PASO-2701 AVALON DR, SACRAMENTO	38.614167	-121.366944	117	76
		0010	1309 T ST., SACRAMENTO	38.558333	-121.491944	116	74
		0011	12490 BRUCEVILLE RD, ELK GROVE	38.301944	-121.422222		
		0012	50 NATOMA STREET, FOLSOM	38.683889	-121.162778	119	81
		0013	3801 AIRPORT ROAD, SACRAMENTO	38.636944	-121.513333	118	73
		1001	1300 LIEDESDORFF, FOLSOM	38.675	-121.185833	119	80
		5002	7926 EARHART DR., SACRAMENTO	38.716944	-121.591944		
Santa Clara	085	0002	9TH & PRINCEVILLE, GILROY	37	-121.574444	73	71
		0004	120B N 4TH ST, SAN JOSE	37.3398	-121.8884	83	64
		0005	158B JACKSON ST, SAN JOSE	37.3485	-121.895	83	64
		1001	306 UNIVERSITY AVE., LOS GATOS	37.226944	-121.978611		
		1002	160 CUESTA DR., MOUNTAIN VIEW	37.373056	-122.077222	84	60
		2004	1866 W SAN CARLOS ST, SAN JOSE	37.323056	-121.926111	82	64

County	County ID	Monitor ID	Address	Lat	Long	IY	IX
		2005	935 PIEDMONT ROAD, SAN JOSE	37.401944	-121.8425	85	66
		2006	13030 MURPHY AVE., SAN MARTIN	37.079444	-121.599167	76	71
		2007	910 TICONDEROGA DRIVE	37.35527	-122.051389	83	61
Contra Costa	013	0002	2956-A TREAT BOULEVARD	37.936	-122.0262	99	62
		0003	1144 13TH ST., RICHMOND	37.95	-122.356111		
		0010	1098 POMONA STREET	38.0313	-122.1318		
		1002	5551 BETHEL ISLAND RD, BETHEL ISLAND	38.010556	-121.641389	101	70
		1003	EL PORTAL SHOPPING CENTER	37.964167	-122.339167	100	55
		1004	1865 D RUMRILL BLVD, SAN PABLO	37.96028	-122.35667		
		3001	583 W. 10TH ST., PITTSBURG	38.029167	-121.902222	101	65
				0003	2614 OLD 1ST ST., LIVERMORE	37.685	-121.766111
Alameda	001	0005	822 ALICE ST., OAKLAND	37.799444	-122.266667	95	57
		0006	15400 FOOTHILL BLVD,SAN LEANDRO	37.707778	-122.120278	93	60
		0007	793 RINCON AVE., LIVERMORE	37.6875	-121.7842	92	67
		0010	6701 INTERNATIONAL BLVD	37.7603	-122.1925		
		1001	40733 CHAPEL WAY., FREMONT	37.5358	-121.9619	88	63
		2001	3466 LA MESA DR., HAYWARD	37.654444	-122.030556		
				0007	4706 E. DRUMMOND ST., FRESNO	36.705556	-119.741389
Fresno	019	0008	3425 N FIRST ST, FRESNO	36.781389	-119.772222	67	111
		0010	NORTH PERIMETER ROAD	37.138333	-119.266667		
		0242	BLYTHE & CHNNLT, FRESNO	36.841389	-119.874444	69	108
		0243	1005 W. WELDON AVENUE	36.76722	-119.8275	67	110
		0244	mobile	36.80306	-119.76917		
		4001	9240 S. RIVERBEND, PARLIER 93648	36.5975	-119.503611	63	117
		5001	908 N VILLA AVE, CLOVIS	36.819167	-119.716389		
San Bernardino	071	0001	200 E. BUENA VISTA, BARSTOW	34.895	-117.023611		
		0005	LAKE GREGORY-LAKE DR, CRESTLINE	34.2431	-117.27235		
		0012	BEEKLEY & PHELAN RDS, PHELAN	34.426111	-117.563056		
		0014	14029 AMARGOSA ROAD, VICTORVILLE	34.5125	-117.33		
		0015	83732 TRONA ROAD, TRONA	35.775	-117.366667		
		0017	6136 ADOBE ROAD, TWENTYNINE PALMS	34.141944	-116.055		
		0217	6945 MT BALDY ROAD	34.239167	-117.620833		
		0306	14306 PARK AVE., VICTORVILLE, CA	34.51	-117.330556		
		1004	1350 SAN BERNARDINO RD., UPLAND	34.10374	-117.62914	46	65
		1234	ATHOL at TELESCOPE roads	35.763889	-117.396111		
		2002	14360 ARROW BLVD., FONTANA	34.10002	-117.49201	66	68
		4001	17288 OLIVE ST., HESPERIA	34.418056	-117.284722	66	68
		4003	500 N. DEARBORN, REDLANDS	34.05977	-117.14731	45	74
		9000	CELLULAR RELAY STATION,LUDLOW	34.724722	-116.157778		
		9002	JOSHUA TREE NATIONAL MONUMENT	34.071389	-116.390556		
		9003	SHADOW MOUNTAIN RELAY STATION	34.737778	-117.565		
9004	24302 4TH ST., SAN BERNARDINO, CA.	34.10688	-117.27411	46	72		
		9006	BALDY MESA	34.375	-117.447778		

County	County ID	Monitor ID	Address	Lat	Long	IY	IX
		9007	FLASH II MOUNTAIN RELAY STATION	34.737778	-117.565		
		9008	QUARTZITE MOUNTAIN	34.611667	-117.288889		
Los Angeles	037	0002	803 N. LOREN AVE., AZUSA	34.1365	-117.92391	47	60
		0016	840 LAUREL, GLENDORA	34.14435	-117.85036	47	62
		0030	651 S. MOTT STREET	34.035278	-118.216667	44	54
		0031	1115 N. MAHAR AVENUE WILMINGTON	33.786111	-118.246389	39	54
		0113	VA HOSPITAL, WEST LOS ANGELES	34.05111	-118.45636	45	50
		0206	21865 E. COPLEY DR., DIAMOND BAR	33.958333	-117.841667	43	62
		1002	228 W. PALM AVE., BURBANK	34.17605	-118.31712	47	53
		1103	1630 N MAIN ST, LOS ANGELES	34.06659	-118.22688	45	54
		1201	18330 GAULT ST., RESEDA	34.19925	-118.53276		
		1301	11220 LONG BEACH BLVD., LYNWOOD	33.92899	-118.21071	42	55
		1601	3713 SAN GABRIEL RIVER PKWY, PICO RIVERA	34.01407	-118.06056	44	57
		1701	924 N. GAREY AVE., POMONA	34.06703	-117.7514	45	63
		2005	752 S. WILSON AVE., PASADENA	34.1326	-118.1272	46	56
		4002	3648 N. LONG BEACH BLVD., LONG BEACH	33.82376	-118.18921		
		Los Angeles, continued		5001	5234 W. 120TH ST., HAWTHORNE	33.92288	-118.37026
5005	7201 W. WESTCHESTER PARKWAY			33.9508	-118.43043		
6002	SAN FERNANDO RD, SANTA CLARITA			34.3875	-118.533611	53	49
6012	22224 PLACERITA CANYON RD, SANTA CLARITA			34.38344	-118.5284		
9002	315 W. PONDERA ST., LANCASTER			34.69	-118.131944	58	56
9006	1030 EAST AVENUE S, PALMDALE			34.556944	-118.111667	56	56
Riverside	065	9033	43301 DIVISION ST., LANCASTER	34.671389	-118.130556		
		0002	135 N. ALLESANDRO, BANNING	33.927778	-116.873611		
		0003	NORCONIAN-US NFAC, NORCO	33.920556	-117.571389	42	66
		0008	JOSHUA TREE NATIONAL PARK	33.7411	-115.8206		
		0012	200 S. HATHAWAY ST., BANNING CA	33.92086	-116.85841		
		1002	880 STATE ST., HEMET	33.741667	-116.958333	38	77
		2002	46-990 JACKSON ST., INDIO	33.70853	-116.21537		
		5001	FS-590 RACQUET CLUB AVE, PALM SPRINGS	33.85275	-116.54101		
		6001	237 1/2 N. "D" ST., PERRIS	33.78942	-117.22764	39	73
		8001	5888 MISSION BLVD., RUBIDOUX	33.99958	-117.41601	43	69
		9001	506 W FLINT ST, LAKE ELSINORE	33.67649	-117.33098		
		9003	445 W MURPHY STREET, BLYTHE	33.612127	-114.600583		

In the following sections, the domain-wide ozone fields and changes are discussed. To begin, we list the domain-wide modeled base-case ozone peaks (ppb) during the episodes analyzed here. These are summarized in Table 12.2.

**Table 12.2: Domain-wide Simulated Base-Case Episodic Ozone Peak**

<b>Episodic Peak 1-hr Ozone</b>			
<b>Central California Episodes</b>	<b>Simulated domain-wide episodic 1-hr peak</b>	<b>Southern California Episodes</b>	<b>Simulated domain-wide episodic 1-hr peak</b>
Jul–Aug 2000, 2000 emissions	127.22	May 23–Jun 16, 2000 (run N)	133.60
Jul–Aug 2000, 2018 emissions	107.25	May 22–Jun 8, 2001 (run O)	136.22
Jul 1999, 1999 emissions	148.65	Aug 13–17, 2011 (run P)	121.99
Jul 1999, 2018 emissions	115.02	Jul 9–24, 2003 (run Q)	152.63
Jun 14–27, 2000 (run A1)	143.66	Jul 12–26, 2005 (run R)	144.61
Jul 19–Aug 1, 2000 (run B)	146.45		
Aug 4–8, 2000 (run C)	105.82		
Aug 11–18, 2000 (run D)	124.81		
May 18–31, 2001 (run E)	148.45		
Jul 10–22, 2002 (runH2)	148.12		
Jul 4–19, 2002 (runH1)	162.18		
Aug 8–20, 2002 (run I)	150.93		
Jun 3–27, 2003 (run J)	128.90		
Jun 25–Jul 17, 2003 (run K)	143.72		
Jul 25–Aug 4, 2005 (run M)	159.50		

## 12.1 2000 Episode (Central California)

### 12.1.1 Air-Quality Impacts with Year2000 Emissions

To evaluate the impacts of increased urban albedo on ozone air quality, some qualitative and quantitative measures are discussed in this section. The qualitative characterizations include cross-section analysis of ozone and its changes in the modeling domain. However, the information to glean from such cross-sections is not straightforward to interpret because there is significant spatial variation. Thus, while these cross-sections are included and discussed in this report, they are meant only for a qualitative assessment. Quantitative measures of peak ozone and monitor-level analysis are more relevant in forming an overall evaluation of UHI-mitigation effectiveness.

It is important to keep in mind in this discussion that throughout the hours of each day there are decreases in ozone, as well some increases (typically small), as a result of albedo increase. Thus, the overall inclusive effect is evaluated later in terms of cumulative metrics, e.g., “parts per billion per hour” statistics. Here, we discuss only the cross sections at the times of the

largest decrease in 1-hour average ozone during daylight hours on each day of the episode. Larger reductions that may occur during nighttime hours are not discussed or shown in these figures, since nighttime reductions are not as relevant as those occurring during daylight hours, when concentrations are higher.

Figures C5-1 through C5-5 in Appendix C depict the changes in ozone resulting from the albedo-increase scenario for the July-August 2000 episode for the SFBA-Sacramento domain with year 2000 emission inventories. Figures C6-1 through C6-5 show the same type of information, but for the Fresno domain. It is important to note that the areas where increased albedo is assumed always have a decrease in ozone (improved air quality). It is only in unmodified areas, which are often downwind, that ozone can increase at times. The areas affected by an increase in ozone, if any, are typically much smaller than those affected by a decrease. The weighted and net effects are captured in the quantitative analysis discussed in this report.

The reason why ozone can increase in downwind areas such as in Tulare County and in El Dorado County, for example, where no urban albedo changes (or only marginal changes) are assumed, was explained earlier in Taha (2007). This is mainly because of reduced mixing in such areas, increased local temperatures, and transport of precursors into them. In the future, simulations with urban modifications in these downwind areas will also be undertaken, so as to evaluate the benefits in those regions as well. This aspect will be discussed again later in this report, when the impacts of wind direction are evaluated. Table 12.3 summarizes the results from Figures C5-1 through C6-5.

**Table 12.3: Largest Changes in Daily Ozone in Central California with Year 2000 Emissions**

<b>Date</b>	<b>Largest decrease in SFBA-SAC domain (ppb) and county location</b>	<b>SFBA decrease at hour of largest decrease (ppb)</b>	<b>SAC decrease at hour of largest decrease (ppb)</b>	<b>Largest decrease in Fresno domain (ppb) and county location</b>	<b>Fresno decrease at hour of largest decrease (ppb)</b>
27 July	6 Contra Costa	6	3	4 Fresno	4
28 July	8 Contra Costa	8	8	6 Fresno	6
29 July	6 Sacramento	4	6	3 Fresno	3
30 July	4 Sacramento	4	4	3 Fresno	3
31 July	9 Contra Costa	9	1	10 Fresno	10

### 12.1.2 Air-Quality Impacts with Future Emissions (Year 2018)

In this section, a similar qualitative analysis is provided for the same scenarios and conditions discussed above, except that the emissions used in the modeling now represent future-year conditions (year 2018 anthropogenic emission). This scenario thus includes all emission caps

and control measures anticipated by that time frame. Figures C7-1 through C7-5 and C8-1 through C8-5 show the corresponding cross sections at the hours of largest decrease in ozone as a result of heat-island control.

Table 12.4 is similar to Table 12.3 above, except that it is for results with year 2018 emissions. The results suggest that, roughly, the impacts on ozone in the year 2018 time frame are 40 to 100 percent of what they are under year 2000 emissions. There are cases, however, where the impacts during 2018 are larger than those in 2000.

**Table 12.4: Largest Changes in Daily Ozone in Central California with Year 2018 Emissions**

Date	Largest decrease in SFBA-SAC domain (ppb) and county location	SFBA decrease at hour of largest decrease (ppb)	SAC decrease at hour of largest decrease (ppb)	Largest decrease in Fresno domain (ppb) and county location	Fresno decrease at hour of largest decrease (ppb)
27 July	4 Contra Costa	4	1	2 Fresno	2
28 July	6 Contra Costa	6	3	3 Fresno	3
29 July	4 Sacramento	4	2	1 Fresno	1
30 July	4 Alameda	4	2	2 Fresno	2
31 July	8 Contra Costa	8	4	5 Fresno	5

## 12.2 1999 Episode (Central California)

### 12.2.1 Air-Quality Impacts with Year 1999 Emissions

As with the previous discussion of the impacts of increased urban albedo on ozone air quality for the July 2000 episode, some qualitative and quantitative measures are discussed in this section for the July 1999 episode, with year 1999 emissions. The qualitative characterizations include cross-section analysis of ozone and its changes in the modeling domain. Quantitative measures of peak ozone and monitor-level analyses are more relevant in forming an overall evaluation of the UHI-mitigation effectiveness, and will be discussed later. Here, we discuss only the cross sections at the times of the largest decrease in 1-hour average ozone on each day of the episode during daylight hours. Larger reductions that may occur during nighttime hours are not discussed, since nighttime reductions are not as important as those occurring during daylight hours.

Figures C13-1 through C13-4 depict the changes in ozone resulting from albedo increases for the July 1999 episode for the SFBA-Sacramento domain with 1999 emissions. Figures C14-1 through C14-4 show the same type of information, but for the Fresno domain. Table 12.5 summarizes the results from all of these figures.

**Table 12.5: Largest Changes in Daily Ozone in Central California with Year 1999 Emissions**

Date	Largest decrease in SFBA-SAC domain (ppb) and county location	SFBA decrease at hour of largest decrease (ppb)	SAC decrease at hour of largest decrease (ppb)	Largest decrease in Fresno domain (ppb) and county location	Fresno decrease at hour of largest decrease (ppb)
7 July	11 Contra Costa	11	2	8 Fresno	8
8 July	6 Santa Clara	6	3	14 Tulare*	8
9 July	7 Santa Clara	7	3	4 Fresno	4
10 July	22 Placer*	4	22*	6 Tulare*	5

\*Not representative, non-local values. These are rather extremes occurring near the domain boundaries or are signals exiting the domain (after advection throughout the day from the modified area).

Note that the scales on the figures are set so as to show equal increase and decrease. An unintended consequence is that other areas where changes in ozone occur are not captured in these figures. However, these are captured in the statistical analysis that follows later.

### 12.2.2 Air-Quality Impacts with Future Emissions (Year 2018)

In this section, a similar qualitative analysis is provided for the same scenarios and conditions discussed above, except that the emissions used in the modeling now represent future years (emissions of 2018). Figures C15-1 through C15-4 and C16-1 through C16-4 show the ozone changes during the hours of largest decrease, as with the discussion above, except for the 2018 emissions.

Table 12.6 shows the largest daily ozone changes from increased albedo for the 2018 emissions. The results show that the effects of heat island control under 2018 emissions are about 40 to 100 percent of what they are under 1999 emissions. In several instances, e.g., in the Sacramento region, the effects in 2018 are larger than they are in 1999.

**Table 12.6: Largest Changes in Daily Ozone in Central California with Year 2018 Emissions**

Date	Largest decrease in SFBA-SAC domain (ppb) and county location	SFBA decrease at hour of largest decrease (ppb)	SAC decrease at hour of largest decrease (ppb)	Largest decrease in Fresno domain (ppb) and county location	Fresno decrease at hour of largest decrease (ppb)
7 July	8 Contra Costa	8	5	4 Fresno	4
8 July	6 Contra Costa	6	4	11 Tulare*	4
9 July	7 El Dorado*	3	7	2 Fresno	2

Date	Largest decrease in SFBA-SAC domain (ppb) and county location	SFBA decrease at hour of largest decrease (ppb)	SAC decrease at hour of largest decrease (ppb)	Largest decrease in Fresno domain (ppb) and county location	Fresno decrease at hour of largest decrease (ppb)
10 July	14 Placer*	3	14	11 Tulare*	1

\*Not representative, non-local values. These are rather extremes occurring near the domain boundaries or are signals exiting the domain (after advection throughout the day from the modified area).

### 12.3 2005 Episode (Southern California)

Following the same discussion pattern above, this section presents a qualitative analysis of the air quality impacts during the hours with the largest decrease in ozone on each day of the southern California July 2005 episode. As discussed earlier, it is important to keep in mind that the overall effects of increased urban albedo will be evaluated later using several statistics. Here, we discuss only the cross sections at the hours of the largest decrease in 1-hour average ozone on each day of the episode during daylight hours.

Figures C19-1 through C19-6 depict the largest daily changes in ozone resulting from albedo increases for the July 2005 episode in southern California domain with 2005 emissions. Table 12.7 summarizes the results from all of these figures.

This episode was not analyzed for future-year emissions, as the year 2005 is not in the too-distant past and emissions for that year can be considered valid for the next few years into the future.

**Table 12.7: Largest Changes in Daily Ozone in Southern California with Year 2005 Emissions**

Date	Largest decrease in southern California domain (ppb) and county location	Los Angeles County decrease at hour of largest decrease (ppb) in that county	Orange County decrease at hour of largest decrease (ppb) in that county	San Bernardino County decrease at hour of largest decrease (ppb) in that county
14 July	18 Los Angeles	18	17	7
15 July	11 Los Angeles	11	5	7
16 July	10 Los Angeles	10	7	9
17 July	8 San Bernardino	7	5	8
18 July	16 Los Angeles	16	6	7
19 July	25 Los Angeles	25	7	10

## 12.4 Multi-Episodic Air-Quality Analysis

In this section, the modeled air quality impacts are discussed for all episodes (listed in Table 6.1) and monitor locations identified earlier (in Table 12.1). The metrics discussed here include the 1-hour peak, cumulative changes in concentrations (ppb-hr), 8-hour average and peak, relative reduction factor (RRF), and emission equivalents.

### 12.4.1 Impacts on the 1-hour Peak Ozone at Monitors

In this section, the impacts of increased urban albedo on air quality are discussed for all episodes and monitors analyzed in this study. The discussion also includes the three regulatory episodes discussed above, as well as impacts under future-year (2018) emissions for the 1999 and 2000 episodes. Figures F1 through F14, in Appendix F, summarize the results for central California and Figures F15 through F19 summarize the results for southern California. It is important to note here that while the impacts on ozone at the locations of the 1-hour peaks in the domain are mostly positive (that is, there is a beneficial reduction in the peaks), the impacts at monitor locations are not always positive.

#### 12.4.1.1 Central California

For the July–August 2000 base episode in central California (Figure F1), the impacts of increased urban albedo on monitor peaks under 2000 emissions (the blue bars in the figure) are mixed (having both increases and decreases), but are mostly decreases. Increases are seen in Placer and Sacramento counties. Decreases in the 1-hour peak are seen in Santa Clara, Contra Costa, Alameda, and Fresno counties. These decreases and increases generally correspond to the changes in air temperature (Figure D1). Where the temperature reduction is small, or there is an increase, there is a corresponding increase in ozone. Where the temperature reduction is larger, there is a corresponding reduction in 1-hour peak ozone. However, overall, the decreases are dominant and generally larger than the increases, i.e., there is a total increase of 5.38 ppb-hr in the peaks versus a decrease of 14.48 ppb-hr (about three times larger). Some of the largest decreases at the monitors are about 2 ppb.

For the same base episode but under year 2018 emissions (red bars in Figure F1), the effects of increased urban albedo on the 1-hour peak are generally smaller than those under 1999 emissions. However, there are certain monitors where the effects in 2018 are larger than in 1999, but generally, the effects are shifted towards relatively less reductions in the peaks. Under this scenario (2018 emissions), the total effects are now almost similar in the positive and negative directions, that is, 8.31 ppb-hr of decrease versus 10.66 ppb-hr of increase. In the carrying-capacity analysis in Section 13 we will discuss that some of these monitors where negative effects occur are generally in locations with reactive organic gases (ROG)/NO<sub>x</sub> regimes where emissions reductions from any strategy (not just heat-island control) could actually result in increased ozone.

For the July 1999 base episode (Figure F2), the impacts of increased urban albedo on monitor peaks under 1999 emissions (blue bars in the figure) are all decreases in the 1-hour peak, except for a monitor in Parlier (about 0.5 ppb increase) and very small increases in two monitors in Sacramento county (less than 0.1 ppb). These are generally downwind monitor locations where

no surface modifications (increased urban albedo) have been assumed (this will be addressed in future efforts where downwind locations will be also modified so as to maximize benefits). The largest reductions at monitors are up to 3–4 ppb, with some larger decreases as well. The reason for the larger effects of heat-island control in this episode compared to the July–August 2000 episode (discussed above) is partially explained by the generally larger air temperature reductions in this episode (compare Figures D2 and D1). The total effects under this episode with 1999 emissions are 38.88 ppb-hr in decrease versus only 1.31 ppb-hr in increase, thus representing a very dominant beneficial impact from increased urban albedo.

Under the 2018 emissions for this same base episode (red bars in Figure F2), the effects are generally smaller. In some cases, there are negative effects, i.e., increases in ozone at monitors where the ROG/NO<sub>x</sub> ratio is negatively affecting the carrying capacity and a few cases where there is larger decrease than in 1999 emissions. Overall, the increases are small compared to the decreases, namely, there are 20.68 ppb-hr of decrease compared to only 3.68 ppb-hr of increase, and the effects in this episode are overwhelmingly positive, i.e., they significantly improved air quality.

During all the other episodes, Figures F3 through F14 show that the effects of increased urban albedo on the 1-hour peak is overwhelmingly positive (that is, there is a decrease in ozone). This is summarized in Table 12.8 for the episodic-average change in the 1-hour peak at each monitor. The table also recaps the above discussion for the 2000 and 1999 regulatory episodes. It is very important to note that one cannot compare an episode to another directly in columns 4 and 5 in Table 12.8 (total ppb-hrs) because of varying lengths of the episodes. Other columns can be used to compare one episode to another directly.

**Table 12.8: Impacts on the 1-hr Peak Ozone in Central California**

Central California						
Episodes	Largest averaged decrease in 1-hr peak (ppb)	Largest averaged increase in 1-hr peak (ppb)	Total ppb-hrs decrease in peak	Total ppb-hrs increase in peak	Ratio of decrease to increase (RDI)	Domain average changes in 1-hr peak (ppb)
Jul–Aug 2000, 2000 emissions	2.05	1.47	14.48	5.38	2.68	-0.28
Jul–Aug 2000, 2018 emissions	1.18	2.75	8.31	10.66	0.78	0.07
Jul 1999, 1999 emissions	5.24	0.65	38.88	1.31	29.56	-1.14
Jul 1999, 2018 emissions	3.20	0.73	20.68	3.68	5.61	-0.52
Jun 14–27, 2000 (run A1)	3.15	2.41	23.77	11.54	2.06	-0.37
Jul 19–Aug 1, 2000 (run B)	3.04	0.81	28.00	1.93	14.44	-0.79

Central California						
Episodes	Largest averaged decrease in 1-hr peak (ppb)	Largest averaged increase in 1-hr peak (ppb)	Total ppb-hrs decrease in peak	Total ppb-hrs increase in peak	Ratio of decrease to increase (RDI)	Domain average changes in 1-hr peak (ppb)
Aug 4–8, 2000 (run C)	2.09	0.44	22.69	0.92	24.56	-0.66
Aug 11–18, 2000 (run D)	3.29	0.43	38.25	0.76	49.92	-1.14
May 18–31, 2001 (run E)	3.11	0.81	30.69	2.28	13.43	-0.86
Jun 20–22, 2001 (run F)	4.57	0.22	42.57	0.68	62.32	-1.27
Jul 10–22, 2002 (runH2)	3.63	0.94	20.78	5.97	3.47	-0.45
Jul 4–19, 2002 (runH1)	3.70	1.64	27.71	7.52	3.68	-0.61
Aug 8–20, 2002 (run I)	4.85	2.25	33.18	8.51	3.89	-0.75
Jun 3–27, 2003 (run J)	2.93	0.28	26.31	0.81	32.34	-0.77
Jun 25–Jul 17, 2003 (run K)	2.90	0.47	27.11	1.50	18.01	-0.78
Jul 25–Aug 4, 2005 (run M)	3.21	1.98	31.76	7.33	4.33	-0.74

It can be seen that except for the July–August 2000 episode, with 2018 emissions, all RDI values are greater than 1, indicating an overall decrease in 1-hour peaks. If the episodes listed in Table 12.8 were to be grouped into categories of “effectiveness” of increased urban albedo, the following could be the result:

**Group 1:** The most effective episodes include those with high RDI, as well as high absolute reductions in the peaks. This category includes: (1) July 1999 with 1999 emissions (RDI=29.56), and (2) June 20–22, 2001 (RDI=62.32). These episodes also have some of the largest decreases in the 1-hour peaks—5.24 ppb and 4.57 ppb, respectively—and the largest domain-averaged changes in 1-hour peak: -1.14 and -1.27 ppb, respectively.

**Group 2:** Highly effective episodes that include high RDI and relatively smaller absolute peak reductions than in Group 1. These include: (1) August 4–8, 2000 (RDI=24.56), (2) August 11–18, 2000 (RDI=49.92), and (3) June 3–27, 2003 (RDI=32.34). These episodes also have some of the higher domain-averaged changes in 1-hour peak, namely -0.66, -1.14, and -0.77 ppb, respectively.

**Group 3:** Effective episodes include the following: (1) July 1999 with 2018 emissions (RDI = 5.61), (2) June 14–27, 2000 (RDI=2.06), (3) July 19–August 1, 2000 (RDI = 14.44), (4) May 18–31, 2001 (RDI=13.43), (5) July 10–22, 2002 (RDI=3.47), (6) July 4–19, 2002 (RDI=3.68), (7) August 8–20, 2002 (RDI=3.89), (8) June 25–Jul 17, 2003 (RDI=18.01), and (9) July 25–August 4, 2005 (RDI=4.33)

**Group 4:** The least effective episodes include: (1) the July–August 2000 episode with 2000 emissions (RDI=2.68) and (2) the July–August 2000 with 2018 emissions (RDI=0.78). This is one of the episodes most modeled for central California in the regulatory environment.

While one of the factors behind the high effectiveness of UHI control in Group 1 episodes is the achievable temperature depression (see Table 10.3), there is generally no clear correlation with the base-case meteorology, and the impacts on ozone concentrations seem relatively consistent. That is, in general, the reductions in ozone in episode Groups 1 through 4 above correlate with the temperature *changes* (degree-hours reductions during the episode, seen in Table 10.3), except for episodes such as H1 and H2. For run July\_1999 and run F, the total degree-hours reductions (Table 10.3) are some of the largest. For both episodes, the domain-wide temperature is 40°C (104°F) or under (cooler than other episodes), thus indicating again that UHI mitigation can sometimes be more effective under non-extreme (i.e., not the hottest) conditions. This was alluded to in Phase II modeling and was one reason for undertaking the multi-episodic modeling in this project. Note that both the July-1999 run and run F have southwesterly flow in the SFBA, Sacramento, and Fresno regions. Also, the least-effective episode, July–August 2000, has some of the highest domain-wide absolute temperatures. The flow in all three sub-regions in this episode is northwest/west without any southwest component or coupling between Sacramento and the SFBA.

Of note in Figures F1 through F14 is that ozone peaks can increase at certain monitor locations. These locations are predominantly downwind of modified areas but are not modified themselves (or only marginally modified) with local increase in albedo. Thus, such locations can get negative impacts on ozone as a result of upwind modifications and reductions in air temperature. Thus, in general, such monitors should not be included in this analysis, as they are not modified, but are nevertheless included here to provide a complete picture of both positive and negative effects on the peaks in all regions (whether modified or not).

The monitors with potential increases in ozone include those in Placer County (almost always downwind of modified areas in Sacramento County) such as monitors 061-0002, 061-0006, and 061-3001; monitors in the Folsom Lake area that are downwind of urban Sacramento (e.g., monitors 067-0012 and 067-1001); and a monitor 019-4001 in Parlier (downwind of urban Fresno). Note that the monitors in Placer County almost always see increases in the local ozone peaks, except during run B (Figure F4), run D (Figure F6), and run M (Figure F14). Checking again in Table 10.1, it can be seen that these three episodes (runs B, D, and M) have no southerly or southwesterly flow in Sacramento county (only northwest or west), meaning that during these three episodes, Placer County is not downwind of Sacramento County but upwind of it, thus the reason why there are no negative impacts on the peaks during these episodes in Placer County.

The same can be seen in the monitor at Parlier (019-4001). The only times this monitor sees reductions in peak ozone are during runs F and J. Table 10.1 shows that during these two episodes, the flow in the Fresno region has westerly and southwesterly components. Thus, in these episodes, Parlier was not downwind of Fresno. Note that the decreases in ozone at Parlier are generally small because the modifications are marginal in this area. For the two monitors in

Sacramento County, 067-0012 and 067-1001, the same observation is made. These monitors see increased peaks except for the episodes in runs C and D. From Table 10.1, it can be seen that the flow during these two episodes in Sacramento County is mainly northwesterly, with some southwesterly flow. Either way, eastern Sacramento County (these monitor locations) is not downwind of urban Sacramento to the west (which would have been the case had the flow been westerly, as in other episodes).

#### 12.4.1.2 Southern California

During the five episodes modeled for southern California, as seen in Figures F15 through F19 (for the episodes-averaged changes in 1-hour peaks at monitors), the overwhelming impact is a decrease in the peak at all monitors, except for two in Riverside County (065-1002 and 065-6001) and one in Los Angeles County (037-6002). The reductions in the peaks are relatively similar across runs N, O, and P but are larger in runs Q and R. Table 12.9 summarizes these results for southern California domain. The ratio of the decrease to increase (RDI) in this table show that the effects are overwhelmingly positive (i.e., improved air quality) as does the domain-averaged change in 1-hour peaks (last column in the table).

**Table 12.9: Impacts on the 1-hr Peak Ozone in Southern California**

Southern California						
Episodes	Largest averaged decrease in 1-hr peak (ppb)	Largest averaged increase in 1-hr peak (ppb)	Total ppb-hrs decrease in peak	Total ppb-hrs increase in peak	Ratio of decrease to increase (RDI)	Domain average changes in 1-hr peak (ppb)
May 23–Jun 16, 2000 (run N)	4.80	0.48	39.00	0.93	41.90	-1.59
May 22–Jun 8, 2001 (run O)	4.92	0.94	47.19	2.51	18.79	-1.86
Aug 13–17, 2011 (run P)	5.02	0.55	48.23	1.15	41.78	-1.96
Jul 9–24, 2003 (run Q)	6.50	0.52	53.35	2.07	25.72	-2.14
Jul 12–26, 2005 (run R)	8.37	0.40	62.13	0.63	98.52	-2.56

Note in general that the impacts of increased urban albedo are larger in southern California than in central California, the main reason being the larger modifiable area in the Los Angeles Basin. Of note in figures F15 through F19 is that ozone peaks can increase at certain monitor locations. As mentioned above, the monitors include 071-2001 and 071-4001 in San Bernardino County; monitor 037-6002 in Los Angeles County, and monitors 065-1002 and 065-6001 in Riverside County. These monitors where the ozone peaks can increase at times are generally downwind of modified areas (that is, areas where albedo is increased) during the daytime, i.e., they are in the eastern-most and northern-most parts of the basin.

Thus, the results from both central and southern California domains show that the impacts of increased urban albedo on the ozone peaks are significant and are heavily positive, meaning a decrease in the peak at most monitors. The RDI provides a measure to evaluate the overall effect in the domain.

#### 12.4.2 Peak 8-hour Ozone and Relative Reduction Factor Analysis

Analysis of the 8-hour average ozone over all domains and episodes was performed. Of interest is the episodic peak of the 8-hour average (i.e., 8-hour maximum ozone), as it is the measure needed to develop a relative reduction factor (RRF). In this section, the modeled domain-wide episodic 8-hour peaks are identified for each episode in Table 12.10, as well as graphically in Figures G1 through G20 in Appendix G. Note that for the July–August 2000 episode, the simulations discussed here are shorter than the full regulatory episode analyzed elsewhere (e.g., Taha 2007), so they may not capture high ozone during later days in the episode.

As seen in Table 12.10, the episodic 8-hour maximum ozone ranges from about 95 to 131 ppb (in the central California episodes) and from about 100 to 130 ppb in the southern California episodes modeled in this study. As seen in Figures G1 through G20 in Appendix G, the episodic 8-hour peaks occur mostly in the urban areas and downwind of them, e.g., downwind of Sacramento (NE, E, SE), the SFBA East Bay (E, SE), Fresno (SE), and Bakersfield (E, SE) in central California. In southern California, the peaks occur in the north and northeast parts of the Los Angeles basin (in the San Bernardino, Riverside, and San Fernando areas), and east of San Diego.

As indicated earlier, one aspect of interest in evaluating the effectiveness of urban heat-island control, e.g., via increased urban albedo, is the impact on the 8-hour peak, that is, the RRF. The RRF is calculated for each monitor location (discussed earlier) and episode to give an overall assessment of this strategy's effectiveness. Figures 12.1 through 12.12 below depict these effects as “ $-(1-RRF)$ ” to make it easier to visually evaluate the impacts. In other words, the figures simply show the changes in the 8-hour episodic peak at each monitor and for each episode.

##### 12.4.2.1 *Central California*

Figures 12.1 and 12.2 show the impacts during the July–August 2000 and July 1999 episodes, both with current and future-year emissions (year 2018). While the impacts are predominantly beneficial (reduction in 8-hour peaks), it can be seen again that the effects during the July 1999 episode are more positive (larger ozone reductions) than those during the July–August 2000 episode. There are also negative impacts at certain monitors (increased ozone); these were identified earlier and the reasons for the negative impacts were highlighted. Here, we evaluate the overall impacts on RRF for the regulatory episodes and then for all other episodes. Rather than give a range or discuss each monitor separately, an average for each episode is discussed next.

**Table 12.10: Domain-Wide, Episodic 8-hr Peak Ozone in Central and Southern California**

<b>Episodic Peak 8-hr Ozone (Base-Case Scenarios Only)</b>			
<b>Central California Episodes</b>	<b>Domain-wide episodic 8-hr peak</b>	<b>Southern California Episodes</b>	<b>Domain-wide episodic 8-hr peak</b>
Jul–Aug 2000, 2000 emissions	106.42	May 23–Jun 16, 2000 (run N)	109.85
Jul–Aug 2000, 2018 emissions	94.56	May 22–Jun 8, 2001 (run O)	106.90
Jul 1999, 1999 emissions	125.86	Aug 13–17, 2011 (run P)	100.13
Jul 1999, 2018 emissions	100.63	Jul 9–24, 2003 (run Q)	130.21
Jun 14–27, 2000 (run A1)	114.88	Jul 12–26, 2005 (run R)	121.69
Jul 19–Aug 1, 2000 (run B)	123.56		
Aug 4–8, 2000 (run C)	94.09		
Aug 11–18, 2000 (run D)	104.51		
May 18–31, 2001 (run E)	116.50		
Jul 10–22, 2002 (runH2)	111.87		
Jul 4–19, 2002 (runH1)	130.98		
Aug 8–20, 2002 (run I)	113.67		
Jun 3–27, 2003 (run J)	106.67		
Jun 25–Jul 17, 2003 (run K)	117.83		
Jul 25–Aug 4, 2005 (run M)	121.69		

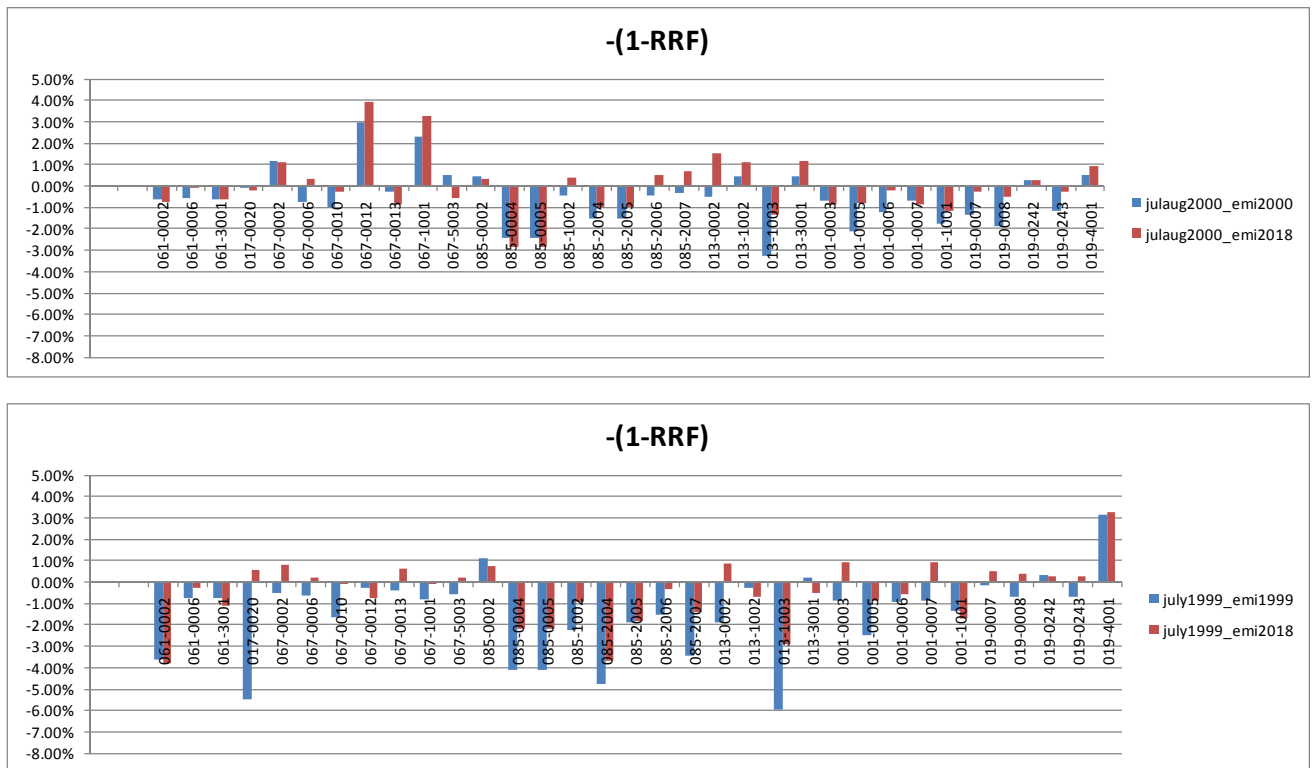
During the July–August 2000 episode, with year 2000 emissions, the “1-RRF” factor, i.e., reduction in episodic 8-hour peak ozone, ranges from -3.2 to +3.0 percent (but note that the large increase happens only during two events) with a domain-average change of -0.6 percent. Under the 2018 emissions, the range becomes -2.8 to +3.9 percent, with a domain-average of 0 percent. For the July 1999 episode with 1999 emissions, the “1-RRF” factor ranges from -5.9 to +3.2 percent and is more dominantly a decrease compared to the effects under the July–August 2000 episode. The domain-average change is -1.5 percent. Under the 2018 emissions scenario, the range of this factor for the July 1999 episode becomes -3.8 to +3.3 percent, with a domain-average of -0.5 percent. It is to be noted, however, that the large increase (of 3.3 percent) is occurring at only one monitor (Parlier), as discussed earlier and for the reasons explained before.

In a similar manner, Figures 12.3 through 12.12 below show the RRF changes for the remaining central California episodes. Table 12.11 summarizes the domain-average change in the “1-RRF” factor(reduction in 8-hour peak) for each episode. All averages are negative, implying improved air quality overall.

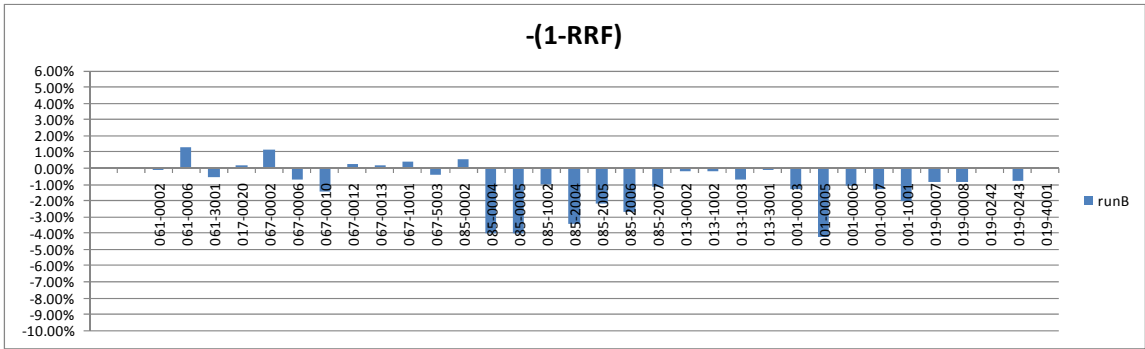
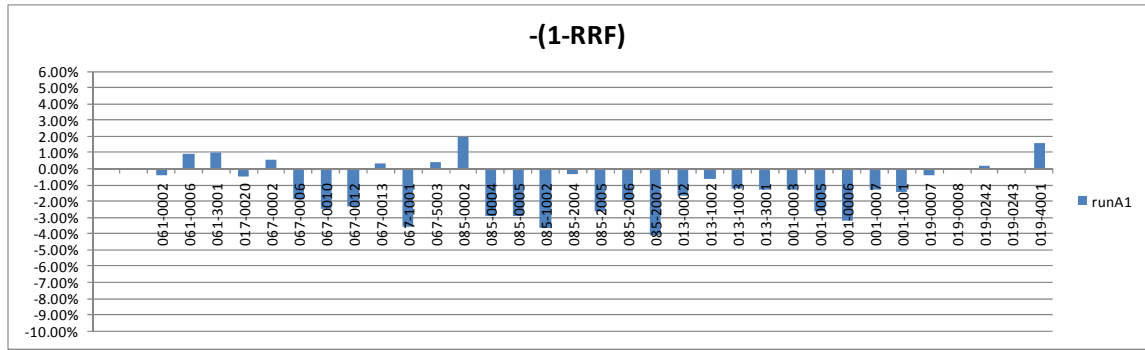
**Table 12.11: Domain-Average Change in 8-hr Episodic Peak in Central California**

runA1	runB	runC	runD	runE	runH1	runI	runJ	runK	runM
-1.1%	-0.9%	-1.4%	-1.6%	-1.0%	-1.3%	-1.2%	-1.9%	-0.9%	-1.0%

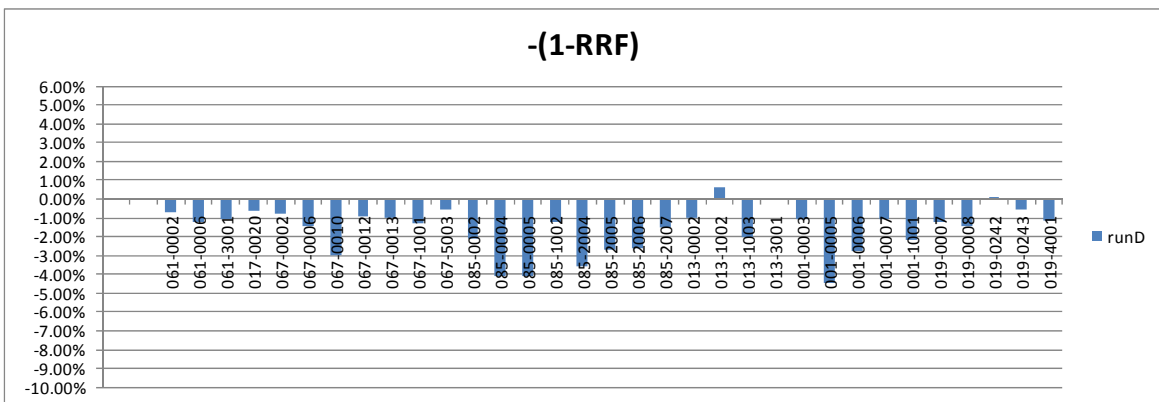
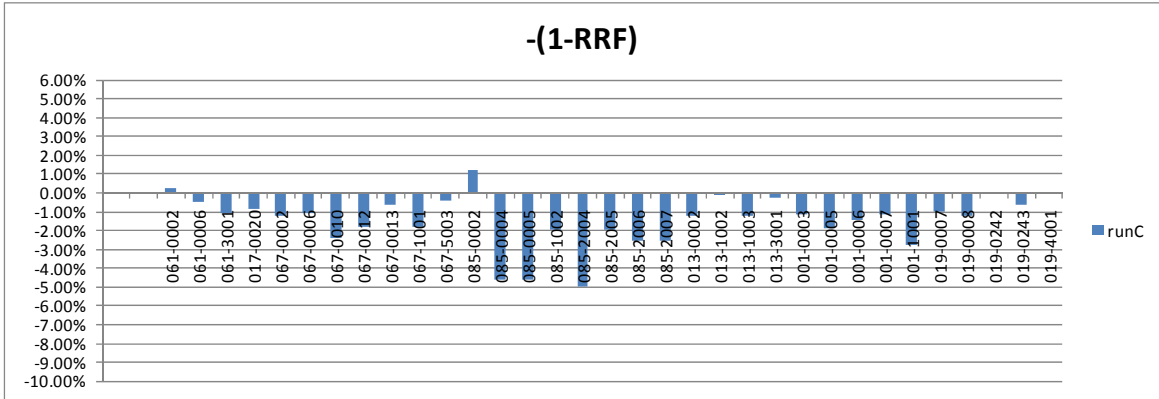
**Figures 12.1 and 12.2: Impacts on the Episodic 8-hour Peak During the 2000 and 1999 Central California Episodes**



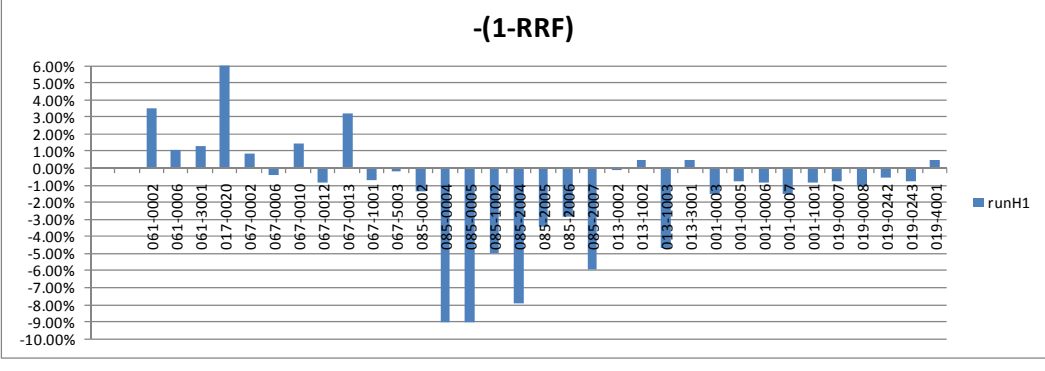
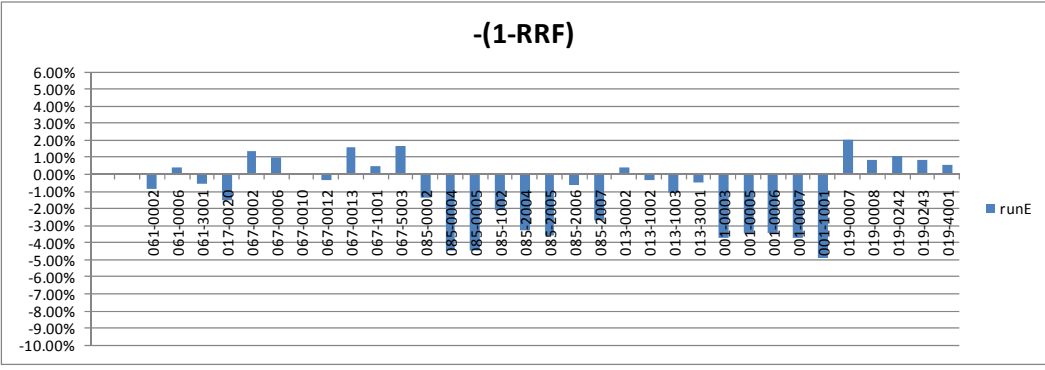
Figures 12.3 and 12.4: Impacts on the Episodic 8-hour Peak for Runs A1 and B for Central California



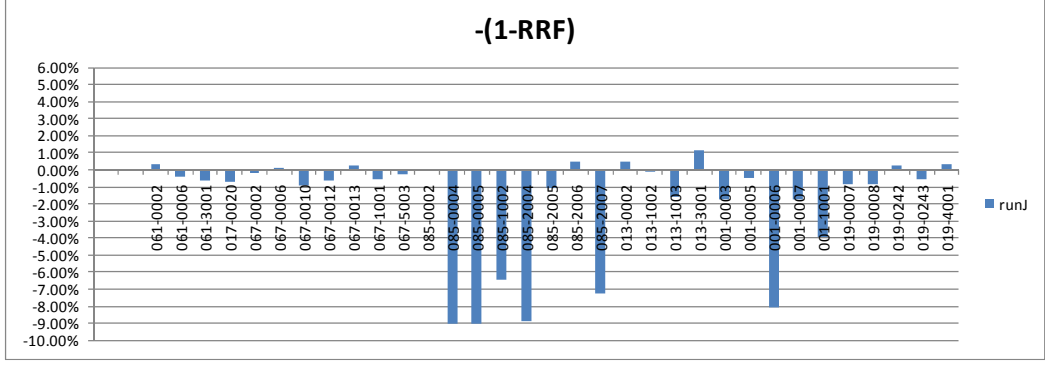
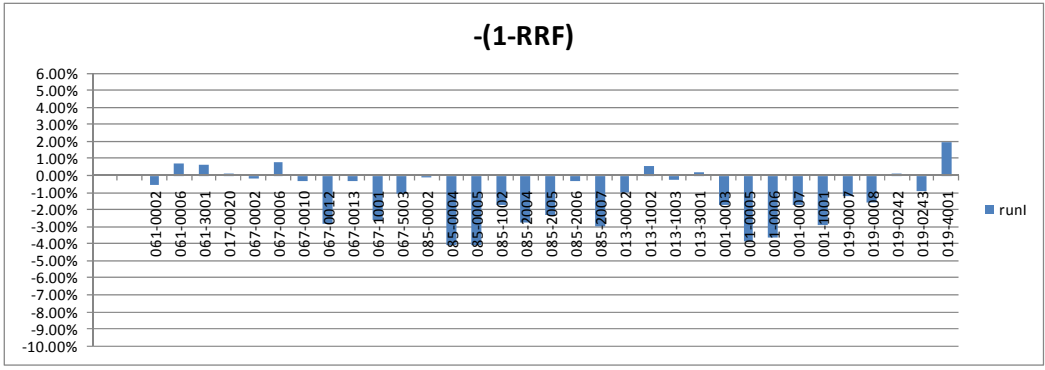
Figures 12.5 and 12.6: Impacts on the Episodic 8-hour Peak for Runs C and D for Central California



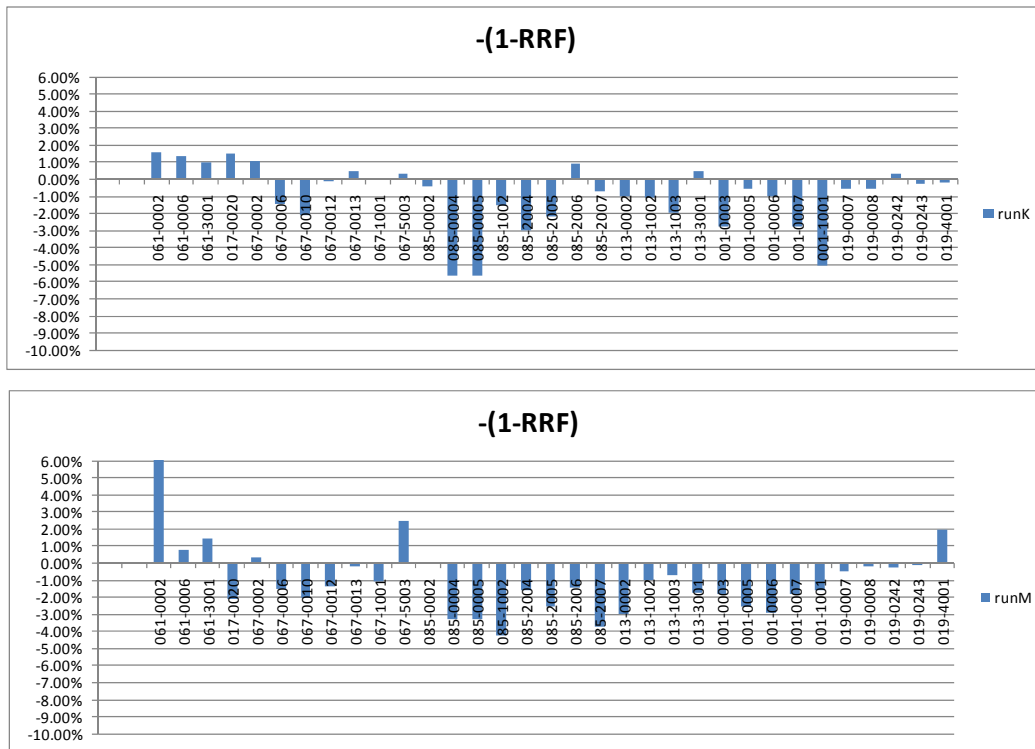
**Figures 12.7 and 12.8: Impacts on the Episodic 8-hour Peak for Runs E and H1 for Central California**



**Figures 12.9 and 12.10: Impacts on the Episodic 8-hour Peak for Runs I and J for Central California**



**Figures 12.11 and 12.12: Impacts on the Episodic 8-hour Peak for Runs K and M for Central California**



#### 12.4.2.2 Southern California

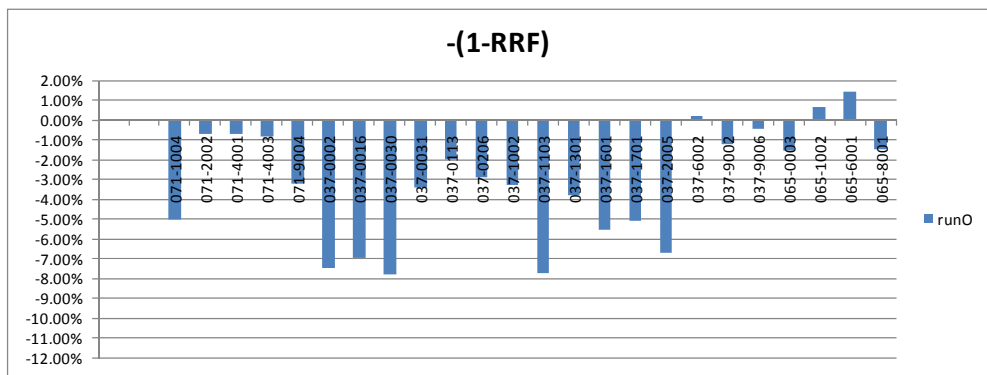
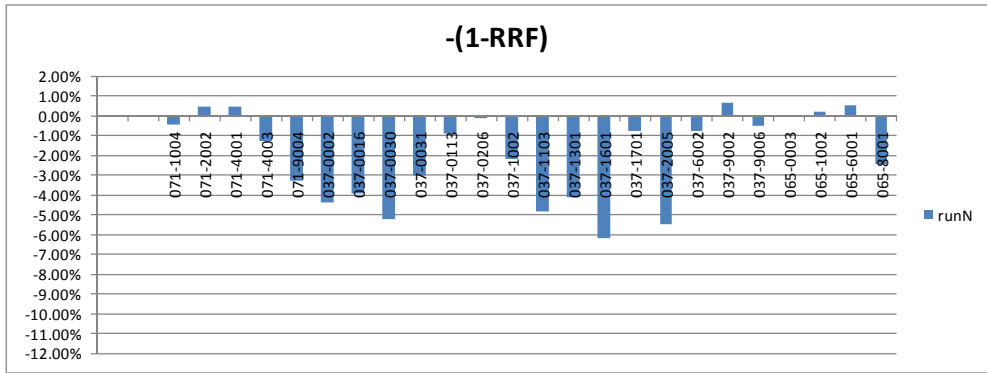
Figures 12.13 through 12.17 below show the same type of information (RRF changes) but for the southern California episodes. The results show an overwhelmingly positive impact (reductions in 8-hour peaks). Table 12.12 shows the domain-averaged changes in the “1-RRF” factor (reductions in 8-hr peak) for each episode. All averages are negative and significant, implying improved air quality overall.

**Table 12.12: Domain-Averaged Changes in the 8-hr Episodic Peak in Southern California**

runN	runO	runP	runQ	runR
-2.0%	-3.1%	-3.6%	-2.6%	-2.7%

It can be noted that the RRF changes in southern California are larger and more beneficial than those in central California, and their range is relatively more consistent. This reflects the fact that the larger modifiable area in the Los Angeles region can benefit more from increased urban albedo and that there is less geographical separation (one contiguous area) than in central California, where the SFBA, Sacramento, and Fresno regions can be affected differently under different synoptic conditions (episodes).

Figures 12.13 and 12.14: Impacts on the Episodic 8-hour Peak for Runs N and O for Southern California



Figures 12.15 and 12.16: Impacts on the Episodic 8-hour Peak for Runs P and Q for Southern California

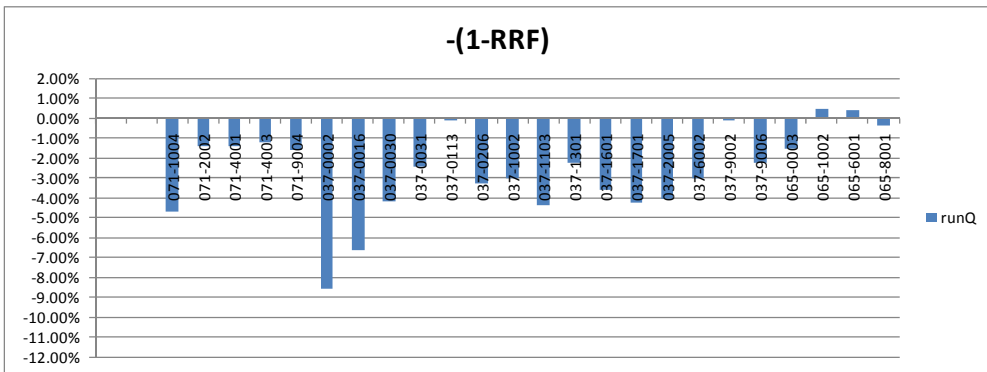
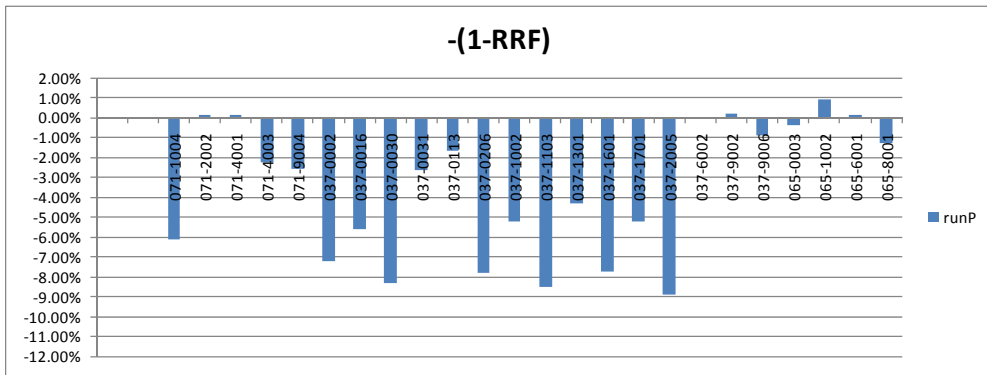
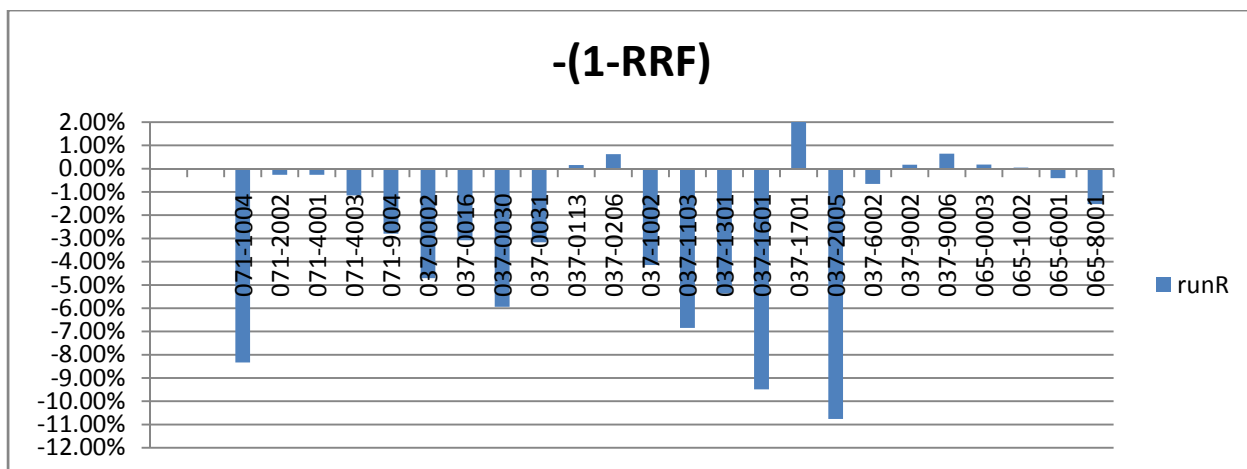


Figure 12.17: Impacts on the Episodic 8-hour Peak for Run R for Southern California



### 12.4.3 Cumulative Concentrations Changes

Another measure that can be used to evaluate the effectiveness of increased urban albedo in affecting air quality is the cumulative, integrated “concentration-time” product, i.e., in units of ppb-hr above a certain threshold. Here, two thresholds are used: 0 ppb and 60 ppb. The first is used to evaluate the overall effects of the strategy (including both day and nighttime impacts); whereas, the second is used to evaluate impacts more during the daytime, when concentrations are higher. In theory any other threshold can be used, but for simplicity, only 0 and 60 ppb are discussed here.

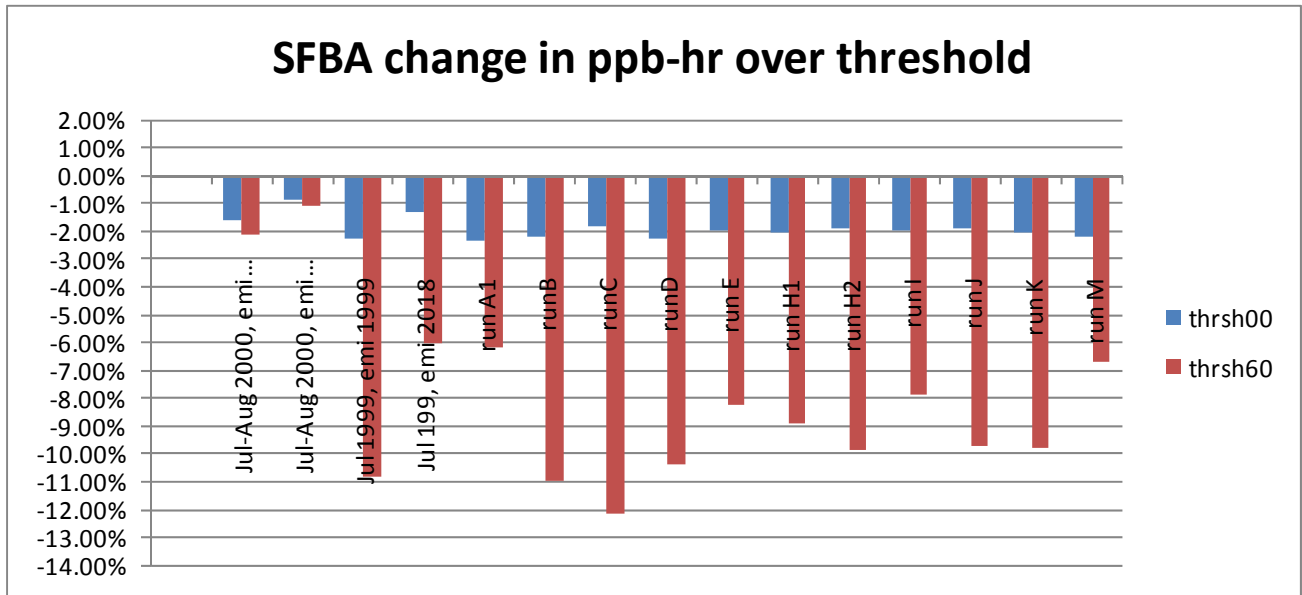
Thus, in Figures 12.18 through 12.20, the measure shown is the percentage-wise change in ppb-hr at all monitors in a region of interest, for the full length of each episode in that area, as discussed above. The regions of interest are the SFBA (Figure 12.18), Sacramento (Figure 12.19), and Fresno (Figure 12.20). The results show significant decreases in ppb-hr in all regions and episodes, except for two small increases in the Sacramento area. The average changes (averaged over all episodes) are as follows (Table 12.13):

Table 12.13: Average Changes in Cumulative Concentration Differences in Central California

	Threshold 0 ppb (%)	Threshold 60 ppb (%)
SFBA	-1.9	-8.0
Sacramento	-1.0	-2.7
Fresno	-1.1	-2.2

Once again we can see that as the urban area decreases in size, the effects of the control measure become smaller (i.e., from the SFBA, to Sacramento, to Fresno). Thus, overall, the effects of UHI mitigation are significant and positive (reduction in exposure above certain thresholds).

**Figure 12.18: Changes in Cumulative Concentration-Time (ppb-hr) above 0 and 60 ppb Thresholds, for the San Francisco Bay Area**



**Figure 12.19: Changes in Cumulative Concentration-Time (ppb-hr) above 0 and 60 ppb Thresholds, for the Sacramento Area**

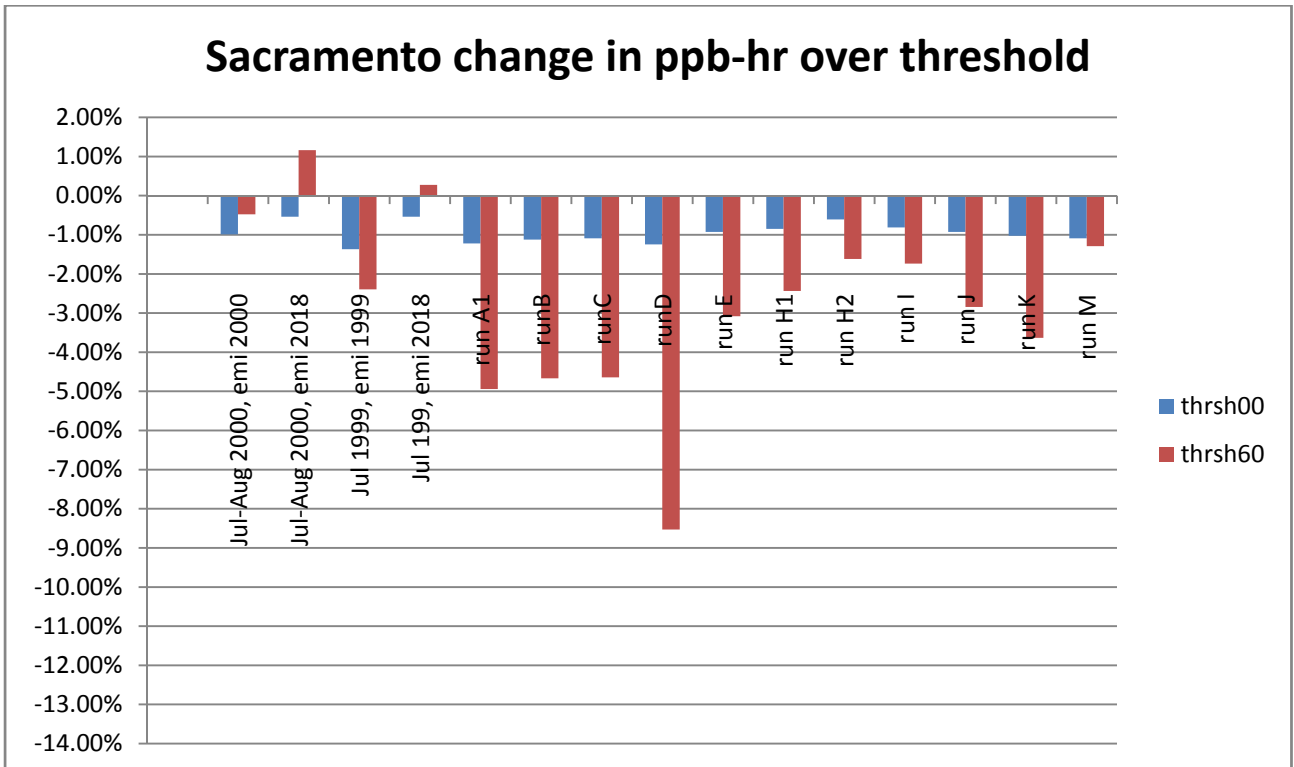
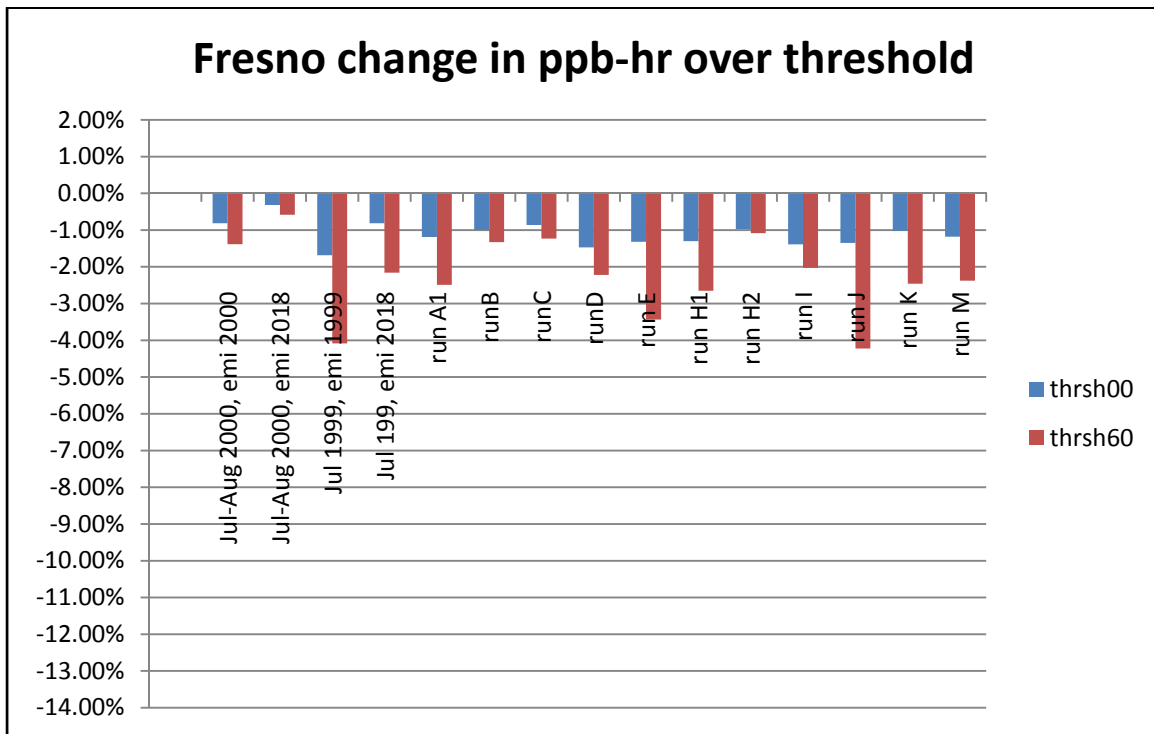


**Figure 12.20: Changes in Cumulative Concentration-Time (ppb-hr) above 0 and 60 ppb Thresholds, for the Fresno Area**



## CHAPTER 13: Emissions Equivalents

To develop emissions equivalents to the ozone air quality changes resulting from increased urban albedo (heat-island control) in this study, the atmospheric carrying capacity for NO<sub>x</sub> and ROG was analyzed via extensive photochemical modeling. The photochemical simulations discussed here were performed in addition to all the multi-episodic runs discussed in Section 12 and listed in Table 6.1.

For this purpose, step-wise emissions reductions and photochemical modeling were performed using emission from the July–August 2000 episode for central California and the July 2005 episode for southern California. Thus, in generating emissions equivalents (and the carrying-capacity diagrams shown in Appendix H), the reference ozone peaks are those from these two episodes, respectively, for central and southern California. The SAPRC99-mechanism speciation of pollutants was used as the basis to identify the NO<sub>x</sub> and ROG species emissions to be controlled (in step-wise reductions) in the sensitivity modeling. Biogenic emissions, of course, are not modified as part of the step-wise reduction; only anthropogenic emissions from area, point, and mobile sources.

For NO<sub>x</sub>, the stepwise controls include reductions in emissions of nitric oxide and nitrogen dioxide (NO<sub>x</sub> = NO + NO<sub>2</sub>). For ROG, the species include aldehydes, ketones, phenols, cresols, methanol, alkanes, alkenes, and aromatics. The photochemical model (CAMx) was re-run for each 20 percent step-wise emission reduction in NO<sub>x</sub>, in ROG, and then in both NO<sub>x</sub> and ROG from 100 to 40 percent, thus a total of 16 runs for each of central and southern California, analyzed at each monitor of interest. Results from the photochemical model runs, i.e., 1-hour ozone peaks, are then plotted on carrying-capacity diagrams and are summarized for each monitor in Figures H7.1 through H7.32 in Appendix G (for central California monitors) and H8.1 through H8.24 (for southern California monitors). The monitor locations were already identified in Table 12.1.

Figures H1 through H6 depict the areas affected by the step-wise emissions reductions for several combinations of NO<sub>x</sub> and ROG curtailment, as an example. Figure H1 (a–g) shows the areas affected by 20 percent reductions in NO<sub>x</sub> emissions (and 0 percent reductions in ROG) in central California. The figures are for species olefins (OLE), nitric oxide (NO), nitrogen dioxide (NO<sub>2</sub>), isoprene (ISOP), ethene (ETHE), alkanes (ALK1), and terpenes (TERP). Note that only anthropogenic ROG emissions are modified in this analysis; BVOC emissions (terpenes and isoprene) are not affected. The reason for including ROG emissions in this set of figures (even though ROG emissions are not changed) is simply for a quality check of various emissions processing steps, and also to provide a consistent set of figures to be reused in subsequent discussions.

Figure H2 (a–g) shows the changes in the same species listed above but for a reduction of 20 percent in ROG (no change in NO<sub>x</sub> emissions) for the central California domain. Figures H3 (a–g) again shows this information but for a scenario of 20 percent decrease in both ROG

and NO<sub>x</sub> emissions. Figures H4, H5, and H6 repeat the same information again but for the southern California modeling domain.

The results from these model runs are summarized graphically in Figures H7 (1–32) and H8 (1–24), showing the response in the 1-hour peak ozone (at each monitor location) to step-wise reductions in precursor emissions. The data (i.e., the pathways to lower ozone represented in these carrying-capacity diagrams) was then roughly classified in one of four ways, as indicated in Table 13.1. These pathways are emission reductions via (1) NO<sub>x</sub>-only control, (2) ROG-only control, (3) NO<sub>x</sub> and ROG control, and (4) NO<sub>x</sub> or ROG control. Type 3 means that decreasing the peak is not feasible by reducing emissions of NO<sub>x</sub> alone or ROG only, but that both must be reduced. The fourth type means that reductions in ozone peaks at that location could be achieved either by reducing NO<sub>x</sub> emissions or those of ROG. Table 13.1 summarizes these findings. The last column in the table provides the emission reductions (percentage-wise) needed to achieve a 1-ppb reduction in the 1-hour ozone peak at the location of the given monitor.

Note that some monitors will not be used in the analysis discussed next. Such monitors include the ones discussed earlier in Placer County, eastern Sacramento County, and in Parlier (southeast of Fresno). These were locations downwind of modified areas but were only marginally modified, and thus have mostly negative air-quality impacts. Thus, using results from these monitors will be meaningless per se but are nevertheless included to provide an overall picture of the potential impacts.

Based on the NO<sub>x</sub> and/or ROG limitations (pathways) identified in Table 13.1 for various areas in the central and southern California domains, the changes in ozone are converted into emissions equivalents, i.e., according to the specific pathway for each monitor. This conversion is shown in Table 13.2 for central California and Table 13.4 for southern California. Of note; in Tables 13.2 and 13.4, only a subset of the monitors is shown. This subset is arrived at after (1) removing the irrelevant monitors (in areas where no surface modifications are assumed), and (2) removing monitors that do not have the relevant pathway, i.e., removing monitors from the NO<sub>x</sub> list when there is no beneficial NO<sub>x</sub> pathway at the monitor location and removing the monitor from the ROG list when there is no ROG beneficial pathway. Then, as a summary, the emission equivalence is averaged over all monitors for each episode (respective run) and summarized in Table 13.3 for central California and Table 13.5 for southern California. Clearly, it is more beneficial to adopt a ROG-control approach, since all resulting changes are a decrease in emission equivalences. As can be seen in Table 13.3, the range of ROG emissions reductions across all episodes in central California is from -3.31 to -9.26 percent and for southern California (Table 13.5) from -5.70 to 8.56 percent.

Since anthropogenic ROG emissions in central California amount to an average of about ~2,000 tons per day (TPD), then the above range of reductions translates into about 66 to 185 TPD of anthropogenic ROG reduction. For southern California, the average daily emission of anthropogenic ROG is about ~900 TPD. Thus, the equivalent emissions reductions range is from 51 to 77 TPD of anthropogenic ROG.

**Table 13.1: Summary of Carrying-Capacity Sensitivities**

County and Monitor	Emission Reduction Pathway				Reduction (NOx,VOC) Needed to Achieve a 1 ppb Reduction in 1-hr Peak
	NOx control	or	and	VOC Control	
Placer					
061-0002	■				10% / ppb
061-3001	■		■	■	20% and 20% / ppb
061-0020	■				3.33% / ppb
Sacramento					
067-0002	■				10% / ppb
067-0006	■		■	■	20% and 20% / ppb
067-0012	■	■		■	3.33% or 3.33% / ppb
067-0013	■				5% / ppb
067-1001	■	■		■	6.66% or 10% / ppb
067-5003	■	■		■	6.66% or 6.66% / ppb
Santa Clara					
085-0002	■	■		■	6.66% or 10% / ppb
085-0004				■	4% / ppb
085-1002				■	5% / ppb
085-2004				■	3.33% / ppb
085-2005				■	4% / ppb
085-2006				■	4% / ppb
085-2007				■	4% / ppb
Contra Costa					
013-0002				■	5% / ppb
013-1002	■	■		■	20% or 5% / ppb
013-1003				■	20% / ppb
013-3001				■	5% / ppb
Alameda					
001-0003				■	3.33% / ppb
001-0005				■	10% / ppb
001-0006				■	6.66% / ppb
001-0007				■	3.33% / ppb
001-1001				■	6.66% / ppb
Fresno					
019-0007	■	■		■	5% or 6.66% / ppb
019-0008	■	■		■	6.66% or 6.66% / ppb
019-0242	■	■		■	5% or 10% / ppb
019-0243	■	■		■	6.66% or 10% / ppb

County and Monitor	Emission Reduction Pathway				Reduction (NO <sub>x</sub> ,VOC) Needed to Achieve a 1 ppb Reduction in 1-hr Peak
	NO <sub>x</sub> control	or	and	VOC Control	
019-4001	■	■		■	5% or 6.66% / ppb
San Bernardino					
071-1004				■	1.42% / ppb
071-2002	■				10% / ppb
071-4001	■				10% / ppb
071-4003				■	1.17% / ppb
071-9004				■	1.17% / ppb
Los Angeles					
037-0002				■	2% / ppb
037-0016				■	1.43% / ppb
037-0030				■	6.66% / ppb
037-0031				■	10% / ppb
037-0113				■	10% / ppb
037-0206				■	2.22% / ppb
037-1002				■	3.33% / ppb
037-1103				■	4% / ppb
037-1301				■	5%/ppb
037-1601				■	3.33% / ppb
037-1701				■	1.81% / ppb
037-2005				■	2.5% / ppb
037-6002				■	3.33% / ppb
037-9002				■	5% / ppb
037-9006				■	2.85% / ppb
Riverside					
065-0003				■	2.5% / ppb
065-1002	■	■		■	5% or 5% / ppb
065-6001				■	3.33% / ppb
065-8001				■	1.66% / ppb

Two important caveats need to be borne in mind here regarding the computation of these emission-reduction equivalents:

1. The above calculations assume that increased urban albedo has been implemented in all urban regions in the domain of interest (i.e., the SFBA, Sacramento, and Fresno in central California; and Los Angeles, San Bernardino, and Riverside in southern California) *simultaneously* to achieve the meteorological, emissions, and air-quality impacts that are used in the calculations of emissions equivalents.

2. That the emission equivalents are computed over all areas as well. For example, the reductions of 66 to 185 TPD of ROG, calculated above for central California, are assumed to come uniformly from all emission sources in the central California domain, particularly the three regions identified above. Similarly, the 51 to 77 TPD of ROG calculated for southern California are assumed to come uniformly from the Los Angeles Basin.

**Table 13.2: NOx and ROG Equivalences for Central California**

Monitors	julaug2000 emi2000	july1999 emi1999	runA1	runB	runC	runD	runE	runF	runH2	runH1	runI	runJ	runK	runM
<b>NOx equivalence</b>														
067-0002	1.10%	-3.56%	2.78%	-2.42%	-2.84%	-3.92%	2.99%	0.41%	-2.72%	5.35%	2.83%	0.09%	-0.14%	5.17%
067-0013	-0.08%	-1.97%	-1.02%	-0.81%	0.17%	-2.08%	-0.37%	-0.93%	2.09%	2.56%	2.79%	-0.36%	-0.59%	-0.71%
<b>ROG equivalence</b>														
067-5003	0.91%	0.86%	16.07%	-0.69%	-0.16%	-1.45%	-3.66%	-3.11%	4.97%	3.33%	-0.15%	-1.20%	-1.92%	6.92%
085-0002	3.98%	1.12%	1.82%	-1.37%	1.72%	-13.51%	-2.65%	-2.24%	0.45%	-0.86%	0.38%	-3.11%	-4.34%	1.56%
085-0004	-8.18%	-13.86%	-12.59%	-12.14%	-8.37%	-13.17%	-11.88%	-18.30%	-14.52%	-14.82%	-19.40%	-11.73%	-11.58%	-12.46%
085-1002	-0.01%	-13.76%	-7.04%	-5.89%	-3.27%	-5.87%	-6.36%	-18.85%	0.34%	-7.84%	-9.73%	-5.91%	-7.17%	-7.32%
085-2004	-5.75%	-14.56%	0.32%	-8.37%	-6.72%	-9.12%	-10.37%	-13.91%	-10.45%	-10.63%	-12.31%	-9.14%	-7.72%	-10.68%
085-2005	-3.52%	-2.21%	-6.35%	-7.99%	-3.85%	-9.49%	-8.48%	-8.56%	-5.79%	-7.30%	-7.61%	-5.72%	-7.50%	-7.74%
085-2006	-0.74%	-4.48%	1.80%	-8.94%	-5.74%	-10.93%	-4.30%	-4.42%	0.35%	-2.78%	6.09%	-3.44%	-6.25%	-0.87%
085-2007	-1.10%	-14.76%	-3.18%	-4.77%	-3.96%	-5.83%	-7.65%	-17.89%	-0.52%	-6.22%	-8.56%	-5.12%	-5.83%	-4.00%
013-0002	-6.54%	-5.35%	-10.22%	-4.27%	-5.74%	0.12%	-3.37%	-4.02%	-4.81%	-4.93%	-8.31%	-3.35%	-1.65%	-8.33%
013-1003	-12.92%	-44.23%	-15.63%	-10.70%	-9.56%	-27.98%	-14.09%	-47.44%	-9.30%	-19.95%	-19.18%	-7.27%	-15.23%	-19.27%
013-3001	-0.38%	-1.78%	-1.87%	-0.05%	-3.72%	0.69%	-0.61%	-0.70%	-3.54%	-1.85%	-2.30%	-0.73%	1.13%	-3.95%
001-0003	-1.35%	-2.50%	-2.50%	-5.68%	-2.66%	-10.24%	-4.91%	-14.77%	-3.12%	-4.58%	-5.90%	-4.06%	-5.91%	-7.59%
001-0005	-6.09%	-8.52%	-24.68%	-15.15%	-7.65%	-25.67%	-23.90%	0.24%	-10.70%	-10.60%	-10.51%	-16.38%	-20.19%	-18.50%
001-0006	-4.22%	-8.60%	-14.41%	-8.22%	-4.38%	-11.02%	-15.65%	0.21%	-5.01%	-11.05%	-12.56%	-12.10%	-11.65%	-12.72%
001-0007	-1.34%	-2.48%	-2.47%	-5.63%	-2.64%	-10.15%	-4.87%	-14.64%	-3.10%	-4.54%	-5.85%	-4.03%	-5.85%	-7.53%
001-1001	-8.88%	-12.12%	-16.80%	-11.27%	-8.23%	-13.82%	-14.19%	-16.58%	-9.67%	-16.33%	-16.80%	-9.07%	-10.58%	-18.18%
019-0007	-2.78%	-0.85%	4.86%	-2.51%	-4.84%	-2.27%	-4.69%	1.49%	0.32%	0.21%	0.51%	-5.50%	-0.89%	8.86%
019-0008	-3.86%	-2.55%	4.41%	-3.43%	-5.36%	-3.16%	-3.97%	-0.20%	-0.03%	0.61%	-1.25%	-7.30%	-2.11%	3.15%
019-0242	0.36%	0.74%	-4.94%	0.31%	-2.73%	-1.21%	-1.63%	-0.03%	1.87%	-1.40%	0.86%	-0.15%	-0.60%	0.21%
019-0243	-3.82%	-3.10%	6.12%	-4.69%	-10.14%	-3.13%	-4.55%	-1.56%	0.02%	-0.07%	-2.90%	-6.61%	-4.26%	11.09%

**Table 13.3: Central California Episode-Averaged Emissions Equivalence**

	julaug2000 emi2000	july1999 emi1999	runA1	runB	runC	runD	runE	runF	runH2	runH1	runI	runJ	runK	runM
<b>NOx equivalence</b>														
	0.51%	-2.76%	0.88%	-1.62%	-1.34%	-3.00%	1.31%	-0.26%	-0.32%	3.96%	2.81%	-0.14%	-0.37%	2.23%
<b>ROG equivalence</b>														
	-3.31%	-7.65%	-4.36%	-6.07%	-4.90%	-8.86%	-7.59%	-9.26%	-3.61%	-6.08%	-6.77%	-6.10%	-6.51%	-5.37%

**Table 13.4: NOx and ROG Emission Equivalence for Southern California**

Monitors	runN	runO	runP	runQ	runR
<b>NOx equivalence</b>					
071-2002	0.8%	2.1%	-0.2%	3.0%	-3.9%
071-4001	0.8%	2.1%	-0.2%	3.0%	-3.9%
<b>ROG equivalence</b>					
071-1004	-5.4%	-5.4%	-5.9%	-6.0%	-8.8%
071-4003	-0.9%	-1.9%	-1.7%	-1.5%	-1.6%
071-9004	-2.5%	-2.6%	-1.8%	-2.8%	-4.2%
037-0002	-8.8%	-8.8%	-7.8%	-13.0%	-13.3%
037-0016	-6.9%	-7.0%	-4.5%	-7.3%	-12.0%
037-0030	-13.0%	-16.8%	-33.4%	-21.7%	-22.7%
037-0031	-12.7%	-13.1%	-15.2%	-11.9%	-10.7%
037-0113	-2.7%	-4.3%	-4.2%	1.8%	-5.7%
037-0206	-5.8%	-6.5%	-9.1%	-7.9%	-7.2%
037-1002	-4.7%	-5.8%	-9.3%	-9.5%	-7.2%
037-1103	-7.9%	-12.7%	-15.5%	-17.1%	-13.2%
037-1301	-8.2%	-12.0%	-9.3%	-11.0%	-8.0%
037-1601	-8.5%	-10.8%	-9.4%	-10.7%	-10.5%
037-1701	-6.2%	-6.9%	-7.2%	-8.9%	-11.1%
037-2005	-6.3%	-8.0%	-8.7%	-10.6%	-11.0%
037-9002	-1.3%	-1.2%	1.5%	2.5%	-3.8%
037-9006	-0.8%	-2.2%	-1.5%	0.1%	-5.7%
065-0003	-3.3%	-5.8%	-3.6%	-3.2%	-3.1%
065-8001	-2.3%	-3.5%	-2.8%	-2.6%	-2.8%

**Table 13.5: Southern California Episode-Averaged Emissions Equivalence**

	runN	runO	runP	runQ	runR
<b>NOx equivalence</b>	0.76%	2.14%	-0.24%	2.98%	-3.93%
<b>ROG equivalence</b>	-5.70%	-7.12%	-7.86%	-7.45%	-8.56%

## CHAPTER 14: Potential Atmospheric Impacts of Urban Solar PV Arrays

As a continuation to the main aspect of the study—that is, urban heat islands, their impacts, and ways to mitigate them—the rest of this report focuses on the potential meso-urban effects of solar technology deployment and the perceived potential for its creation of heat islands in urban areas. The purpose of this task is to evaluate any such effects, both positive and negative, under existing conditions as well as under cool-city scenarios, and propose ways to mitigate them, if any negative impacts could arise. This part of the project, while involving full atmospheric modeling, is mainly a scoping study, with the goal of identifying the relevant parameters in evaluating such impacts.

The deployment of solar arrays (e.g., photovoltaic or solar thermal systems) can have two types of impacts. The *direct* effect is that of generating electricity (or hot water/air); whereas, the *indirect* effect is the impact of solar systems on the ambient environment, such as air temperature. Depending on the configuration of the solar arrays (envelope-embedded or detached/elevated), additional effects can be included in the direct effect, such as the shading from such elevated arrays on the underlying roof system or parking lots, and other effects. In addition, solar power generation (or heating) contributes to air quality and greenhouse gas emission reductions by avoiding power-plant electricity generation (or natural gas, if solar water heating, for example) and by reducing energy use in buildings, e.g., via shading.

This scoping analysis and report discussion focuses only on the *indirect* effect, i.e., the potential atmospheric impacts of solar PV deployment in urban areas.

California's ambitious portfolio for inclusion of energy efficiency and renewable energy measures dictates that a variety of energy technologies are implemented both in the short and long terms. In terms of renewables, there is a large focus on solar and wind energy sources, both of which are abundant in the state. For solar generation, Governor Brown's *Clean Energy Jobs Plan* (CEC 2011) suggests that solar systems up to 2 megawatts (MW) be installed on the roofs of warehouses, parking lot structures, schools, and other commercial buildings throughout the state, and that solar energy projects up to 20 MW in size would be built on public and private property throughout the state. For example, the State would create the California Solar Highway by placing solar panels along the banks of state highways. This is not counting voluntary installations of solar systems by homeowners and business owners.

Navigant (2007) estimated that by the year 2016, it would be possible to attain the goal of 3,000 MW, set out by the California Solar Initiative, if an aggressive program of PV development and incentives is put in place. They also report that the technical deployment potential on rooftops in California amounts to about 40 GW in 2006 (with a potential of up to 68 GW by 2016).

Thus, keeping in mind that to generate 10 W of electricity, roughly 1 square foot [ft<sup>2</sup>](~0.1 square meter [m<sup>2</sup>]) of a PV collector is required (CEC 2003), then a large penetration of solar systems in California would be needed to attain these goals. In this discussion and in the calculations of deploy ability and roof area needs for PV systems, we will use this factor of 10 W ft<sup>-2</sup> (~ 110 W m<sup>-2</sup>). Generally, the implementation of solar technologies can take two forms. One is concentrated solar energy generation, and the second is distributed generation. The first is typically found in solar power plants, such as those licensed by the Energy Commission; whereas, the second is typically an urban-scale deployment of solar systems. This report summarizes a scoping analysis for the latter situation and identifies thermal environmental considerations (e.g., temperature and heat islands) that could be affected.

In this scoping analysis, we do not concern ourselves with the direct effects of solar systems, i.e., the power they generate (or hot water) and their effects on heat flow through the building envelope (such as the effects of shading the underlying roof structure), and thus the impact on energy use for cooling and heating. Several tools, such as the DOE Roof Calculator<sup>6</sup> or the calculator developed by the National Renewable Energy Laboratory (NREL 2012), can be used to evaluate such tradeoffs and their impacts on energy use in buildings. Also, an important beneficial environmental effect of solar systems is that they avoid air pollution and help improve air quality by reducing the amount of power needed to produce electricity, and thus emissions from power plants. Again, we are not considering this beneficial effect in this study.

In this analysis, we concern ourselves with the indirect (ambient) effects of solar systems, i.e., the atmospheric impacts. Thus, we examine the potential impacts of solar systems on local meteorology, focusing on air temperature changes in urban areas where the solar PV systems are deployed. That is, the analysis attempts at answering only the following questions:

Does the large-scale deployment of solar systems generate a heat island? Does it generate it under existing conditions or under future, cool-city conditions? And, if it does, what are the potential associated impacts on meteorology and air quality? Or can such solar systems contribute to lowering ambient temperatures and thus help mitigate the local heat island? If so, under what conditions?

The report also does not examine the effects of solar power plants. These are studied and modeled differently, and some initial estimates are available. For example Millstein and Menon (2011) show, via regional modeling, that a hypothetical 1 terawatt (TW) capacity solar array in the California Mojave desert increased average temperatures by 0.4°C (0.7°F) and affected wind flow over an area of 300 km radius around the power plant.

## 14.1 Deployability (Technical Potential)

In this scoping study, we assume that the deploy ability of solar systems in urban settings is a function of several aspects, including:

1. Land-use / Land-cover (LULC)

---

<sup>6</sup> DOE Roof Calculator website: <http://www.ornl.gov/sci/roofs+walls/facts/CoolCalcEnergy.htm>.

2. Total available roof surface area that is available for solar installations
3. Solar (sunshine) availability and access

To estimate deploy ability (technical potential) of solar systems, several approaches can be followed. For example, Chaves and Bahill (2010) developed technical potential using a digital elevation model (DEM) based on LiDAR data. Navigant (2007) used a market-based penetration model to compute the technical potential for solar photovoltaic technologies in urban areas in California. Taha (2007,2011) develops deploy ability technical potential based on LULC analysis, e.g., based on data from USGS Level-II LULC (Anderson et al. 2001).

Here, a crude comparison is made between the approaches of Navigant (2007) and Taha (2011). Using Navigant’s megawatt potential (MWp) data, and assuming a factor of  $\sim 110 \text{ W m}^{-2}$ , we can compute the following (in  $\text{km}^2$ ) in Table 14.1:

**Table 14.1: Technical Potential for Solar PV (Based on Navigant 2007)**

Region	Total MWp			Total PV Area Potential( $\text{km}^2$ )		
	Year 2006	Year 2010	Year 2016	Year 2006	Year 2010	Year 2016
Los Angeles	15658	19457	26204	145	180	243
Sacramento	2938	3855	5607	27	36	52
Fresno	962	1227	1707	9	11	16

On the other hand, the LULC analysis of Taha (2011) develops technical potential based on deployability values assigned to various LULC and gridded into a modeling domain. For the three regions in Table 14.1, and for conditions representing the past 5–10 years, Taha (2011) estimates a total technical potential as follows (in Table 14.2):

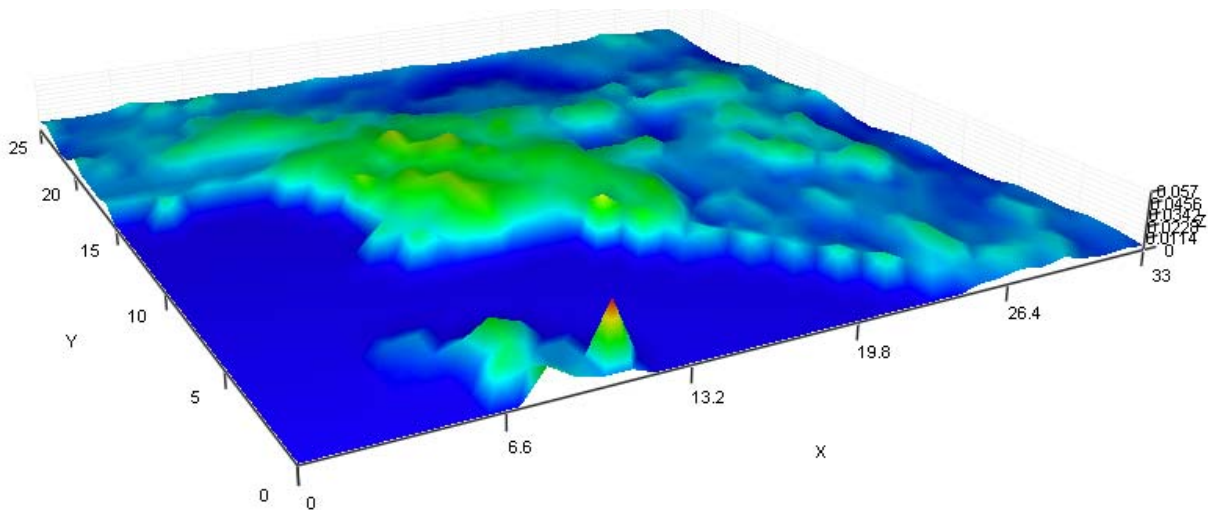
**Table 14.2: Technical Potential for Solar PV Based on Taha (2011)**

Region	Total PV Area Potential( $\text{km}^2$ )	
	Low scenario	High scenario
Los Angeles	71	137
Sacramento	18	36
Fresno	9	18

While the results from Navigant and Taha are not exactly comparable, they are nevertheless of the same magnitude. In this scoping study and modeling analysis, the deployability calculations of Taha (2011) will be used, since they are gridded at the desired atmospheric model resolutions

and domains. Figure 14.1 shows an example calculation of solar PV deploy ability (percent of 200 m cells) computed for the Los Angeles Basin (Taha 2011).

**Figure 14.1: Solar Photovoltaic Deployment Potential (% of 200 m Cells) for the Los Angeles Basin**



Source: Taha 2011.

## 14.2 Effective Albedo of Solar PV Systems

For any surface and at a specific wavelength ( $\lambda$ ), the following equation holds:

$$\alpha_{\lambda} + \rho_{\lambda} + \tau_{\lambda} = 1$$

where  $\alpha$ ,  $\rho$ , and  $\tau$  are respectively the absorptivity, reflectivity, and transmissivity at the given wavelength. For atmospheric modeling purposes, e.g., for UHI modeling and impact on ambient temperatures, a more generalized form of this equation for a solar photovoltaic or solar thermal system is:

$$\alpha_{eff} = 1 - \rho - \varepsilon$$

where  $\alpha_{eff}$ ,  $\rho$ , and  $\varepsilon$  are respectively effective absorptivity, reflectivity, and the solar conversion efficiency (annual averages over 365 days for sunrise-to-sunset hours).

Typical values of  $\rho$  range from 0.06 to 0.1 (thus an average of 0.08 is used here). Some sources state a value as low as 0.04 (SolarWorld 2010) and 0.05 (Nemet 2009) or as high as 0.1 (Protogeropoulos and Zachariou 2010). Note that in this report, we are interested only in the

“atmospheric impact” aspect of PV systems, and thus reflectively is characterized in that sense. We are not interested in low-sun (small angle of incidence) reflectivity where the reflected beam from the PV system can cause glare on the other side. In such cases, “reflectivity” can reach up to 0.20 to 0.30 (Protogeropoulos and Zachariou 2010). While this aspect is important for glare consideration (not thermal energy balance calculations and atmospheric modeling), a value of 0.08 is used here for  $\rho$ .

For  $\varepsilon$ , the literature and field-measurement studies give various ranges. For example, Fanney et al. (2001) give  $\varepsilon$  values of between 5 and 12 percent, with most panels having an efficiency of between 10 and 12 percent. Other sources give values for  $\varepsilon$  between 14 and 18 percent (Hester et al. 2005) and between 6 and 19 percent (Simons and McCabe 2005); thus an overall average of 10 to 15 percent seems representative. Accordingly,  $\alpha_{eff}$  has a value of around 0.77 (these are example calculations). Thus, if effective albedo is defined as:

$$A_{eff} = 1 - \alpha_{eff}$$

or in other words,

$$A_{eff} = \rho + \varepsilon$$

then a representative value for effective albedo of a solar PV panel is between 0.18 and 0.23. Note that in the long term, it is anticipated that the solar conversion efficiency of PV systems would reach up to 0.28 by the year 2100 (Nemet 2009). With such high efficiencies, solar systems will provide a larger cooling effect than with currently feasible efficiencies.

### 14.3 Evaluation of Potential Radiative Impacts

From a radiative balance standpoint, it is straightforward to see that for a defined area, such as a model’s grid cell or a neighborhood/city block targeted for implementation of solar arrays, that an initial estimate can be made as follows.

If the base albedo of the grid cell or target area is  $A_b$ , then the modified albedo  $A_m$  of that area or cell after introduction of solar PV is:

$$A_m = A_b[1 - PVd] + PVd \times A_{eff}$$

where  $PVd$  is the aerial deployment potential for solar PV in that grid cell or target area, and  $A_{eff}$  is as defined earlier. Thus, whenever  $A_{eff} > A_b$ , the grid cells’s albedo (or area’s albedo) increases, and one can expect a decrease in ambient air temperature, generally speaking. This is correct from a radiative balance point of view; however, there are non-linear effects in terms of temperature change that need to be quantified, e.g., via meso-urban meteorological modeling, to evaluate their magnitudes. On the other hand, if  $A_{eff} < A_b$ , then some compensation in albedo is needed in theory, i.e., there is need to increase roof albedo or pavement albedo by an amount

opposite to and equal to the reduction in albedo due to the introduction of the solar PV systems in that grid cell or area (keeping in mind that the impacts on air temperature may not be large enough to require compensation—this will be discussed later). Thus, in summary:

$$\text{Radiative impact: } \left\{ \begin{array}{l} A_{eff} \geq A_b : \text{ no action necessary} \\ A_{eff} < A_b : \text{ compensation necessary} \end{array} \right.$$

Since in current conditions, most urban average albedo in U.S. cities; that is, albedo averaged over areas of a few square kilometers at a time, is in the range of 0.16 to 0.22, e.g., an average of 0.18 (see calculations explained later), it is anticipated that solar systems will have no negative impacts, even at a low, 10 percent conversion efficiency ( $\varepsilon$ ) assuming a solar panel reflectivity of 0.08, as discussed earlier. For  $\varepsilon$  values greater than 10 percent, the solar PV systems will actually provide a cooling effect. Again, this is from a radiative balance standpoint, and meteorological modeling is still needed to evaluate the effects on air temperature. Of note, in other parts of the world, e.g., the Middle East or Africa, where urban albedo can be higher, e.g., 0.20 to 0.30, it may be that  $\varepsilon$  needs to attain values of around 20 percent to break even.

On the other hand, the typical future-year urban albedo in cool cities (if heat-island mitigation strategies are implemented) will likely range from 0.25 to 0.28, as discussed below. In such cases, the conversion efficiency of the solar systems will need to reach 0.17 to 0.20 to break even (i.e., to exert no negative effects). Such efficiencies are anticipated in the near future. Of note, if efficiencies increase beyond the value of 0.25 (as is predicted to occur by 2100), then solar systems can provide cooling even under scenarios of cool cities.

As emphasized earlier, the above discussion pertains to the radiative effects only. The impacts on air temperature are a result of interaction between the surface and the atmosphere. These impacts involve several factors, some of which are non-linear, that must be evaluated independently, e.g., via meteorological modeling (as discussed below). Also, even though there are certain cases where PV systems decrease the overall urban albedo, their negative effects may not be large enough to affect air temperature by a significant amount.

#### **14.4 Modeling of Potential Meteorological Impacts**

The meteorological modeling performed in this study and presented here is only meant to serve as an example for the proposed methodology and approach used in determining the potential atmospheric impacts of solar PV deployment. The results are not intended to serve as a specific guide or reference (especially in light of the various variables that can differ significantly from one region to another). Thus, while the results from the modeling performed in this study can provide some general idea as to anticipated effects and magnitudes, it is the planners, energy specialists, regulators, and engineers working on the deployment of solar arrays in specific areas who will have to evaluate the atmospheric impacts and benefits on a case-by-case basis. The list of parameters at the end of this section identifies certain information and variables that

need to be collected and characterized for each area to allow for the local analysis of the potential impacts of solar systems.

With that in mind, we now proceed to discuss some findings from the example meteorological modeling performed in this study. The geographical area analyzed is southern California (the Los Angeles Basin). The meteorological models were discussed earlier in Section 8, and the episode modeled here is based on “run R” for the southern California domain, as shown in Table 6.1. The episode in this run is part of the July 2005 period simulated earlier. The specific dates modeled for this solar PV analysis are 11 through 16 July, 2005.

Two main scenarios, and several sub-scenarios, are modeled and discussed here. The main scenarios represent (1) current conditions, and (2) future-year, cool-cities conditions. Current conditions, as used here, refer to existing regional land-use/land-cover, urban fabric, albedo, and other surface physical properties in urban areas. Cool-cities conditions, on the other hand, represent potential future-year scenarios where high-albedo roofs, pavements, and streets would have been implemented on a large scale. For each of these two scenarios (present and future-year), a number of sensitivity simulations with and without solar PV arrays were performed, as discussed next.

As discussed earlier, the assumptions we make here are that roof-area availability (technical potential) for deployment of solar PV is based on LULC analysis and not market conditions or actual roof-specific factors such as orientation, solar access, slope, vegetation blocking, permit requirements, and so on. These aspects are too detailed and very site-specific for this scoping analysis, but should be undertaken in future studies. It is important to note that the change in large-scale albedo as a result of regional deployment of solar arrays varies from one region to another. The larger the area, e.g., Los Angeles Basin versus Fresno, for example, the larger the effect a certain albedo change would have. As seen earlier in this report, similar levels of albedo modifications in Fresno and Los Angeles can cause only up to 1°C (2°F) change in Fresno but up to almost 4°C (7°F) change in Los Angeles.

For the sake of performing this scoping and modeling analysis, an episode of four days was used. Ideally, when evaluating such impacts, much longer time periods (seasonal or annual, such as those discussed earlier in this report) should be modeled.

The deploy ability (technical potential) of solar PV systems was computed as a fraction of roof area available for PV installation. The roof area was computed based on land-use/land-cover analysis as discussed in Taha (2011). The roof cover (fraction) arrived at through these calculations is summarized in Table 14.3. The PV technical potential was then calculated based on available roof area. For each of the present-year and cool-cities scenarios, two PV deployment scenarios could be considered: (1) low deployment and (2) high deployment. The roof fraction area covered with PV (in each 200 m grid cell) in such low- and high-deployment scenarios would be as follows in Table 14.3:

**Table 14.3: Deployment Scenarios (Technical Potential) at 200 m Resolution**

LULC ID	Roof fraction (200 m cells)	Roof Fraction Covered with PV		
		Reasonably low deploy (%)	Reasonably high deploy (%)	High deploy (%)
11	0.20	10	20	60
12	0.23	15	30	80
13	0.19	30	50	90
14	0.12	20	40	90
15	0.22	20	20	80
16	0.23	10	20	70
17	0.23	10	20	70

The technical potential is then computed from the product of roof fraction and one of the deployment levels (last 3 columns in the table). It must be re-emphasized again that these are examples for the sake of calculations and modeling. These numbers must be generated site-specifically for each area or region where the effects need to be evaluated.

Then, within each of the three scenarios in Table 14.3, a number of perturbations were simulated assuming a constant average solar panel reflectivity ( $\rho$ ) of 0.08 for PV systems, but a range of solar conversion efficiencies ( $\varepsilon$ ) as summarized in Table 14.4:

**Table 14.4: Perturbation Scenarios for  $\varepsilon$**

Solar Conversion Efficiency	Effective Albedo
$\varepsilon = 0.10$	$A_{eff} = 0.18$
$\varepsilon = 0.15$	$A_{eff} = 0.23$
$\varepsilon = 0.20$	$A_{eff} = 0.28$
$\varepsilon = 0.25$ **	$A_{eff} = 0.33$
$\varepsilon = 0.30$ **	$A_{eff} = 0.38$

\*\* Such efficiencies are expected to become technically attainable by the year 2100  
Source: Nemet 2009

The scenarios of roof fractions available for PV deployment have been assumed to be reasonable (as in Table 14.3 above). Extreme scenarios where PV systems cover entire roofs on all buildings are not evaluated here, except one scenario (a “high” scenario, last column in Table 14.3). This scenario is constructed with the assumption that the roof fraction available for PV deployment is higher than reasonable. The scenario was tested with a range of conversion efficiencies for cool cities (future years) and deployability ( $\varepsilon = 10$  percent through  $\varepsilon = 30$  percent). It was also tested with an albedo-increase compensation scenario, where the albedo of all roof types was

increased by 0.05 (e.g., if a roof has an initial albedo of 0.20, it becomes 0.25). The purpose of this latter scenario is to evaluate the need (how much) to increase roof albedo to compensate for the effects of PV if heat islands are negatively affected at the low  $\varepsilon$  level, e.g., when  $\varepsilon = 10$  percent under cool-cities scenarios.

Note that the values listed in the above tables are those at the solar panel level (PV panel). These values are further aggregated and averaged in the meso-urban model by roof type, deployability, land-use land-cover, etc., and for each grid cell of the domain. In the following discussion, only the “reasonably high” and “high” deployment scenarios (last two columns in Table 14.3) are simulated along with several perturbations of  $\varepsilon$  as listed in Table 14.4. The Los Angeles basin is simulated and discussed as an example, but the calculations and methodologies can apply anywhere. Thus, the simulations discussed here are as shown in Table 14.5:

**Table 14.5: Modeling Scenarios of Solar PV Deployment in Southern California**

Los Angeles		Scenario ID
Present Conditions	Without PV (reference scenario)	PnoPV
	With PV (reasonably high deployment), 5 $\varepsilon$ levels (##)	PwPV $\varepsilon$ ##
	Without PV (reference scenario)	FnoPV
Cool Cities (future)	Without PV (reference scenario)	FnoPV
	With PV (reasonably high deployment), 5 $\varepsilon$ levels (##)	FwPV $\varepsilon$ ##
	With PV (high deployment), 5 $\varepsilon$ levels (#)	FwPV $x\varepsilon$ ##
	With PV (high deployment), $\varepsilon = 0.10$ , and 0.05 roof albedo increase	FwPV $x\varepsilon 10A$

where ## is the value of conversion efficiency ( $\varepsilon$ ) used in the particular run. That is, ## can take on five values: 0.10, 0.15, 0.20, 0.25, and 0.30 (per Table 14.4). Thus, for example, FwPV $x\varepsilon 10A$  is a future-year (cool cities) scenario, with PV (wPV), using the high (higher than reasonable) deployment of PV (x), with a conversion efficiency of 10 percent ( $\varepsilon 10$ ), and an increase in albedo of 0.05 to compensate for the PV effects (A).

For present conditions, scenario PnoPV serves as a reference (base) that characterizes the meteorology in the Los Angeles areas without large-scale introduction of PV. Scenarios PwPV $\varepsilon 10$  through PwPV $\varepsilon 30$  are perturbations to PnoPV to evaluate the effects of large-scale implementation of solar PV in urban areas (of southern California) on the meteorology at several  $\varepsilon$  levels (0.10, 0.15, 0.20, 0.25, and 0.30). Similarly, for future cool-cities scenarios, FnoPV serves as a reference (base) to evaluate the meteorological effects of increasing urban albedo without large-scale implementation of solar PV. Thus, the difference between FnoPV and PnoPV is the effect of increased urban albedo (roofs, streets, pavements) in cool-cities strategies. Scenarios FwPV $\varepsilon$ ## and FwPV $x\varepsilon$ ## quantify the effects of large-scale implementation of solar PV in future-year, cool-cities conditions at the “reasonably high” and “high” PV deployment levels, respectively (per Table 14.3). Again, the ## indicate that five sub-scenarios of conversion

efficiency are modeled and quantified here. Finally, scenario FwPV $\epsilon$ 10A is analyzed to evaluate the potential of increased roof albedo to compensate for or offset the effects of high deployment of solar PV (with  $\epsilon$  of 10 percent) in cool-cities scenarios on air temperature in southern California.

From this point on in the report, the scenario ID (last column of Table 14.5) will be used to reference the simulation cases and corresponding results.

## 14.5 Results and Discussion

It is emphasized again that the modeling and simulations discussed here as part of the scoping analysis are provided as examples of the methodology or approach used in evaluating the regional impacts of solar PV deployment. These are not results to be used for planning purposes at this time. They are provided to demonstrate the steps needed, information collected, and approach taken to quantify the atmospheric effects of PV deployment.

The base-case simulated meteorological fields for the July 2005 episode in southern California were discussed earlier in Section 10.1.3. In this section, only the differences for each scenario from the corresponding base case will be discussed. The focus in this discussion will be on the changes in air temperature at the lowest level of the model. In addition, we are interested here in daytime effects of solar PV on the air temperature as nighttime effects are small and not directly relevant to the issue of urban heat islands and daytime cooling needs. Finally, the following analysis examines changes in air temperature in the urban areas where solar PV is deployed, not other remote areas in the domain where model noise or carry-over effects can sometimes be detected.

### *Impacts during present conditions with reasonably high deployment of PV*

The full July 2005 episode, used in the simulations, was discussed earlier in this report. In this section, only five days (11 through 16 July) of that episode were re-run as an example to discuss the methodology and approach for solar PV scoping. The results from these simulations show that the effects (magnitudes and spatial characteristics in the domain) are generally similar from one day to another in the episode. For compactness, we discuss here only the middle day of the episode (14 July) as an example.

The background urban albedo in this case (present-day conditions) is between 0.14 and 0.15 (averaged at 5 km resolution in urbanized cells of the model). The derivation of urban albedo was described earlier and the deployment level for PV is the “reasonably high” scenario (the middle column in Table 14.3).

The meteorological modeling at a solar conversion efficiency ( $\epsilon$ ) of 10 percent shows that the impacts of deploying solar PV in the Los Angeles Basin are virtually non-existent. In other words, there are no negative impacts (nor positive) on air temperature because the effective albedo of the solar PV is roughly similar to that of the background urban albedo in the area. Figure S1 in Appendix I shows the air temperature difference between scenario PwPV $\epsilon$ 10 and

PnoPV on 14 July (selected as the middle day of the episode) at 1500 PDT. As can be seen, areas in the Los Angeles Basin display no air-temperature changes.

At an  $\varepsilon$  of 15 percent, there still is not detectable impact (positive or negative) on air temperature, as seen for example in Figure S2, for 14 July at 1500 PDT, which shows the difference between scenario PwPV $\varepsilon$ 15 and scenario PnoPV. When the  $\varepsilon$  reaches 20 percent, some regional cooling can be detected. The cooling is very small, up to 0.05°C (0.09°F), but covers a large area corresponding to that where the solar PV deployment occurs. This can be seen in Figure S3, showing the difference between PwPV $\varepsilon$ 20 and PnoPV at 1500 PDT on 14 July.

At an  $\varepsilon$  of 25 percent, the cooling effect increases slightly to between 0.05°C and 0.1°C (0.09°F and 0.2°F), as seen in Figure S4, for the hour at 1500 PDT on 14 July. The figure shows the difference between PwPV $\varepsilon$ 25 and PnoPV. Finally, for an  $\varepsilon$  of 30 percent, the cooling effects reaches up to 0.15°C (0.27°F) (Figure S5) at that same date and hour. Figure S5 shows the difference between scenario PwPV $\varepsilon$ 30 and PnoPV. However, this  $\varepsilon$  value for solar PV ( $\varepsilon$  = 30 percent) is expected only in the future, by the year 2100, as discussed before, so this impact on air temperature cannot be expected in present day.

Thus, if land-use/land-cover characteristics; surface physical properties; and materials on roofs, pavements, and streets are assumed unchanged relative to present-day conditions, the example simulations here show that a threshold of  $\varepsilon$  = 20 percent is where cooling begins as a result of deploying solar PV in the Los Angeles Basin. Again, it should be re-emphasized that (1) this is simply an example, and (2) these effects and threshold will differ from one area to another and from one set of synoptic conditions to another. Also since  $\varepsilon$  values higher than 20 percent are expected in the future, it is feasible to state here that cooling effects will not be experienced during the present or in the next few years.

#### *Impacts during future-year conditions (cool cities) with reasonably high deployment of PV*

In the case of cool-cities deployment, based on albedo-increase values assumed in this study, the background urban albedo (in urbanized cells of the model) is between 0.24 and 0.26, representing a high-increase scenario. The regional albedo of the modeling domains is, of course, much lower than that. Also note that the deployment level for PV, discussed here, is the “reasonably high” scenario (the fourth column in Table 14.3 above).

The modeling of this scenario shows that with an  $\varepsilon$  value of 10 percent, and a cool-city scenario as characterized above, the impact on air temperature is negligible. This is seen in Figure S6 representing the difference between scenarios FwPV $\varepsilon$ 10 and FnoPV at 1500 PDT on 14 July. A similar situation (no effect) is seen for an  $\varepsilon$  value of 15 percent, 20 percent, and 25 percent as in Figures S7, S8, and S9. It is only at an  $\varepsilon$  value of 30 percent that some of cooling effects of solar PV deployment becomes noticeable. As seen in Figure S10 (showing the difference between scenarios FwPV $\varepsilon$ 30 and FnoPV at 1500 PDT on 14 July), there is some very small cooling effect of 0.05°C (0.09°F). In other words, the increase in albedo in the cool-city scenario (relative to present-day conditions) requires a larger  $\varepsilon$  to initiate a cooling impact than during present-day albedo. That is, under present-day conditions, PV cooling starts at  $\varepsilon$  of 20 percent; whereas, under cool-city scenarios, the cooling effect starts at  $\varepsilon$  of 30 percent.

To summarize the discussion so far, the “reasonably high” deployment of PV in both cases of present and cool cities scenarios incurs no negative air temperature impacts. The cooling effect from PV deployment starts at an  $\varepsilon$  of 20 percent in present day-conditions and at an  $\varepsilon$  of 30 percent in future-year, cool-city scenarios.

We now examine the effects of “high” deployment of solar PV in the following section.

*Impacts during future-year conditions (cool cities) with high deployment of PV*

In this scenario, the meteorological effects of “high” deployment of solar PV (last column in Table 14.3) are evaluated in the framework of the future-year cool-cities scenarios. As before, five levels of  $\varepsilon$  values are tested (modeled). In this scenario, larger effects from solar PV deployment are expected (both negative and positive), since the deployment is now at higher densities.

At an  $\varepsilon$  of 10 percent, the “high” deployment level of solar PV causes an increase in air temperatures in the Los Angeles Basin. Thus, a small UHI is generated due to the density of deployment. The increase in air temperature reaches 0.1°C (0.2°F), such as that seen in Figure S11, which shows the difference between scenarios FwPVx $\varepsilon$ 10 and FnoPV at 1500 PDT on 14 July. While the increase is small, the area affected by the temperature increase is relatively large and spans several counties.

With an  $\varepsilon$  of 15 percent, the “high” deployment of solar PV can cause some very small (almost negligible) increases in air temperatures, reaching up to 0.05°C (0.09°F) in some small areas. This is seen, for example, in Figure S12 (which shows the difference between scenario FwPVx $\varepsilon$ 15 and FnoPV). At an  $\varepsilon$  value of 20 percent, the effects are non-existent (no increase or decrease in air temperature), as seen in Figure S13 (which shows the difference between FwPVx $\varepsilon$ 20 and FnoPV). In other words, the  $\varepsilon$  level of 20 percent is the “break even” level where the impacts of increased albedo (cool cities) and increased  $\varepsilon$  balance each other.

Indeed, at an  $\varepsilon$  level of 25 percent, the effects turn into cooling the area by as much as 0.15°C (0.27°F), as seen in Figure S14, which shows the difference between FwPVx $\varepsilon$ 25 and FnoPV at 1500 PDT on 14 July. This reinforces the above statement that the  $\varepsilon$  level at 20 percent is a break-even level, below which there is an increase in temperature and above which there is cooling. The cooling effect increases further at the  $\varepsilon$  level of 30 percent to reach a decrease of 0.2°C (0.4°F), and the cooling covers a large swath of the Los Angeles Basin, as seen in Figure S15 (which shows the difference between FwPVx $\varepsilon$ 30 and FnoPV).

Thus, this indicates that a high deployment level for solar PV (higher density) can have larger negative effects at low  $\varepsilon$  values in the future-year cool-cities scenario, but also larger cooling (at high  $\varepsilon$  values) compared to scenarios with “reasonably high” deployment of solar PV.

Based on findings from the extensive meteorological, energy, emissions, and air quality modeling performed in this and prior phases of heat-island modeling efforts, it can be stated that in practical terms, a temperature change in a range smaller than +0.1°C to -0.2°C (+0.2°F to -0.4°F) likely has very minimal or no measurable effects in terms of energy use, emissions, and photochemical production of ozone (air quality). However, this is different from the potential

impacts of clustered and high-density solar power plants, e.g., those in the high desert, which might have larger impacts on meteorology.

*Impacts during future-year conditions (cool cities) with high deployment of PV and additionally increased albedo for compensation*

One last scenario was also evaluated in the context of future-year cool cities conditions. This scenario involves further increasing the albedo of all roof types by 0.05 while keeping solar conversion efficiency at the 10 percent level. The purpose is to evaluate whether increasing albedo in the absence of conversion-efficiency improvements in the future can offset some or all of the possible negative effects caused by solar PV deployment in scenario FwPVx $\epsilon$ 10 (which resulted in an increase of 0.1°C (0.2°F) in air temperature as discussed above). Thus, the scenario examined here is essentially scenario FwPVx $\epsilon$ 10, but rather than increase  $\epsilon$  to offset its negative temperature impacts, the roof albedo in the region is increased instead.

The simulations of this scenario (scenario FwPVx $\epsilon$ 10A) show no impacts on air temperature relative to FnoPV, as seen in Figure S16, which shows difference of this scenario from FnoPV. This means that the effect of increased roof albedo (for all roof types) in the Los Angeles Basin by 0.05 (in the cool-city context) is equivalent to increasing  $\epsilon$  from a value of 10 to 20 percent (the latter being the break-even  $\epsilon$  level discussed earlier). Recall that the albedo increase of 0.05 is that at the roof scale; over the urban cells in the modeling domain, the increase in albedo is much smaller—up to 0.01. Recall also that these findings are specific to the assumptions made and characterizations done in this scoping analysis. These values may be different for actual applications with measured data or site-specific information. But the modeling suggests that increasing the albedo slightly (by 0.05 for roofs) can cancel any potential negative impacts from urban deployment of solar PV in the future, cool-cities scenarios.

### *Summary*

To summarize the discussion so far, and based on the specific assumptions and modeling done here as an example, the following general statements can be made:

- During present-day, existing urban conditions, the “reasonably high” deployment of solar PV systems has no negative impacts on air temperature (does not increase air temperature or cause heat islands).
- At some level of solar conversion efficiency, e.g., in this case, at conversion efficiency of 20 percent, some regional cooling can be detected. The cooling is small, up to 0.05°C (0.09°F).
- As the conversion efficiency increases (assuming no changes in LULC or regional surface characteristics), the cooling effect also increases. In this example modeling, as the conversion efficiency approaches 30 percent, the regional cooling in the Los Angeles Basin reaches up to 0.15°C (0.27°F).
- During future-year, cool-cities scenarios in the Los Angeles Basin, the “reasonably high” deployment of solar PV has no negative impacts on air temperature. However,

the cooling effect from PV starts at a higher conversion-efficiency level. In other words: under present-day conditions, PV cooling starts at a conversion efficiency of 20 percent; whereas, under cool-city scenarios, the cooling effect starts at 30 percent.

- During future-year, cool-cities scenarios, the “high” deployment of solar PV systems in the Los Angeles Basin can cause negative impacts on air temperatures at the conversion-efficiency level of 10 percent. The increase is small, about 0.1°C (0.2°F). But this scenario can also produce relatively larger cooling of 0.15°C–0.2°C (0.27°F–0.4°F) at  $\epsilon$  values of 25 to 30 percent.
- A solar conversion efficiency value of 20 percent is a break-even threshold in this high-deployment scenario (no increase or decrease in air temperature), where the impacts of increased albedo from cool cities and increased conversion efficiency balance each other.
- Under future-year scenarios of cool cities, and at the “high” level of solar PV deployment in the Los Angeles Basin, an increase in roof albedo of by 0.05 (in the cool-city context) is equivalent to increasing solar conversion efficiency from a value of 10 to 20 percent.
- The example modeling performed here assumes clear-sky conditions, i.e., maximum solar resources availability in southern California. In practical terms, the modeling should also account for cloudiness, whether specific or approximated (e.g., via probability distribution functions during longer episodic modeling), to evaluate the site-specific potential impacts of solar PV deployment.

The foregoing discussion presented a brief scoping study of the aspects that need to be considered and addressed in evaluating the potential atmospheric impacts of large-scale deployment of solar PV arrays in urban areas. Thus, the following are considerations to evaluate these effects on a case-by-case basis (region-specific):

- Define a range of reasonable and high PV deployment levels for the target area.
- Characterize and quantify the roof area, or cover, in the region of interest (target area), e.g., neighborhood, city block, or model grid cell.
- Characterize the fraction of flat roofs, sloped roofs, and parking lots that can be covered with solar PV for all building types and structures, or open space, in the target area.
- Characterize the existing background albedo of the target area from observational data, e.g., aircraft / remote sensing, satellite data or other in-situ measurements, such as with airborne pyranometers.
- Characterize/measure the actual albedo of the solar panels to be installed.
- Characterize the conversion efficiency of the solar PV systems planned for deployment.

- Characterize the effective albedo of the solar panels (the albedo value that also incorporates the rated solar conversion efficiency).
- Determine potential future-year albedo changes as a result of land-use modifications or from deployment of cool-cities measures (strategies of increased urban albedo on roofs, pavements, and streets).
- Quantify and characterize the solar availability at the locations or sites where PV deployment is planned.
- Perform a multi-seasonal assessment of the potential atmospheric impacts of solar PV deployment, via mesoscale and meso-urban meteorological modeling of various scenarios and configurations.
- Perform CFD modeling in specific situations or for specific buildings to account for all other effects, both direct and indirect, from PV deployment.

# CHAPTER 15:

## Summary and Conclusions

This study evaluated the effectiveness of heat-island control measures on local meteorology, emissions, and ozone air quality under a range of summer conditions typically experienced in several California regions. The research focused on the potential impacts and benefits from increased urban albedo in several regions. The goal of the multi-episodic modeling was to further the analysis beyond the time scales and limited episodic conditions modeled in previous studies.

Thus, the focus in this modeling effort was on quantifying the impacts of increasing albedo in several California urban areas, including the Sacramento Valley, San Francisco Bay Area, Fresno region, and South Coast Air Basin (Los Angeles region). The research sought to evaluate and quantify the potential positive and negative impacts in each of these regions that can arise following surface modifications over several episodes, various synoptic conditions, and different interactions among regions (e.g., pollutant transport). To accomplish these goals, the study developed several episodes to cover a range of meteorological conditions, associated emissions, and photochemical/ozone air-quality.

Another study goal was to evaluate the potential atmospheric impacts of large-scale urban solar photovoltaic (PV) deployment on local meteorology. The purpose of this scoping analysis, with example modeling results, was to provide a basis for and identify the important factors and parameters needed in evaluating the local and regional meteorological impacts of solar PV arrays. The scoping analysis included extensive model runs to evaluate various scenarios and assumptions, as was discussed in the report.

### 15.1 Heat-Island Control

#### 15.1.1 Meteorology

The multi-episodic impacts of increased urban albedo on local meteorology were evaluated. The modeling shows that significant cooling can be achieved, particularly during the daytime, via heat island mitigation. For example, during the July–August 2000 episode, the largest daily cooling ranged from 0.6°C to 1.1°C (1.1°F to 2°F) or more in various parts of the central California domain; whereas, in the July 1999 episode, it ranged from 0.7°C to 2.2°C (1.3°F to 4°F). During the southern California episode of July 2005, the largest daily reduction ranged from 1.1°C to 3.9°C (2°F to 7°F) in different parts of the domain. In some days, the models showed warming as well but, in general, the warming was smaller in magnitude than the cooling, was short-lived, and affected much smaller areas than the cooling.

In terms of cumulative impacts on air temperature, a “degree-hour” metric is used to quantify the effects from increased urban albedo. More specifically, the differences in degree-hours per day (DH/D) across the various region-episodes combinations were evaluated at several monitor locations in the domain. Four different ambient-air temperature thresholds were selected: 15°C

(59°F), 20°C (68°F), 25°C (77°F), and 30°C (86°F). The purpose was to show the effectiveness of increased urban albedo in changing air temperature in different temperature ranges.

An overall assessment of the meteorological modeling results for central California shows that the effects of increased urban albedo on temperature are relatively consistent and of the same magnitude (at each monitor) and are relatively independent of meteorological conditions during the selected summer episodes. Of course, there *are* actual differences in impacts from one episode to another, due to variations in cloud cover and wind flow patterns, but they are not significantly large (Table 15.1). The modeling also shows that, in general, the impacts on temperature are greater in the larger urban areas because of the larger surface area available for modification, i.e., for increasing albedo.

**Table 15.1: Changes in Degree-Hours (per day) Totalized over All Monitors in the Central California Domain for Each Episode (Relative to the 15°C Threshold)**

Episode / Run ID	Change in Degree-Hours/Day**	Episode / Run ID	Change in Degree-Hours / Day**
Jul 27–Aug 4, 2000	-117	Jul 1–2, 2002 (run G)	-119
Jul 4–14, 1999	-132	Jul 4–19, 2002 (runH1)	-90
Jun 14–27, 2000 (run A1)	-120	Jul 10–22, 2002 (runH2)	-155
Jun 14–15, 2000 (run A2)	-133	Aug 8–20, 2002 (run I)	-141
Jul 19–Aug 1, 2000 (run B)	-126	Jun 3–27, 2003 (run J)	-116
Aug 4–8, 2000 (run C)	-108	Jun 25–Jul 17, 2003 (run K)	-134
Aug 11–18, 2000 (run D)	-134	Jul 13–14, 2005 (run L)	-112
May 18–31, 2001 (run E)	-124	Jul 25–Aug 4, 2005 (run M)	-134
Jun 20–22, 2001 (run F)	-130		

\*\* Total degree-hours/day (DH/D) change over all monitors in central California, rounded to nearest 1 DH/D

Thus, as can be seen in Table 15.1, the impacts of increased urban albedo are relatively consistent, in the range of about -110 to -140 DH/D, regardless of meteorology, except for two episodes that deviate somewhat from this range (runs H1 and H2). In terms of percentage-wise changes at monitors averaged over all episodes, the model results show that the change (decrease) in degree-hours becomes larger as the temperature threshold increases. Table 15.2 summarizes the ranges of change in counties and for the four temperature thresholds discussed above. The impacts differ from one county to another depending on the temperature threshold, but the changes are significant overall.

For southern California, Table 15.3 summarizes the changes in DH/D as a total over all monitors in the domain, totalized for each episode (for the 15°C (59°F) (threshold). It can be seen again from the table that the range of total changes is narrow, between 142 and 155 DH/D, and that there is little difference in impacts on air temperature among the summer episodes considered here.

**Table 15.2: Range of Percentage-wise Changes in Degree-Hours across Monitors in Counties (Averaged over All Episodes) for Central California**

Temperature Threshold	Range of Percentage Change in Degree-Hours					
	Placer		Sacramento		Santa Clara	
	From (%)	To (%)	From (%)	To (%)	From (%)	To (%)
15°C (59°F)	-1.46	-2.33	-1.22	-2.10	-0.24	-5.71
20°C (68°F)	-2.63	-3.81	-2.02	-3.39	-0.44	-8.99
25°C (77°F)	-4.77	-6.67	-3.46	-5.66	-1.45	-17.32
30°C (86°F)	-10.18	-11.62	-7.91	-31.93	-8.80	-31.06
	Contra Costa		Alameda		Fresno	
	From (%)	To (%)	From (%)	To (%)	From (%)	To (%)
	15°C (59°F)	-0.41	-4.22	-4.54	-6.80	-0.13
20°C (68°F)	-0.75	-9.54	-9.24	-15.82	-0.20	-3.49
25°C (77°F)	-1.41	-25.54	-21.92	-40.03	-0.33	-5.73
30°C (86°F)	-3.47	-26.95	-34.19	53.21	-0.89	-10.81

**Table 15.3: Changes in Degree-Hours (Per Day) Totalized over All Monitors in the Southern California Domain for Each Episode (Using the 15°C Threshold)**

Episode/Run ID	Change in Degree-Hours/Day**
May 23–Jun 16, 2000 (run N)	-142
May 22–Jun 8, 2001 (run O)	-151
Aug 13–17, 2001 (run P)	-155
Jul 9–24, 2003 (run Q)	-145
Jul 12–26, 2005 (run R)	-155

\*\* Total degree-hours/day (DH/D) change over all monitors in southern California, rounded to nearest 1 DH/D

**Table 15.4: Range of Percentage-wise Changes in Degree-Hours across Monitors in Counties (Averaged over All Episodes) for Southern California**

Temperature Threshold	Range of Percentage Change in Degree-Hours					
	San Bernardino		Los Angeles		Riverside	
	From (%)	To (%)	From (%)	To (%)	From (%)	To (%)
15°C (59°F)	-1.42	-2.46	-0.09	-9.64	-0.04	-2.03
20°C (68°F)	-2.51	-4.06	-0.14	-16.97	-0.12	-3.47
25°C (77°F)	-5.35	-8.43	-0.27	-39.17	-0.23	-6.23
30°C (86°F)	-13.09	-20.45	-0.30	-83.33	-0.76	-14.12

For percentage-wise changes at monitors (averaged over all episodes), Table 15.4 summarizes the results for southern California, i.e., change in three counties and for the four temperature thresholds discussed earlier.

In these tables (15.2 and 15.4), the lower end of the range (within each county) typically corresponds to monitors located in small or remote urban areas with relatively small albedo modifications; whereas, the upper end of the range corresponds to highly urbanized (high density) regions. Note that the percentage-wise reductions are larger in Los Angeles than in San Bernardino or Riverside. This is due to (1) the larger modifiable areas, and (2) the relatively lower air temperature in Los Angeles compared to those in the other two regions.

### 15.1.2 Air Quality

In order to evaluate the impacts of heat-island control on ozone air quality, several metrics were discussed in the report. Here, we reiterate a few highlights from the results for only a few of the metrics discussed in the report.

In terms of impacts on the 1-hour peak, the analysis of model results shows that there can be both increases and decreases in ozone as a result of increased urban albedo. However, as discussed in the report, the increases are smaller, short-lived, and affect much smaller areas relative to the decreases in ozone. To summarize these effects, Table 15.5 shows the ratio of decrease-to-increase (RDI) in the 1-hour peaks' total ppb-hours, as well as the domain-averaged changes in 1-hour peaks. It is seen again that the impacts of heat-island control on the 1-hour peak are generally larger in southern than in central California.

Following the assessment of impacts on 1-hour ozone peaks, the analysis of the 8-hour average ozone over all domains and episodes was performed. Of interest is the change in the episodic peak of the 8-hour average (i.e., 8-hour maximum ozone) as it is the measure needed to develop a relative reduction factor (RRF). The episodic 8-hour maximum ozone ranges from about 95 to 131 ppb (in the central California episodes) and from about 100 to 130 ppb in the southern California episodes selected here for analysis. The RRF is calculated for each monitor location and episode to give an overall assessment of this strategy's effectiveness in improving air quality.

During the central California episode of July-August 2000, with year 2000 emissions, the 8-hour episodic peak changes in the range from -3.2 to +3.0 percent with a domain average of -0.6 percent (but note that the large increase happens only during two events). Under the 2018 emissions, the range becomes -2.8 to +3.9 percent, with a domain average of ~0 percent. However, there are instances where the benefits are actually larger under the 2018 emissions scenario and other instances where the negative impacts are larger. For the July 1999 episode with 1999 emissions, the change in 8-hour episodic peak ranges from -5.9 to +3.2 percent, with a domain average of -1.5 percent, and is more dominantly a decrease compared to the July-August 2000 episode. Under the 2018 emissions scenario, the range becomes -3.8 to +3.3 percent, with a domain average of -0.5 percent. It is to be noted, that the large increase (of 3.3 percent) is occurring at only one monitor (Parlier) for the reasons explained in the report (the downwind

location of this monitor relative to Fresno). Table 15.6 summarizes the domain-averaged changes in the episodic 8-hour maximum for other episodes/scenarios.

**Table 15.5: Ratio of Decrease-to-Increase (RDI) in 1-hr Peaks' Total ppb-hr**

Central California			Southern California		
Episodes/Scenarios	Ratio of decrease to increase (RDI)**	Domain averaged changes in 1-hr peaks (ppb)	Episodes/Scenarios	Ratio of decrease to increase (RDI)**	Domain averaged changes in 1-hr peaks (ppb)
Jul 27–Aug 4, 2000, 2000 emis	2.7	-0.28	May 23–Jun 16, 2000 (run N)	41.9	-1.59
Jul 27–Aug 4, 2000, 2018 emis	0.8	0.07	May 22–Jun 8, 2001 (run O)	18.8	-1.86
Jul 4–13, 1999, 1999 emissions	29.6	-1.14	Aug 13–17, 2011 (run P)	41.8	-1.96
Jul 4–14, 1999, 2018 emissions	5.6	-0.52	Jul 9–24, 2003 (run Q)	25.7	-2.14
Jun 14–27, 2000 (run A1)	2.1	-0.37	Jul 12–26, 2005 (run R)	98.5	-2.56
Jul 19–Aug 1, 2000 (run B)	14.4	-0.79			
Aug 4–8, 2000 (run C)	24.6	-0.66			
Aug 11–18, 2000 (run D)	50.0	-1.14			
May 18–31, 2001 (run E)	13.4	-0.86			
Jun 20–22, 2001 (run F)	62.3	-1.27			
Jul 10–22, 2002 (runH2)	3.5	-0.45			
Jul 4–19, 2002 (runH1)	3.7	-0.61			
Aug 8–20, 2002 (run I)	3.9	-0.75			
Jun 3–27, 2003 (run J)	32.3	-0.77			
Jun 25–Jul 17, 2003 (run K)	18.0	-0.78			
Jul 25–Aug 4, 2005 (run M)	4.3	-0.74			

\*\*Rounded to the nearest tenth

**Table 15.6: Domain-Averaged Changes in 8-hr Episodic Maximum for Central California**

runA1	runB	runC	runD	runE	runH1	runI	runJ	runK	runM
-1.1%	-0.9%	-1.4%	-1.6%	-1.0%	-1.3%	-1.2%	-1.9%	-0.9%	-1.0%

For southern California, Table 15.7 summarizes the domain-averaged change in the episodic 8-hour maximum.

**Table 15.7: Domain-Averaged Changes in 8-hr Episodic Maximum for Southern California**

runN	runO	runP	runQ	runR
-2.0%	-3.1%	-3.6%	-2.6%	-2.7%

It can be noted that the changes in the episodic 8-hour maximum ozone in southern California are larger than those in central California and are relatively more consistent. This reflects the fact that the modifiable area in the Los Angeles Basin is larger and can benefit more from increased urban albedo, as there is less geographical separation (one contiguous area) than in central California, where the SFBA, Sacramento, and Fresno regions can be affected differently under different conditions (episodes).

Another measure that can be used to evaluate the effectiveness of increased urban albedo in affecting air quality is the cumulative change in concentrations, i.e., in units of ppb-hr, above a certain threshold. In the report, two thresholds were discussed—0 ppb and 60 ppb—and the measure is the change in ppb-hr at all monitors in a region of interest, for the full length of each episode, and for all episodes discussed above. Table 15.8 summarizes the findings from this analysis.

**Table 15.8: Average Changes in Cumulative Concentrations above 0 and 60 ppb for Central California**

	<b>Threshold 0 ppb</b>	<b>Threshold 60 ppb</b>
	(%)	(%)
SFBA	-1.9	-8.0
Sacramento	-1.0	-2.7
Fresno	-1.1	-2.2

Once again we can see that as the urban area decreases in size, the effects of the control strategy become smaller (i.e., from the SFBA, to Sacramento, to Fresno). Overall, the effects of UHI mitigation are significant and positive (reduction in exposure above certain thresholds).

In terms of the frequency of occurrence with which certain changes in ozone occur, Table 15.9 summarizes the results for four counties. The results show that some of the larger impacts of heat-island control occur during those conditions that are more prevailing (i.e., occur more frequently than conditions of top ozone concentrations). For example, in Fresno, the largest decreases in the 1-hour peak ozone occur in the range of peak concentrations of 90–120 ppb (representing about 35 percent of occurrences); in Sacramento the largest decreases occur in the 90–110 ppb range (representing about 12 percent of occurrences), and in San Bernardino, they occur in the range of 100–140 ppb, representing about 21 percent of occurrences. Similarly for the 8-hour episodic maximum ozone, the largest decreases occur in the 90–100 ppb range in Fresno (representing about 27 percent of occurrences), in the 90–110 ppb range in Sacramento (representing about 12 percent of occurrences), and in the 100–120 ppb range in San Bernardino (representing about 17 percent of occurrences). A similar statement can be made regarding the cumulative (ppb-hour) changes in peak 1-hour ozone (last column in Table 15.9).

The ozone air quality changes resulting from the increases in urban albedo assumed in this study were also converted to emission-equivalents by analyzing the atmospheric carrying

capacity for NOx and ROG in the central and southern California domains. This analysis was performed via photochemical modeling of stepwise reductions in NOx and/or ROG emissions in the domains of interest. Table 15.10 summarizes the emissions equivalence of heat island-control impacts in terms of ROG emission equivalents for each of the episodes/scenarios that were modeled for central California. The table provides an average for each episode for all monitors of interest in that domain.

**Table 15.9. Occurrence of Changes in 1-hr and 8-hr Peaks, and Cumulative Concentration Differences**

County	Concentration Range in 10-ppb Bins	Occurrence (%)	Representative Runs	Monitors: Averaged Change in 1-hr Peak (ppb)	Monitors: Averaged Change in 8-hr Peak (1-RRF)	Monitors: Averaged Change in ppb-hour > 60 ppb
Fresno	120-130	1.81	H2	0	-0.8%	-1.1%
	100-120	8.76	C,D	-0.71,-0.31	-0.7%, -0.8%	-1.2%,-2.2%
	90-100	26.66	A1,E	0.37,-0.48	0, -1.2%	-2.5%,-3.4%
Sacramento	130-140	0.74		***	***	***
	110-130	2.67	F,J	-0.31,-0.14	-0.3%	-2.8%
	90-110	11.73	B,C,D,H1,M	0,-0.33, -0.47,0.49,0	-0.1%, -1.3%, -1.3%, 0.5%, -0.5%	-4.7%, -4.6%, -8.5%, -2.4%, -1.3%
Santa Clara	120-130	1.25		***	***	***
	100-120	3.28	K	-1.86	-1.7%	-9.8%
	90-100	6.87		***	***	***
San Bernardino	140-160	0.66	Q	-1.48	-2.1%	
	120-140	4.24	O,Q	-1.44, -1.48	-2.1%, -2.1%	
	100-120	16.91	N,P,R	-1.31, -1.43, -2.38	-0.8%, -2.2%, -2.6%	

\*\*\* No sufficient data for computing parameter

**Table 15.10. Central California Episode-Averaged Emissions Equivalence (percent change in emissions)**

julaug200														
0 july1999														
emi2000	emi1999	runA1	runB	runC	runD	runE	runF	runH2	runH1	runI	runJ	runK	runM	
ROG equivalence														
	-3.31%	-7.65%	-4.36%	-6.07%	-4.90%	-8.86%	-7.59%	-9.26%	-3.61%	-6.08%	-6.77%	-6.10%	-6.51%	-5.37%

For southern California, Table 15.11 summarizes the averages in ROG emission equivalences.

**Table 15.11. Southern California Episode-Averaged Emissions Equivalence (percent change in emissions)**

	runN	runO	runP	runQ	runR
ROG equivalence	-5.70%	-7.12%	-7.86%	-7.45%	-8.56%

Since anthropogenic ROG emissions in central California amount to an average of about ~2,000 TPD, then the above range of reductions translates into about 66 to 185 TPD of anthropogenic ROG reduction. For southern California, the average daily emission of anthropogenic ROG is about ~900 TPD. Thus, the equivalent emissions reductions range is from 51 to 77 TPD of anthropogenic ROG.

## 15.2 Solar PV Deployment

The potential meso-urban atmospheric effects of solar photovoltaic (PV) deployment were evaluated in this study via simple calculations and full atmospheric modeling. The purpose of this scoping analysis was to evaluate whether large-scale deployment of urban solar PV arrays could impart any positive or negative effects and, if the latter, how to mitigate them. Of note, the actual results from modeling provided in this report are only meant to show an example (approach, methodology, and modeling aspects) but the emphasis is not on the results. This type of modeling evaluation will need to be performed on a region-by-region basis to assess the potential local impacts of solar PV.

From a simple radiative standpoint, and since in current conditions, most urban average albedo in U.S. cities is in the range of 0.16 to 0.22 (e.g., an average of 0.18), it is anticipated that deployment of solar PV systems will have no negative impacts even at a low 10 percent solar conversion efficiency ( $\epsilon$ ), assuming a solar panel reflectivity of 0.08. For  $\epsilon$  values greater than 10 percent, the solar PV systems will actually provide a cooling effect. On the other hand, the typical future-year urban albedo of cool cities (if heat-island mitigation strategies are implemented) will likely range from 0.25 to 0.28. In such cases, the conversion efficiency of the solar systems would have to reach 0.17 to 0.20 to break even (i.e., to exert no negative effects). Such findings pertain to the radiative effects only; meteorological modeling is needed to evaluate the effects on air temperature on a region-wide basis. The impact on air temperature is a result of interactions, some of which are non-linear, between the surface and the atmosphere. Thus, even though there are certain cases where PV systems decrease the overall urban albedo, their effects may not be large enough to negatively impact air temperature by any significant amount. That is, a threshold may exist below which the impacts on air temperature are negligible.

Two overall scenarios were modeled, representing (1) current conditions, and (2) future-year, cool-cities conditions. Within each of these two scenarios, further cases were modeled. The results were presented for four situations and several solar conversion efficiencies. The four situations are:

1. Impacts during present conditions with reasonably high deployment of PV

2. Impacts during future-year conditions (cool cities) with reasonably high deployment of PV
3. Impacts during future-year conditions (cool cities) with high deployment of PV
4. Impacts during future-year conditions (cool cities) with high deployment of PV and additional increase in albedo to compensate for the effects of low solar conversion efficiencies.

The levels of deployment are discussed in the report. The Los Angeles Basin is selected as an example for modeling. Results for these situations are briefly discussed here.

*(a) Impacts during present conditions with reasonably high deployment of PV*

The meteorological modeling of this scenario and at a solar conversion efficiency ( $\varepsilon$ ) of 10 or 15 percent shows that the impacts of deploying solar PV in the Los Angeles Basin are virtually non-existent. In other words, there are no negative nor positive impacts on air temperature because the effective albedo of the solar PV is roughly similar to that of the background urban albedo in the area. When  $\varepsilon$  reaches 20 percent, some regional cooling can be detected in the area. For  $\varepsilon$  of 30 percent the cooling effects reach up to 0.15°C (0.27°F). However, this  $\varepsilon$  value for solar PV (30 percent) is expected in the future, by the years 2050–2100, as discussed in the report, so this cooling effect, even though very small, is not expected under present day conditions.

*(b) Impacts during future-year conditions (cool cities) with reasonably high deployment of PV*

In the case of future cool-cities scenarios where high-albedo is implemented on urban surfaces, the modeling shows no impacts on air temperature all the way through  $\varepsilon$  value of 25 percent. It is only at an  $\varepsilon$  value of 30 percent that some very small cooling effects (0.05°C [0.09°F]) from solar PV deployment become noticeable. In other words, the increase in albedo in the cool-city scenario (relative to present-day conditions) requires that PV systems have a larger  $\varepsilon$  to initiate a cooling impact than during present-day albedo conditions. However, the important point here is that there are no negative impacts from solar PV arrays over a large range of conversion efficiencies.

*(c) Impacts during future-year conditions (cool cities) with high deployment of PV*

In this scenario, the meteorological effects of “high” deployment of solar PV are evaluated in the framework of the future-year cool-cities scenarios. At  $\varepsilon$  of 10 percent, the “high” deployment level of solar PV causes an increase in air temperatures in the Los Angeles Basin. The increase is small, reaching up to 0.1°C (0.2°F). At  $\varepsilon$  value of 20 percent, the effects are non-existent (no increase or decrease in air temperature). In other words, the  $\varepsilon$  level of 20 percent can be considered as a “break even” level where the impacts of increased albedo from cool cities and increased solar-conversion efficiency balance each other.

Past that point, at  $\varepsilon$  level of 25 percent, the effects turn into cooling the area by as much as 0.15°C (0.27°F). The cooling increases further at the  $\varepsilon$  level of 30 percent to reach a decrease of 0.2°C (0.4°F). Thus, a “high” deployment level for solar PV (higher density) can have larger

negative effects at low  $\varepsilon$  values but also larger cooling (at high  $\varepsilon$  values) compared to scenarios with “reasonably high” deployment of solar PV.

*(d) Impacts during future-year conditions (cool cities) with high deployment of PV and additional increase in albedo for compensation of low conversion efficiencies.*

One last scenario was evaluated in the context of future-year cool-cities conditions. This scenario involves further increasing the albedo of all roof types by 0.05 beyond the increase from cool cities. The purpose is to evaluate whether additional increase in albedo in the absence of solar conversion-efficiency improvements in the future can offset some or all of the possible negative effects caused by the “high” solar PV deployment. The modeling shows that the effect of increased roof albedo in the Los Angeles Basin by 0.05 (in the cool-city context) is equivalent to increasing solar conversion efficiency from 10 to 20 percent.

### **15.3 Recommendations**

Based on findings from the heat-island modeling performed in this study, it is recommended that the following aspects be addressed further in the future:

- Evaluating the effects of proximity between urban areas (e.g., up- and down-wind) when one is modified by increasing albedo and the other is not (this can increase ozone in non-modified downwind areas if close enough to upwind, modified ones). In such cases, considerations should be given to also modifying downwind urban areas, e.g., by increasing their albedo. This should be modeled and evaluated on a region-by-region basis.
- Modeling the effects of site-specific changes in albedo that are market-based and neighborhood-specific, not theoretical/ idealized or maximum feasible values.
- Evaluating the impacts of heat-island control strategies under conditions of future urbanization, per projected building and population growth trends.
- Evaluating the benefits of these strategies under scenarios of potential future climate change in California, to characterize impacts on radiative forcing, local cooling and air temperatures, emissions, and air quality.

## LIST OF ACRONYMS

ARB	California Air Resources Board
AFB	Air force base
AIRS	Aerometric Information Retrieval System
ALK1	Alkanes
AQS	Air Quality System (EPA AIRS)
BVOC	Biogenic volatile organic compounds
CAMx	Comprehensive Air quality Model with extensions
CART	Classification and Regression Tree
CB-IV	Carbon Bond chemical mechanism
CCOS	Central California Ozone Study
CFD	Computational Fluid Dynamics
CMAQ	Community Multiscale Air Quality model
DA	A drag-force-based scheme
DEM	Digital elevation model
DH/D	degree-hours per day
DOE	United States Department of Energy
DRI	Desert Research Institute
$\varepsilon$	Conversion efficiency
ETA	NCEP limited-area mesoscale model
ETHE	Ethene
FDDA	Four-dimensional data assimilation
GUIDE	Generalized, Unbiased, Interaction Detection and Estimation
hPa	Hectopascal
ISOP	Isoprene
K	Kelvin
KOAK	Metropolitan Oakland International Airport
LiDAR	Light Detection and Ranging

LSM	Land-surface models
LULC	Land-use / Land-cover
MBO	Methyl butenol
MM5	PSU/ NCAR mesoscale model
MOST	Monin-Obukhov Similarity Theory
MRF	Medium Range Forecast
MW	Megawatts
MWp	Megawatt potential
NAS	Naval air station
NCAR	National Center for Atmospheric Research
NCEP	National Centers for Environmental Prediction
NNRP	NCEP-NCAR Reanalysis Project
NO	Nitric oxide
NO <sub>2</sub>	Nitrogen dioxide
NOAA	National Oceanic and Atmospheric Administration
NO <sub>x</sub>	Nitrogen oxide
NREL	National Renewable Energy Laboratory
NSJV	North San Joaquin Valley
NWC	Naval Weapons Center
O <sub>3</sub>	Ozone
OAK	Oakland airport soundings and profilers
OLE	Olefins
OSAT	Ozone source apportionment technology
OSU	Oregon State University
OVOC	Oxygenated volatile organic compounds
PA	Process analysis
PAR	Photosynthetically active radiation
PBL	Planetary Boundary Layer

PDT	Pacific Daylight Time
PiG	Plume-in grid
PM	Particulate matter
PMNAS	Point Mugu Naval Air Station
ppb	parts per billion
PSU	Pennsylvania State University
PV	Photovoltaic
RA	roughness-length-based scheme
RADM	Regional Acid Deposition Model
RDI	Ratio of decrease to increase
ROG	Reactive organic gases
RRF	Relative reduction factor
RRTM	Rapid Radiation Transfer Model
SAPRC	Statewide Air Pollution Research Center chemical mechanism
SoCAB	South Coast Air Basin
SCOS	Southern California Ozone Study
SFBA	San Francisco Bay Area
SSJV	South San Joaquin Valley
TERP	Terpenes
TPD	Tons per day
TUV	Tropospheric Ultraviolet and Visible radiation model
TW	Terawatt
UAM-V	Urban Airshed Model
UCL	Urban canopy layer
UCP	Urban Canopy Parameterization
UHI	Urban heat island
uMM5	Urban PSU/ NCAR mesoscale model
U.S. EPA	United States Environmental Protection Agency

USGS	United States Geological Survey
UTC	Coordinated Universal Time
VAFB	Vandenberg Air Force Base
VOC	Volatile organic compounds

## REFERENCES

- Anderson, J. R., Hardy, E. E., Roach, J. T., and Witmer, R. E. 2001. "A land use and land cover classification system for use with remote sensor data." USGS Professional Paper 964. U.S. Government Printing Office.
- Betts, A. K., and Miller, M. J. 1986. "A new convective adjustment scheme. Part II: Single column tests using GATE wave, BOMEX, ATEX, and Arctic air mass data sets." *Quarterly Journal of the Royal Meteorological Society*, 112, 693–709.
- Burk, S.D., and Thompson, W.T. 1989. "A vertically nested regional numerical prediction model with second order closure physics." *Monthly Weather Review*, 117, 2305–2324.
- California Energy Commission (CEC). 2003. *Buying a photovoltaic solar electricity system*. Handbook, P500-03-014F, Renewable Energy Program. Sacramento, California.
- California Energy Commission (CEC). 2011. *Developing renewable generation on state property*. Staff Report. CEC-150-2011-001. Sacramento, California.
- Chaves, A., and Bahill, A. T. 2010. "Locating sites for photovoltaic solar panels." *Arcuser*, 13, 4 (Fall 2010), 24–27.
- Chang, J. S., R. A. Brost, I. S. A. Isaksen, S. Madronich, P. Middleton, W. R. Stockwell, and C. J. Walcek. 1987. "A three-dimensional Eulerian acid deposition model: Physical concepts and formulation." *J. Geophys. Res.* 92, 14,681–14,700, doi:10.1029/JD092iD12p14681.
- Chen, F., and J. Dudhia, 2001. "Coupling an advanced land-surface/hydrology model with the Penn State/NCAR MM5 modeling system. Part I: Model implementation and sensitivity." *Monthly Weather Review*, 129, 569–585.
- Chen, F., Kusaka, H., Tewari, M., Bao, J-W., and Hirakuchi, H. 2004. "Utilizing the coupled WRF/LSM/urban modeling system with detailed urban classification to simulate the urban heat island phenomenon over the greater Houston area." Paper 9.11, American Meteorological Society Fifth Symposium on the Urban Environment, 23–27 August 2004, Vancouver, British Columbia.
- Ching, J., Dupont, S., Gilliam, R., Burian, S., and Tang, R. 2004. "Neighborhood scale air quality modeling in Houston using urban canopy parameters in MM5 and CMAQ with improved characterization of mesoscale lake-land breeze circulation." Paper 9.2. American Meteorological Society Fifth Symposium on the Urban Environment, 23–27 August 2004, Vancouver, British Columbia.
- Cox, W., and Chu, S. 1996. "Assessment of interannual ozone variation in urban areas from a climatological perspective." *Atmospheric Environment*, 30, 2615–2625.
- Davis, J. M., Eder, B. K., and Bloomfield, P. 1998. Regional and temporal models for ozone along the Gulf Coast. In: Nychka, D., Piegorsch, W. W., Cox, L. H. (eds.), *Case Studies in Environmental Statistics, Lecture Notes in Statistics*. 132, 27–50, Springer.

DOE (U.S. Department of Energy). Cool Roof Calculator

<http://www.ornl.gov/sci/roofs+walls/facts/CoolCalcEnergy.htm>.

- Dudhia, J. 1993. "A non-hydrostatic version of the Penn State/NCAR mesoscale model: Validation tests and simulation of an Atlantic cyclone and cold front." *Monthly Weather Review*, 121, 1493–1513.
- Dupont, S., Otte, T., and Ching, J. 2004. "Simulation of meteorological fields within and above urban and rural canopies with a mesoscale model." *Boundary-Layer Meteorology*, 113,111–158.
- Environ Corp. 2004. "Comprehensive Air Quality Model with Extensions Version 4." Environ Corp., Air Sciences, 2003.
- Environ. 2005. "Development of a photochemical modeling system for the BAAQMD to support ongoing ozone air quality analysis." Final Report to BAAQMD, from Environ International Corp., Alpine Geophysics LLC, Atmet LLC, and SJSU, 275 pp.
- Environ. 2006. "CAMx User's Guide: Version 4.40." Environ Corp., Air Sciences, 2006.
- Fanney, A. H., Dougherty, B. P., and Davis, M. W. 2001. "Measured Performance of Building Integrated Photovoltaic Panels." *ASME Journal of Solar Energy Engineering*, 123, 187–193.
- Fuentes, J. D., Lerdau, M., Atkinson, R., Baldocchi, D., Bottenheim, D., Ciccioli, P., Lamb, B., Geron, C., Gu, L., Guenther, A., Sharkley, T. D., and Stockwell, W. 2000. "Biogenic hydrocarbons in the atmospheric boundary layer: A review." *Bulletin of the American Meteorological Society*, 81(7), 1537–1575.
- Grell, G. A., Kuo, Y. H., and Pasch, R. 1991. "Semi prognostic test of cumulus parameterization schemes in the middle latitudes." *Monthly Weather Review*, 119, 5–31.
- Grell, G. A., Dudhia, J., and Stauffer, D. R. 1994. "A description of the fifth generation PSU/NCAR mesoscale modeling system (MM5)." Technical Note NCAR/TN–379+STR, NCAR.
- Guenther, A. B., Zimmerman, P. R., Harley, P. C., Monson, R. K., and Fall, R. 1993. "Isoprene and monoterpene emission rate variability–model evaluations and sensitivity analyses." *Journal of Geophysical Research*, 98(D7), 12609–12617.
- Hester, S., Willey, T., Serfass, J., 2005. "Photovoltaic Markets and Technologies." California Energy Commission, PIER Renewable Energy Technologies Program. CEC-500-2009-057.
- Hong, S. H. and Pan, H. L. 1996. "Nonlocal boundary layer vertical diffusion in a medium-range forecast model." *Monthly Weather Review*, 124, 2322–2339.
- Horie, Y., 1988. "Air Quality Management Plan 1988 Revision, Appendix V-P: Ozone episode representativeness study for the South Coast Air Basin." Report prepared for the South Coast Air Quality Management District, El Monte, California, by Valley Research Corporation, Van Nuys, California. VRC Project Number 057, March 1988.

- Hsie, E. Y., and Anthes, R. A. 1984. "Simulations of frontogenesis in a moist atmosphere using alternative parameterizations of condensation and precipitation." *Journal of Atmospheric Science*, 41, 2701–2716.
- Kain, J. S., and Fritsch, J. M. 1993. "Convective parameterization for mesoscale models: The Kain-Fritsch scheme," in *The Representation of Cumulus Convection in Numerical Models*. Meteorological Monographs, K. A. Emanuel and D. J. Raymond, eds. No. 46, 165–170, American Meteorological Society.
- Kistler, R., Kalnay, E., Collins, W., et al. 2001. "The NCEP-NCAR 50-year reanalysis: Monthly means CD-ROM and documentation." *Bulletin of the American Meteorological Society*, 82, 247–267.
- Loh, W.-Y. 2002. "Regression trees with unbiased variable selection and interaction detection." *Statistica Sinica*, 12, 361–386.  
<http://www3.stat.sinica.edu.tw/statistica/j12n2/j12n21/j12n21.htm>.
- Loh, W.-Y. 2006. Regression tree models for designed experiments, in J. Rojo (ed.) *The Second Erich L. Lehmann Symposium—Optimality*, Vol. 49, Institute of Mathematical Statistics Lecture Notes-Monograph Series, pp. 210–228.<http://arxiv.org/abs/math.ST/0611192>.
- Loh, W.-Y., 2008. Classification and regression tree methods, in F. Ruggeri, R. Kenett and F. W. Faltin (eds), *Encyclopedia of Statistics in Quality and Reliability*, Wiley, Chichester, UK, pp. 315–323.<http://www.stat.wisc.edu/~loh/treeprogs/guide/eqr.pdf>.
- Millstein, D., and Menon, S. 2011. "Regional climate consequences of large-scale cool roof and photovoltaic array deployment." *Environmental Research Letters*, 6(2011) 034001 (9 pp).  
[doi:10.1088/1748-9326/6/3/034001](https://doi.org/10.1088/1748-9326/6/3/034001).
- Mlawer, E. J., Taubman, S. J., Brown, P. D., Iacono, M. J., and Clough, S. A., 1997. "Radiative transfer for inhomogeneous atmosphere: RRTM, a validated correlated-k model for the longwave." *Journal of Geophysical Research*, 102 (D14), 16663–16682.
- Navigant Consulting, Inc. 2007. "California Rooftop Photovoltaic (PV) Resource Assessment and Growth Potential by County." California Energy Commission, PIER Program. CEC-500-2007-048.
- Nemet, G. F. 2009. "Net radiative forcing from widespread deployment of photovoltaics." *Environmental Science & Technology*, 43, 2173–8.
- NREL (National Renewable Energy Laboratory). 2012. PV Watts Calculator.  
<http://rredc.nrel.gov/solar/calculators/PVWATTS/version1/>.
- Pan, H. L., and Mahrt, L. 1987. "Interaction between soil hydrology and boundary-layer development." *Boundary Layer Meteorology*, 38, 185–202.

- Protogeropoulos, C., and Zachariou, A. 2010. "Photovoltaic module laboratory reflectivity measurements and comparison analysis with other reflecting surfaces." 25th European Photovoltaic Solar Energy Conference, 6–10 September 2010, Valencia, Spain.
- Pryor, S. C., McKendry, I. G., and Steyn, D. G. 1995. "Synoptic-scale meteorological variability and surface ozone concentrations in Vancouver, British Columbia." *Journal of Applied Meteorology*, 34, 1824–1833.
- Reisner, J., R. J. Rasmussen, and R. T. Bruintjes. 1998. "Explicit forecasting of supercooled liquid water in winter storms using the MM5 mesoscale model." *Quarterly Journal of the Royal Meteorological Society*, 124B, 1071–1107.
- Schultz, P., 1995. "An explicit cloud physics parameterization for operational numerical weather prediction." *Monthly Weather Review*, 123, 3331–3343.
- Seaman, N. L., and Stauffer, D. R. 1996. *SARMAP meteorological model final report*. Prepared for the San Joaquin Valleywide Air Pollution Study Agency, Department of Meteorology, Pennsylvania State University, University Park, Pennsylvania.
- Seaman, N. L. et al. 1997. "The use of the San Joaquin Valley meteorological model in preparation of a field program in the South Coast Air Basin and surrounding regions of Southern California," Volume II: Numerical modeling studies for the development and application of a guidance technique to support the design of the 1997 Southern California Ozone Study field program." Prepared for the California Air Resources Board, Department of Meteorology, Pennsylvania State University, University Park, Pennsylvania.
- Seinfeld, J. H., and Pandis, S. N. 1998. *Atmospheric chemistry and physics*. John Wiley and Sons: New York.
- Simons, G., and McCabe, J. 2005. "California Solar Resources." Staff Paper, CEC-500-2005-072-D. California Energy Commission, Sacramento, California.
- SolarWorld. 2010. "Reflectivity of SolarWorld Sunmodule Plus Photovoltaic Modules." Technical Bulletin, SolarWorld.  
<http://www.solarworld-usa.com/system-designers/~media/Global/PDFs/reflectivity-photovoltaic-modules-1006-tb.pdf>.
- Stauffer, D. R., and Seaman, N. L. 1990. "Use of four-dimensional data assimilation in a limited area mesoscale model. Part I: Experiments with synoptic-scale data." *Monthly Weather Review*, 118, 1250–1277.
- Taha, H. 2005. *Surface modifications as a potential ozone air-quality improvement strategy in California: Part I: Mesoscale Modeling*. Report prepared for the California Energy Commission, for Contract 500-02-013. Report 04-B, Altostratus Inc.  
<http://www.energy.ca.gov/2005publications/CEC-500-2005-128/CEC-500-2005-128.PDF>.

- Taha, H. 2006. "The urbanized MM5 model (uMM5) and its application to the Houston-Galveston Region." Presentation at the First EPA-NCAR NUDAPT Workshop, National Center For Atmospheric Research, May 10–12, 2006, Boulder, Colorado.
- Taha, H. 2007. *Surface modifications as a potential ozone air-quality improvement strategy in California: Part II: Fine-resolution meteorological and photochemical modeling of urban heat islands*. Report to the California Energy Commission, prepared by Altostratus Inc.
- Taha, H. 2008a. "Meso-urban meteorological and photochemical modeling of heat island mitigation." *Atmospheric Environment*, 2008. doi:10.1016/j.atmosenv.2008.06.036.
- Taha, H. 2008b. "Episodic performance and sensitivity of the urbanized MM5 (uMM5) to perturbations in surface properties in Houston TX." *Boundary-Layer Meteorology* 127(2). May 2008. pp. 193–218. doi:10.1007/s10546-007-9258-6.
- Taha, H. 2008c. "Urban surface modification as a potential ozone air-quality improvement strategy in California: A mesoscale modeling study." *Boundary-Layer Meteorology*, 127(2). May 2008. pp. 219–239. doi:10.1007/s10546-007-9259-5.
- Tao, W. K. and Simpson, J. 1993. "Goddard cumulus ensemble model. Part I: model description." *Terrestrial, Atmospheric, and Oceanic Science*, 4, 35–72.
- Tesche, T. W. 1988. "Accuracy of ozone air-quality models." *Journal of Environmental Engineering*, 114(4): 739–752.
- Tesche, T. W., McNally, D. E., Emery, C. A., and Tai, E. 2001. "Evaluation of the MM5 model over the Midwestern U.S. for three 8-hour oxidant episodes." Prepared for the Kansas City Ozone Technical Workgroup. Alpine Geophysics LLC and Environ Corp. Thompson, M. L., Reynolds, J., Cox, L. H., Guttorp, P., and Sampson, P. D. 2000. "A review of statistical methods for the meteorological adjustment of tropospheric ozone." *Atmospheric Environment*, 35 (2001):617–630.
- U. S. EPA. 1999. "Draft guidance on the use of models and other analyses in attainment demonstrations for the 8-hour ozone national ambient air quality standard." EPA-454/R-99-004. EPA OAQPS, RTP, NC 27711. May 1999.
- Yamada, T., and Mellor, G. 1975. "A simulation of the Wangara atmospheric boundary layer." *Atmospheric Environment*, 32, 2309–2329.
- Yarwood, G., Morris, R. E., Yocke, M. A., Hogo, H., and Chico, T. 1996. "Development of a methodology for source apportionment of ozone concentration estimates from a photochemical grid model." 89th AWMA Annual Meeting, Nashville, Tennessee. June 1996.
- Zhang, D. L., and Anthes, R. A. 1982. "A high resolution model of the planetary boundary layer – Sensitivity tests and comparisons with SESAME 79 data." *Journal of Applied Meteorology*, 21, 1594–1609.

# **Appendix A: Monitor Locations**

Figure A-1. Monitor Locations in Placer and El Dorado Counties

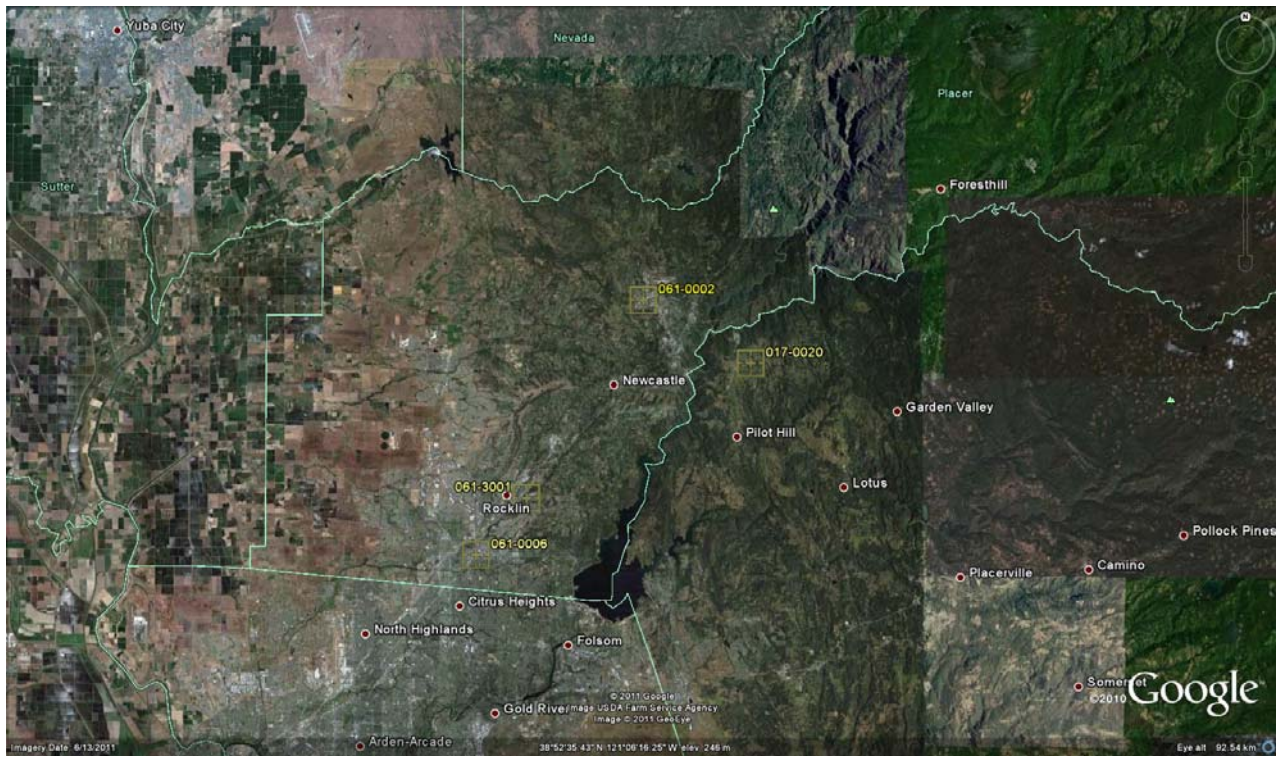


Figure A-2. Monitor Locations in Sacramento County

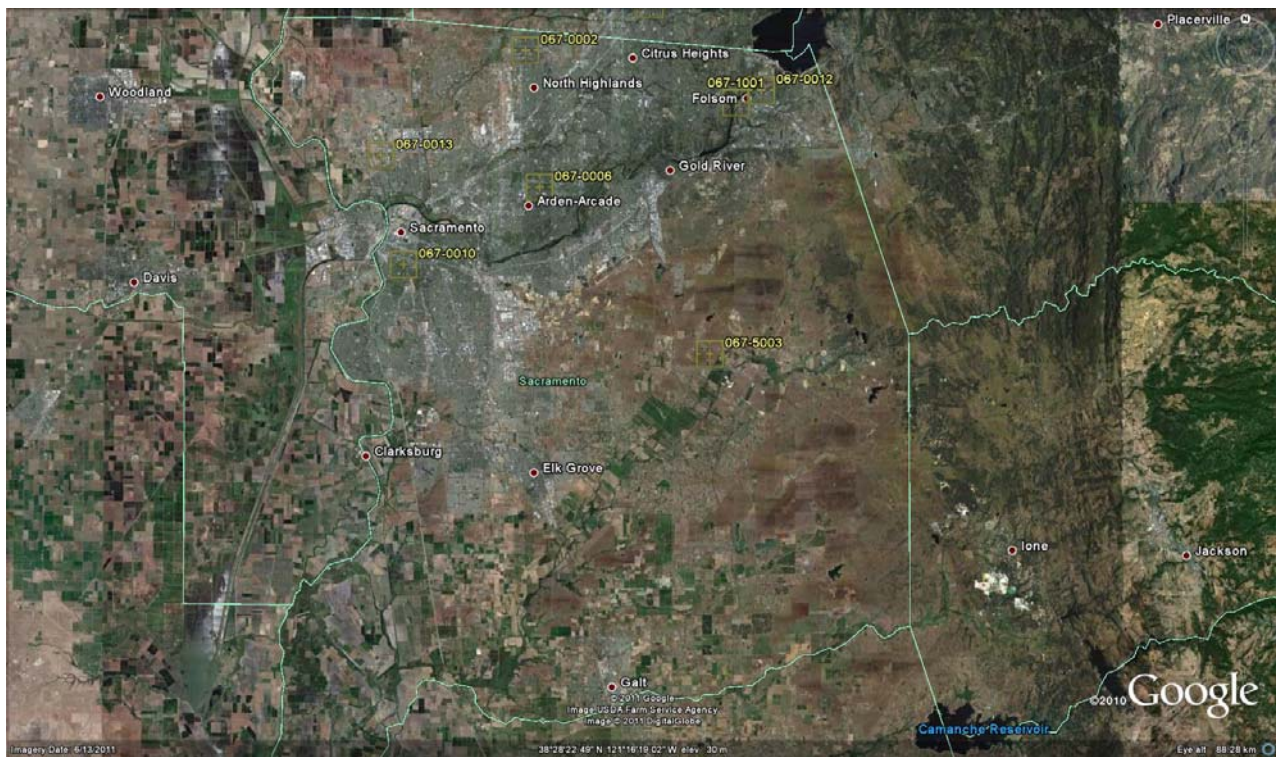


Figure A-3. Monitor Locations in Santa Clara County

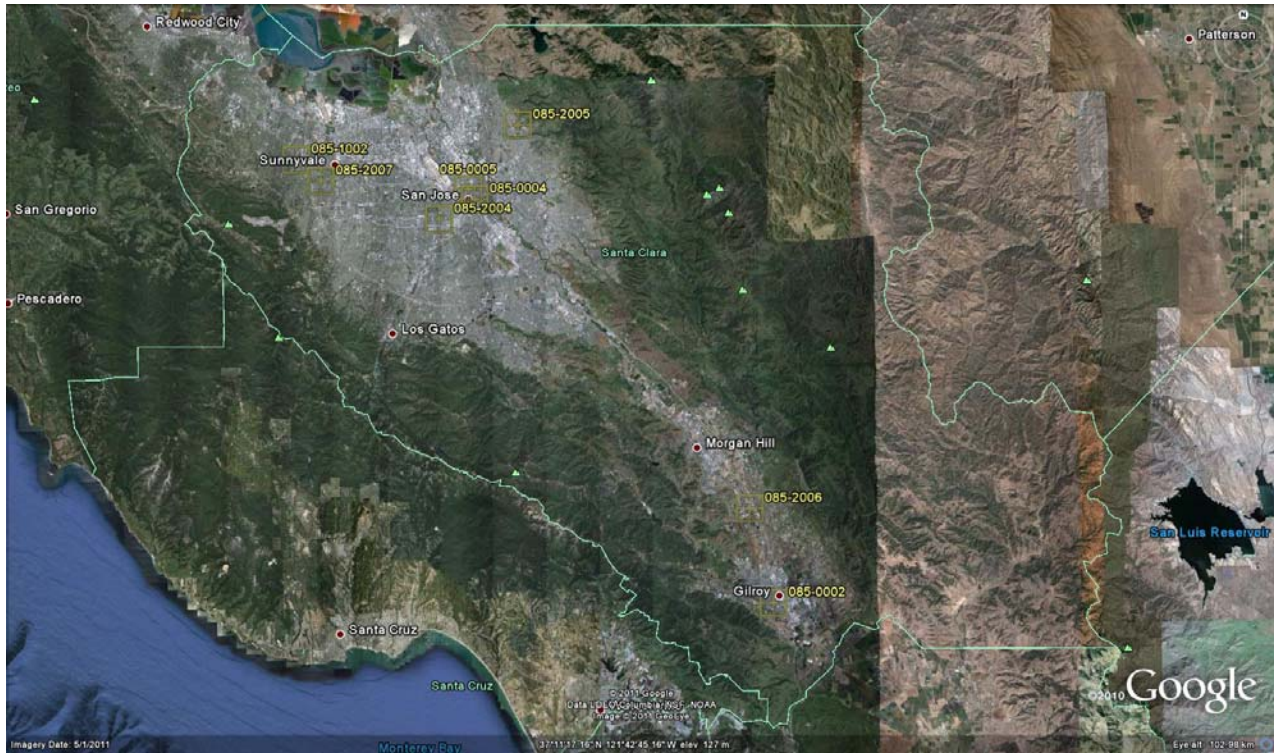


Figure A-5. Monitor Locations in Alameda County

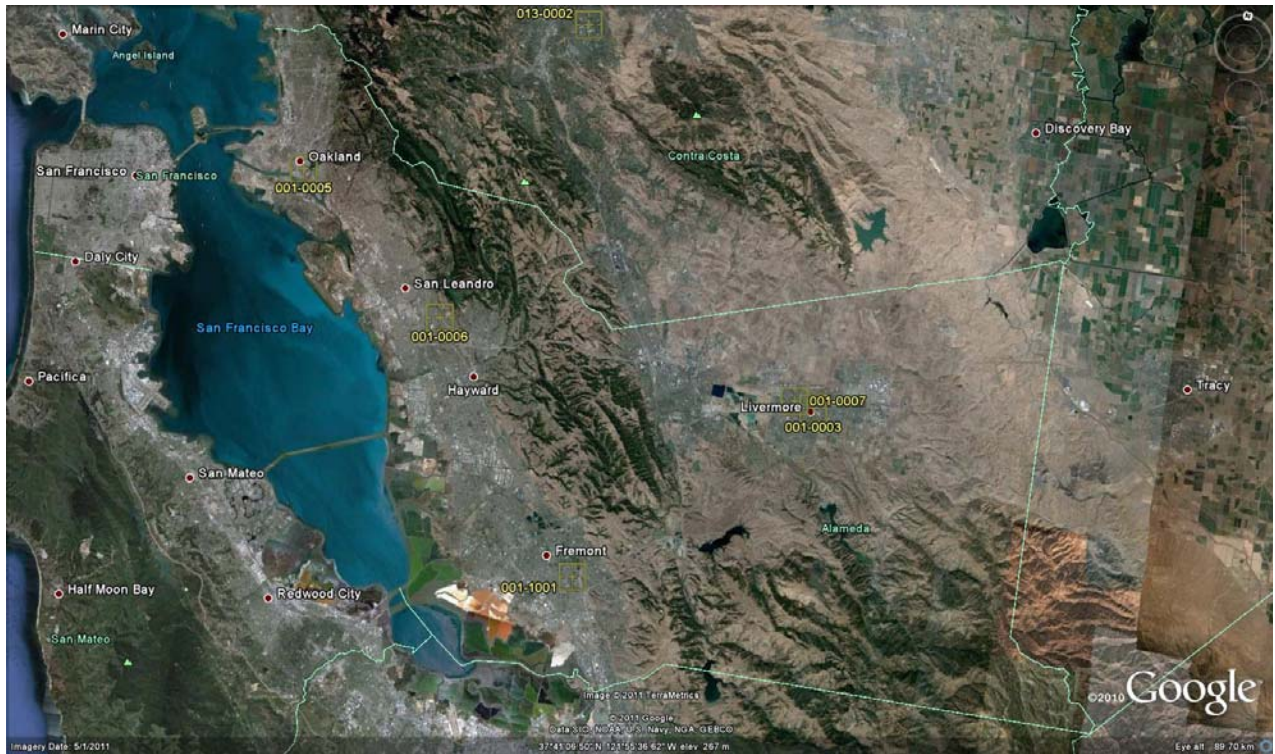


Figure A-6. Monitor Locations in Fresno County



Figure A-7. Monitor Locations in San Bernardino County

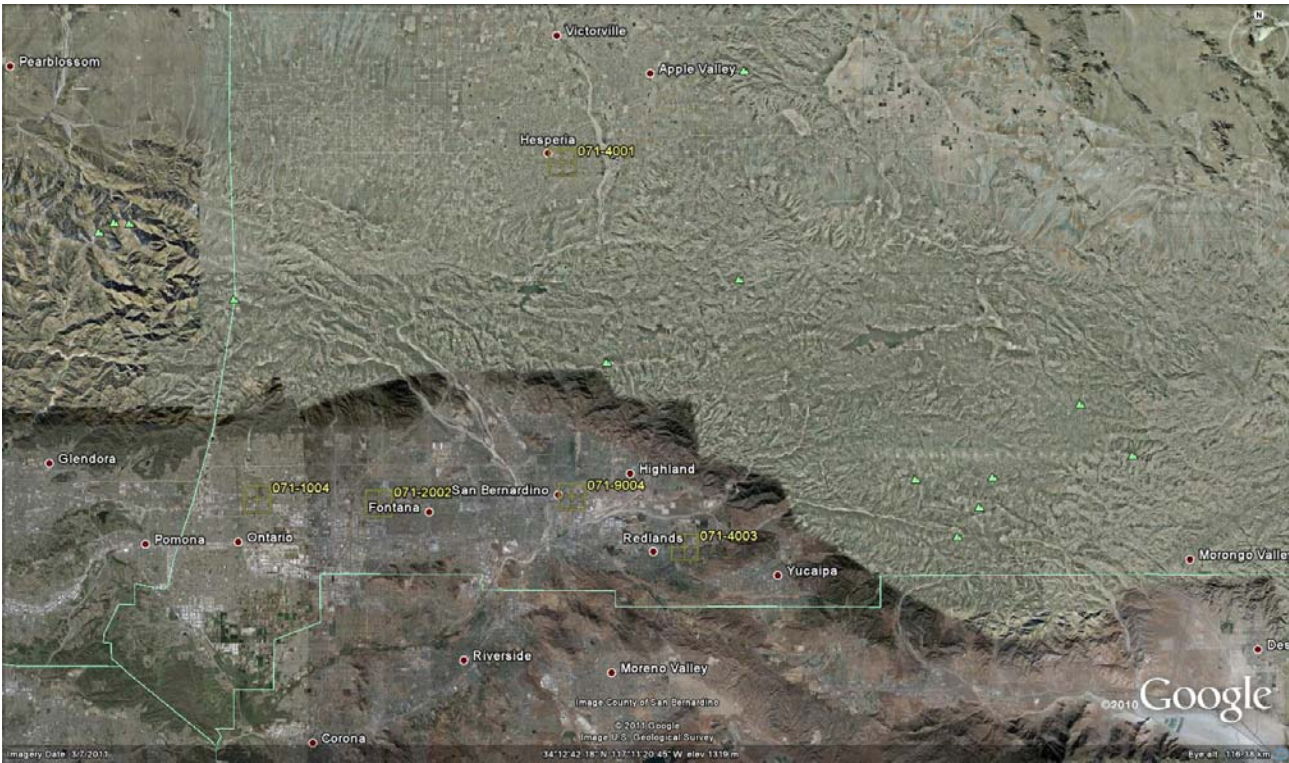


Figure A-8. Monitor Locations in Los Angeles County

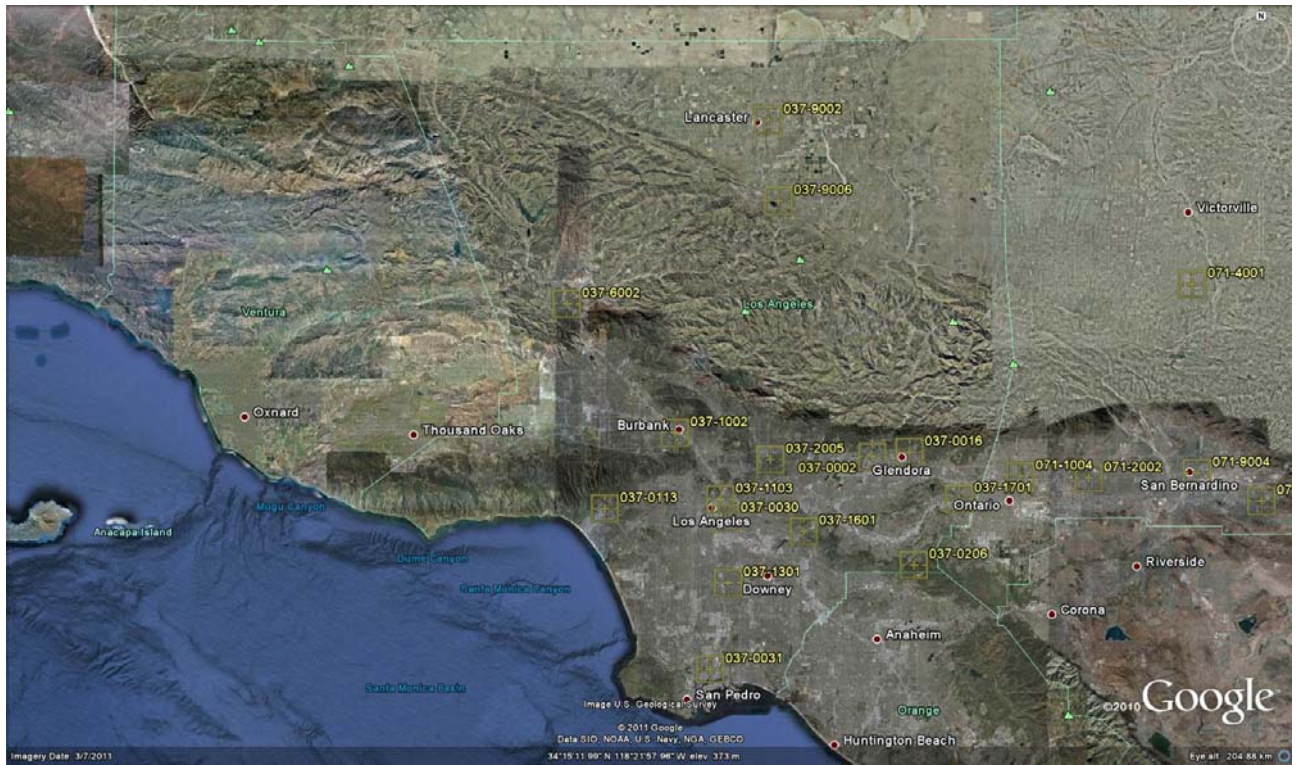
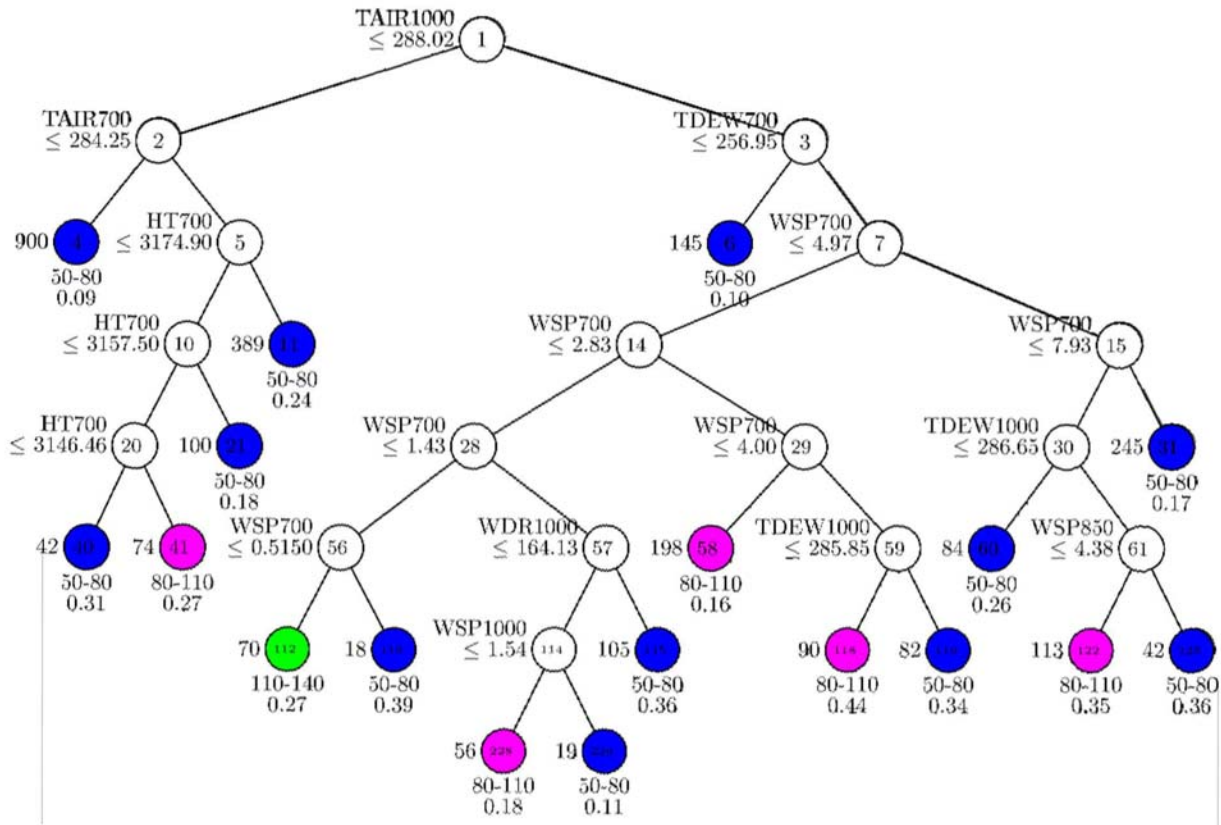


Figure A-9. Monitor Locations in Riverside County



# **Appendix B: Classification and Regression Trees**

**Figure B1 (1–5):** Examples from classification tree analysis of binned ozone versus meteorological parameters. Of note is that air temperature at various levels, e.g., 1,000, 850, or 700 hectopascals (hPa) (the top node of the trees shown here), is generally the most important splitting variable (predictor). In each figure, the units are as follows: HT in meters, TAIR in K, TDEW in K, WSP in  $m\ s^{-1}$ , WDR in degrees. The following CARTs are for  $[O_3] \geq 50$  ppb, years 2000–2005, and weekdays only.



**Figure B1-1. Alameda Example**

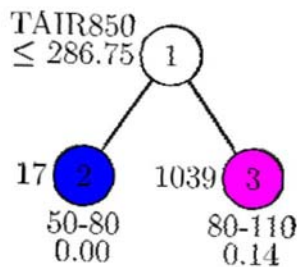


**Figure B1-2. Contra Costa Example (simple tree)**



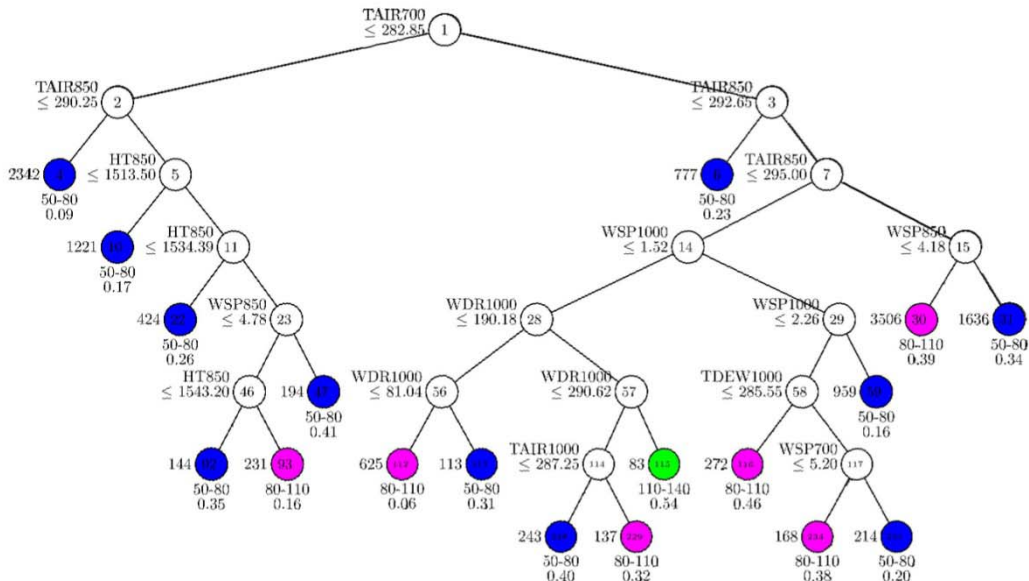
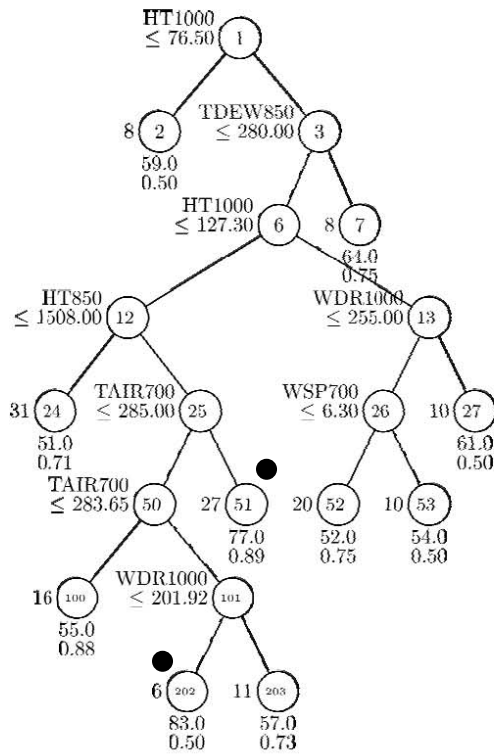
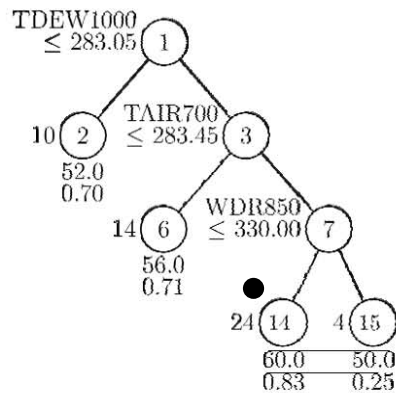


Figure B1-5. Sacramento Example

**Figure B2 (1–51):** Examples from regression tree analysis of ozone versus meteorological parameters. In each figure, the units are as follows: HT in meters, TAIR in K, TDEW in K, WSP in m s<sup>-1</sup>, WDR in degrees. The following CARTs are for [O<sub>3</sub>] ≥ 50 ppb, years 2000–2005, and weekdays only. The black circles next to some nodes refer to the path of splitting variables and conditions reported in Table 5.6.



**Figure B2-1. Alameda Monitor 0007**



**Figure B2-2. Alameda Monitor 1001**

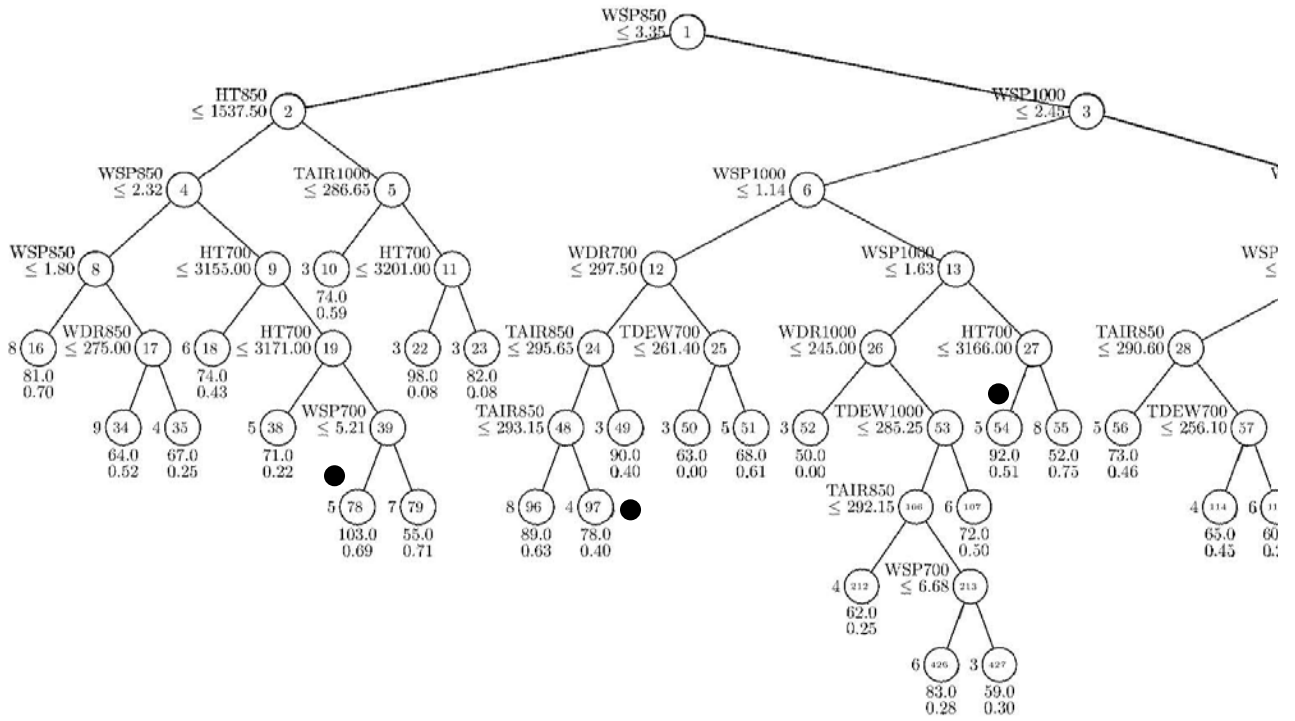


Figure B2-3. Contra Costa Monitor 0002

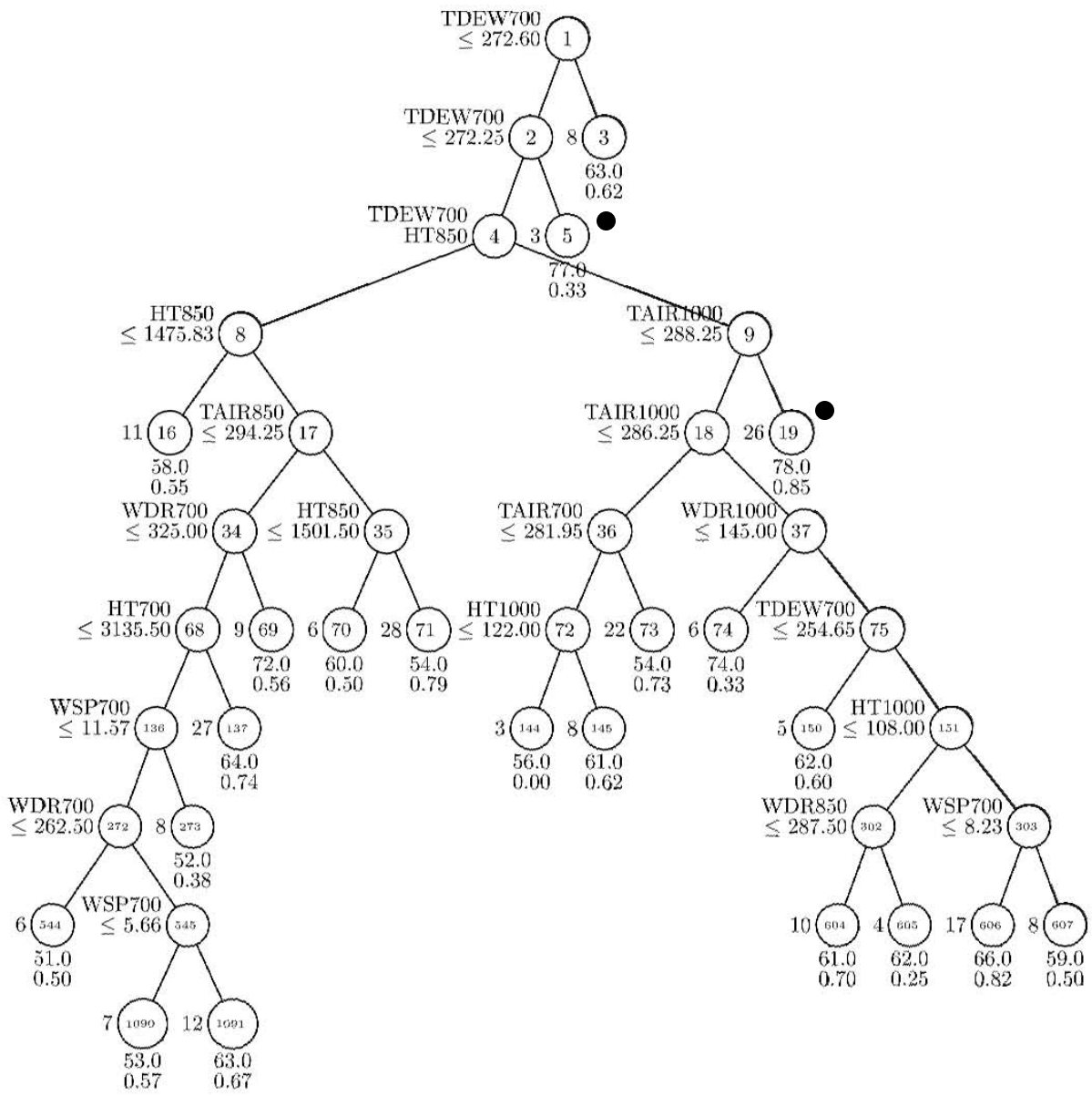


Figure B2-4. Contra Costa Monitor 1002

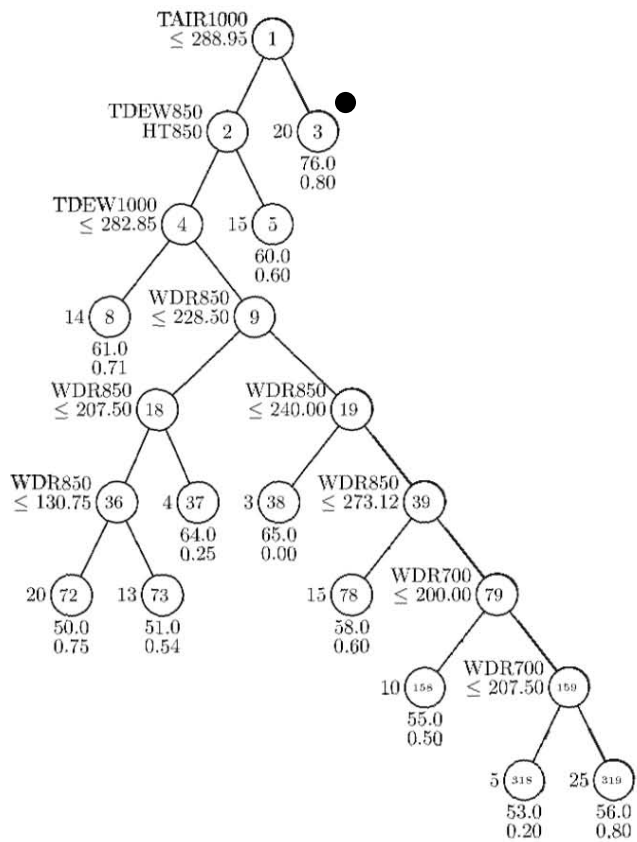


Figure B2-5. Santa Clara Monitor 0002

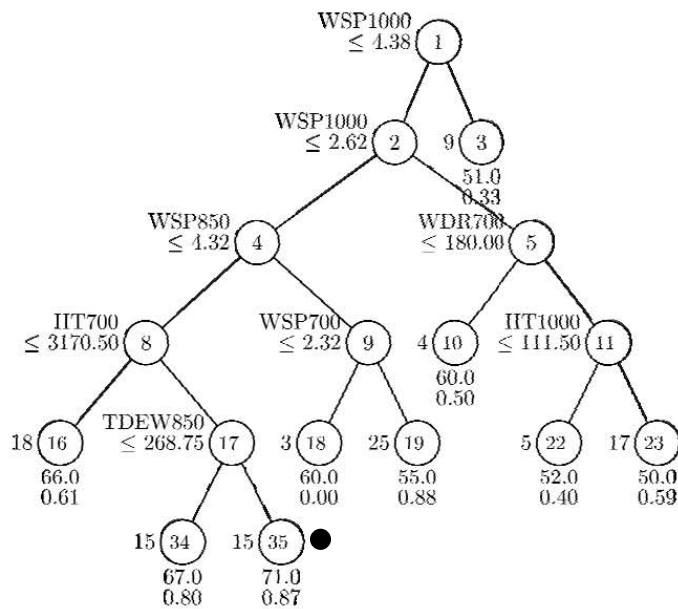


Figure B2-6. Santa Clara Monitor 1001

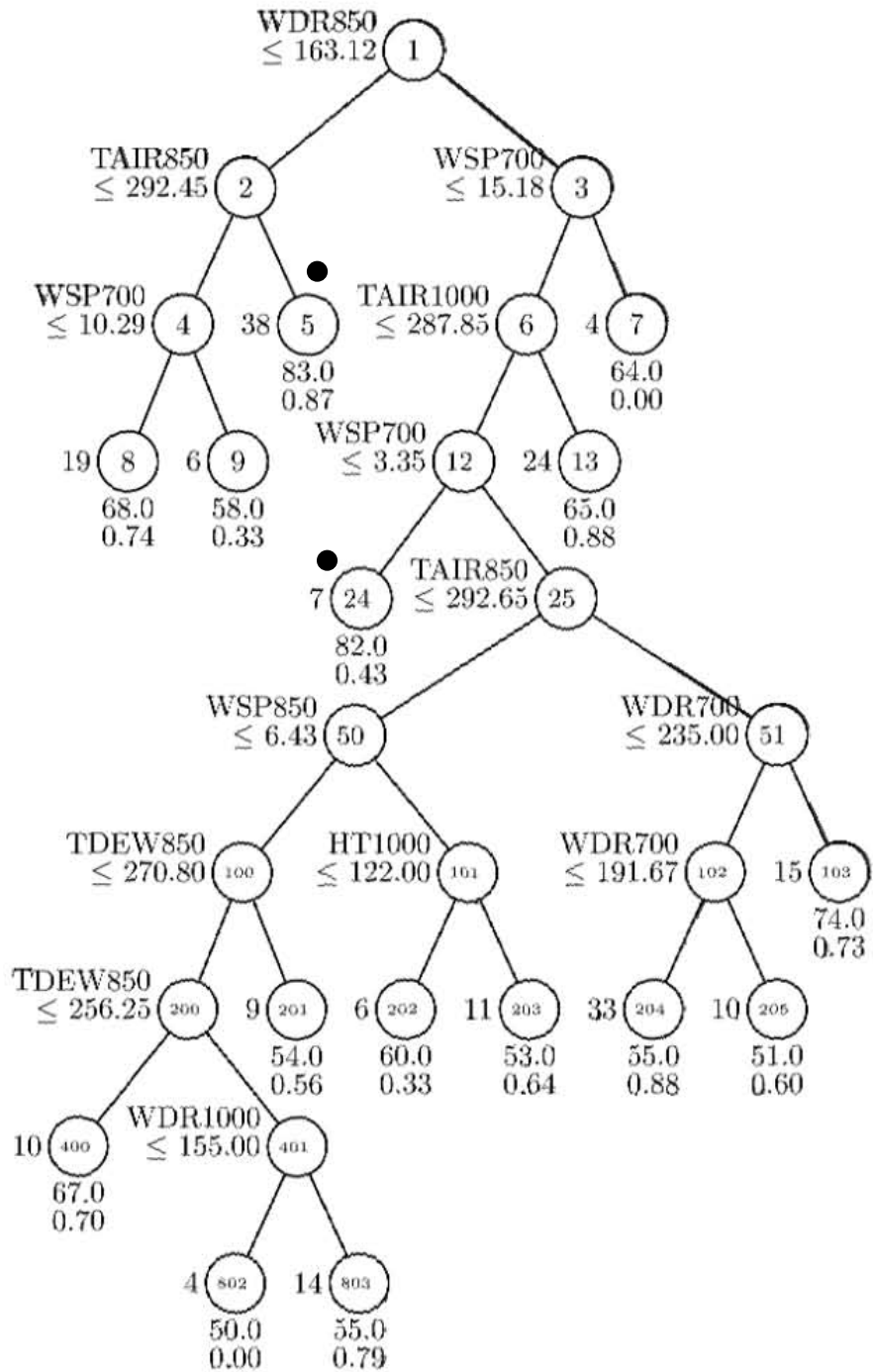


Figure B2-7. San Joaquin Monitor 3003

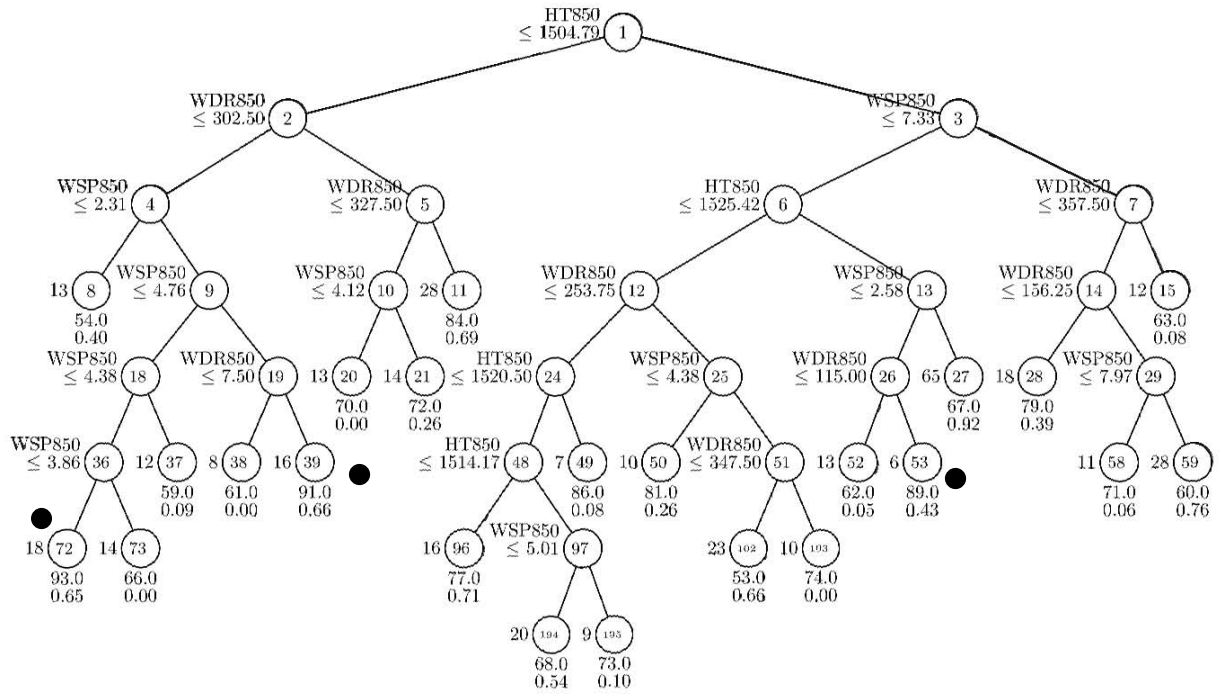


Figure B2-8. San Bernardino Monitor 0001

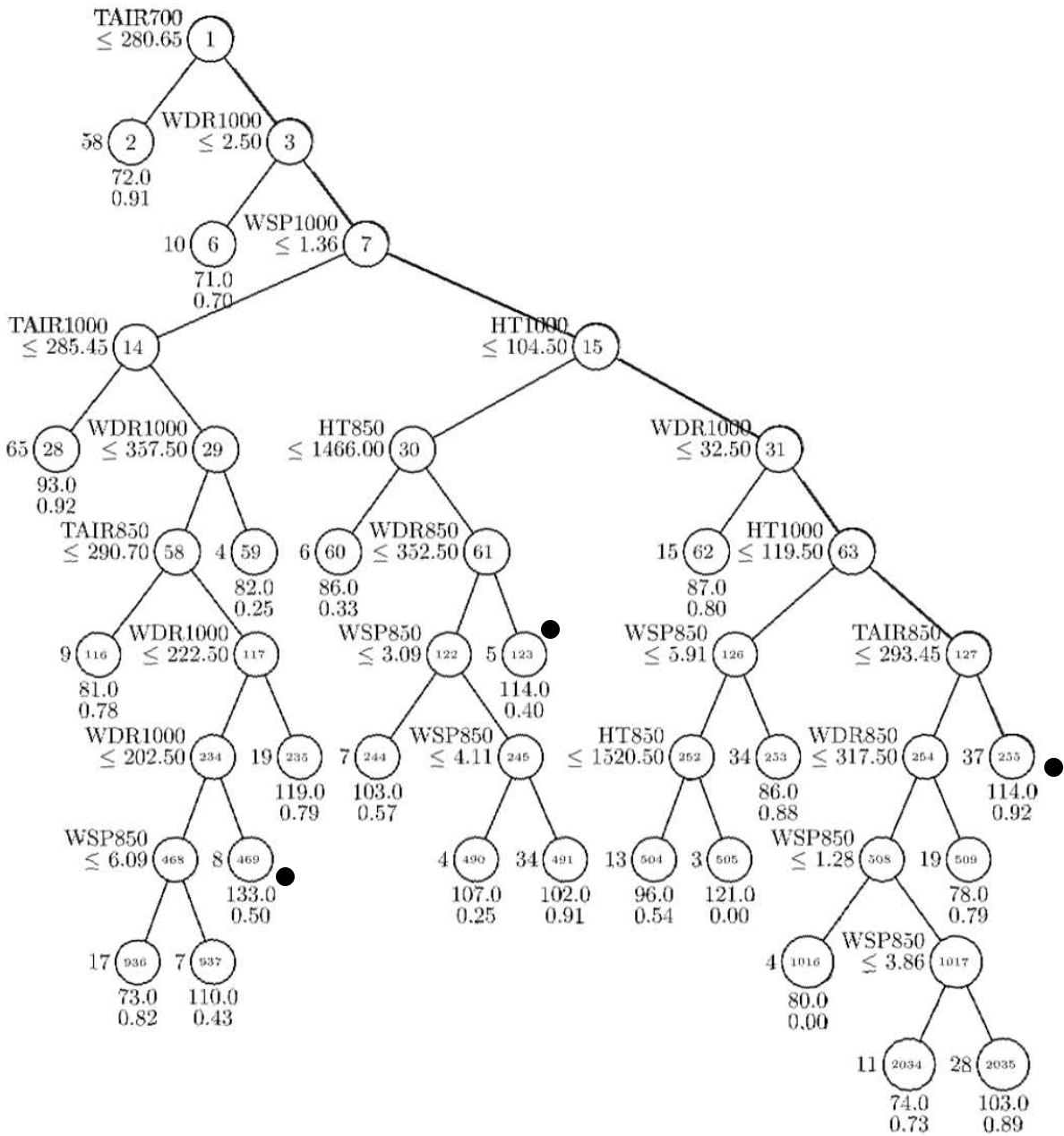


Figure B2-9. San Bernardino Monitor 0005



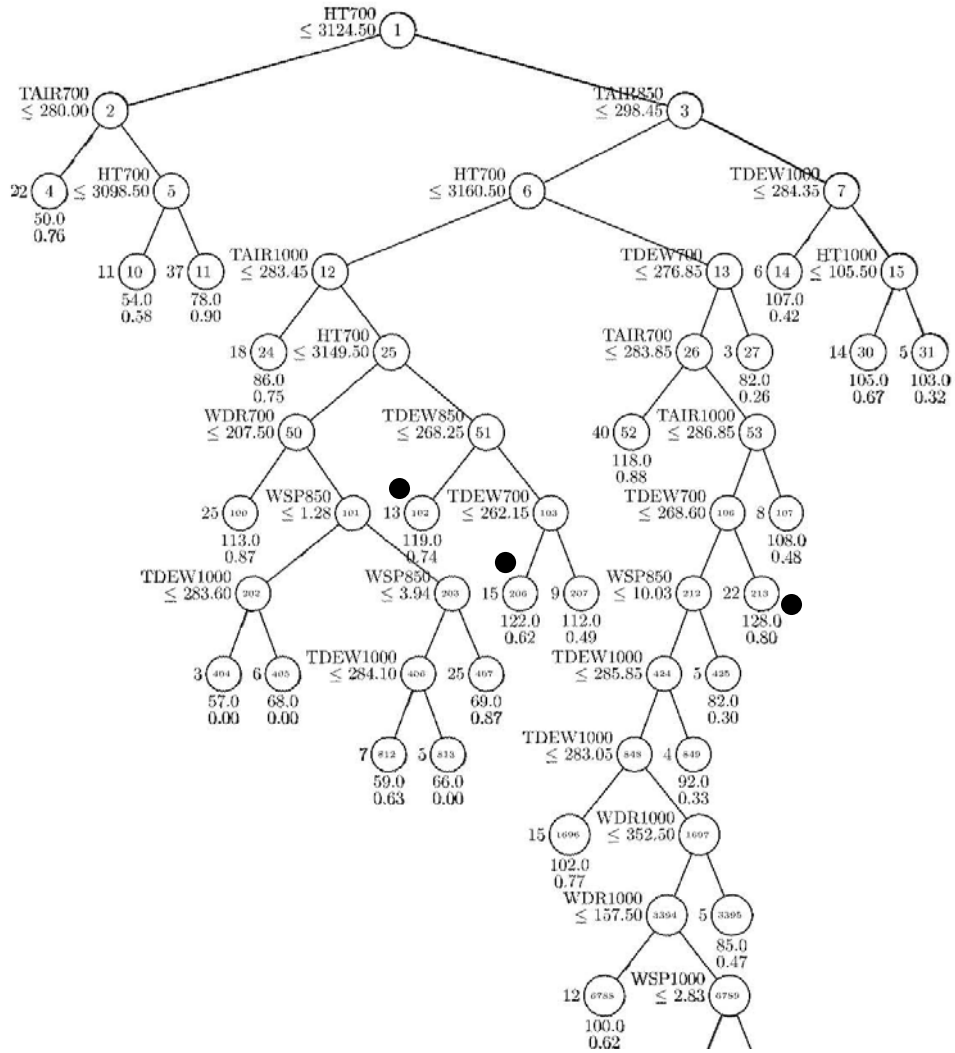


Figure B2-12. San Bernardino Monitor 1004

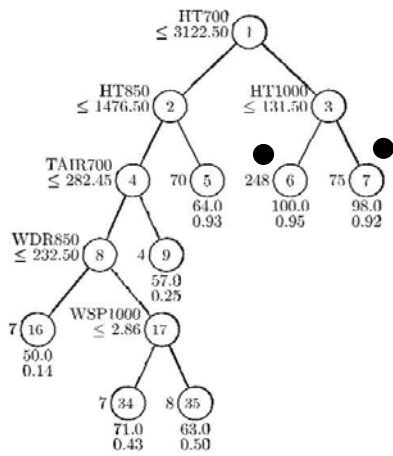


Figure B2-13. San Bernardino Monitor 4003

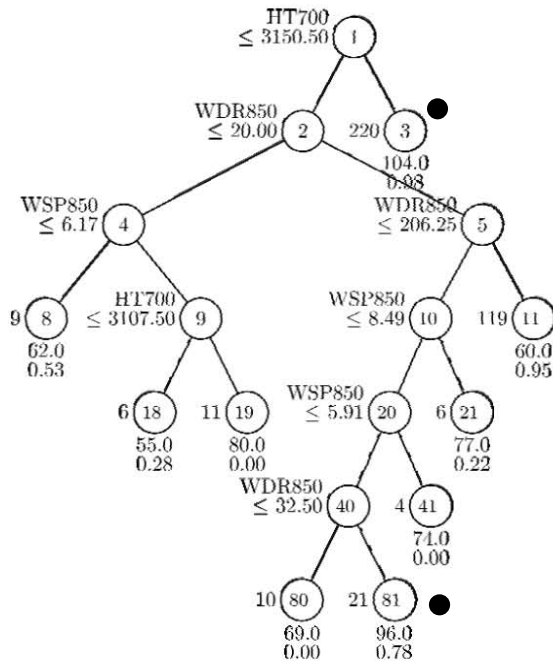


Figure B2-14. San Bernardino Monitor 9004

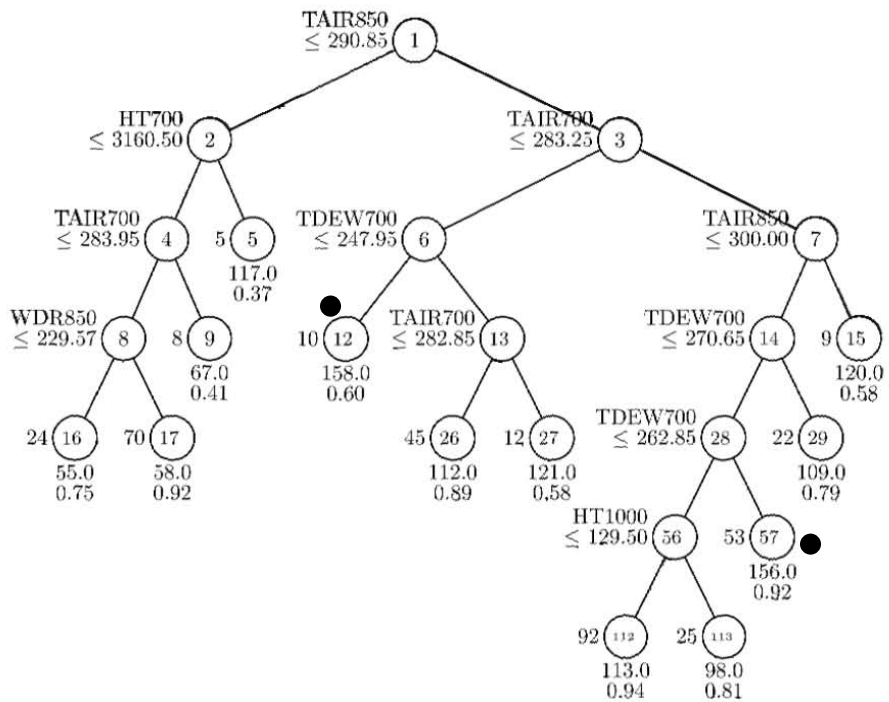


Figure B2-15. San Bernardino Monitor 2002

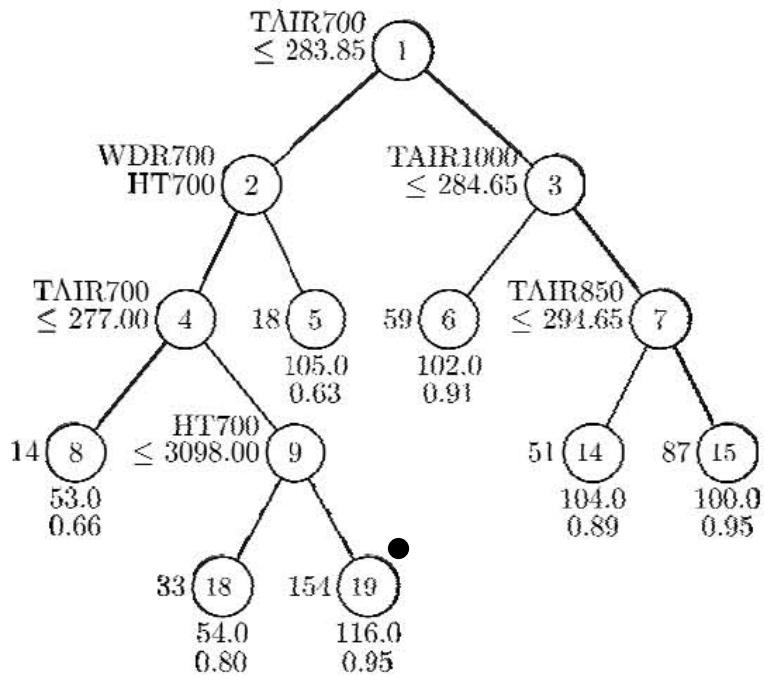


Figure B2-16. San Bernardino Monitor 4001

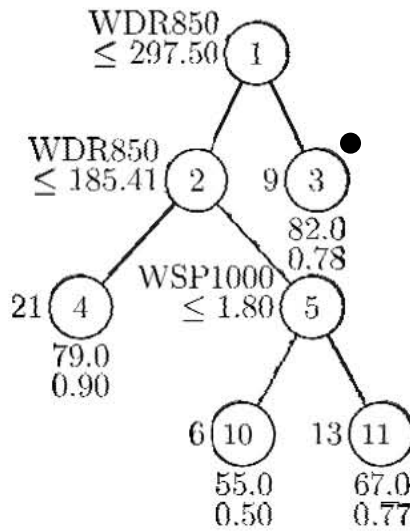


Figure B2-17. Riverside Monitor 6001

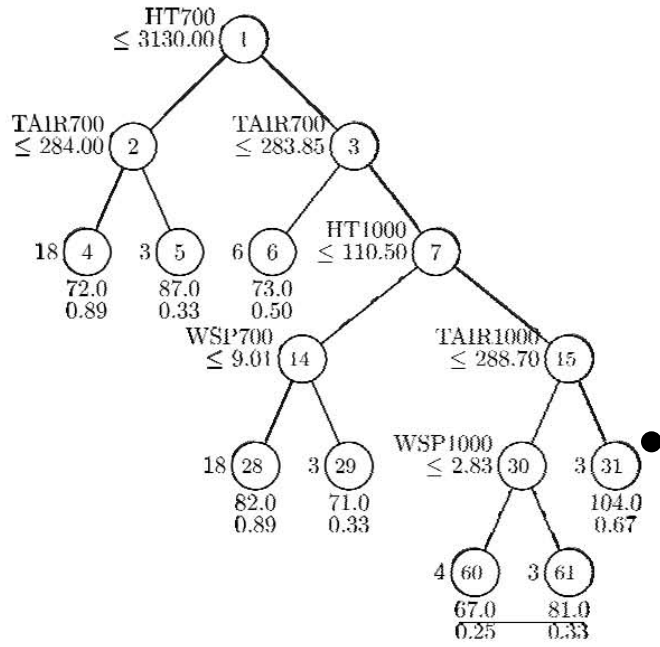


Figure B2-18. Riverside Monitor 8001

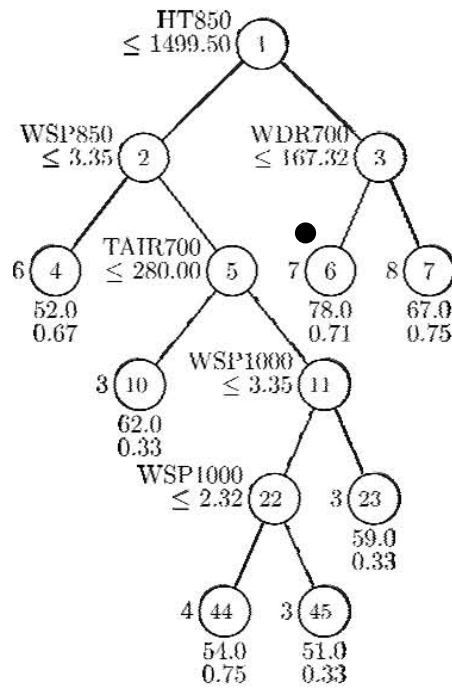


Figure B2-19. Orange Monitor 2022

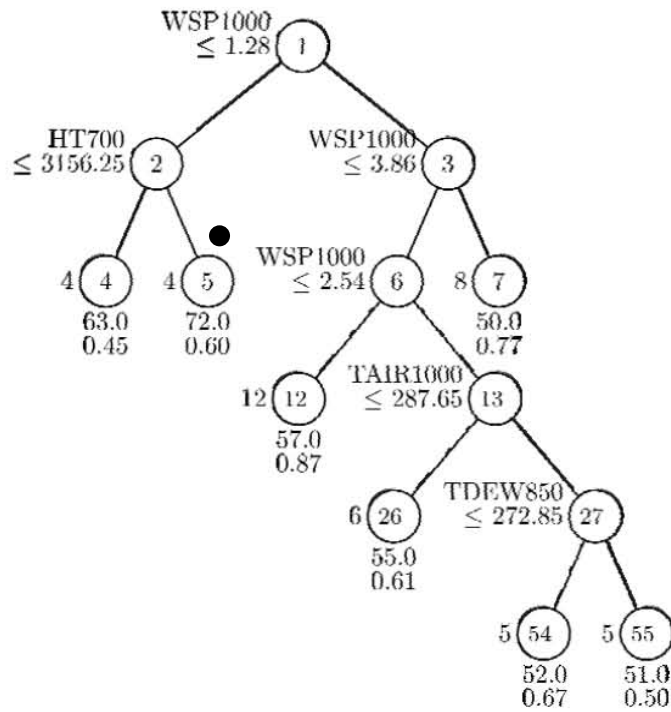


Figure B2-20. Orange Monitor 0007

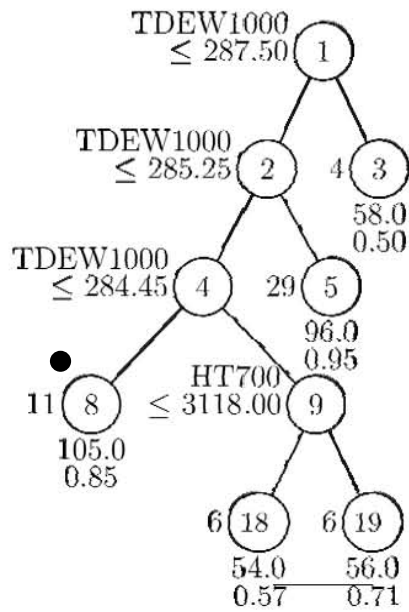


Figure B2-21. Los Angeles Monitor 1701

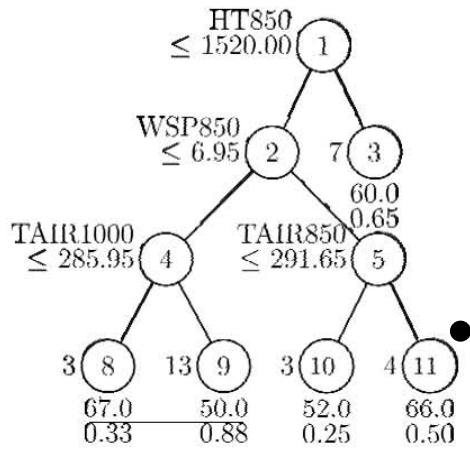


Figure B2-22. Los Angeles Monitor 5005

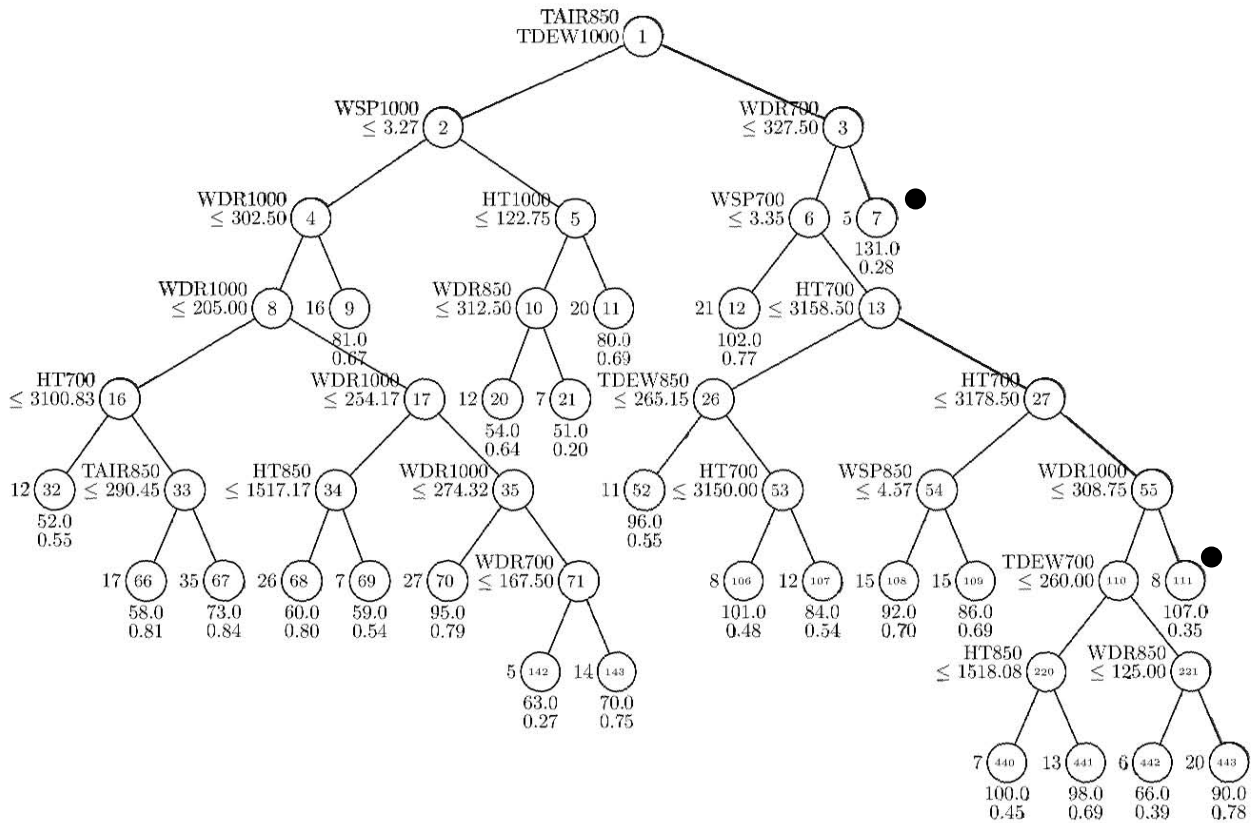


Figure B2-23. Sacramento Monitor 0002

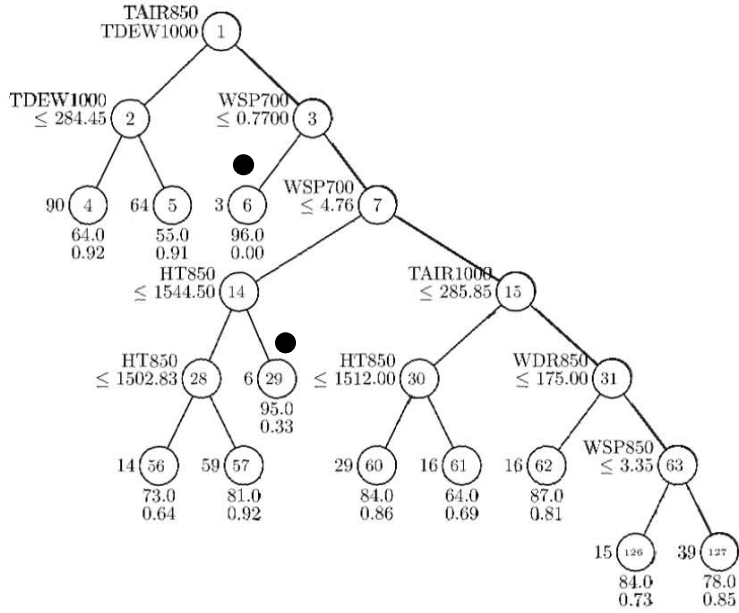


Figure B2-24. Sacramento Monitor 0006

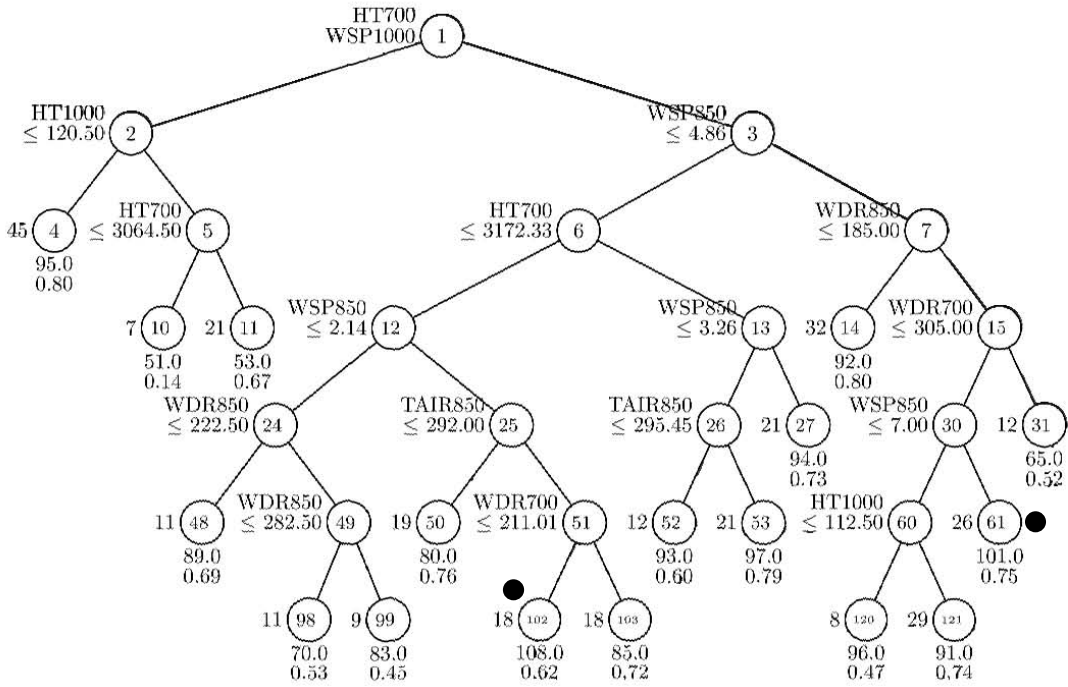


Figure B2-25. Sacramento Monitor 0011

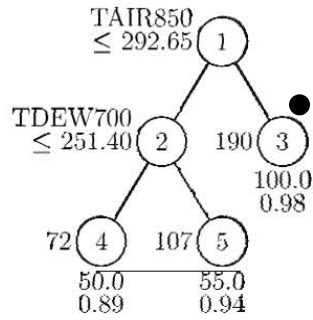


Figure B2-26. Sacramento Monitor 0012

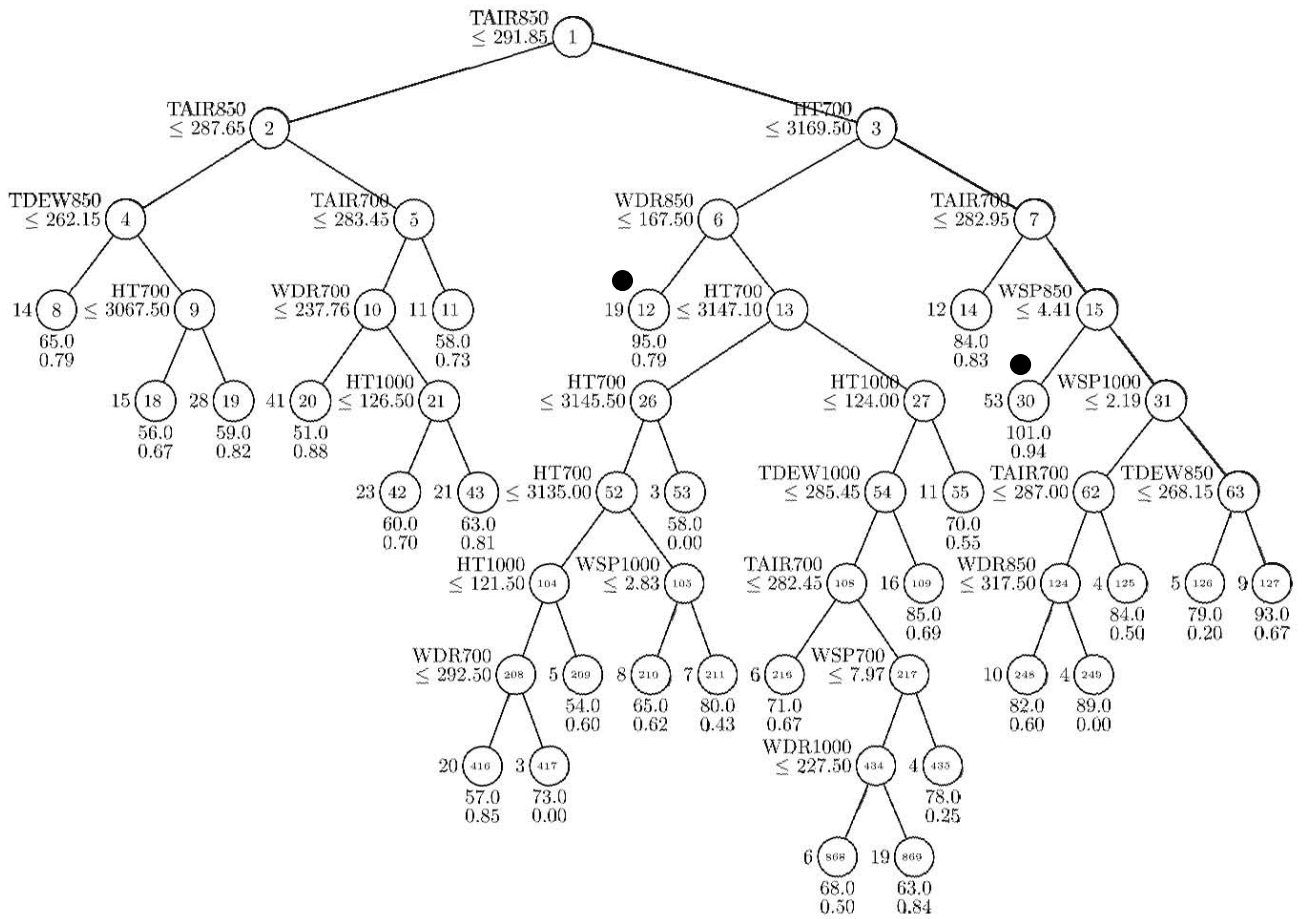


Figure B2-27. Sacramento Monitor 5003

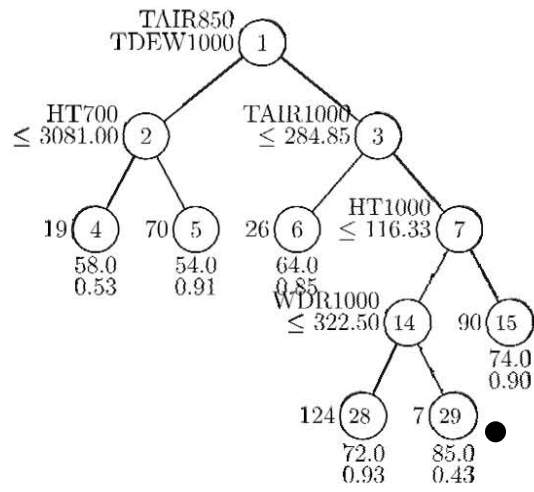


Figure B2-28. Placer Monitor 0002

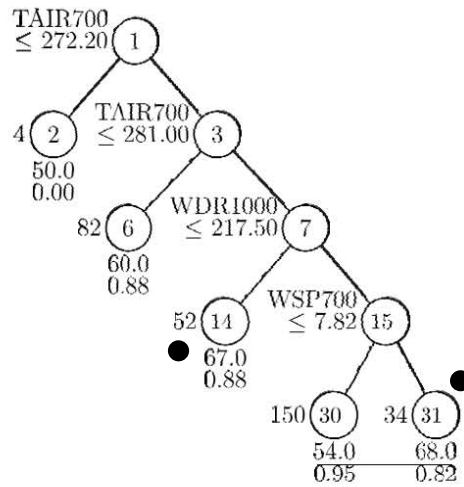


Figure B2-29. Placer Monitor 0006

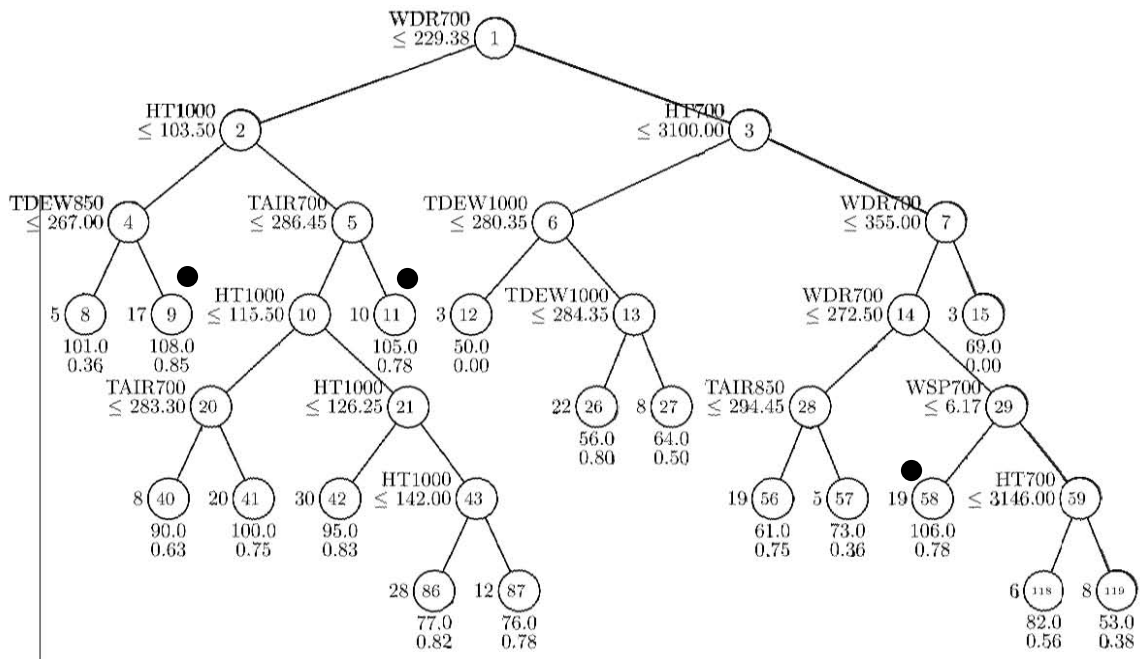


Figure B2-30. Placer Monitor 0004

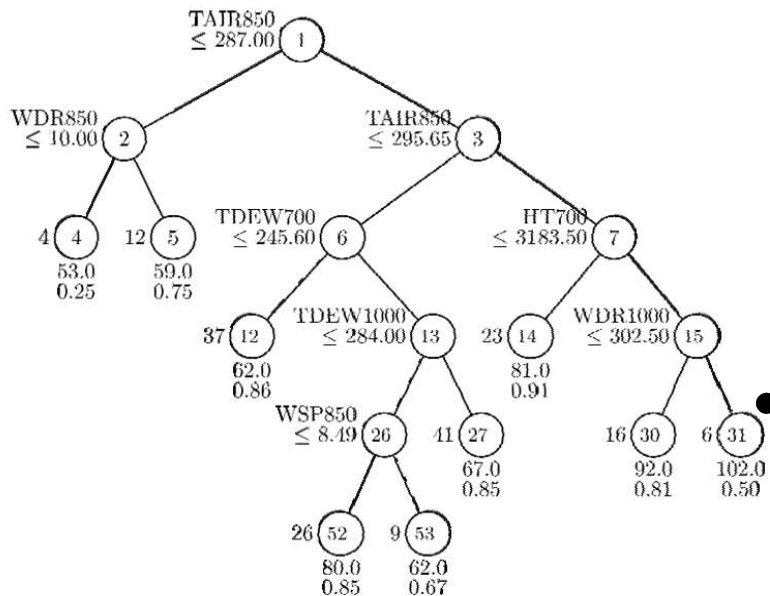


Figure B2-31. Placer Monitor 3001

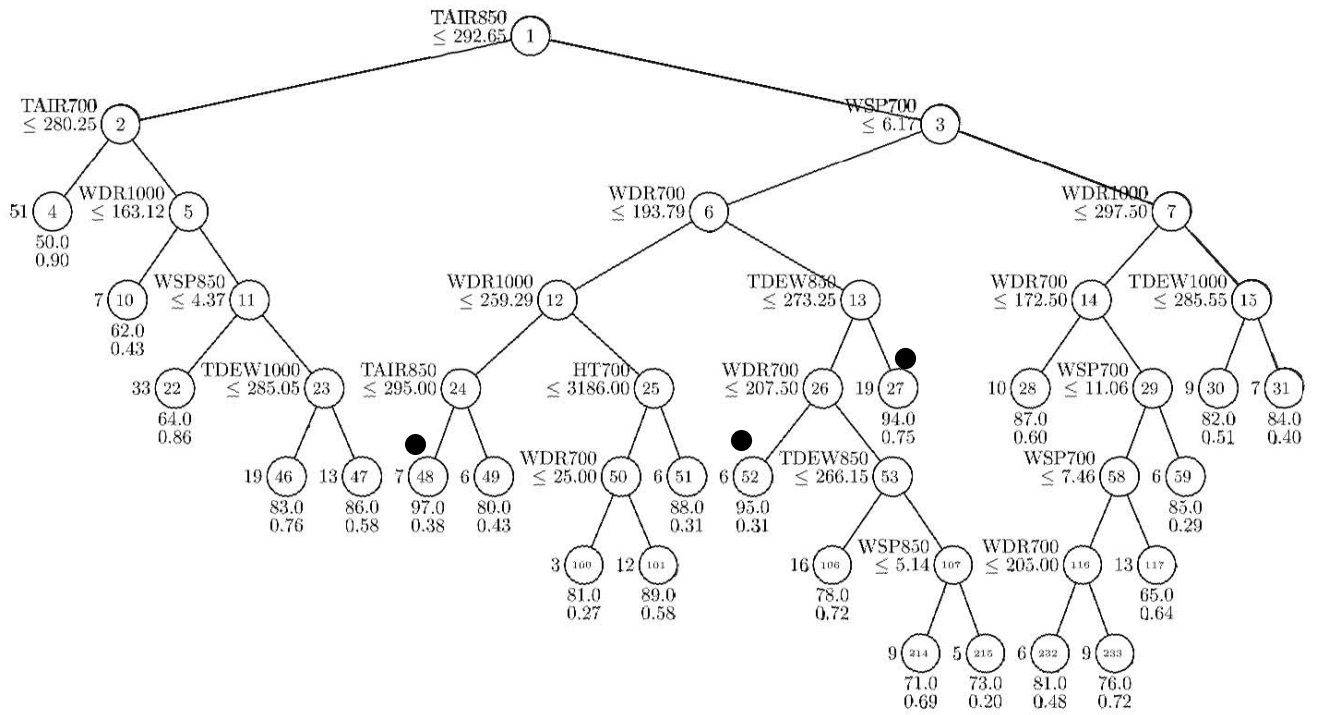


Figure B2-32. Yolo Monitor 0004

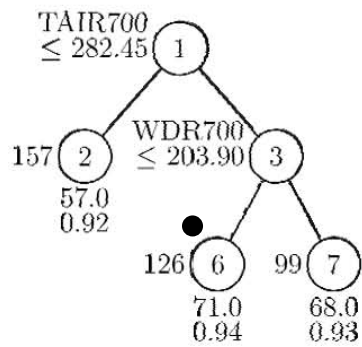


Figure B2-33. Eldorado Monitor 0010

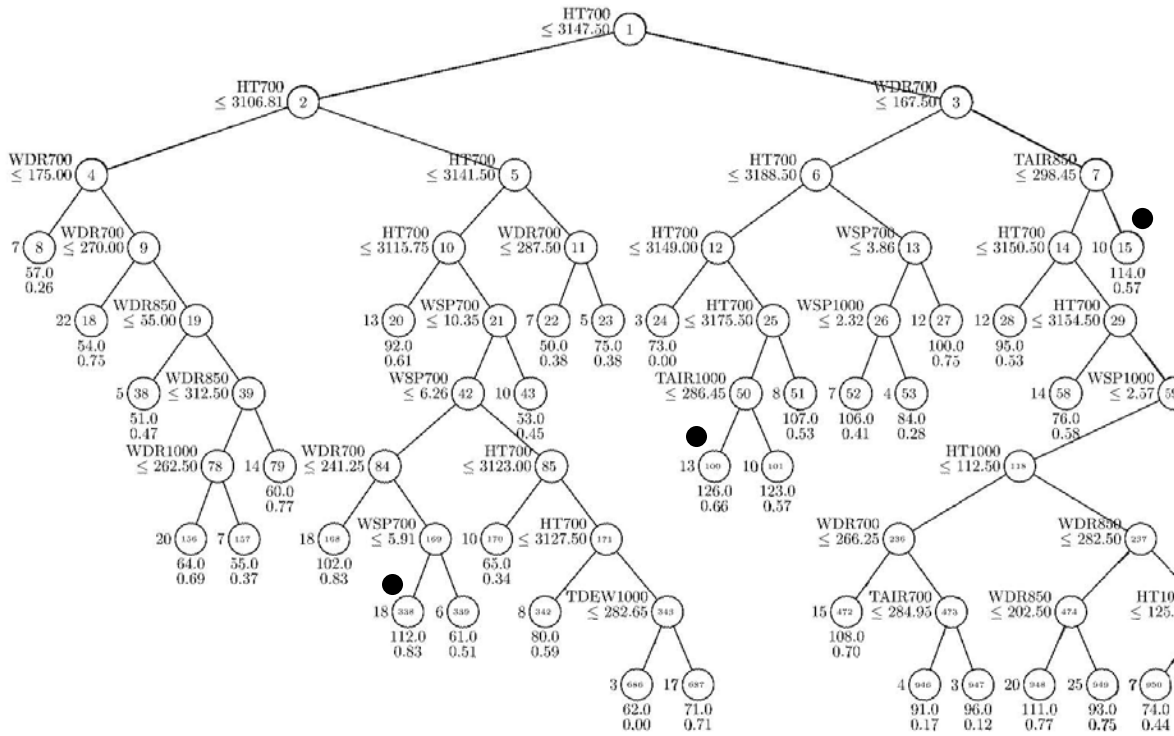


Figure B2-34. Eldorado Monitor 0020

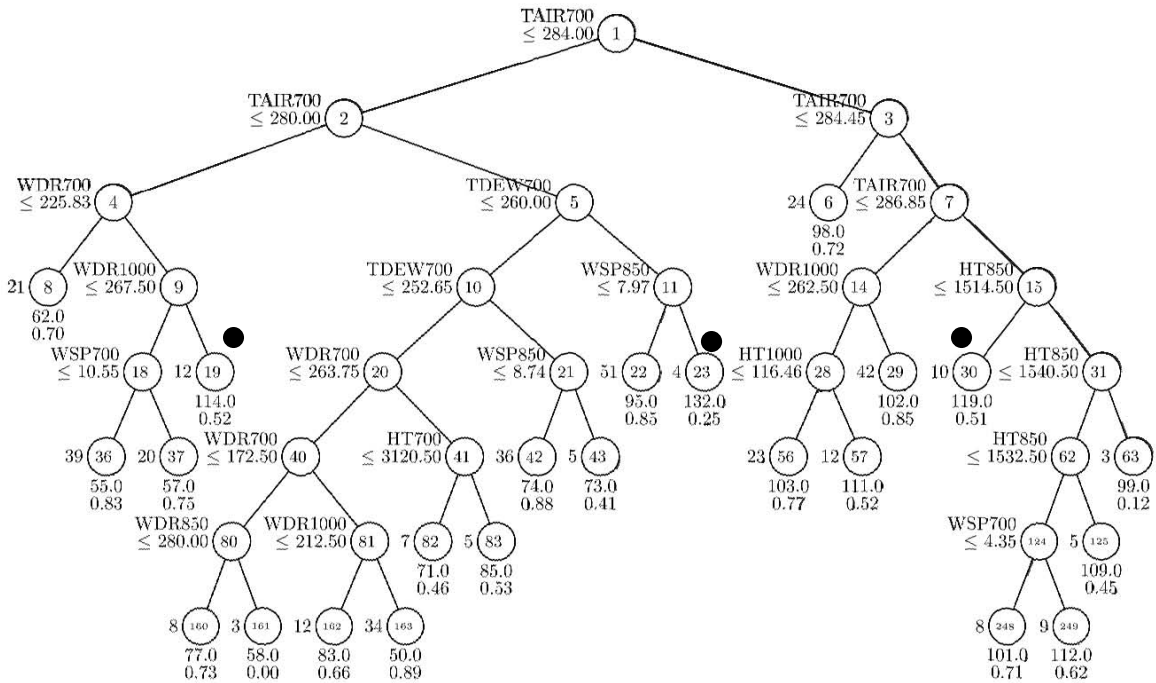


Figure B2-34. Fresno Monitor 0007

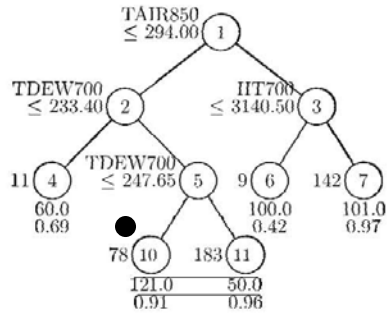


Figure B2-36. Fresno Monitor 0008

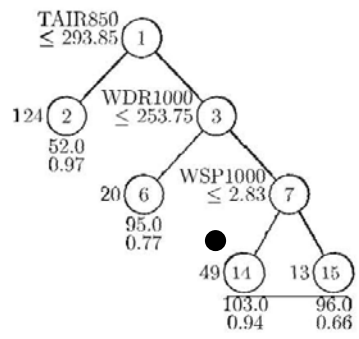


Figure B2-37. Fresno Monitor 0010

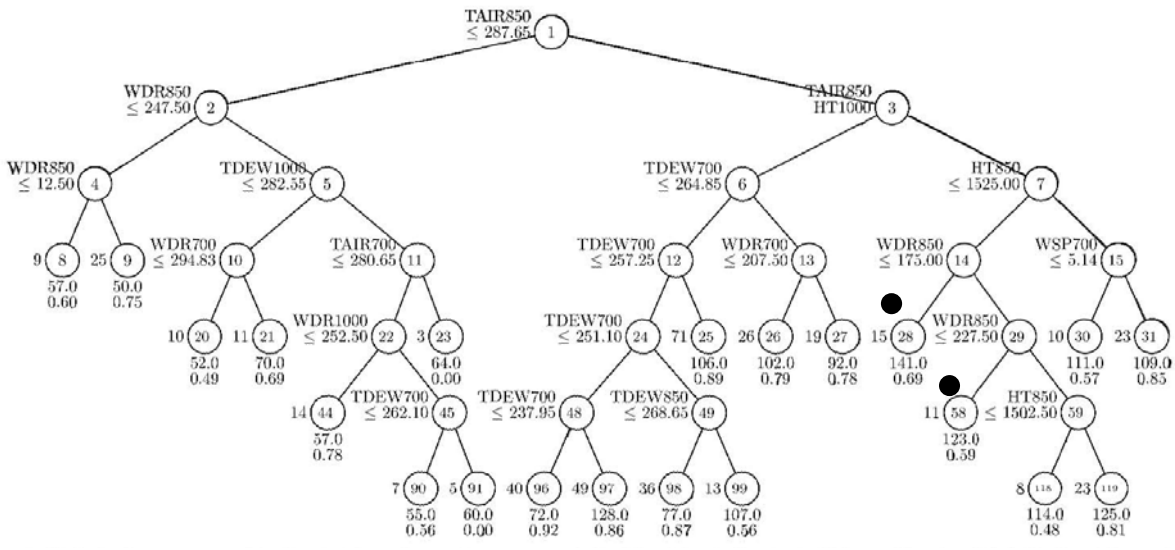


Figure B2-38. Fresno Monitor 0242



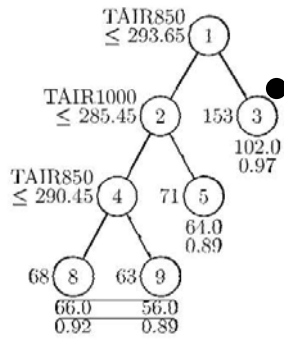


Figure B2-41. Kern Monitor 0008

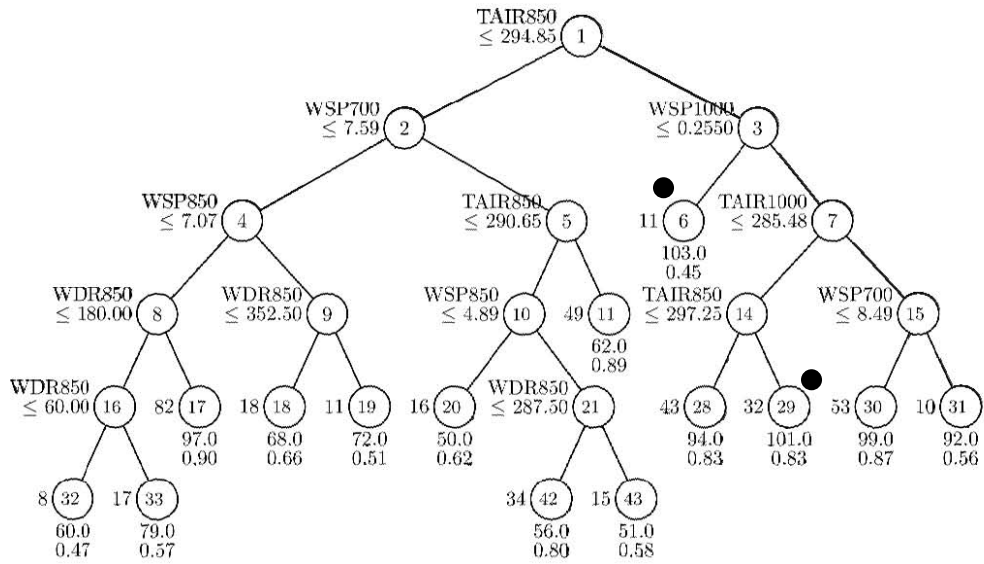


Figure B2-42. Kern Monitor 0010

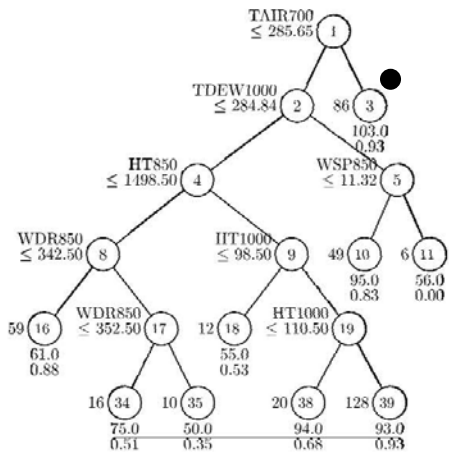


Figure B2-43. Kern Monitor 0011

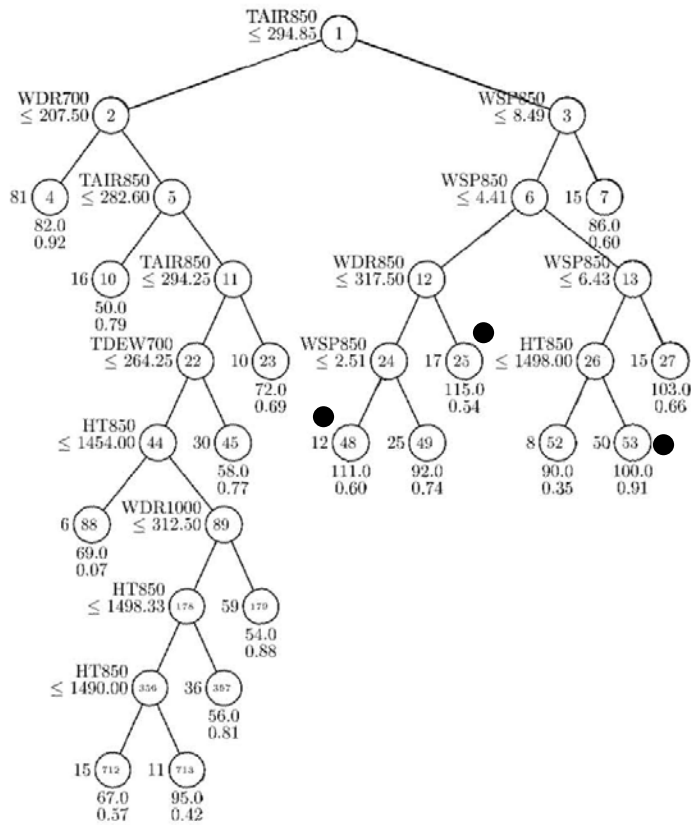


Figure B2-44. Kern Monitor 0014

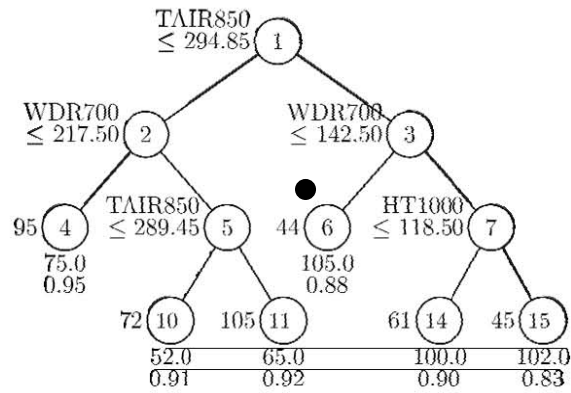


Figure B2-45. Kern Monitor 0232

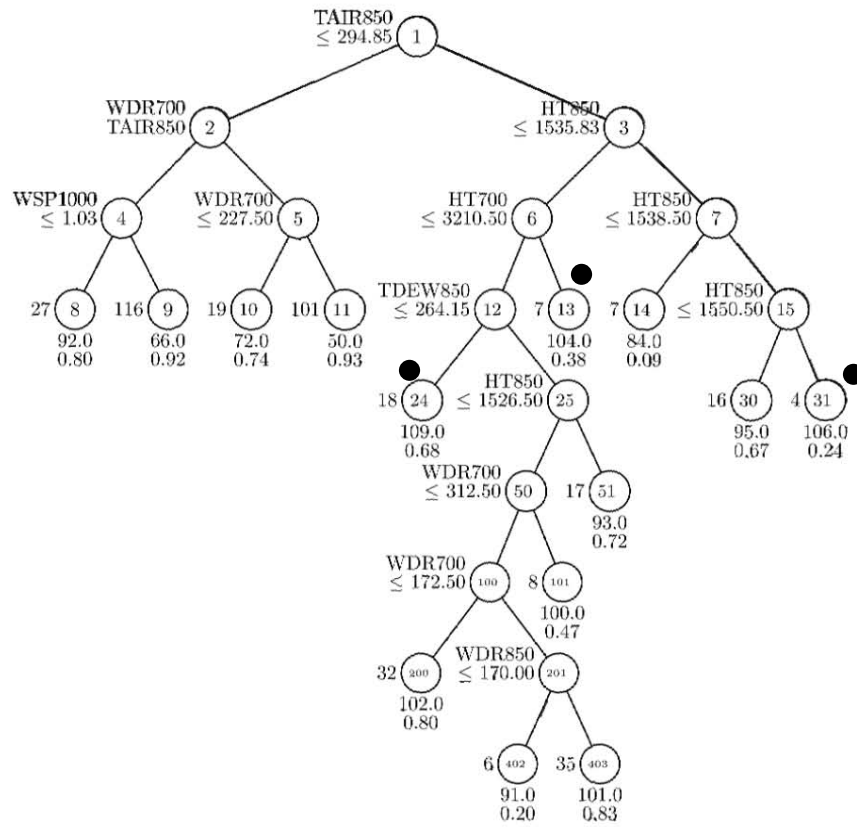
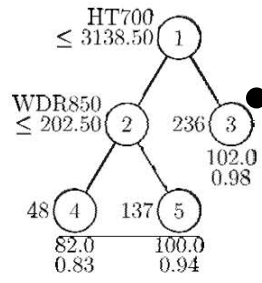
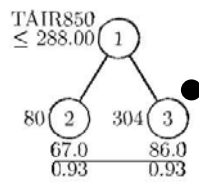


Figure B2-46. Kern Monitor 6001



**Figure B2-47. Kings Monitor 1004**



**Figure B2-48. Tulare Monitor 0006**

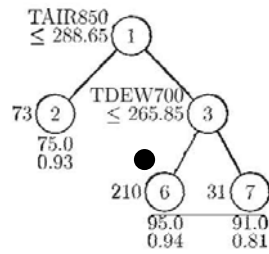


**Figure B2-49. Tulare Monitor 0008**

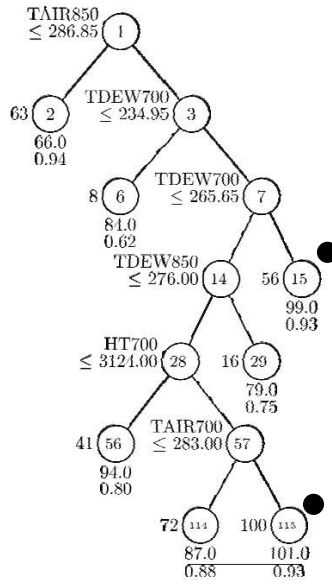


Figure B2-50. Tulare Monitor 0009

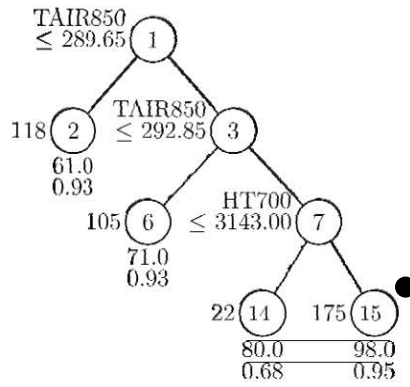


Figure B2-51. Tulare Monitor 2002

**Appendix C:  
Meteorological and Air-Quality Impact Cross-Section  
Figures**

Dataset: case00 RIP: ripexecute.SF SAC Init: 0000 UTC Thu 27 Jul 00  
Fcst: 22.00 h Valid: 2200 UTC Thu 27 Jul 00 (1500 PDT Thu 27 Jul 00)  
Temperature at k-index = 32  
Horizontal wind vectors at k-index = 32

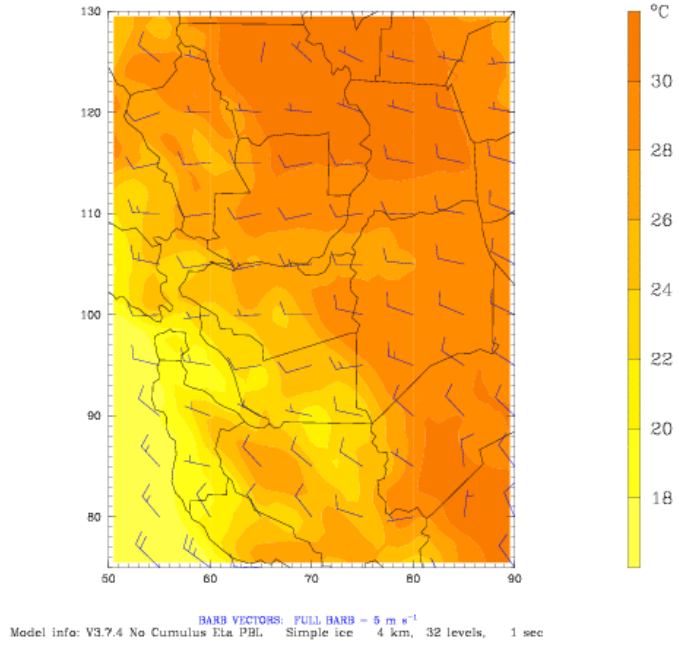


Figure C1-1. Base Case Meteorology Episode 2000 SF-SAC Domain

Dataset: case00 RIP: ripexecute.SF SAC Init: 0000 UTC Thu 27 Jul 00  
Fcst: 46.00 h Valid: 2200 UTC Fri 28 Jul 00 (1500 PDT Fri 28 Jul 00)  
Temperature at k-index = 32  
Horizontal wind vectors at k-index = 32

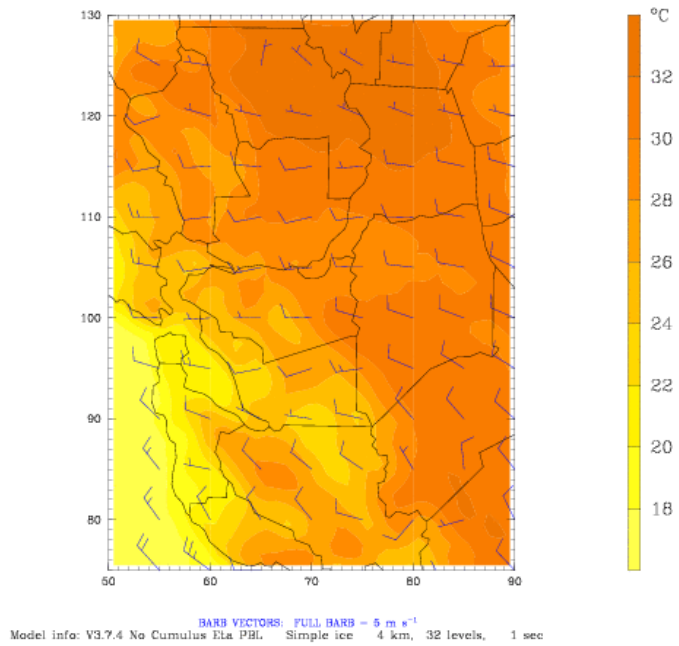


Figure C1-2. Base Case Meteorology Episode 2000 SF-SAC Domain

Dataset: case00 RIP: ripexecute.SF SAC Init: 0000 UTC Thu 27 Jul 00  
Fest: 70.00 h Valid: 2200 UTC Sat 29 Jul 00 (1500 PDT Sat 29 Jul 00)  
Temperature at k-index = 32  
Horizontal wind vectors at k-index = 32

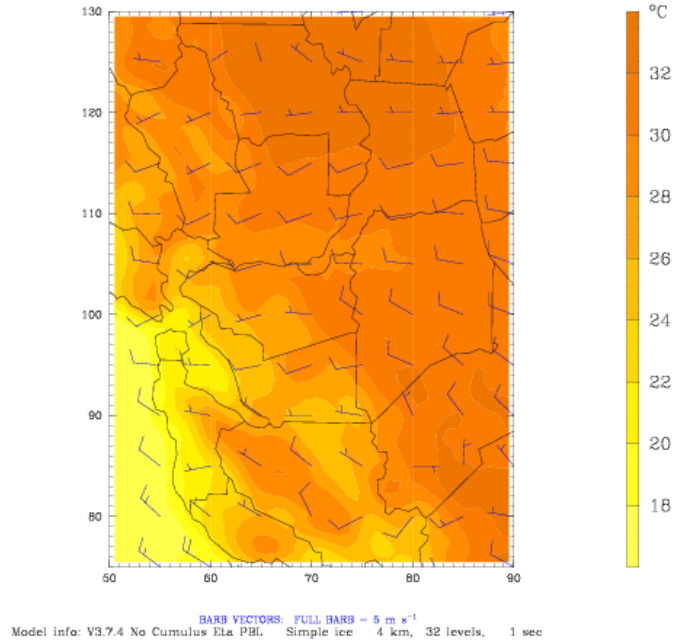


Figure C1-3. Base Case Meteorology Episode 2000 SF-SAC Domain

Dataset: case00 RIP: ripexecute.SF SAC Init: 0000 UTC Thu 27 Jul 00  
Fest: 94.00 h Valid: 2200 UTC Sun 30 Jul 00 (1500 PDT Sun 30 Jul 00)  
Temperature at k-index = 32  
Horizontal wind vectors at k-index = 32

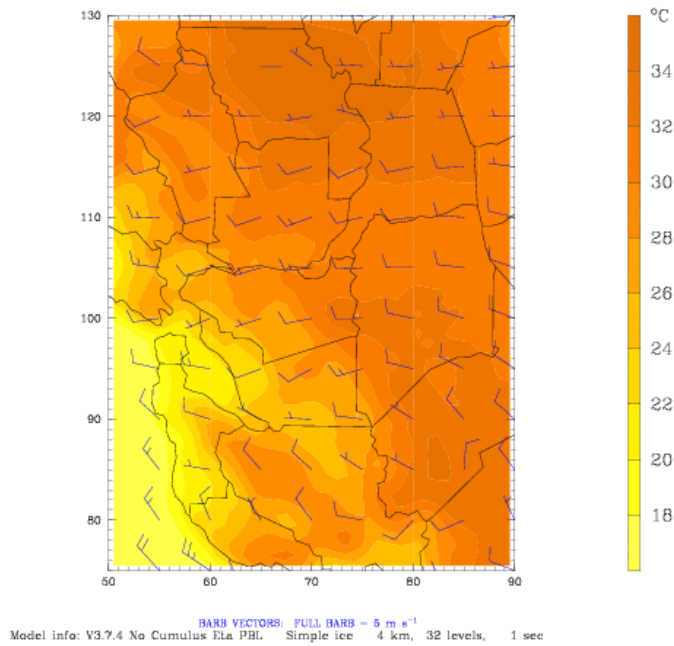
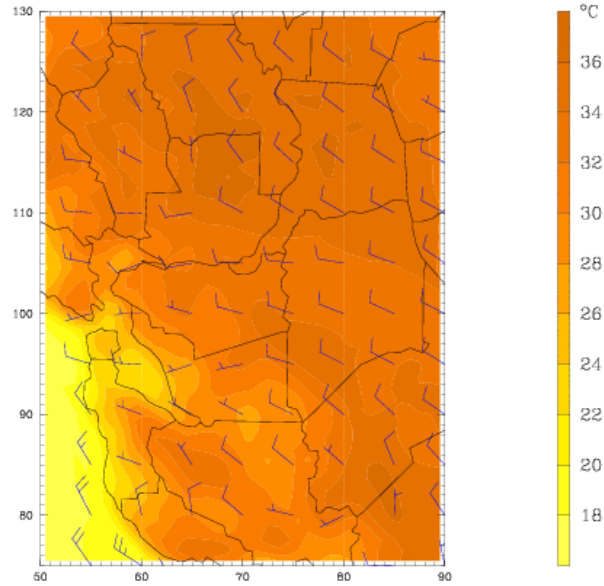


Figure C1-4. Base Case Meteorology Episode 2000 SF-SAC Domain

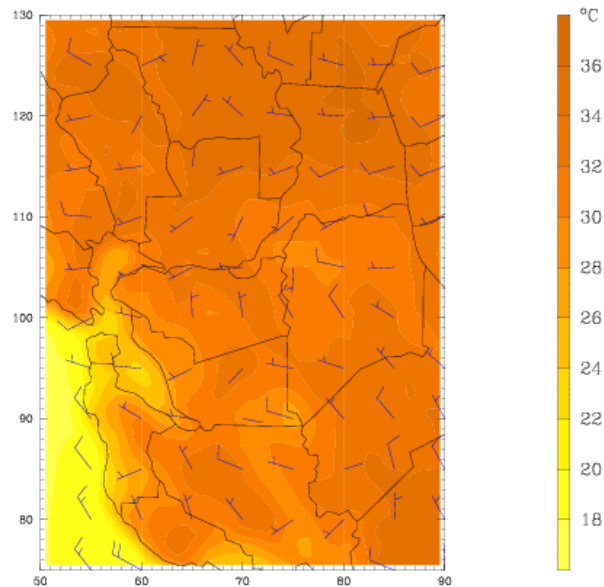
Dataset: case00 RIP: ripexecute.SF SAC Init: 0000 UTC Thu 27 Jul 00  
 Fcst: 118.00 h Valid: 2200 UTC Mon 31 Jul 00 (1500 PDT Mon 31 Jul 00)  
 Temperature at k-index = 32  
 Horizontal wind vectors at k-index = 32



BARB VECTORS: FULL BARB = 5 m s<sup>-1</sup>  
 Model info: V3.7.4 No Cumulus Eta PBL Simple ice 4 km, 32 levels, 1 sec

**Figure C1. Base Case Meteorology Episode 2000 SF-SAC Domain**

Dataset: case00 RIP: ripexecute.SF SAC Init: 0000 UTC Thu 27 Jul 00  
 Fcst: 142.00 h Valid: 2200 UTC Tue 01 Aug 00 (1500 PDT Tue 01 Aug 00)  
 Temperature at k-index = 32  
 Horizontal wind vectors at k-index = 32



BARB VECTORS: FULL BARB = 5 m s<sup>-1</sup>  
 Model info: V3.7.4 No Cumulus Eta PBL Simple ice 4 km, 32 levels, 1 sec

**Figure C1-6. Base Case Meteorology Episode 2000 SF-SAC Domain**

Dataset: case00 RIP: ripexecute.SF SAC Init: 0000 UTC Thu 27 Jul 00  
Post: 166.00 h Valid: 2200 UTC Wed 02 Aug 00 (1500 PDT Wed 02 Aug 00)  
Temperature at k-index = 32  
Horizontal wind vectors at k-index = 32

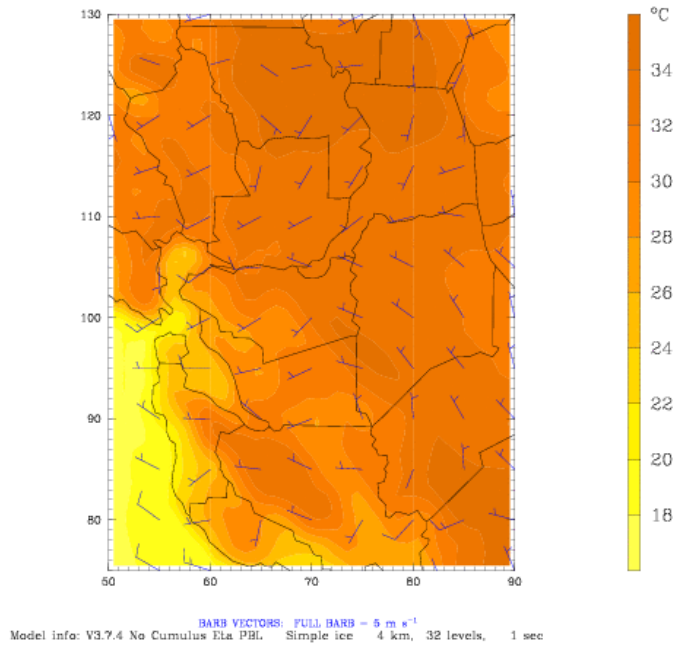
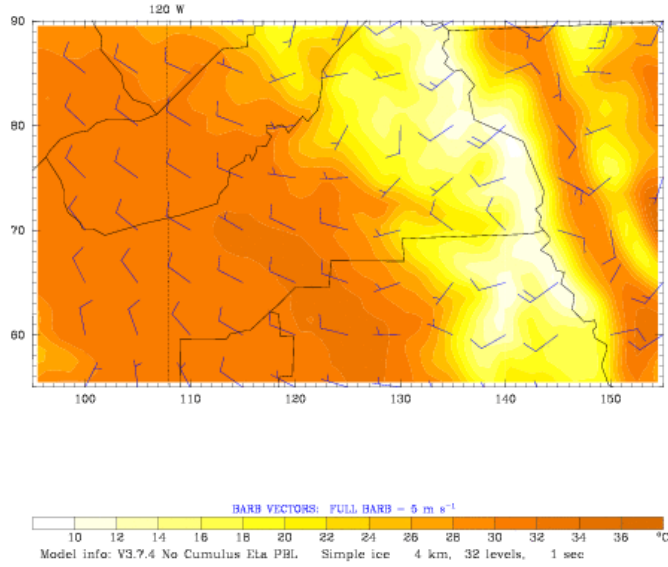


Figure C1-7. Base Case Meteorology Episode 2000 SF-SAC Domain

Dataset: case00 RIP: ripexecute.FRESNO Init: 0000 UTC Thu 27 Jul 00  
 Fcst: 24.00 h Valid: 0000 UTC Fri 28 Jul 00 (1700 PDT Thu 27 Jul 00)  
 Temperature at k-index = 32  
 Horizontal wind vectors at k-index = 32



**Figure C2-1. Base Case Meteorology Episode 2000 – Fresno-Visalia Domain**

Dataset: case00 RIP: ripexecute.FRESNO Init: 0000 UTC Thu 27 Jul 00  
 Fcst: 46.00 h Valid: 2200 UTC Fri 28 Jul 00 (1500 PDT Fri 28 Jul 00)  
 Temperature at k-index = 32  
 Horizontal wind vectors at k-index = 32

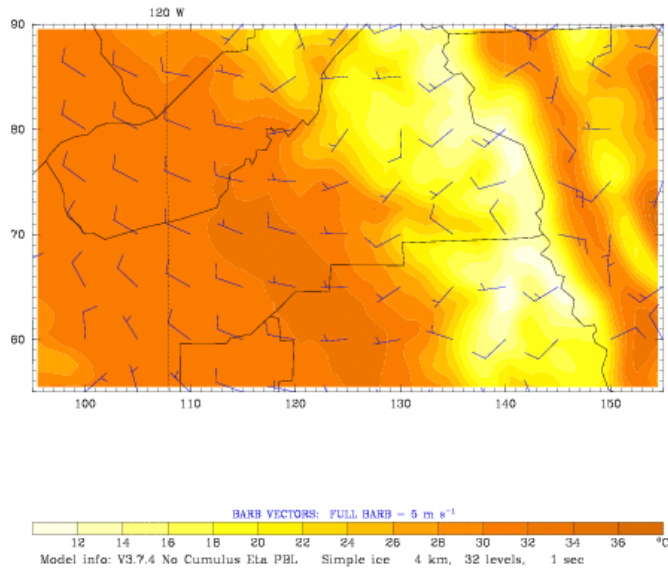


**Figure C2-2. Base Case Meteorology Episode 2000 – Fresno-Visalia Domain**

Dataset: case00 RIP: ripexecute.FRESNO Init: 0000 UTC Thu 27 Jul 00  
 Fcst: 72.00 h Valid: 0000 UTC Sun 30 Jul 00 (1700 PDT Sat 29 Jul 00)  
 Temperature at k-index = 32  
 Horizontal wind vectors at k-index = 32

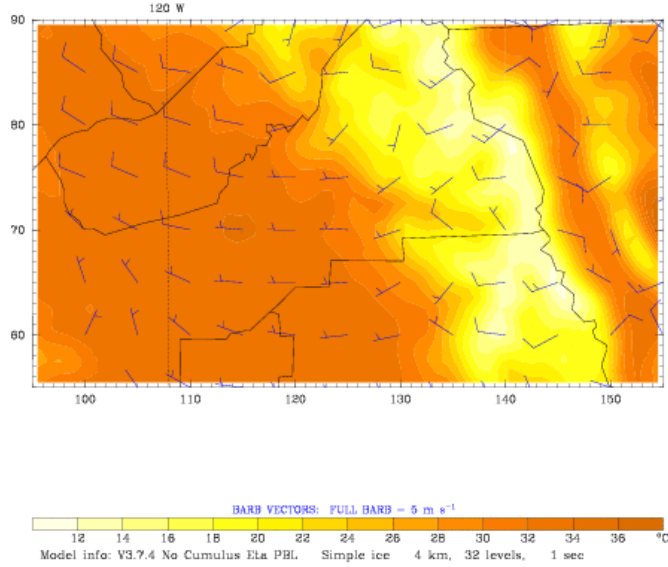


**Figure C2-3. Base Case Meteorology Episode 2000 – Fresno-Visalia Domain**

Dataset: case00 RIP: ripexecute.FRESNO Init: 0000 UTC Thu 27 Jul 00  
 Fcst: 94.00 h Valid: 2200 UTC Sun 30 Jul 00 (1500 PDT Sun 30 Jul 00)  
 Temperature at k-index = 32  
 Horizontal wind vectors at k-index = 32

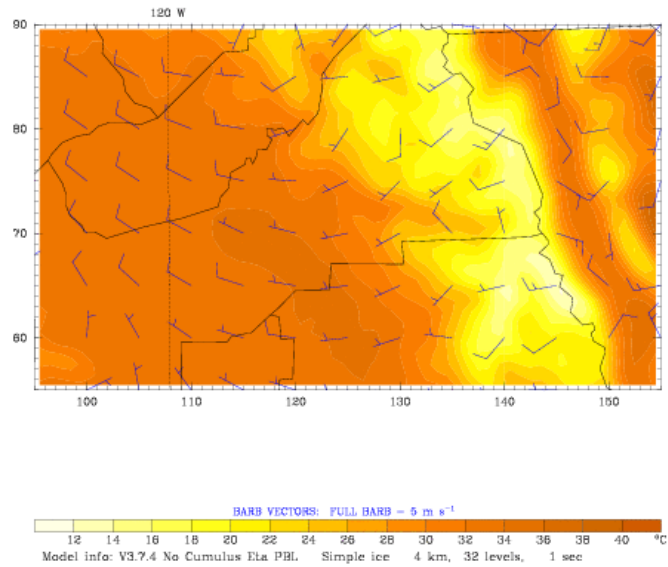


**Figure C2-4. Base Case Meteorology Episode 2000 – Fresno-Visalia Domain**

Dataset: case00 RIP: ripexecute.FRESNO Init: 0000 UTC Thu 27 Jul 00  
 Fcst: 120.00 h Valid: 0000 UTC Tue 01 Aug 00 (1700 PDT Mon 31 Jul 00)  
 Temperature at k-index = 32  
 Horizontal wind vectors at k-index = 32

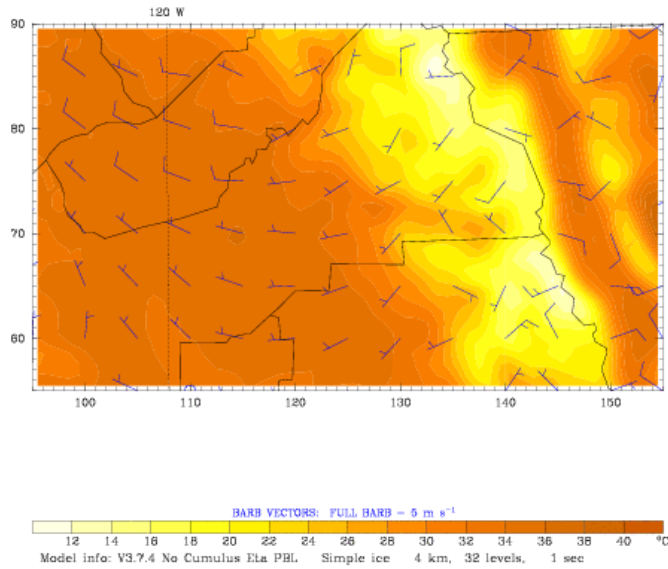


**Figure C2-5. Base Case Meteorology Episode 2000 – Fresno-Visalia Domain**

Dataset: case00 RIP: ripexecute.FRESNO Init: 0000 UTC Thu 27 Jul 00  
 Fcst: 140.00 h Valid: 2000 UTC Tue 01 Aug 00 (1300 PDT Tue 01 Aug 00)  
 Temperature at k-index = 32  
 Horizontal wind vectors at k-index = 32

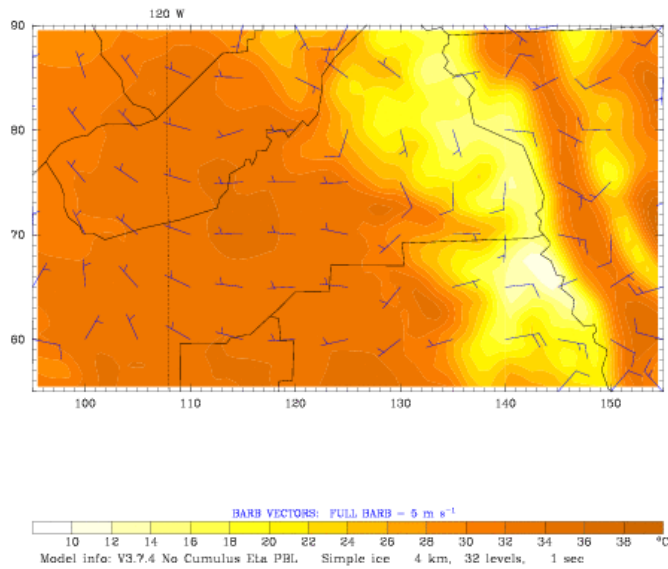


**Figure C2-6. Base Case Meteorology Episode 2000 – Fresno-Visalia Domain**

Dataset: case00 RIP: ripexecute.FRESNO Init: 0000 UTC Thu 27 Jul 00  
Fest: 166.00 h Valid: 2200 UTC Wed 02 Aug 00 (1500 PDT Wed 02 Aug 00)  
Temperature at k-index = 32  
Horizontal wind vectors at k-index = 32

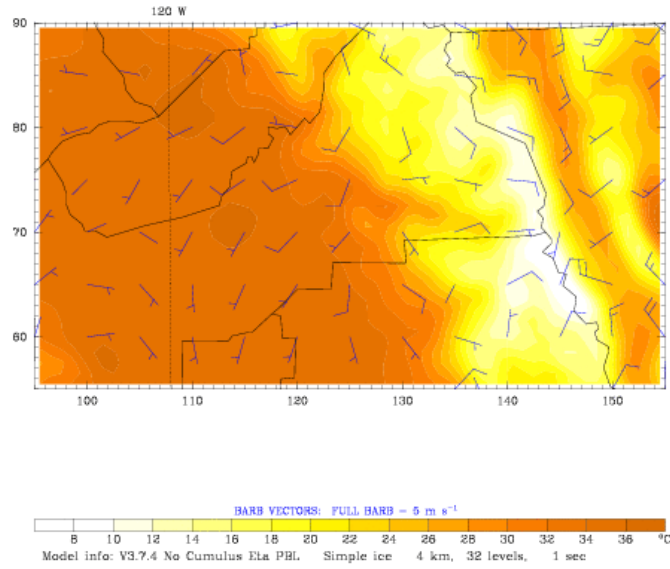


**Figure C2-7. Base Case Meteorology Episode 2000 – Fresno-Visalia Domain**

Dataset: case20 RIP: ripexecute.diff.SF SAC Init: 0000 UTC Thu 27 Jul 00  
 Fcst: 20.00 h Valid: 2000 UTC Thu 27 Jul 00 (1300 PDT Thu 27 Jul 00)  
 Temperature at k-index = 32  
 (diff. from case=case00, time= 20.00)  
 Horizontal wind vectors at k-index = 32

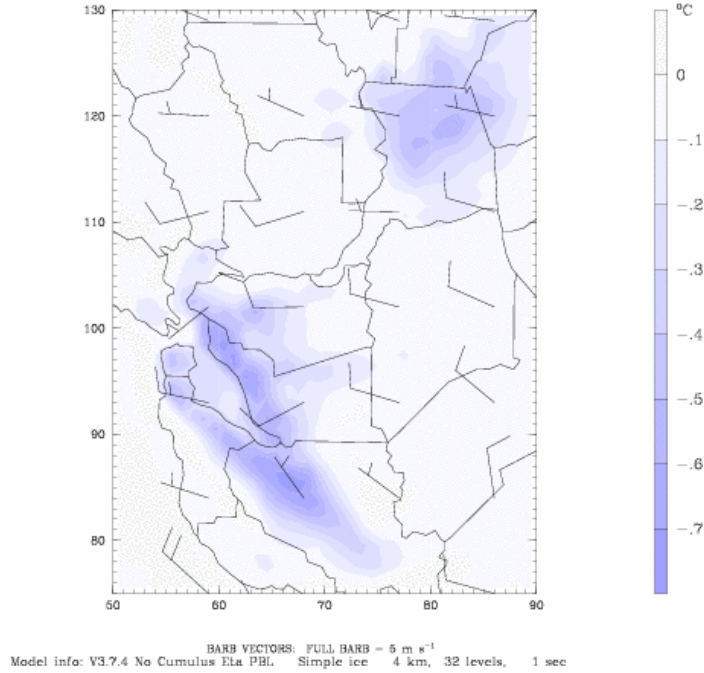


**Figure C3-1. High-albedo Case Minus Base Case; 2000 Episode for SF-SAC Domain**

Dataset: case20 RIP: ripexecute.diff.SF SAC Init: 0000 UTC Thu 27 Jul 00  
 Fcst: 42.00 h Valid: 1800 UTC Fri 28 Jul 00 (1100 PDT Fri 28 Jul 00)  
 Temperature at k-index = 32  
 (diff. from case=case00, time= 42.00)  
 Horizontal wind vectors at k-index = 32

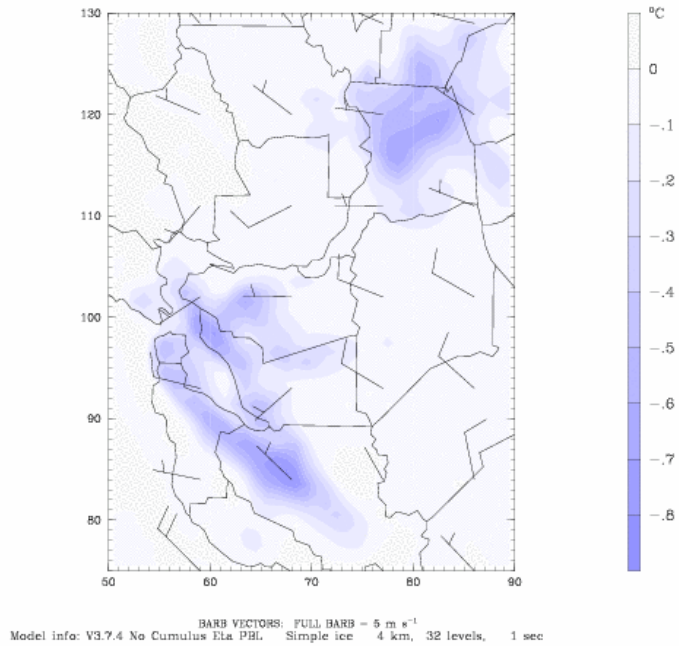


**Figure C3-2. High-albedo Case Minus Base Case; 2000 Episode for SF-SAC Domain**

Dataset: case20 RIP: ripexecute.diff.SF SAC Init: 0000 UTC Thu 27 Jul 00  
 Fcst: 66.00 h Valid: 1800 UTC Sat 29 Jul 00 (1100 PDT Sat 29 Jul 00)  
 Temperature at k-index = 32  
 (diff. from case=case00, time= 66.00)  
 Horizontal wind vectors at k-index = 32

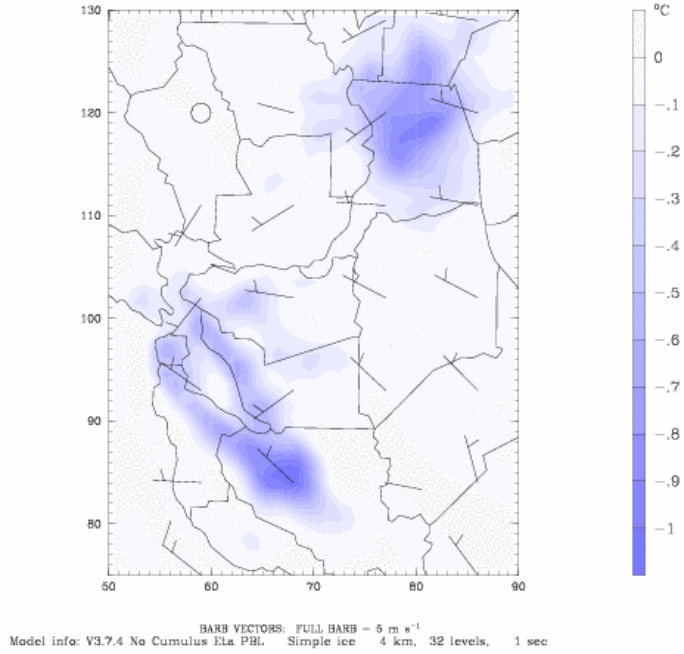


**Figure C3-3. High-albedo Case Minus Base Case; 2000 Episode for SF-SAC Domain**

Dataset: case20 RIP: ripexecute.diff.SF SAC Init: 0000 UTC Thu 27 Jul 00  
 Fcst: 90.00 h Valid: 1800 UTC Sun 30 Jul 00 (1100 PDT Sun 30 Jul 00)  
 Temperature at k-index = 32  
 (diff. from case=case00, time= 90.00)  
 Horizontal wind vectors at k-index = 32

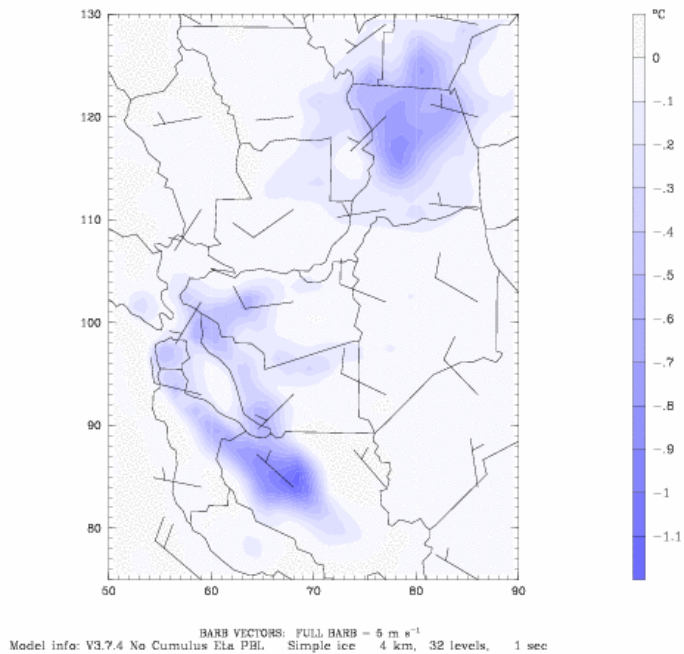
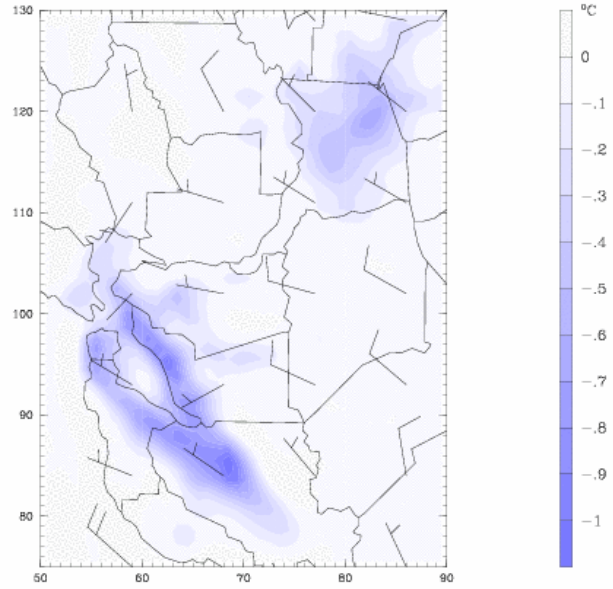


**Figure C3-4. High-albedo Case Minus Base Case; 2000 Episode for SF-SAC Domain**

Dataset: case20 RIP: ripexecute.diff.SF SAC Init: 0000 UTC Thu 27 Jul 00  
Fest: 114.00 h Valid: 1800 UTC Mon 31 Jul 00 (1100 PDT Mon 31 Jul 00)  
Temperature at k-index = 32  
(diff. from case=case00, time=114.00)  
Horizontal wind vectors at k-index = 32



BARB VECTORS: FULL BARB = 5 m s<sup>-1</sup>  
Model info: V3.7.4 No Cumulus Eta PBL Simple ice 4 km, 32 levels, 1 sec

**Figure C3-5. High-albedo Case Minus Base Case; 2000 Episode for SF-SAC Domain**

Dataset: case20 RIP: ripexecute.diff.FRESNO Init: 0000 UTC Thu 27 Jul 00  
 Fcst: 18.00 h Valid: 1800 UTC Thu 27 Jul 00 (1100 PDT Thu 27 Jul 00)  
 Temperature at k-index = 32  
 (diff. from case=case00, time= 18.00)  
 Horizontal wind vectors at k-index = 32

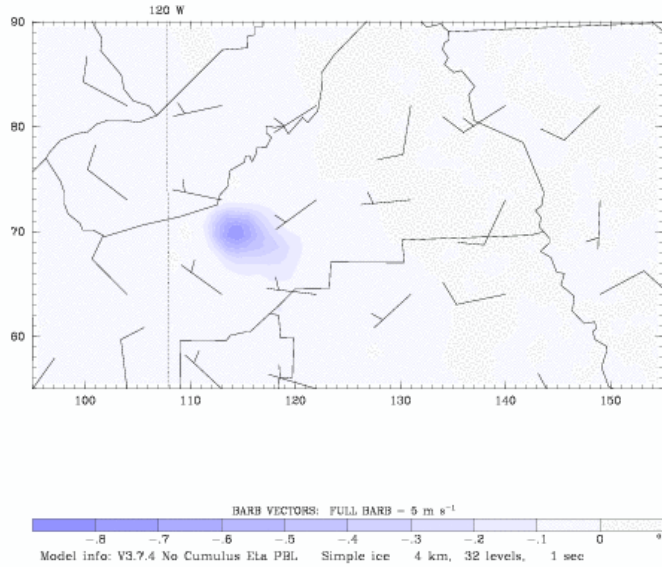


**Figure C4-1. High-albedo Case Minus Base Case; 2000 Episode for Fresno-Visalia Domain**

Dataset: case20 RIP: ripexecute.diff.FRESNO Init: 0000 UTC Thu 27 Jul 00  
 Fcst: 42.00 h Valid: 1800 UTC Fri 28 Jul 00 (1100 PDT Fri 28 Jul 00)  
 Temperature at k-index = 32  
 (diff. from case=case00, time= 42.00)  
 Horizontal wind vectors at k-index = 32

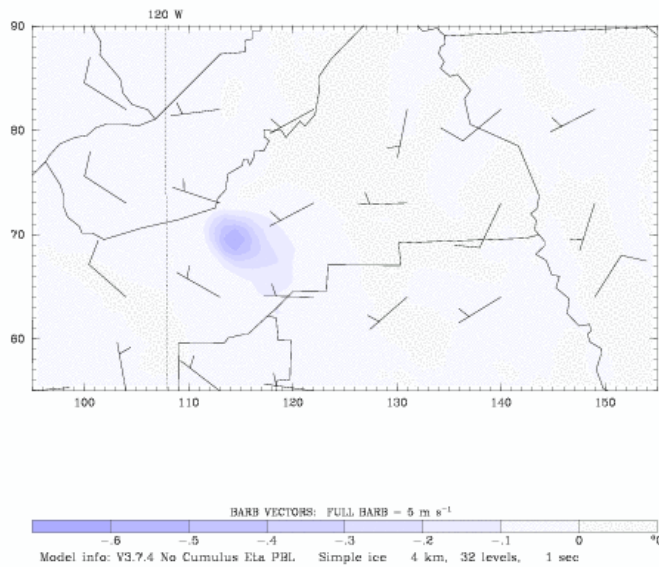


**Figure C4-2. High-albedo Case Minus Base Case; 2000 Episode for Fresno-Visalia Domain**

Dataset: case20 RIP: ripexecute.diff.FRESNO Init: 0000 UTC Thu 27 Jul 00  
 Fcst: 66.00 h Valid: 1800 UTC Sat 29 Jul 00 (1100 PDT Sat 29 Jul 00)  
 Temperature at k-index = 32  
 (diff. from case=case00, time= 66.00)  
 Horizontal wind vectors at k-index = 32

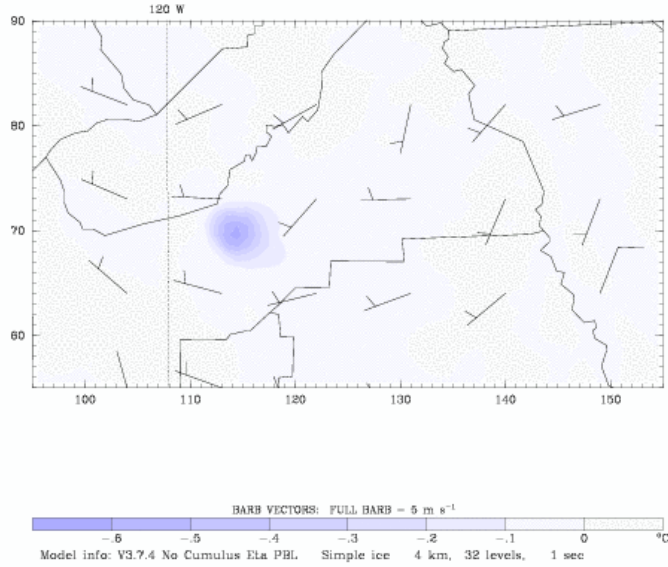


**Figure C4-3. High-albedo Case Minus Base Case; 2000 Episode for Fresno-Visalia Domain**

Dataset: case20 RIP: ripexecute.diff.FRESNO Init: 0000 UTC Thu 27 Jul 00  
 Fcst: 90.00 h Valid: 1800 UTC Sun 30 Jul 00 (1100 PDT Sun 30 Jul 00)  
 Temperature at k-index = 32  
 (diff. from case=case00, time= 90.00)  
 Horizontal wind vectors at k-index = 32

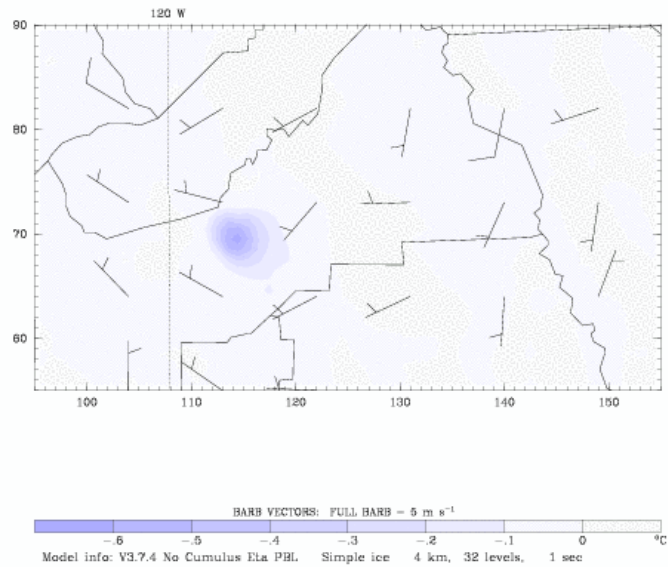


**Figure C4-4. High-albedo Case Minus Base Case; 2000 Episode for Fresno-Visalia Domain**

Dataset: case20 RIP: ripexecute.diff.FRESNO Init: 0000 UTC Thu 27 Jul 00  
Fest: 114.00 h Valid: 1800 UTC Mon 31 Jul 00 (1100 PDT Mon 31 Jul 00)  
Temperature at k-index = 32  
(diff. from case=case00, time=114.00)  
Horizontal wind vectors at k-index = 32

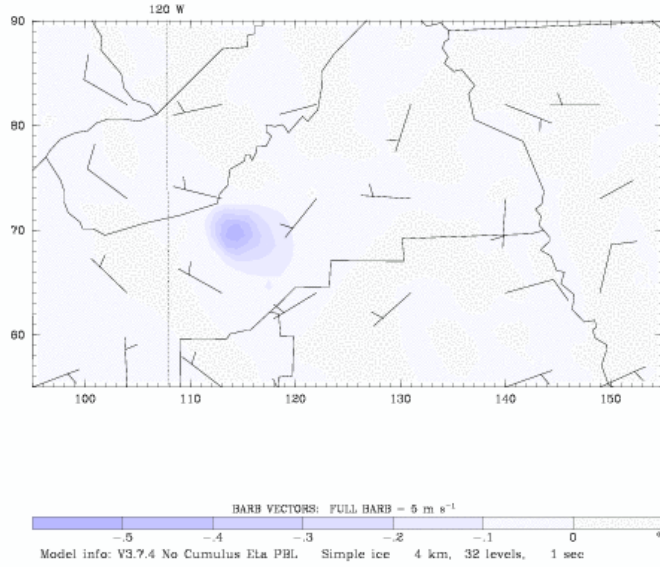


**Figure C4-5. High-albedo Case Minus Base Case; 2000 Episode for Fresno-Visalia Domain**

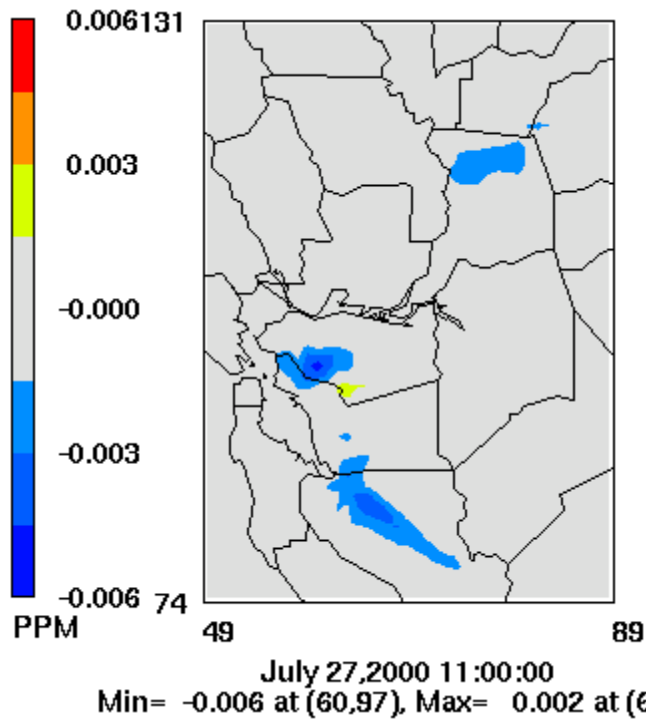


Figure C5-1. High-albedo Case Minus Base Case; 2000 Episode, 2000 Emissions SF-SAC; Hour with Largest Reduction in Ozone

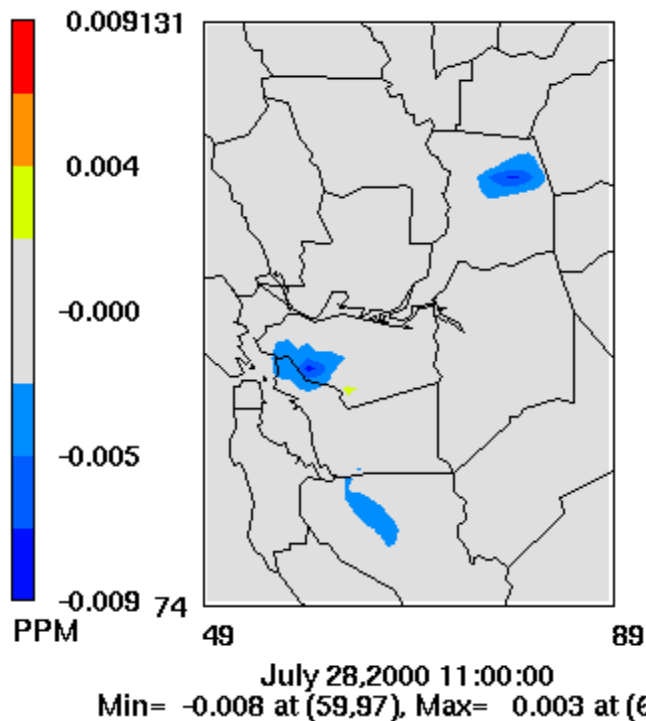


Figure C5-2. High-albedo Case Minus Base Case; 2000 Episode, 2000 Emissions SF-SAC; Hour with Largest Reduction in Ozone

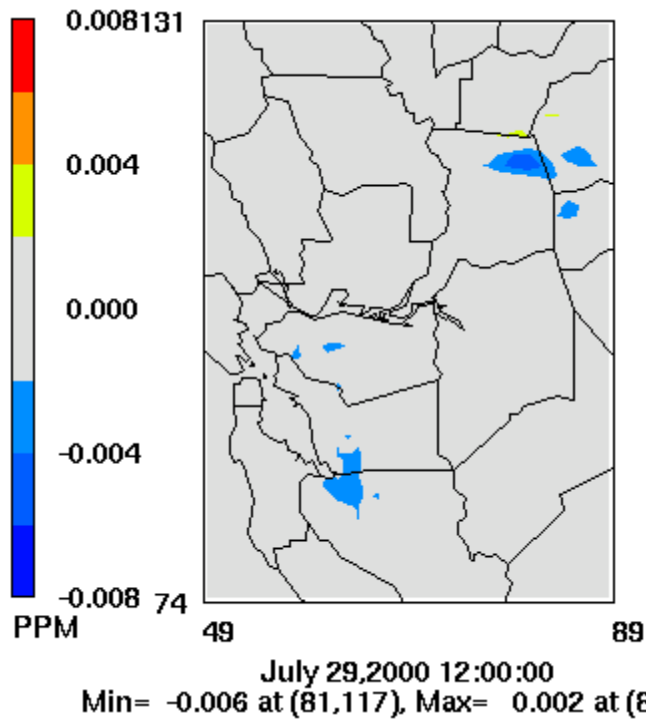


Figure C5-3. High-albedo Case Minus Base Case; 2000 Episode, 2000 Emissions SF-SAC; Hour with Largest Reduction in Ozone

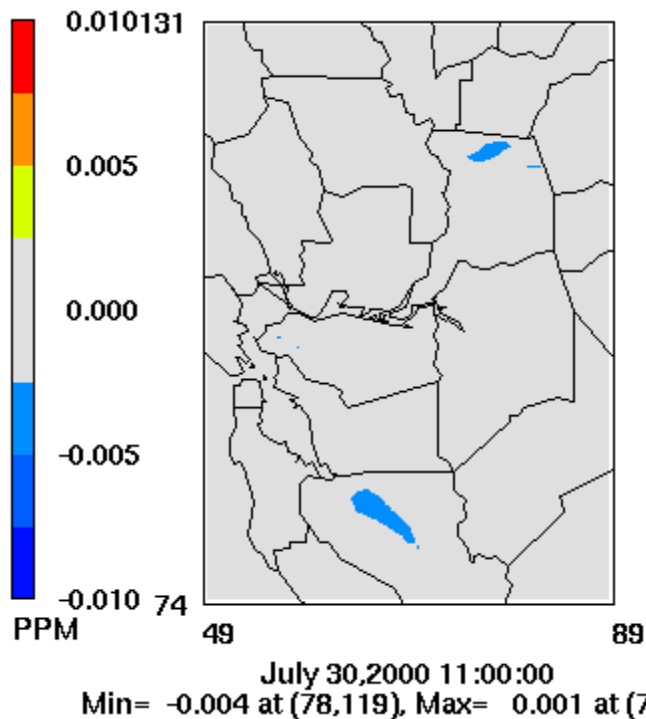
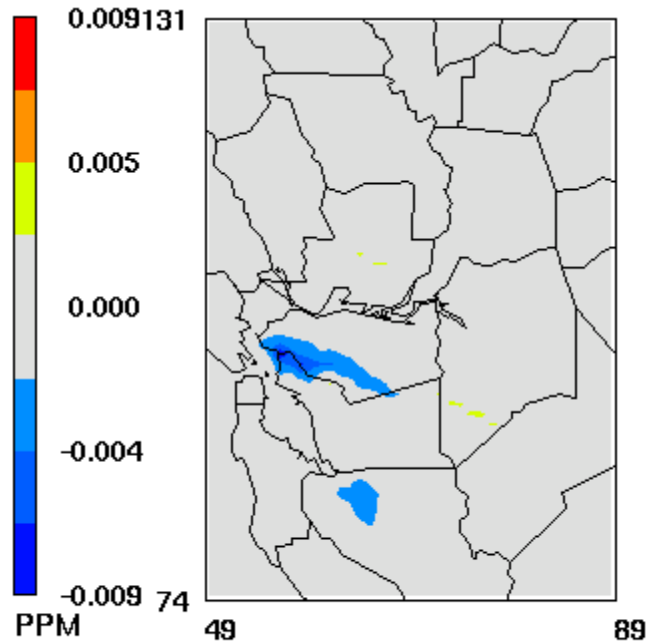


Figure C5-4. High-albedo Case Minus Base Case; 2000 Episode, 2000 Emissions SF-SAC; Hour with Largest Reduction in Ozone



July 31, 2000 14:00:00  
Min= -0.009 at (56,98), Max= 0.003 at (76,92)

Figure C5-5. High-albedo Case Minus Base Case; 2000 Episode, 2000 Emissions SF-SAC; Hour with Largest Reduction in Ozone

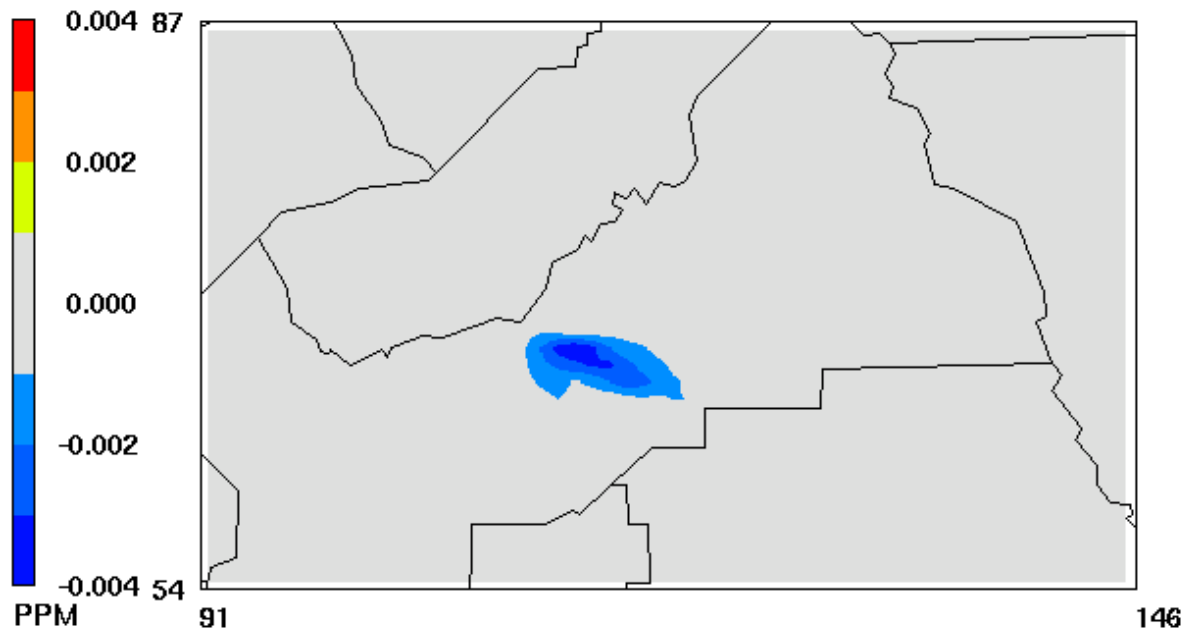


Figure C6-1. High-albedo Case Minus Base Case; 2000 Episode, 2000 Emissions Fresno; Hour with Largest Reduction in Ozone

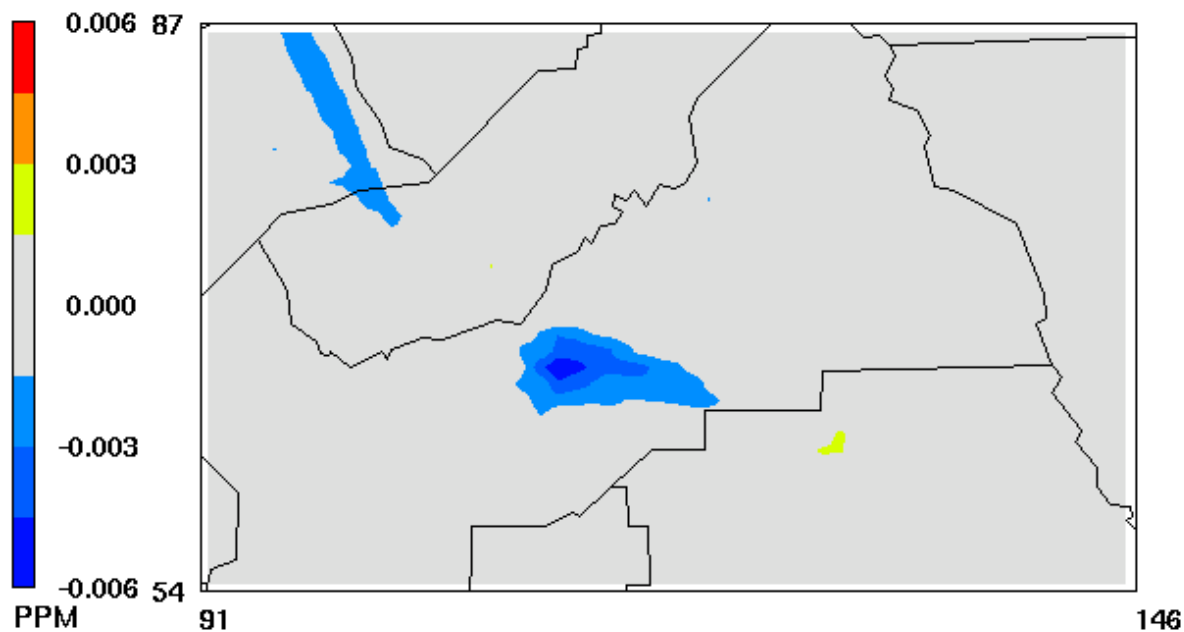
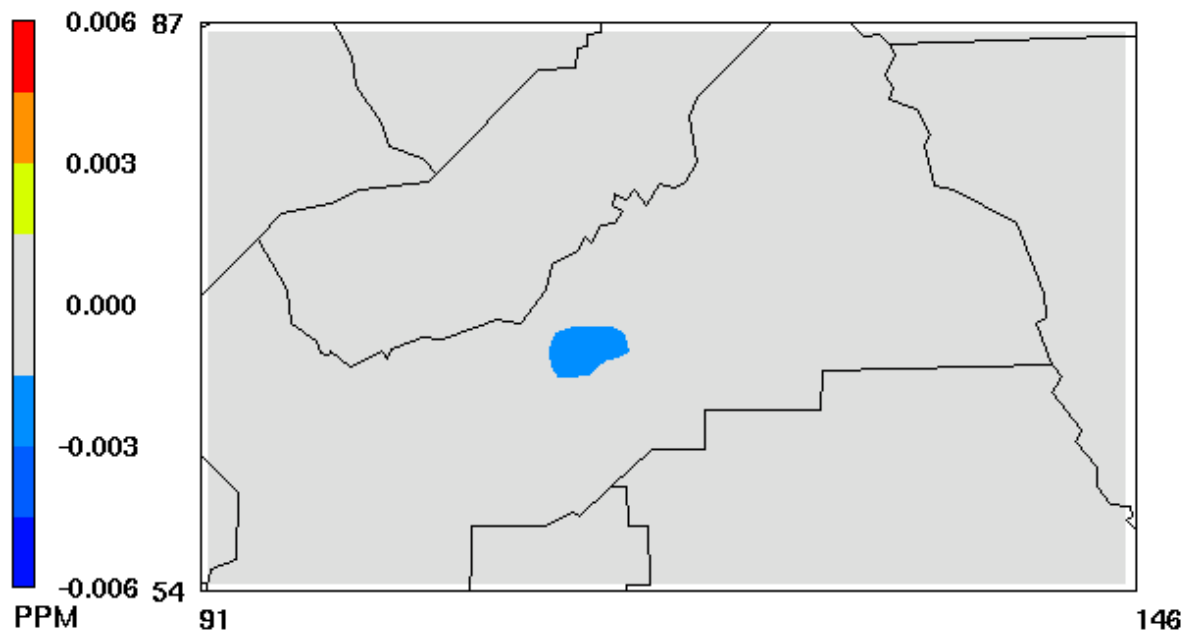
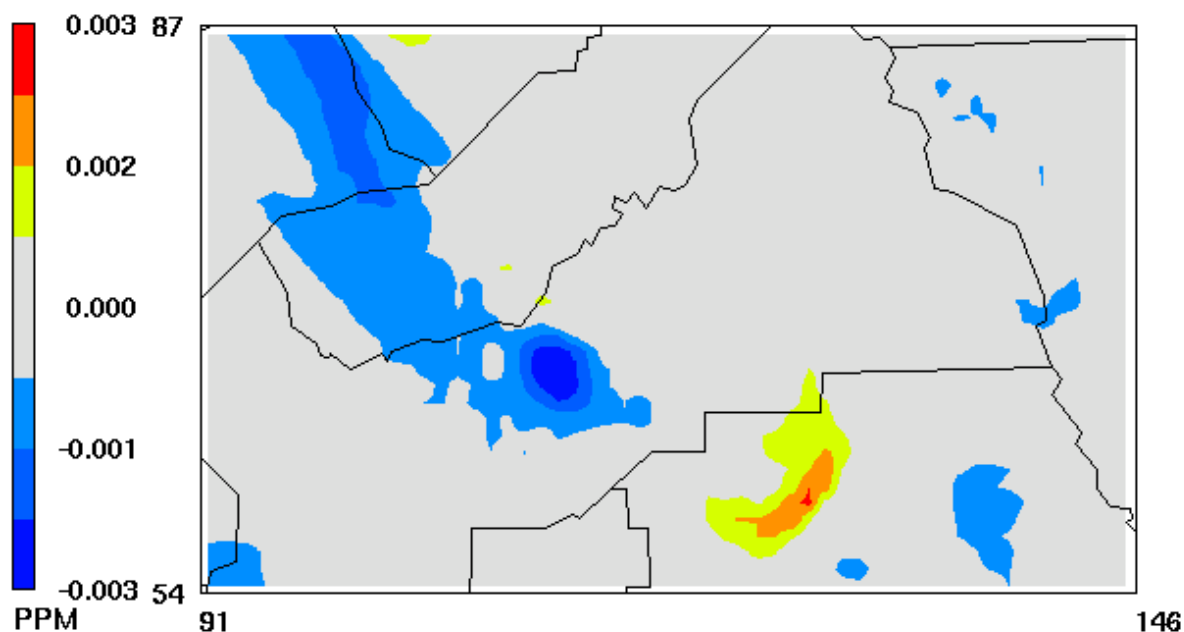


Figure C6-2. High-albedo Case Minus Base Case; 2000 Episode, 2000 Emissions Fresno; Hour with Largest Reduction in Ozone



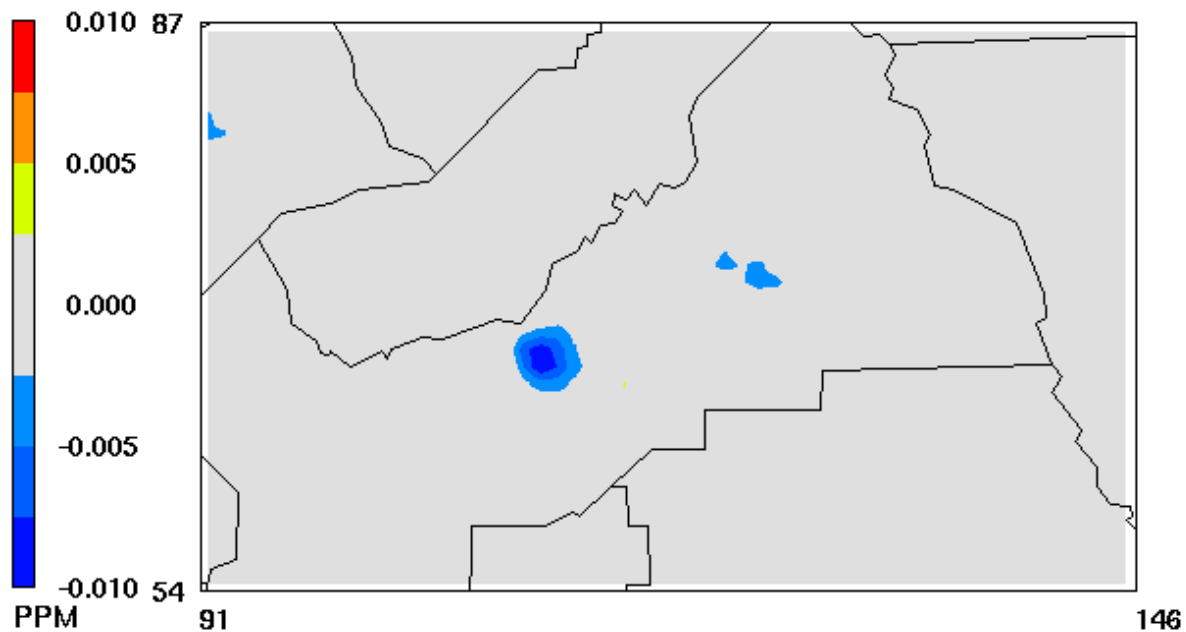
July 29,2000 10:00:00  
Min= -0.003 at (113,68), Max= 0.001 at (116,64)

Figure C6-3. High-albedo Case Minus Base Case; 2000 Episode, 2000 Emissions Fresno; Hour with Largest Reduction in Ozone



July 30,2000 18:00:00  
Min= -0.003 at (112,67), Max= 0.003 at (127,59)

Figure C6-4. High-albedo Case Minus Base Case; 2000 Episode, 2000 Emissions Fresno; Hour with Largest Reduction in Ozone



July 31, 2000 19:00:00  
Min= -0.010 at (111,67), Max= 0.003 at (116,66)

Figure C6-5. High-albedo Case Minus Base Case; 2000 Episode, 2000 Emissions Fresno; Hour with Largest Reduction in Ozone

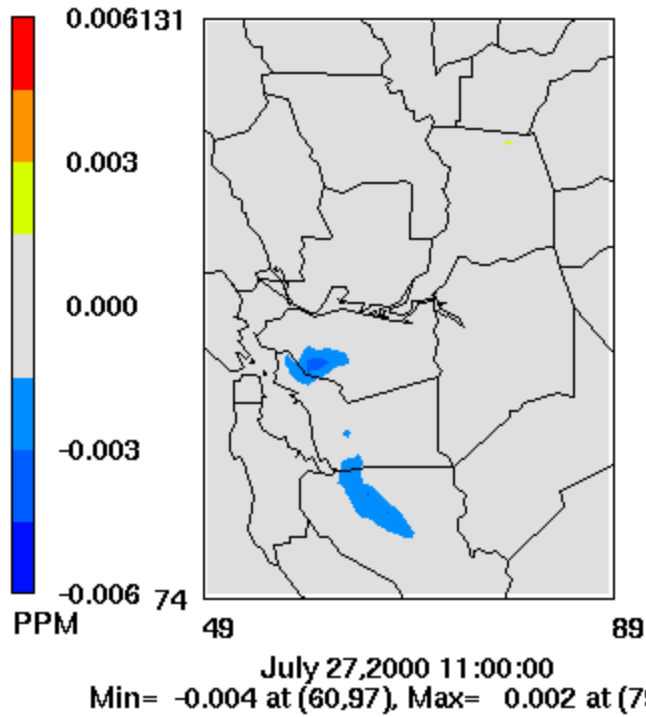


Figure C7-1. High-albedo Case Minus Base Case; 2000 Episode, 2018 Emissions SF-SAC; Hour with Largest Reduction in Ozone

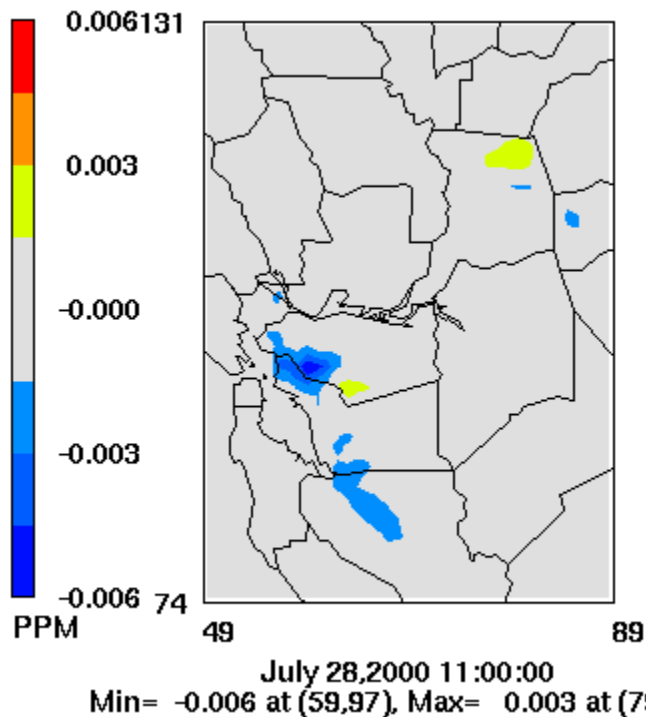


Figure C7-2. High-albedo Case Minus Base Case; 2000 Episode, 2018 Emissions SF-SAC; Hour with Largest Reduction in Ozone

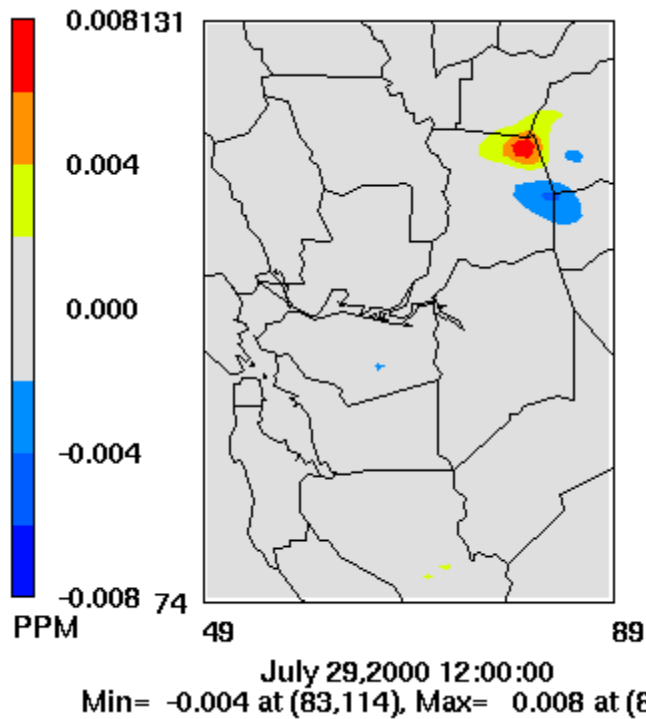


Figure C7-3. High-albedo Case Minus Base Case; 2000 Episode, 2018 Emissions SF-SAC; Hour with Largest Reduction in Ozone

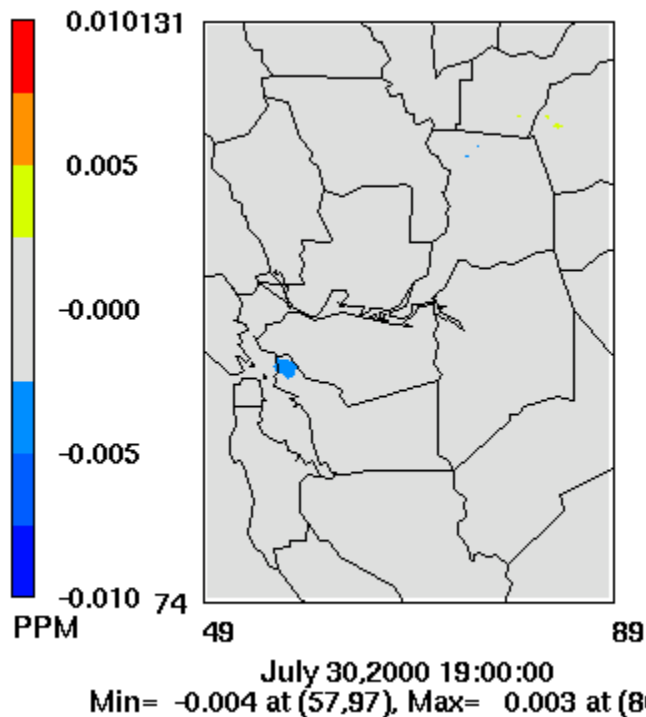
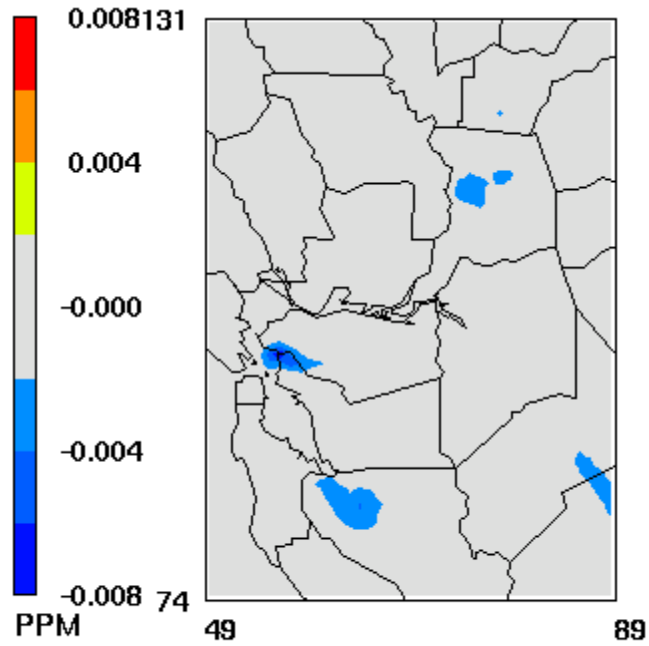
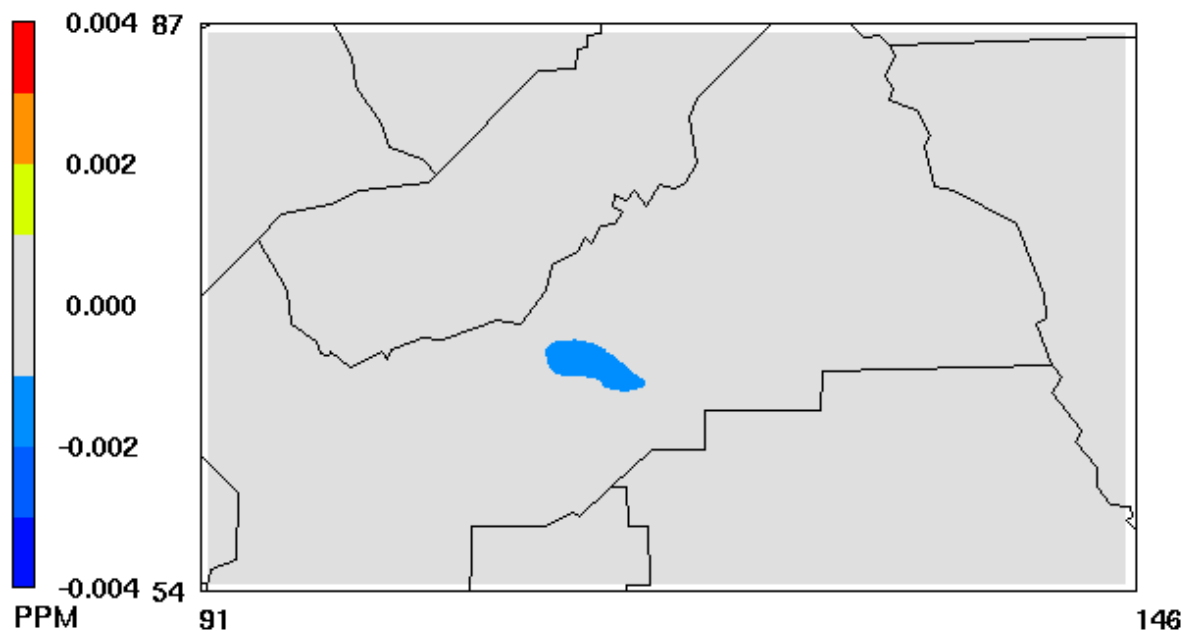


Figure C7-4. High-albedo Case Minus Base Case; 2000 Episode, 2018 Emissions SF-SAC; Hour with Largest Reduction in Ozone



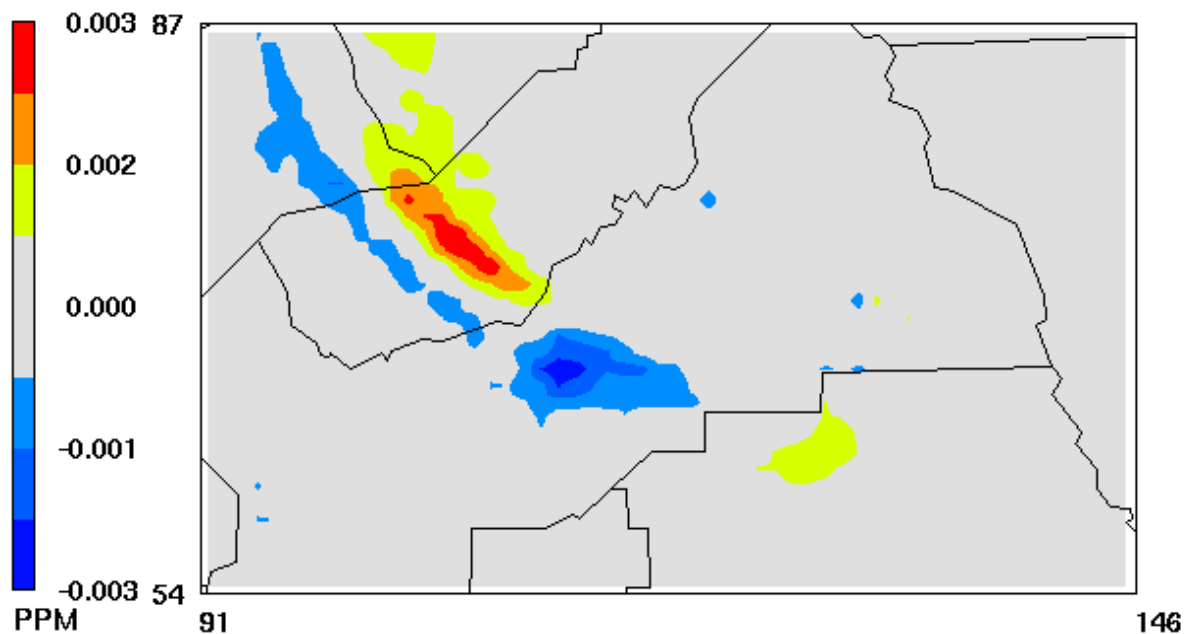
July 31, 2000 19:00:00  
Min= -0.008 at (56,98), Max= 0.002 at (81,98)

Figure C7-5. High-albedo Case Minus Base Case; 2000 Episode, 2018 Emissions SF-SAC; Hour with Largest Reduction in Ozone



July 27,2000 10:00:00  
Min= -0.002 at (113,68), Max= 0.000 at (113,61)

Figure C8-1. High-albedo Case Minus Base Case; 2000 Episode, 2018 Emissions Fresno; Hour with Largest Reduction in Ozone



July 28,2000 19:00:00  
Min= -0.003 at (112,67), Max= 0.003 at (108,73)

Figure C8-2. High-albedo Case Minus Base Case; 2000 Episode, 2018 Emissions Fresno; Hour with Largest Reduction in Ozone

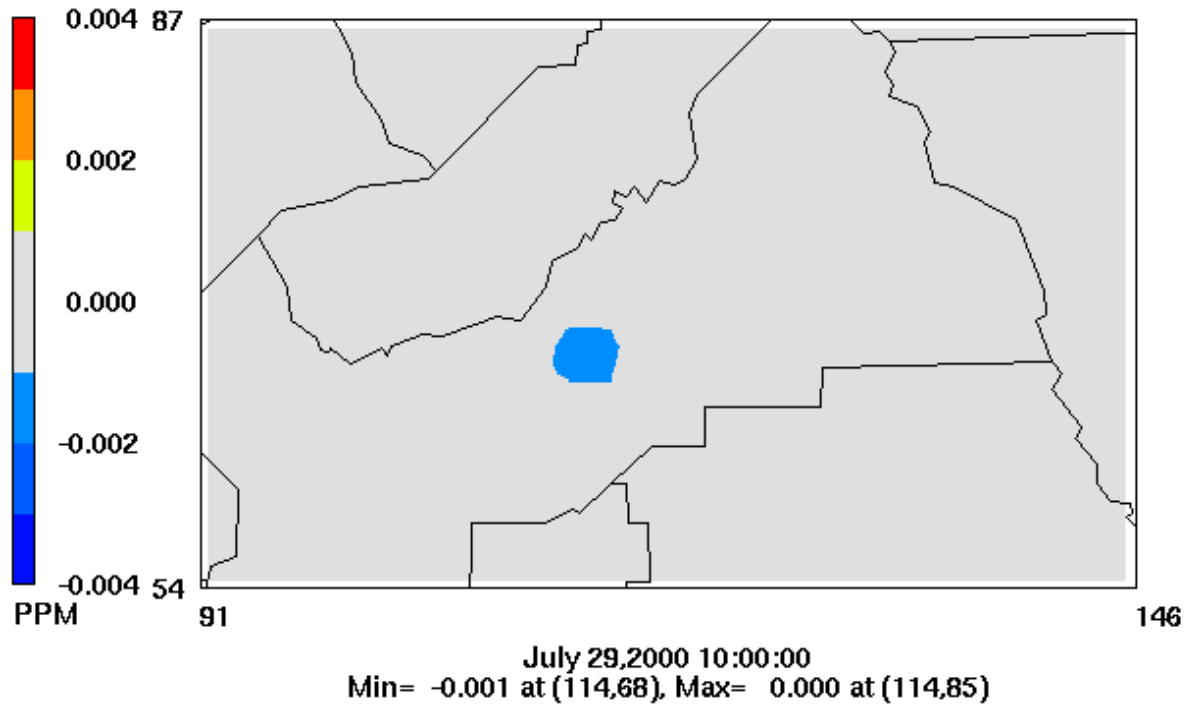


Figure C8-3. High-albedo Case Minus Base Case; 2000 Episode, 2018 Emissions Fresno; Hour with Largest Reduction in Ozone

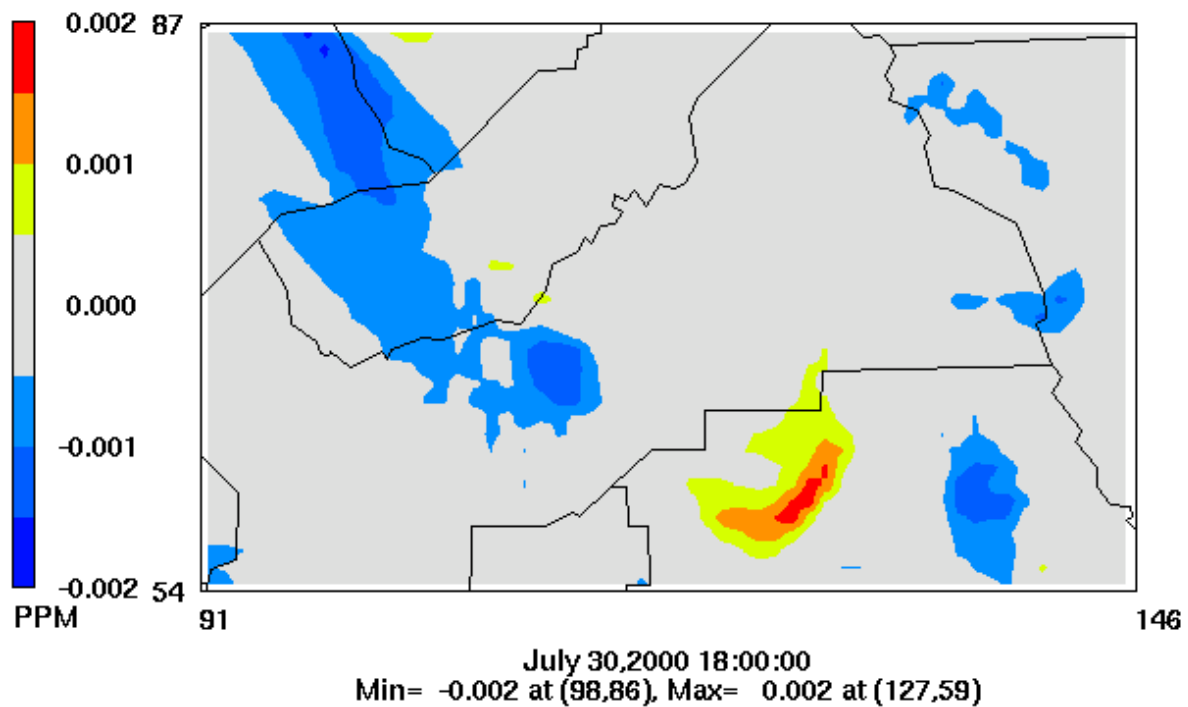


Figure C8-4. High-albedo Case Minus Base Case; 2000 Episode, 2018 Emissions Fresno; Hour with Largest Reduction in Ozone

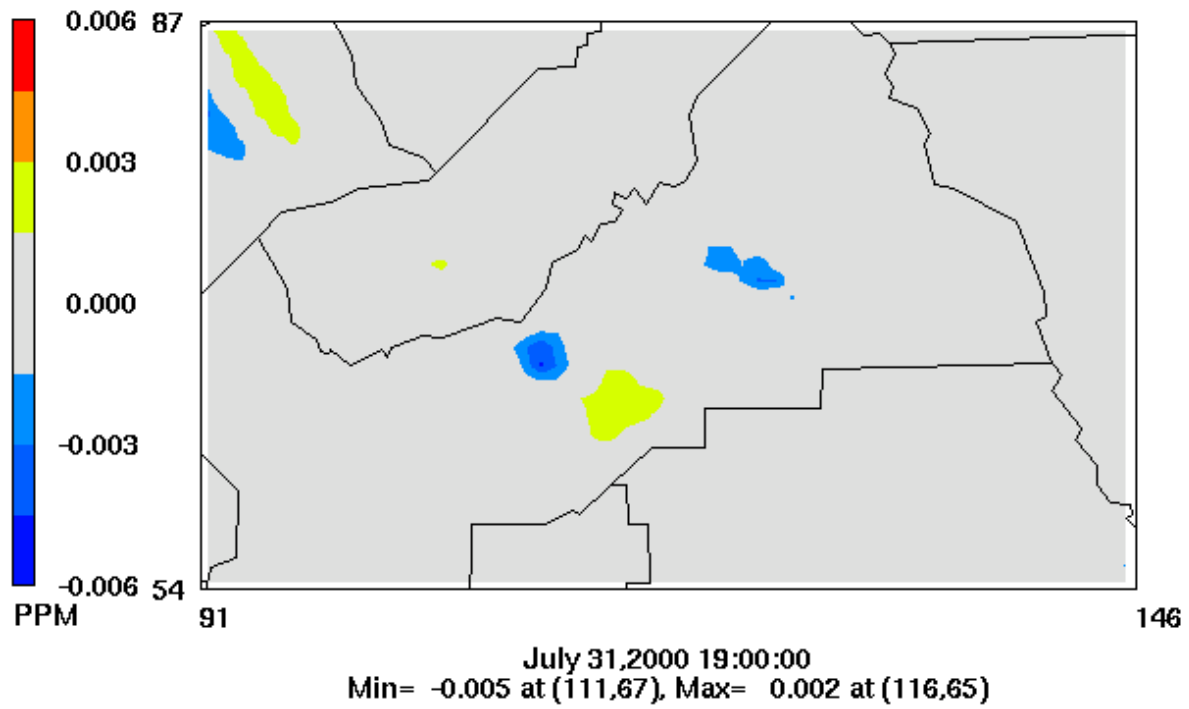
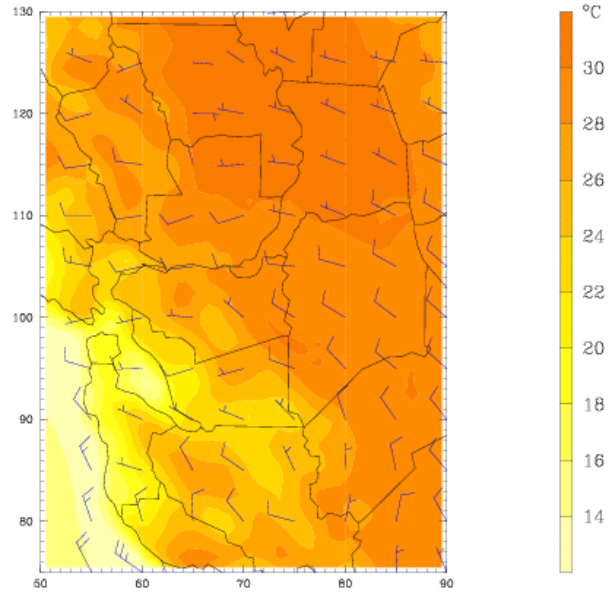


Figure C8-5. High-albedo Case Minus Base Case; 2000 Episode, 2018 Emissions Fresno; Hour with Largest Reduction in Ozone

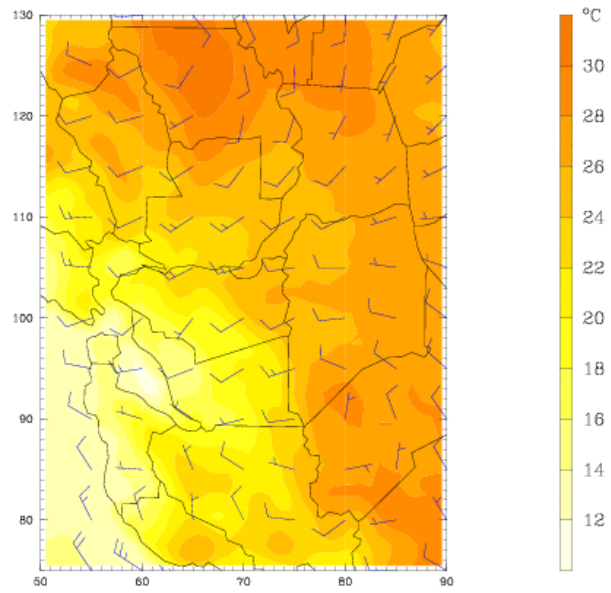
Dataset: case00 RIP: ripexecute.SF SAC Init: 1200 UTC Mon 05 Jul 99  
 Fcst: 10.00 h Valid: 2200 UTC Mon 05 Jul 99 (1500 PDT Mon 05 Jul 99)  
 Temperature at k-index = 32  
 Horizontal wind vectors at k-index = 32



BARB VECTORS: FULL BARB = 5 m s<sup>-1</sup>  
 Model info: V3.7.4 No Cumulus Eta PBL Simple ice 4 km, 32 levels, 1 sec

**Figure C9-1. Base Case Meteorology Episode 1999 SF-SAC Domain**

Dataset: case00 RIP: ripexecute.SF SAC Init: 1200 UTC Mon 05 Jul 99  
 Fcst: 34.00 h Valid: 2200 UTC Tue 06 Jul 99 (1500 PDT Tue 06 Jul 99)  
 Temperature at k-index = 32  
 Horizontal wind vectors at k-index = 32



BARB VECTORS: FULL BARB = 5 m s<sup>-1</sup>  
 Model info: V3.7.4 No Cumulus Eta PBL Simple ice 4 km, 32 levels, 1 sec

**Figure C9-2. Base Case Meteorology Episode 1999 SF-SAC Domain**

Dataset: case00 RIP: ripexecute.SF SAC Init: 1200 UTC Mon 05 Jul 99  
 Fcst: 60.00 h Valid: 0000 UTC Thu 08 Jul 99 (1700 PDT Wed 07 Jul 99)  
 Temperature at k-index = 32  
 Horizontal wind vectors at k-index = 32

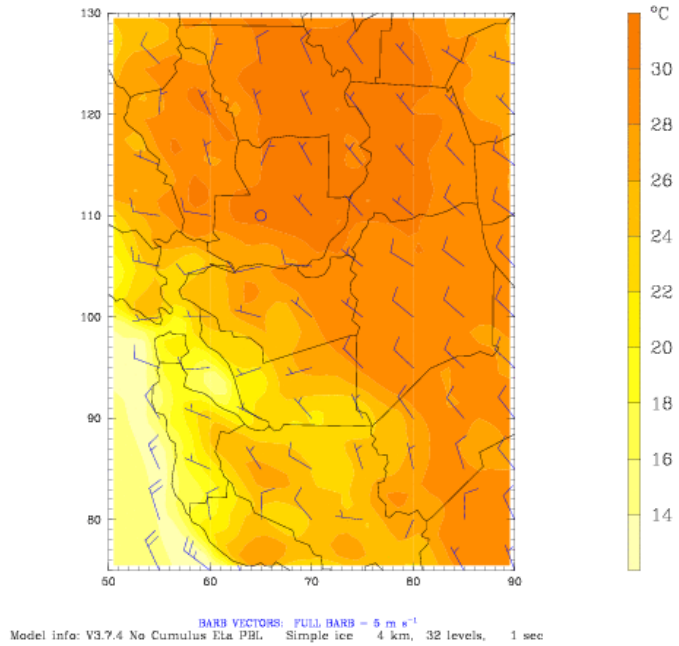


**Figure C9-3. Base Case Meteorology Episode 1999 SF-SAC Domain**

Dataset: case00 RIP: ripexecute.SF SAC Init: 1200 UTC Mon 05 Jul 99  
 Fcst: 82.00 h Valid: 2200 UTC Thu 08 Jul 99 (1500 PDT Thu 08 Jul 99)  
 Temperature at k-index = 32  
 Horizontal wind vectors at k-index = 32

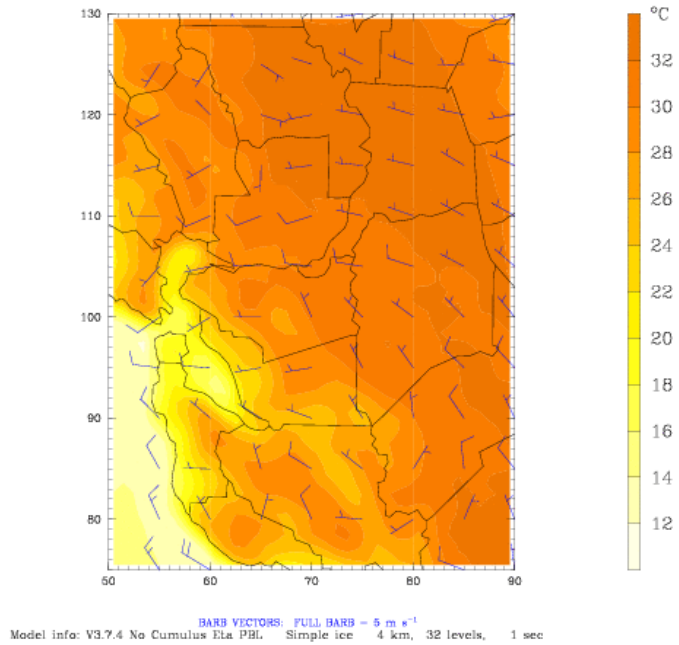
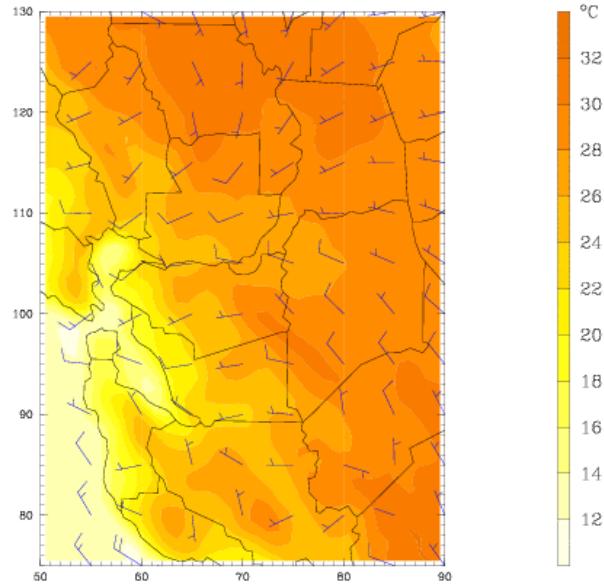


**Figure C9-4. Base Case Meteorology Episode 1999 SF-SAC Domain**

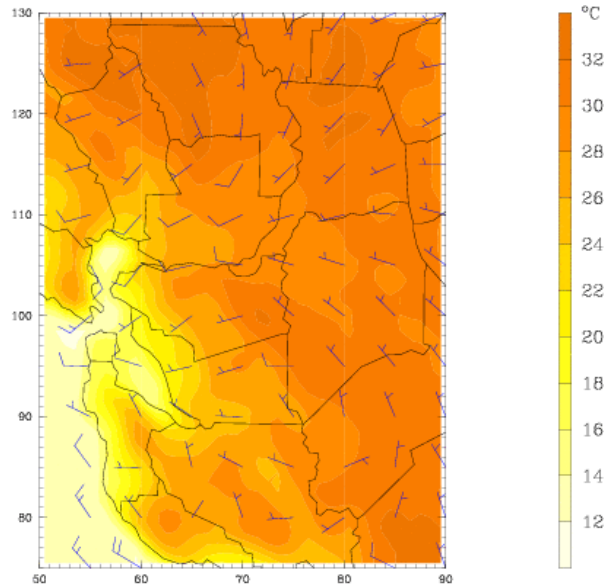
Dataset: case00 RIP: ripexecute.SF SAC Init: 1200 UTC Mon 05 Jul 99  
 Fcst: 106.00 h Valid: 2200 UTC Fri 09 Jul 99 (1500 PDT Fri 09 Jul 99)  
 Temperature at k-index = 32  
 Horizontal wind vectors at k-index = 32



Model info: V3.7.4 No Cumulus Eta PBL Simple ice 4 km, 32 levels, 1 sec  
 BARB VECTORS: FULL BARB = 5 m s<sup>-1</sup>

**Figure C9-5. Base Case Meteorology Episode 1999 SF-SAC Domain**

Dataset: case00 RIP: ripexecute.SF SAC Init: 1200 UTC Mon 05 Jul 99  
 Fcst: 130.00 h Valid: 2200 UTC Sat 10 Jul 99 (1500 PDT Sat 10 Jul 99)  
 Temperature at k-index = 32  
 Horizontal wind vectors at k-index = 32



Model info: V3.7.4 No Cumulus Eta PBL Simple ice 4 km, 32 levels, 1 sec  
 BARB VECTORS: FULL BARB = 5 m s<sup>-1</sup>

**Figure C9-6. Base Case Meteorology Episode 1999 SF-SAC Domain**

Dataset: case00 RIP: ripexecute.SF SAC Init: 1200 UTC Mon 05 Jul 99  
 Fcst: 154.00 h Valid: 2200 UTC Sun 11 Jul 99 (1500 PDT Sun 11 Jul 99)  
 Temperature at k-index = 32  
 Horizontal wind vectors at k-index = 32

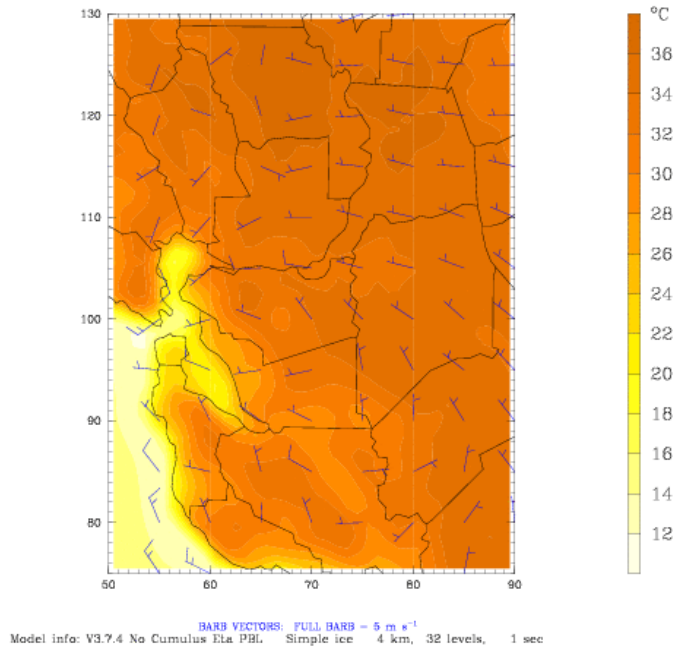


**Figure C9-7. Base Case Meteorology Episode 1999 SF-SAC Domain**

Dataset: case00 RIP: ripexecute.SF SAC Init: 1200 UTC Mon 05 Jul 99  
 Fcst: 178.00 h Valid: 2200 UTC Mon 12 Jul 99 (1500 PDT Mon 12 Jul 99)  
 Temperature at k-index = 32  
 Horizontal wind vectors at k-index = 32

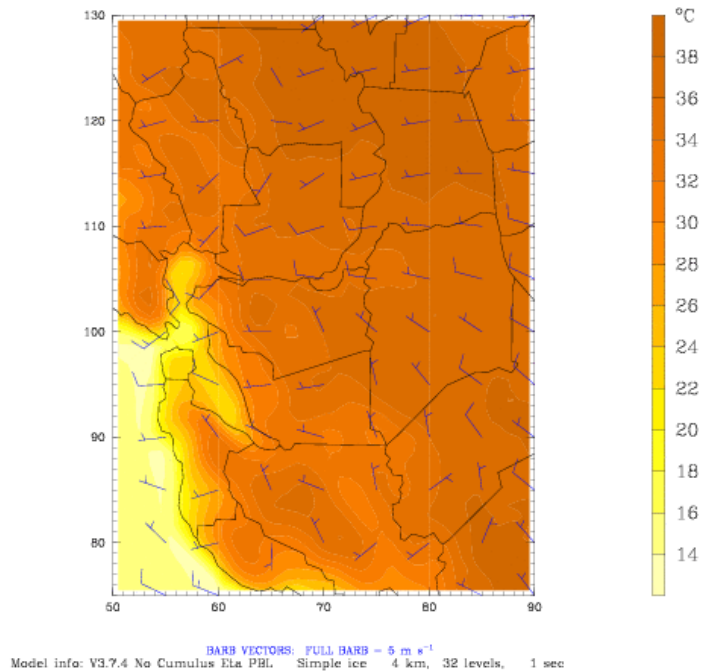
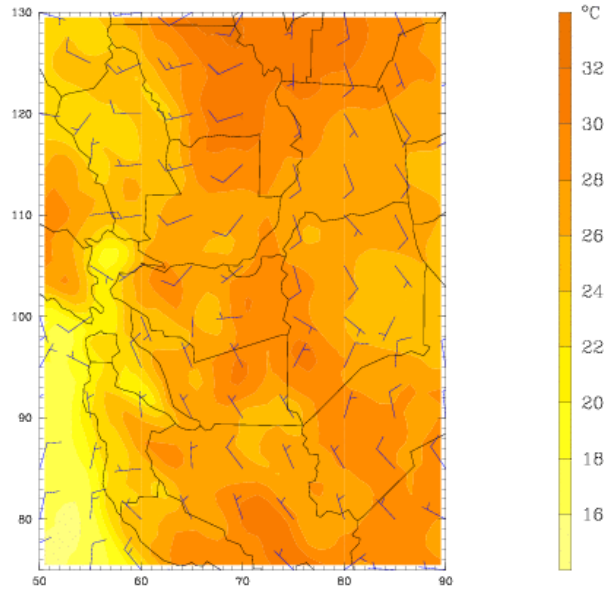


**Figure C9-8. Base Case Meteorology Episode 1999 SF-SAC Domain**

Dataset: case00 RIP: ripexecute.SF SAC Init: 1200 UTC Mon 05 Jul 99  
Fcst: 200.00 h Valid: 2000 UTC Tue 13 Jul 99 (1300 PDT Tue 13 Jul 99)  
Temperature at k-index = 32  
Horizontal wind vectors at k-index = 32



Model info: V3.7.4 No Cumulus Eta PBL Simple ice 4 km, 32 levels, 1 sec  
BARB VECTORS: FULL BARB = 5 m s<sup>-1</sup>

**Figure C9-9. Base Case Meteorology Episode 1999 SF-SAC Domain**

Dataset: case00 RIP: ripexecute.FRESNO Init: 1200 UTC Mon 05 Jul 99  
 Fcst: 14.00 h Valid: 0200 UTC Tue 06 Jul 99 (1900 PDT Mon 05 Jul 99)  
 Temperature at k-index = 32  
 Horizontal wind vectors at k-index = 32

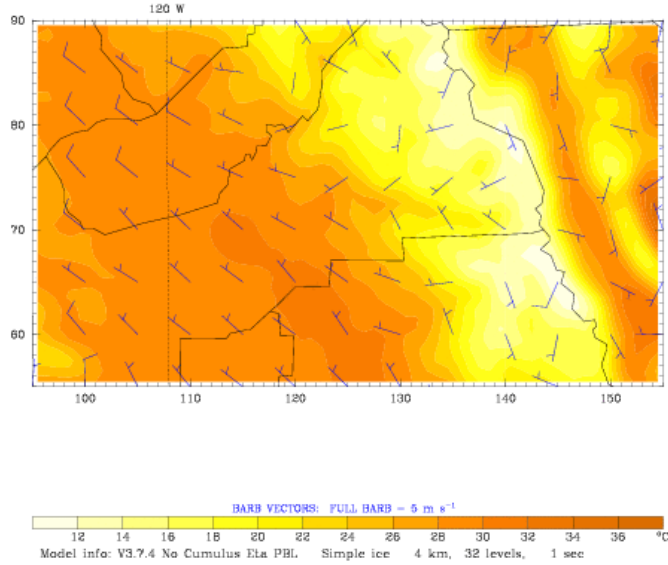


**Figure C10-1. Base Case Meteorology Episode 1999 – Fresno-Visalia Domain**

Dataset: case00 RIP: ripexecute.FRESNO Init: 1200 UTC Mon 05 Jul 99  
 Fcst: 32.00 h Valid: 2000 UTC Tue 06 Jul 99 (1300 PDT Tue 06 Jul 99)  
 Temperature at k-index = 32  
 Horizontal wind vectors at k-index = 32

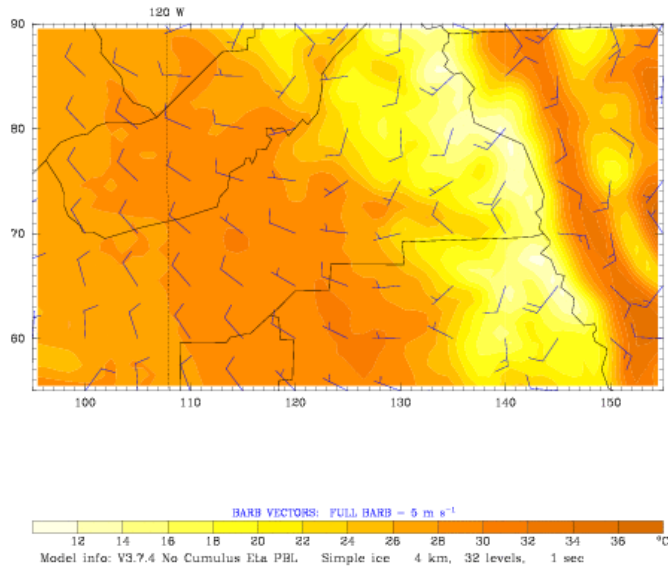


**Figure C10-2. Base Case Meteorology Episode 1999 – Fresno-Visalia Domain**

Dataset: case00 RIP: ripexecute.FRESNO Init: 1200 UTC Mon 05 Jul 99  
 Fcst: 56.00 h Valid: 2000 UTC Wed 07 Jul 99 (1300 PDT Wed 07 Jul 99)  
 Temperature at k-index = 32  
 Horizontal wind vectors at k-index = 32

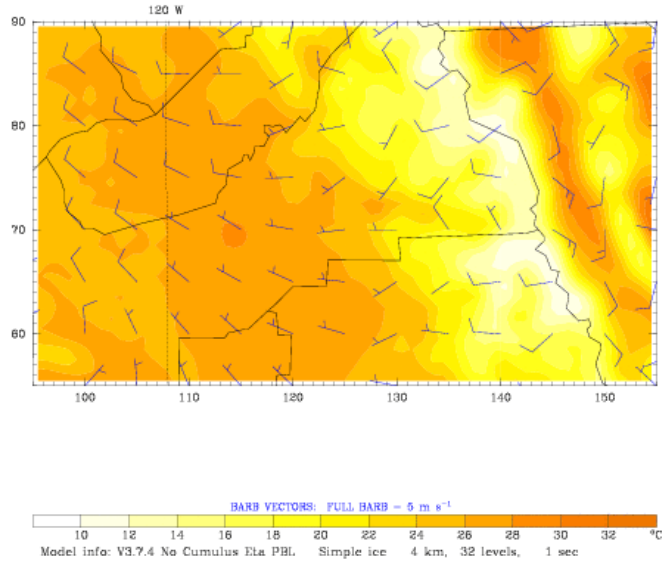


**Figure C10-3. Base Case Meteorology Episode 1999 – Fresno-Visalia Domain**

Dataset: case00 RIP: ripexecute.FRESNO Init: 1200 UTC Mon 05 Jul 99  
 Fcst: 82.00 h Valid: 2200 UTC Thu 08 Jul 99 (1500 PDT Thu 08 Jul 99)  
 Temperature at k-index = 32  
 Horizontal wind vectors at k-index = 32

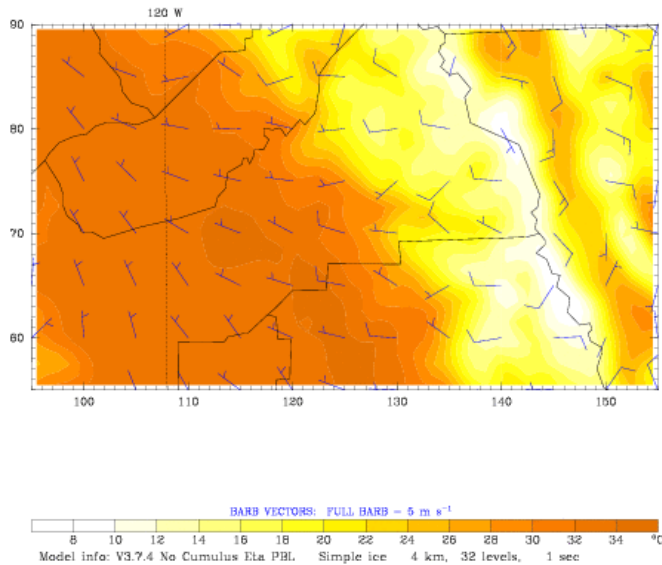


**Figure C10-4. Base Case Meteorology Episode 1999 – Fresno-Visalia Domain**

Dataset: case00 RIP: ripexecute.FRESNO Init: 1200 UTC Mon 05 Jul 99  
 Fcst: 104.00 h Valid: 2000 UTC Fri 09 Jul 99 (1300 PDT Fri 09 Jul 99)  
 Temperature at k-index = 32  
 Horizontal wind vectors at k-index = 32

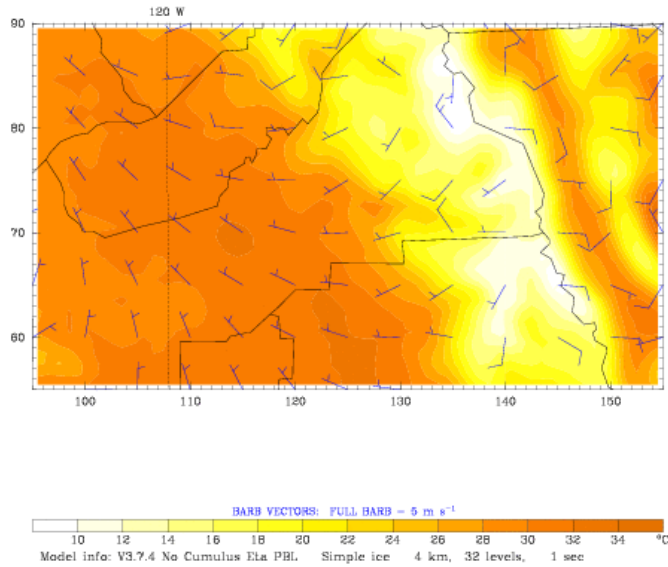


**Figure C10-5. Base Case Meteorology Episode 1999 – Fresno-Visalia Domain**

Dataset: case00 RIP: ripexecute.FRESNO Init: 1200 UTC Mon 05 Jul 99  
 Fcst: 132.00 h Valid: 0000 UTC Sun 11 Jul 99 (1700 PDT Sat 10 Jul 99)  
 Temperature at k-index = 32  
 Horizontal wind vectors at k-index = 32

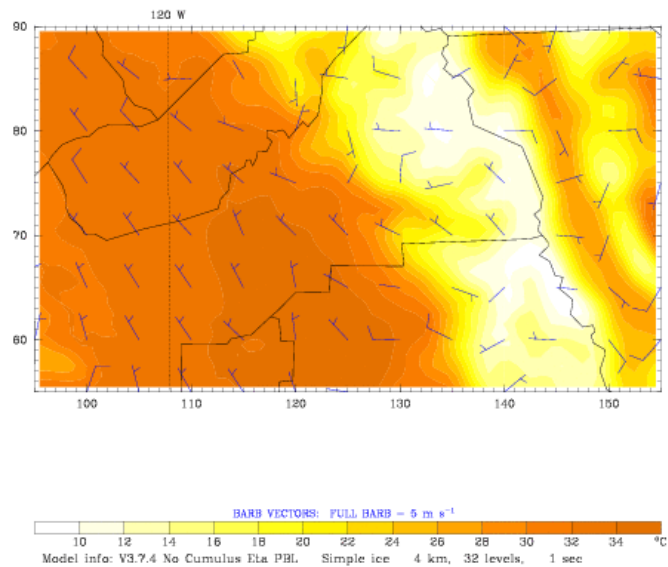


**Figure C10-6. Base Case Meteorology Episode 1999 – Fresno-Visalia Domain**

Dataset: case00 RIP: ripexecute.FRESNO Init: 1200 UTC Mon 05 Jul 99  
 Fcst: 154.00 h Valid: 2200 UTC Sun 11 Jul 99 (1500 PDT Sun 11 Jul 99)  
 Temperature at k-index = 32  
 Horizontal wind vectors at k-index = 32

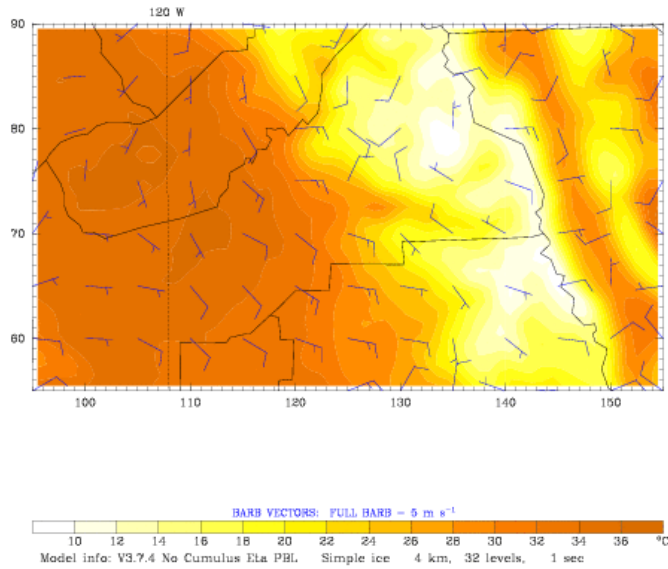


**Figure C10-7. Base Case Meteorology Episode 1999 – Fresno-Visalia Domain**

Dataset: case00 RIP: ripexecute.FRESNO Init: 1200 UTC Mon 05 Jul 99  
 Fcst: 178.00 h Valid: 2200 UTC Mon 12 Jul 99 (1500 PDT Mon 12 Jul 99)  
 Temperature at k-index = 32  
 Horizontal wind vectors at k-index = 32

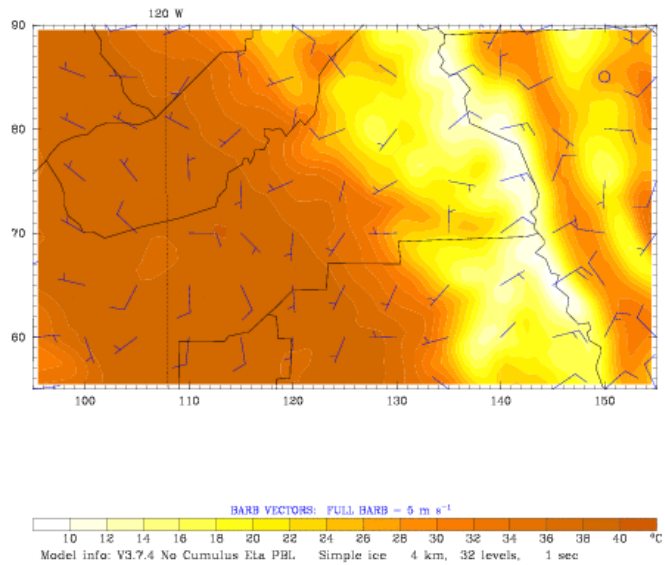


**Figure C10-8. Base Case Meteorology Episode 1999 – Fresno-Visalia Domain**

Dataset: case00 RIP: ripexecute.FRESNO Init: 1200 UTC Mon 05 Jul 99  
Fest: 204.00 h Valid: 0000 UTC Wed 14 Jul 99 (1700 PDT Tue 13 Jul 99)  
Temperature at k-index = 32  
Horizontal wind vectors at k-index = 32

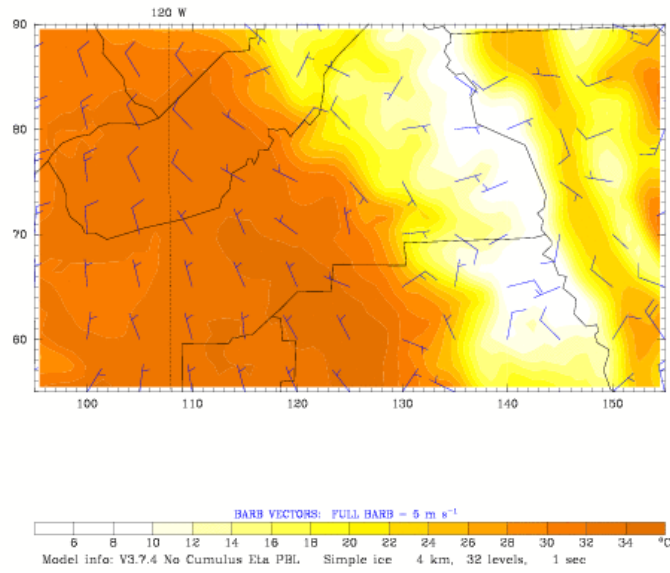


**Figure C10-9. Base Case Meteorology Episode 1999 – Fresno-Visalia Domain**

Dataset: case20 RIP: ripexecute.diff.SF SAC Init: 1200 UTC Mon 05 Jul 99  
 Fcst: 6.00 h Valid: 1800 UTC Mon 05 Jul 99 (1100 PDT Mon 05 Jul 99)  
 Temperature at k-index = 32  
 (diff. from case=case00, time= 6.00)  
 Horizontal wind vectors at k-index = 32

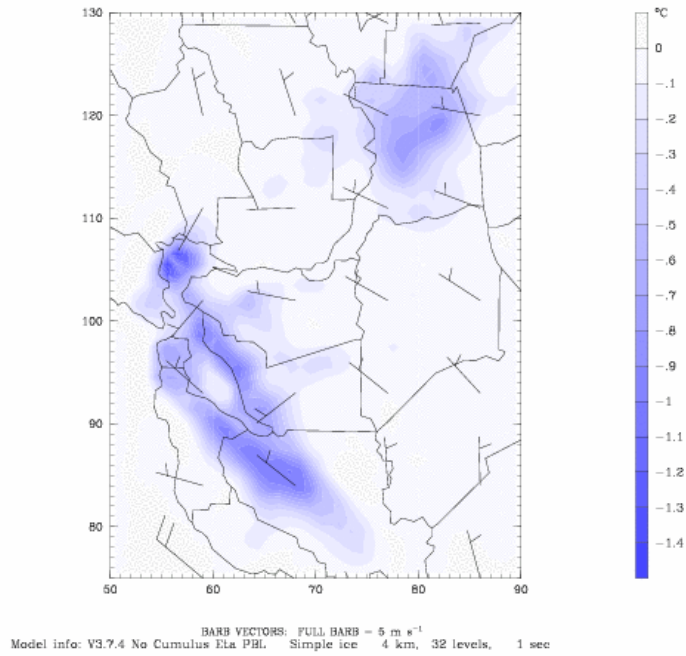


**Figure C11-1. High-albedo Case Minus Base Case; 1999 Episode for SF-SAC Domain**

Dataset: case20 RIP: ripexecute.diff.SF SAC Init: 1200 UTC Mon 05 Jul 99  
 Fcst: 30.00 h Valid: 1800 UTC Tue 06 Jul 99 (1100 PDT Tue 06 Jul 99)  
 Temperature at k-index = 32  
 (diff. from case=case00, time= 30.00)  
 Horizontal wind vectors at k-index = 32

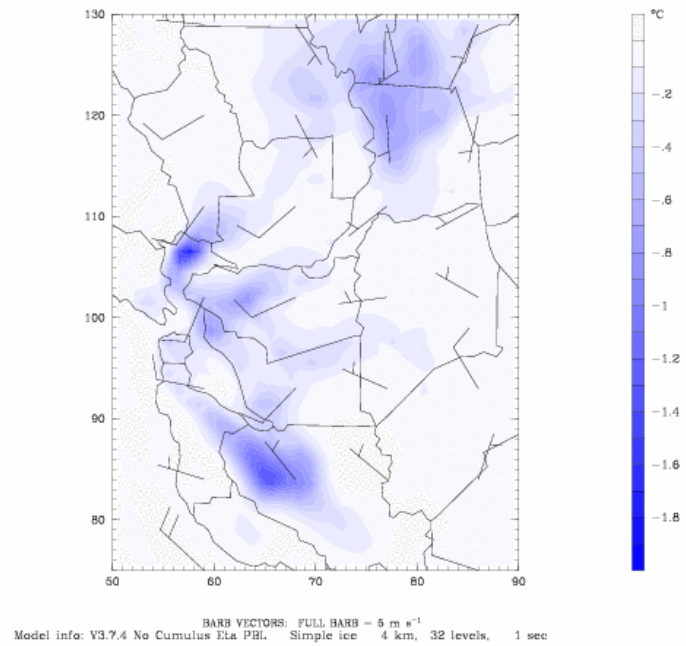


**Figure C11-2. High-albedo Case Minus Base Case; 1999 Episode for SF-SAC Domain**

Dataset: case20 RIP: ripexecute.diff.SF SAC Init: 1200 UTC Mon 05 Jul 99  
 Fcst: 56.00 h Valid: 2000 UTC Wed 07 Jul 99 (1300 PDT Wed 07 Jul 99)  
 Temperature at k-index = 32  
 (diff. from case=case00, time= 56.00)  
 Horizontal wind vectors at k-index = 32

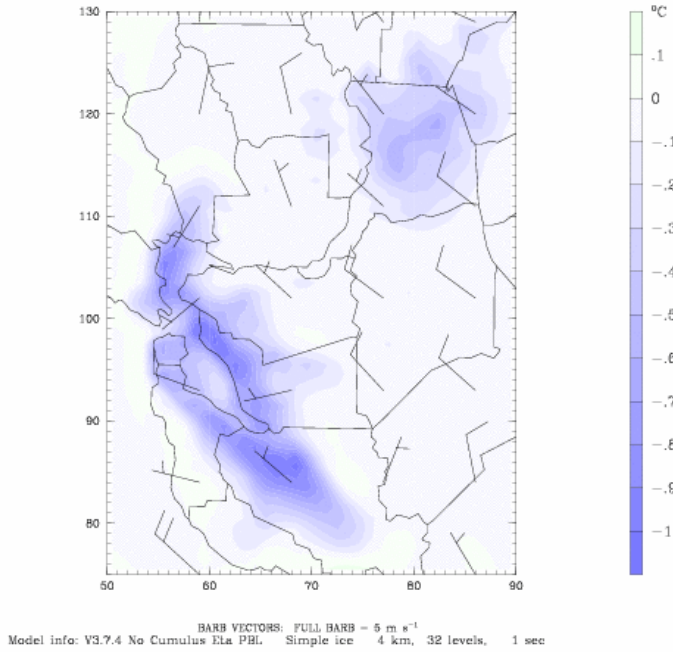


**Figure C11-3. High-albedo Case Minus Base Case; 1999 Episode for SF-SAC Domain**

Dataset: case20 RIP: ripexecute.diff.SF SAC Init: 1200 UTC Mon 05 Jul 99  
 Fcst: 78.00 h Valid: 1800 UTC Thu 08 Jul 99 (1100 PDT Thu 08 Jul 99)  
 Temperature at k-index = 32  
 (diff. from case=case00, time= 78.00)  
 Horizontal wind vectors at k-index = 32

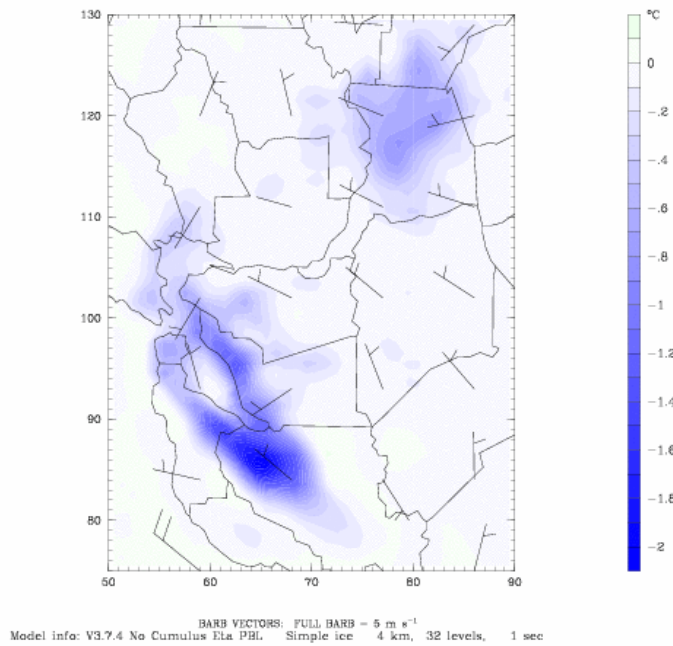
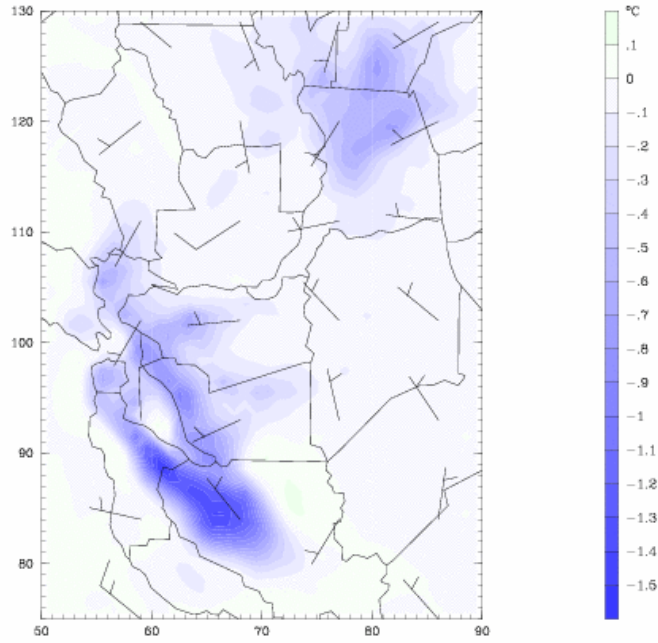


**Figure C11-4. High-albedo Case Minus Base Case; 1999 Episode for SF-SAC Domain**

Dataset: case20 RIP: ripexecute.diff.SF SAC Init: 1200 UTC Mon 05 Jul 99  
Pest: 104.00 h Valid: 2000 UTC Fri 09 Jul 99 (1300 PDT Fri 09 Jul 99)  
Temperature at k-index = 32  
(diff. from case=case00, time=104.00)  
Horizontal wind vectors at k-index = 32



Model info: V3.7.4 No Cumulus Eta PBL Simple ice 4 km, 32 levels, 1 sec  
BARB VECTORS: FULL BARB = 5 m s<sup>-1</sup>

**Figure C11-5. High-albedo Case Minus Base Case; 1999 Episode for SF-SAC Domain**

Dataset: case20 RIP: ripexecute.diff.SF SAC Init: 1200 UTC Mon 05 Jul 99  
 Fcst: 126.00 h Valid: 1800 UTC Sat 10 Jul 99 (1100 PDT Sat 10 Jul 99)  
 Temperature at k-index = 32  
 (diff. from case=case00, time=126.00)  
 Horizontal wind vectors at k-index = 32

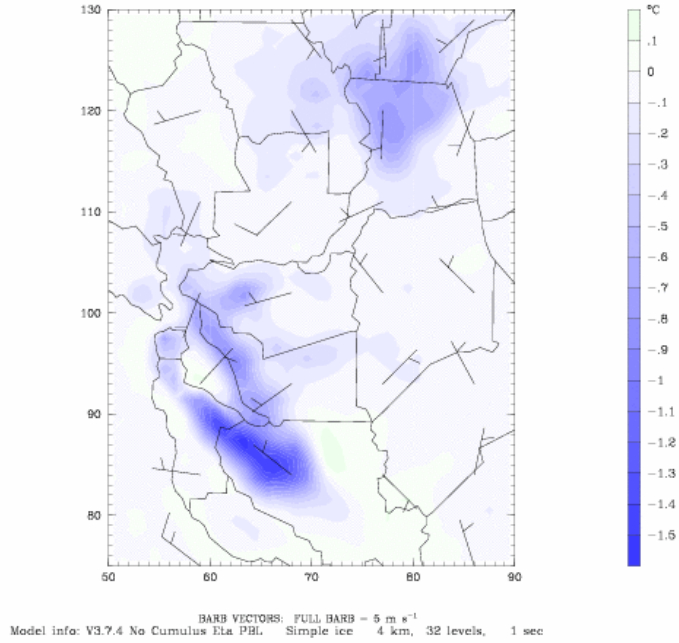


**Figure C11-6. High-albedo Case Minus Base Case; 1999 Episode for SF-SAC Domain**

Dataset: case20 RIP: ripexecute.diff.SF SAC Init: 1200 UTC Mon 05 Jul 99  
 Fcst: 150.00 h Valid: 1800 UTC Sun 11 Jul 99 (1100 PDT Sun 11 Jul 99)  
 Temperature at k-index = 32  
 (diff. from case=case00, time=150.00)  
 Horizontal wind vectors at k-index = 32

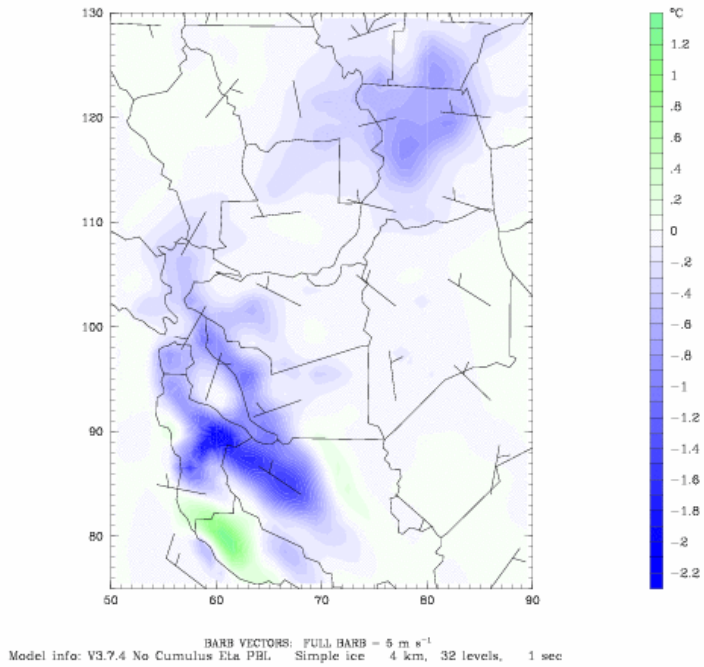


**Figure C11-7. High-albedo Case Minus Base Case; 1999 Episode for SF-SAC Domain**

Dataset: case20 RIP: ripexecute.diff.FRESNO Init: 1200 UTC Mon 05 Jul 99  
 Fcst: 6.00 h Valid: 1800 UTC Mon 05 Jul 99 (1100 PDT Mon 05 Jul 99)  
 Temperature at k-index = 32  
 (diff. from case=case00, time= 6.00)  
 Horizontal wind vectors at k-index = 32

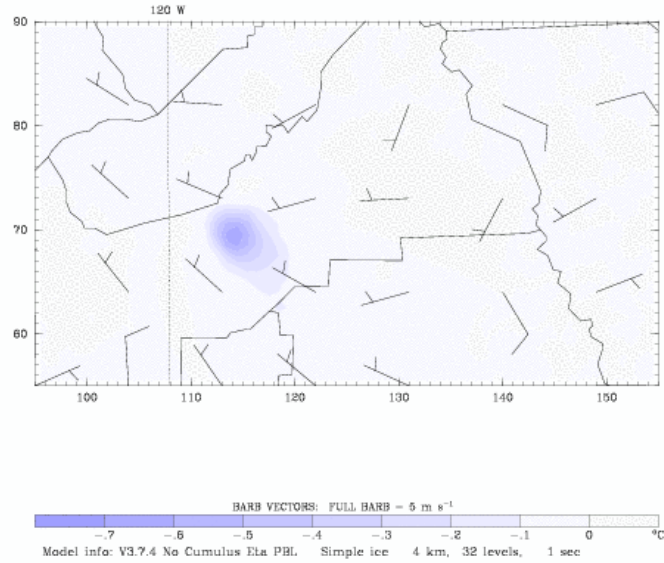


**Figure C12-1. High-albedo Case Minus Base Case; 1999 Episode for Fresno-Visalia Domain**

Dataset: case20 RIP: ripexecute.diff.FRESNO Init: 1200 UTC Mon 05 Jul 99  
 Fcst: 28.00 h Valid: 1600 UTC Tue 06 Jul 99 (0900 PDT Tue 06 Jul 99)  
 Temperature at k-index = 32  
 (diff. from case=case00, time= 28.00)  
 Horizontal wind vectors at k-index = 32

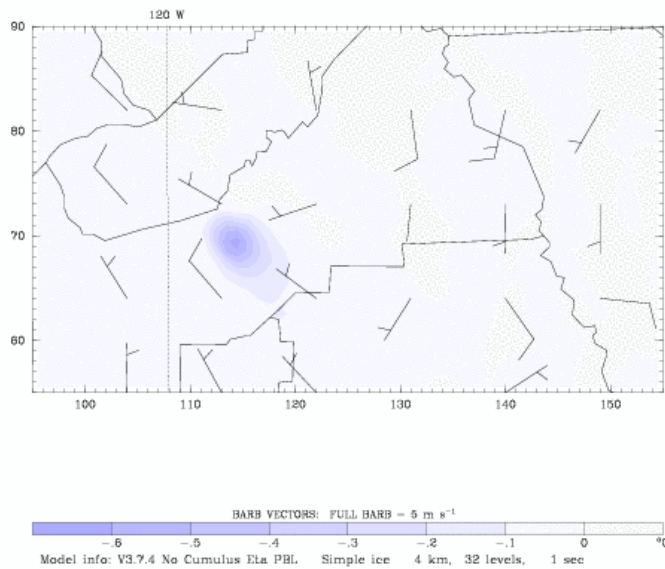


**Figure C12-2. High-albedo Case Minus Base Case; 2000 Episode for Fresno-Visalia Domain**

Dataset: case20 RIP: ripexecute.diff.FRESNO Init: 1200 UTC Mon 05 Jul 99  
 Fcst: 54.00 h Valid: 1800 UTC Wed 07 Jul 99 (1100 PDT Wed 07 Jul 99)  
 Temperature at k-index = 32  
 (diff. from case=case00, time= 54.00)  
 Horizontal wind vectors at k-index = 32

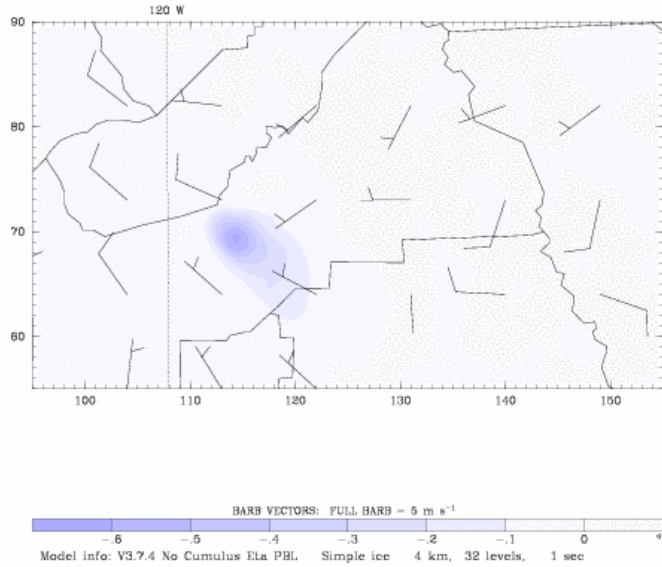
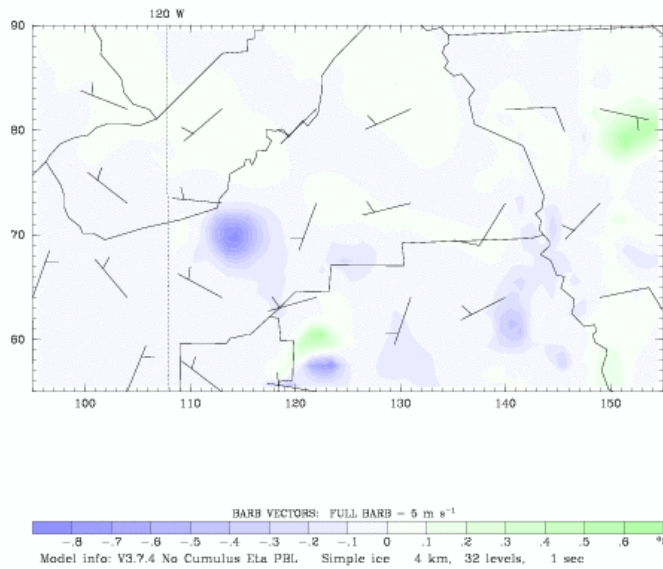


**Figure C12-3. High-albedo Case Minus Base Case; 2000 Episode for Fresno-Visalia Domain**

Dataset: case20 RIP: ripexecute.diff.FRESNO Init: 1200 UTC Mon 05 Jul 99  
 Fcst: 78.00 h Valid: 1800 UTC Thu 08 Jul 99 (1100 PDT Thu 08 Jul 99)  
 Temperature at k-index = 32  
 (diff. from case=case00, time= 78.00)  
 Horizontal wind vectors at k-index = 32



4

**Figure C12-4. High-albedo Case Minus Base Case; 2000 Episode for Fresno-Visalia Domain**

Dataset: case20 RIP: ripexecute.diff.FRESNO Init: 1200 UTC Mon 05 Jul 99  
 Fcst: 104.00 h Valid: 2000 UTC Fri 09 Jul 99 (1300 PDT Fri 09 Jul 99)  
 Temperature at k-index = 32  
 (diff. from case=case00, time=104.00)  
 Horizontal wind vectors at k-index = 32

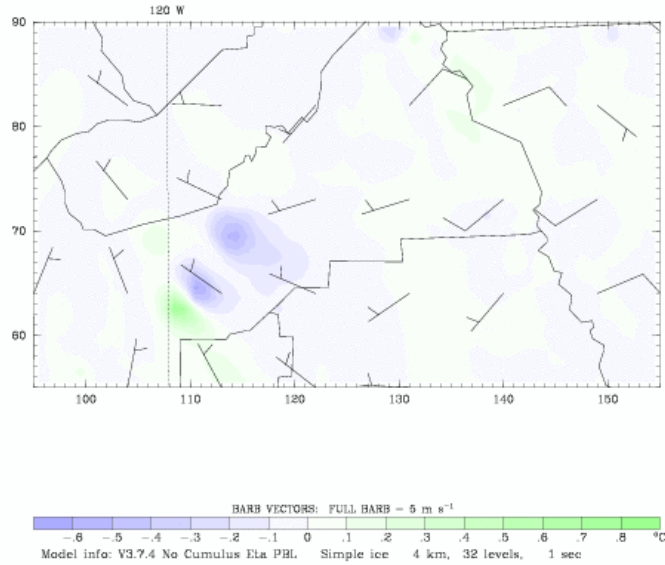


**Figure C12-5. High-albedo Case Minus Base Case; 2000 Episode for Fresno-Visalia Domain**

Dataset: case20 RIP: ripexecute.diff.FRESNO Init: 1200 UTC Mon 05 Jul 99  
 Fcst: 126.00 h Valid: 1800 UTC Sat 10 Jul 99 (1100 PDT Sat 10 Jul 99)  
 Temperature at k-index = 32  
 (diff. from case=case00, time=126.00)  
 Horizontal wind vectors at k-index = 32

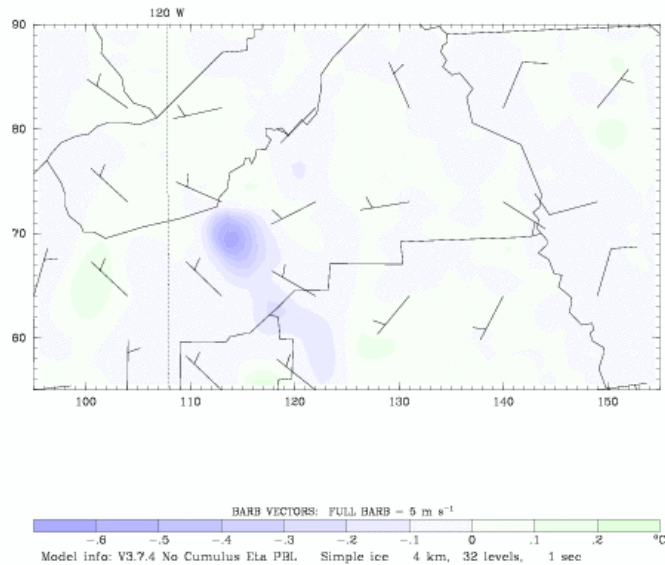
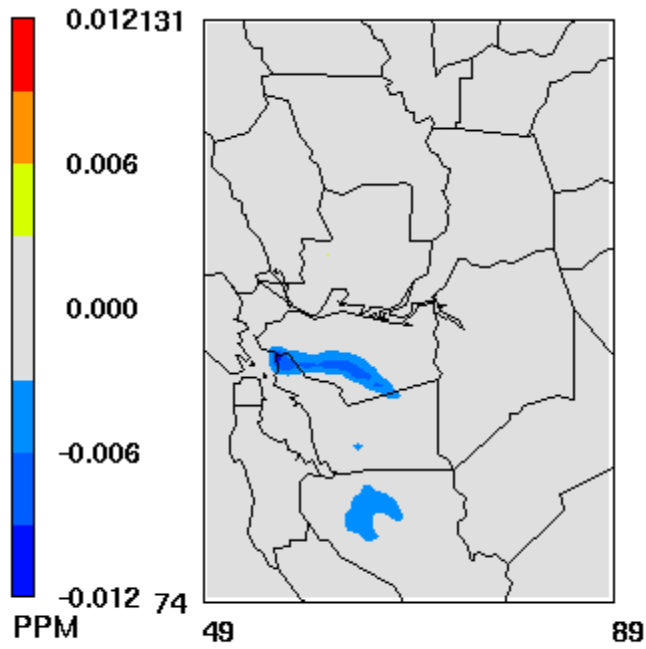
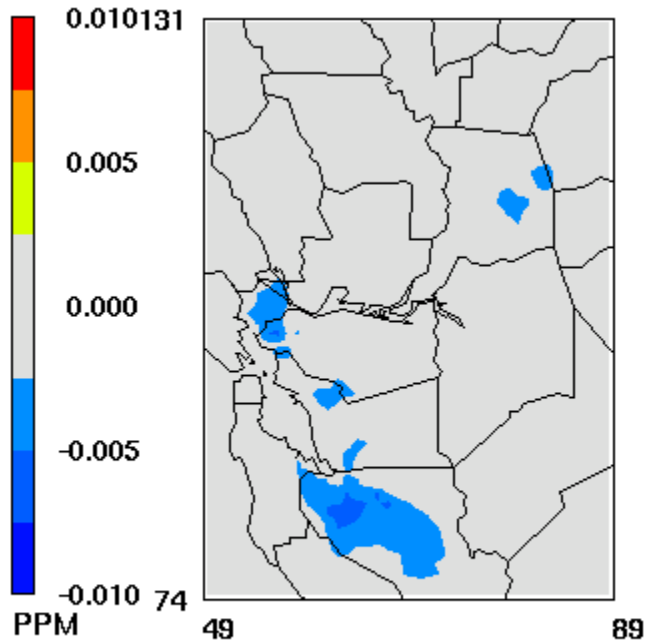


**Figure C12-6. High-albedo Case Minus Base Case; 2000 Episode for Fresno-Visalia Domain**



July 7, 1999 16:00:00  
Min= -0.011 at (56,98), Max= 0.003 at (61,108)

Figure C13-1. High-albedo Case Minus Base Case; 1999 Episode, 1999 Emissions SF-SAC; Hour with Largest Reduction in Ozone



July 8, 1999 13:00:00  
Min= -0.006 at (63,82), Max= 0.003 at (67,97)

Figure C13-2. High-albedo Case Minus Base Case; 1999 Episode, 1999 Emissions SF-SAC; Hour with Largest Reduction in Ozone

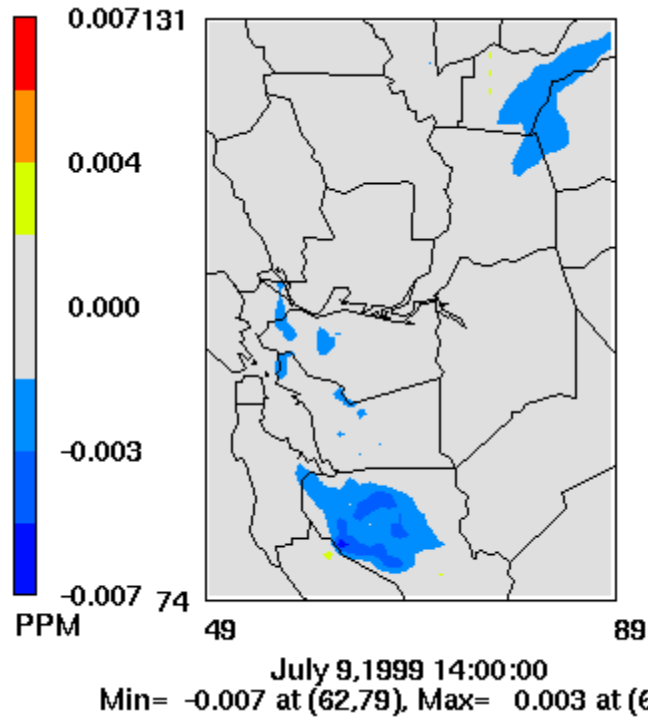


Figure C13-3. High-albedo Case Minus Base Case; 1999 Episode, 1999 Emissions SF-SAC; Hour with Largest Reduction in Ozone

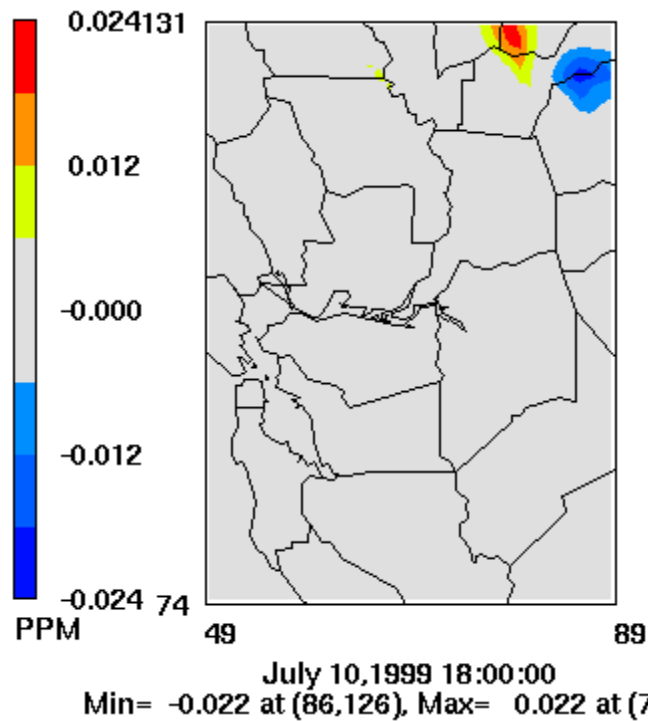


Figure C13-4. High-albedo Case Minus Base Case; 1999 Episode, 1999 Emissions SF-SAC; Hour with Largest Reduction in Ozone

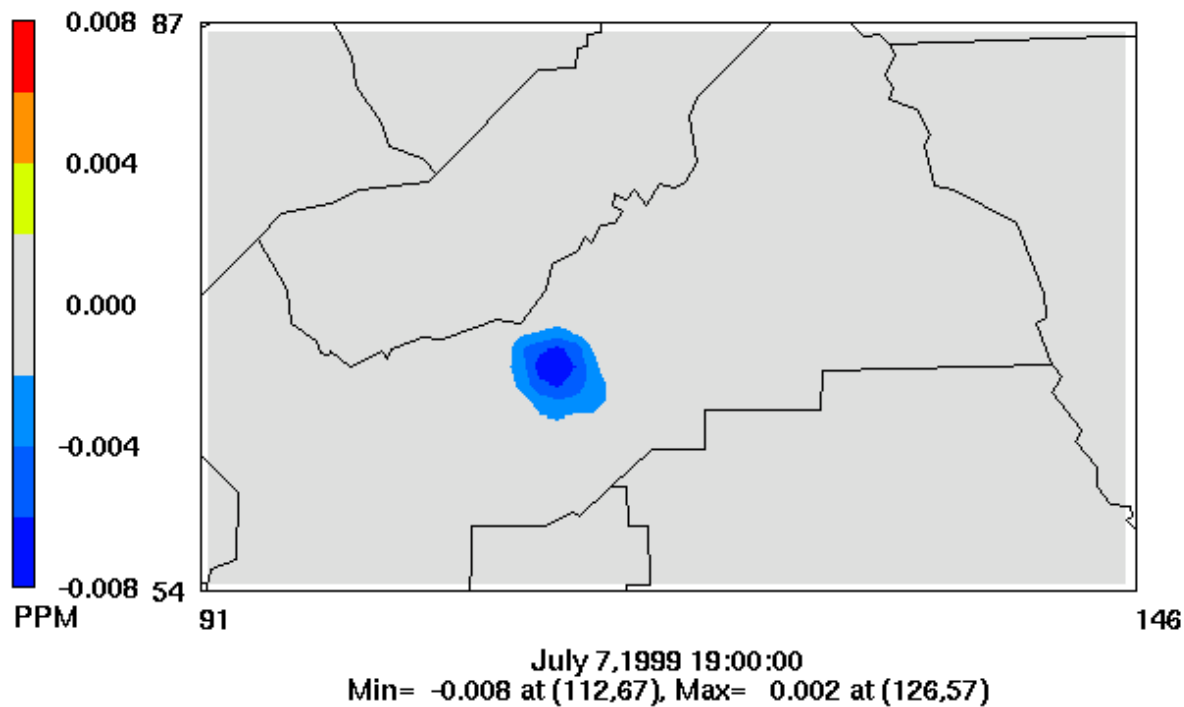


Figure C14-1. High-albedo Case Minus Base Case; 1999 Episode, 1999 Emissions Fresno; Hour with Largest Reduction in Ozone

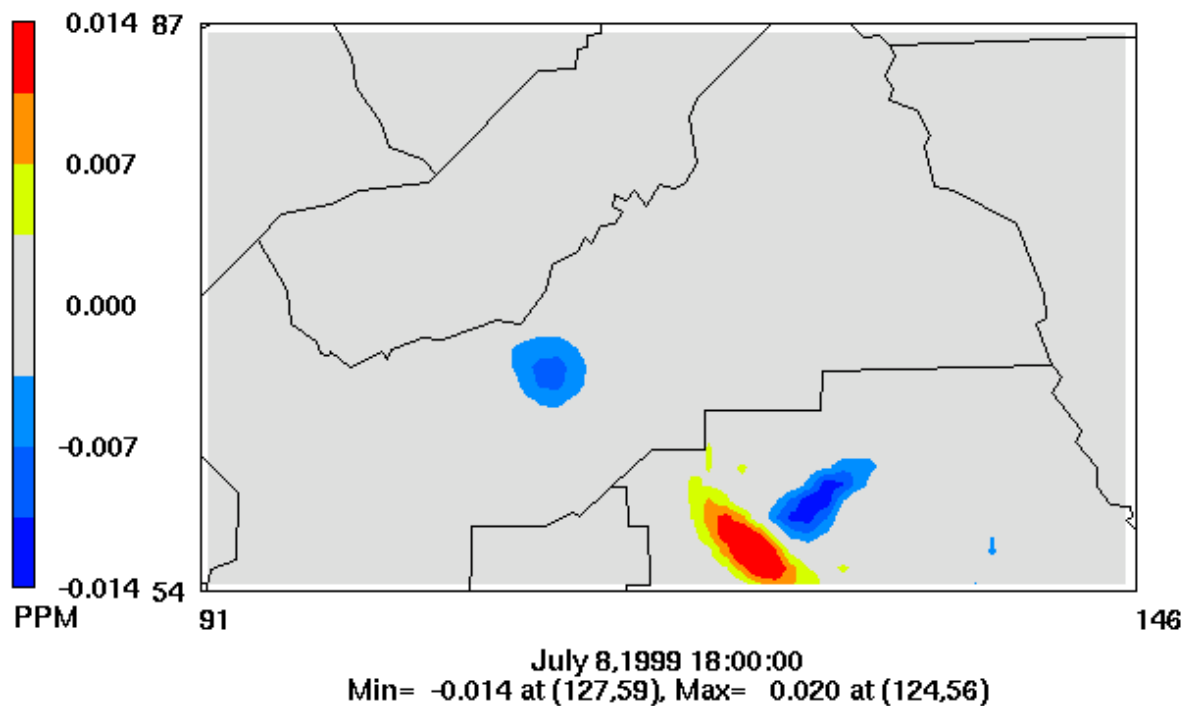
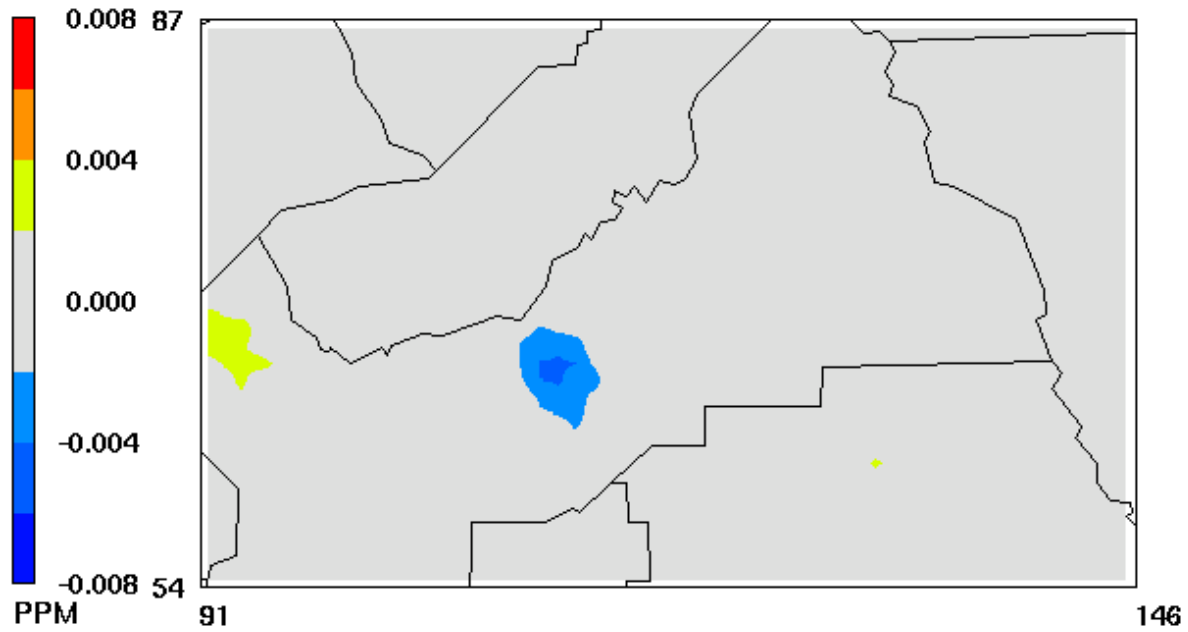
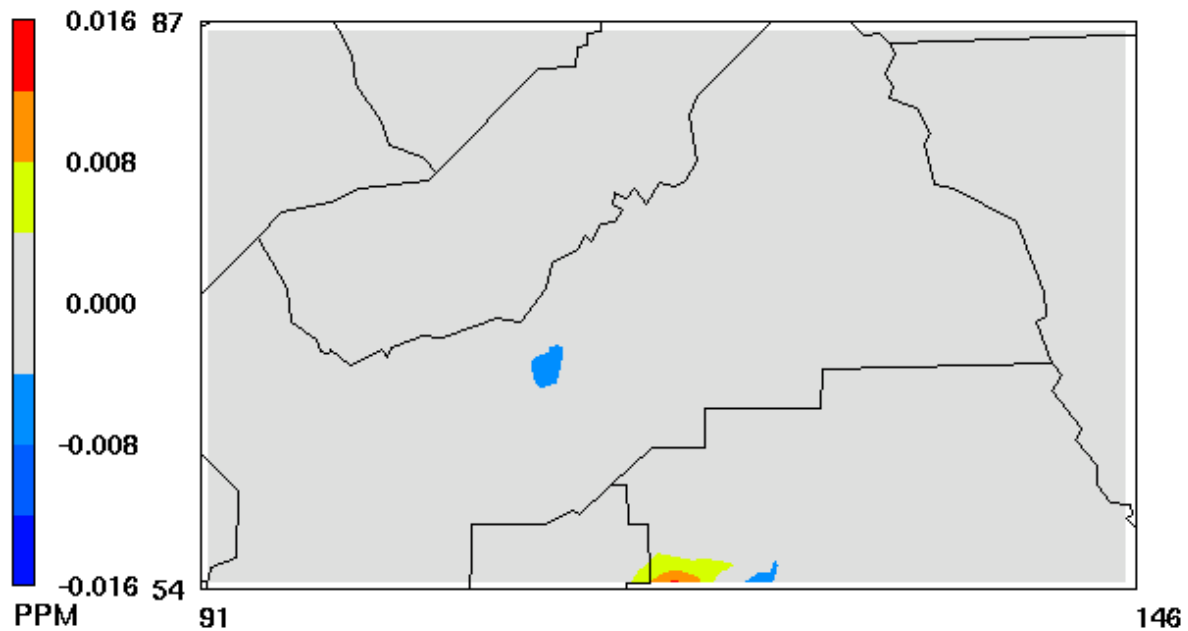


Figure C14-2. High-albedo Case Minus Base Case; 1999 Episode, 1999 Emissions Fresno; Hour with Largest Reduction in Ozone



July 9, 1999 18:00:00  
Min= -0.004 at (112,66), Max= 0.003 at (93,69)

Figure C14-3. High-albedo Case Minus Base Case; 1999 Episode, 1999 Emissions Fresno; Hour with Largest Reduction in Ozone



July 10, 1999 19:00:00  
Min= -0.006 at (124,54), Max= 0.013 at (119,54)

Figure C14-4. High-albedo Case Minus Base Case; 1999 Episode, 1999 Emissions Fresno; Hour with Largest Reduction in Ozone

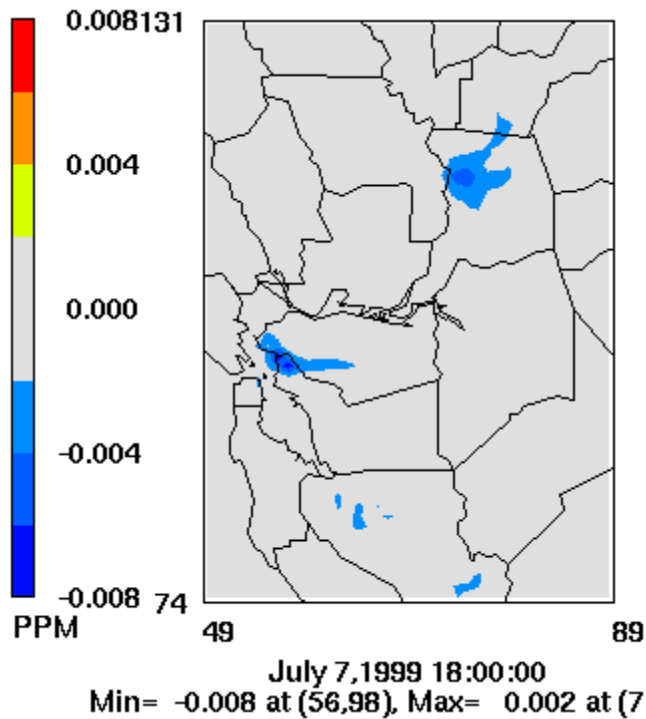


Figure C15-1. High-albedo Case Minus Base Case; 1999 Episode, 2018 Emissions SF-SAC; Hour with Largest Reduction in Ozone

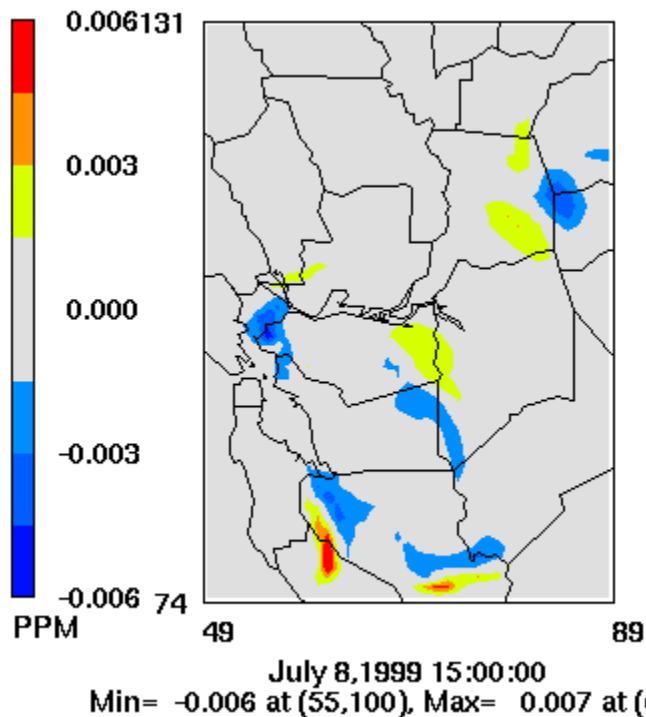


Figure C15-2. High-albedo Case Minus Base Case; 1999 Episode, 2018 Emissions SF-SAC; Hour with Largest Reduction in Ozone

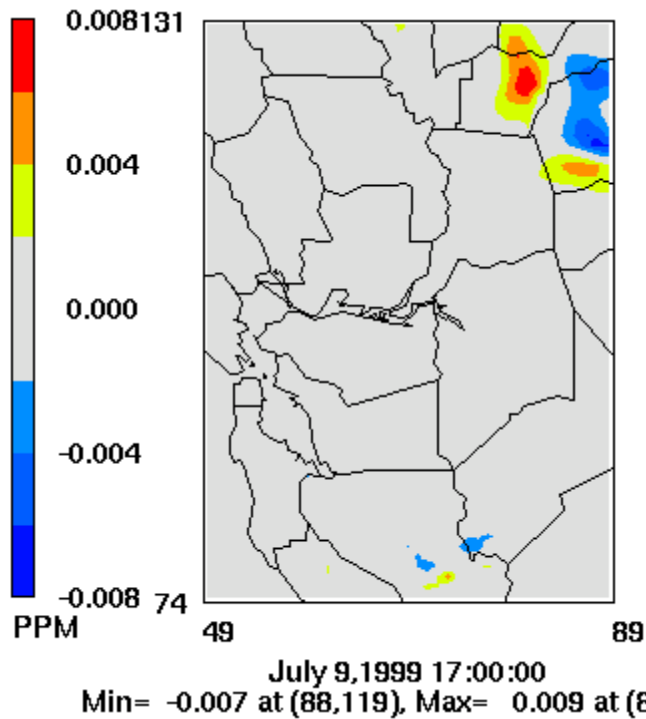


Figure C15-3. High-albedo Case Minus Base Case; 1999 Episode, 2018 Emissions SF-SAC; Hour with Largest Reduction in Ozone

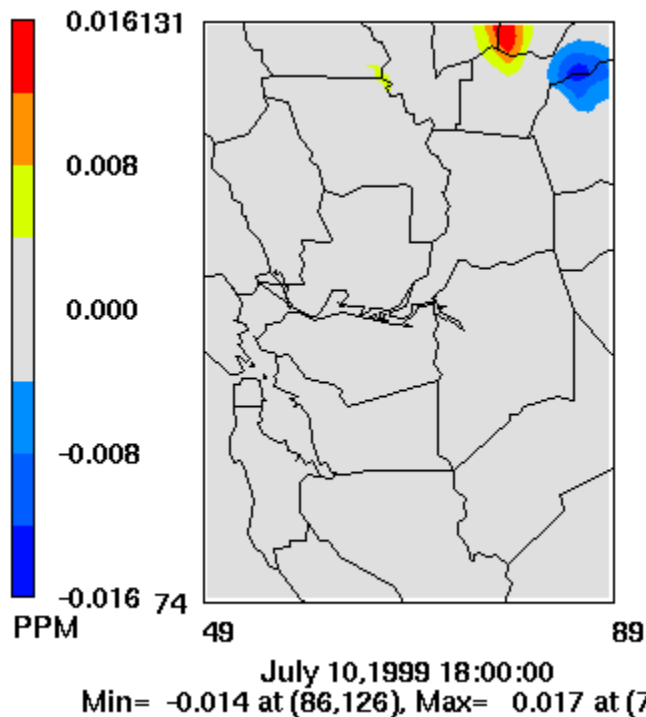


Figure C15-4. High-albedo Case Minus Base Case; 1999 Episode, 2018 Emissions SF-SAC; Hour with Largest Reduction in Ozone

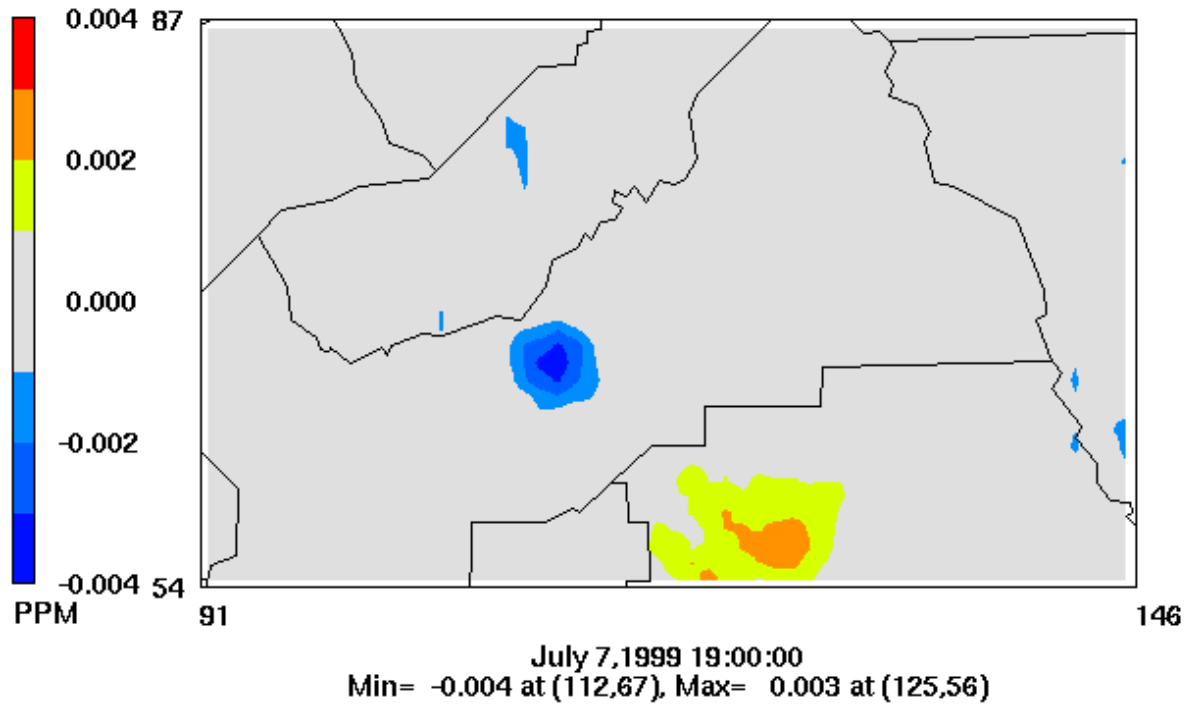


Figure C16-1. High-albedo Case Minus Base Case; 1999 Episode, 2018 Emissions Fresno; Hour with Largest Reduction in Ozone

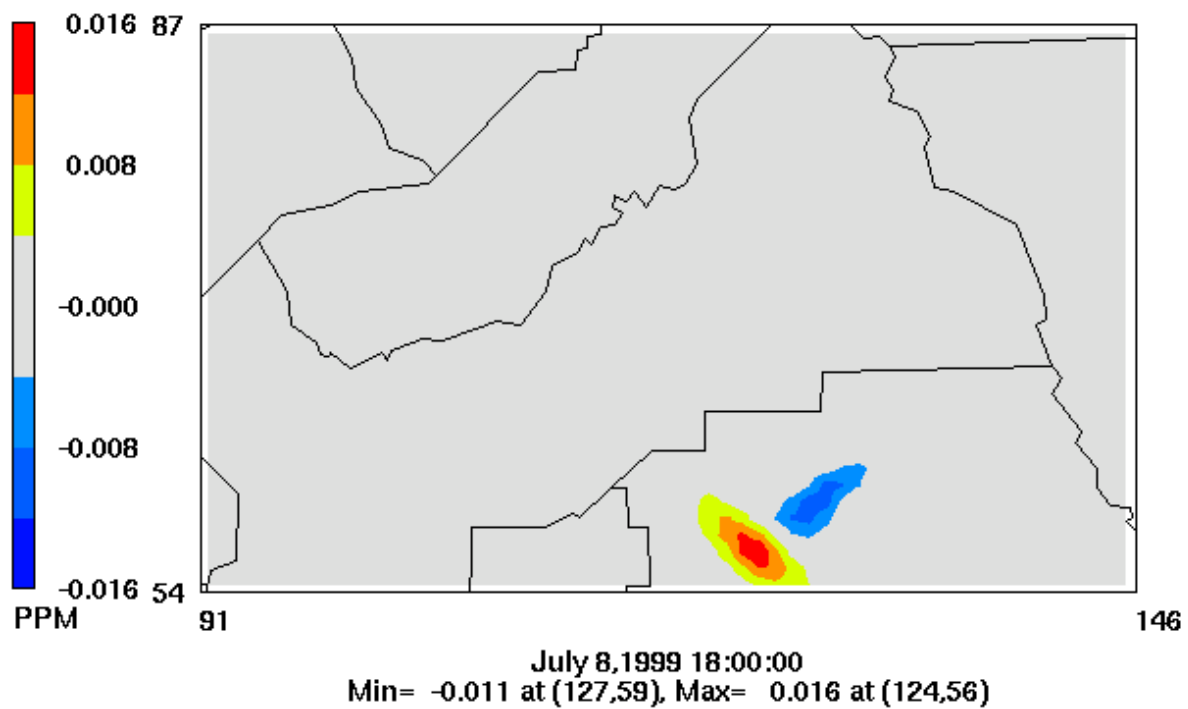
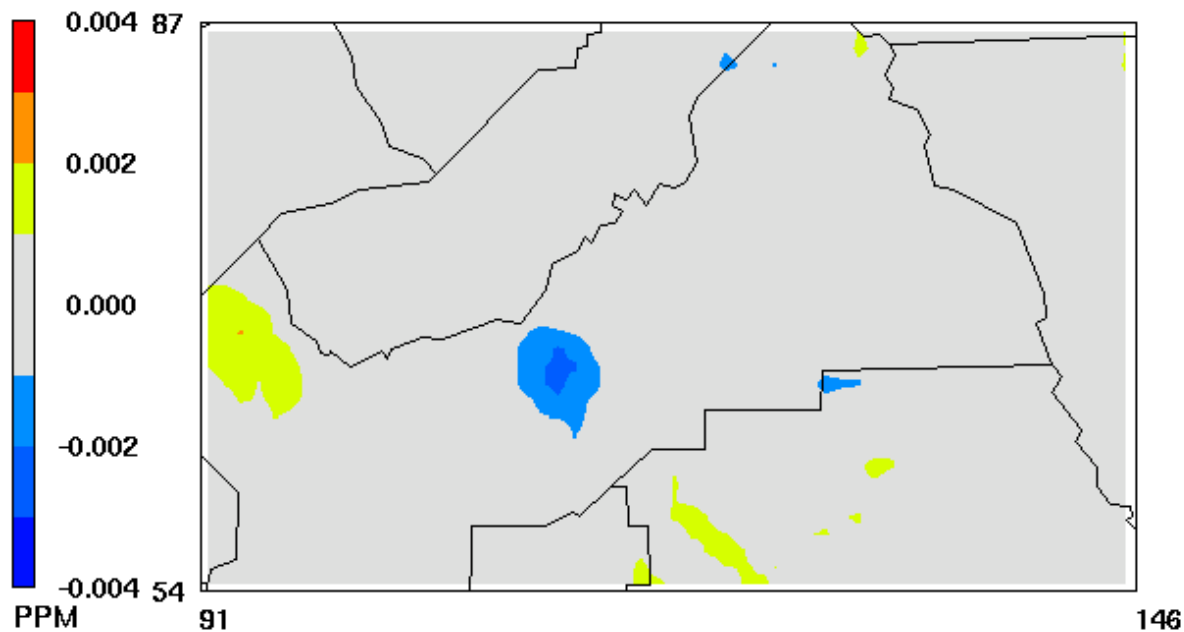
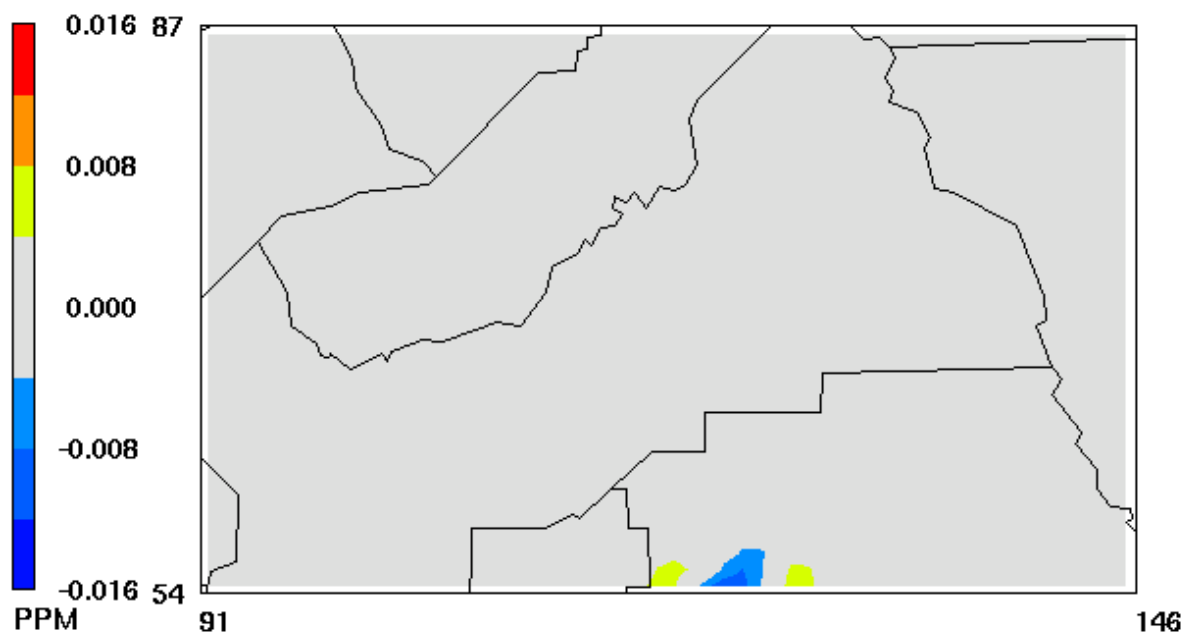


Figure C16-2. High-albedo Case Minus Base Case; 1999 Episode, 2018 Emissions SF-SAC; Hour with Largest Reduction in Ozone



July 9, 1999 18:00:00  
Min= -0.002 at (112,66), Max= 0.002 at (93,69)

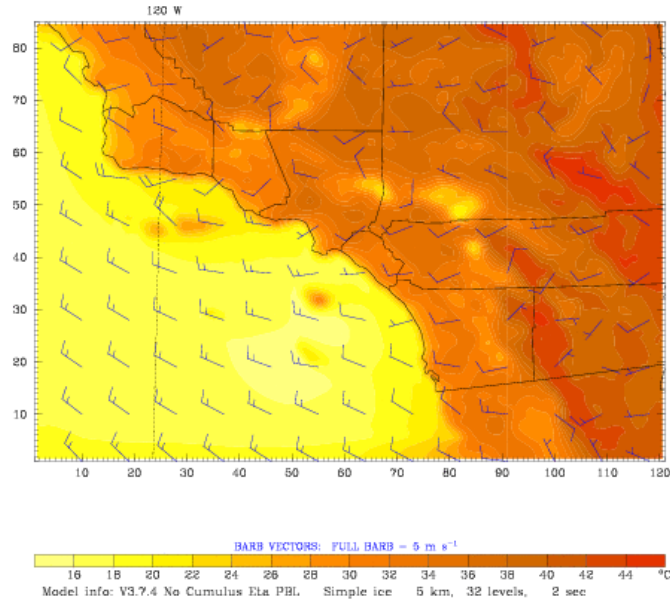
Figure C16-3. High-albedo Case Minus Base Case; 1999 Episode, 2018 Emissions SF-SAC; Hour with Largest Reduction in Ozone



July 10, 1999 20:00:00  
Min= -0.011 at (122,54), Max= 0.006 at (126,54)

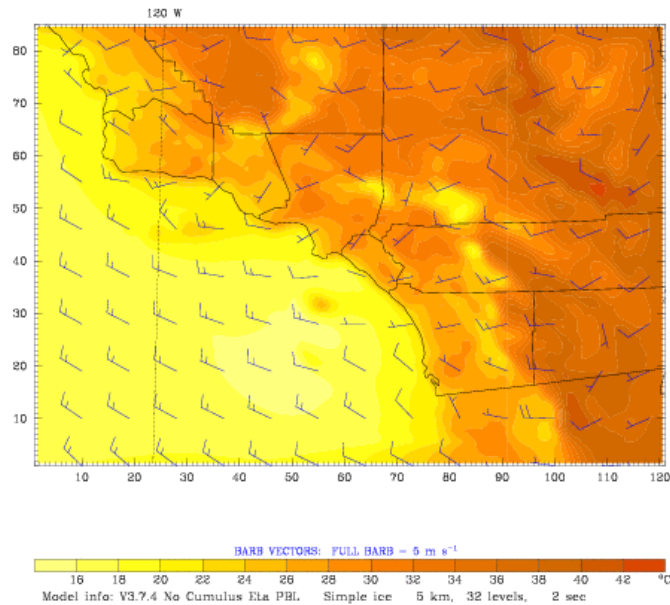
Figure C16-4. High-albedo Case Minus Base Case; 1999 Episode, 2018 Emissions SF-SAC; Hour with Largest Reduction in Ozone

Dataset: case00 RIP: ripexecute Init: 0000 UTC Tue 12 Jul 05  
 Fcst: 70.00 h Valid: 2200 UTC Thu 14 Jul 05 (1500 PDT Thu 14 Jul 05)  
 Temperature at k-index = 32  
 Horizontal wind vectors at k-index = 32



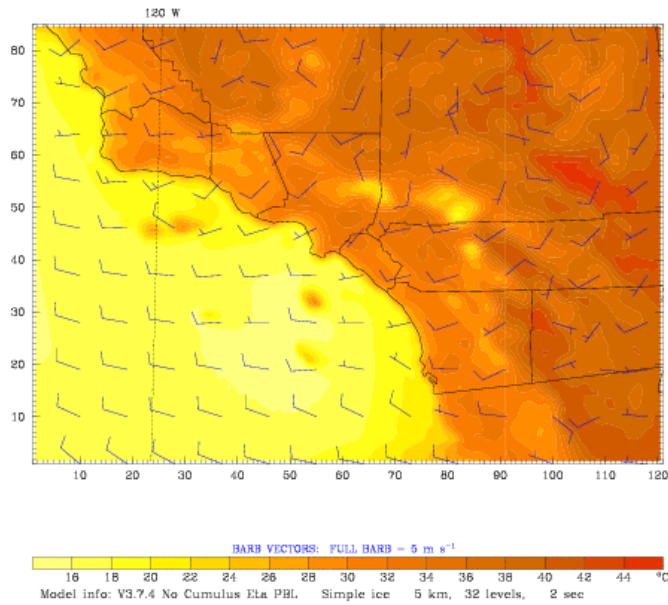
**Figure C17-1. Base Case Meteorology Episode 14–19 July, 2005 Southern California Domain**

Dataset: case00 RIP: ripexecute Init: 0000 UTC Tue 12 Jul 05  
 Fcst: 98.00 h Valid: 0200 UTC Sat 16 Jul 05 (1900 PDT Fri 15 Jul 05)  
 Temperature at k-index = 32  
 Horizontal wind vectors at k-index = 32



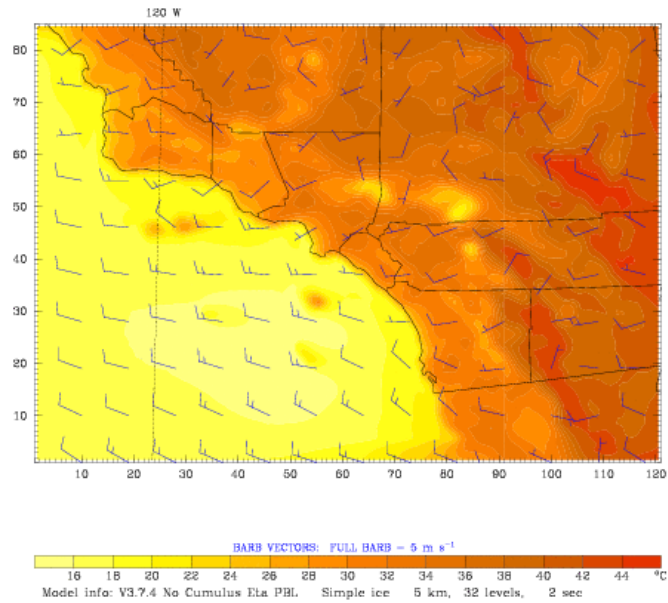
**Figure C17-2. Base Case Meteorology Episode 14–19 July, 2005 Southern California Domain**

Dataset: case00 RIP: ripexecute Init: 0000 UTC Tue 12 Jul 05  
 Fcst: 118.00 h Valid: 2200 UTC Sat 16 Jul 05 (1500 PDT Sat 16 Jul 05)  
 Temperature at k-index = 32  
 Horizontal wind vectors at k-index = 32



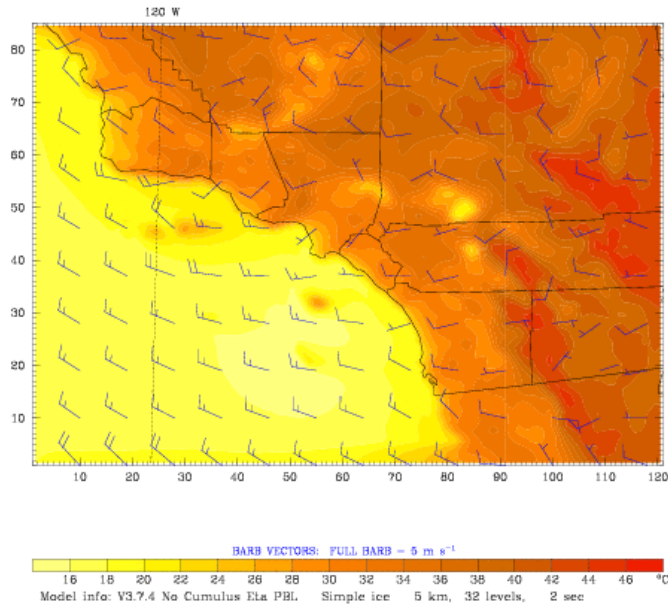
**Figure C17-3. Base Case Meteorology Episode 14–19 July, 2005 Southern California Domain**

Dataset: case00 RIP: ripexecute Init: 0000 UTC Tue 12 Jul 05  
 Fcst: 142.00 h Valid: 2200 UTC Sun 17 Jul 05 (1500 PDT Sun 17 Jul 05)  
 Temperature at k-index = 32  
 Horizontal wind vectors at k-index = 32



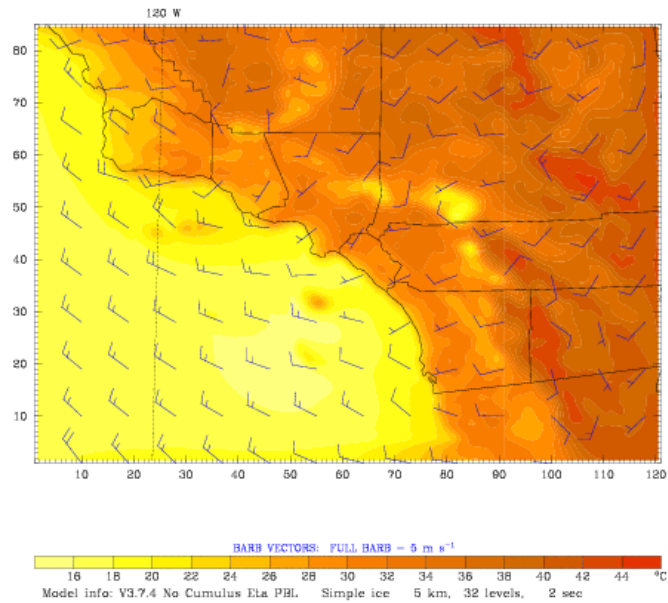
**Figure C17-4. Base Case Meteorology Episode 14–19 July, 2005 Southern California Domain**

Dataset: case00 RIP: ripexecute Init: 0000 UTC Tue 12 Jul 05  
 Fcst: 166.00 h Valid: 2200 UTC Mon 18 Jul 05 (1500 PDT Mon 18 Jul 05)  
 Temperature at k-index = 32  
 Horizontal wind vectors at k-index = 32



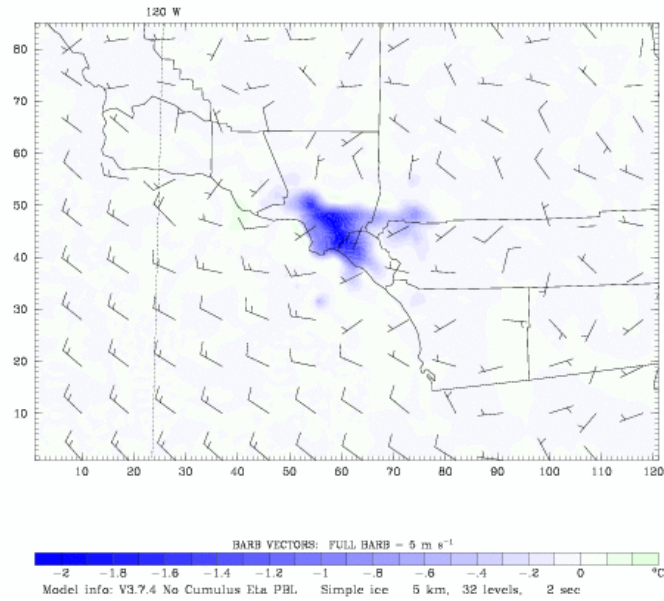
**Figure C17-5. Base Case Meteorology Episode 14–19 July, 2005 Southern California Domain**

Dataset: case00 RIP: ripexecute Init: 0000 UTC Tue 12 Jul 05  
 Fcst: 192.00 h Valid: 0000 UTC Wed 20 Jul 05 (1700 PDT Tue 19 Jul 05)  
 Temperature at k-index = 32  
 Horizontal wind vectors at k-index = 32



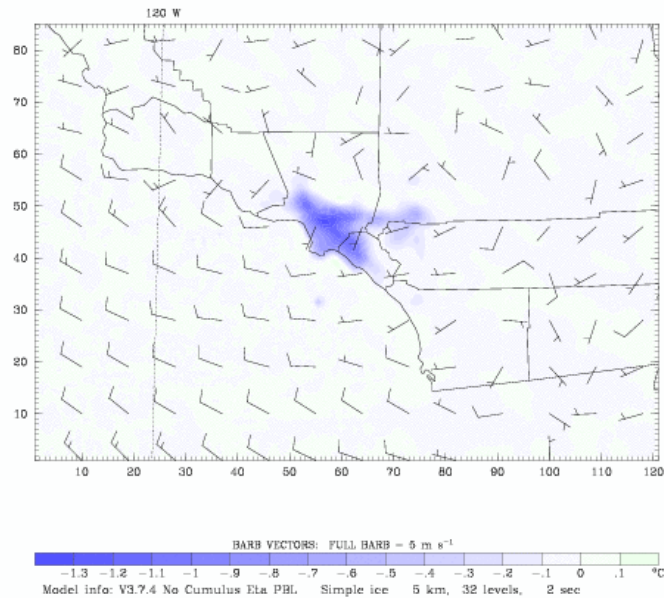
**Figure C17-6. Base Case Meteorology Episode 14–19 July, 2005 Southern California Domain**

Dataset: case20 RIP: ripexecute.diff Init: 0000 UTC Tue 12 Jul 05  
 Fcst: 66.00 h Valid: 1800 UTC Thu 14 Jul 05 (1100 PDT Thu 14 Jul 05)  
 Temperature at k-index = 32  
 (diff. from case=case00, time= 66.00)  
 Horizontal wind vectors at k-index = 32



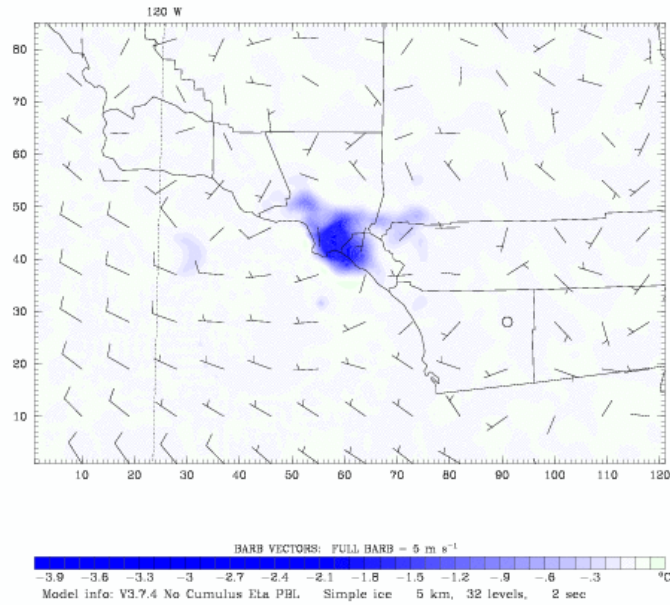
**Figure C18-1. High-albedo Case Minus Base Case; 2005 Episode, Southern California Domain**

Dataset: case20 RIP: ripexecute.diff Init: 0000 UTC Tue 12 Jul 05  
 Fcst: 90.00 h Valid: 1800 UTC Fri 15 Jul 05 (1100 PDT Fri 15 Jul 05)  
 Temperature at k-index = 32  
 (diff. from case=case00, time= 90.00)  
 Horizontal wind vectors at k-index = 32



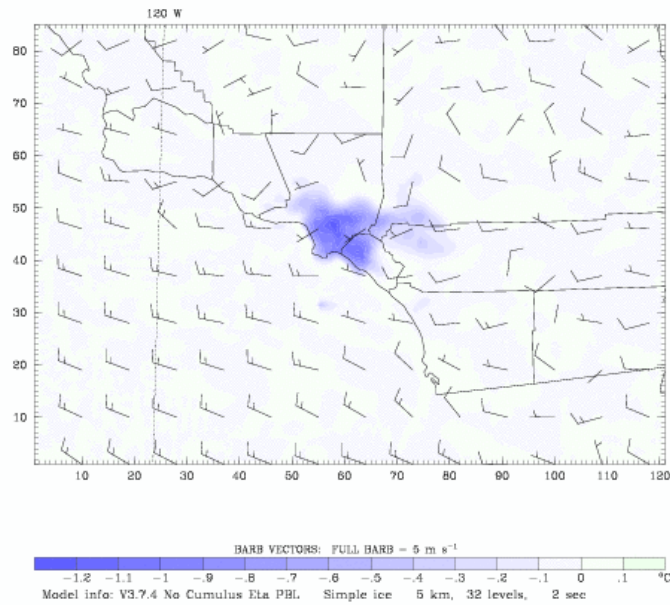
**Figure C18-2. High-albedo Case Minus Base Case; 2005 Episode, Southern California Domain**

Dataset: case20 RIP: ripexecute.diff Init: 0000 UTC Tue 12 Jul 05  
 Fcst: 112.00 h Valid: 1600 UTC Sat 16 Jul 05 (0900 PDT Sat 16 Jul 05)  
 Temperature at k-index = 32  
 (diff. from case=case00, time=112.00)  
 Horizontal wind vectors at k-index = 32



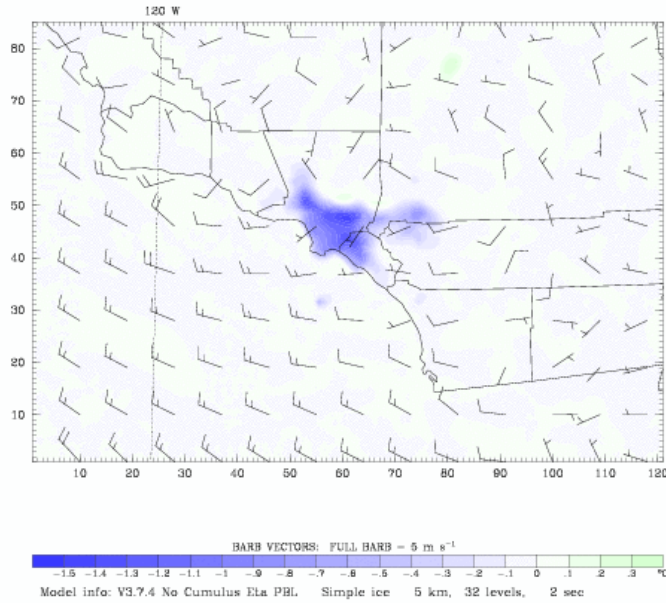
**Figure C18-3. High-albedo Case Minus Base Case; 2005 Episode, Southern California Domain**

Dataset: case20 RIP: ripexecute.diff Init: 0000 UTC Tue 12 Jul 05  
 Fcst: 144.00 h Valid: 0000 UTC Mon 18 Jul 05 (1700 PDT Sun 17 Jul 05)  
 Temperature at k-index = 32  
 (diff. from case=case00, time=144.00)  
 Horizontal wind vectors at k-index = 32



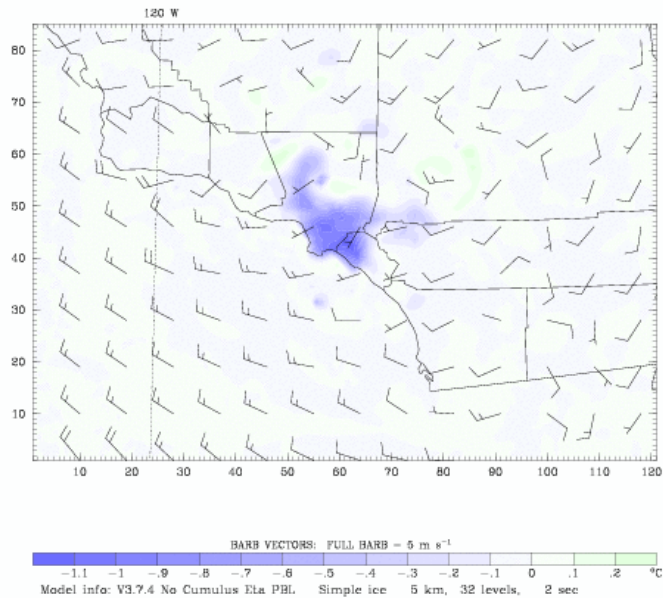
**Figure C18-4. High-albedo Case Minus Base Case; 2005 Episode, Southern California Domain**

Dataset: case20 RIP: ripexecute.diff Init: 0000 UTC Tue 12 Jul 05  
 Fcst: 164.00 h Valid: 2000 UTC Mon 18 Jul 05 (1300 PDT Mon 18 Jul 05)  
 Temperature at k-index = 32  
 (diff. from case=case00, time=164.00)  
 Horizontal wind vectors at k-index = 32

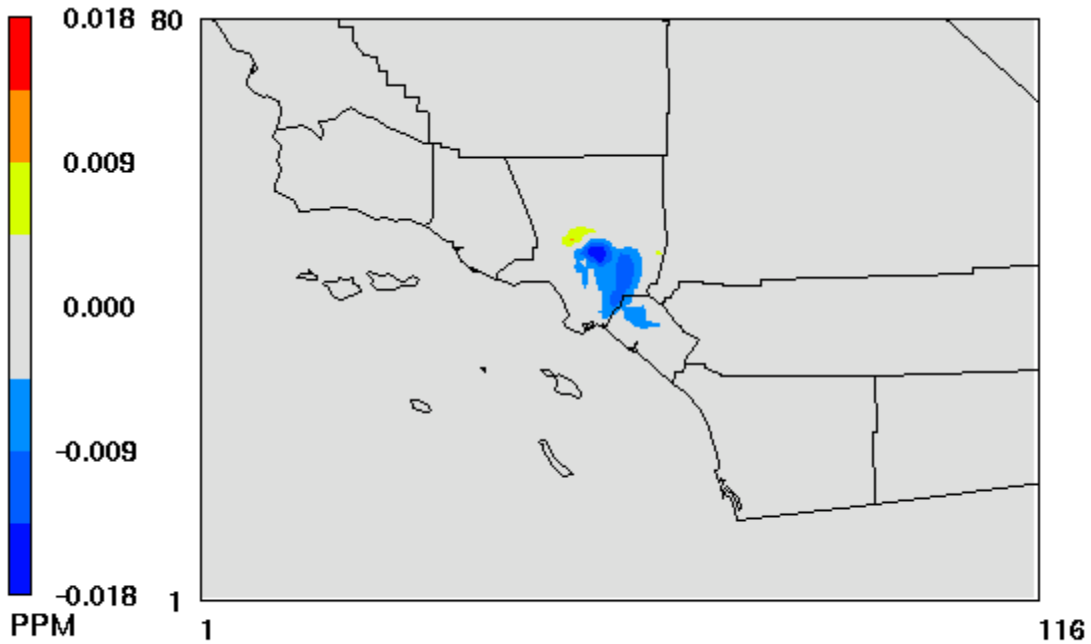


**Figure C18-5. High-albedo Case Minus Base Case; 2005 Episode, Southern California Domain**

Dataset: case20 RIP: ripexecute.diff Init: 0000 UTC Tue 12 Jul 05  
 Fcst: 190.00 h Valid: 2200 UTC Tue 19 Jul 05 (1500 PDT Tue 19 Jul 05)  
 Temperature at k-index = 32  
 (diff. from case=case00, time=190.00)  
 Horizontal wind vectors at k-index = 32

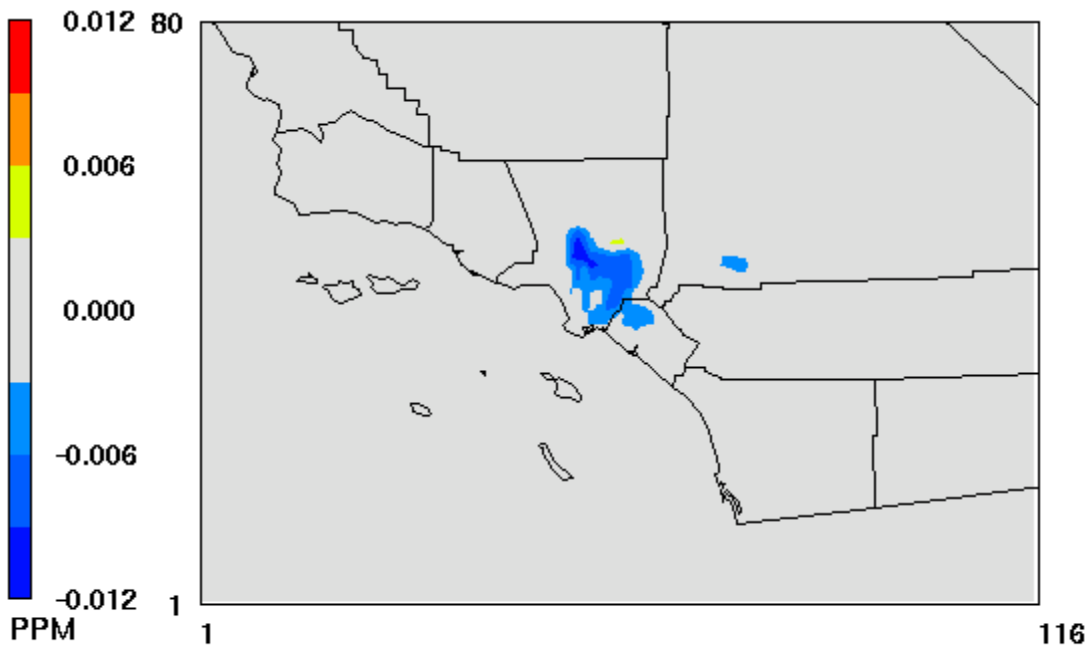


**Figure C18-6. High-albedo Case Minus Base Case; 2005 Episode, Southern California Domain**



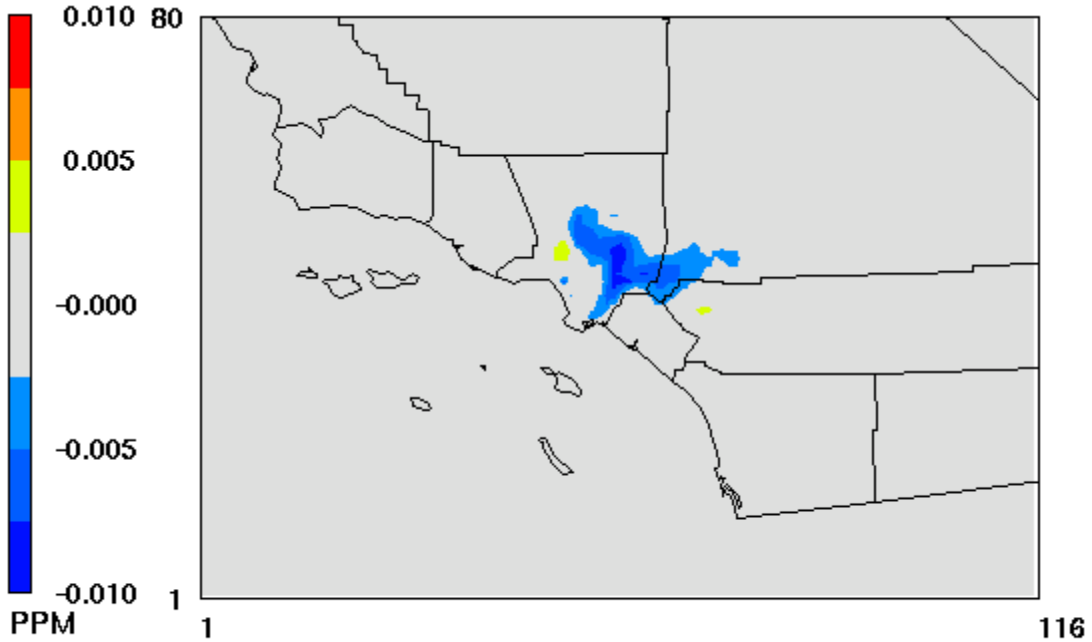
July 14,2005 12:00:00  
Min= -0.018 at (56,48), Max= 0.010 at (52,50)

Figure C19-1. High-albedo Case Minus Base Case; 2005 Episode, 2005 Emissions Southern California; Hour with Largest Reduction in Ozone



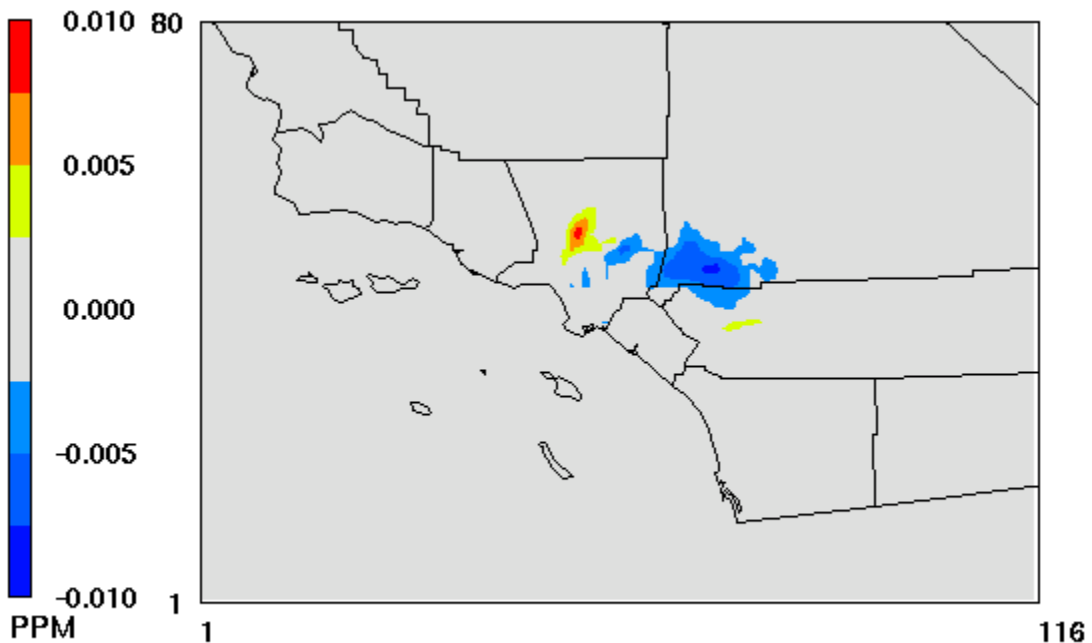
July 15,2005 12:00:00  
Min= -0.011 at (53,49), Max= 0.005 at (59,50)

Figure C19-2. High-albedo Case Minus Base Case; 2005 Episode, 2005 Emissions Southern California; Hour with Largest Reduction in Ozone



July 16,2005 12:00:00  
Min= -0.010 at (59,47), Max= 0.004 at (51,49)

Figure C19-3. High-albedo Case Minus Base Case; 2005 Episode, 2005 Emissions Southern California; Hour with Largest Reduction in Ozone



July 17,2005 14:00:00  
Min= -0.008 at (71,46), Max= 0.009 at (53,51)

Figure C19-4. High-albedo Case Minus Base Case; 2005 Episode, 2005 Emissions Southern California; Hour with Largest Reduction in Ozone

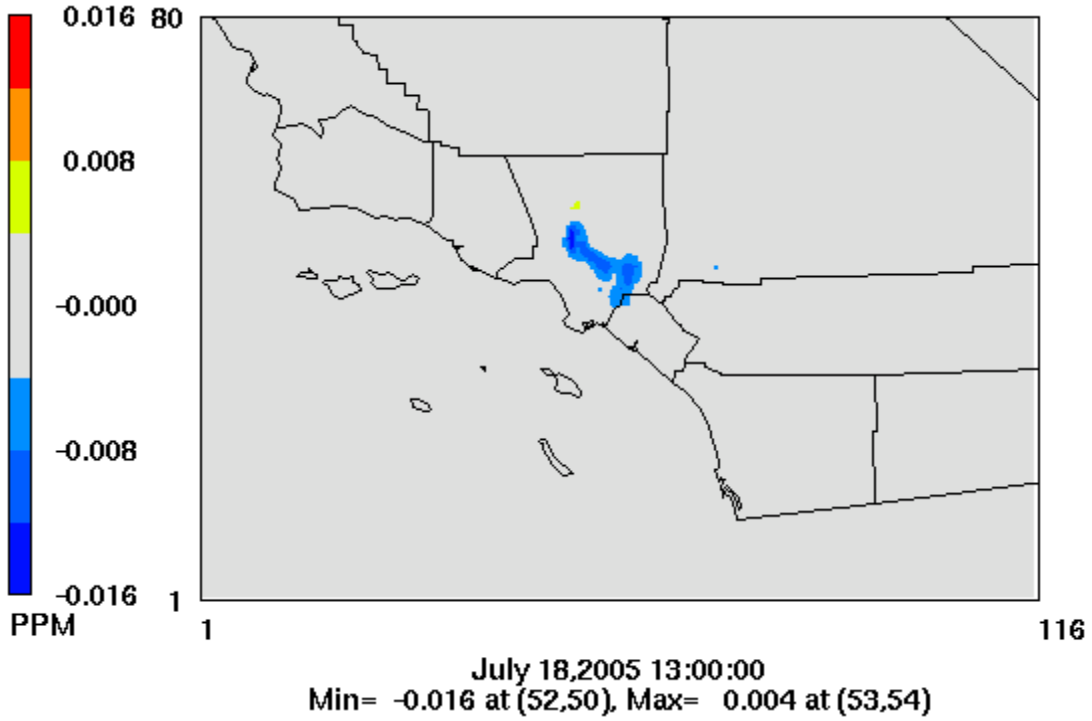


Figure C19-5. High-albedo Case Minus Base Case; 2005 Episode, 2005 Emissions Southern California; Hour with Largest Reduction in Ozone

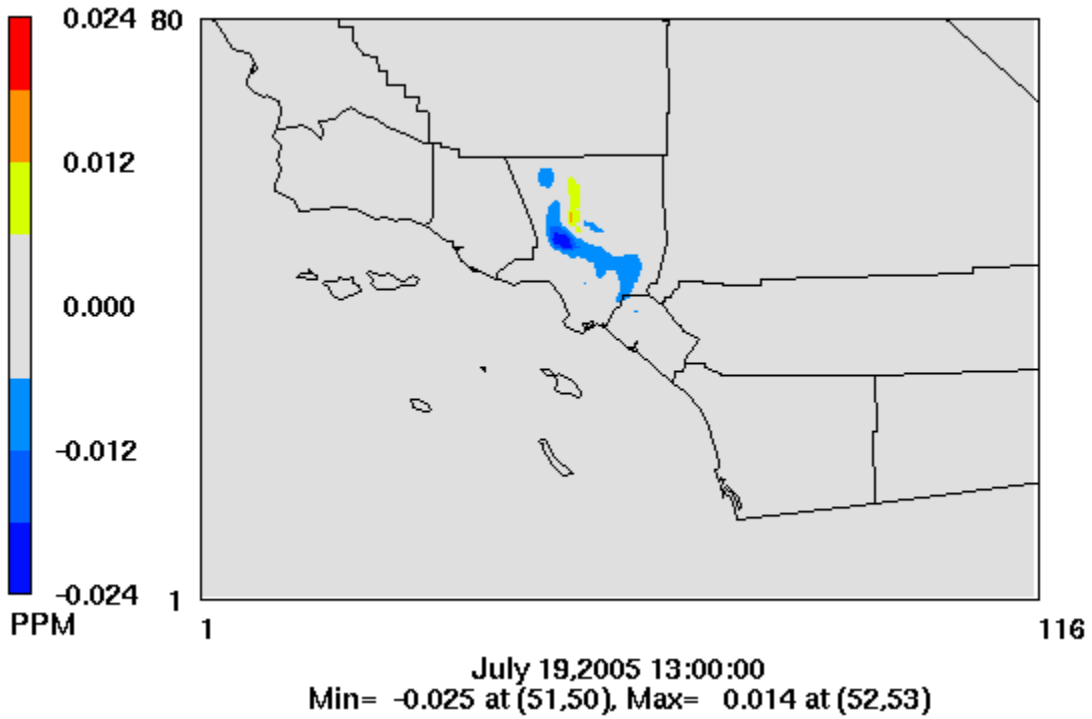
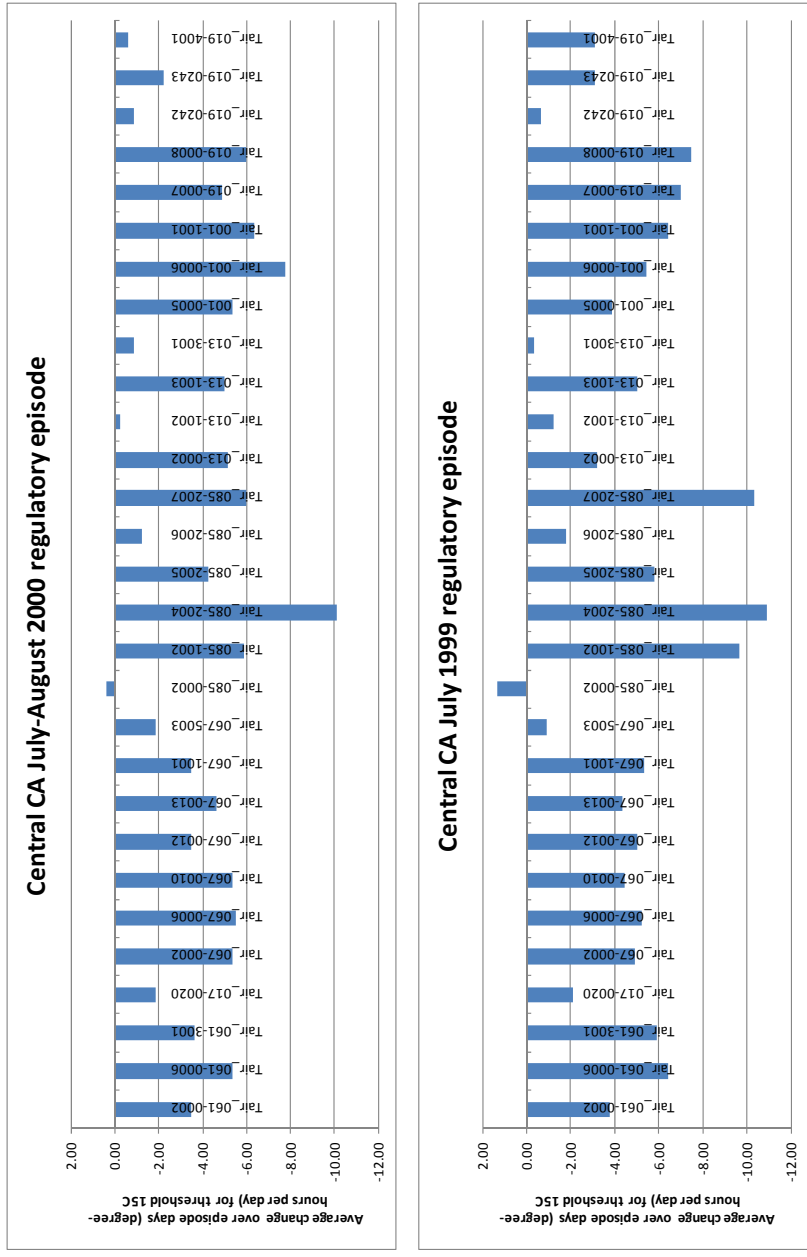
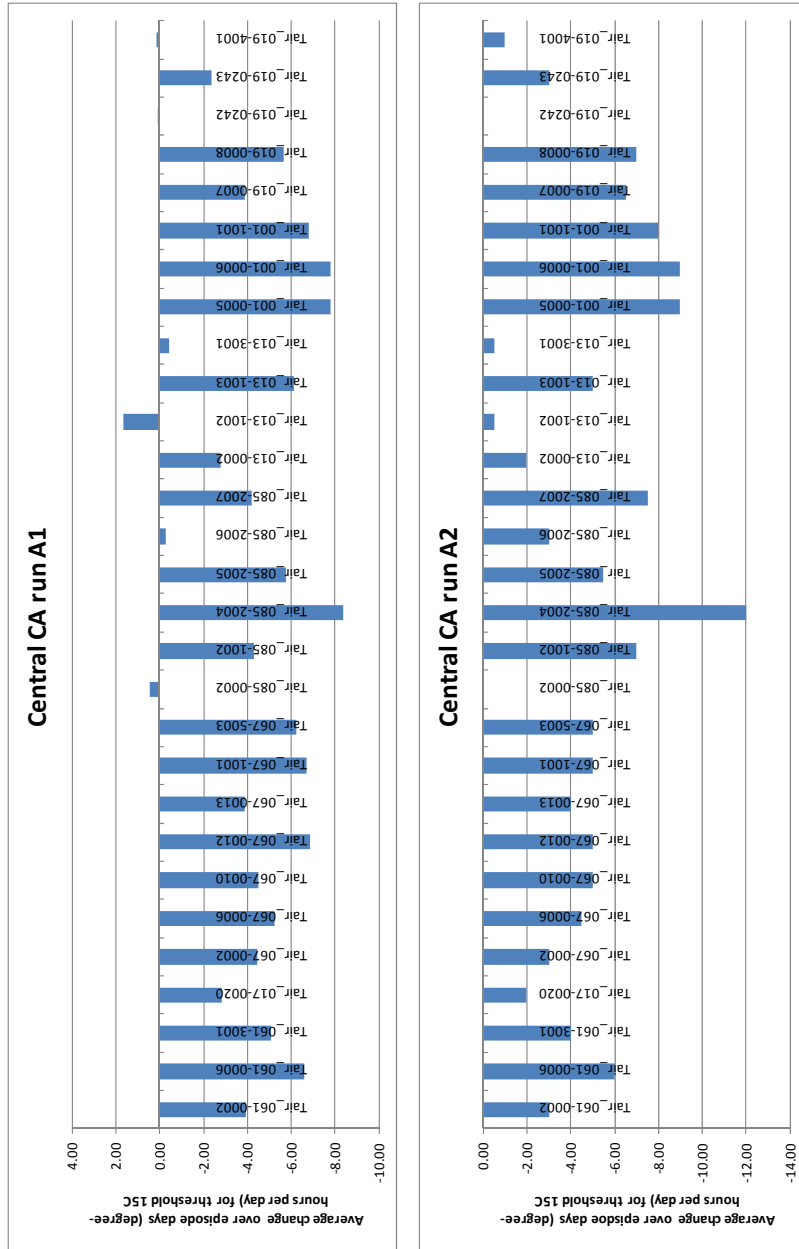


Figure C19-6. High-albedo Case Minus Base Case; 2005 Episode, 2005 Emissions Southern California; Hour with Largest Reduction in Ozone

# **Appendix D: Degree-hour Changes**



Figures D1 and D2. Differences in Degree-hours per Day (C-hr/day) at Monitors in Central California for Runs 2000 and 1999



Figures D3 and D4. Differences in Degree-hours per Day (C-hr/day) at Monitors in Central California for Runs A1 and A2

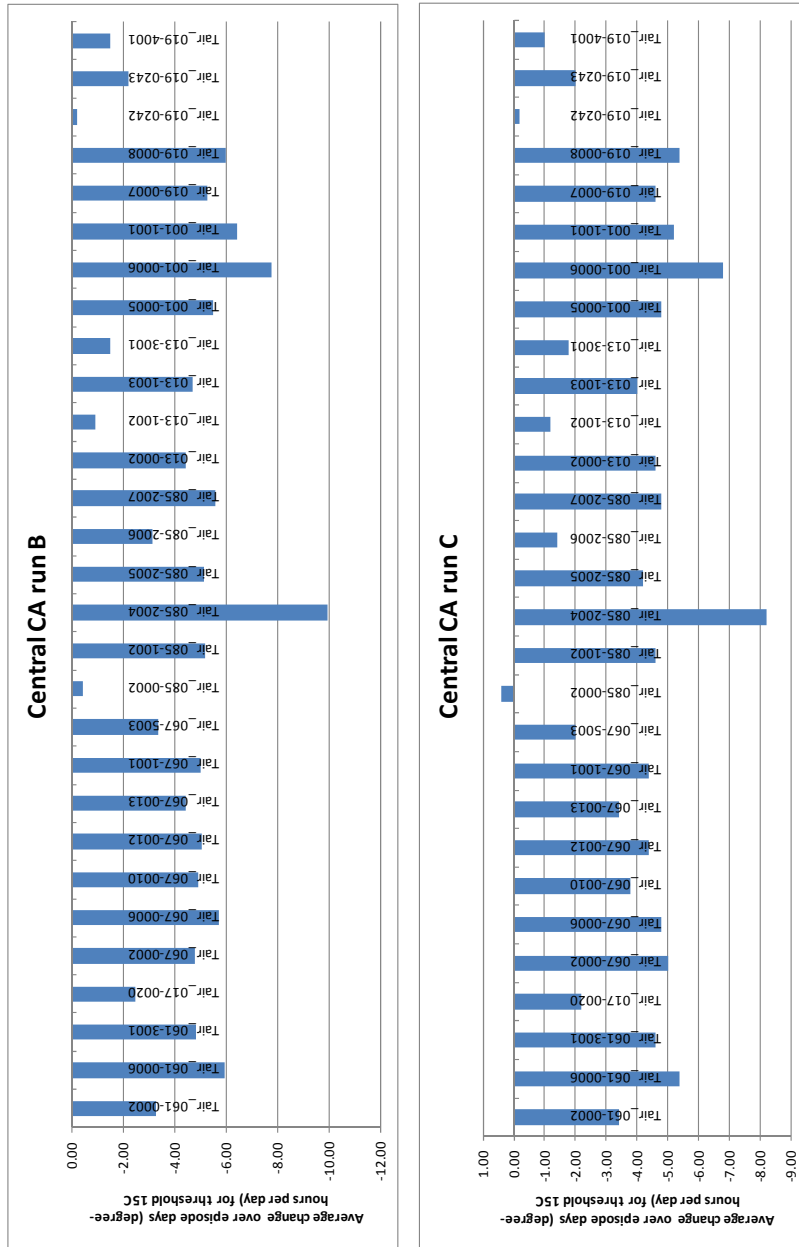


Figure D5 and D6. Differences in Degree-hours per Day (C-hr/day) at Monitors in Central California for Runs B and C

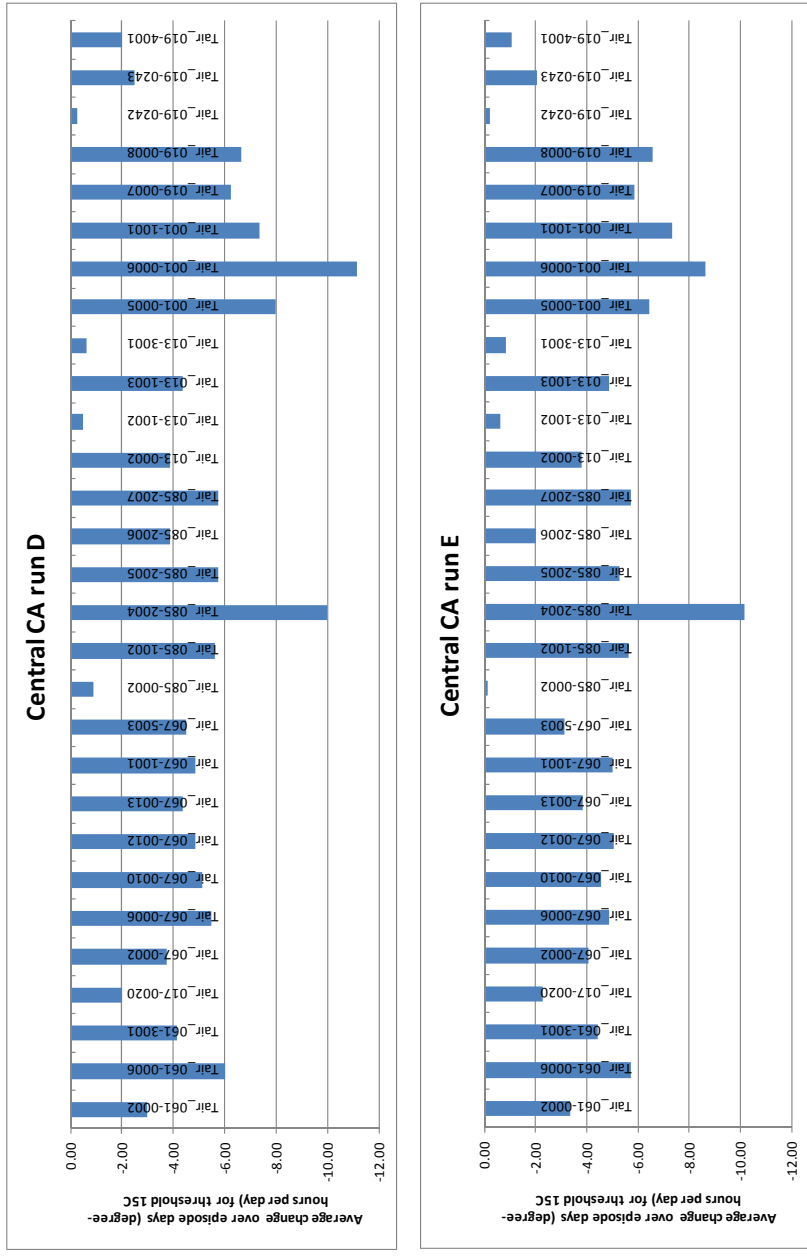
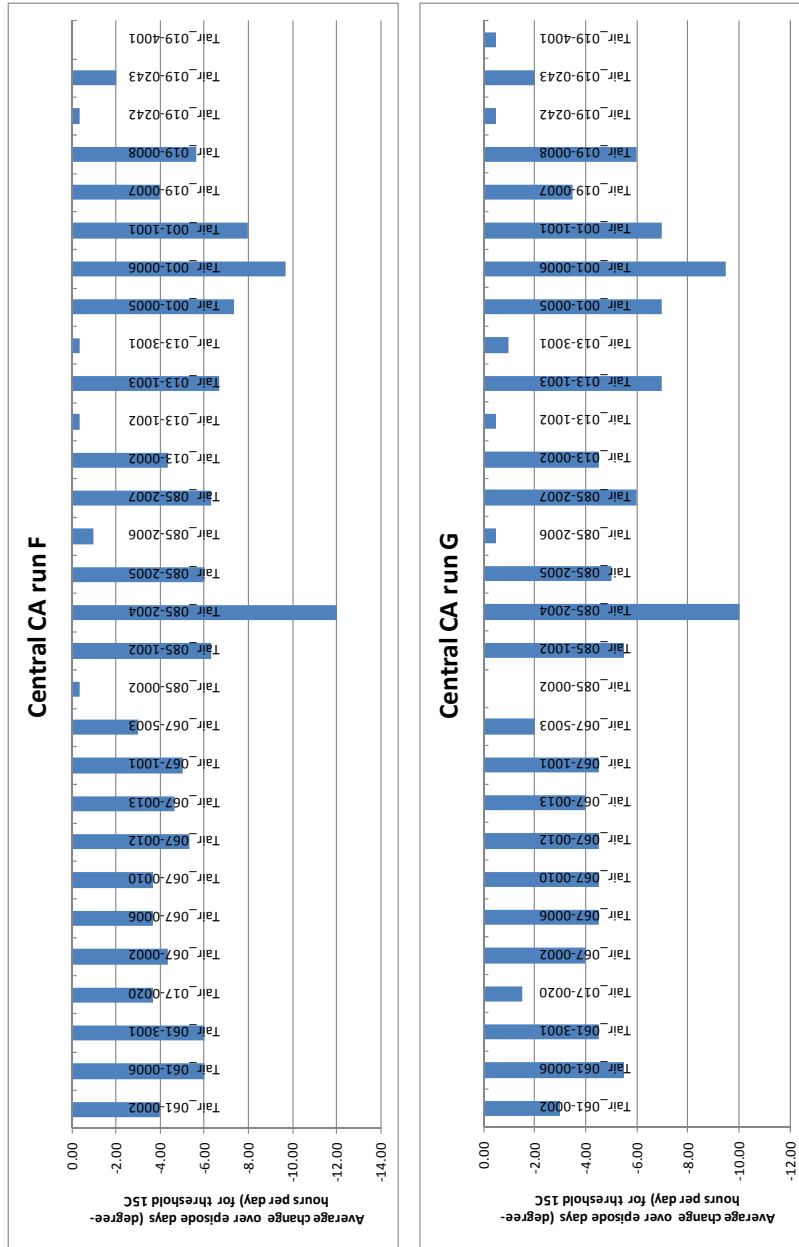
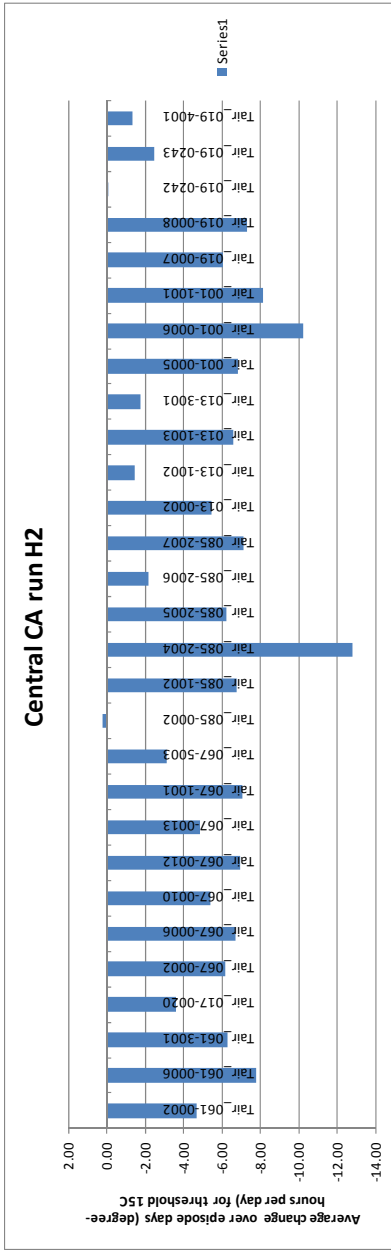
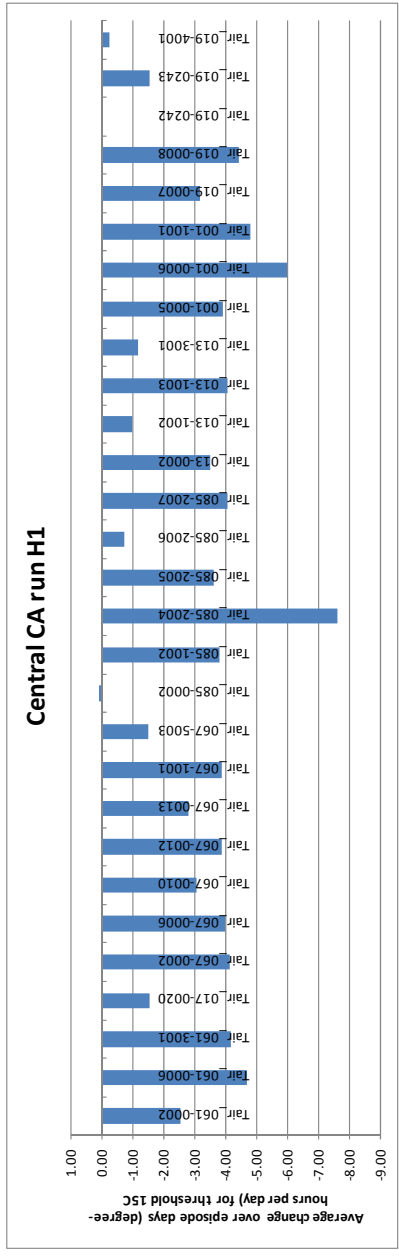


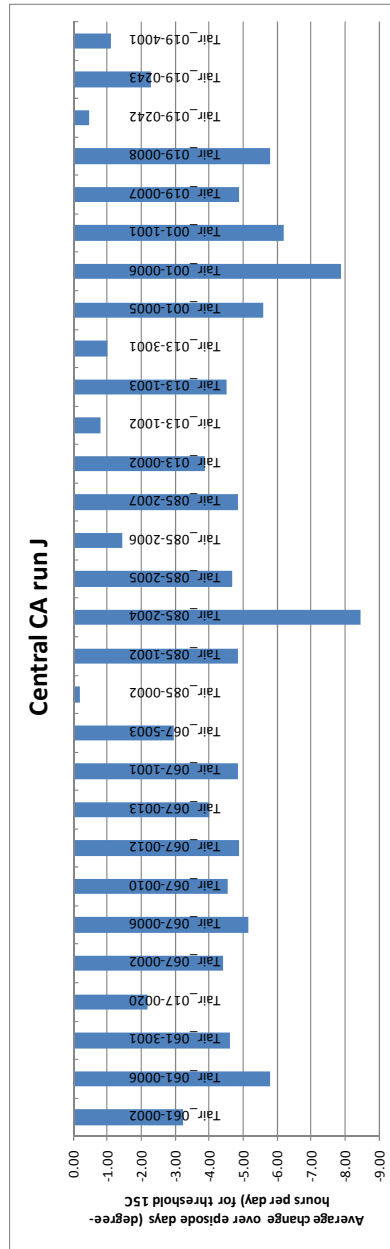
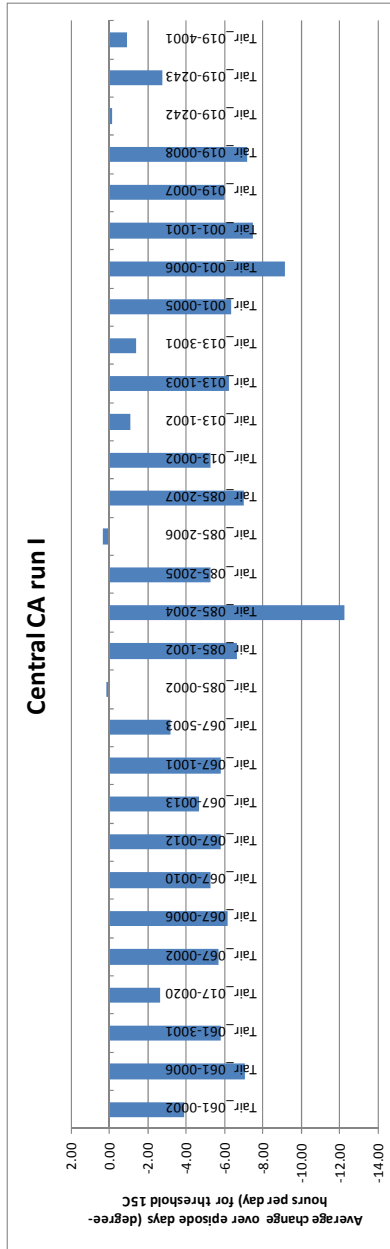
Figure D7 and D8. Differences in Degree-hours per Day (C-hr/day) at Monitors in Central California for Runs D and E



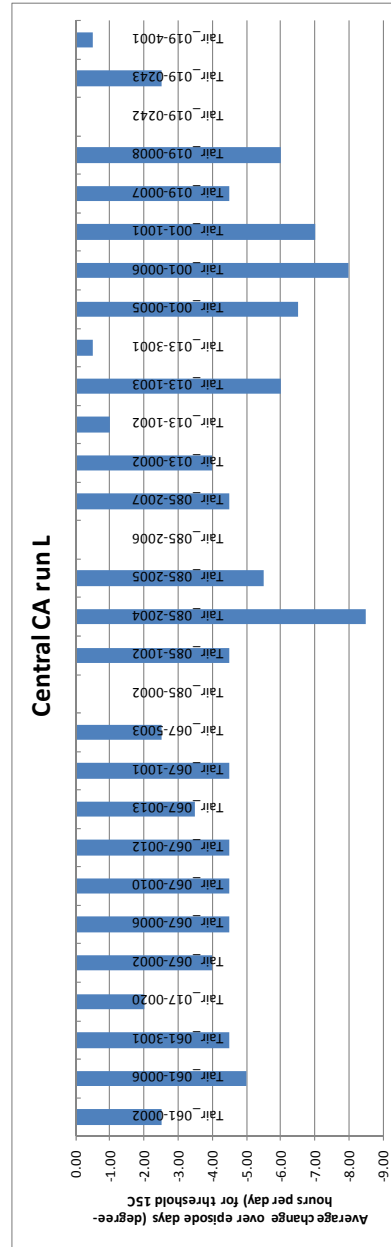
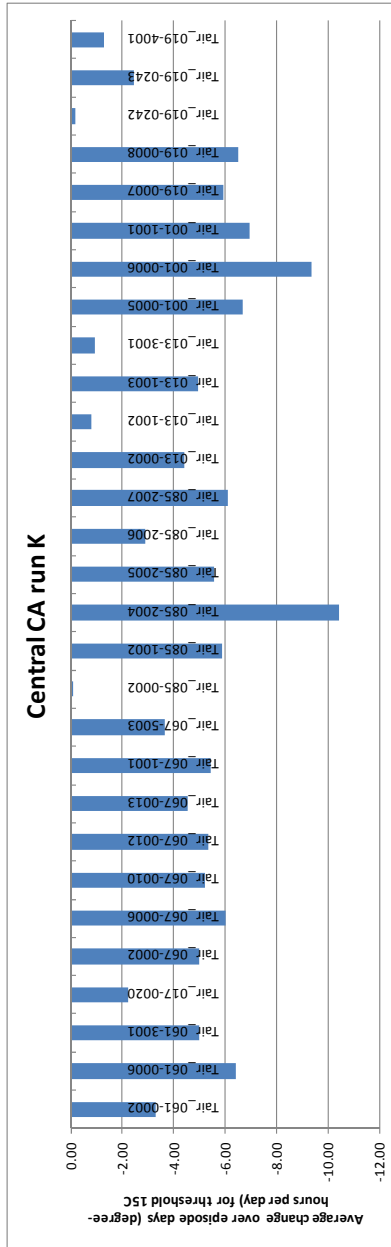
Figures D9 and D10. Differences in Degree-hours per Day (C-hr/day) at Monitors in Central California for Runs F and G



**Figures D11 and D12. Differences in Degree-hours per Day (C-hr/day) at Monitors in Central California for Runs H1 and H2**



Figures D13 and D14. Differences in Degree-hours per Day (C-hr/day) at Monitors in Central California for Runs I and J



Figures D15 and D16. Differences in Degree-hours per Day (C-hr/day) at Monitors in Central California for Runs K and L

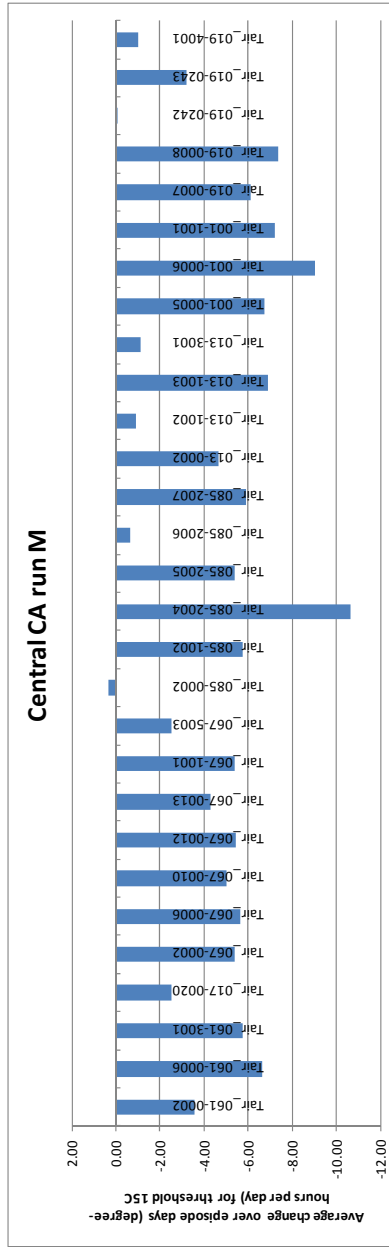


**Figure D17. Differences in Degree-hours per Day (C-hr/day) at Monitors in Central California for Run M**

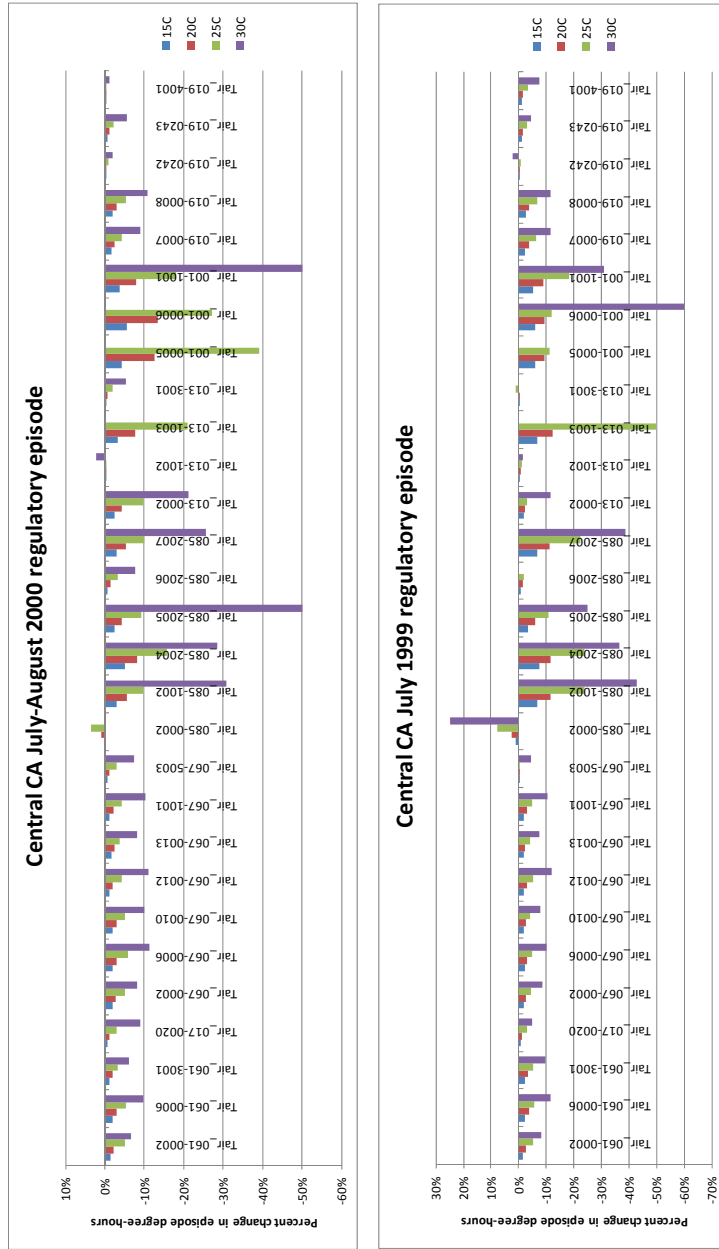
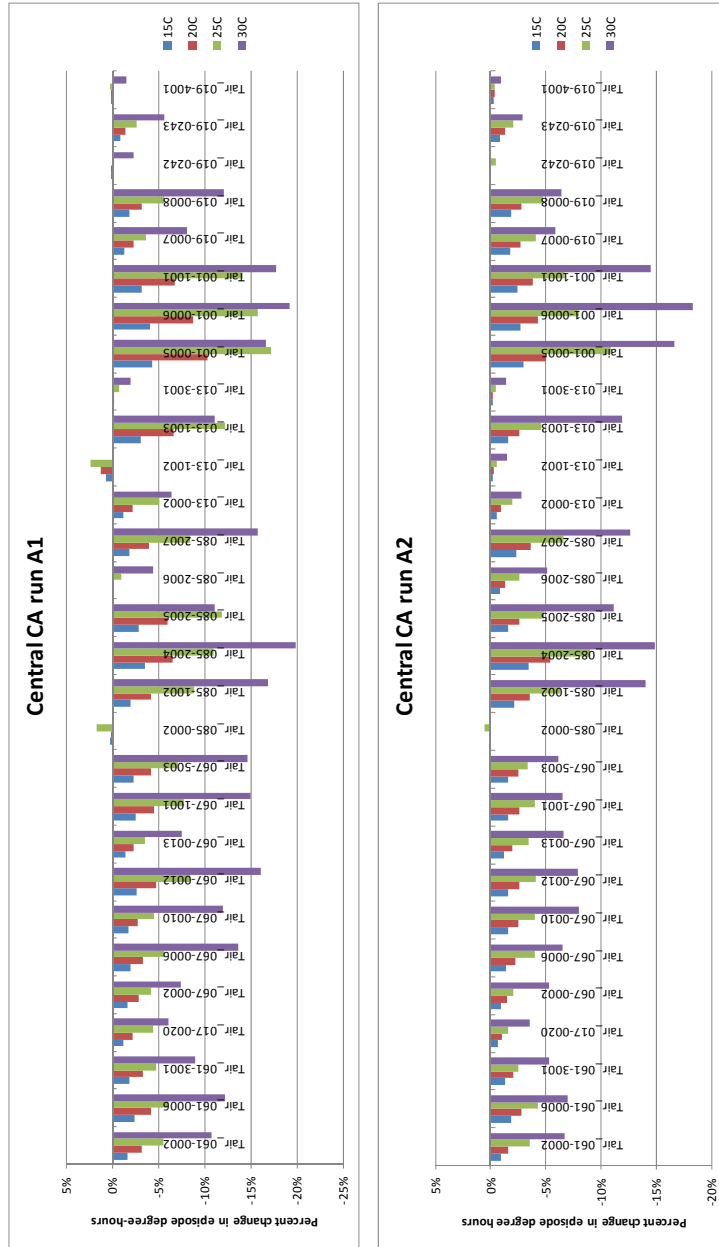
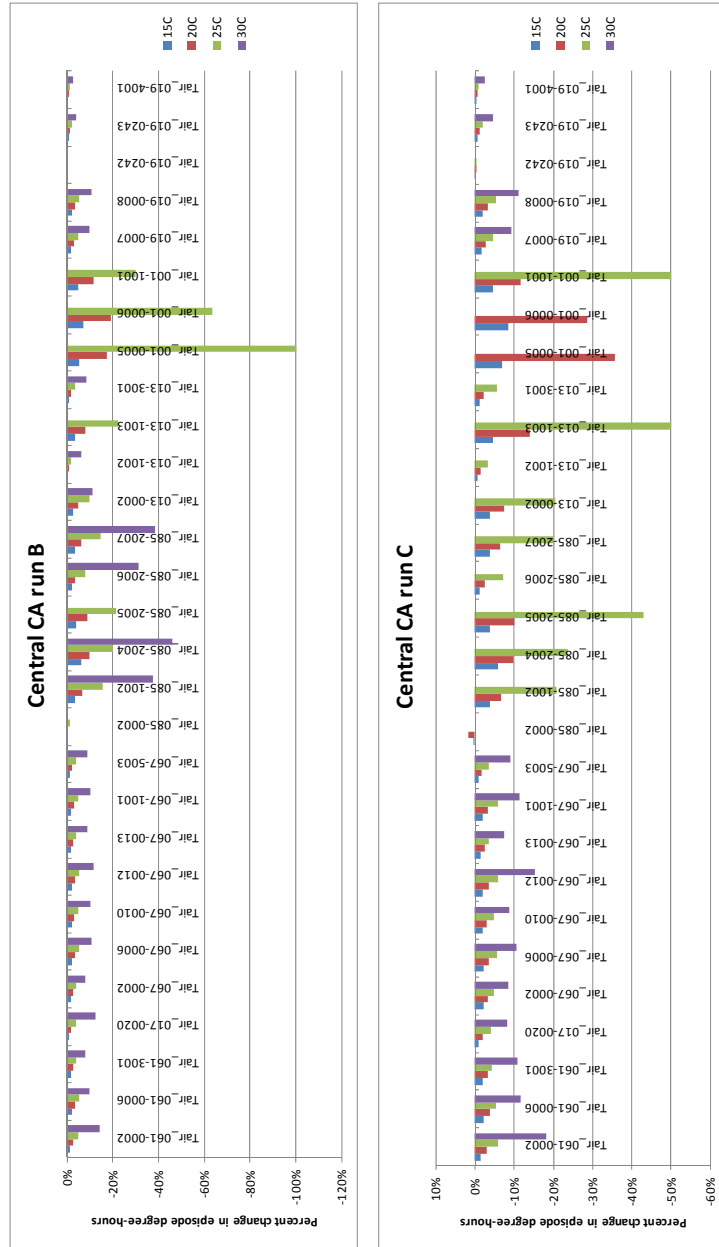


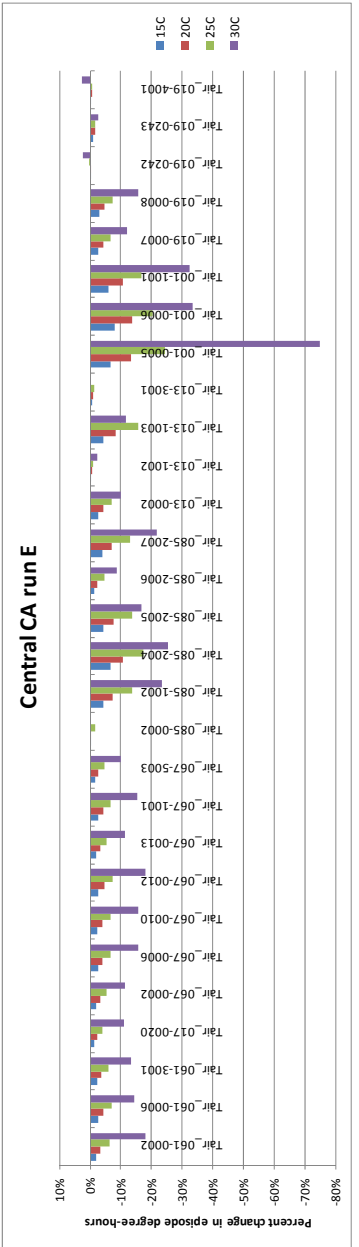
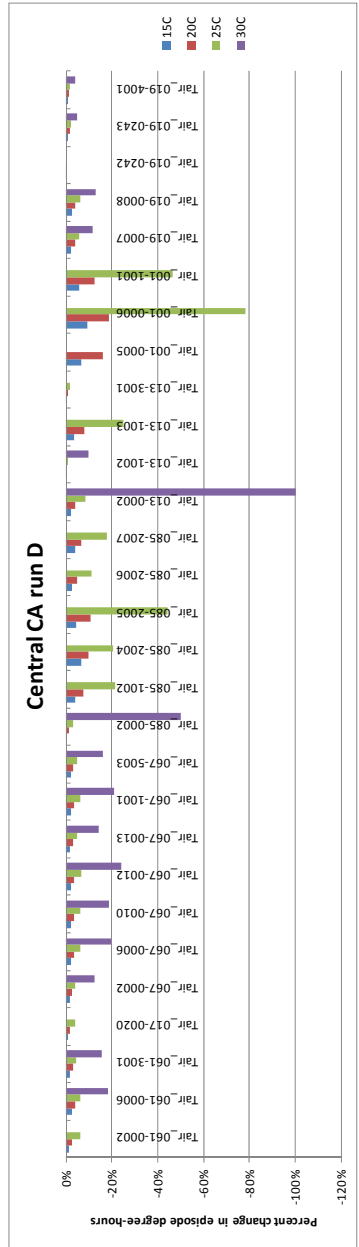
Figure D18 and D19. Relative Changes (%) in Degree-hours at Monitors in Central California for Runs 2000 and 1999 and Four Temperature Thresholds



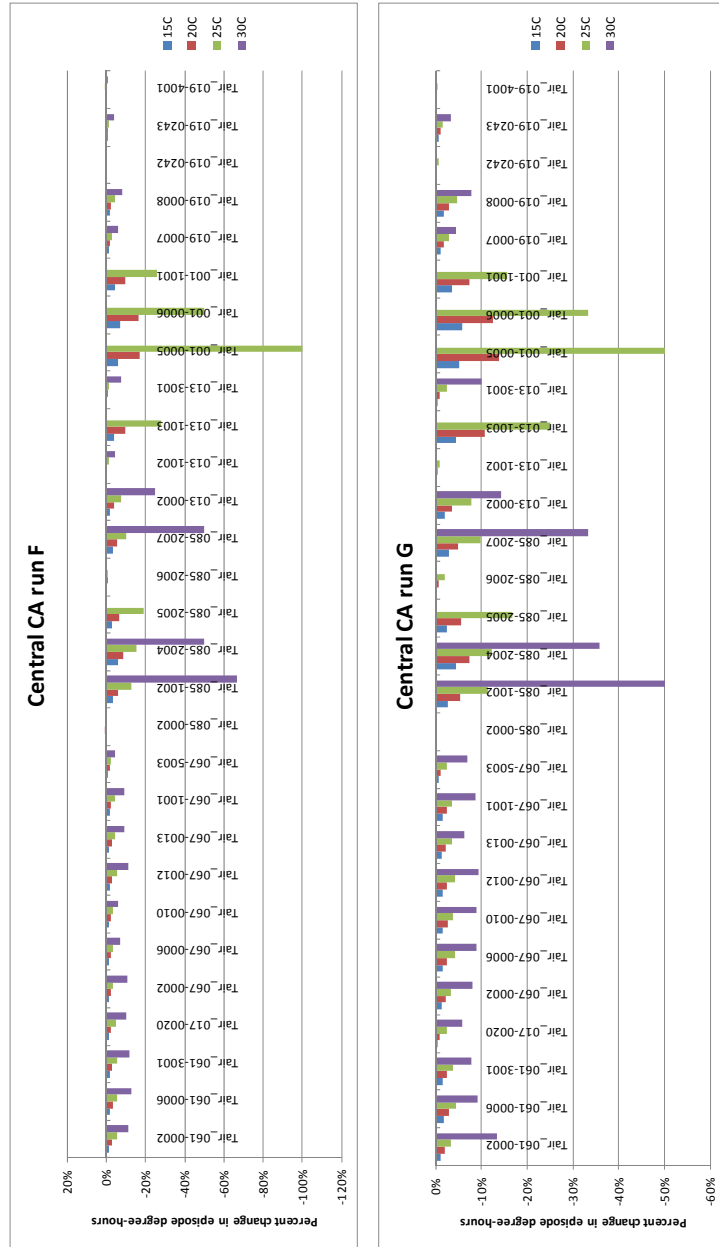
Figures D20 and D21. Relative Changes (%) in Degree-hours at Monitors in Central California for Runs A1 and A2 and Four Temperature Thresholds



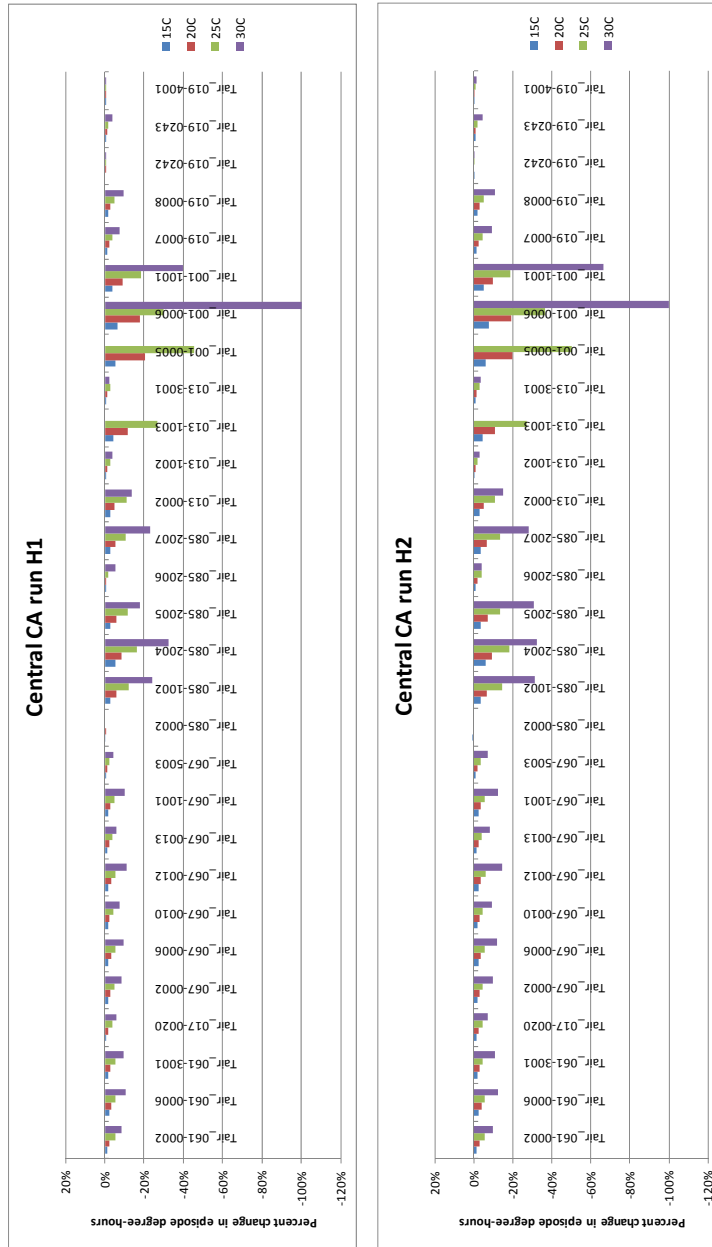
Figures D22 and D23. Relative Changes (%) in Degree-hours at Monitors in Central California for Runs B and C and Four Temperature Thresholds



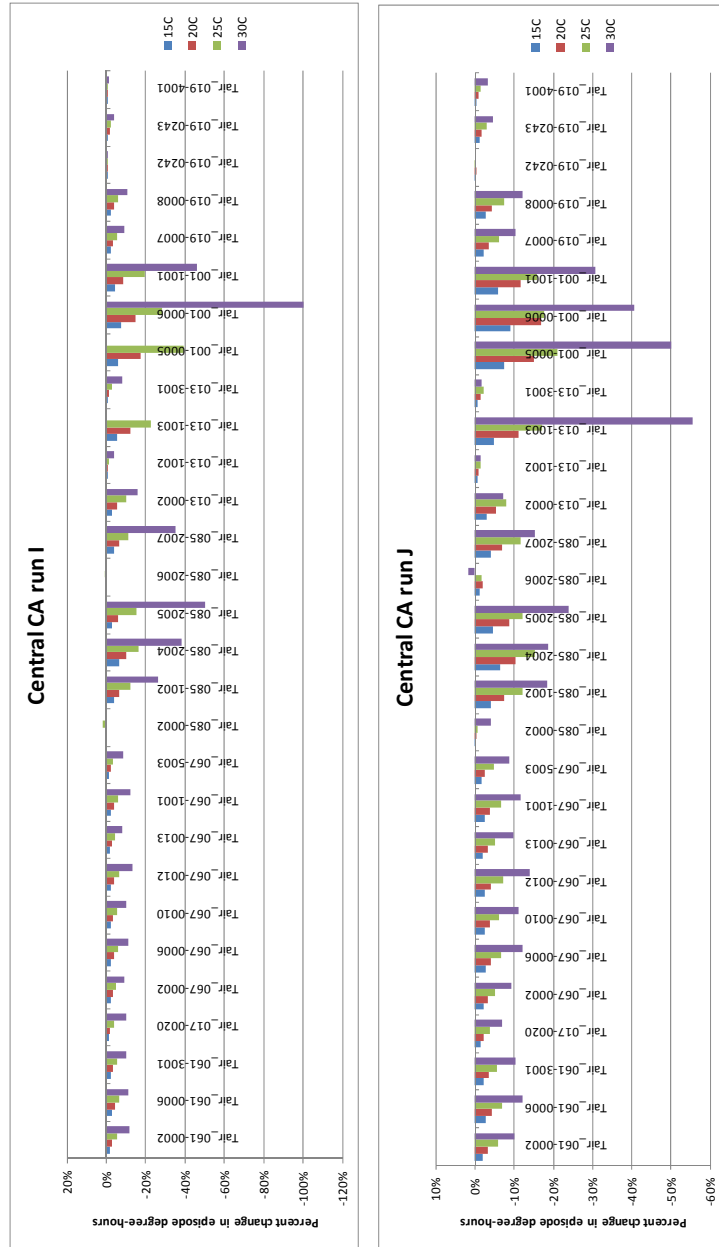
**Figures D24 and D25. Relative Changes (%) in Degree-hours at Monitors in Central California for Runs D and E and Four Temperature Thresholds**



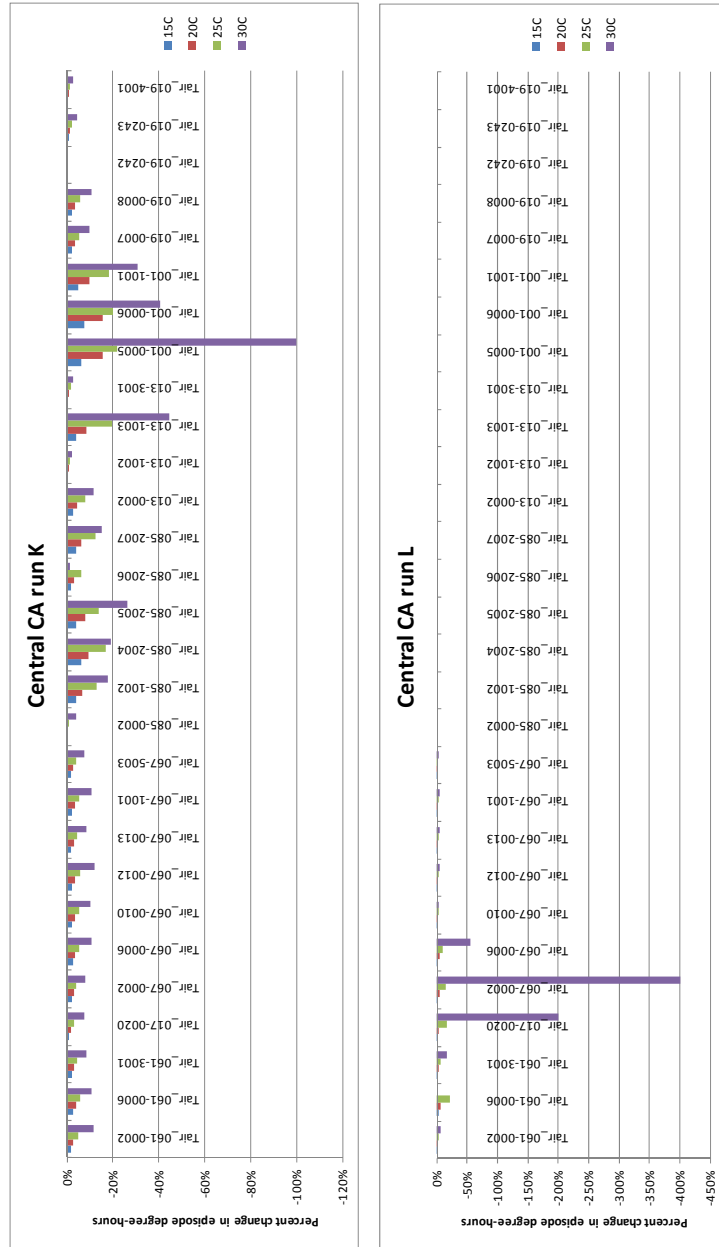
Figures D26 and D27. Relative Changes (%) in Degree-hours at Monitors in Central California for Runs F and G and Four Temperature Thresholds



Figures D28 and D29. Relative Changes (%) in Degree-hours at Monitors in Central California for Runs H1 and H2 and Four Temperature Thresholds



Figures D30 and D31. Relative Changes (%) in Degree-hours at Monitors in Central California for Runs I and J and Four Temperature Thresholds



Figures D32 and D33. Relative Changes (%) in Degree-hours at Monitors in Central California for Runs K and L and Four Temperature Thresholds

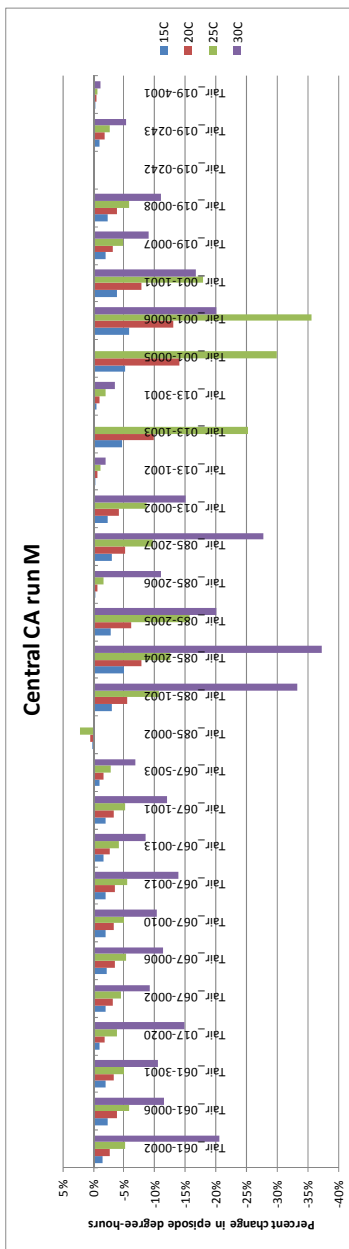
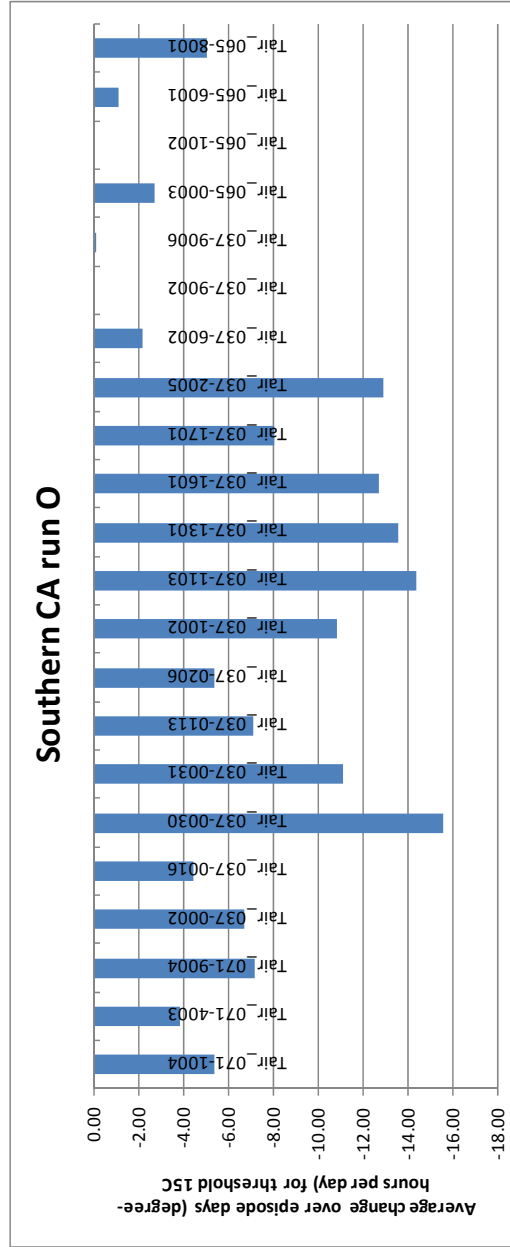
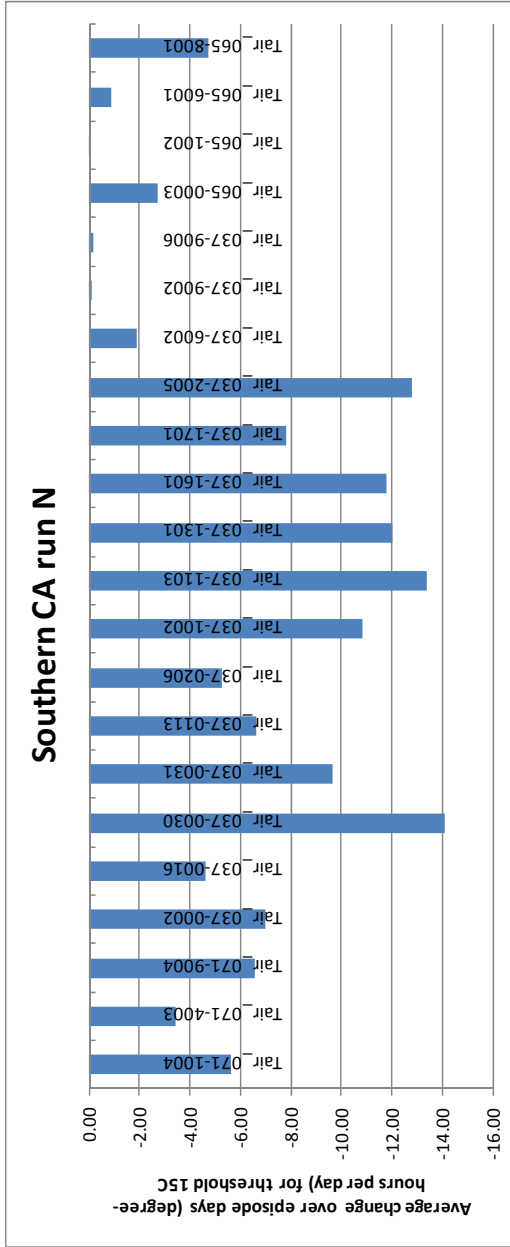
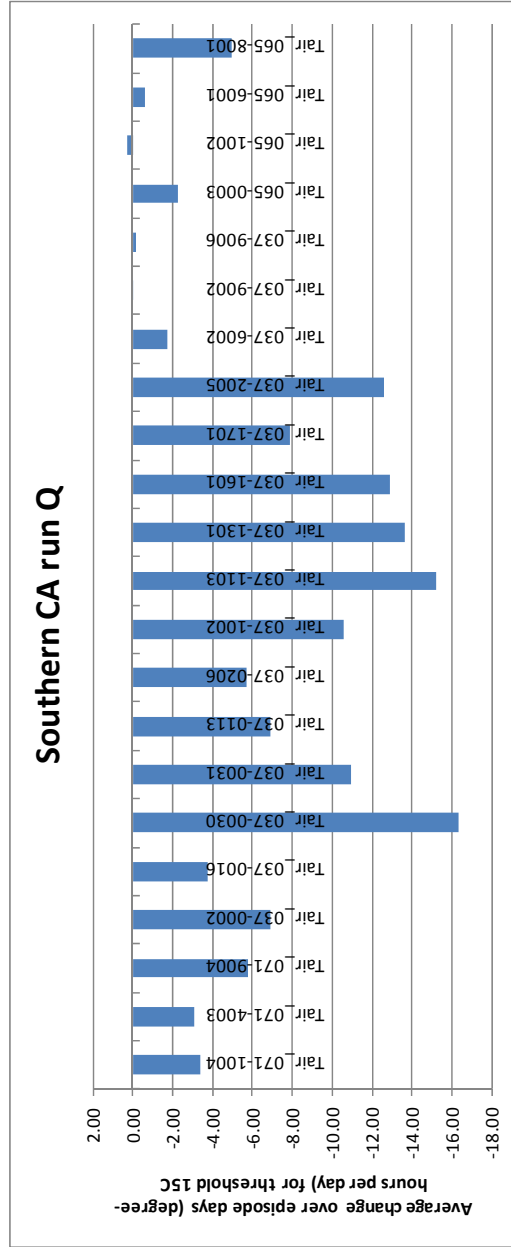
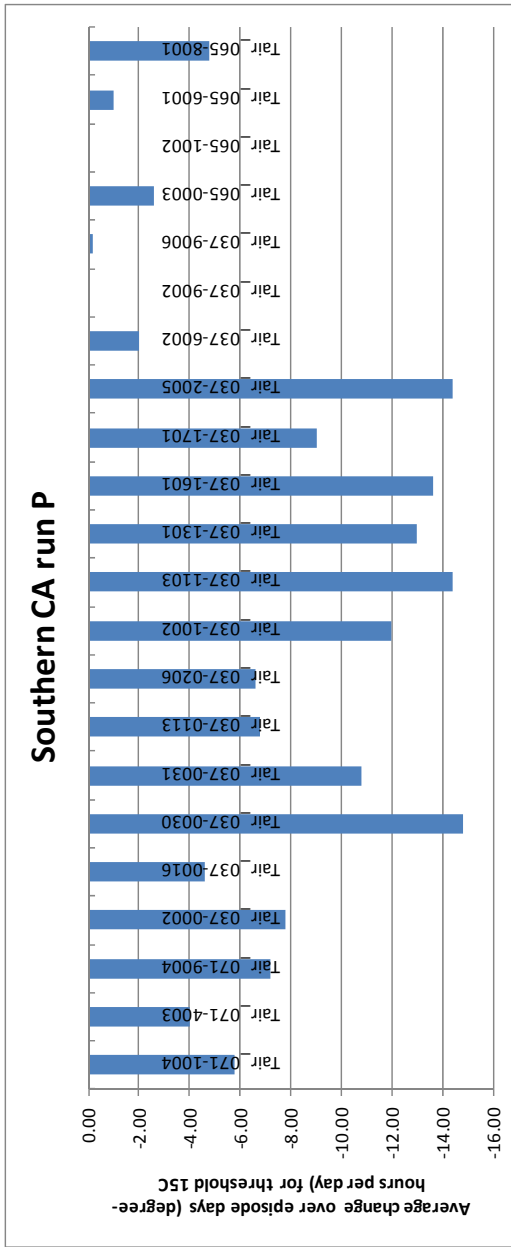


Figure D34. Relative Changes (%) in Degree-hours at Monitors in Central California for Run M and Four Temperature Thresholds



Figures D35 and D36. Differences in Degree-hours per Day (C-hr/day) at Monitors in Southern California for Runs N and O



Figures D37 and D38. Differences in Degree-hours per Day (C-hr/day) at Monitors in Southern California for Runs P and Q

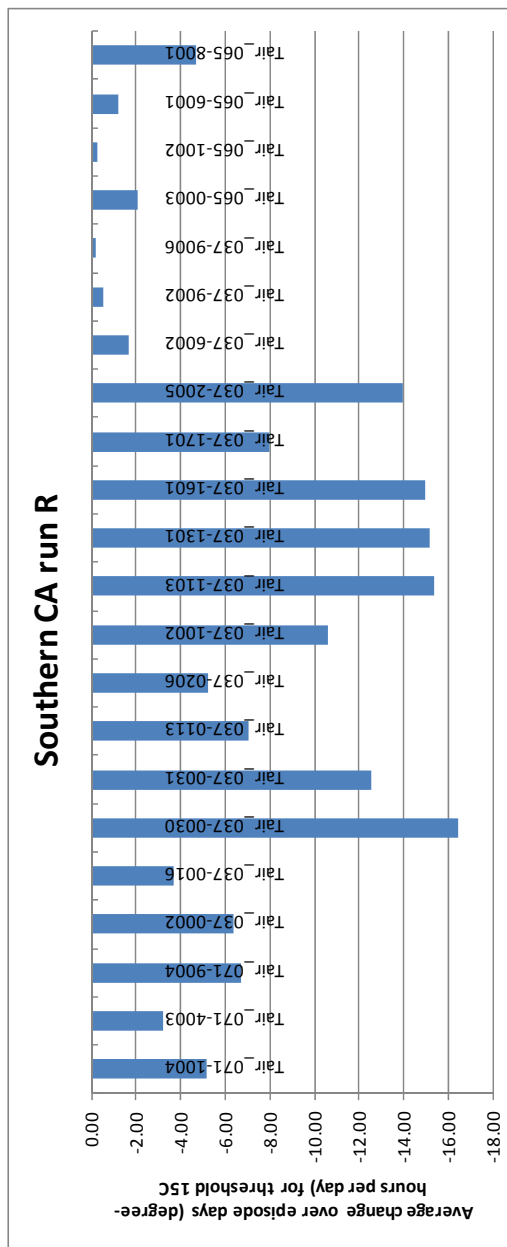
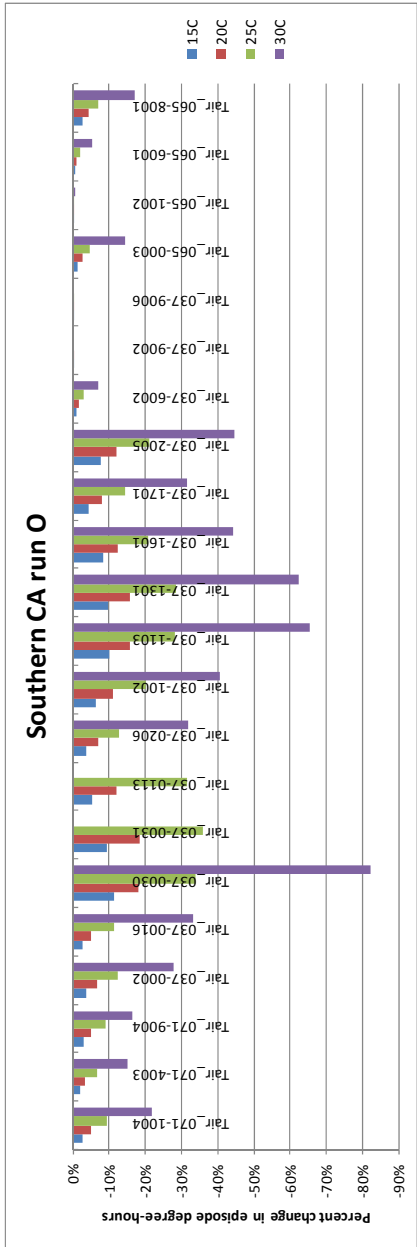
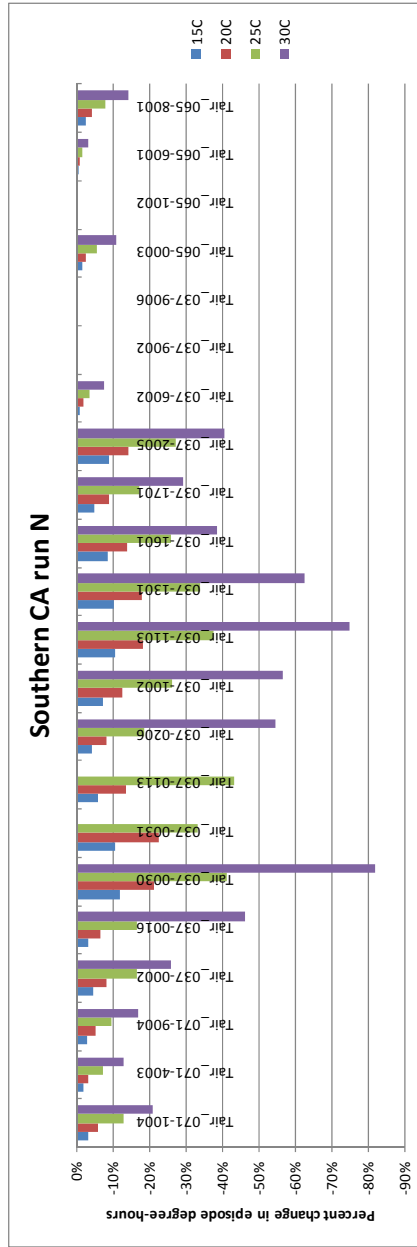
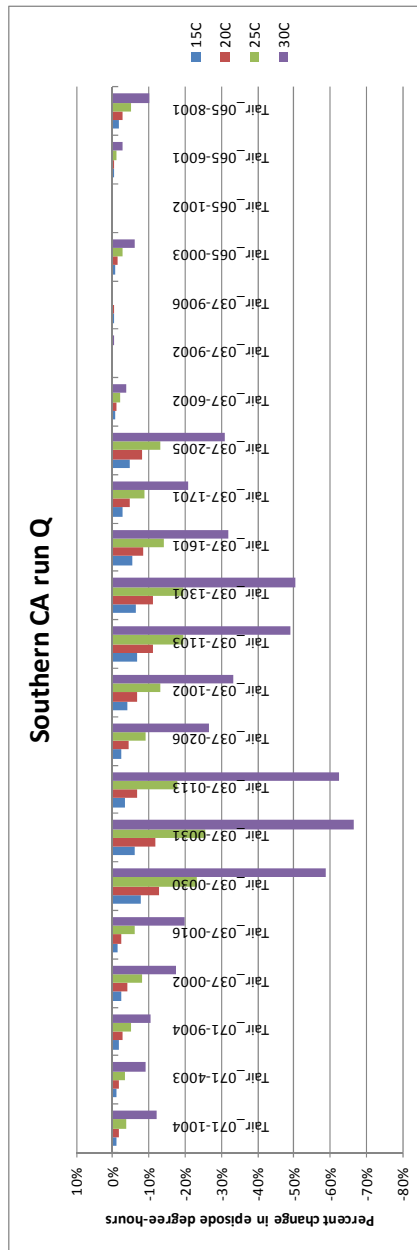
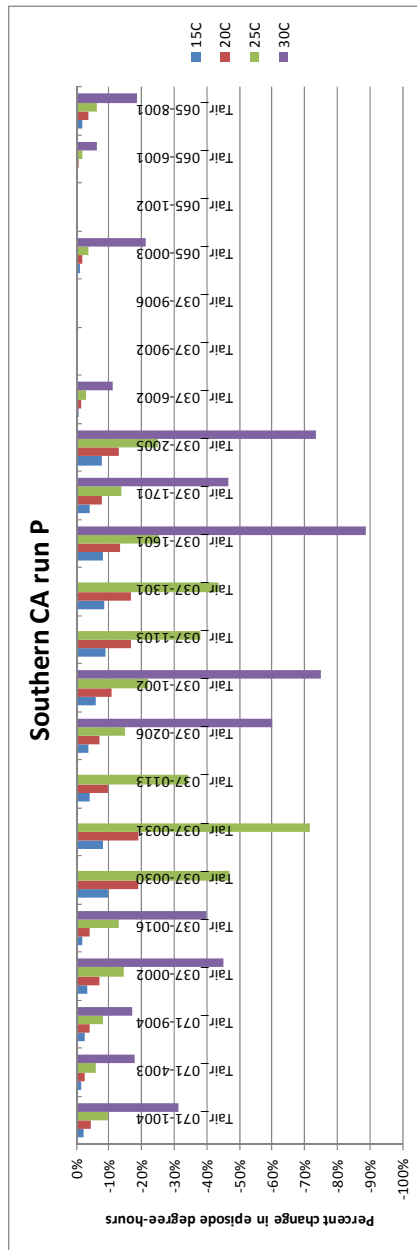


Figure D39. Differences in Degree-hours per Day (C-hr/day) at Monitors in Southern California for Run R



Figures 40 and 41. Relative Changes (%) in Degree-hours at Monitors in Southern California for Runs N and O and Four Temperature Thresholds



Figures D42 and D43. Relative Changes (%) in Degree-hours at Monitors in Southern California for Runs P and Q and Four Temperature Thresholds

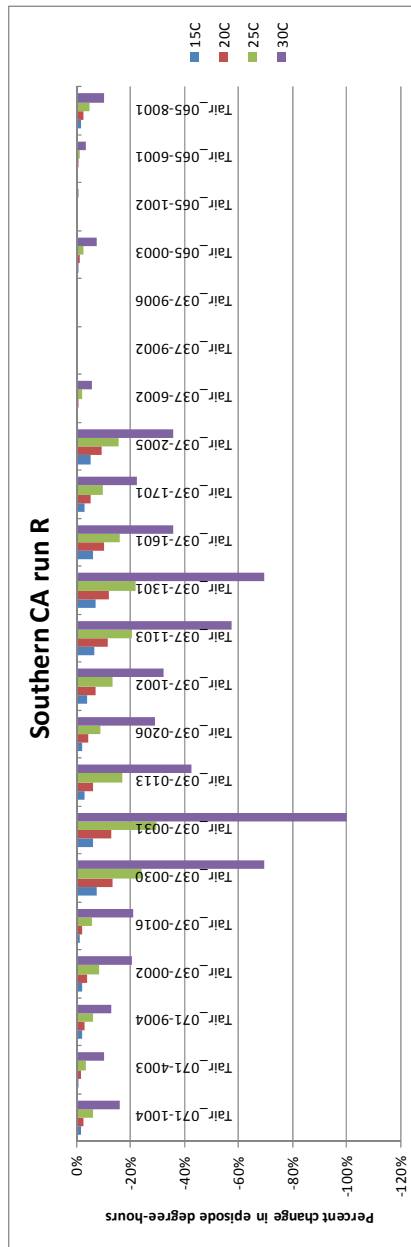


Figure D44. Relative Changes (%) in Degree-hours at Monitors in Southern California for Run R and Four Temperature Thresholds

# **Appendix E: Degree-hour Changes Time Series**

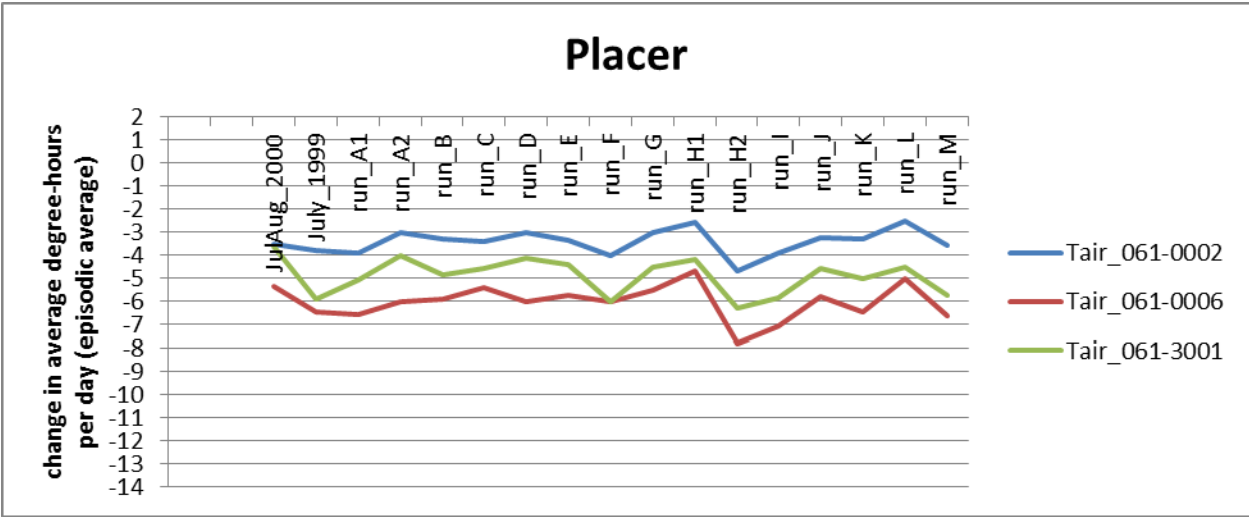


Figure E-1. Changes in Degree-hours per Day (C-hr/day) at Monitors in Placer County

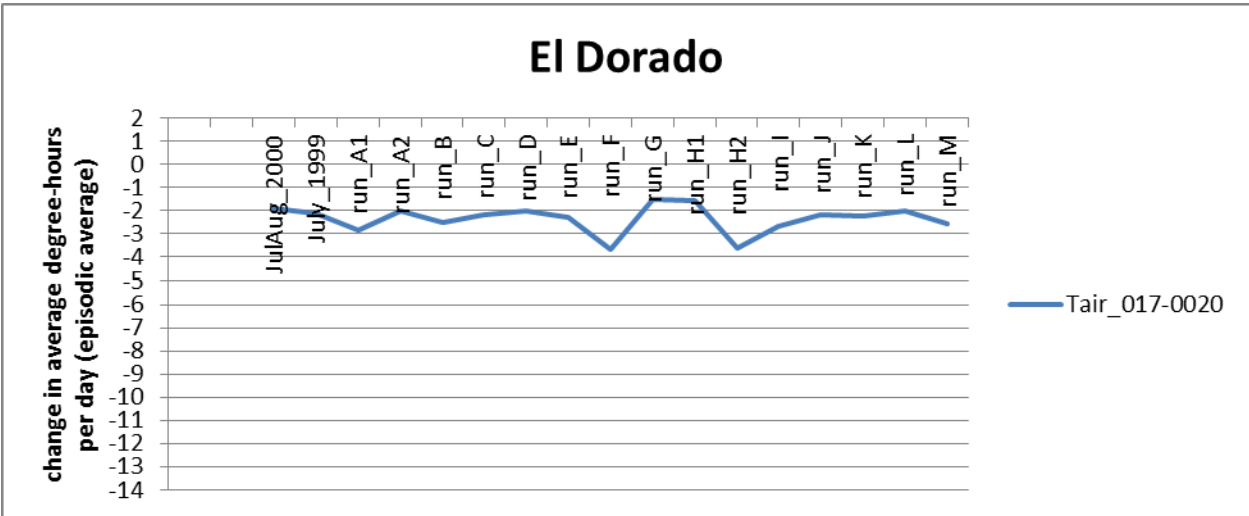


Figure E-2. Changes in Degree-hours per Day (C-hr/day) at Monitors in El Dorado County

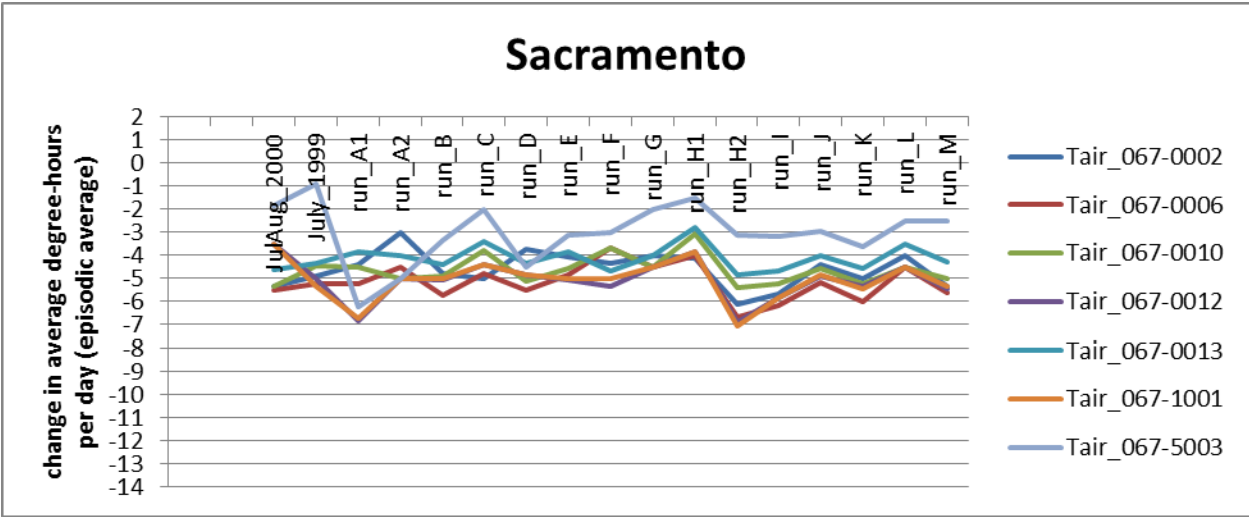


Figure E-3. Changes in Degree-hours per Day (C-hr/day) at Monitors in Sacramento County

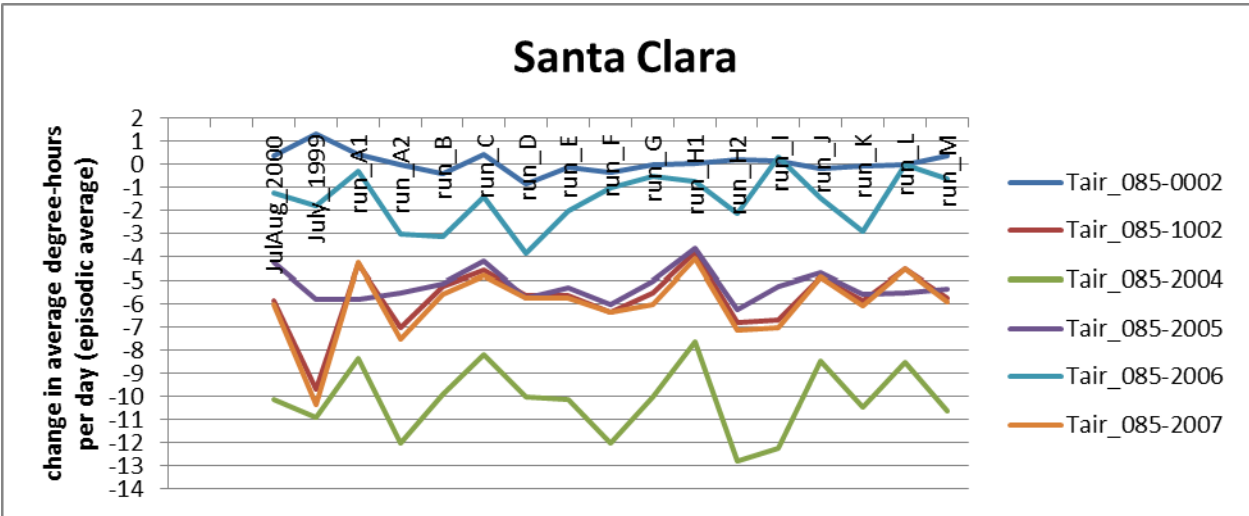


Figure E-4. Changes in Degree-hours per Day (C-hr/day) at Monitors in Santa Clara County

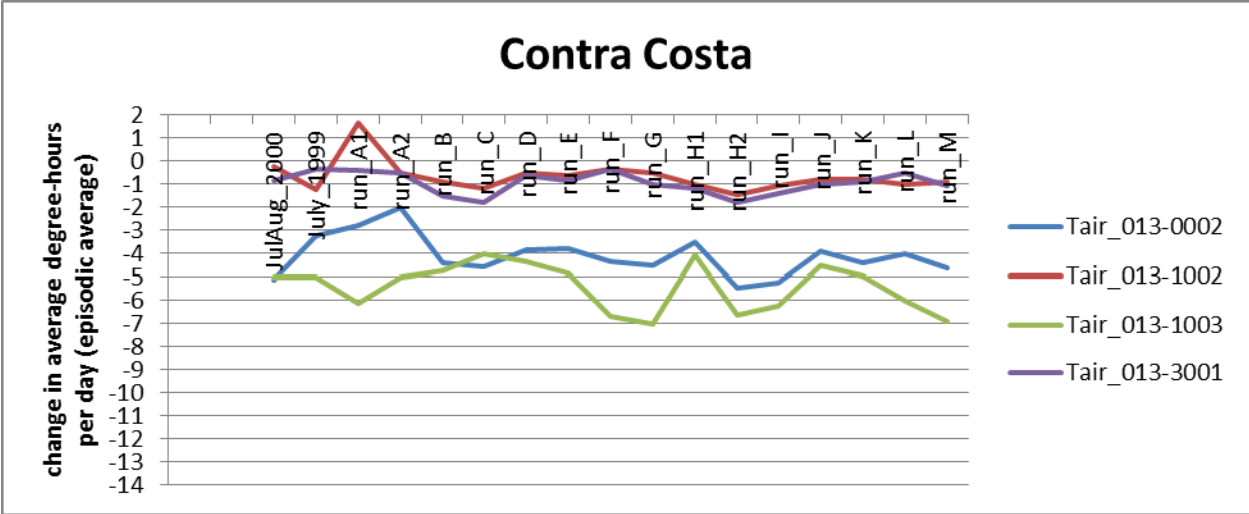


Figure E-5. Changes in Degree-hours per Day (C-hr/day) at Monitors in Contra Costa County

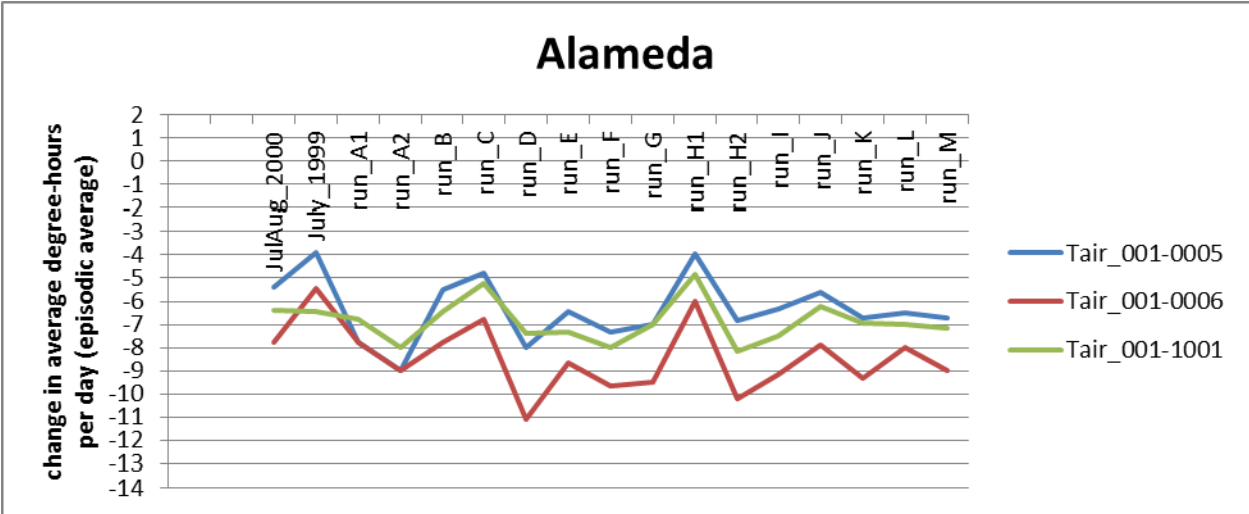


Figure E-6. Changes in Degree-hours per Day (C-hr/day) at Monitors in Alameda County

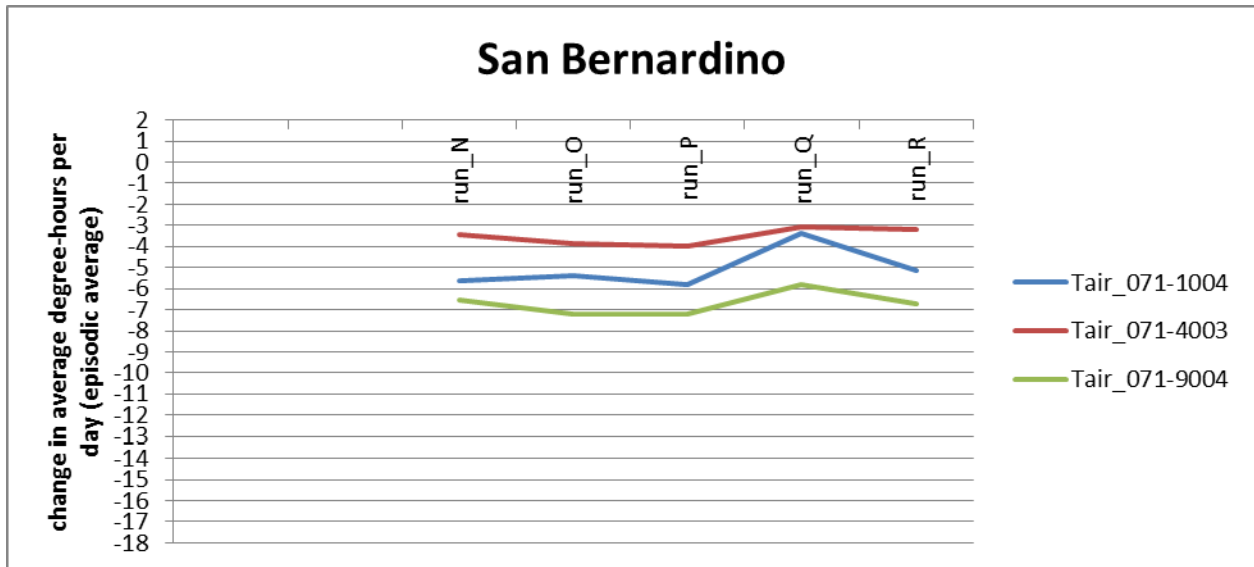


Figure E-7. Changes in Degree-hours per Day (C-hr/day) at Monitors in San Bernardino County

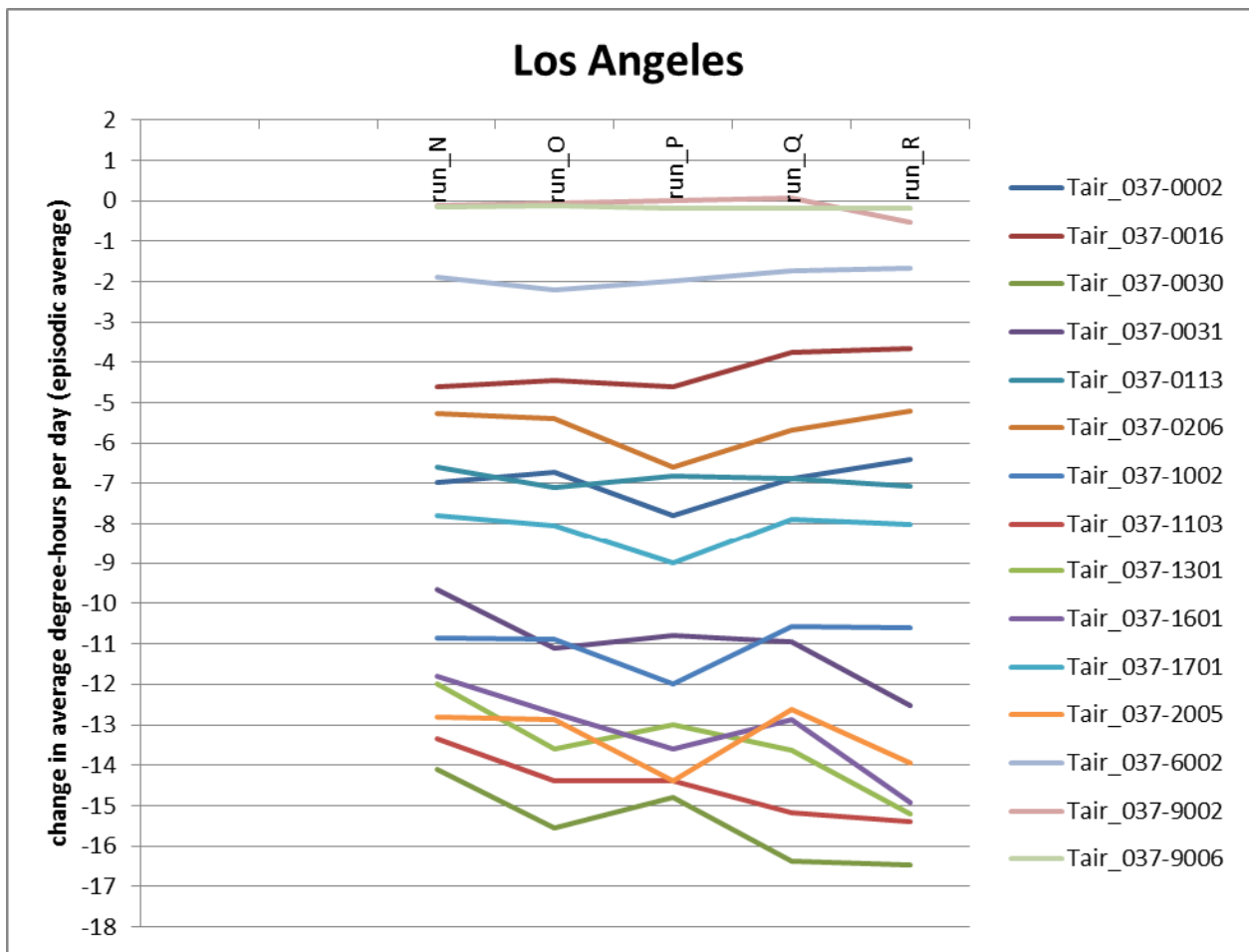


Figure E-8. Changes in Degree-hours per Day (C-hr/day) at Monitors in Los Angeles County

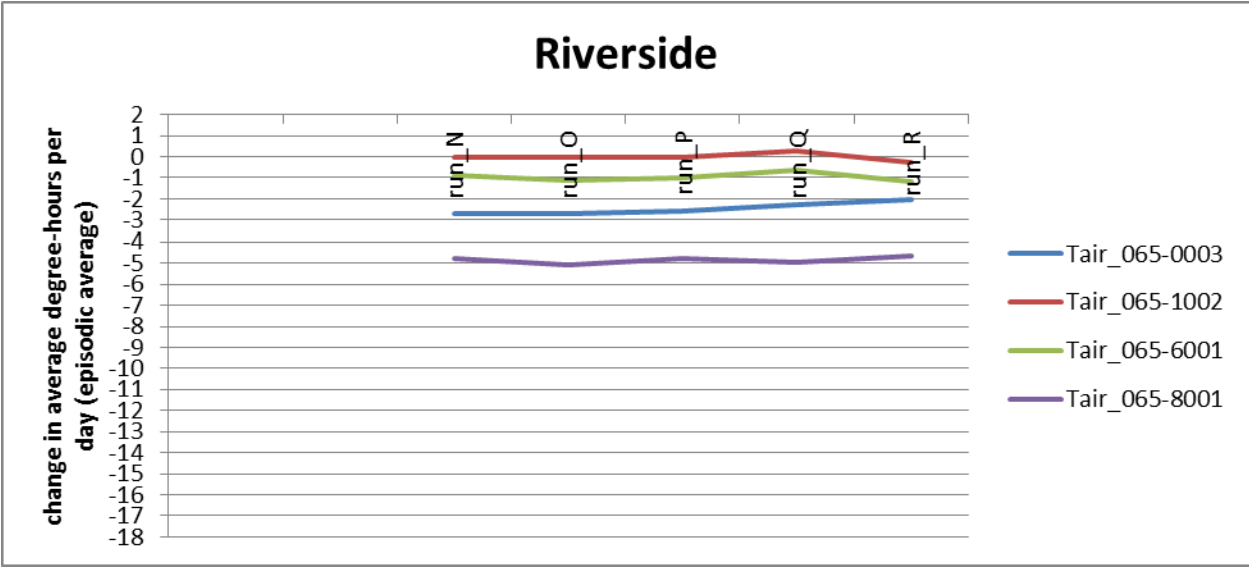


Figure E-9. Changes in Degree-hours per Day (C-hr/day) at Monitors in Riverside County

Dataset: case00 RIP: ripexecute.cloud Init: 0000 UTC Thu 04 Jul 02  
Fcst: 18.00 h Valid: 1800 UTC Thu 04 Jul 02 (1100 PDT Thu 04 Jul 02)  
Cloud water mixing ratio at k-index = 26  
Horizontal wind vectors at k-index = 26

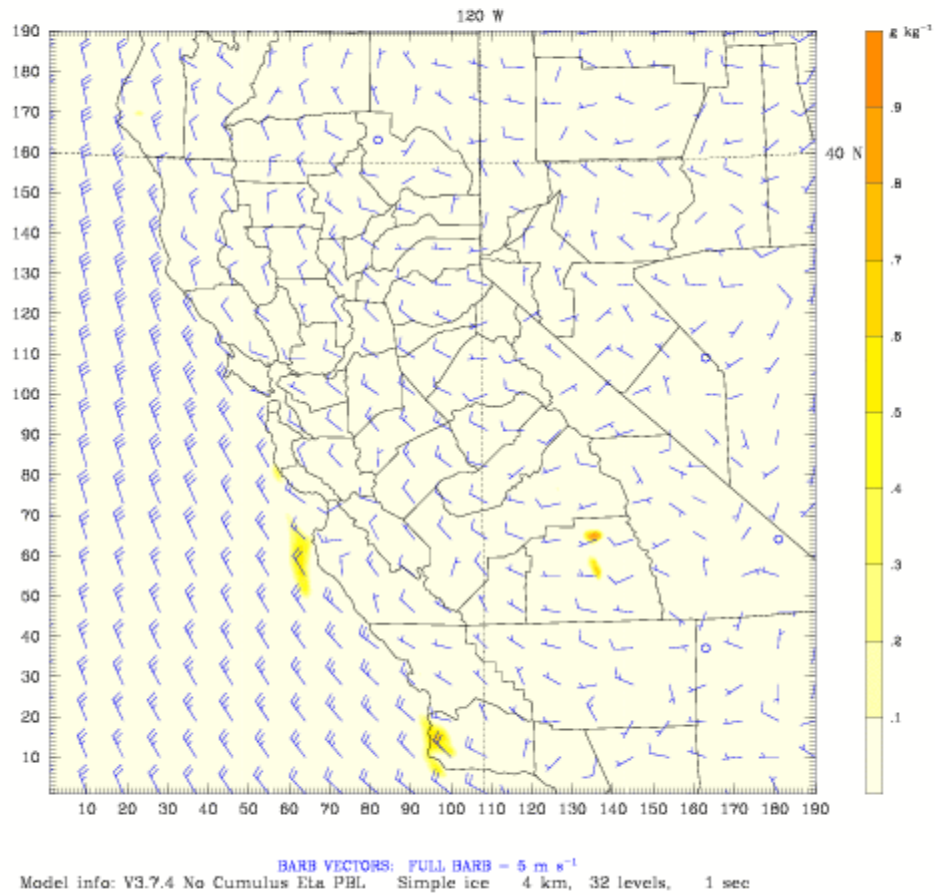


Figure E-10. Sample Output from Run H1 (Episode H1) Showing Flow Field and Low-Level Clouds (Cloud Water  $\text{g kg}^{-1}$ ) on 4 July 2002 at 1100 PDT

Dataset: case20 RIP: ripexecute.cloud Init: 0000 UTC Wed 10 Jul 02  
Pest: 279.00 h Valid: 1500 UTC Sun 21 Jul 02 (0800 PDT Sun 21 Jul 02)  
Cloud water mixing ratio at k-index = 28  
Horizontal wind vectors at k-index = 28

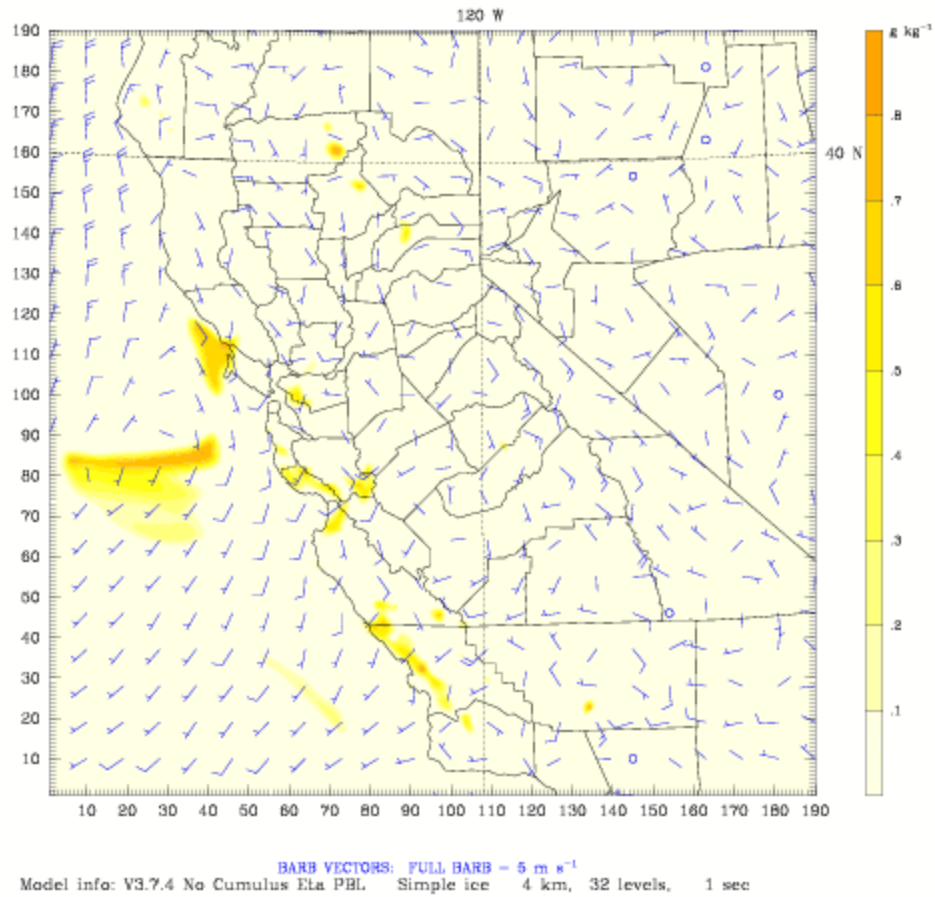


Figure E-11. Sample Output from Run H2 (Episode H2) Showing Flow Field and Low-Level Clouds (Cloud Water  $\text{g kg}^{-1}$ ) on 21 July 2002 at 0800 PDT

Dataset: case20 RIP: ripexecute.cloud Init: 0000 UTC Wed 10 Jul 02  
Pcst: 285.00 h Valid: 2100 UTC Sun 21 Jul 02 (1400 PDT Sun 21 Jul 02)  
Cloud water mixing ratio at k-index = 13  
Horizontal wind vectors at k-index = 13

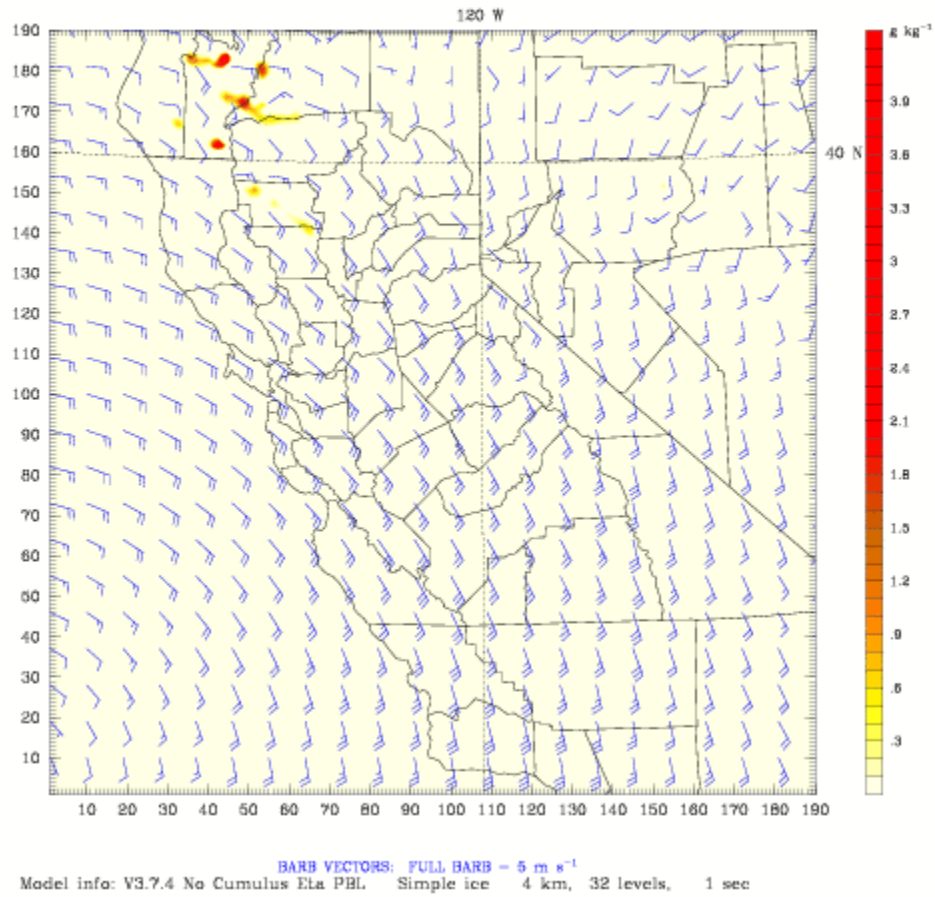
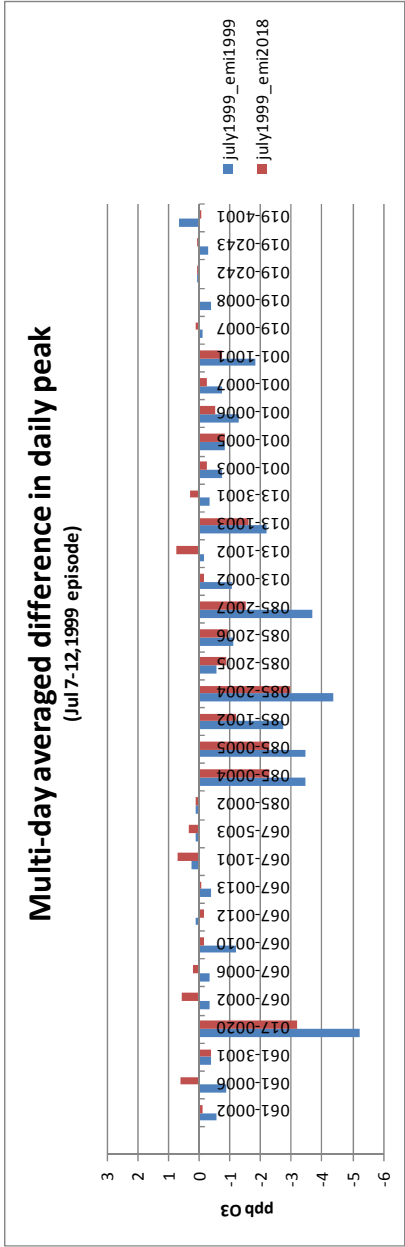
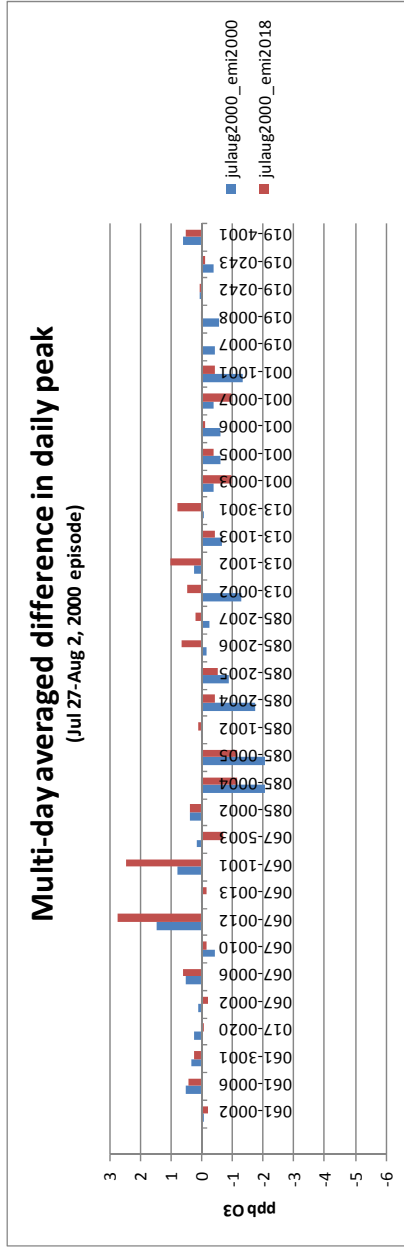
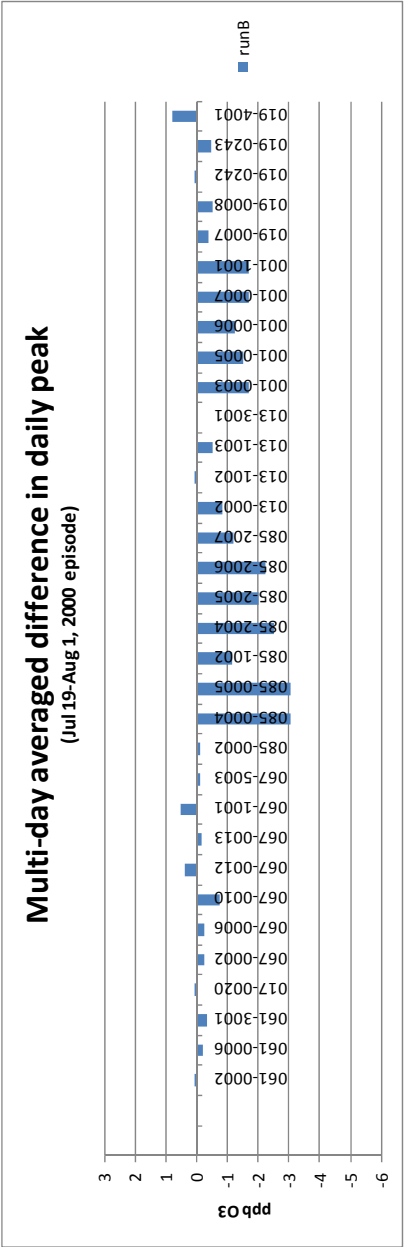
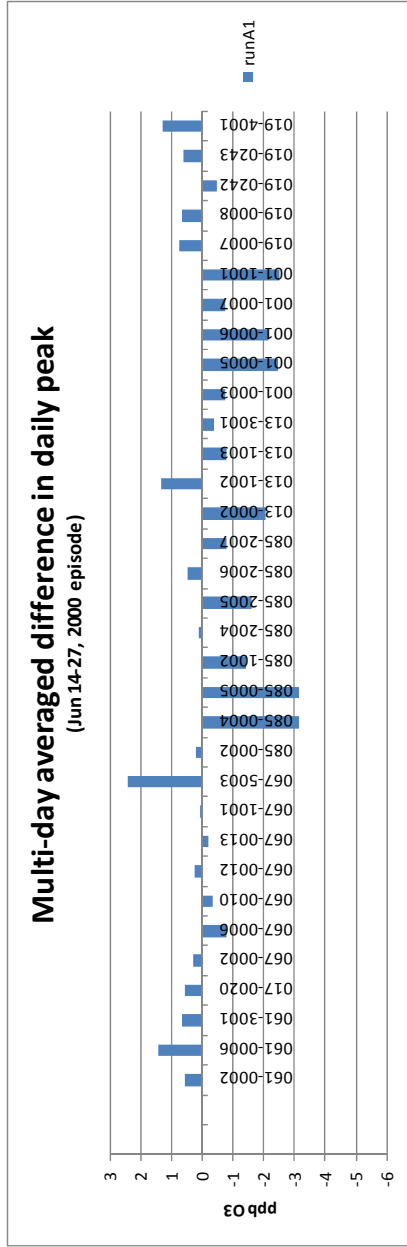


Figure E-12. Sample Output from Run H2 (Episode H2) Showing Flow Field and Middle Clouds (Cloud Water  $\text{g kg}^{-1}$ ) on 21 July 2002 at 1400 PDT

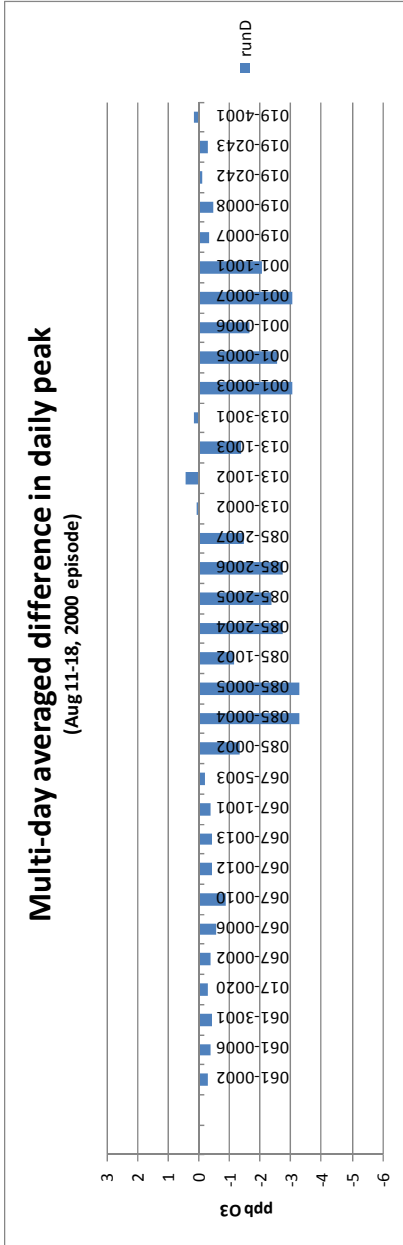
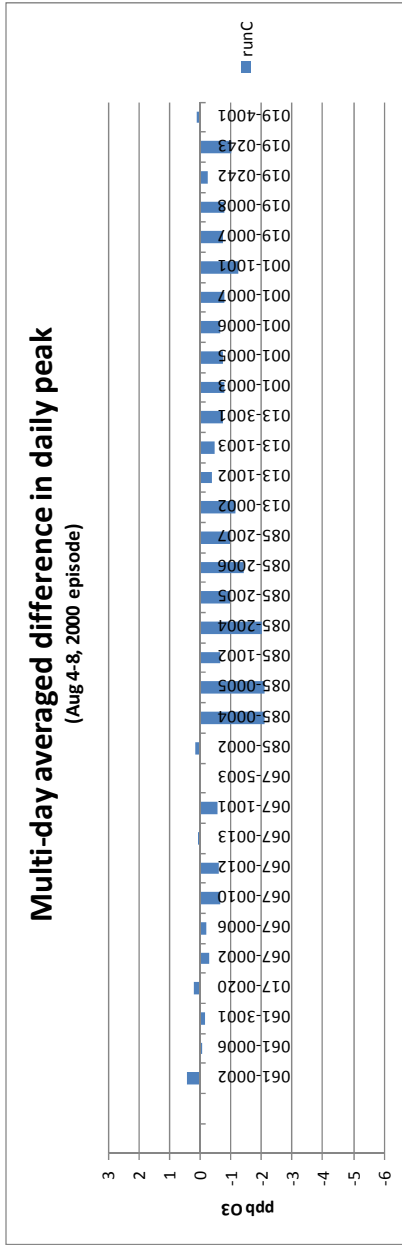
# **Appendix F: Impacts on 1-hour Peak Ozone**



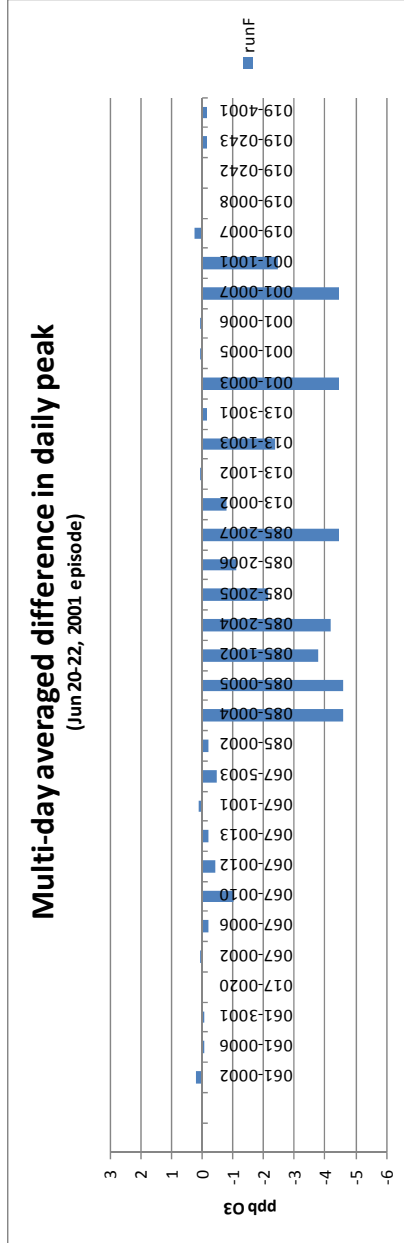
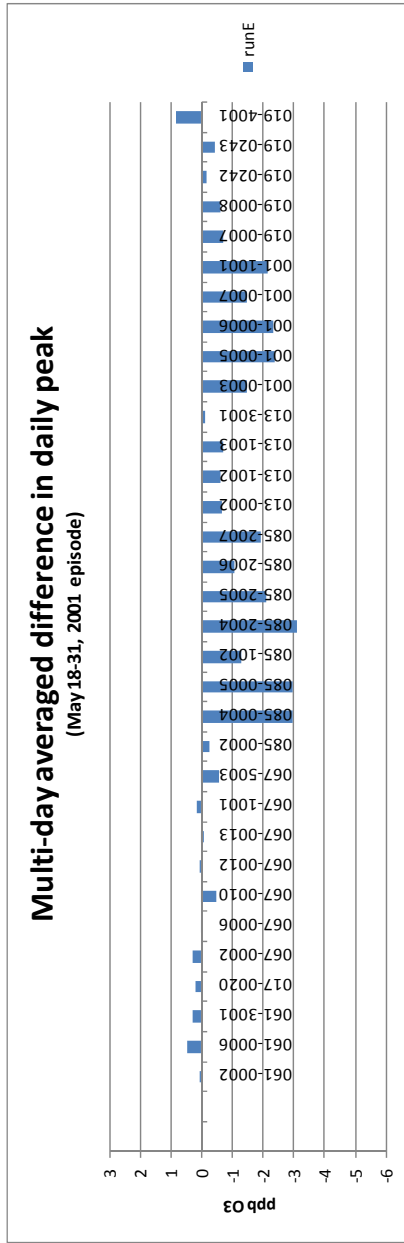
**Figures F1 and F2. Impacts on the 1-hr Peak Ozone at Monitors in Central California for Runs 2000 and 1999**



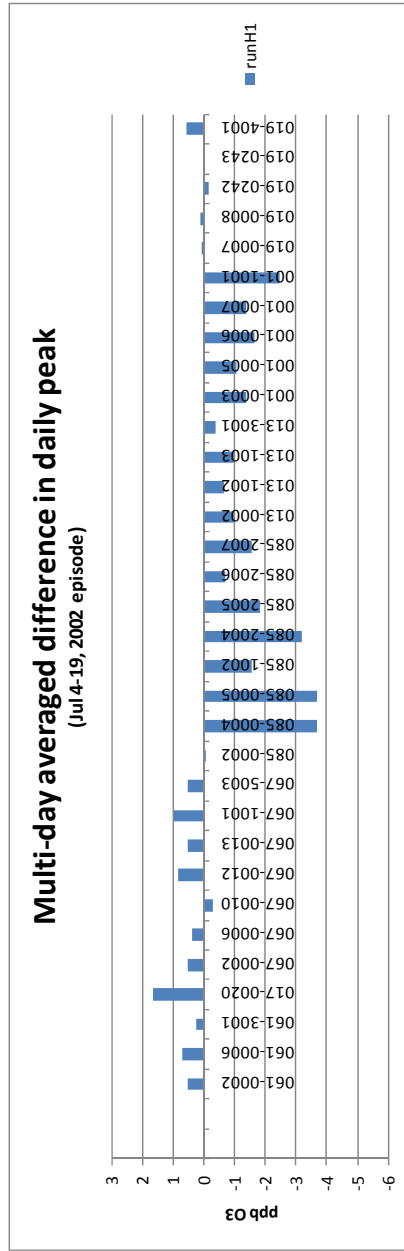
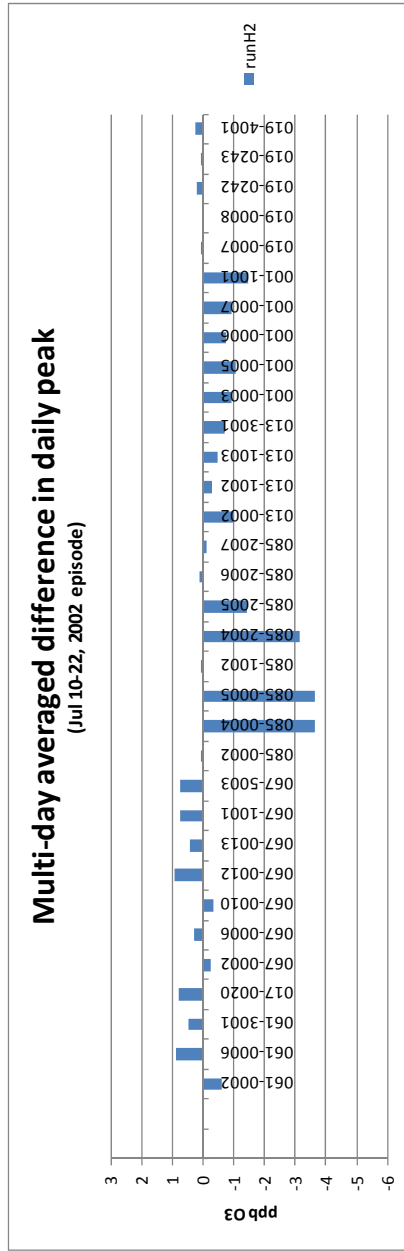
**Figures F3 and F4. Impacts on the 1-hr Peak Ozone at Monitors in Central California for Runs A1 and B**



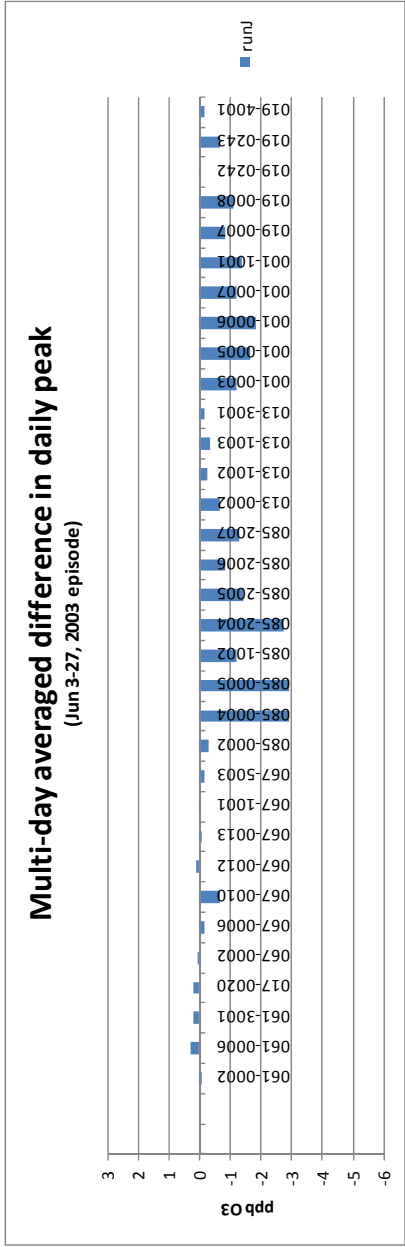
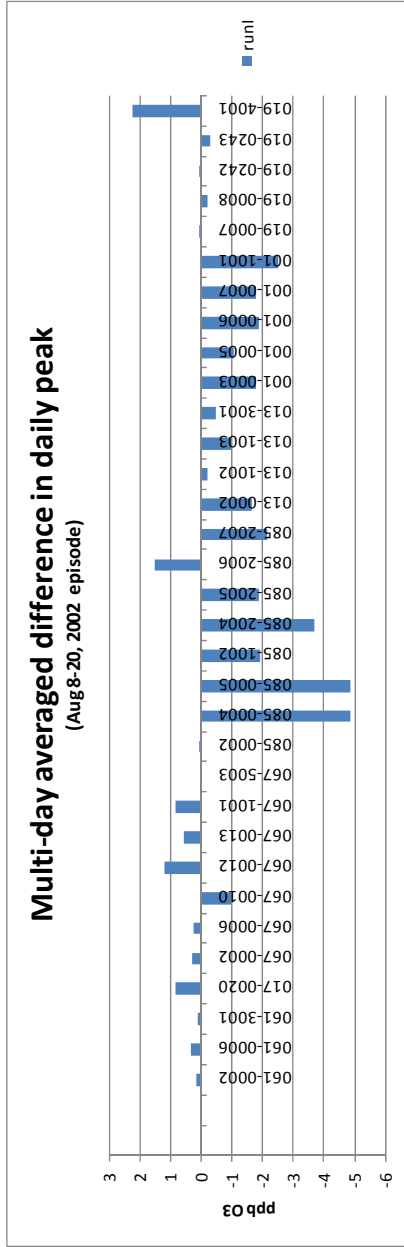
**Figures F5 and F6. Impacts on the 1-hr Peak Ozone at Monitors  
in Central California for Runs C and D**



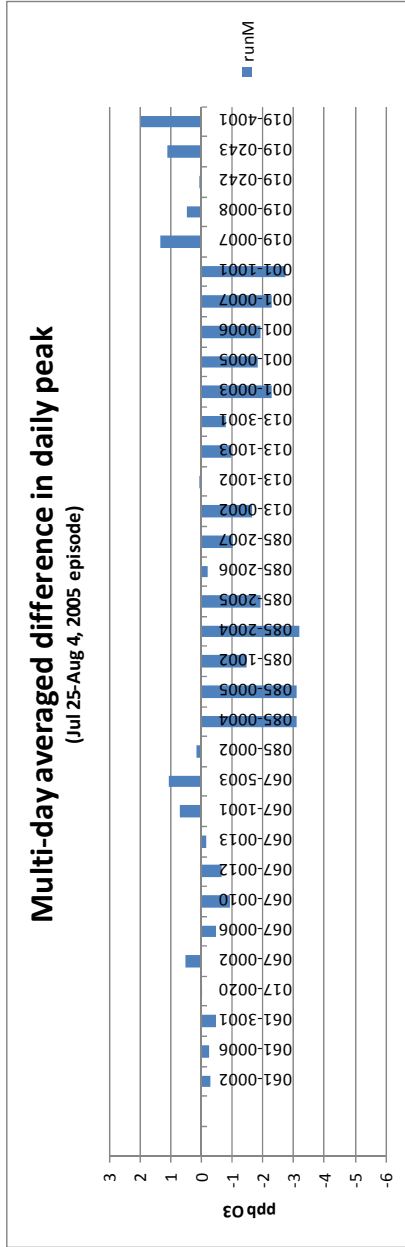
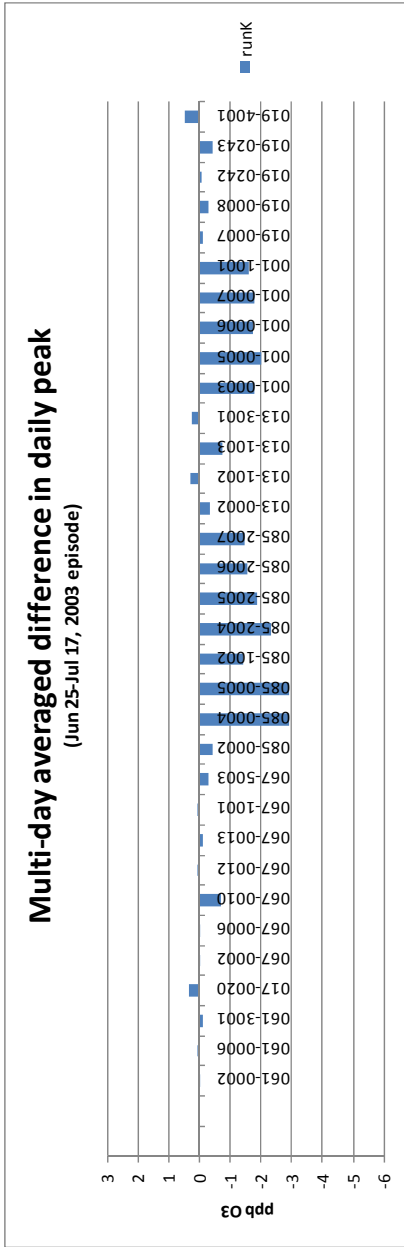
**Figures F7 and F8. Impacts on the 1-hr Peak Ozone at Monitors  
in Central California for Runs E and F**



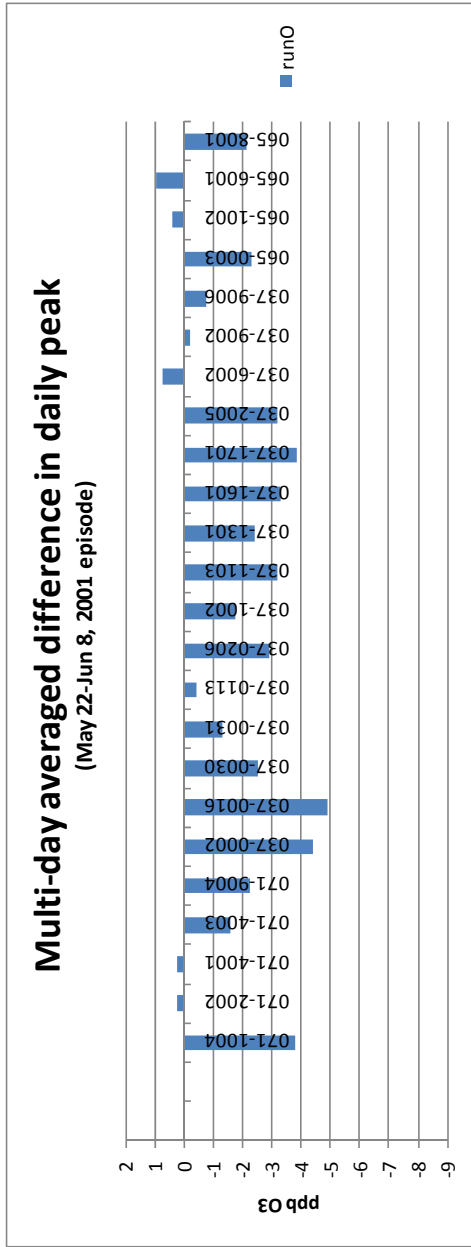
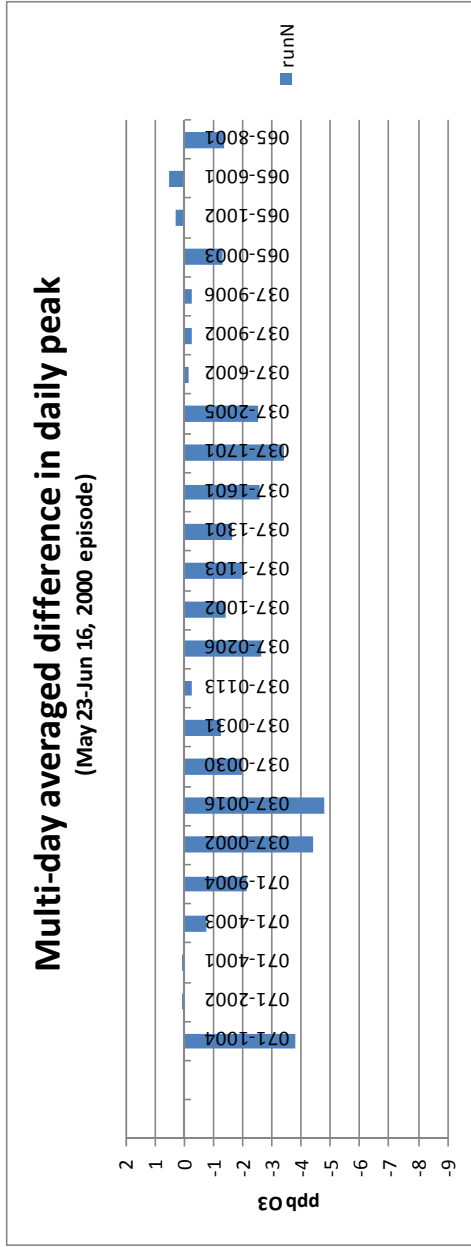
**Figures F19 and F10. Impacts on the 1-hr Peak Ozone at Monitors in Central California for Runs H1 and H2**



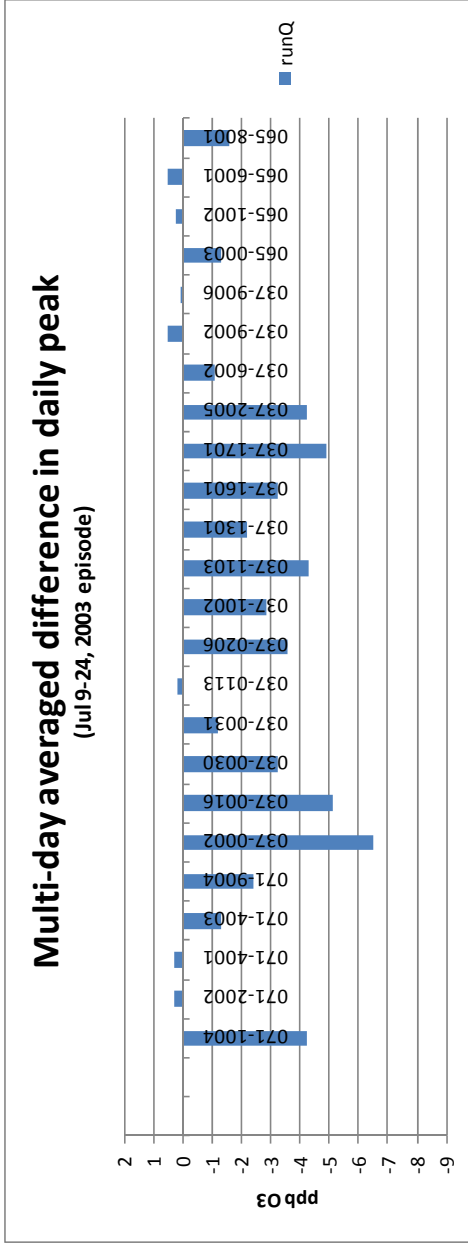
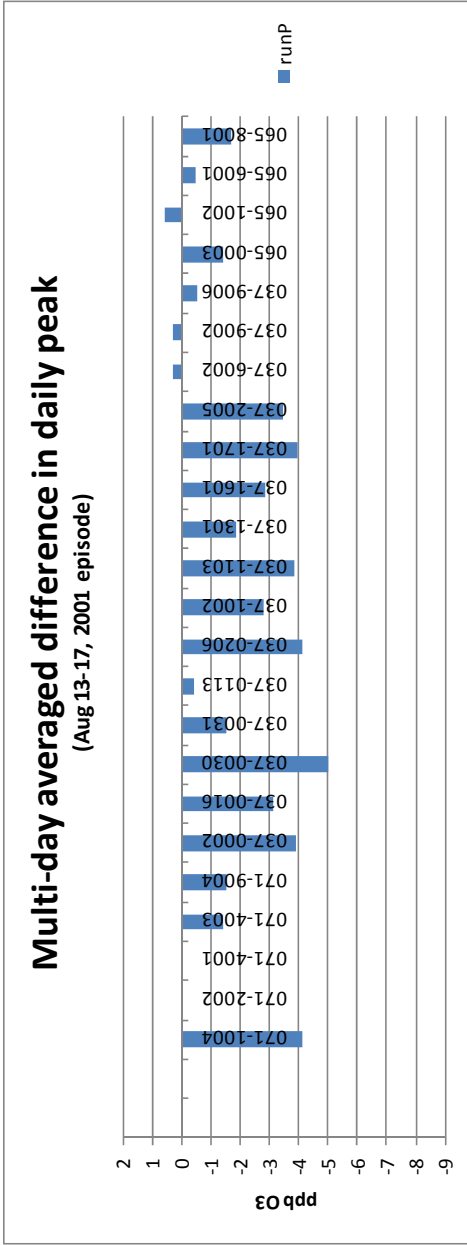
**Figures F11 and F12. Impacts on the 1-hr Peak Ozone at Monitors in Central California for Runs I and J**



**Figures F13 and F14. Impacts on the 1-hr Peak Ozone at Monitors in Central California for Runs K and M**



**Figures F15 and F16. Impacts on the 1-hr Peak Ozone at Monitors  
in Southern California for Runs N and O**



**Figures F17 and F18. Impacts on the 1-hr Peak Ozone at Monitors in Southern California for Runs P and Q**

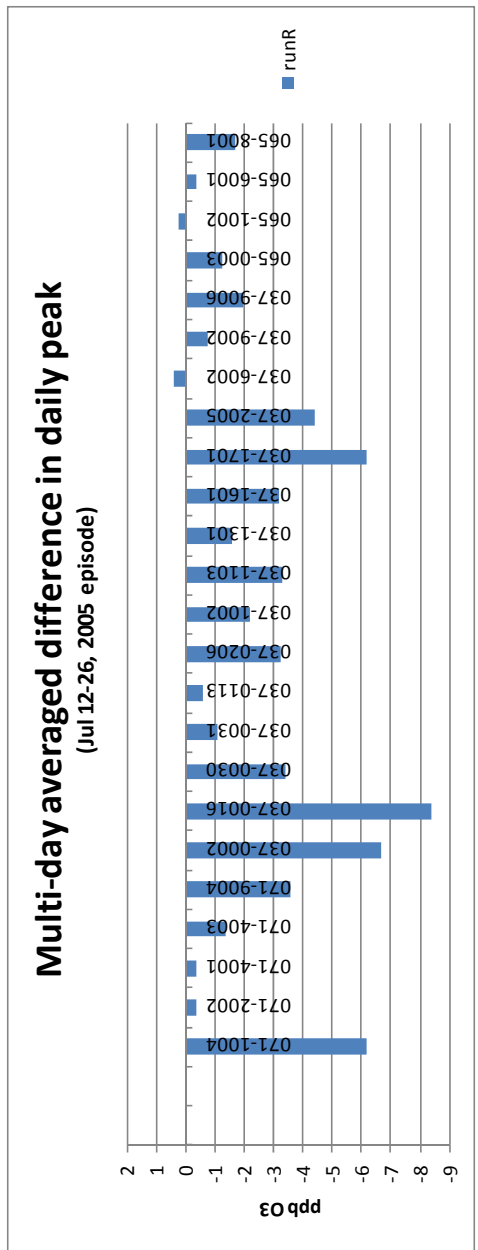


**Figure F19. Impacts on the 1-hr Peak Ozone at Monitors in Southern California for Run R**

**Appendix G:  
Emission Reduction Cross Sections and Carrying  
Capacity Diagrams**

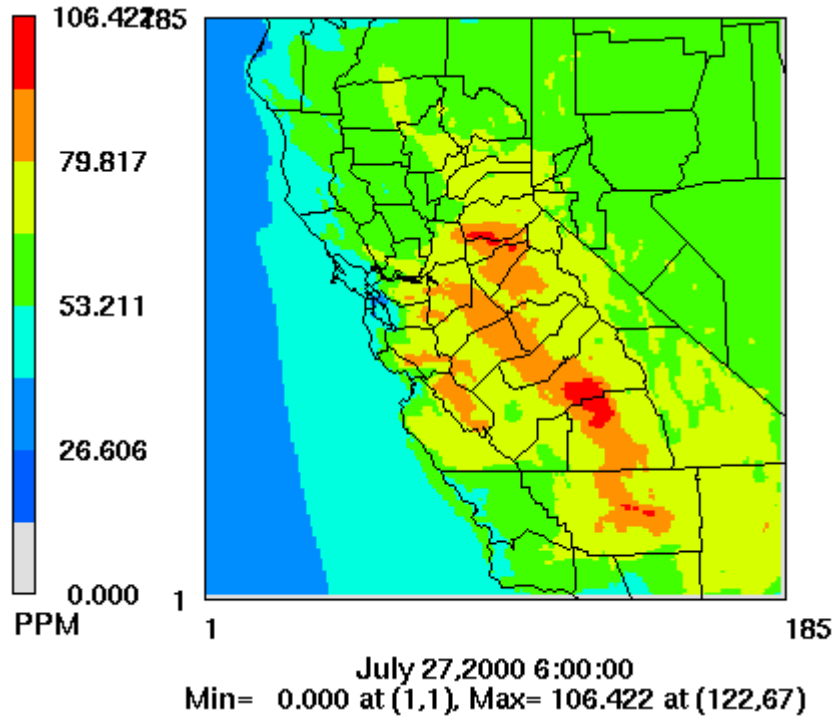


Figure G1. Base-case Episodic Peak 8-hour Ozone for the July–August 2000 Episode with 2000 Emissions

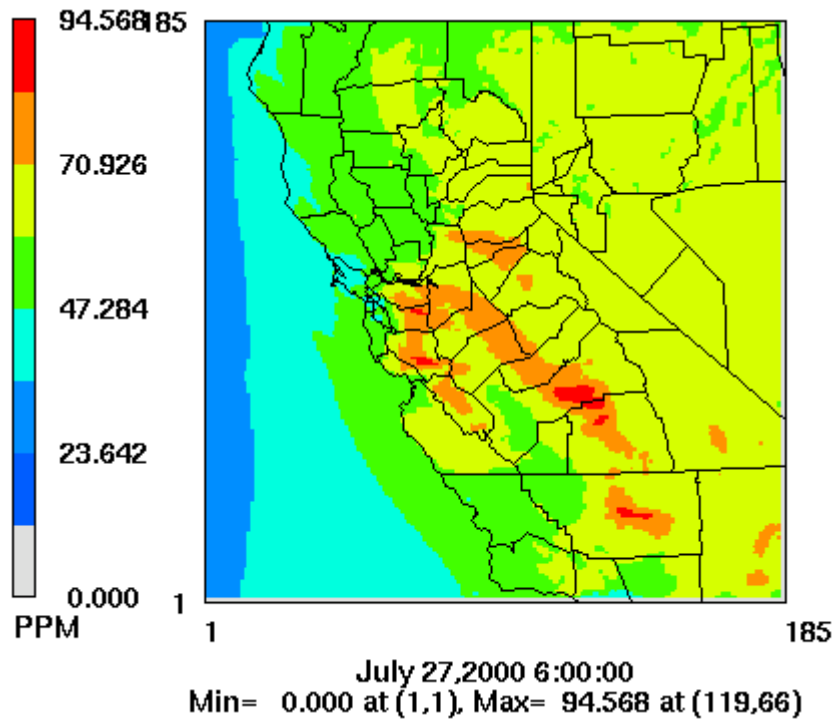


Figure G2. Base-case Episodic Peak 8-hour Ozone for the July–August 2000 Episode with 2018 Emissions

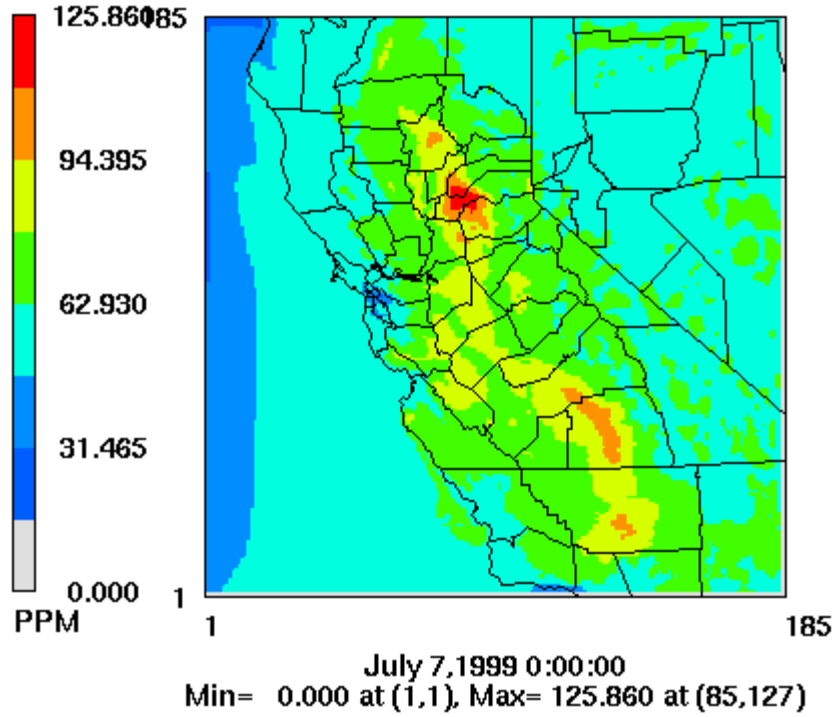


Figure G3. Base-case Episodic Peak 8-hour Ozone for the July 1999 Episode with 1999 Emissions

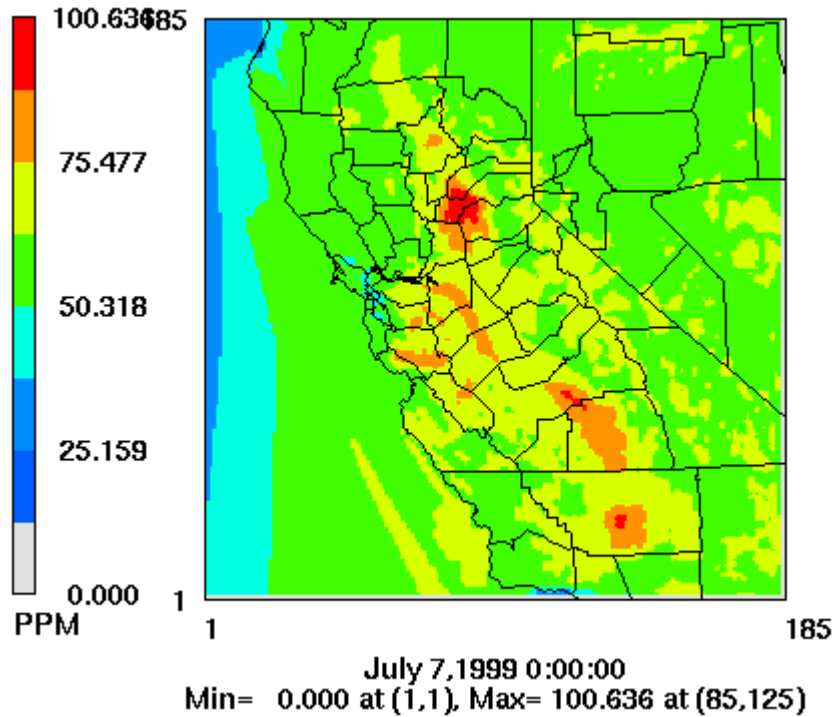
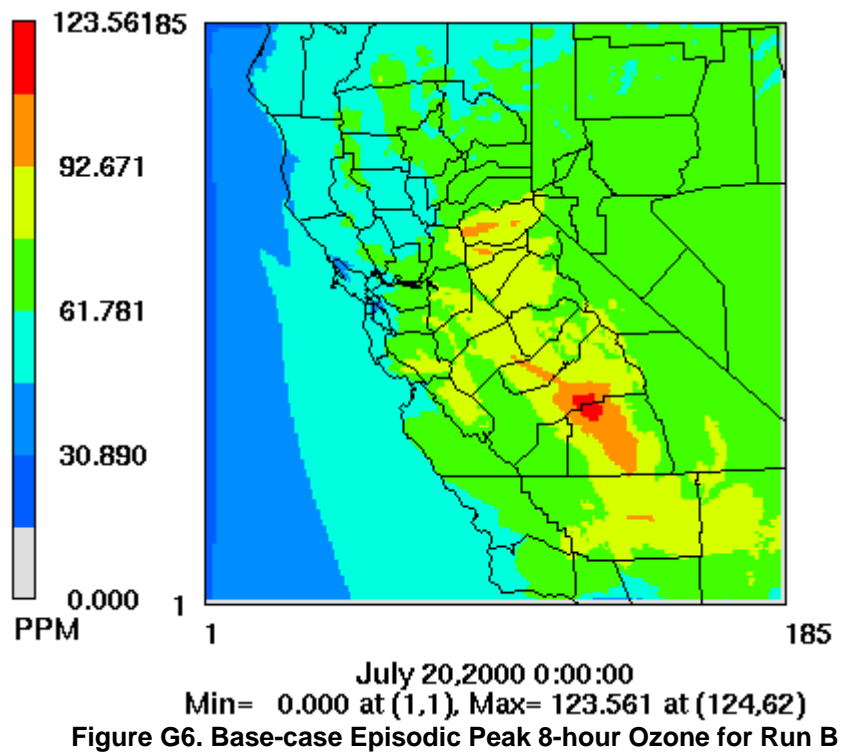
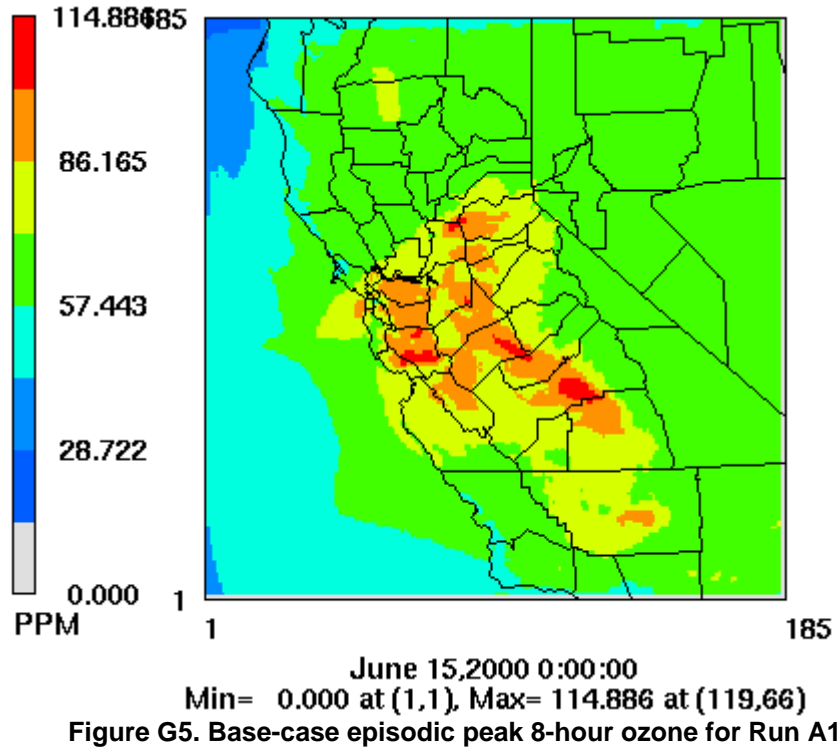
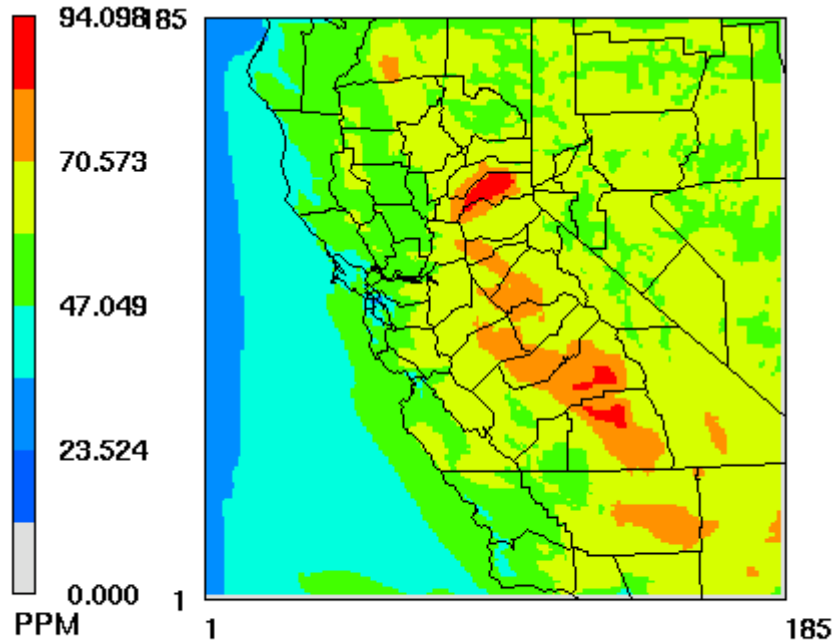


Figure G4. Base-case Episodic Peak 8-hour Ozone for the July 1999 Episode with 2018 Emissions

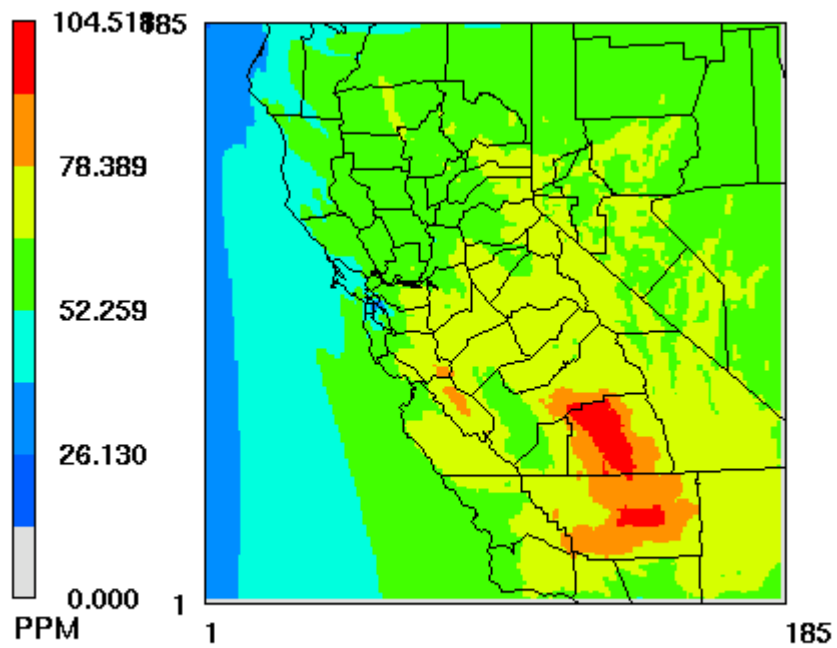




August 5,2000 0:00:00

Min= 0.000 at (1,1), Max= 94.098 at (94,133)

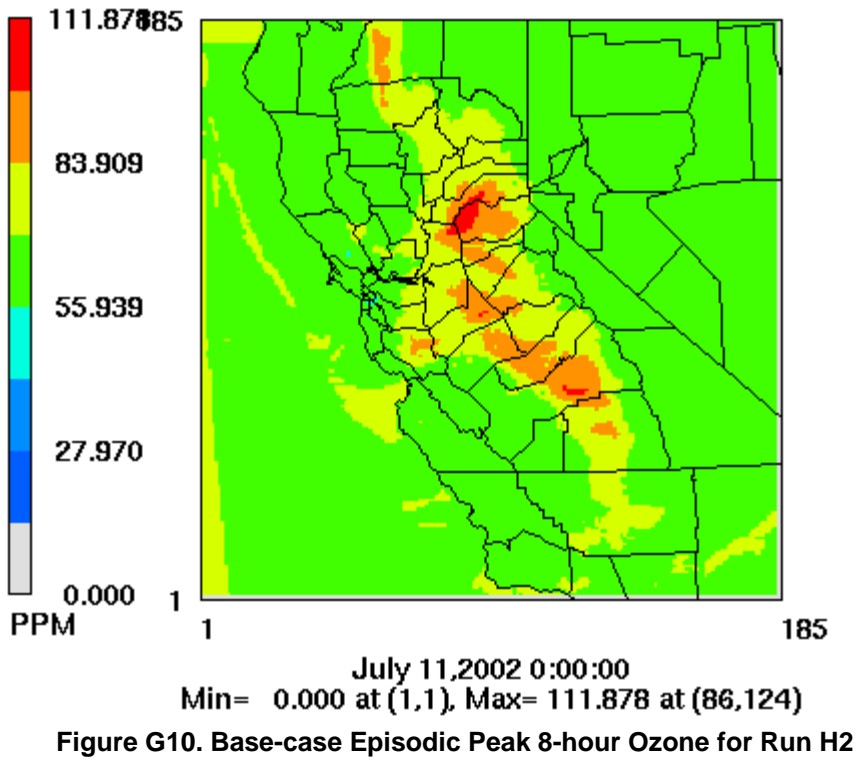
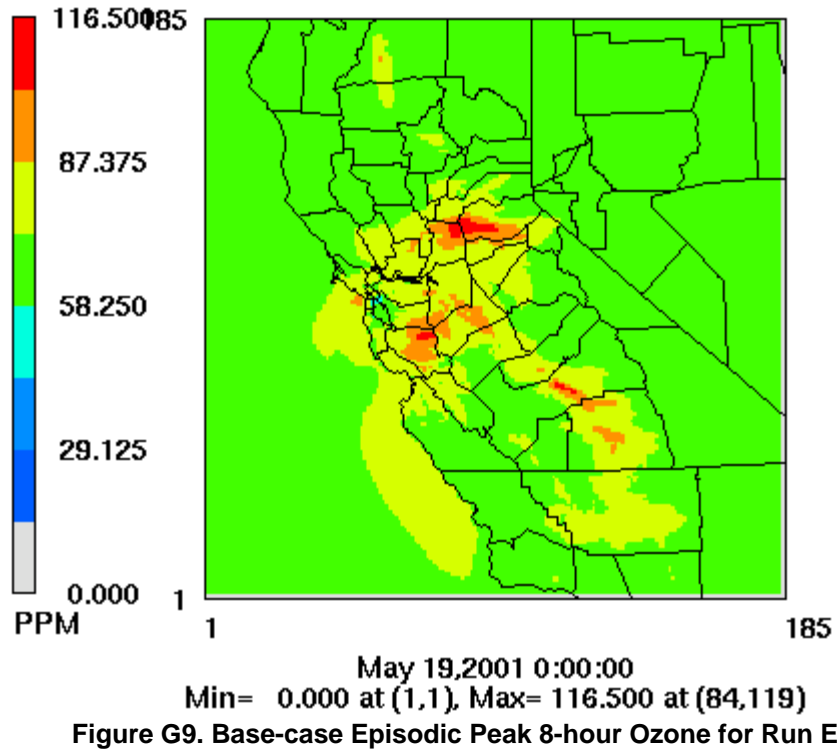
Figure G7. Base-case Episodic Peak 8-hour Ozone for Run C



August 12,2000 0:00:00

Min= 0.000 at (1,1), Max= 104.518 at (128,55)

Figure G8. Base-case Episodic Peak 8-hour Ozone for Run D



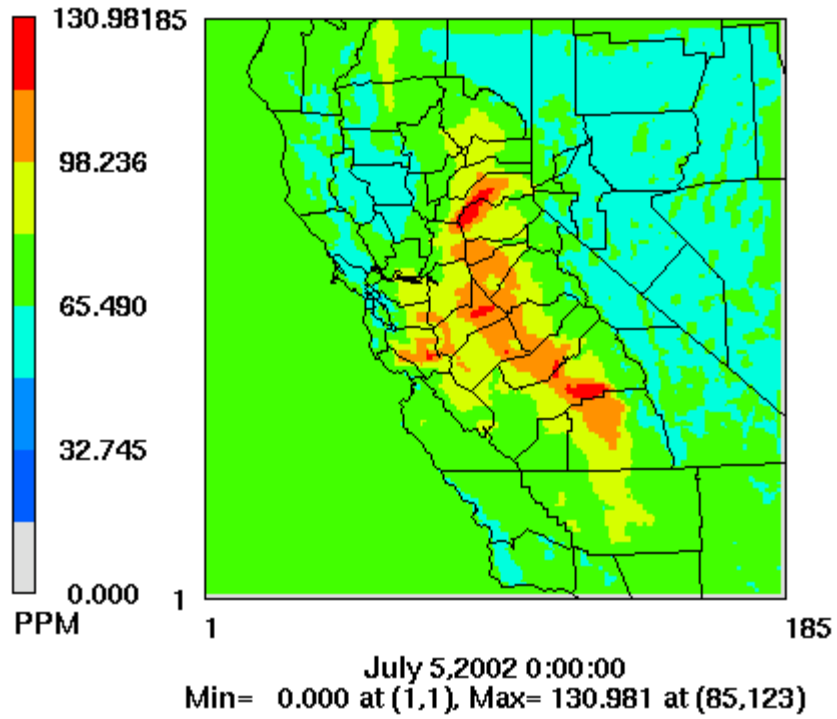


Figure G11. Base-case Episodic Peak 8-hour Ozone for Run H1

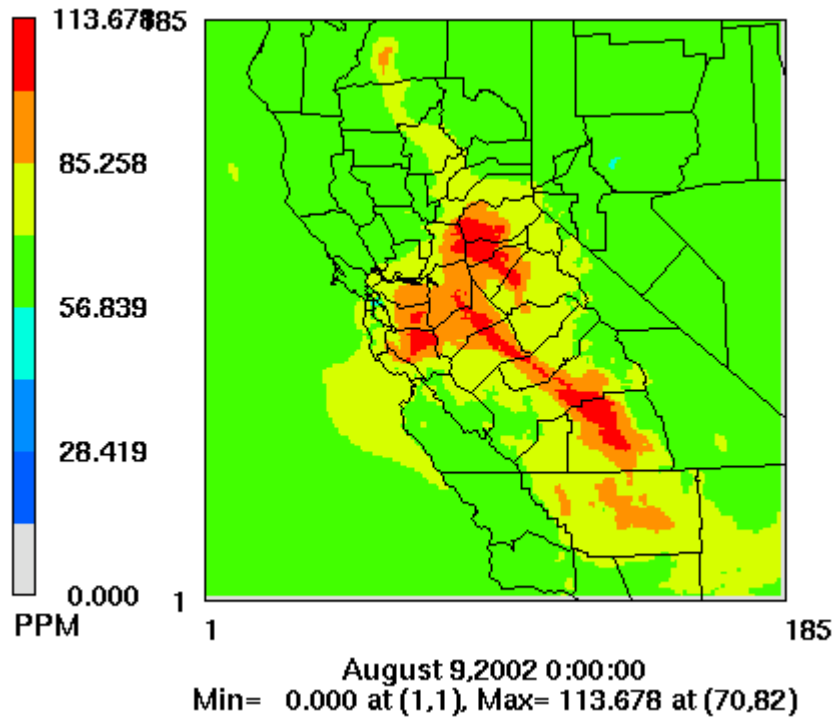


Figure G12. Base-case Episodic Peak 8-hour Ozone for Run I

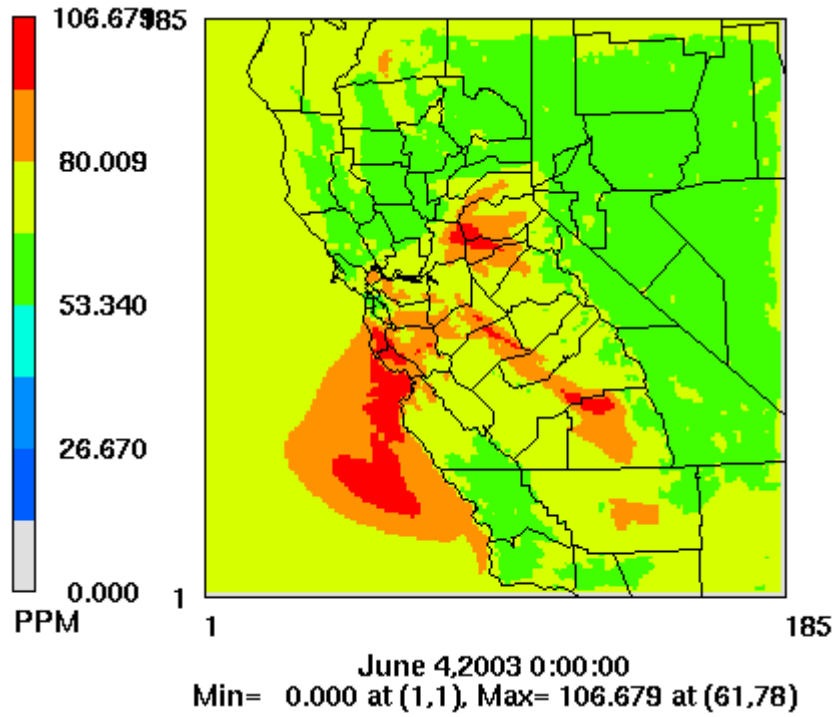


Figure G13. Base-case Episodic Peak 8-hour Ozone for Run J

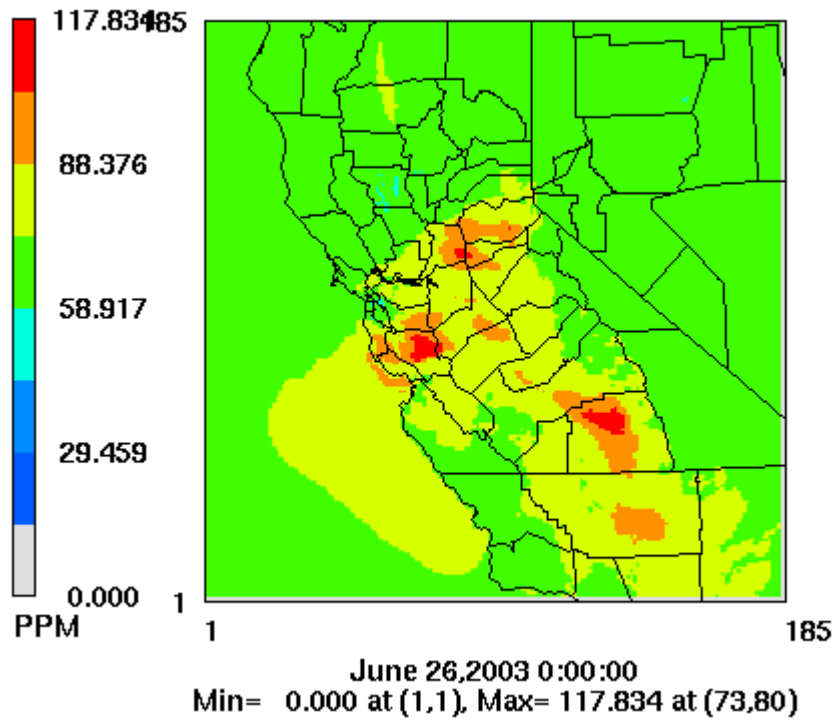
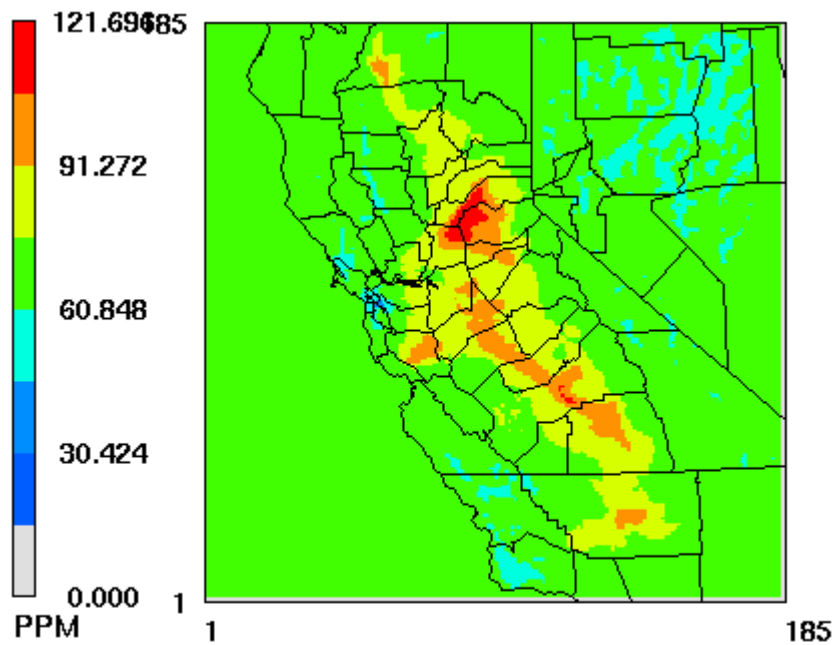
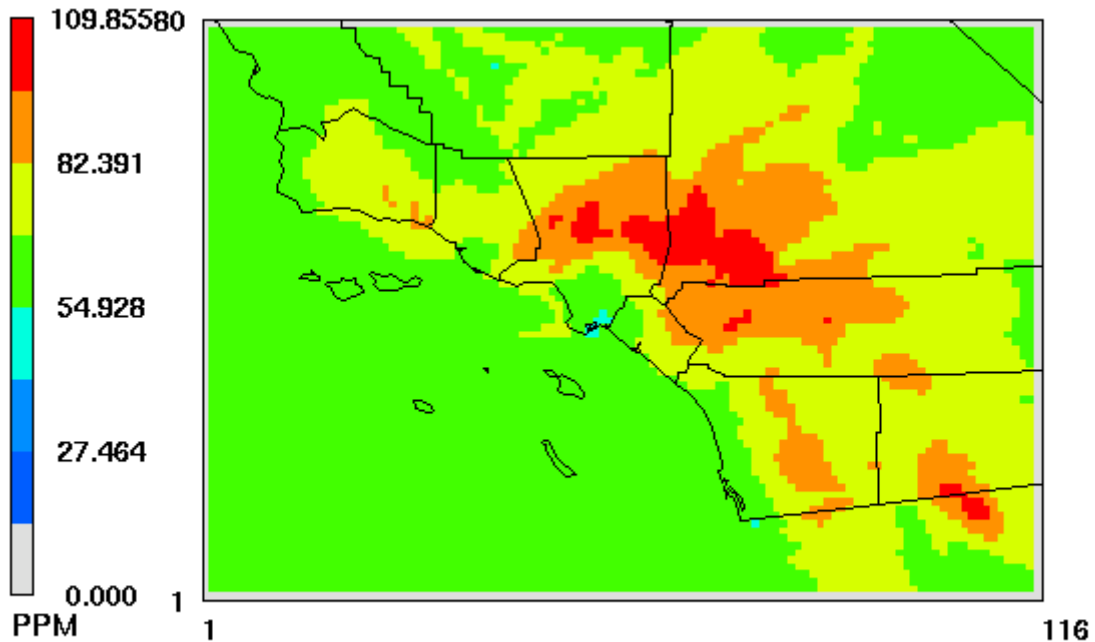


Figure G14. Base-case Episodic Peak 8-hour Ozone for Run K



July 26,2005 0:00:00  
Min= 0.000 at (1,1), Max= 121.696 at (82,119)

Figure G15. Base-case Episodic Peak 8-hour Ozone for Run M



May 24,2000 0:00:00  
Min= 0.000 at (1,1), Max= 109.855 at (67,49)

Figure G16. Base-case Episodic Peak 8-hour Ozone for Run N

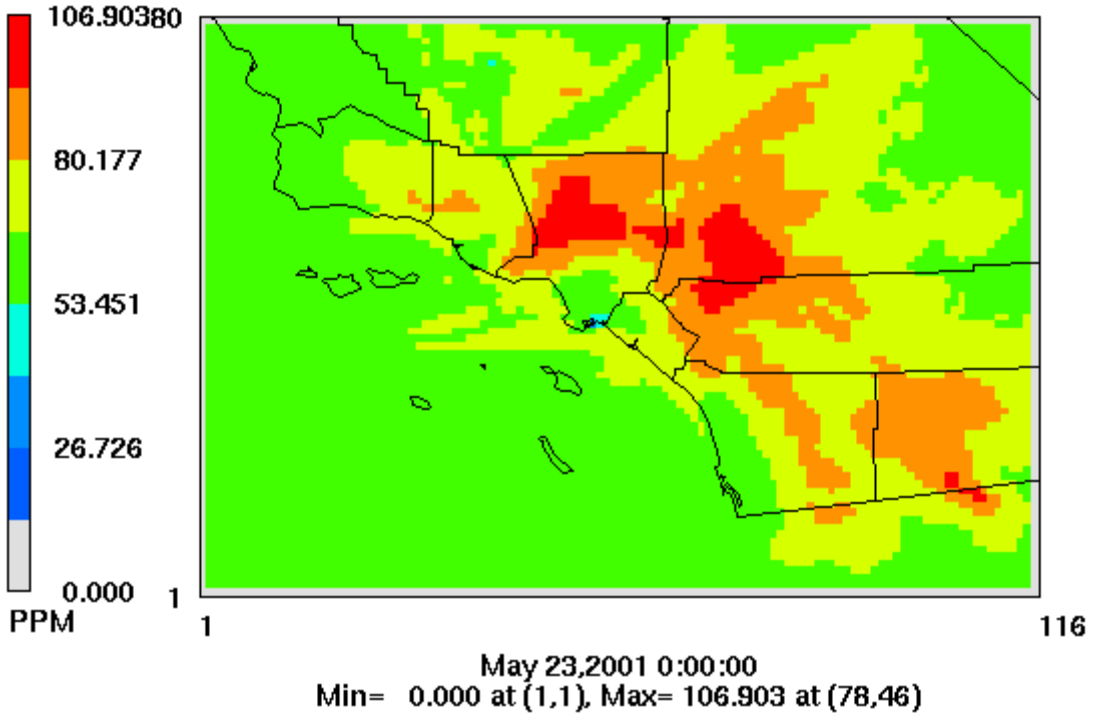


Figure G17. Base-case Episodic Peak 8-hour Ozone for Run O

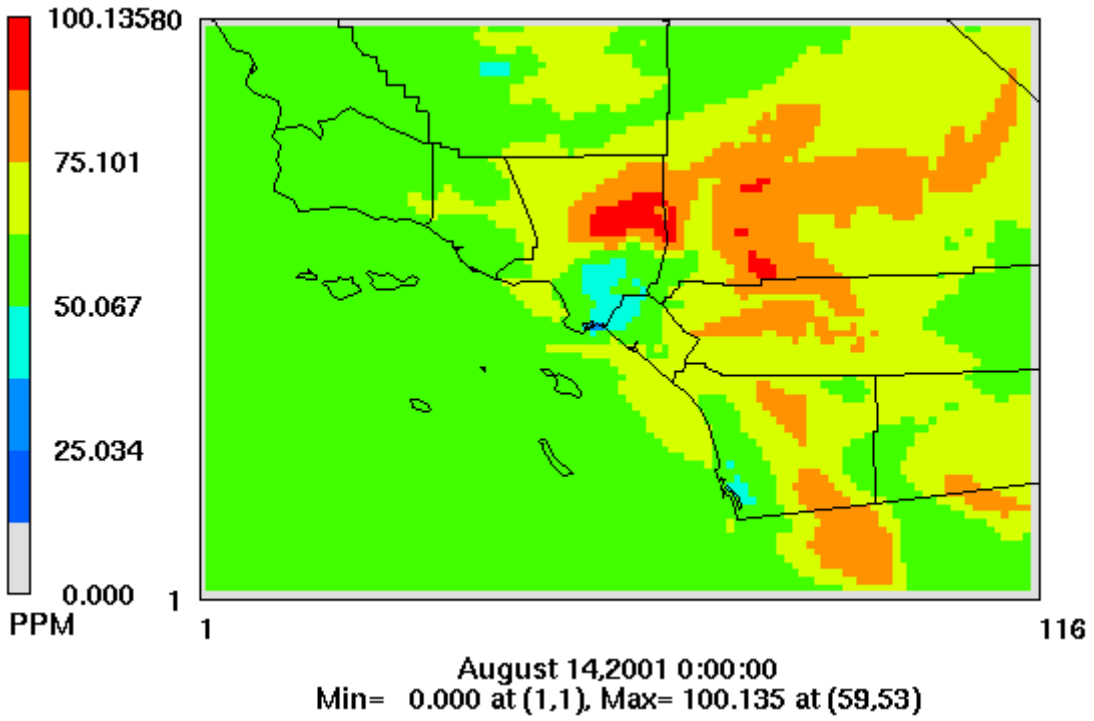


Figure G18. Base-case Episodic Peak 8-hour Ozone for Run P

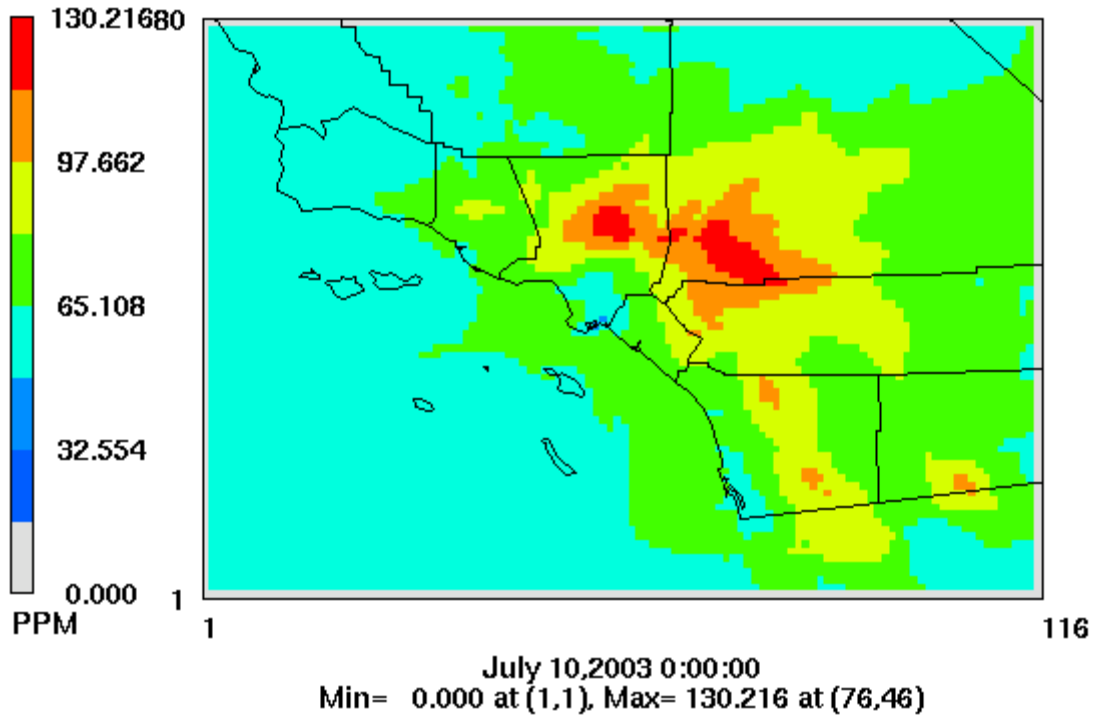


Figure G19. Base-case Episodic Peak 8-hour Ozone for Run Q

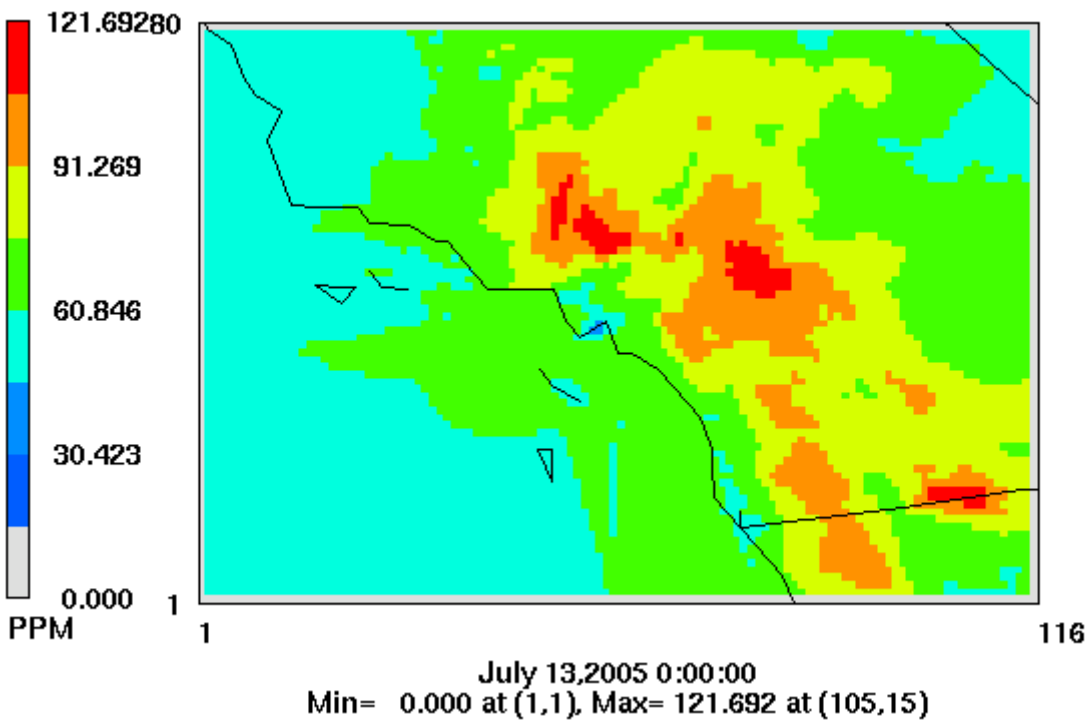
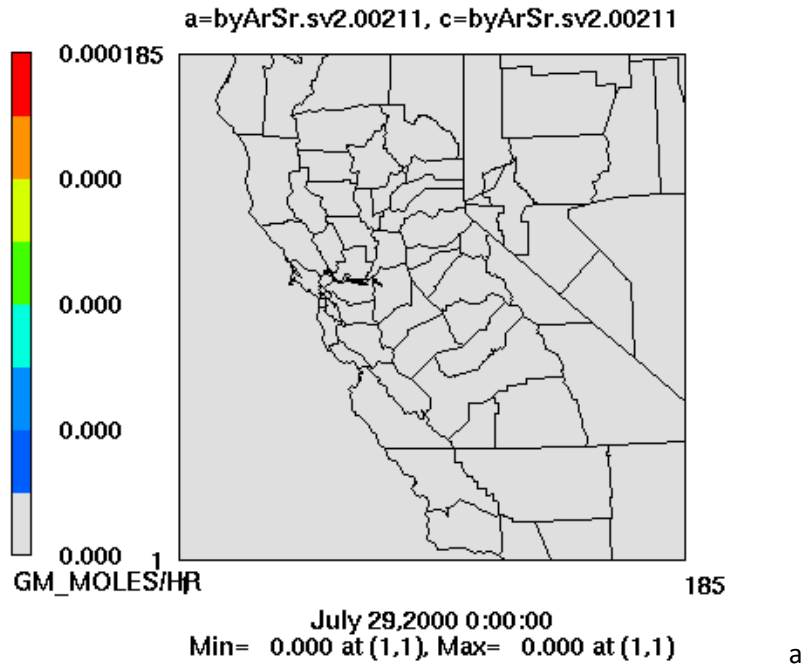


Figure G20. Base-case Episodic Peak 8-hour Ozone for Run R

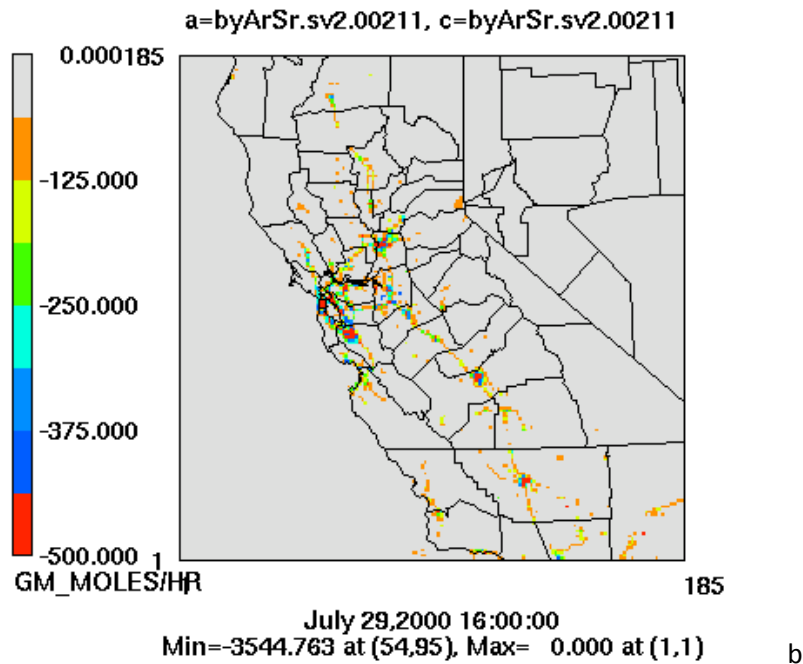
# **Appendix H: 8-hour Peak Ozone Cross Sections**

Figure H1 (a-g): 0% Reduction in ROG Emissions; 20% Reduction in NOx Emissions

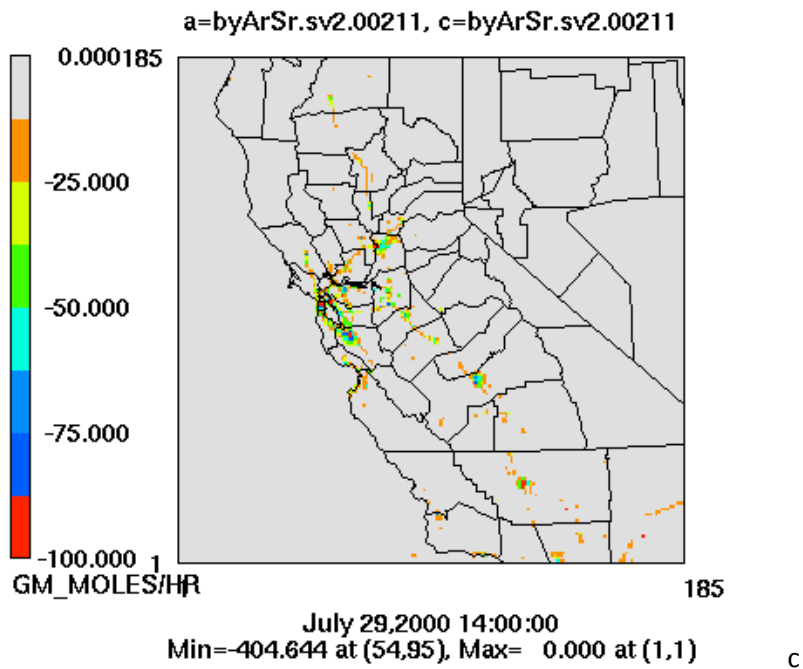
### Layer 1 OLE1c-OLE1a



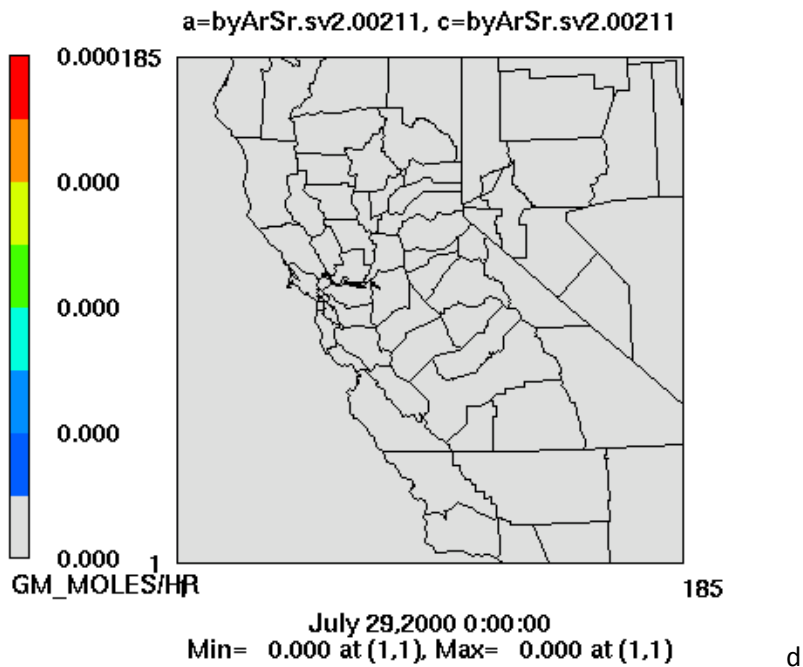
### Layer 1 NOc-NOa



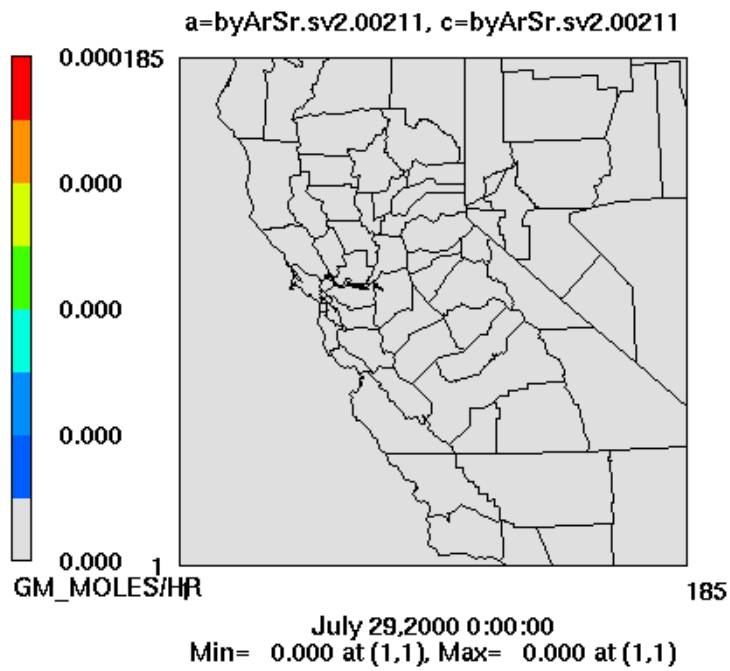
## Layer 1 NO2c-NO2a



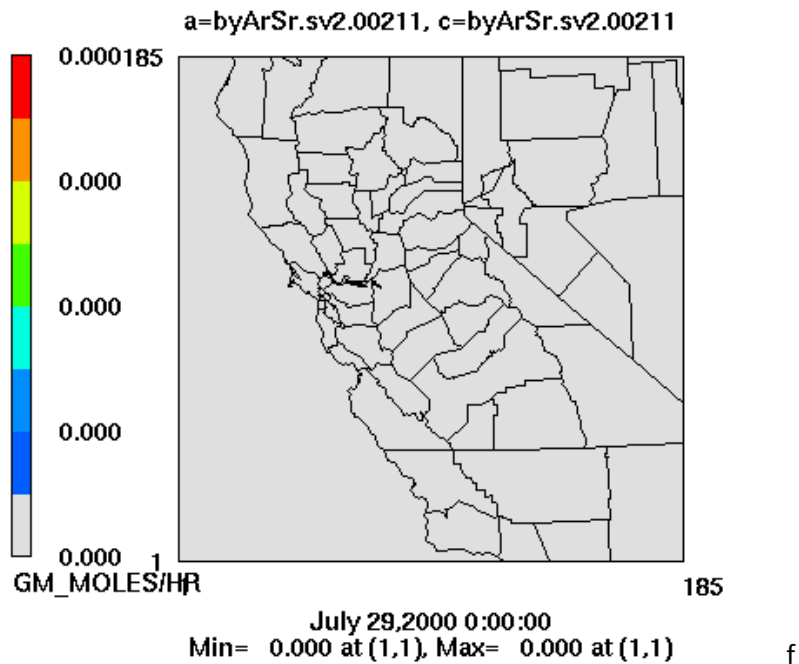
## Layer 1 ISOPc-ISOPa



## Layer 1 ETHEc-ETHEa



## Layer 1 ALK1c-ALK1a



# Layer 1 TERPc-TERPa

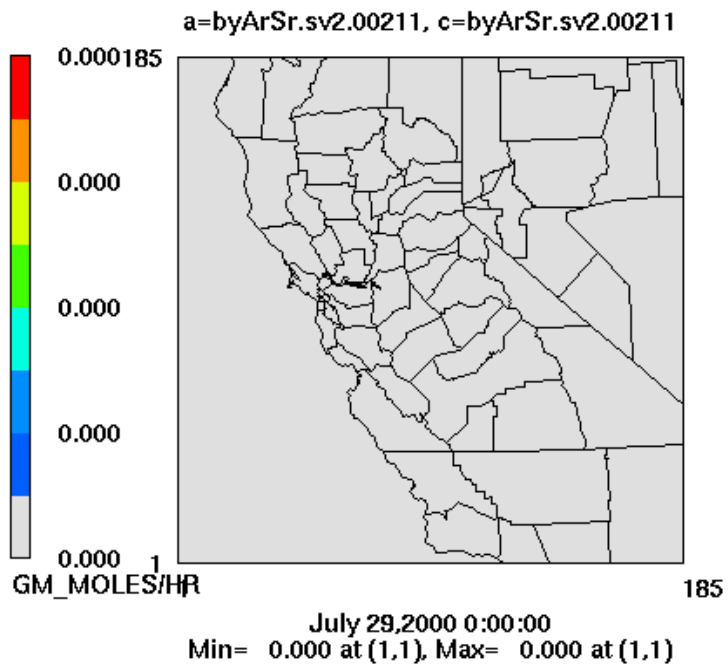
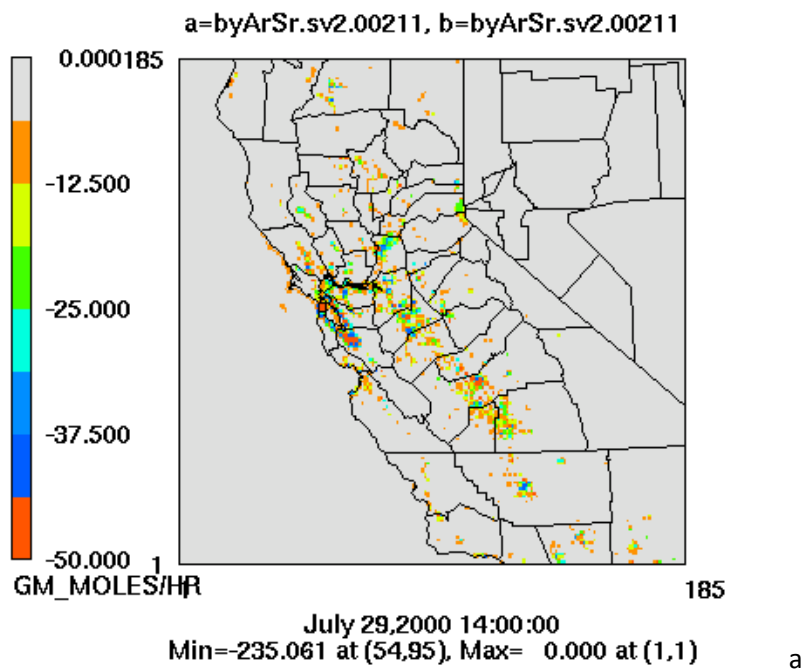
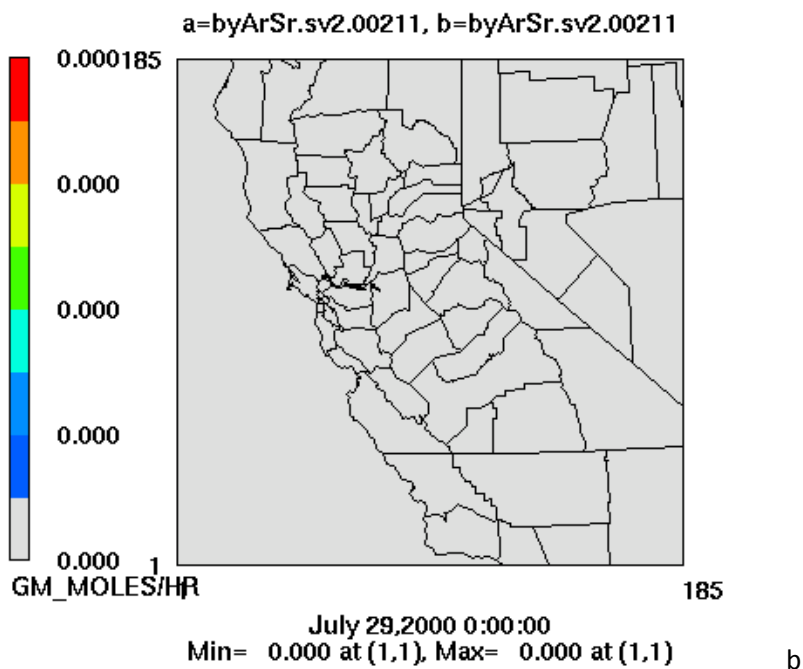


Figure H2 (a-g): 20% Reduction in ROG Emissions; 0% Reduction in NOx Emissions

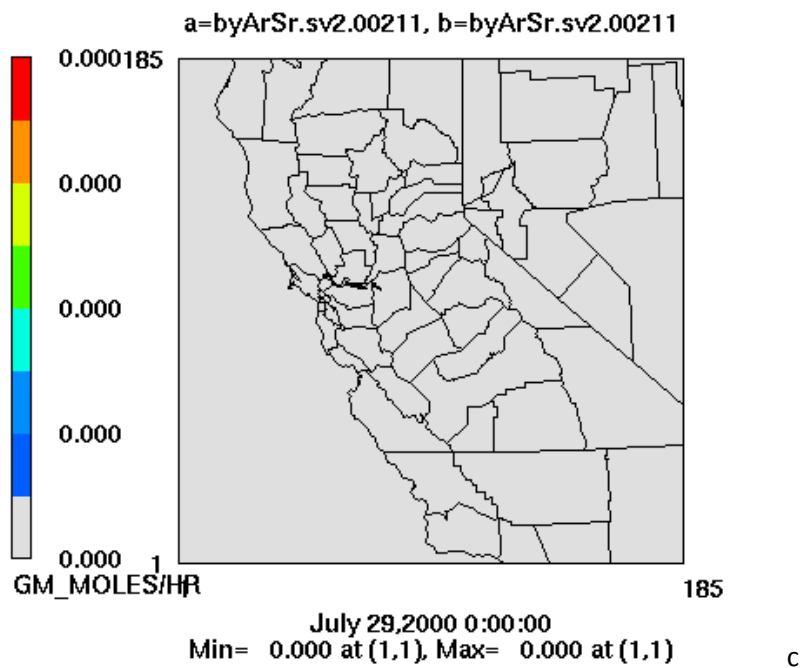
### Layer 1 OLE1b-OLE1a



## Layer 1 NOb-NOa

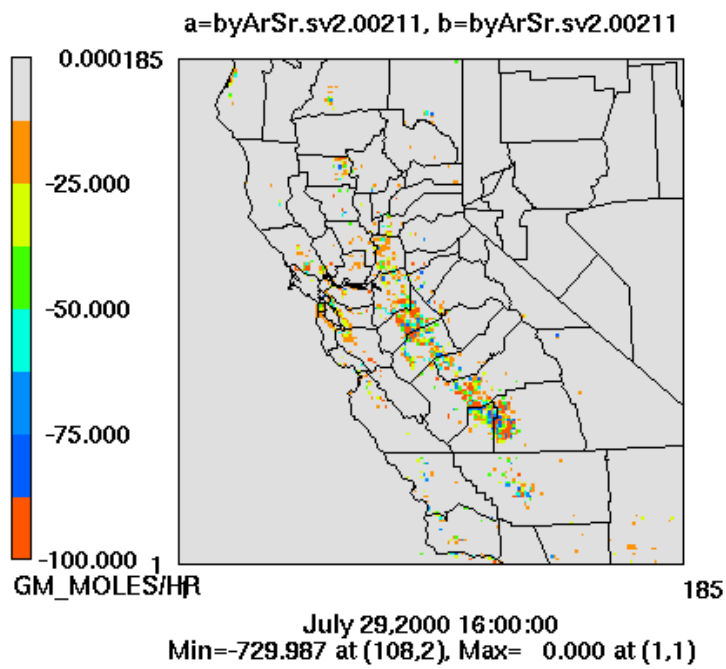


## Layer 1 NO2b-NO2a





## Layer 1 ALK1b-ALK1a



## Layer 1 TERPb-TERPa

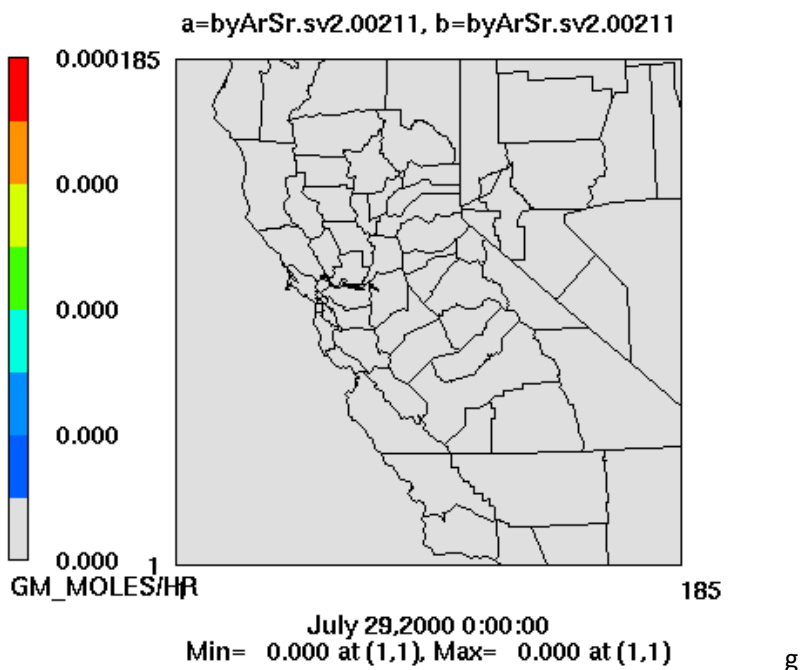
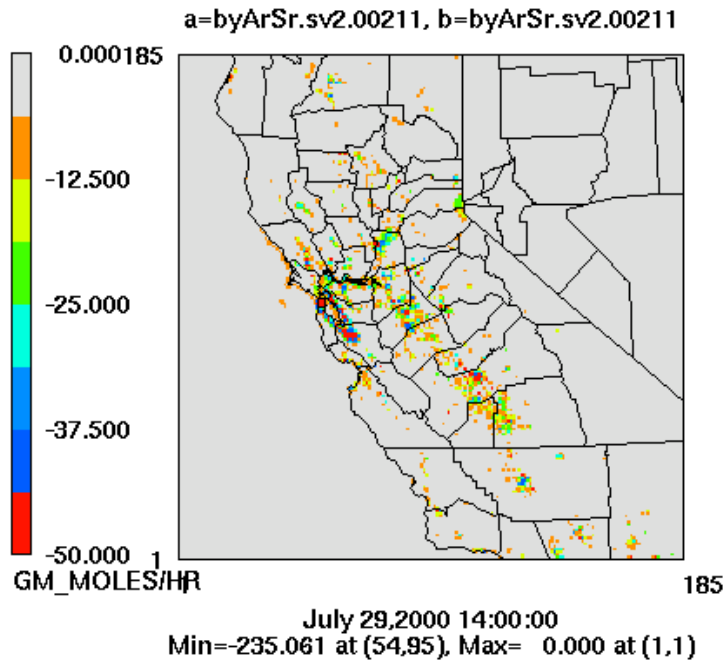


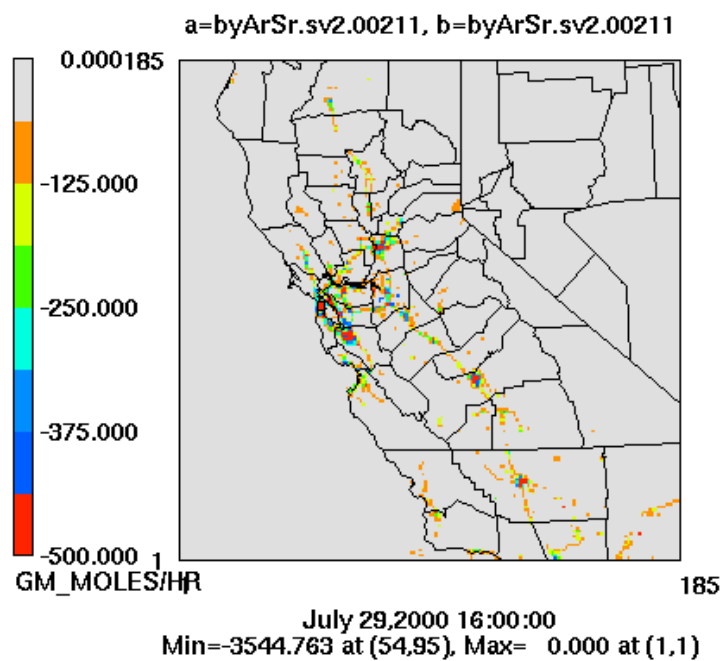
Figure H3 (a-g): 20% Reduction in ROG Emissions; 20% Reduction in NOx Emissions

### Layer 1 OLE1b-OLE1a



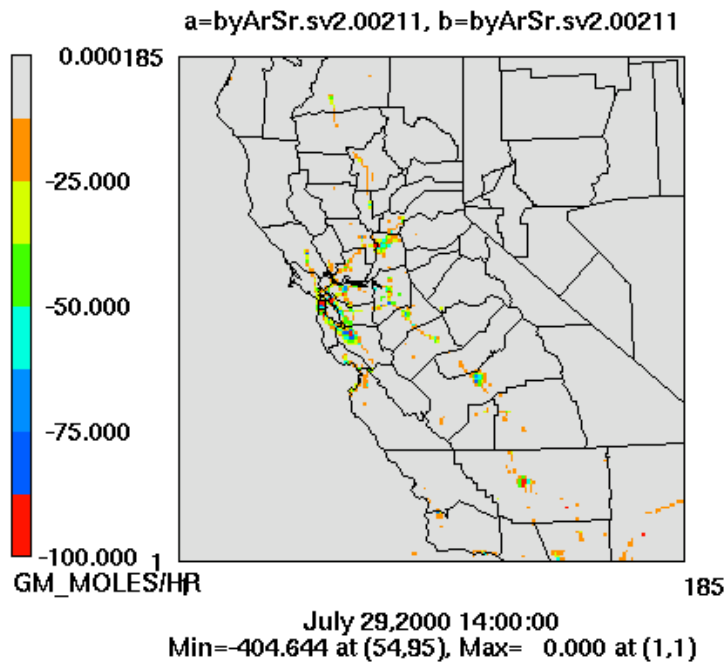
a

### Layer 1 NOb-NOa

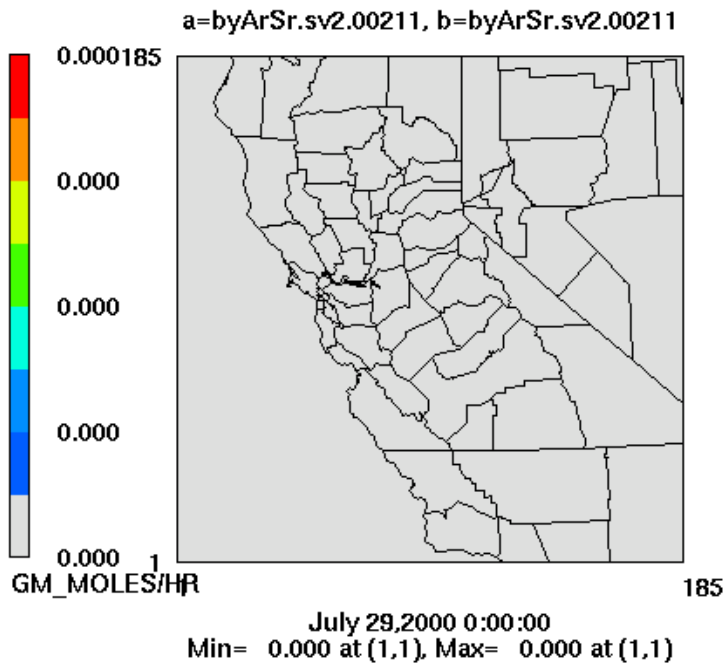


b

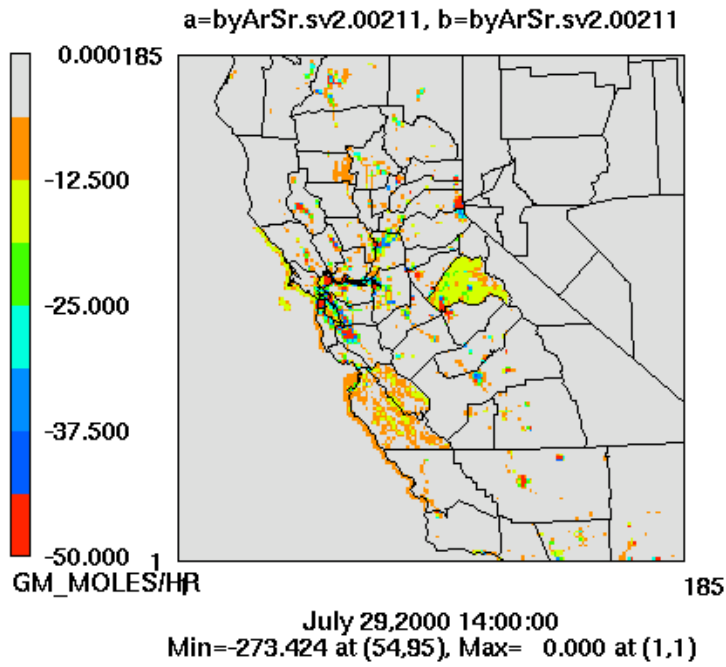
## Layer 1 NO2b-NO2a



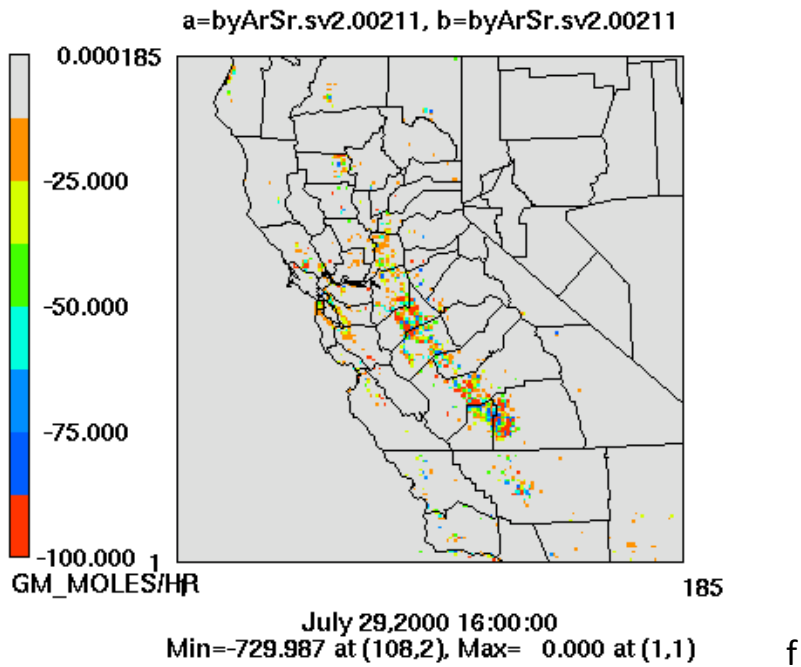
## Layer 1 ISOPb-ISOPa



## Layer 1 ETHEb-ETHEa



## Layer 1 ALK1b-ALK1a



# Layer 1 TERPb-TERPa

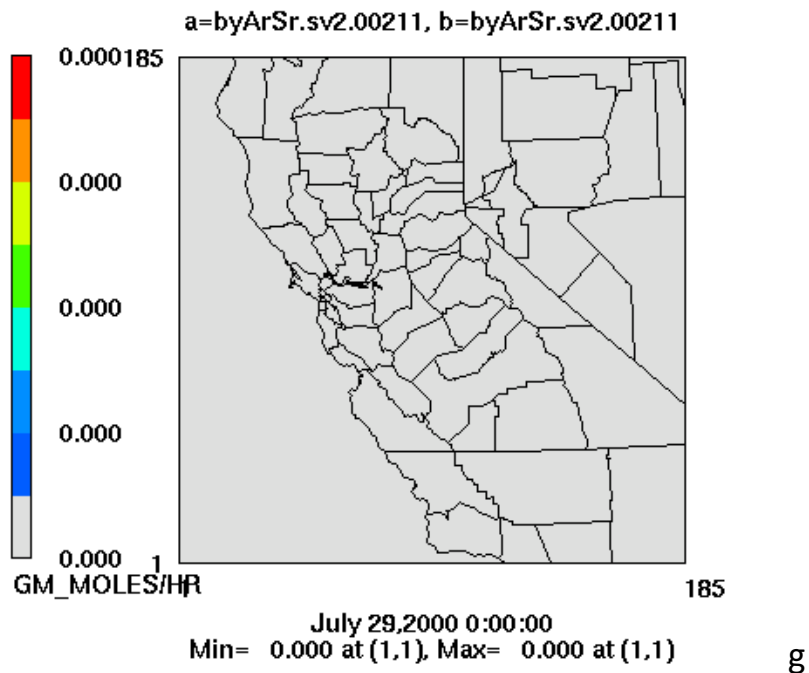
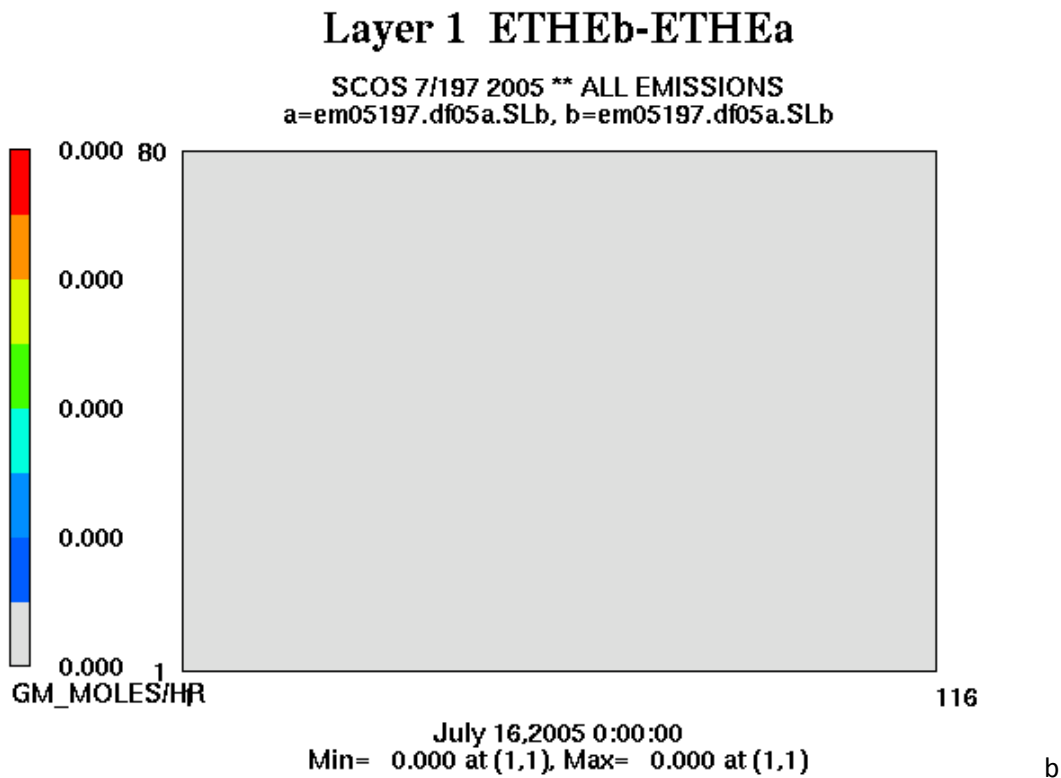
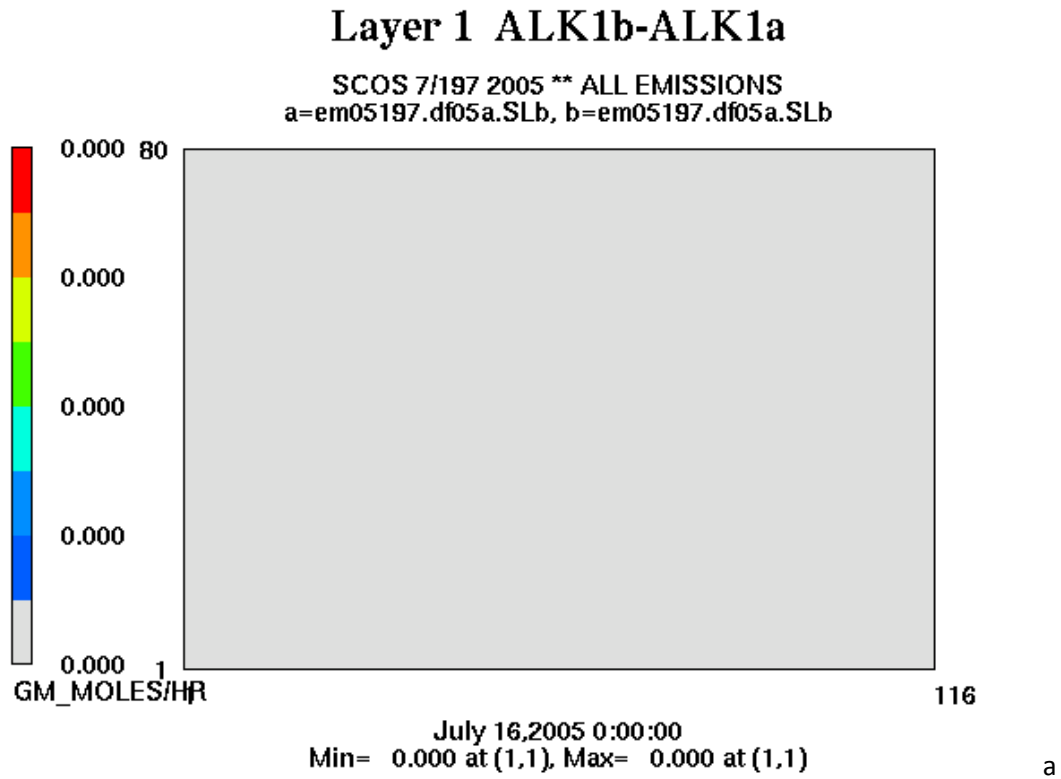
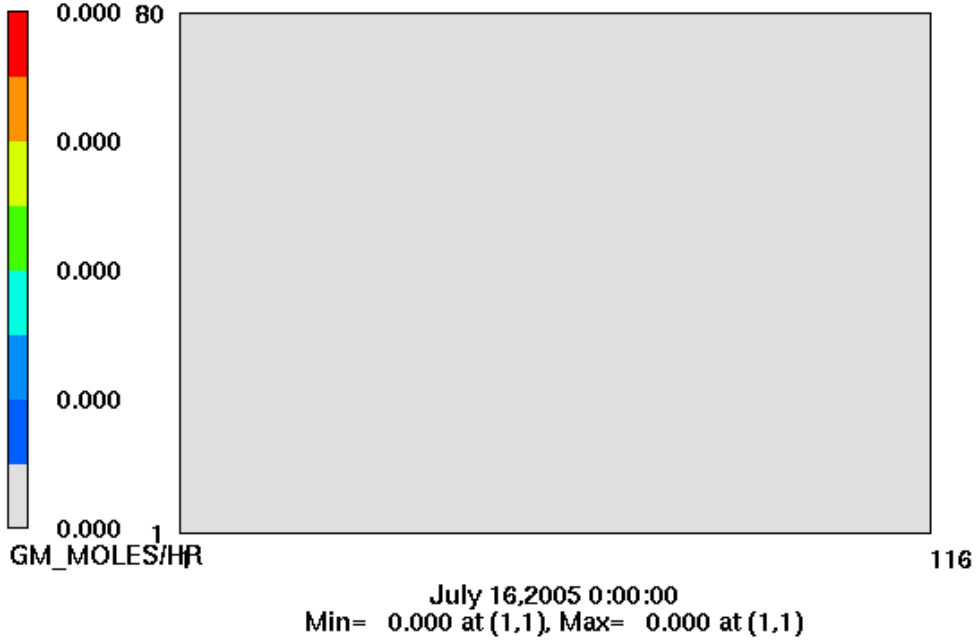


Figure H4 (a-g): 0% Reduction in ROG Emissions; 20% Reduction in NOx Emissions



# Layer 1 ISOPb-ISOPa

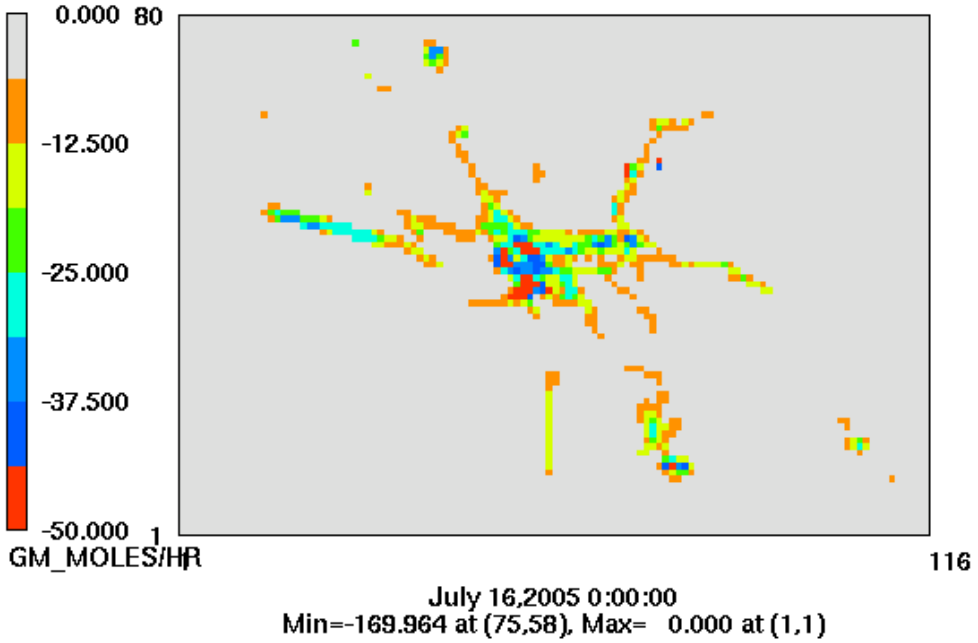
SCOS 7/197 2005 \*\* ALL EMISSIONS  
a=em05197.df05a.SLb, b=em05197.df05a.SLb



c

# Layer 1 NO2b-NO2a

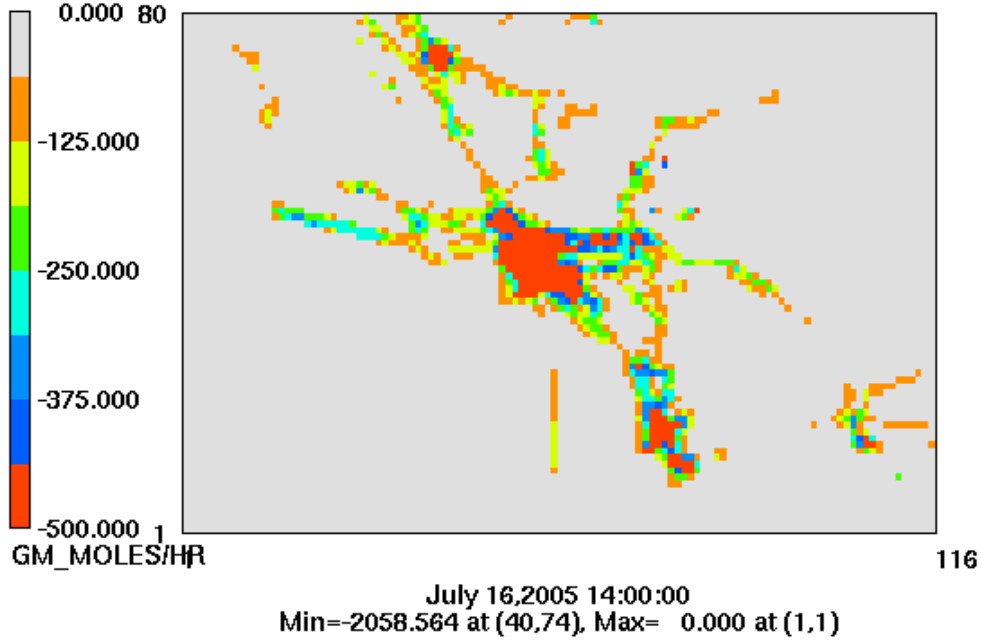
SCOS 7/197 2005 \*\* ALL EMISSIONS  
a=em05197.df05a.SLb, b=em05197.df05a.SLb



d

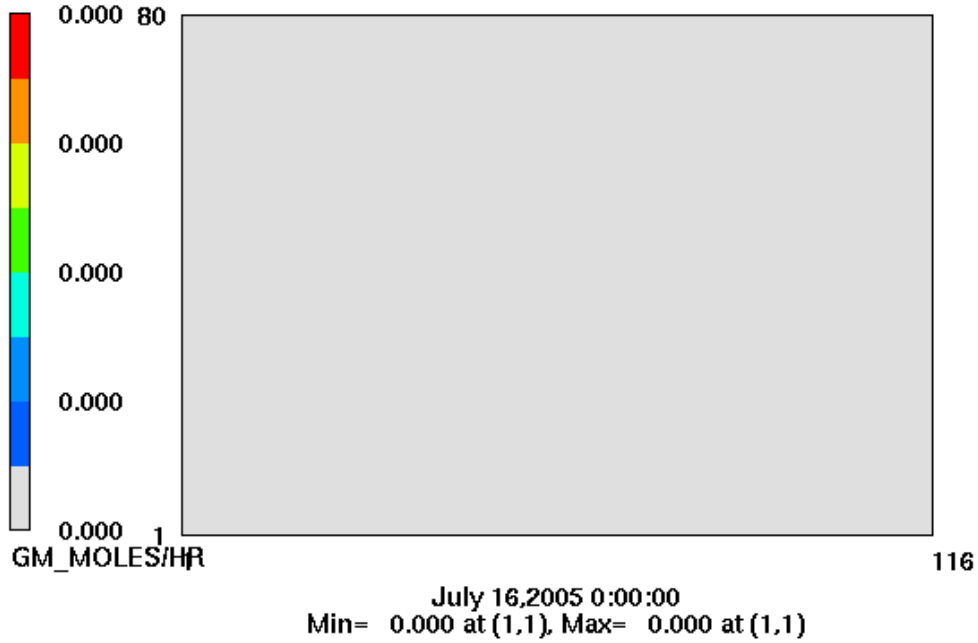
## Layer 1 NOb-NOa

SCOS 7/197 2005 \*\* ALL EMISSIONS  
a=em05197.df05a.SLb, b=em05197.df05a.SLb



## Layer 1 OLE1b-OLE1a

SCOS 7/197 2005 \*\* ALL EMISSIONS  
a=em05197.df05a.SLb, b=em05197.df05a.SLb



# Layer 1 TERPb-TERPa

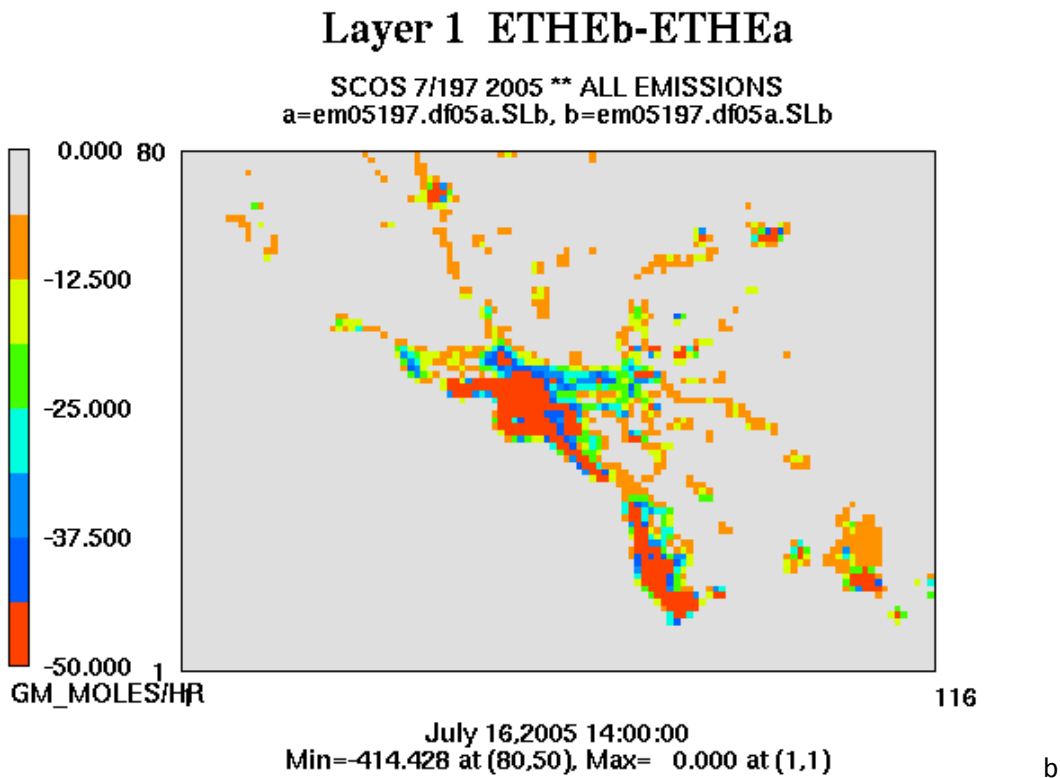
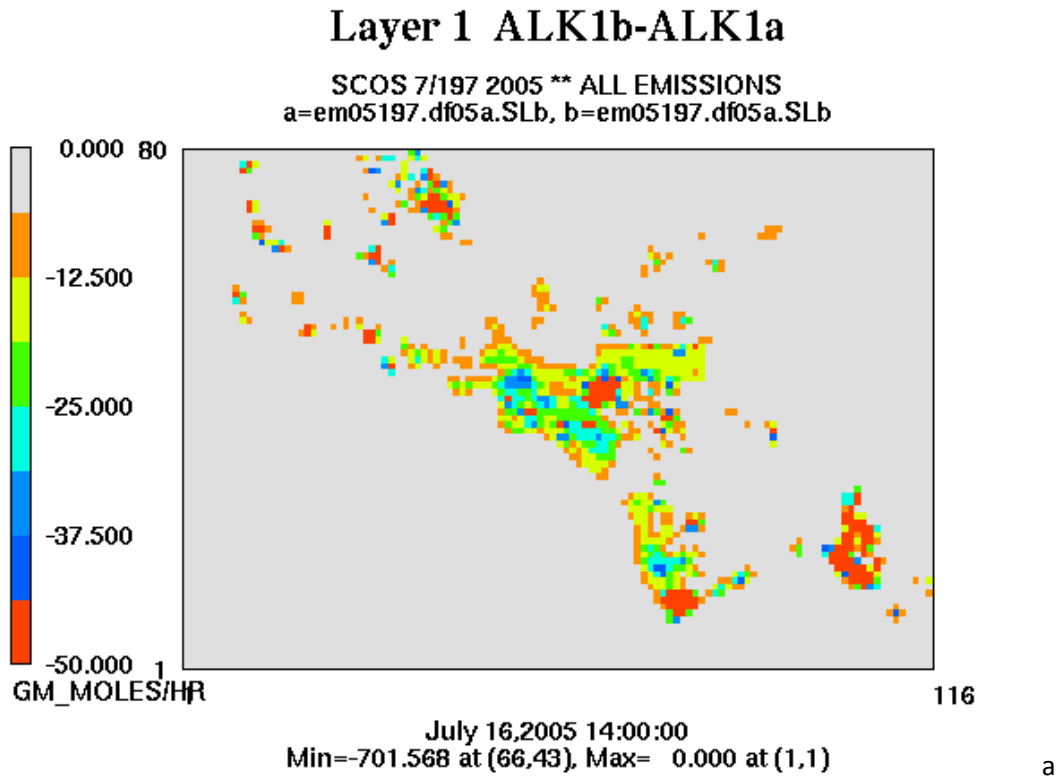
SCOS 7/197 2005 \*\* ALL EMISSIONS  
a=em05197.df05a.SLb, b=em05197.df05a.SLb



July 16,2005 0:00:00  
Min= 0.000 at (1,1), Max= 0.000 at (1,1)

g

Figure H5 (a-g): 20% Reduction in ROG Emissions; 0% Reduction in NOx Emissions



## Layer 1 ISOPb-ISOPa

SCOS 7/197 2005 \*\* ALL EMISSIONS  
a=em05197.df05a.SLb, b=em05197.df05a.SLb



July 16,2005 0:00:00  
Min= 0.000 at (1,1), Max= 0.000 at (1,1)

c

## Layer 1 NO2b-NO2a

SCOS 7/197 2005 \*\* ALL EMISSIONS  
a=em05197.df05a.SLb, b=em05197.df05a.SLb



July 16,2005 0:00:00  
Min= 0.000 at (1,1), Max= 0.000 at (1,1)

d

## Layer 1 NOb-NOa

SCOS 7/197 2005 \*\* ALL EMISSIONS  
a=em05197.df05a.SLb, b=em05197.df05a.SLb

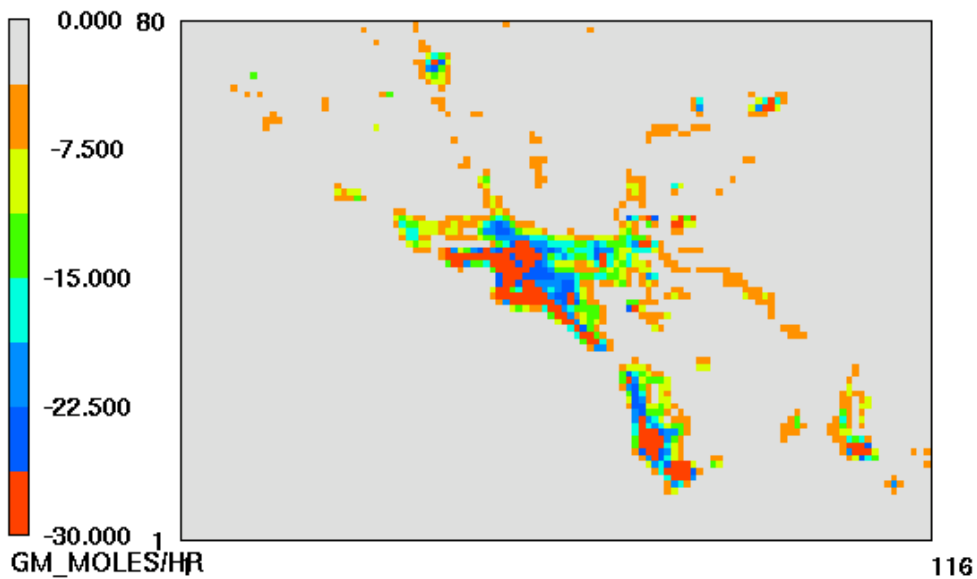


July 16, 2005 0:00:00  
Min= 0.000 at (1,1), Max= 0.000 at (1,1)

e

## Layer 1 OLE1b-OLE1a

SCOS 7/197 2005 \*\* ALL EMISSIONS  
a=em05197.df05a.SLb, b=em05197.df05a.SLb

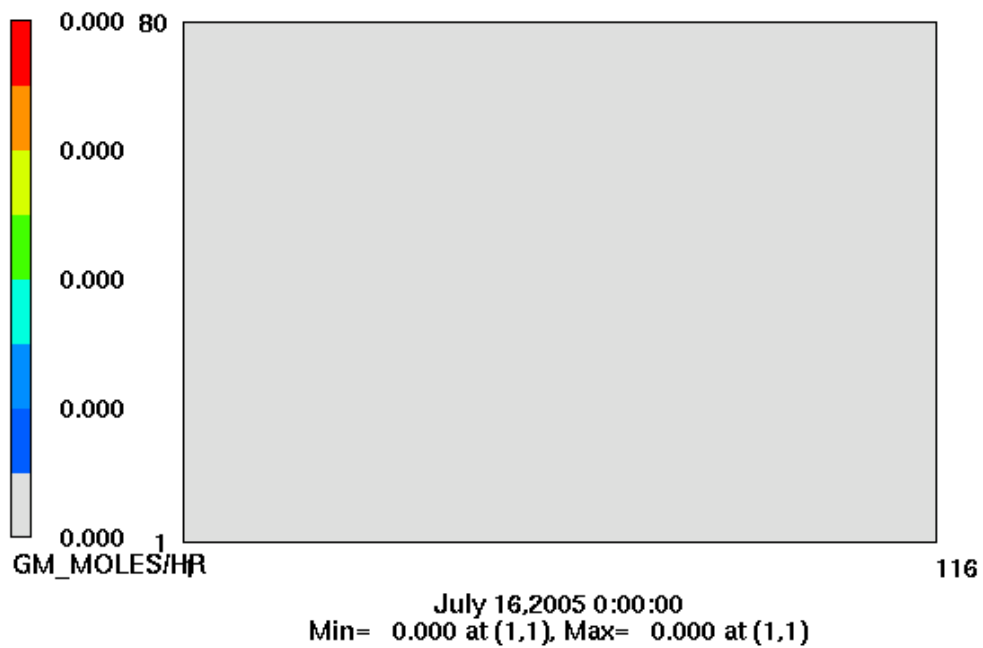


July 16, 2005 14:00:00  
Min=-176.756 at (80,50), Max= 0.000 at (1,1)

f

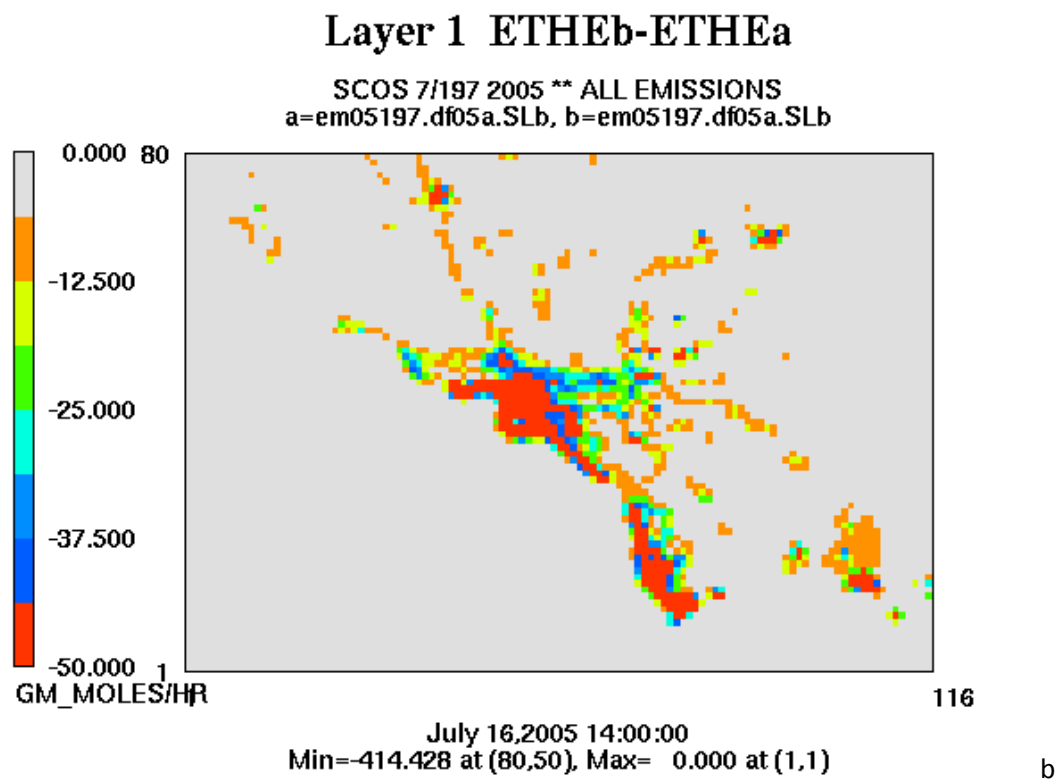
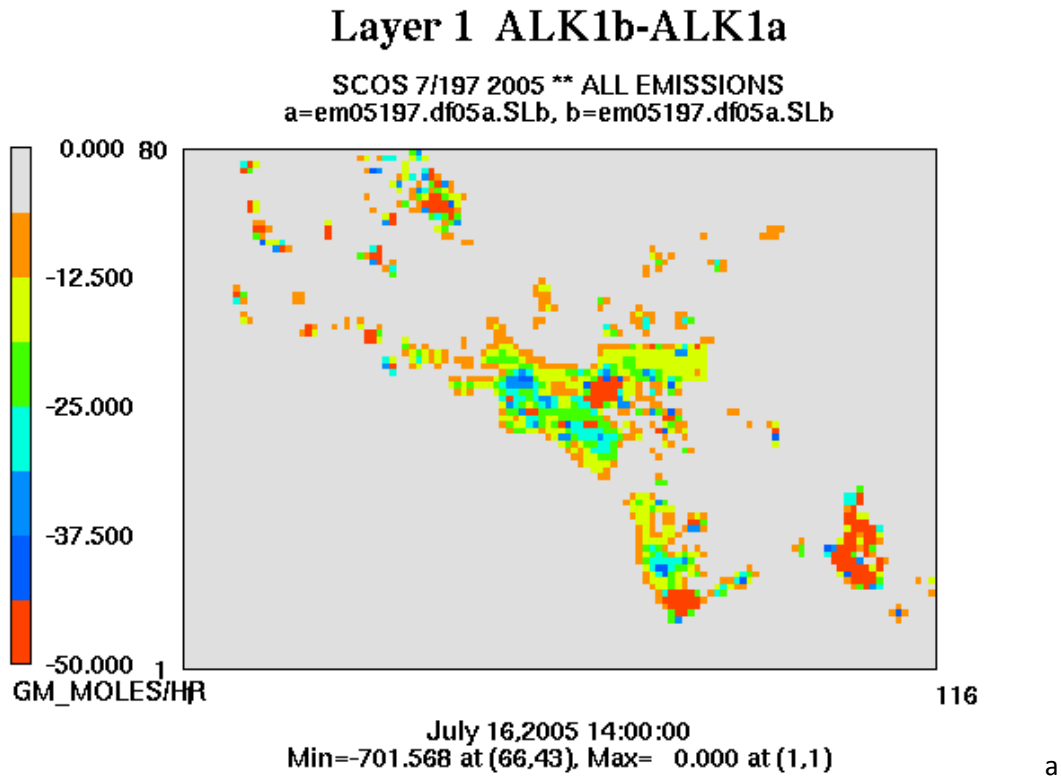
# Layer 1 TERPb-TERPa

SCOS 7/197 2005 \*\* ALL EMISSIONS  
a=em05197.df05a.SLb, b=em05197.df05a.SLb



g

Figure H6 (a-g): 20% Reduction in ROG Emissions; 20% Reduction in NOx Emissions



## Layer 1 ISOPb-ISOPa

SCOS 7/197 2005 \*\* ALL EMISSIONS  
a=em05197.df05a.SLb, b=em05197.df05a.SLb

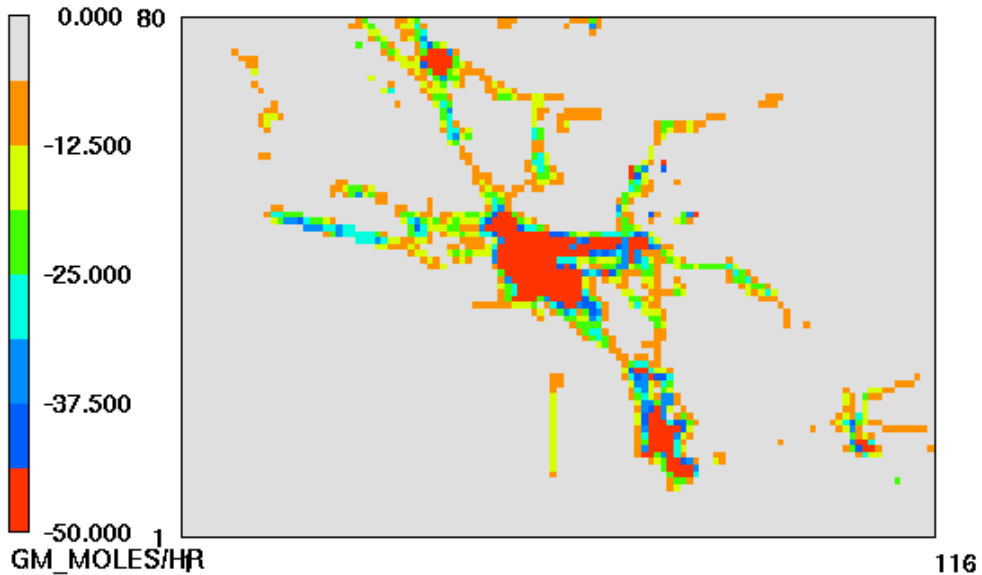


July 16,2005 0:00:00  
Min= 0.000 at (1,1), Max= 0.000 at (1,1)

c

## Layer 1 NO2b-NO2a

SCOS 7/197 2005 \*\* ALL EMISSIONS  
a=em05197.df05a.SLb, b=em05197.df05a.SLb

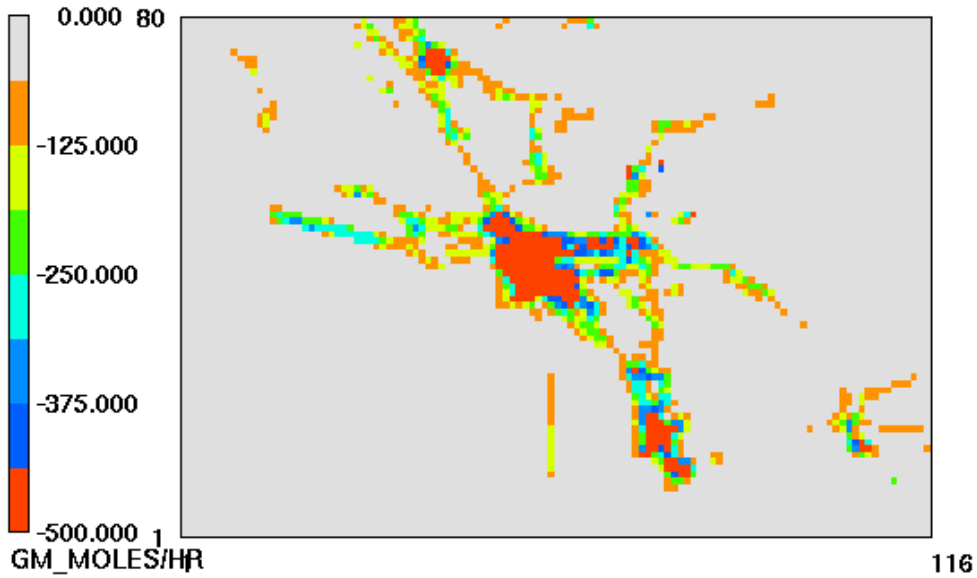


July 16,2005 14:00:00  
Min=-233.909 at (40,74), Max= 0.000 at (1,1)

d

## Layer 1 NOb-NOa

SCOS 7/197 2005 \*\* ALL EMISSIONS  
a=em05197.df05a.SLb, b=em05197.df05a.SLb

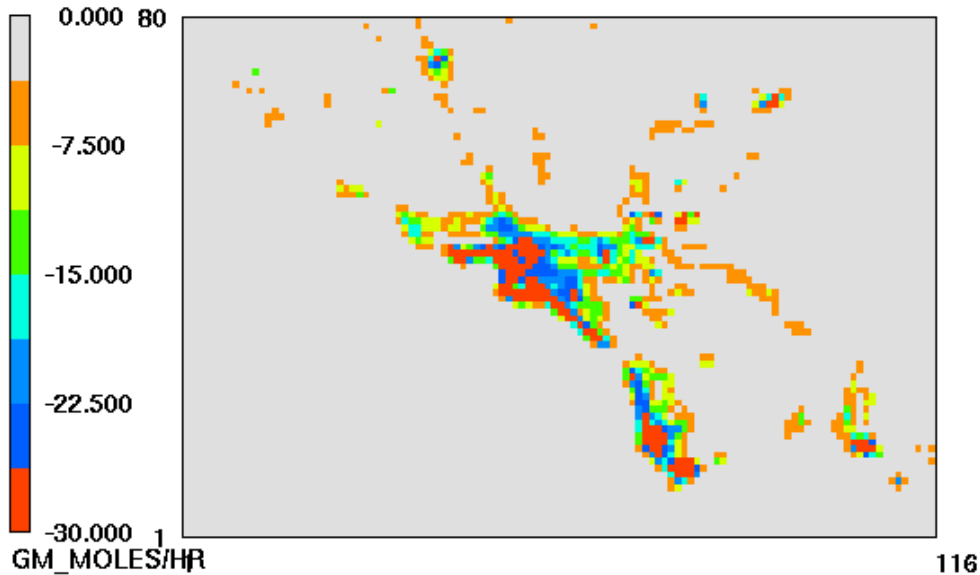


July 16,2005 14:00:00  
Min=-2058.564 at (40,74), Max= 0.000 at (1,1)

e

## Layer 1 OLE1b-OLE1a

SCOS 7/197 2005 \*\* ALL EMISSIONS  
a=em05197.df05a.SLb, b=em05197.df05a.SLb

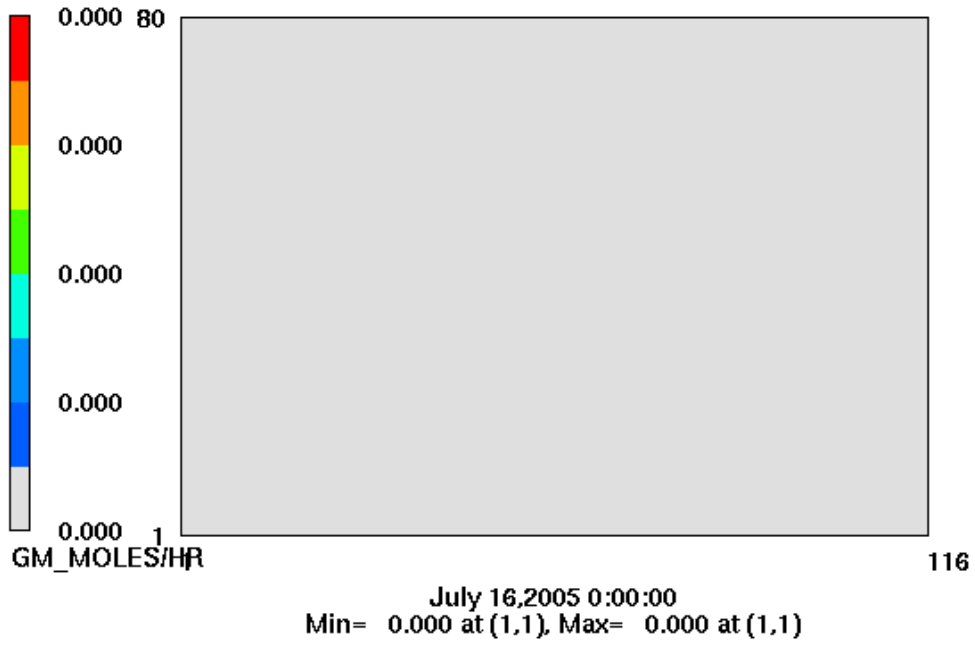


July 16,2005 14:00:00  
Min=-176.756 at (80,50), Max= 0.000 at (1,1)

f

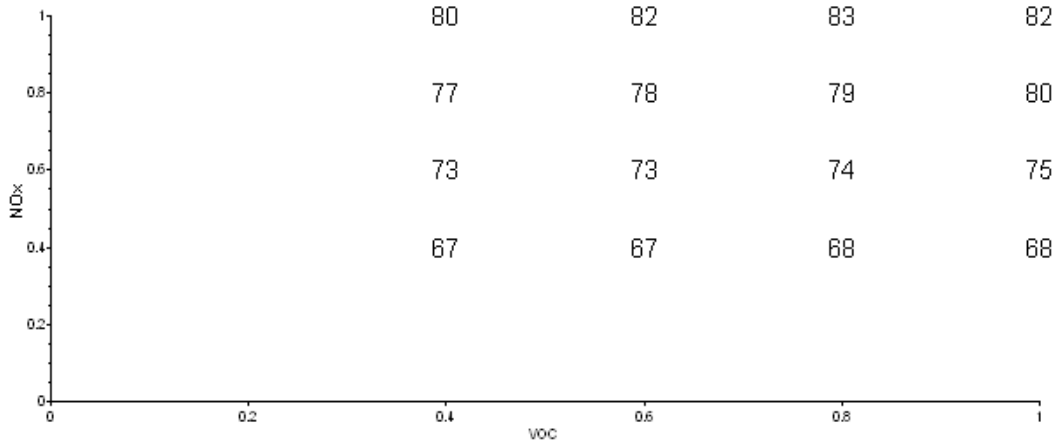
# Layer 1 TERPb-TERPa

SCOS 7/197 2005 \*\* ALL EMISSIONS  
a=em05197.df05a.SLb, b=em05197.df05a.SLb



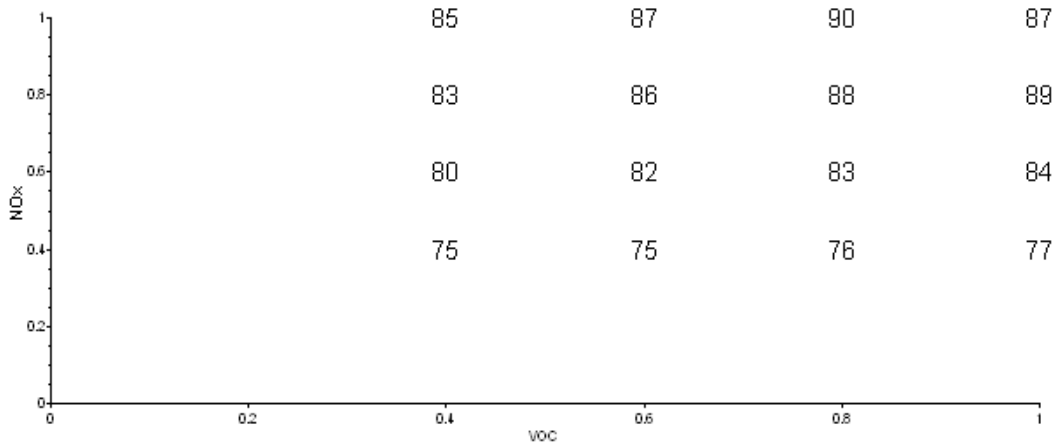
g

**Figure H7.1 through H7.32: Central California Carrying Capacity  
for NOx and ROG**



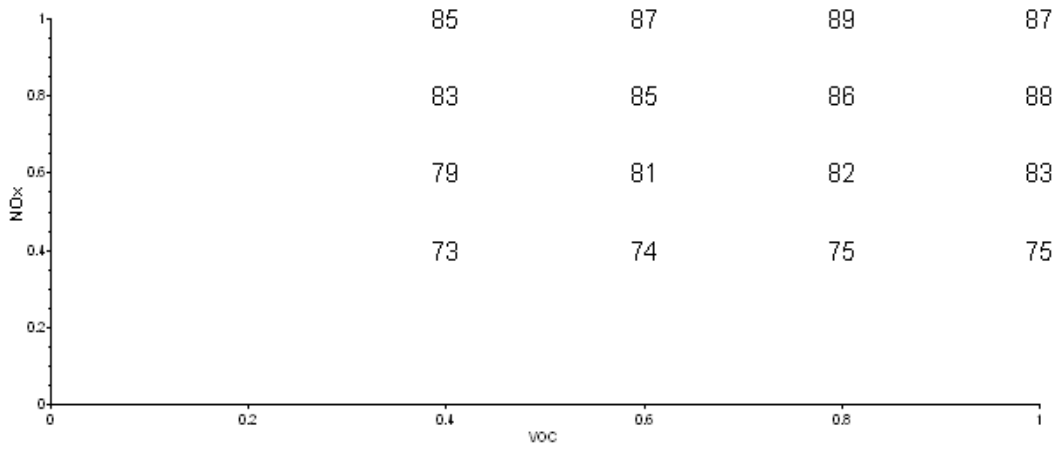
1

061-0002 Placer / Auburn / C Avenue



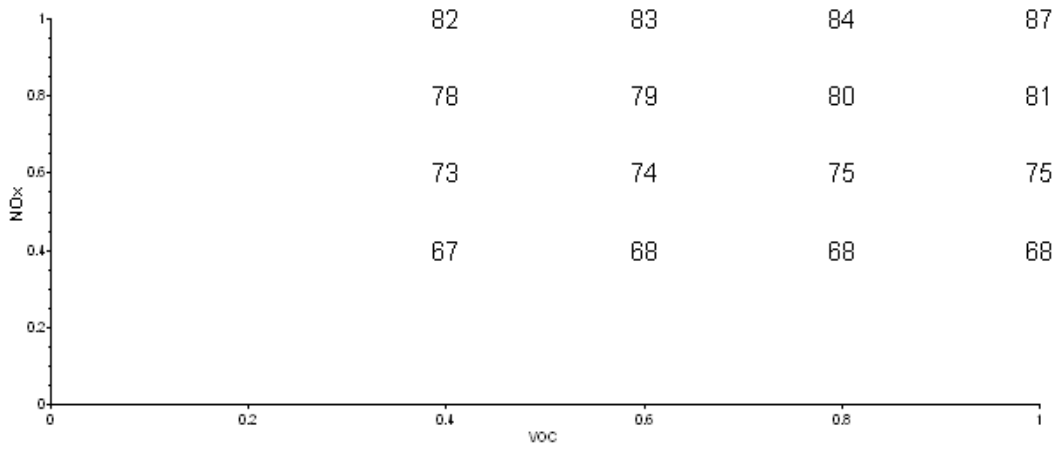
2

061-0006 Placer / Roseville / Sunrise Blvd.



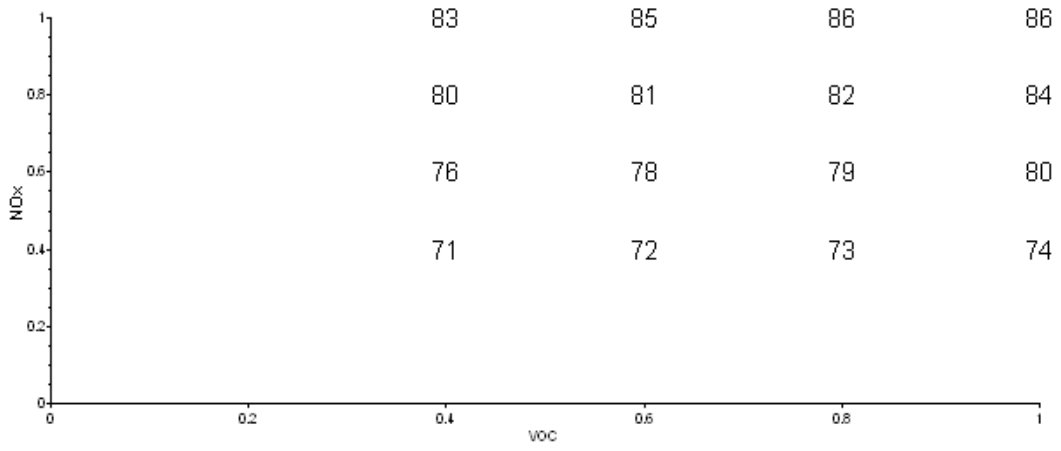
3

061-3001 Placer / Rocklin / Rocklin Road



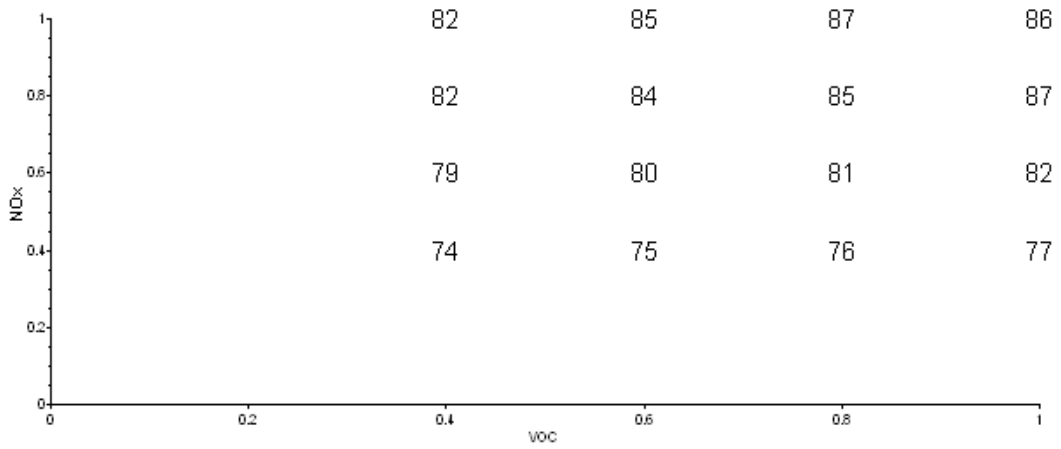
4

017-0020 El Dorado / Cool / American River Trail



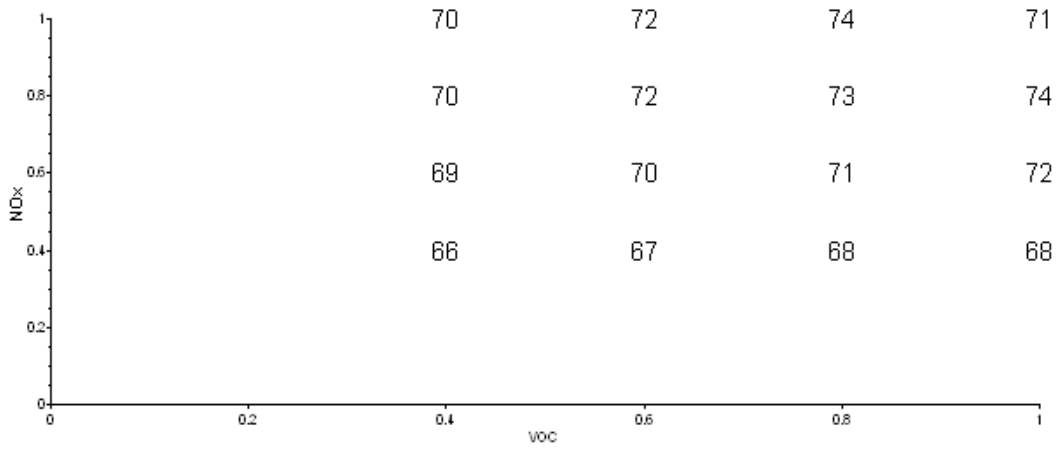
5

067-0002 Sacramento / North Highlands / Black Foot Way



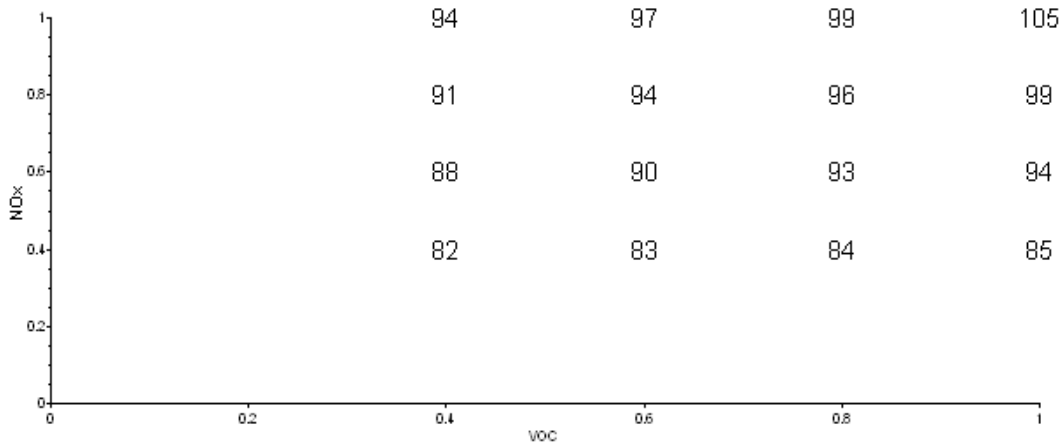
6

067-0006 Sacramento / Del Paso / Avalon Drive



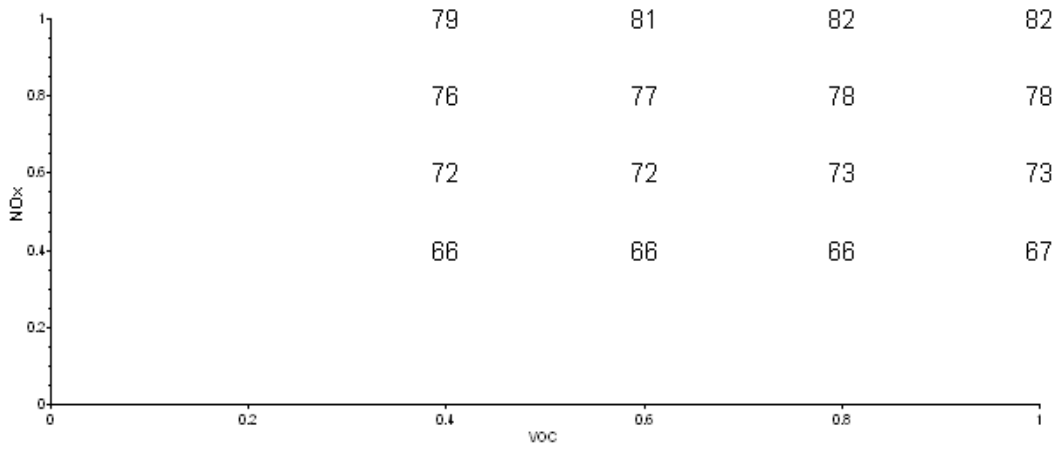
7

067-0010 Sacramento / Sacramento / T Street



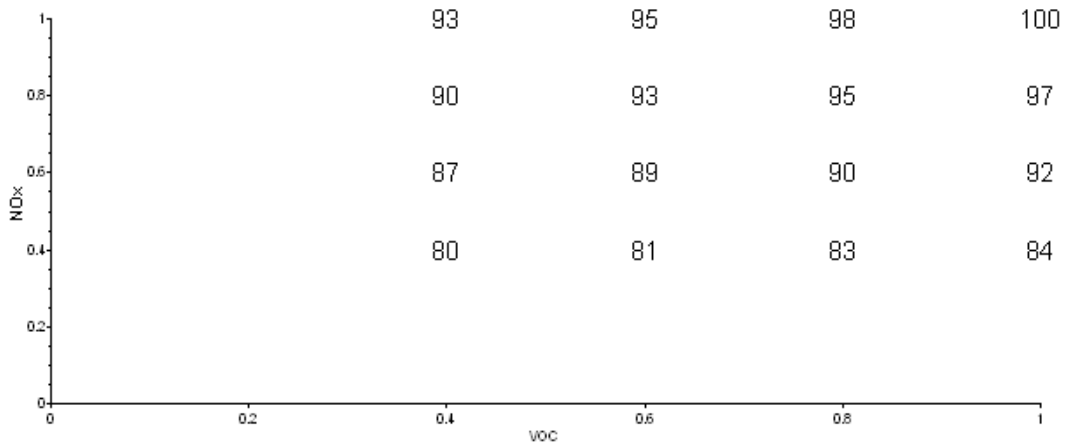
8

067-0012 Sacramento / Folsom / Natoma



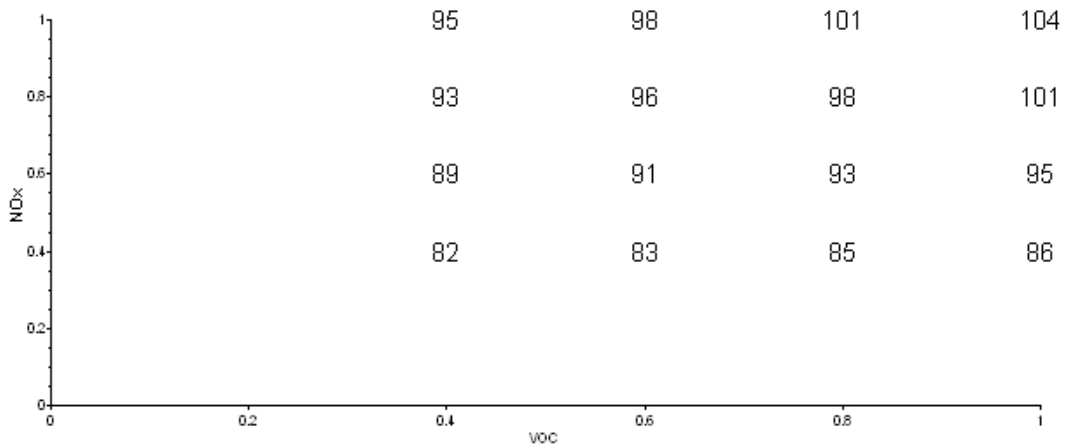
067-0013 Sacramento / Sacramento / Airport Road

9



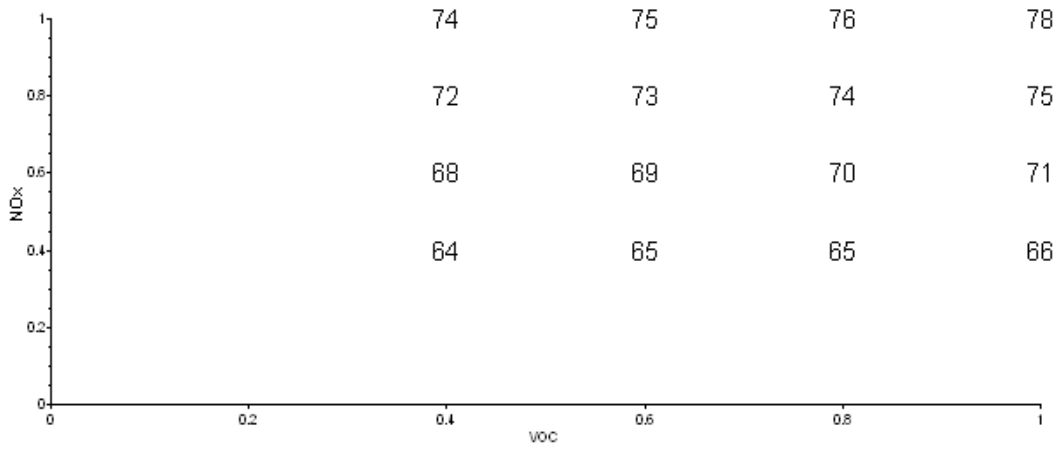
067-1001 Sacramento / Folsom / Liedesdorff

10



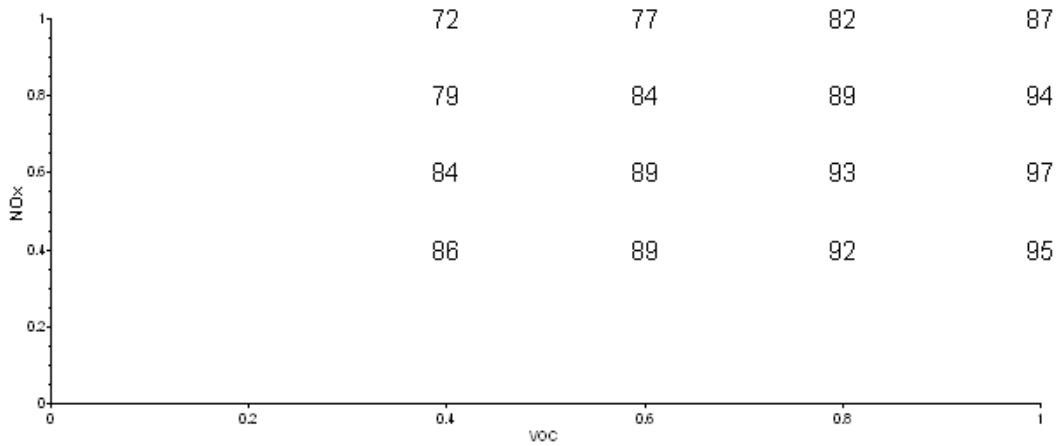
067-5003 Sacramento / Sloughhouse / Sloughhouse Road

11



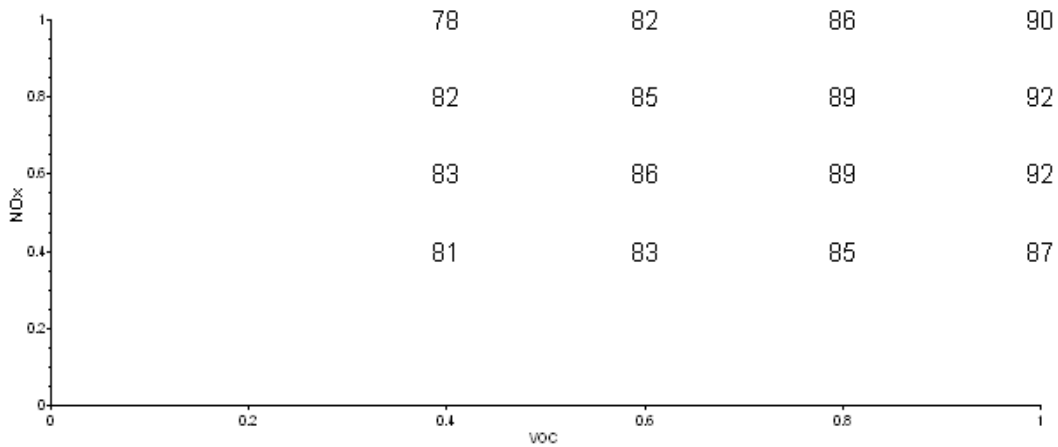
12

085-0002 Santa Clara / Gilroy / Princeville Street



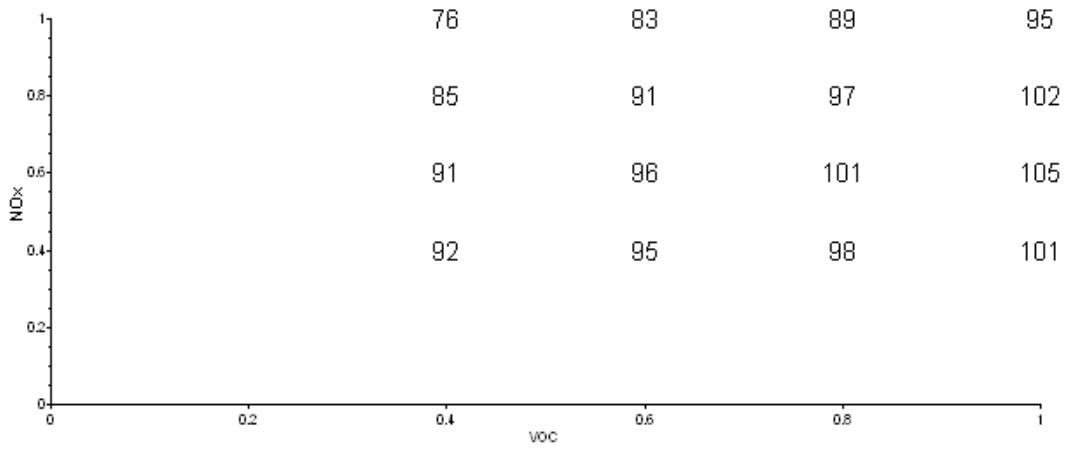
13

085-0004 and 085-0005 Santa Clara / San Jose / 4<sup>th</sup> Street also San Jose / Jackson Street



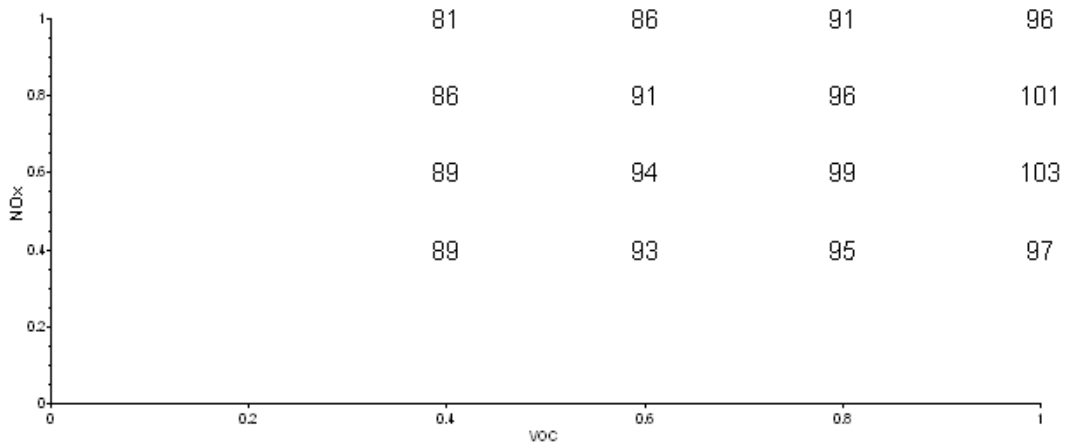
14

085-1002 Santa Clara / Mountain View / Cuesta Drive



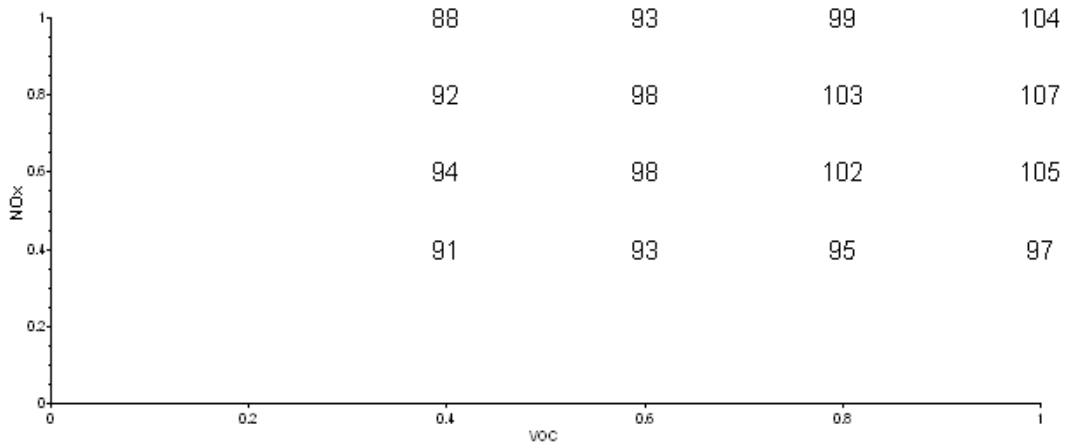
15

085-2004 Santa Clara / San Jose / W. San Carlos



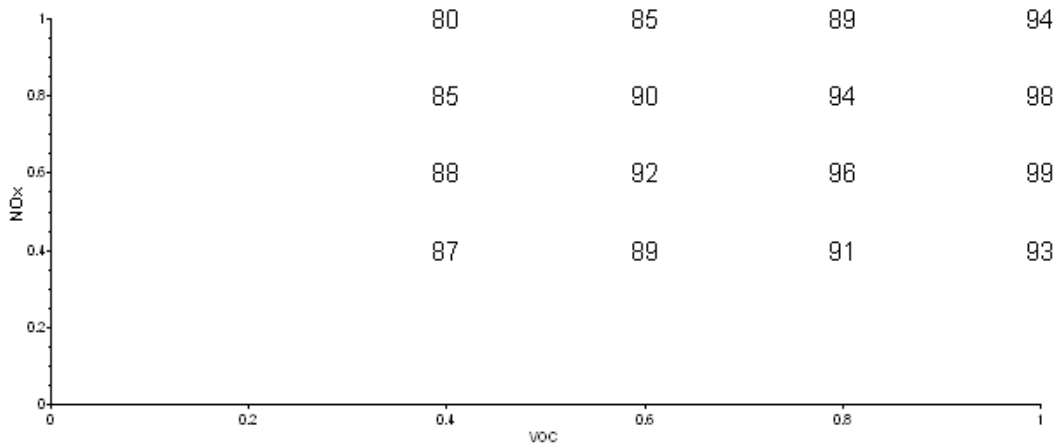
16

085-2005 Santa Clara / San Jose / Piedmont Road



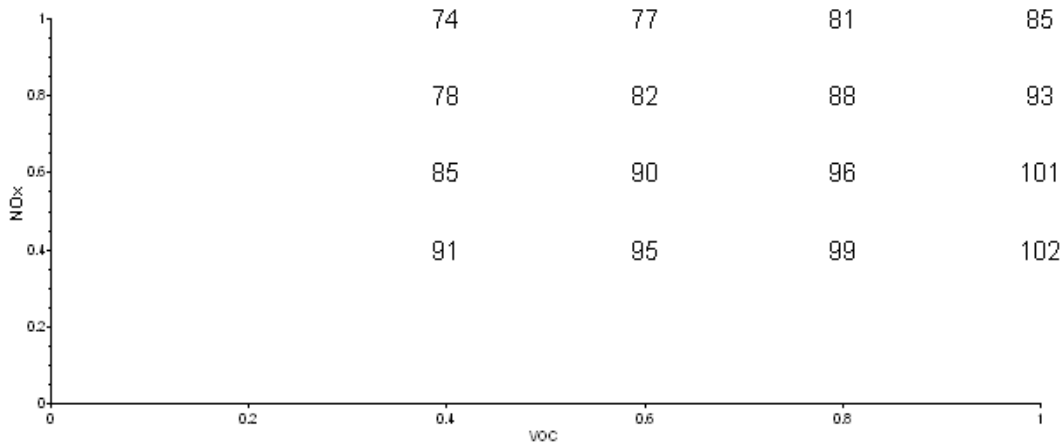
17

085-2006 Santa Clara / San Martin / Murphy Avenue



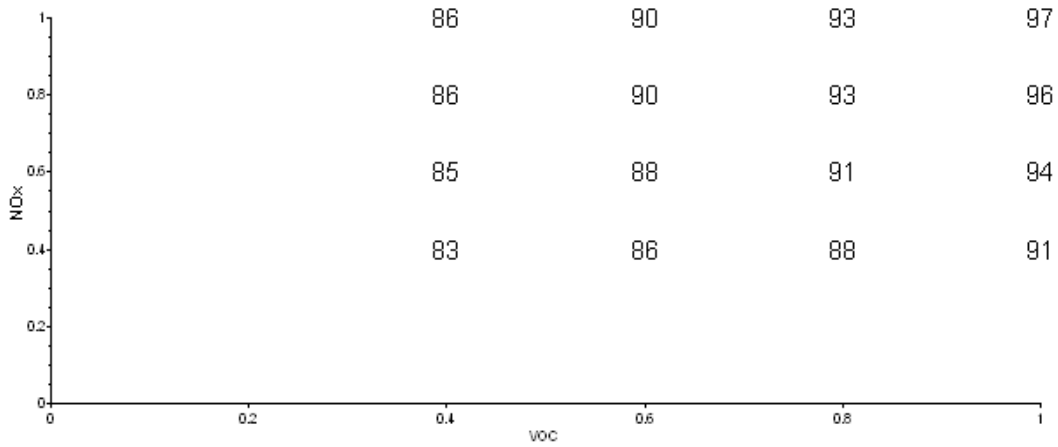
085-2007 Santa Clara / Ticonderoga Drive

18



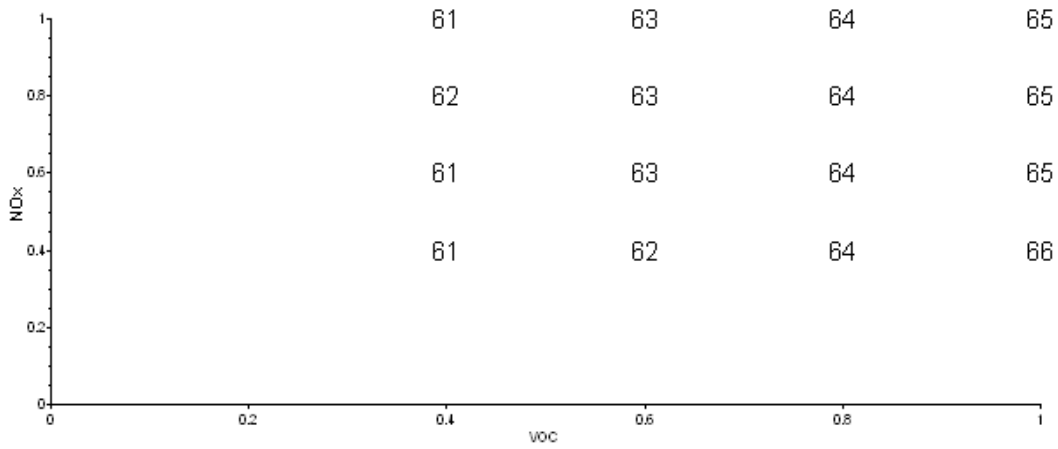
013-0002 Contra Costa / Treat Blvd.

19



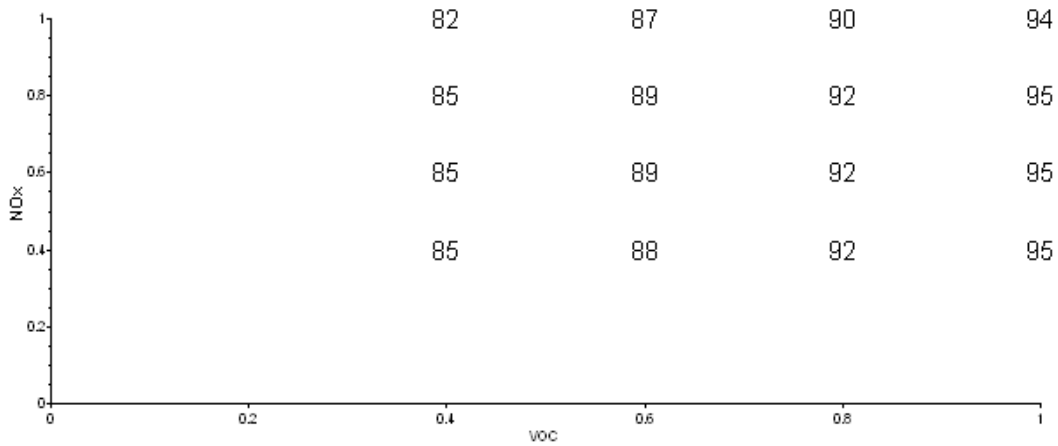
013-1002 Contra Costa / Bethel Island / Bethel Island Road

20



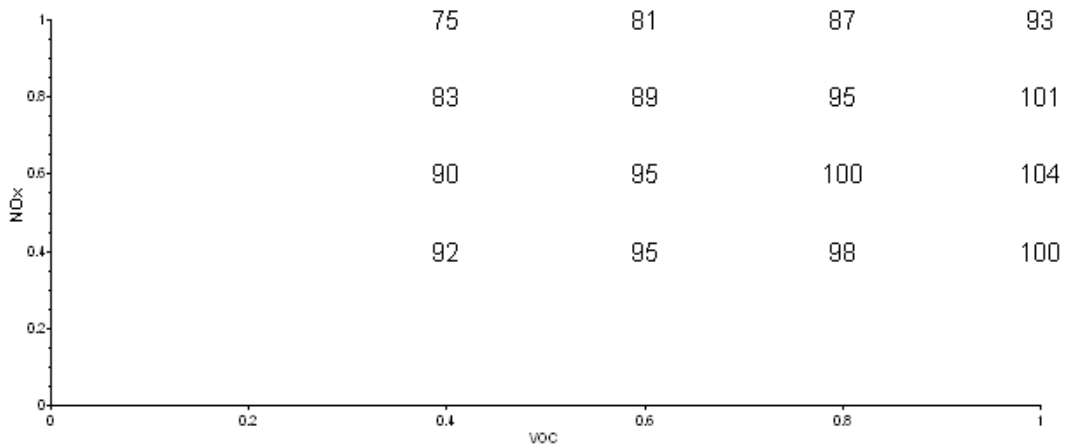
21

013-1003 Contra Costa / El Portal Shopping Center



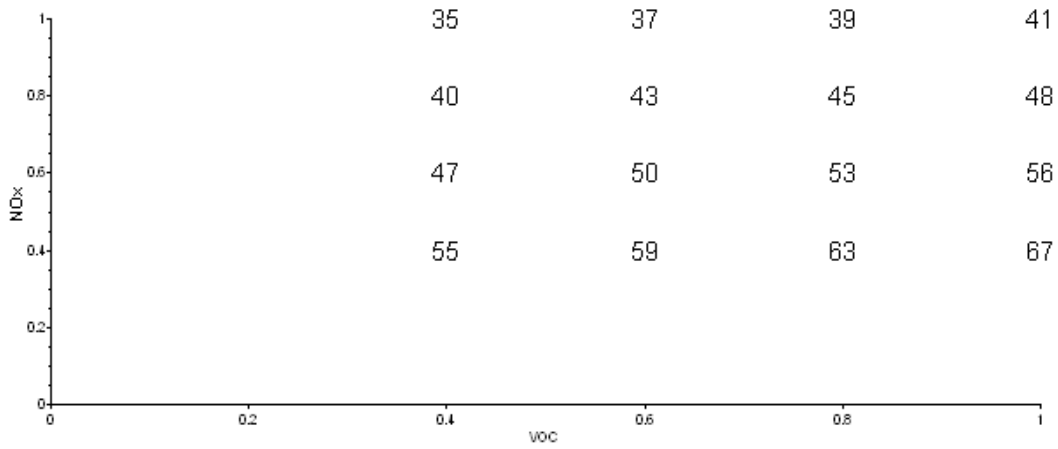
22

013-3001 Contra Costa / Pittsburg, W. 10<sup>th</sup> Street



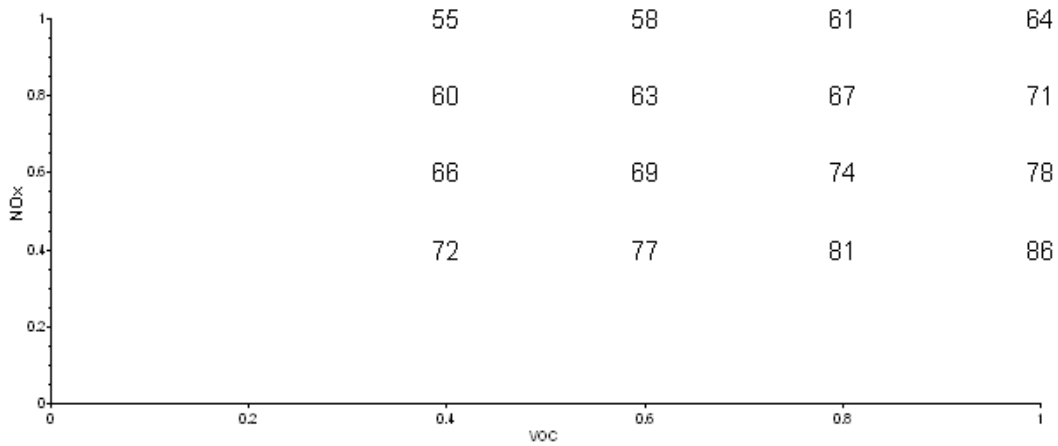
23

001-0003 Alameda / Livermore / Old 1<sup>st</sup> Street



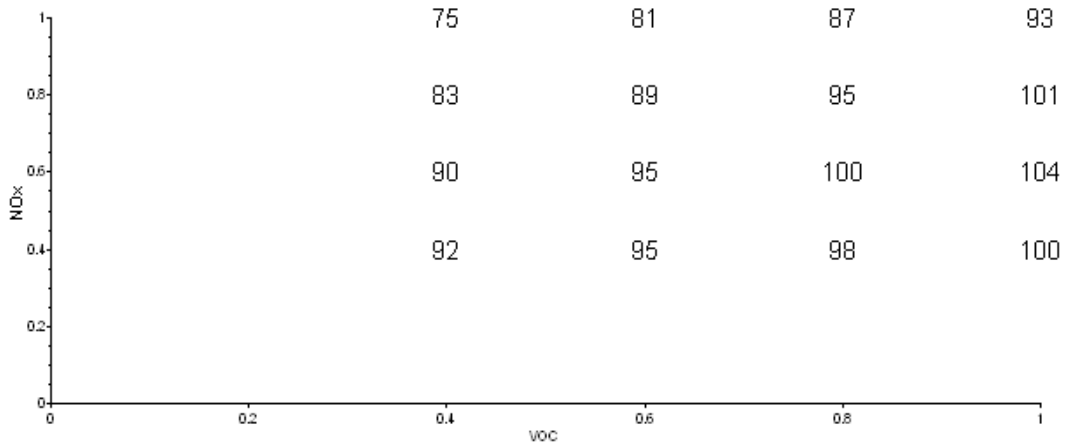
24

001-0005 Alameda / Oakland / Alice Street



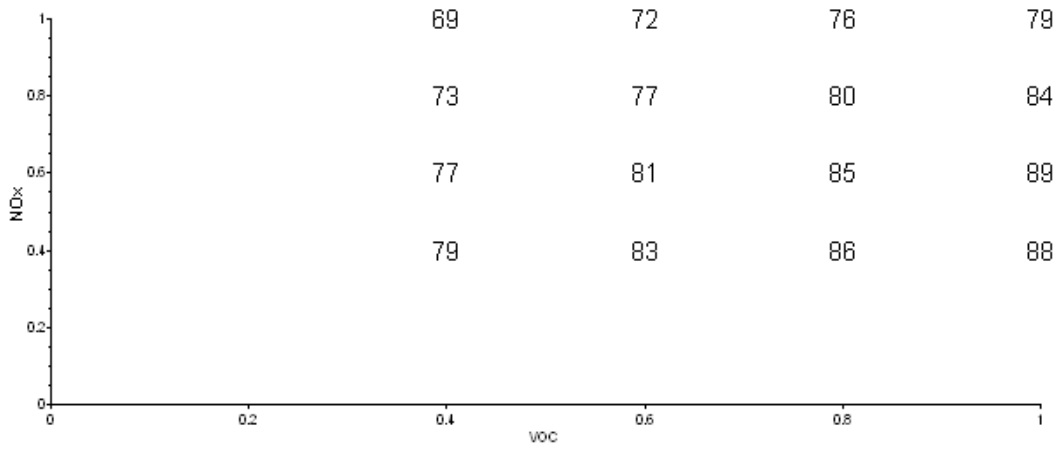
25

001-0006 Alameda / San Leandro / Foothill Blvd.



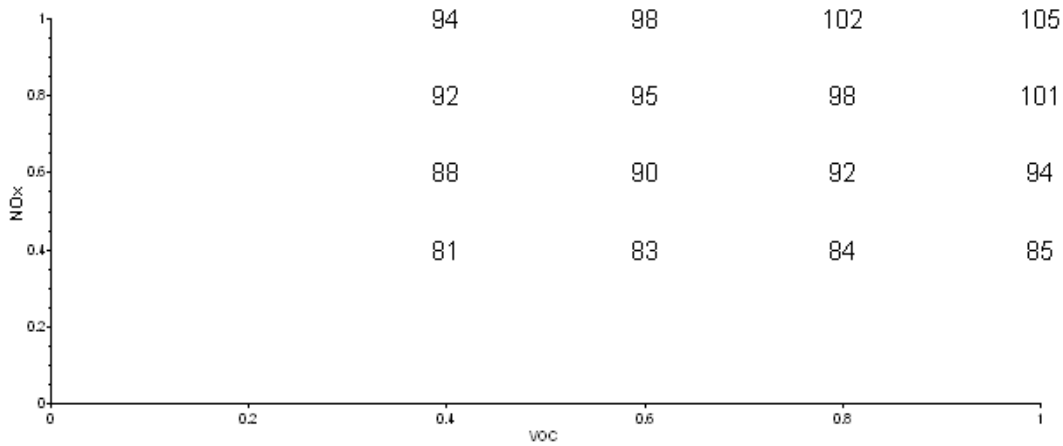
26

001-0007 Alameda / Livermore / Rincon Avenue



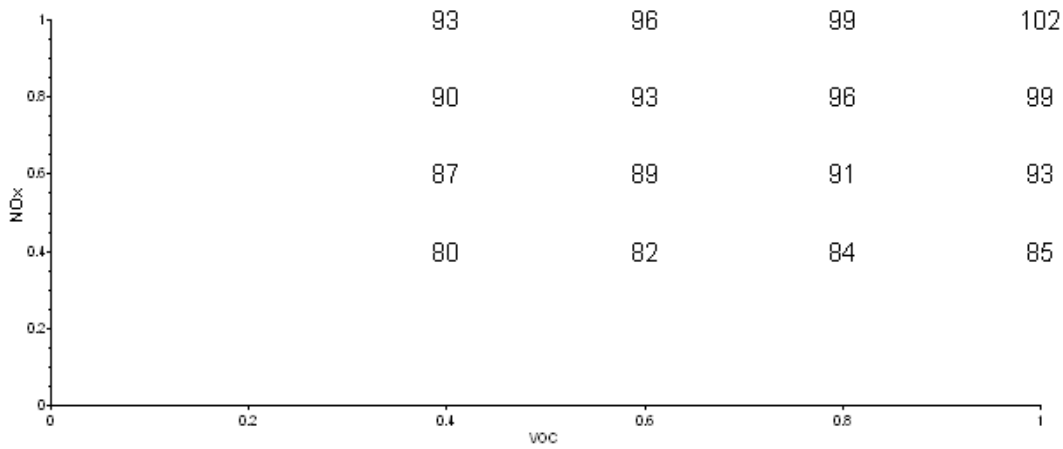
27

001-1001 Alameda / Fremont / Chapel Way



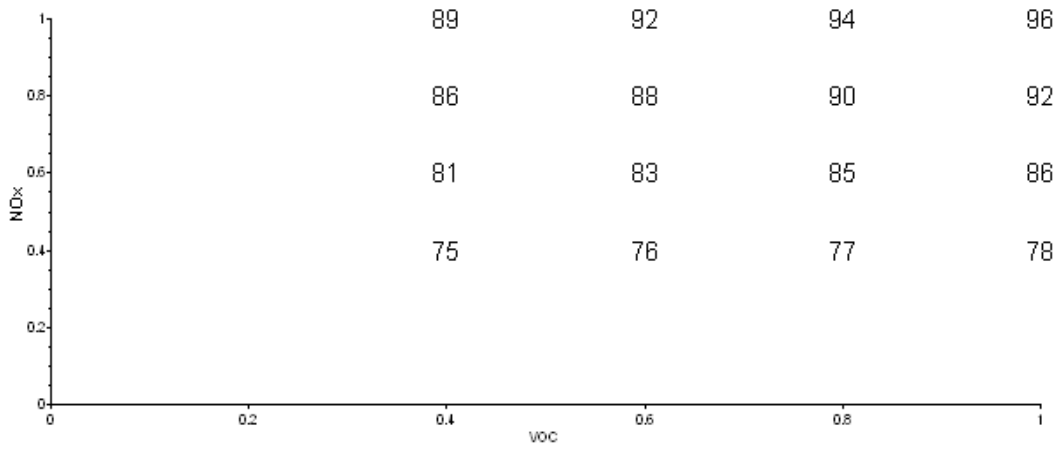
28

019-0007 Fresno / Fresno / Drummond Street



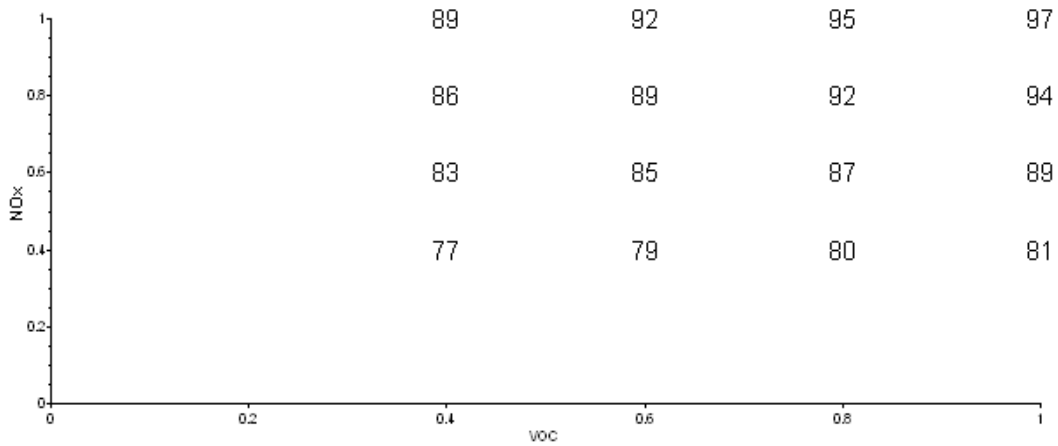
29

019-0008 Fresno / Fresno / First Street



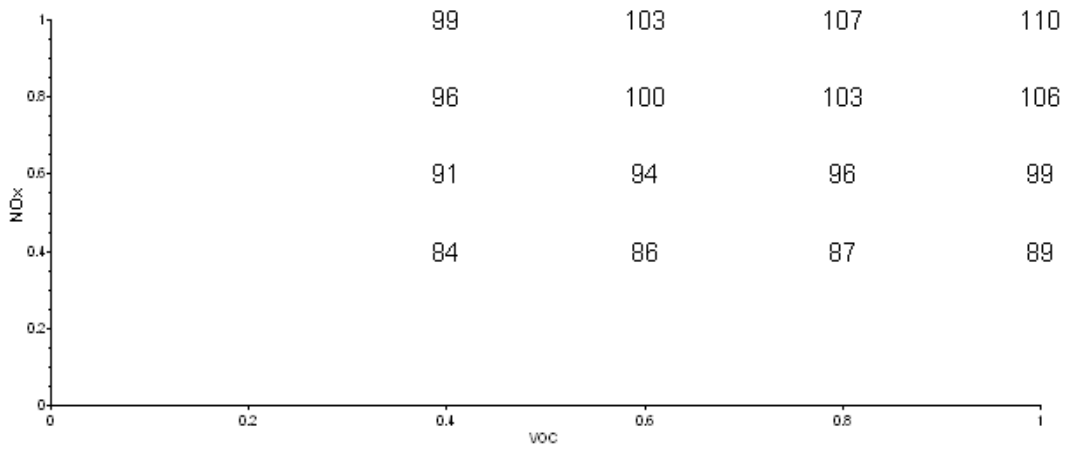
30

019-0242 Fresno / Fresno / Blythe



31

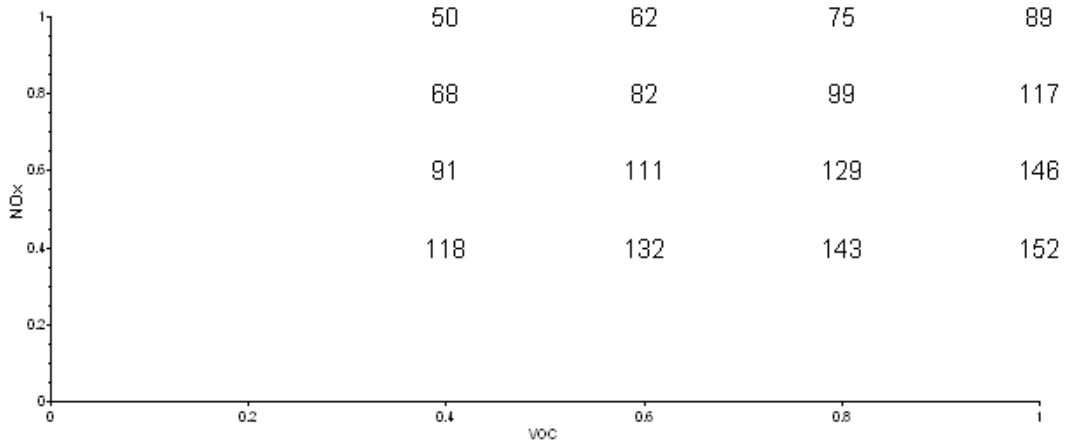
019-0243 Fresno / Fresno / W. Weldon



32

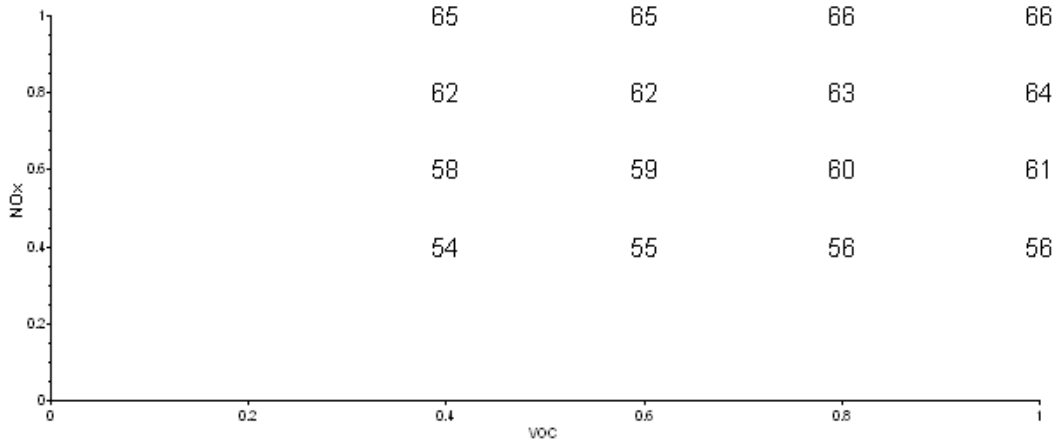
019-4001 Fresno / Parlier / S. Riverbend

**Figures H8.1 through H8.24 Southern California Carrying Capacity  
for NOx and ROG**



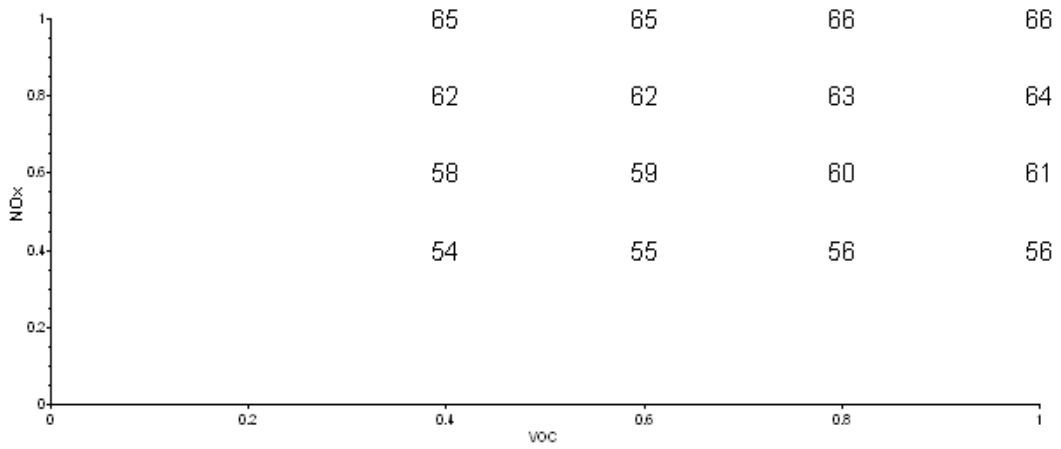
1

071-1004 San Bernardino Rd., Upland



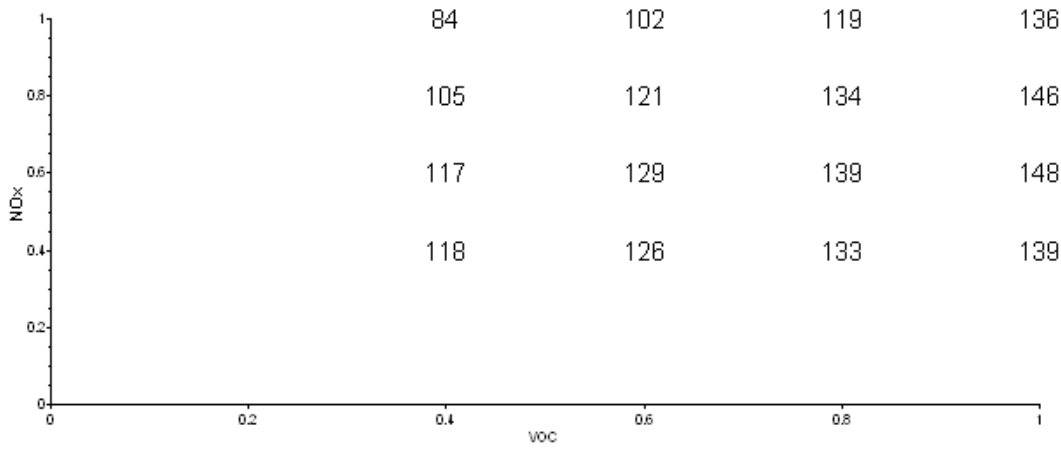
2

071-2002 Arrow Blvd., Fontana



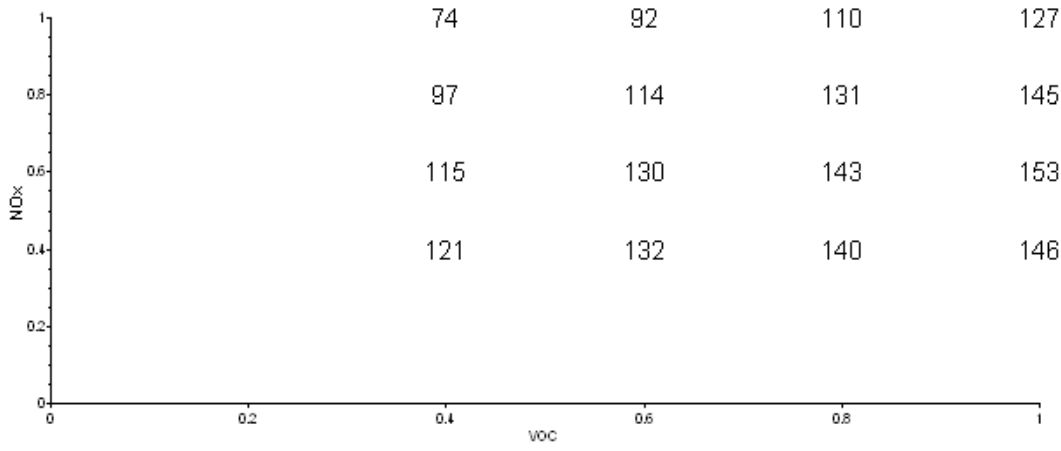
3

071-4001 Olive Street, Hesperia



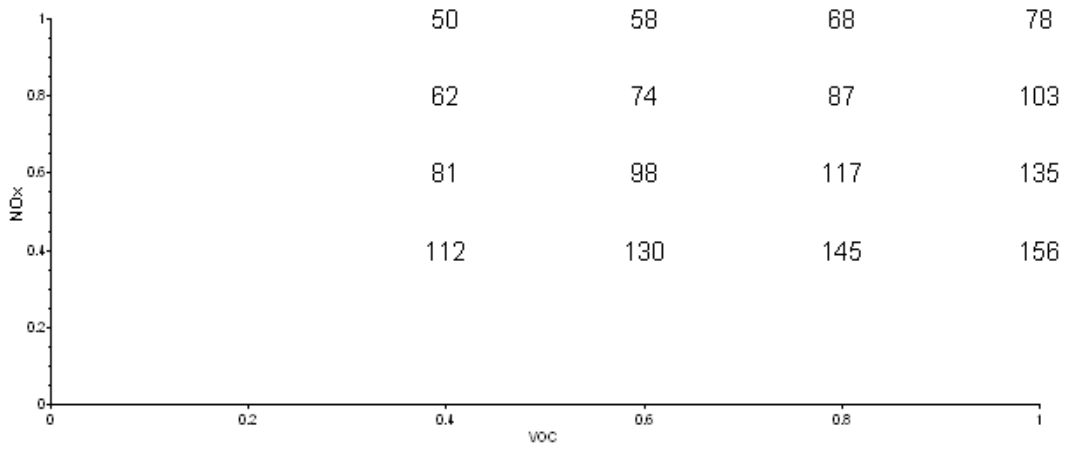
4

071-4003 North Dearborn, Redlands



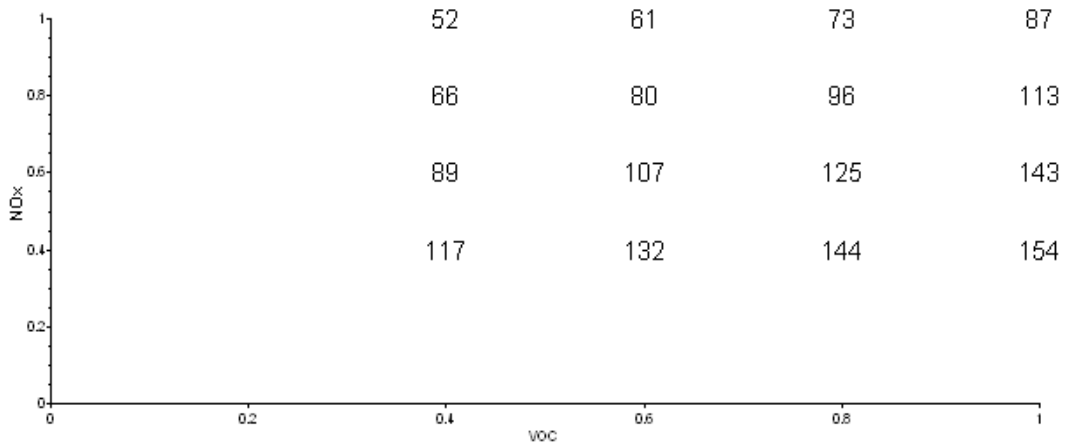
5

071-9004 4<sup>th</sup> Street, San Bernardino



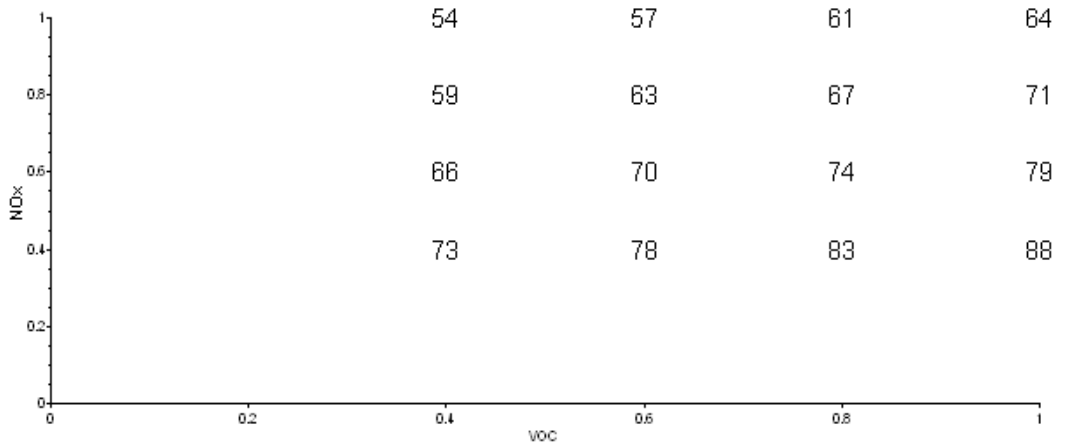
6

037-0002 N. Loren Avenue, Azusa



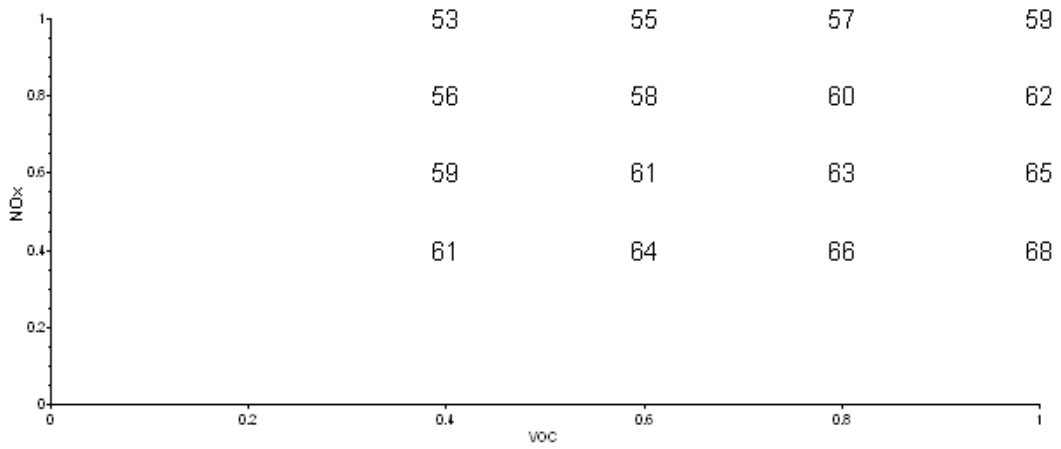
7

037-0016 Laurel, Glendora



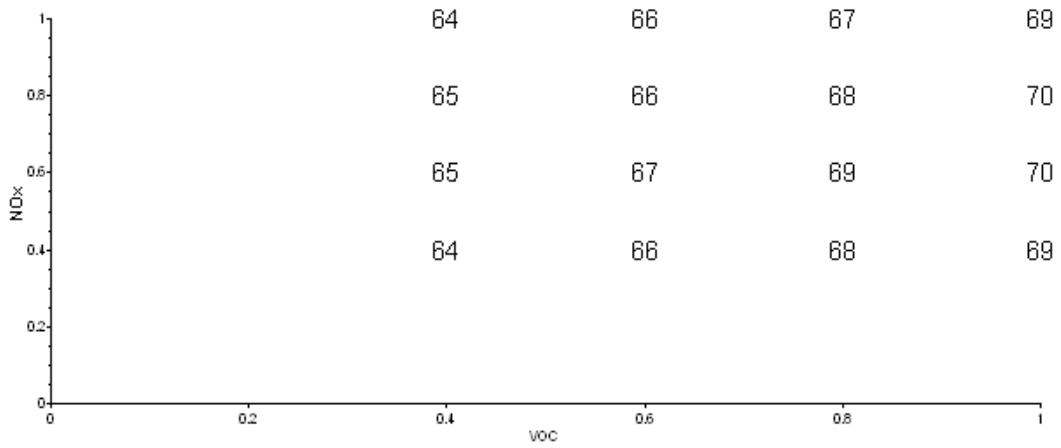
8

037-0030 Mott Street, Los Angeles



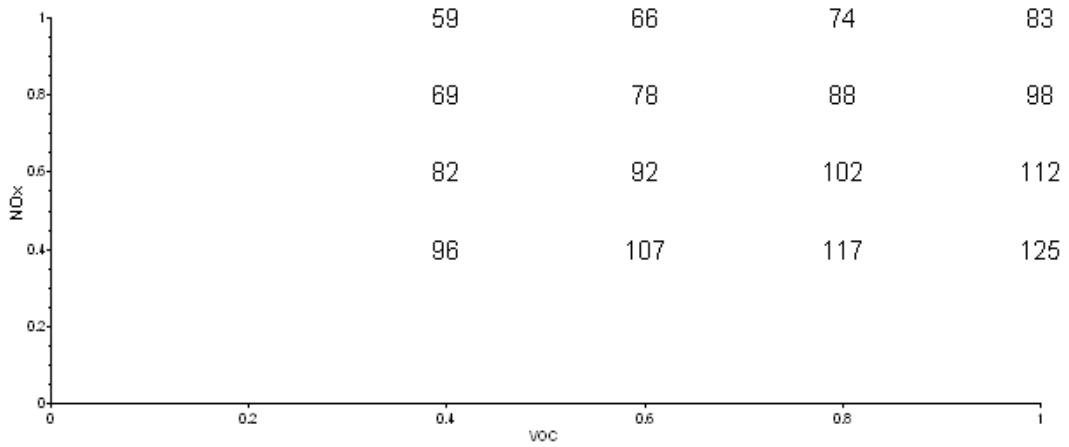
9

037-0031 Mahar Avenue, Wilmington



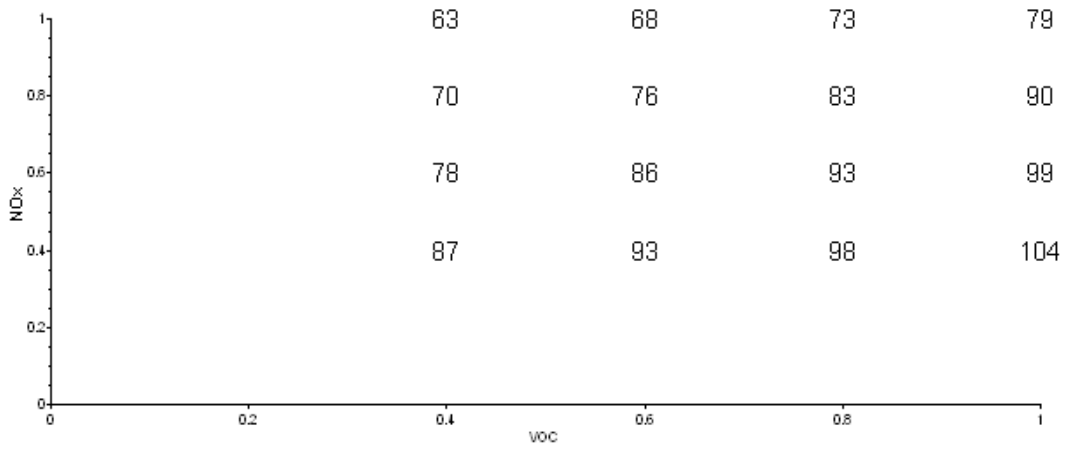
10

037-0113 VA Hospital, West Los Angeles



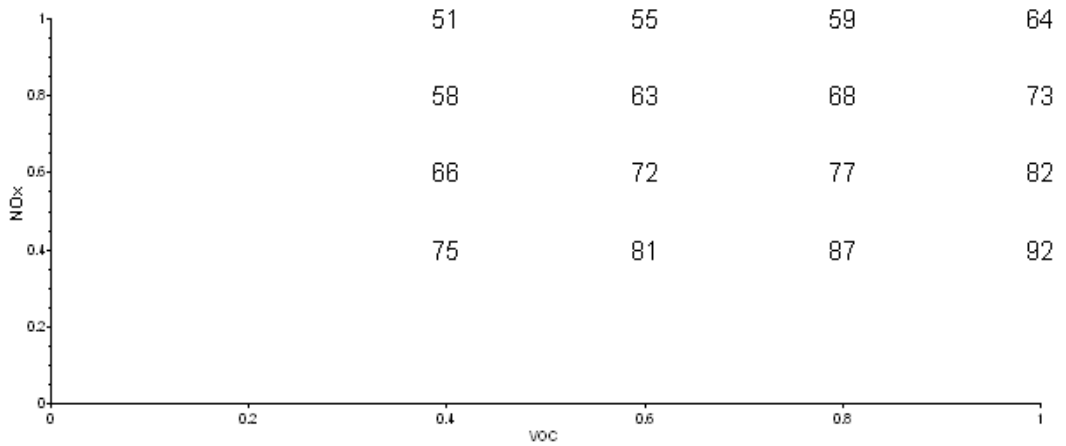
11

037-0206 Copley Drive, Diamond Bar



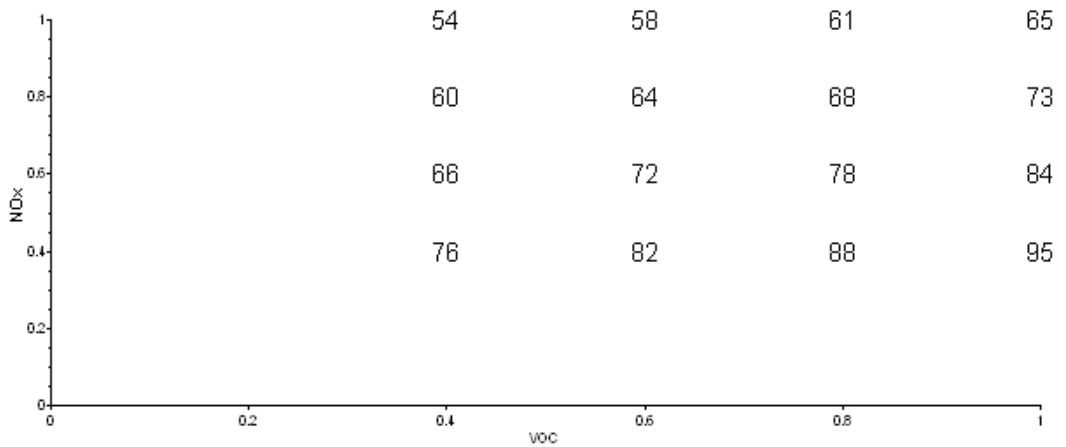
12

037-1002 W. Palm Avenue, Burbank



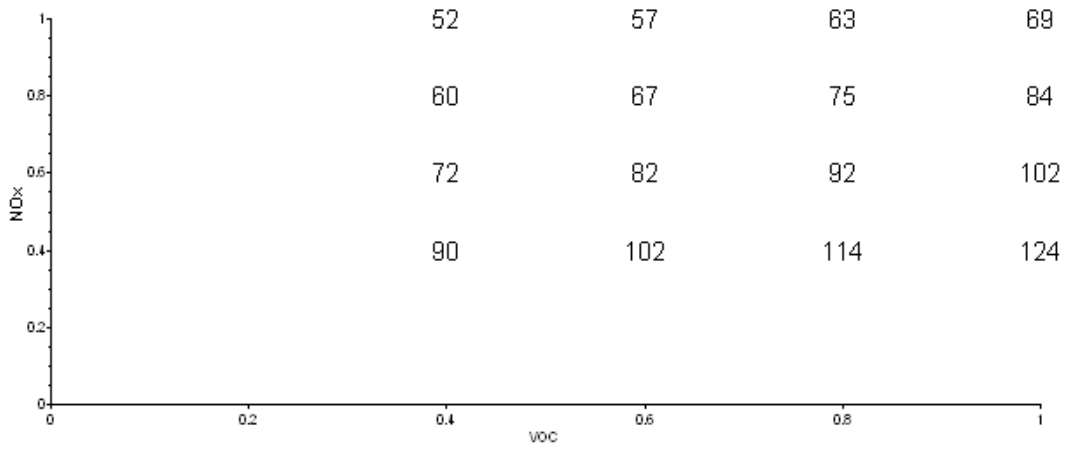
13

037-1103 N. Main Street, Los Angeles



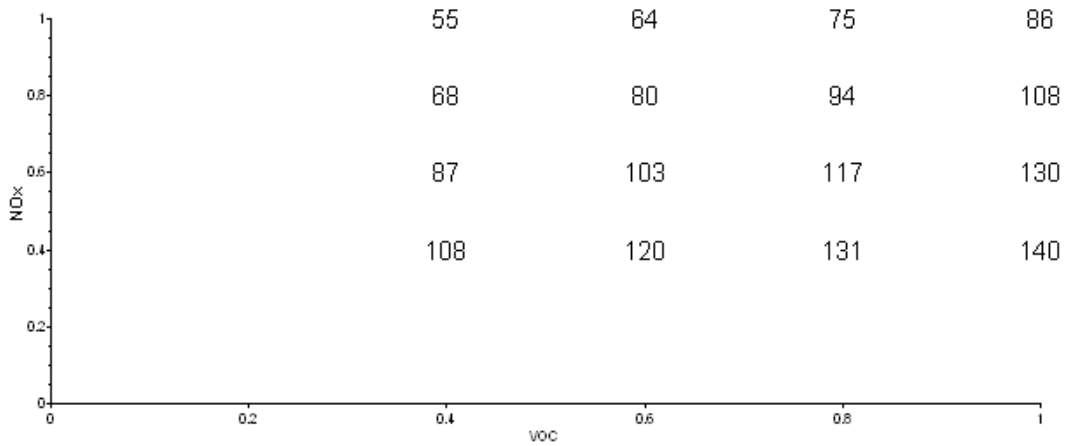
14

037-1301 Long Beach Blvd., Lynwood



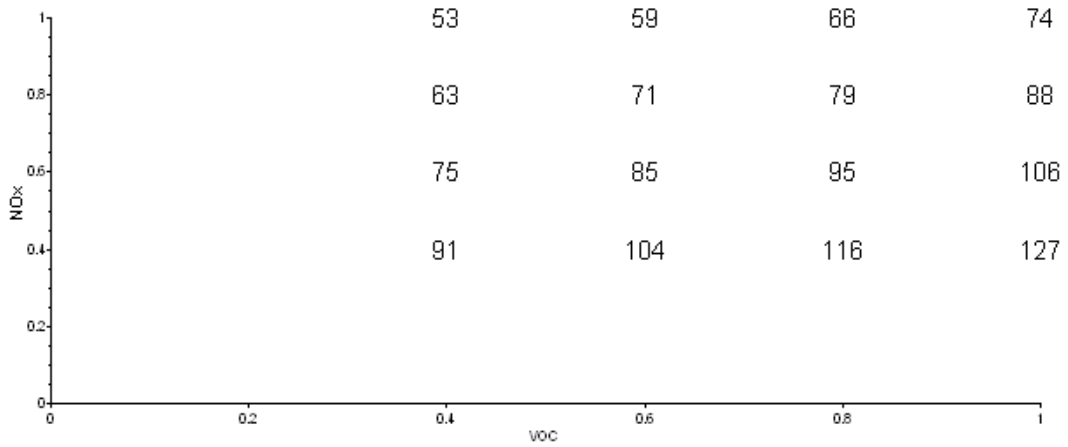
15

037-1601 San Gabriel River Pkwy, Pico Rivera



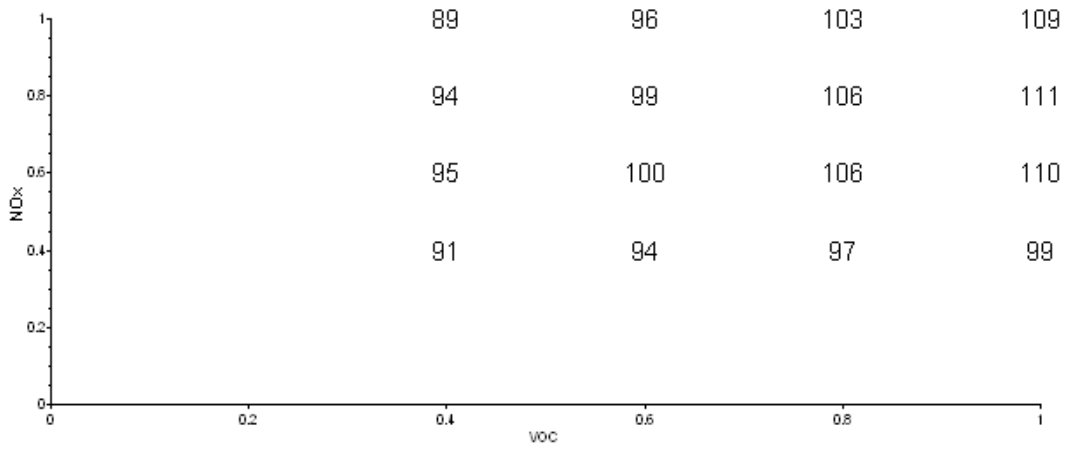
16

037-1701 N. Garey Avenue, Pomona



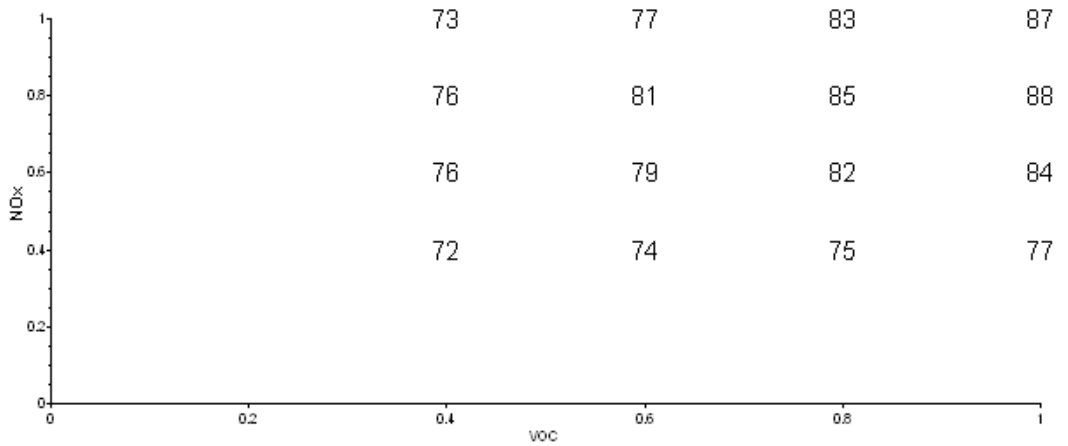
17

037-2005 S. Wilson Avenue, Pasadena



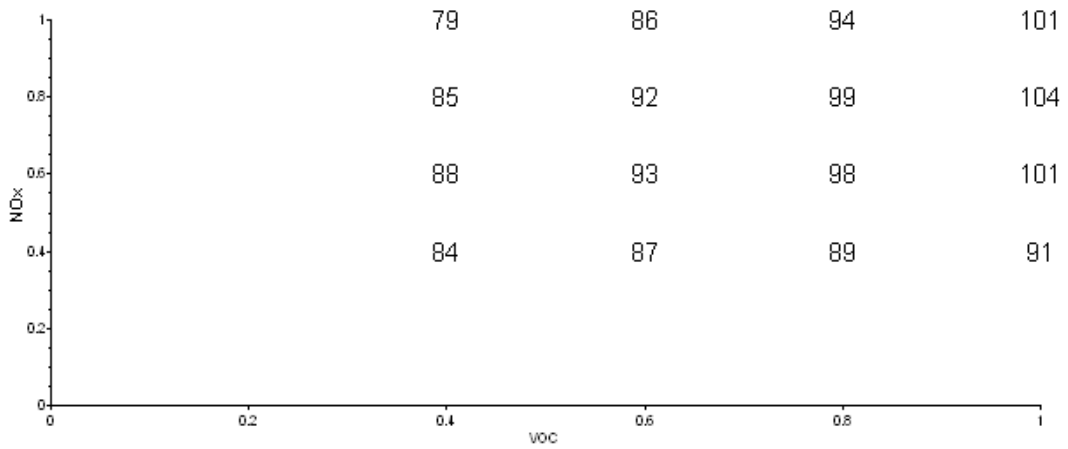
18

037-6002 San Fernando Rd., Santa Clarita



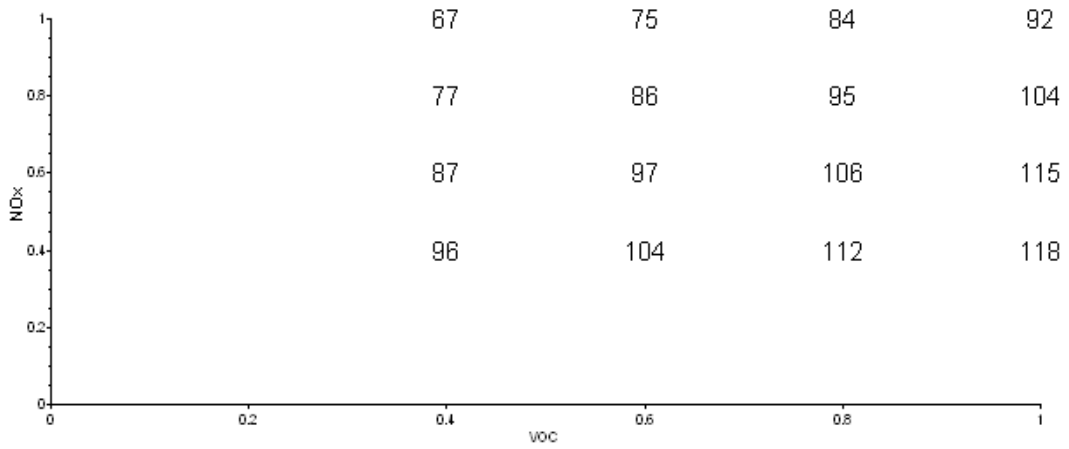
19

037-9002 W. Pondera Street, Lancaster



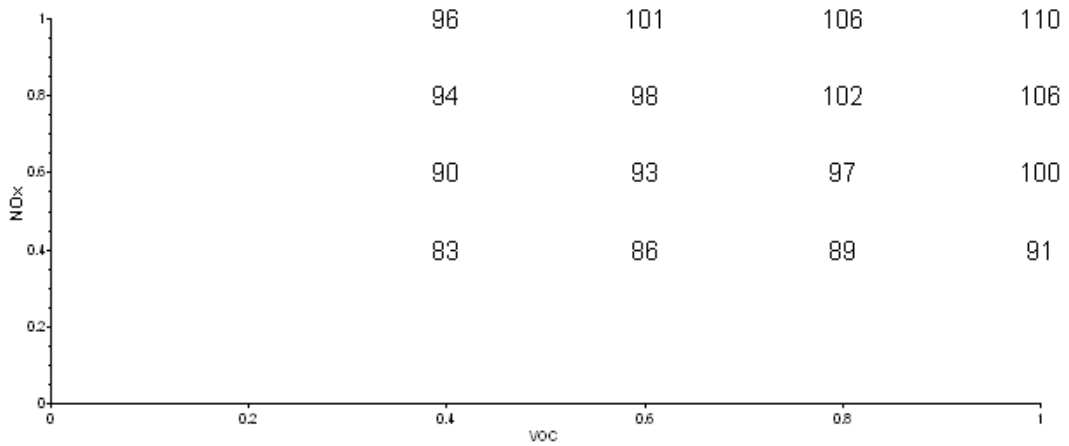
20

037-9006 E. Avenue S, Palmdale



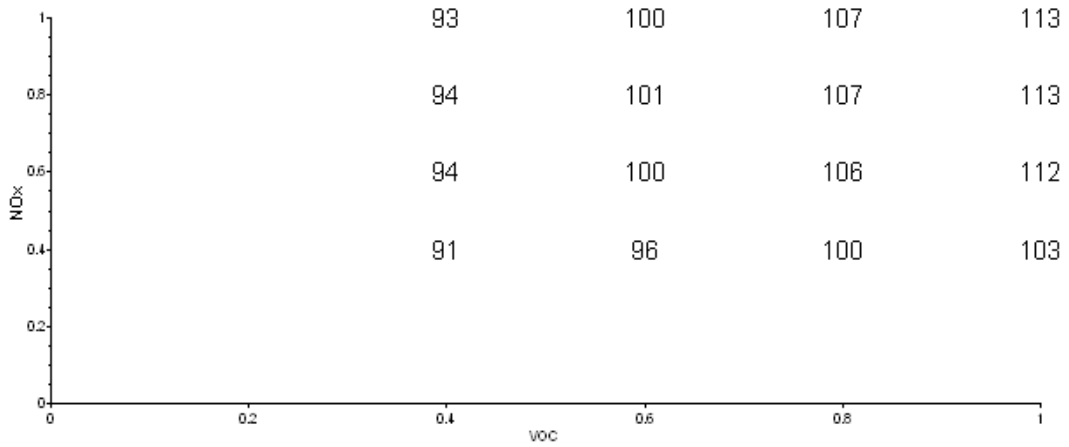
21

065-0003 Norco



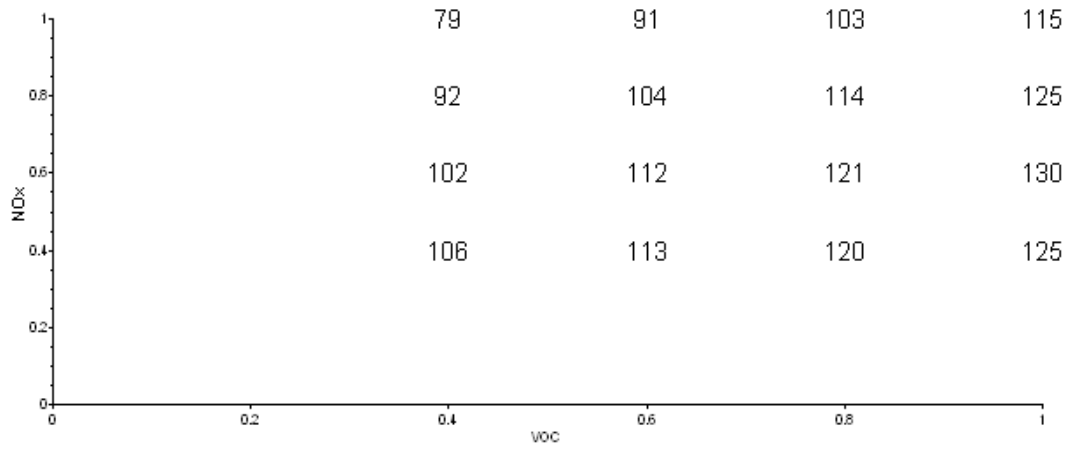
22

065-1002 State Street, Hemet



23

065-6001 D Street, Perris



065-8001 Mission Blvd., Rubidoux

# **Appendix I: Impacts of Solar PV Deployment Cross Sections**

Dataset: case20 RIP: ripexecute.PV Init: 0000 UTC Tue 12 Jul 05  
 Fcst: 70.00 h Valid: 2200 UTC Thu 14 Jul 05 (1500 PDT Thu 14 Jul 05)  
 Temperature at k-index = 32  
 (diff. from case=case00, time= 70.00)  
 Horizontal wind vectors at k-index = 32

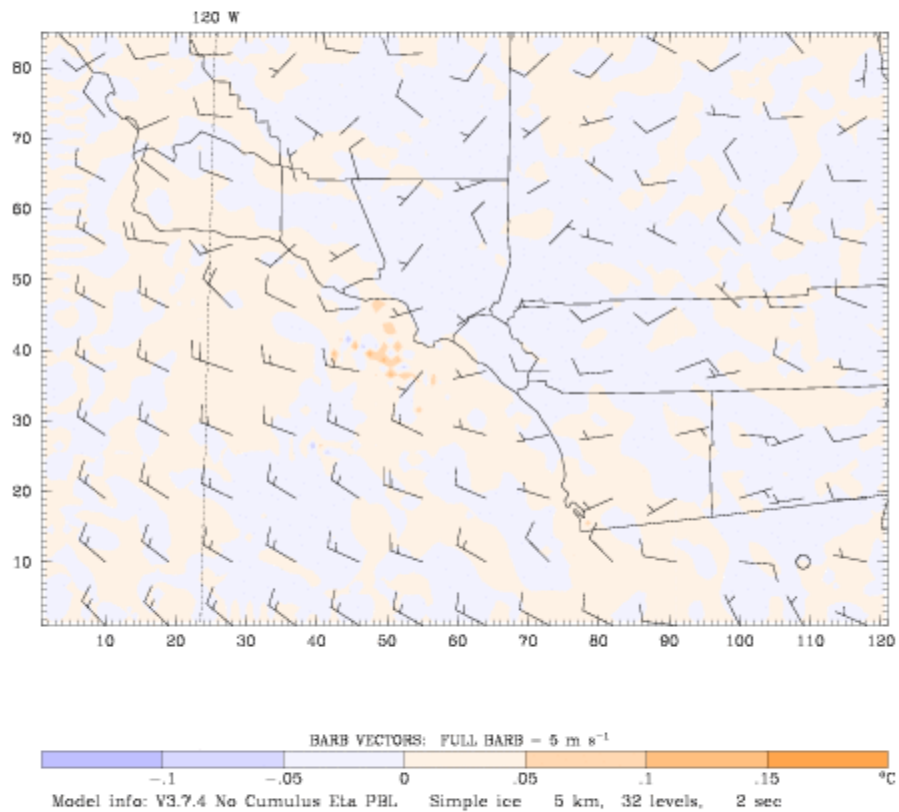


**Figure I1. Air-temperature Difference (C) for Scenario PwPV $\epsilon$ 10 Relative to PnoPV on 14 July at 1500 PDT. Wind filed for scenario PwPV $\epsilon$ 10 is overlaid.**

Dataset: case20 RIP: ripexecute.PV Init: 0000 UTC Tue 12 Jul 05  
Fcst: 70.00 h Valid: 2200 UTC Thu 14 Jul 05 (1500 PDT Thu 14 Jul 05)  
Temperature at k-index = 32  
(diff. from case=case00, time= 70.00)  
Horizontal wind vectors at k-index = 32

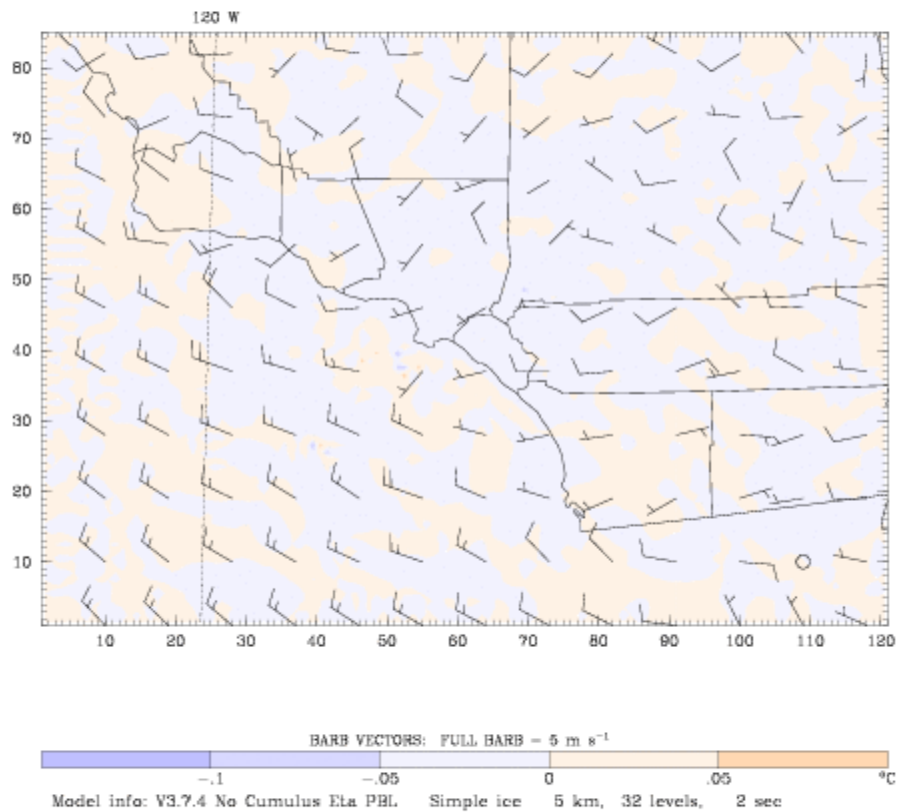
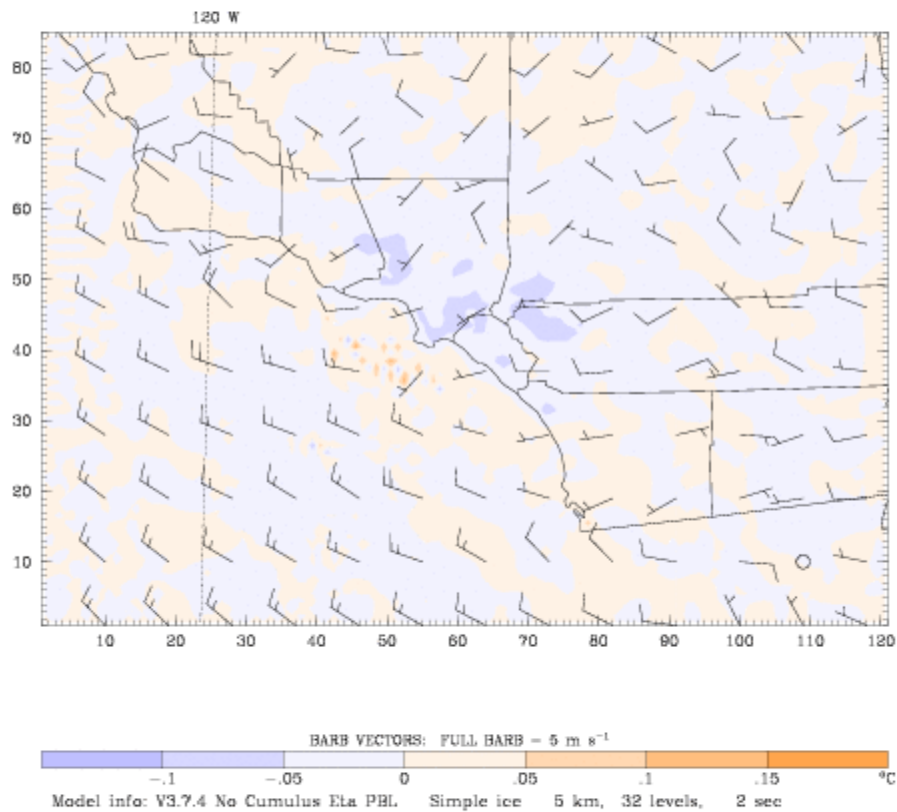


Figure I2. Air-temperature Difference (C) for Scenario PwPV<sub>ε</sub>15 Relative to PnoPV on 14 July at 1500 PDT. Wind filed for scenario PwPV<sub>ε</sub>15 is overlaid.

Dataset: case20 RIP: ripexecute.PV Init: 0000 UTC Tue 12 Jul 05  
 Fcst: 70.00 h Valid: 2200 UTC Thu 14 Jul 05 (1500 PDT Thu 14 Jul 05)  
 Temperature at k-index = 32  
 (diff. from case=case00, time= 70.00)  
 Horizontal wind vectors at k-index = 32



**Figure I3. Air-temperature Difference (C) for Scenario PwPV $\epsilon$ 20 Relative to PnoPV on 14 July at 1500 PDT. Wind filed for scenario PwPV $\epsilon$ 20 is overlaid.**

Dataset: case20 RIP: ripexecute.PV Init: 0000 UTC Tue 12 Jul 05  
 Fcst: 70.00 h Valid: 2200 UTC Thu 14 Jul 05 (1500 PDT Thu 14 Jul 05)  
 Temperature at k-index = 32  
 (diff. from case=case00, time= 70.00)  
 Horizontal wind vectors at k-index = 32

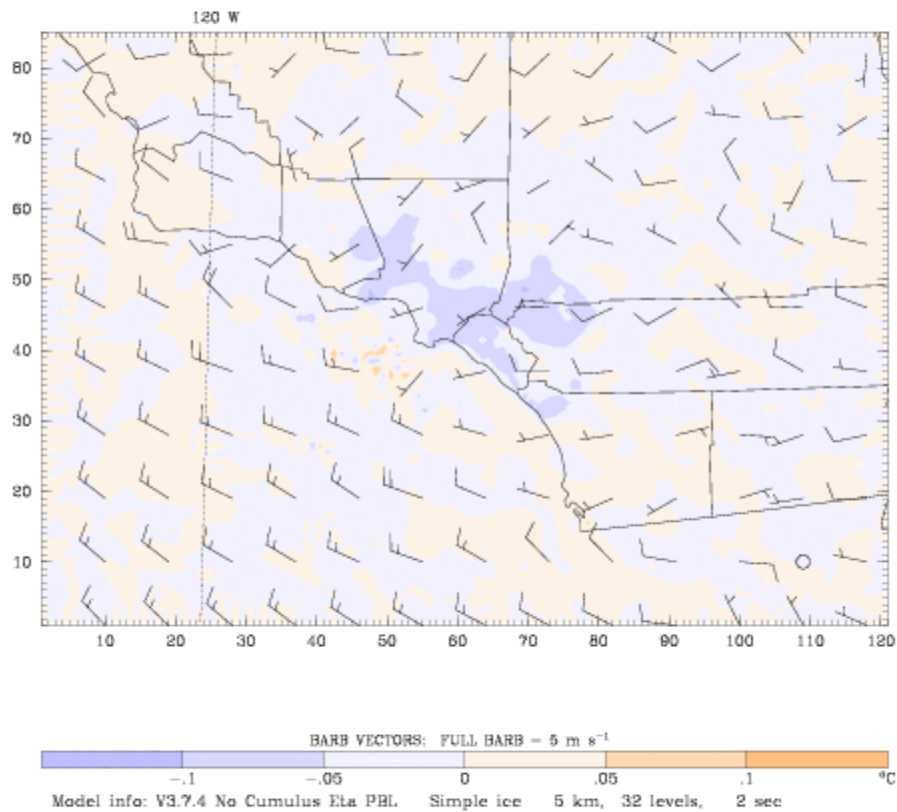


**Figure I4. Air-temperature Difference (C) for Scenario PwPV<sub>ε</sub>25 Relative to PnoPV on 14 July at 1500 PDT. Wind filed for scenario PwPV<sub>ε</sub>25 is overlaid.**

Dataset: case20 RIP: ripexecute.PV Init: 0000 UTC Tue 12 Jul 05  
 Fcst: 70.00 h Valid: 2200 UTC Thu 14 Jul 05 (1500 PDT Thu 14 Jul 05)  
 Temperature at k-index = 32  
 (diff. from case=case00, time= 70.00)  
 Horizontal wind vectors at k-index = 32

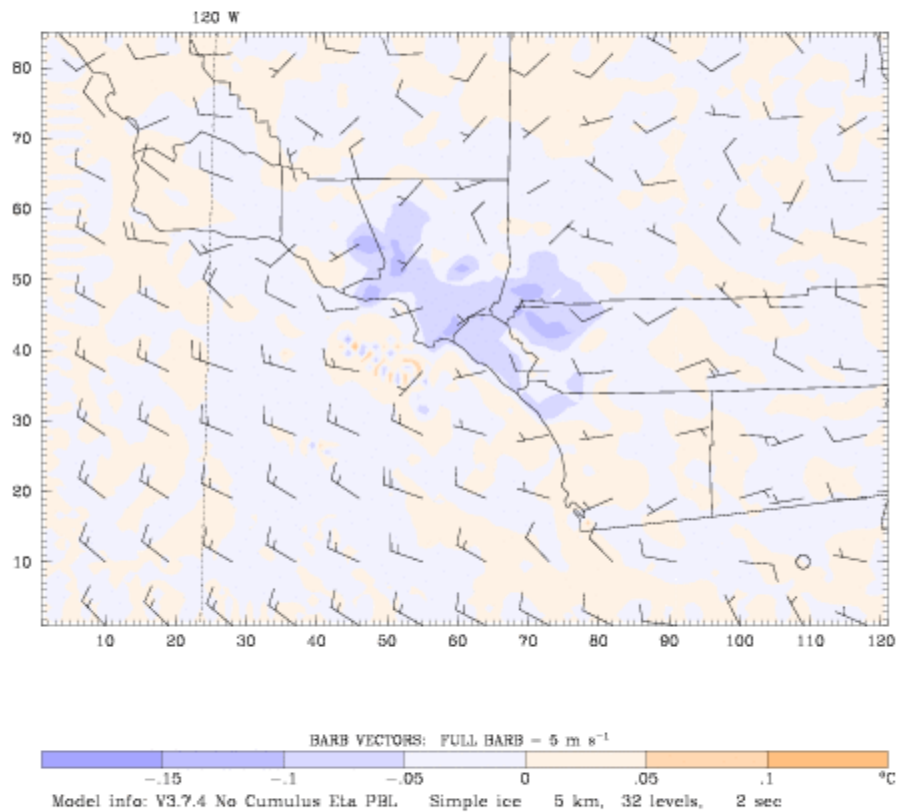


**Figure I5. Air-temperature Difference (C) for Scenario PwPV $\epsilon$ 30 Relative to PnoPV on 14 July at 1500 PDT. Wind filed for scenario PwPV $\epsilon$ 30 is overlaid.**

Dataset: case20 RIP: ripexecute.PV Init: 0000 UTC Tue 12 Jul 05  
 Fcst: 70.00 h Valid: 2200 UTC Thu 14 Jul 05 (1500 PDT Thu 14 Jul 05)  
 Temperature at k-index = 32  
 (diff. from case=case00, time= 70.00)  
 Horizontal wind vectors at k-index = 32

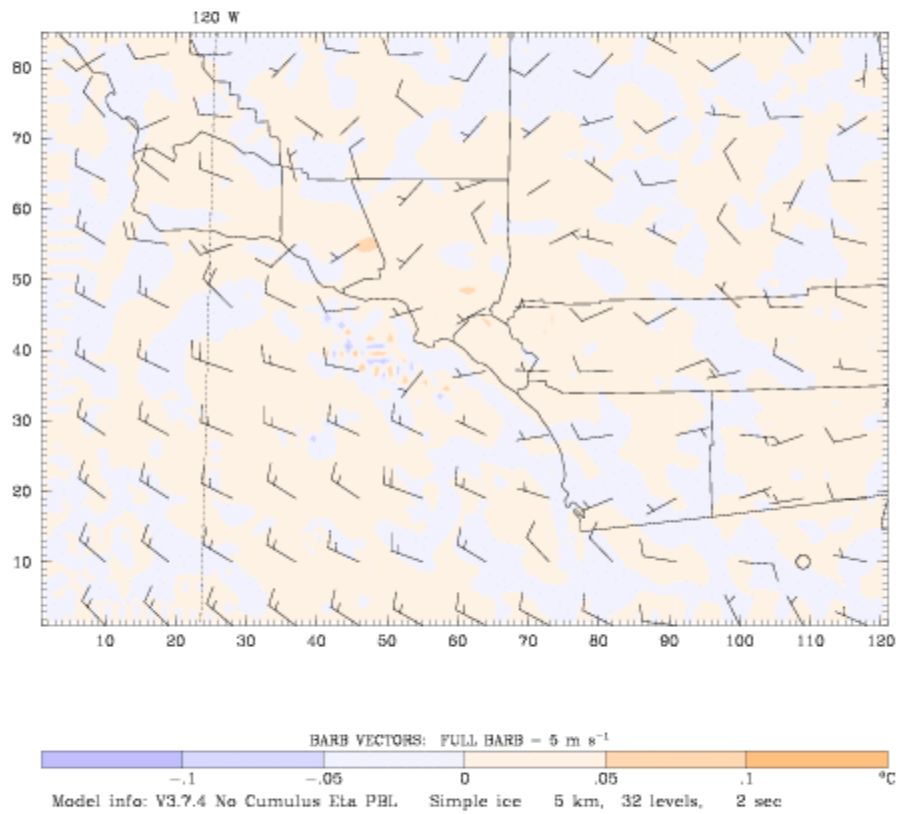


**Figure I6. Air-temperature Difference (C) for Scenario FwPV<sub>ε</sub>10 Relative to FnoPV on 14 July at 1500 PDT. Wind filed for scenario FwPV<sub>ε</sub>10 is overlaid.**

Dataset: case20 RIP: ripexecute.PV Init: 0000 UTC Tue 12 Jul 05  
 Fcst: 46.00 h Valid: 2200 UTC Wed 13 Jul 05 (1500 PDT Wed 13 Jul 05)  
 Temperature at k-index = 32  
 (diff. from case=case00, time= 46.00)  
 Horizontal wind vectors at k-index = 32

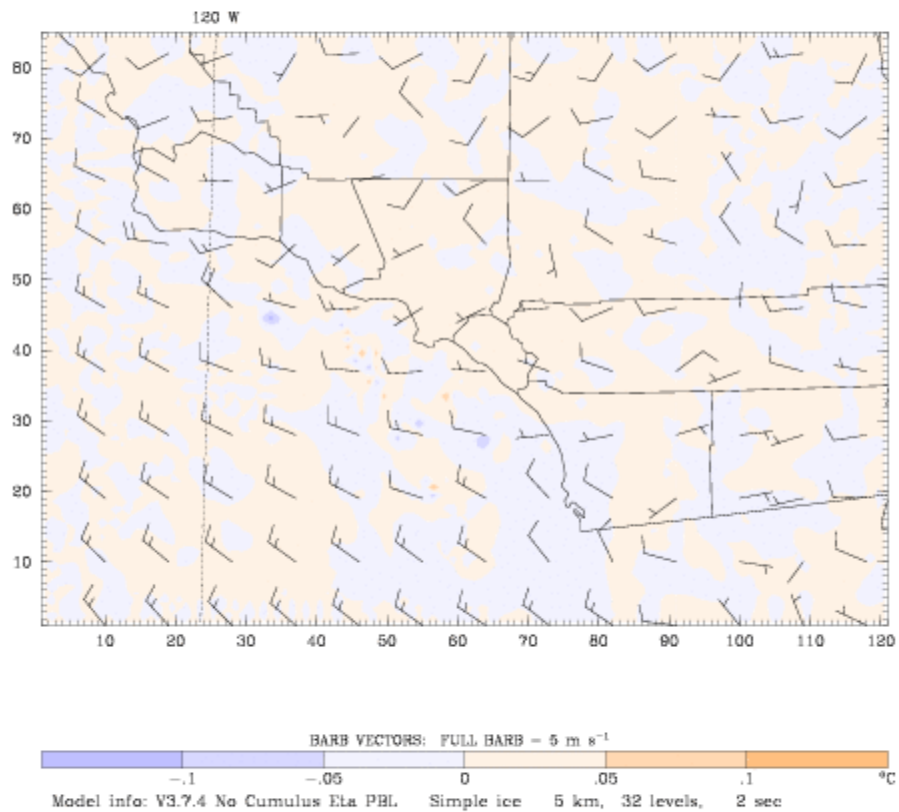


**Figure I7. Air-temperature Difference (C) for Scenario FwPV<sub>ε</sub>15 Relative to FnoPV on 14 July at 1500 PDT. Wind filed for scenario FwPV<sub>ε</sub>15 is overlaid.**

Dataset: case20 RIP: ripexecute.PV Init: 0000 UTC Tue 12 Jul 05  
 Fcst: 70.00 h Valid: 2200 UTC Thu 14 Jul 05 (1500 PDT Thu 14 Jul 05)  
 Temperature at k-index = 32  
 (diff. from case=case00, time= 70.00)  
 Horizontal wind vectors at k-index = 32

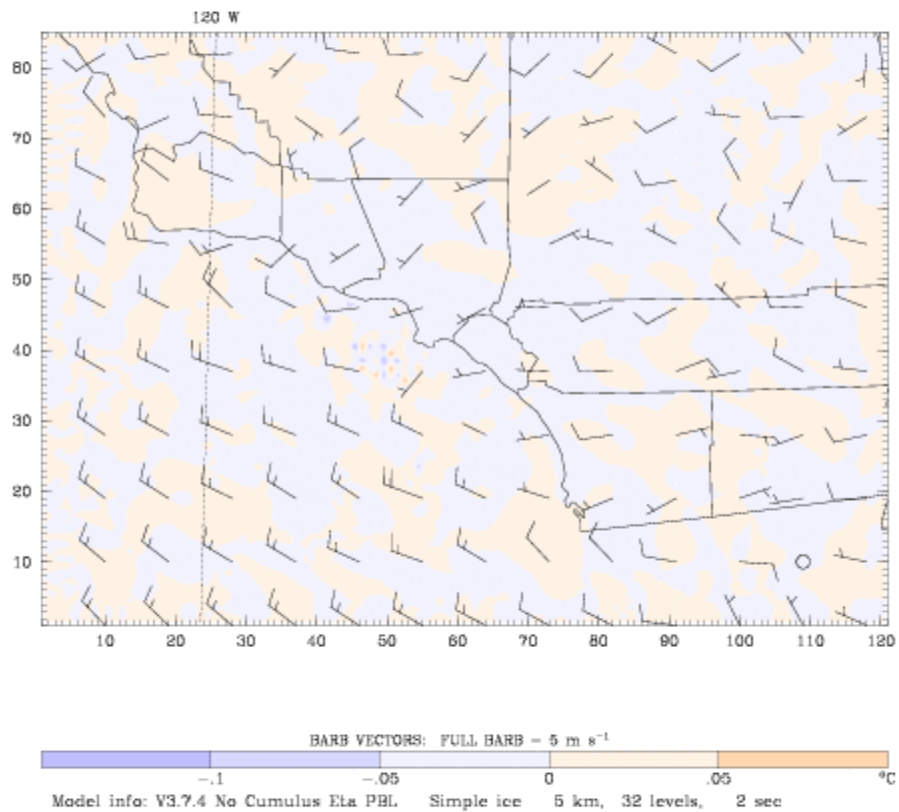


**Figure I8. Air-temperature Difference (C) for Scenario FwPVε20 Relative to FnoPV on 14 July at 1500 PDT. Wind filed for scenario FwPVε20 is overlaid.**

Dataset: case20 RIP: ripexecute.PV Init: 0000 UTC Tue 12 Jul 05  
 Fcst: 70.00 h Valid: 2200 UTC Thu 14 Jul 05 (1500 PDT Thu 14 Jul 05)  
 Temperature at k-index = 32  
 (diff. from case=case00, time= 70.00)  
 Horizontal wind vectors at k-index = 32

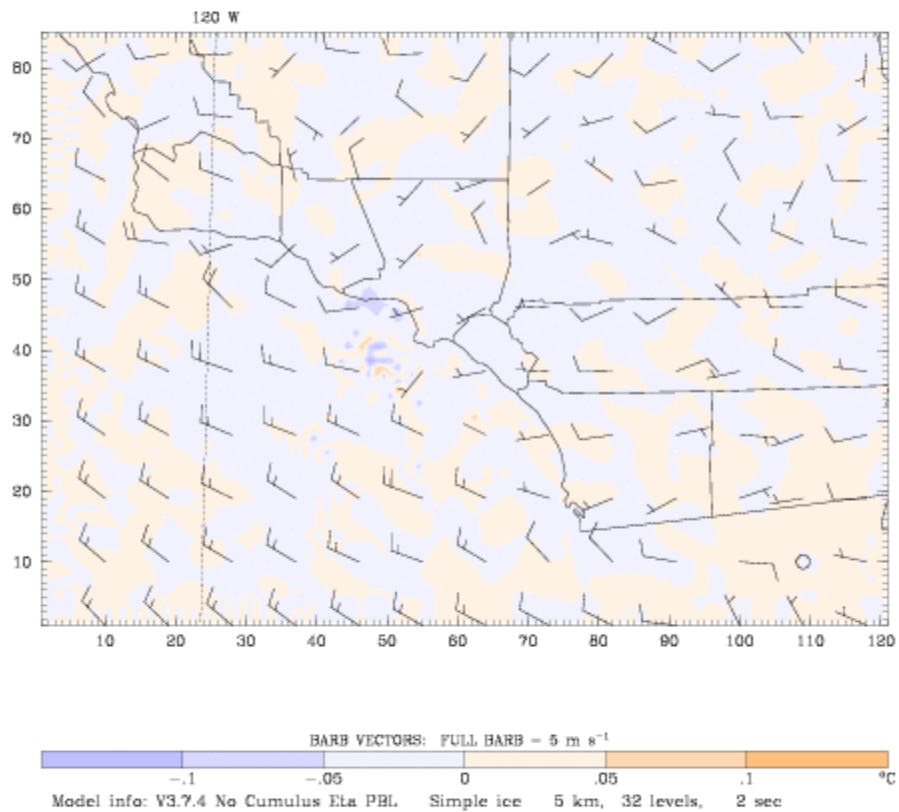


**Figure I9. Air-temperature Difference (C) for Scenario FwPVε25 Relative to FnoPV on 14 July at 1500 PDT. Wind filed for scenario FwPVε25 is overlaid.**

Dataset: case20 RIP: ripexecute.PV Init: 0000 UTC Tue 12 Jul 05  
Fcst: 70.00 h Valid: 2200 UTC Thu 14 Jul 05 (1500 PDT Thu 14 Jul 05)  
Temperature at k-index = 32  
(diff. from case=case00, time= 70.00)  
Horizontal wind vectors at k-index = 32

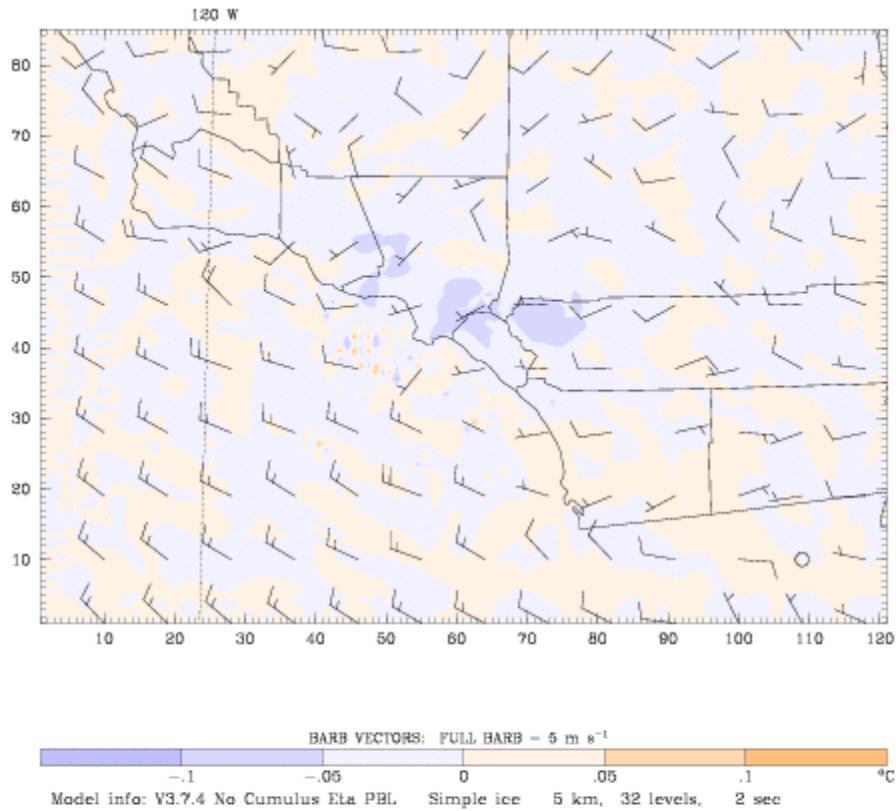


Figure I10. Air-temperature Difference (C) for Scenario FwPV<sub>ε</sub>30 Relative to FnoPV on 14 July at 1500 PDT. Wind filed for scenario FwPV<sub>ε</sub>30 is overlaid.

Dataset: case20 RIP: ripexecute.PV Init: 0000 UTC Tue 12 Jul 05  
Fcst: 70.00 h Valid: 2200 UTC Thu 14 Jul 05 (1500 PDT Thu 14 Jul 05)  
Temperature at k-index = 32  
(diff. from case=case00, time= 70.00)  
Horizontal wind vectors at k-index = 32

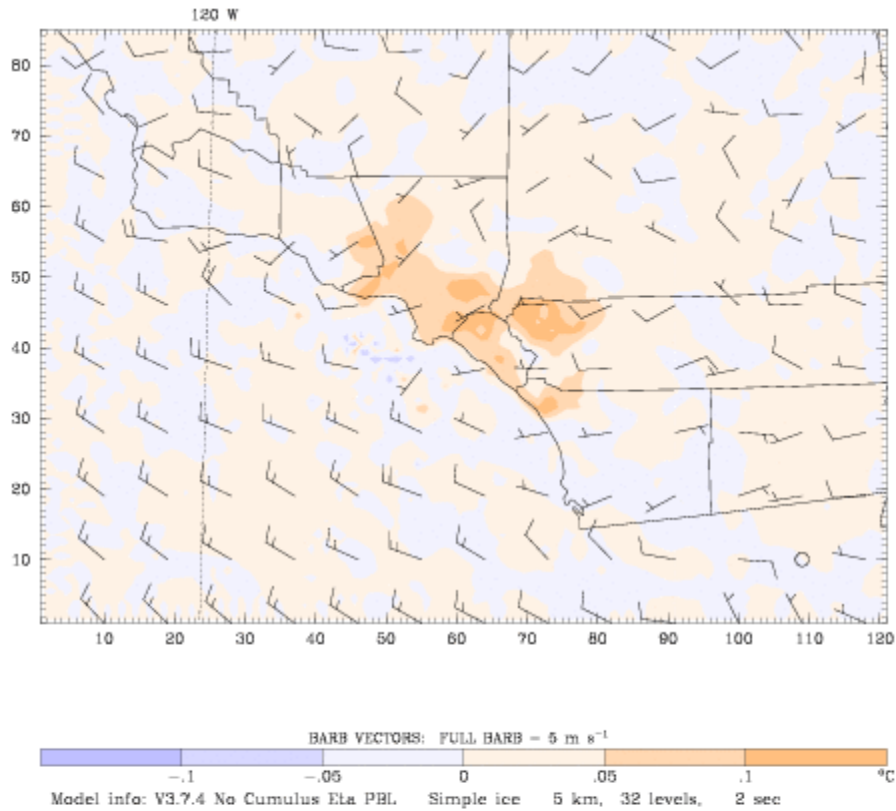
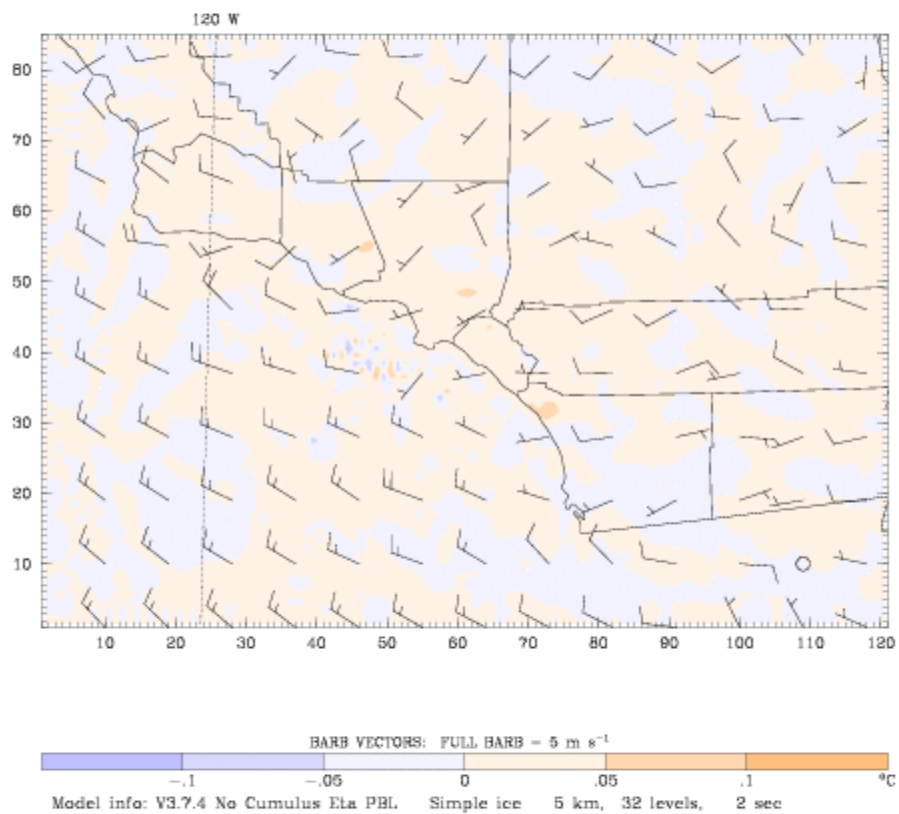


Figure I11. Air-temperature Difference (C) for Scenario FwPVxε10 Relative to FnoPV on 14 July at 1500 PDT. Wind filed for scenario FwPVxε10 is overlaid.

Dataset: case20 RIP: ripexecute.PV Init: 0000 UTC Tue 12 Jul 05  
 Fcst: 70.00 h Valid: 2200 UTC Thu 14 Jul 05 (1500 PDT Thu 14 Jul 05)  
 Temperature at k-index = 32  
 (diff. from case=case00, time= 70.00)  
 Horizontal wind vectors at k-index = 32



**Figure I12. Air-temperature Difference (C) for Scenario FwPVxε15 Relative to FnoPV on 14 July at 1500 PDT. Wind filed for scenario FwPVxε15 is overlaid.**

Dataset: case20 RIP: ripexecute.PV Init: 0000 UTC Tue 12 Jul 05  
 Fcst: 70.00 h Valid: 2200 UTC Thu 14 Jul 05 (1500 PDT Thu 14 Jul 05)  
 Temperature at k-index = 32  
 (diff. from case=case00, time= 70.00)  
 Horizontal wind vectors at k-index = 32

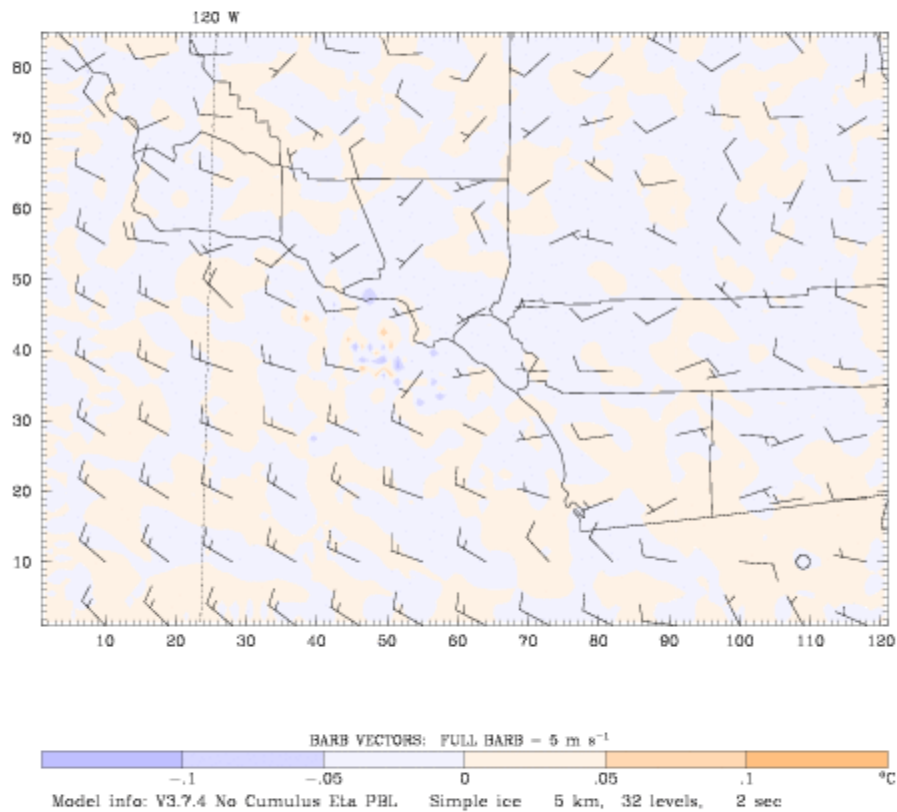


**Figure I13. Air-temperature Difference (C) for Scenario FwPVx20 Relative to FnoPV on 14 July at 1500 PDT. Wind filed for scenario FwPVx20 is overlaid.**

Dataset: case20 RIP: ripexecute.PV Init: 0000 UTC Tue 12 Jul 05  
 Fcst: 70.00 h Valid: 2200 UTC Thu 14 Jul 05 (1500 PDT Thu 14 Jul 05)  
 Temperature at k-index = 32  
 (diff. from case=case00, time= 70.00)  
 Horizontal wind vectors at k-index = 32

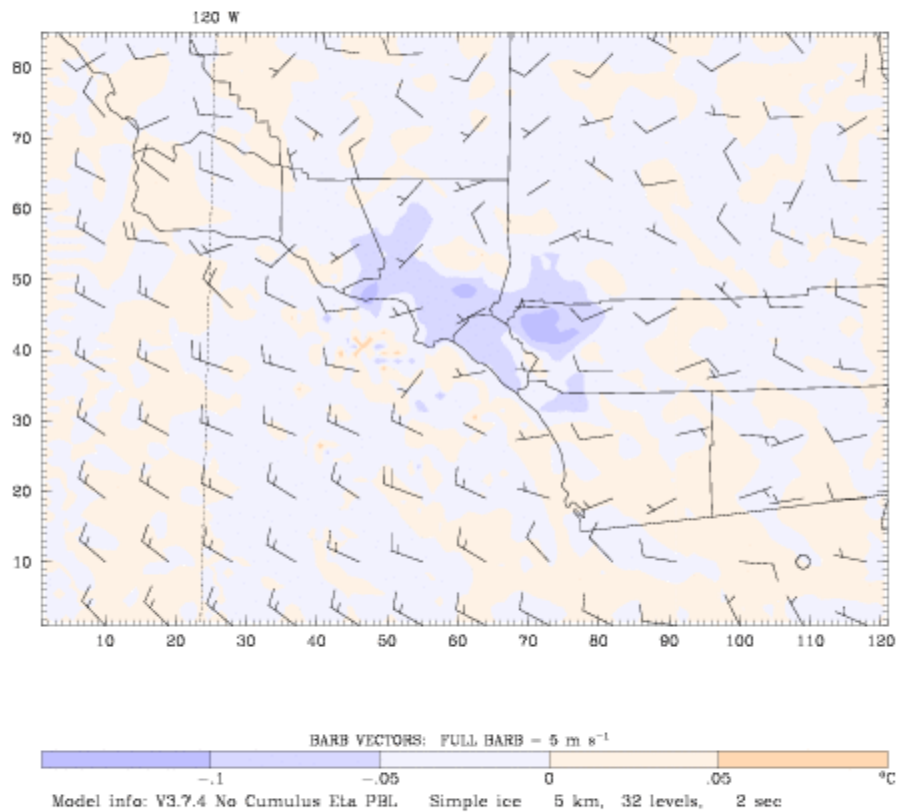


**Figure I14. Air-temperature Difference (C) for Scenario FwPVxε25 Relative to FnoPV on 14 July at 1500 PDT. Wind filed for scenario FwPVxε25 is overlaid.**

Dataset: case20 RIP: ripexecute.PV Init: 0000 UTC Tue 12 Jul 05  
 Fcst: 70.00 h Valid: 2200 UTC Thu 14 Jul 05 (1500 PDT Thu 14 Jul 05)  
 Temperature at k-index = 32  
 (diff. from case=case00, time= 70.00)  
 Horizontal wind vectors at k-index = 32

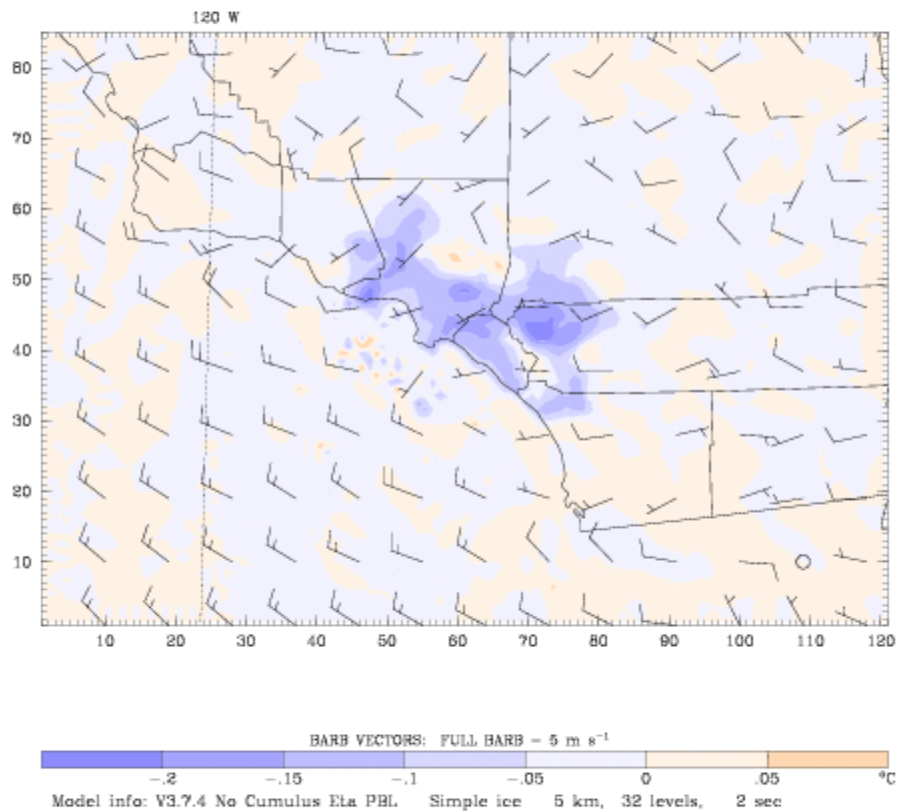


**Figure I15. Air-temperature Difference (C) for Scenario FwPVxε30 Relative to FnoPV on 14 July at 1500 PDT. Wind filed for scenario FwPVxε30 is overlaid.**

Dataset: case20 RIP: ripexecute.PV Init: 0000 UTC Tue 12 Jul 05  
 Fcst: 70.00 h Valid: 2200 UTC Thu 14 Jul 05 (1500 PDT Thu 14 Jul 05)  
 Temperature at k-index = 32  
 (diff. from case=case00, time= 70.00)  
 Horizontal wind vectors at k-index = 32

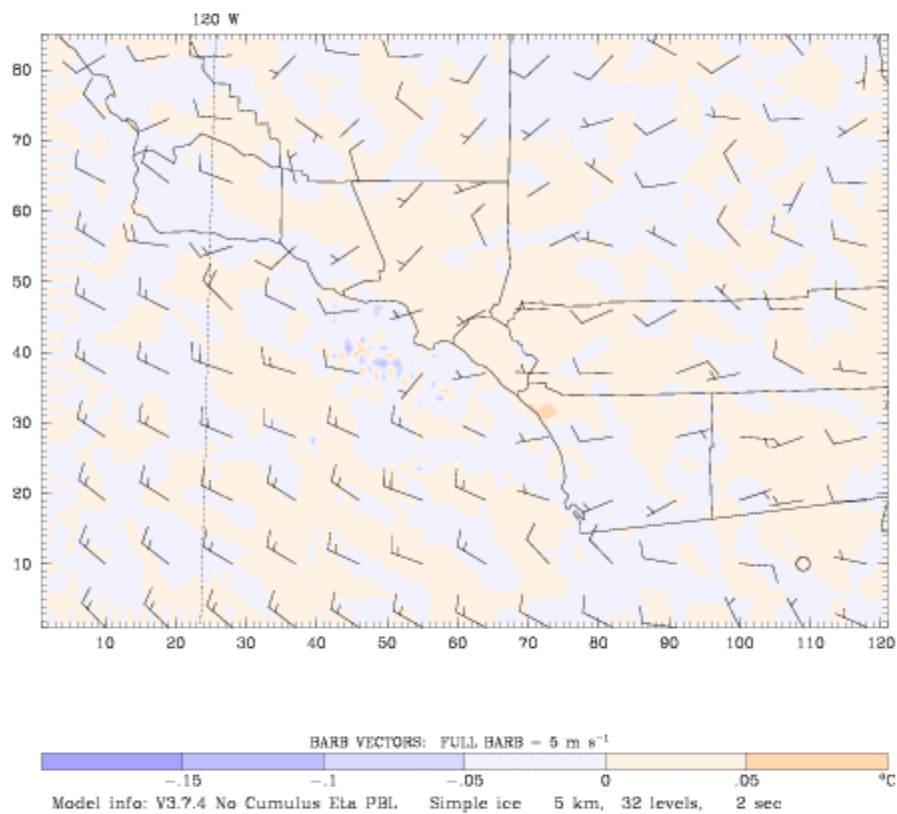


**Figure I16. Air-temperature Difference (C) for Scenario FwPVxε10A Relative to FnoPV on 14 July at 1500 PDT. Wind filed for scenario FwPVxε10A is overlaid.**